NanoScience and Technology

Seizo Morita
Franz J. Giessibl
Ernst Meyer
Roland Wiesendanger *Editors*

Noncontact Atomic Force Microscopy

Volume 3

Springer

NanoScience and Technology

Series editors

Phaedon Avouris, Yorktown Heights, USA
Bharat Bhushan, Columbus, USA
Dieter Bimberg, Berlin, Germany
Klaus von Klitzing, Stuttgart, Germany
Roland Wiesendanger, Hamburg, Germany

The series NanoScience and Technology is focused on the fascinating nano-world, mesoscopic physics, analysis with atomic resolution, nano and quantum-effect devices, nanomechanics and atomic-scale processes. All the basic aspects and technology-oriented developments in this emerging discipline are covered by comprehensive and timely books. The series constitutes a survey of the relevant special topics, which are presented by leading experts in the field. These books will appeal to researchers, engineers, and advanced students.

More information about this series at http://www.springer.com/series/3705

Seizo Morita · Franz J. Giessibl
Ernst Meyer · Roland Wiesendanger
Editors

Noncontact Atomic Force Microscopy

Volume 3

Springer

Editors
Seizo Morita
Nanoscience and Nanotechnology Center,
Institute of Scientific and Industrial
Research
Osaka University
Osaka, Ibaraki
Japan

Franz J. Giessibl
Institute of Experimental and Applied
Physics
University of Regensburg
Regensburg
Germany

Ernst Meyer
Department of Physics
University of Basel
Basel
Switzerland

Roland Wiesendanger
ERC Advanced Research Group
"FURORE"
University of Hamburg
Hamburg
Germany

ISSN 1434-4904 ISSN 2197-7127 (electronic)
NanoScience and Technology
ISBN 978-3-319-15587-6 ISBN 978-3-319-15588-3 (eBook)
DOI 10.1007/978-3-319-15588-3

Library of Congress Control Number: 2015936380

Springer Cham Heidelberg New York Dordrecht London
© Springer International Publishing Switzerland 2015
This work is subject to copyright. All rights are reserved by the Publisher, whether the whole or part of the material is concerned, specifically the rights of translation, reprinting, reuse of illustrations, recitation, broadcasting, reproduction on microfilms or in any other physical way, and transmission or information storage and retrieval, electronic adaptation, computer software, or by similar or dissimilar methodology now known or hereafter developed.
The use of general descriptive names, registered names, trademarks, service marks, etc. in this publication does not imply, even in the absence of a specific statement, that such names are exempt from the relevant protective laws and regulations and therefore free for general use.
The publisher, the authors and the editors are safe to assume that the advice and information in this book are believed to be true and accurate at the date of publication. Neither the publisher nor the authors or the editors give a warranty, express or implied, with respect to the material contained herein or for any errors or omissions that may have been made.

Printed on acid-free paper

Springer International Publishing AG Switzerland is part of Springer Science+Business Media (www.springer.com)

Preface

Atomic force microscopy (AFM) was invented in 1985 by G. Binnig, C.F. Quate, and Ch. Gerber. Since then it has successfully achieved many outstanding results on micro-/nanoscales and even on atomic/molecular scales by simple contact measurements, although contact AFM cannot achieve atomic resolution in a stable manner. In 1994 F.J. Giessibl succeeded in obtaining an atomically resolved AFM (noncontact [NC]-AFM) image of the Si(111)-(7 × 7) surface under a weak attractive tip–sample interaction in UHV at room temperature (RT) by utilizing a frequency modulation (FM) detection method. Soon the NC-AFM successfully accomplished atomically resolved imaging on various surfaces.

In 2002 "Noncontact Atomic Force Microscopy" (NC-AFM Volume 1) edited by S. Morita, R. Wiesendanger and E. Meyer was published from Springer, which introduced the principles of NC-AFM and remarkable progress achieved by NC-AFM such as true atomic resolution and observation of insulators with atomic resolution. Then in 2009 NC-AFM Volume 2 edited by S. Morita, F.J. Giessibl, and R. Wiesendanger was published by Springer, which introduced achievement of three-dimensional (3D) measurements (mapping) of atomic forces, mechanical manipulation of individual atoms, and atom-by-atom mechanical assembly such as construction of embedded atom letters at RT. One of the most surprising unexpected progresses was atomic/submolecular resolution imaging even in liquids. Since then the NC-AFM has developed further. This book deals with the outstanding progresses and applications obtained after the publication of NC-AFM Volume 2.

At first, in Chap. 1, S. Morita briefly introduces the history, present status, and remarkable technical progresses. Then, in Chap. 2, M.Z. Baykara and U. Schwarz highlight the present status and future prospects of 3D force field spectroscopy. In this NC-AFM Volume 3, many groups utilize 3D or multidimensional force field spectroscopy including current. In Chap. 3, P. Hapala et al. discuss the history and recent progress of simultaneous AFM/STM measurements with atomic resolution.

In Chap. 4, Y. Sugimoto et al. explain a novel atom manipulation using internanospace transfer to assemble various atom clusters composed of a defined number of atoms confined in nanospace at RT. In Chap. 11, R. Pawlak et al. report

on the various manipulation modes of a molecule such as the rotation of the dicyanophenyl end group, vertical manipulation of long molecular chains, and lateral manipulation of single porphyrin at low temperature (LT). In Chap. 5, A.J. Weymouth and F.J. Giessibl introduce the phantom force induced by the potential difference within the sample that reduces the potential drop in the junction. Hence it causes a decrease in the electrostatic attraction between tip and sample. If the resistance within the sample is high enough, the phantom force can be dominant. In Chap. 6, M. Kisiel et al. report on mechanisms of energy loss under noncontact friction condition different from the most common Joule dissipation.

In Chap. 7, A. Schwarz and S. Heinze report that magnetic exchange force spectroscopy has possibilities to compare the data quantitatively with first principles electronic structure calculations and to open a new route to induce magnetization reversal events. In Chap. 8, M. Ashino and R. Wiesendanger review damping force spectroscopy and show its possibility to reveal subsurface vibrational modes.

In Chap. 9, F. Kling et al. introduce self-assembly of organic molecules on insulating surfaces with special emphasis on structures stable at RT. Chapters 10–12 introduce atomic-scale contrast in AFM images on molecular systems by Pauli repulsive force at LT. In Chap. 10, F. Schulz et al. discuss the factors influencing the atomic scale imaging of graphene nanoribbon, the graphene moiré on Ir(111), and BPPA molecules. In Chap. 11, R. Pawlak et al. report 3D-force field of C_{60}, a single porphyrin, and LCPD mapping of metal-phtalocyanin on thin insulating films at LT. In Chap. 12, B. Schuler et al. review the contrast mechanism of atomic resolution on molecules with functionalized tips and compare different tip functionalizations. In Chap. 3, P. Hapala et al. discuss high-resolution Pauli repulsive force, scanning tunneling hydrogen microscope (STHM), and IETS-STM images of molecular systems with functionalized tips. In Chap. 14, R. Temirov and S. Tautz explain the mechanism of STM with single molecule force sensors.

In Chap. 13, S. Jarvis et al. discuss a prototype of a mechanically-actuated atomic switch: the flipping of bistable dimers on the Si(100)-c(4 × 2) active surface, and compare it with H:Si(100) passivated and chemically inert surface. In Chap. 15, C. Barth discusses the identification of surface ions on the nanostructured (001) Suzuki surface of Mg^{2+} and Cd^{2+} doped NaCl single crystals. In Chap. 16, M. Heyde et al. report on the atomic structure of two-dimensional (2D) vitreous silica simultaneously obtained by AFM/STM. In Chap. 17, D. Gao et al. describe how one can produce, control, and characterize sharp metal coated tips and how these tips can achieve atomic resolution on insulating bulk surfaces.

In Chap. 18, B. Reischl et al. simulate solid–liquid interfaces in model AFM systems. In Chap. 19, K. Kobayashi and H. Yamada review recent progress in FM-AFM in liquids based on 2D/3D force mapping, and visualize molecular-scale hydration structures as well as that of local electric double layer forces. In Chap. 20, T. Fukuma reports on advanced instrumentation of FM-AFM using a small cantilever and high-speed phase detector to enable direct visualization of atomic-scale interfacial phenomena at 1 frame/sec. In Chap. 21, Y. Yokota and K. Fukui report on electrochemical issues, especially potential-dependent interface structures of adsorbates and electrolyte solutions. In Chap. 22, T. Uchihashi et al. review

high-speed AFM that can capture protein molecules in action at submolecular spatial and sub-100 ms temporal resolution, without disturbing their biological function. They demonstrate various observations of dynamic events on proteins.

We thank all the authors for their contributions to this book. We also thank Springer for their fruitful collaborations. It is hoped that this book will accelerate this field toward rapid and continuing growth and that it will stimulate further efforts to develop atomic/molecular tools based on mechanical methods.

Osaka, Japan — Seizo Morita
Regensburg, Germany — Franz J. Giessibl
Basel, Switzerland — Ernst Meyer
Hamburg, Germany — Roland Wiesendanger

Contents

Contributors

Masayuki Abe Graduate School of Engineering Science, Center for Science and Technology Under Extreme Conditions, Osaka University, Toyonaka, Osaka, Japan

Toshio Ando Department of Physics, Institute of Science and Engineering, Kanazawa University, Kanazawa, Japan; Bio-AFM Frontier Research Center, Institute of Science and Engineering, Kanazawa University, Kanazawa, Japan; CREST, Japan Science and Technology Agency, Kawaguchi, Japan

Makoto Ashino Kanazawa Institute of Technology, Kanazawa, Japan

Clemens Barth Aix-Marseille Université, CNRS, CINaM UMR 7325, Marseille, France

Mehmet Z. Baykara Department of Mechanical Engineering and UNAM-Institute of Materials Science and Nanotechnology, Bilkent University, Ankara, Turkey

Ralf Bechstein Johannes Gutenberg Universität, Mainz, Germany

Christin Büchner Fritz-Haber-Institute of the Max-Planck-Society, Berlin, Germany

Filippo Federici Canova WPI-AIMR Tohoku University, Sendai, Japan

Adam Foster Department of Applied Physics, COMP Centre of Excellence, Aalto University School of Science, Helsinki, Finland

Hans-Joachim Freund Fritz-Haber-Institute of the Max-Planck-Society, Berlin, Germany

Ken-ichi Fukui Division of Chemistry, Department of Materials Engineering Science, Graduate School of Engineering Science, Osaka University, Osaka, Japan

Takeshi Fukuma Division of Electrical Engineering and Computer Science, Kanazawa University, Kanazawa, Japan

David Z. Gao Department of Physics and Astronomy, University College London, London, UK

Franz J. Giessibl University of Regensburg, Regensburg, Germany

Thilo Glatzel Department of Physics, University of Basel, Basel, Switzerland

Leo Gross IBM Research—Zurich, Rüschlikon, Switzerland

Urs Gysin Department of Physics, Univeristy of Basel, Basel, Switzerland

P. Hapala Institute of Physics, Academy of Sciences of the Czech Republic, Prague, Czech Republic

Stefan Heinze Institute of Theoretical Physics and Astrophysics, University of Kiel, Kiel, Germany

Markus Heyde Fritz-Haber-Institute of the Max-Planck-Society, Berlin, Germany

Sampsa Hämäläinen Department of Applied Physics, Aalto University School of Science, Aalto, Finland

Samuel Paul Jarvis School of Physics and Astronomy, University of Nottingham, Nottingham, UK

P. Jelínek Institute of Physics, Academy of Sciences of the Czech Republic, Prague, Czech Republic

Shigeki Kawai Department of Physics, University of Basel, Basel, Switzerland

Marcin Kisiel Department of Physics, Univeristy of Basel, Basel, Switzerland

Felix Kling Johannes Gutenberg Universität, Mainz, Germany

Kei Kobayashi The Hakubi Center for Advanced Research, Kyoto University, Kyoto, Japan

Noriyuki Kodera Bio-AFM Frontier Research Center, Institute of Science and Engineering, Kanazawa University, Kanazawa, Japan; PRESTO, Japan Science and Technology Agency, Kawaguchi, Japan

Angelika Kühnle Johannes Gutenberg Universität, Mainz, Germany

Leonid Lichtenstein Fritz-Haber-Institute of the Max-Planck-Society, Berlin, Germany

Peter Liljeroth Department of Applied Physics, Aalto University School of Science, Aalto, Finland

Ernst Meyer Department of Physics, University of Basel, Basel, Switzerland

Gerhard Meyer IBM Research—Zurich, Rüschlikon, Switzerland

Fabian Mohn IBM Research—Zurich, Rüschlikon, SwitzerlandABB Corporate Research, Baden-Dättwil, Switzerland

Nikolaj Moll IBM Research—Zurich, Rüschlikon, Switzerland

Philip Moriarty School of Physics and Astronomy, University of Nottingham, Nottingham, UK

Seizo Morita Nanoscience and Nanotechnology Center, The Institute of Scientific and Industrial Research, Osaka University, Ibaraki, Osaka, Japan

M. Ondráček Institute of Physics, Academy of Sciences of the Czech Republic, Prague, Czech Republic

Rémy Pawlak Department of Physics, University of Basel, Basel, Switzerland

Philipp Rahe School of Physics and Astronomy, The University of Nottingham, Nottingham, UK

Bernard Reischl Department of Applied Physics, COMP Centre of Excellence, Aalto University School of Science, Helsinki, Finland

Jascha Repp Institute of Experimental and Applied Physics, University of Regenburg, Regensburg, Germany

Markus Samadashvili Department of Physics, Univeristy of Basel, Basel, Switzerland

Bruno Schuler IBM Research—Zurich, Rüschlikon, Switzerland

Fabian Schulz Department of Applied Physics, Aalto University School of Science, Aalto, Finland

Alexander Schwarz Institute of Applied Physics and Microstructure Research Center, University of Hamburg, Hamburg, Germany

Udo D. Schwarz Department of Mechanical Engineering and Materials Science, Yale University, New Haven, USA; Department of Chemical and Environmental Engineering, Yale University, New Haven, USA; Center for Research on Interface Structures and Phenomena (CRISP), Yale University, New Haven, USA

Alexander L. Shluger Department of Physics and Astronomy, University College London, London, UK

Peter Spijker Department of Applied Physics, COMP Centre of Excellence, Aalto University School of Science, Helsinki, Finland

O. Stetsovych Institute of Physics, Academy of Sciences of the Czech Republic, Prague, Czech Republic

Yoshiaki Sugimoto Department of Electrical, Electronic and Information Engineering, Graduate School of Engineering, Osaka University, Suita, Japan

M. Švec Institute of Physics, Academy of Sciences of the Czech Republic, Prague, Czech Republic

Adam Sweetman School of Physics and Astronomy, University of Nottingham, Nottingham, UK

F.S. Tautz Jülich Aachen Research Alliance (JARA)—Fundamentals of Future Information Technology, Jülich, Germany

R. Temirov Peter Grünberg Institut (PGI-3), Jülich, Germany

Takayuki Uchihashi Department of Physics, Institute of Science and Engineering, Kanazawa University, Kanazawa, Japan; Bio-AFM Frontier Research Center, Institute of Science and Engineering, Kanazawa University, Kanazawa, Japan; CREST, Japan Science and Technology Agency, Kawaguchi, Japan

Matt Watkins Department of Physics and Astronomy, London Centre for Nanotechnology, University College London, London, UK

Alfred John Weymouth University of Regensburg, Regensburg, Germany

Roland Wiesendanger Interdisciplinary Nanoscience Center Hamburg (INCH), University of Hamburg, Hamburg, Germany

Hirofumi Yamada Department of Electronic Science and Engineering, Kyoto University, Kyoto, Japan

Yasuyuki Yokota Division of Chemistry, Department of Materials Engineering Science, Graduate School of Engineering Science, Osaka University, Osaka, Japan

Chapter 1
Introduction

Seizo Morita

Abstract Since the publication of *Noncontact Atomic Force Microscopy Vol*. 2 in 2009, the noncontact atomic force microscope (NC-AFM), which can image even insulators with atomic resolution, has achieved remarkable technical progress especially on (a) *Tip Modification*, (b) *Control of Atomic Force*, and (c) *qPlus Sensor/Quartz Tuning Fork*. This third volume deals with the following outstanding progress obtained with atomic resolution after the publication of the previous book: (1) *Force Spectroscopy and Force-Mapping with Atomic Resolution*, (2) *Repulsive Force Imaging*, (3) *AFM/STM combined measurements*, (4) *Atomic/Molecular Manipulation*, (5) *Atomic/Submolecular Imaging in Liquids*. These results and technologies are varying the NC-AFM with imaging function on an atomic scale toward characterization and manipulation tools of individual atoms/molecules and nanostructures with atomic/subatomic resolution noticeably. Therefore, the NC-AFM is becoming a crucial tool for nanoscience and nanotechnology much more.

1.1 Rapidly Developing High Performance AFM

In the former NC-AFM book (Vol. 1) published in 2002 [1], we mentioned that the atomic force microscope (AFM) is a unique microscope based on a mechanical method with the following features:

- true atomic resolution,
- observation of insulators,
- three-dimensional (3D) measurements and mapping of atomic forces,
- control of atomic forces,
- measurement of mechanical response,
- mechanical manipulation of individual atoms,
- atom-by-atom mechanical assembly.

S. Morita (✉)
Nanoscience and Nanotechnology Center, Institute of Scientific and Industrial Research (ISIR), Osaka University, Mihogaoka 8-1, Ibaraki, Osaka 567-0047, Japan
e-mail: smorita@eei.eng.osaka-u.ac.jp

© Springer International Publishing Switzerland 2015

S. Morita et al. (eds.), *Noncontact Atomic Force Microscopy*,
NanoScience and Technology, DOI 10.1007/978-3-319-15588-3_1

Then, in the previous NC-AFM book (Vol. 2) published in 2009 [2], we evaluated the achievement on the above potential abilities of NC-AFM anticipated in the Vol. 1 (2002). In the case of true atomic resolution and observation of insulators with atomic resolution, these abilities of NC-AFM were fully proved at the early stage in the Vol. 1 age (1995–2002) [1]. Concerning three-dimensional (3D) measurements and mapping of atomic forces, atomically resolved NC-AFM images were acquired only at 2∼3 limited tip-sample distance before 2002. Nonetheless, in the Vol. 2 age (2003–2009), precise 3D force-mapping with atomic resolution were reported even at room temperature (RT) on various samples. We note that such achievement has been accomplished by the precise control of tip position at the atomic/subatomic scale and also of tip-surface interaction forces at piconewton level. Regard to precise control of tip-sample distance, however, was incomplete before 2002 [1], as a result, measurement of mechanical response and mechanical manipulation of individual atoms were described only a little bit in Vol. 1. Nevertheless, in the Vol. 2 age (2003–2009), precise controls of both tip position and atomic forces were achieved. As a result, not only measurement of mechanical response but also mechanical manipulation of individual atoms was accomplished even at RT as introduced in the Vol. 2. It should be noted that feed-back [3] and feed-forward [4] techniques using the atom-tracking method are indispensable to suppress the thermal drift and to achieve quasi drift-free measurements at RT similar to that at liquid He temperature. For atom-by-atom mechanical assembly, that is, construction of nanostructures by mechanical atom manipulation with AFM, it was a dream yet in the AFM field around the Vol. 1 age. However, in the Vol. 2 age (2003–2009), "Atom Inlay", that is, the embedded atom letters consisted of two atom species was successfully constructed even at RT using AFM as introduced in the Vol. 2.

Thus, in 2009, we accredited that all above special features inspired in the Vol. 1 are fulfilled by AFM as introduced in the Vol. 2 [2]. The performance of NC-AFM functions anticipated in the Vol. 1 (2002), however, has advanced further by accomplishing remarkable technical progress especially on (a) *Tip Modification*, (b) *Control of Atomic Force*, and (c) *qPlus Sensor/Quartz Tuning Fork* after 2009.

1.1.1 Tip Modification

Now, at liquid He temperature, it is possible to fabricate various defined functionalized AFM tips by picking up single atom/molecule from the sample surface [5] similar to the STM tips [6], which include Cu, Au, Ag, Xe, Cl, Br, H_2, D_2, CO, NO, CH_4, pentacene atoms/molecules [5–7]. Here not only single H_2 molecule adsorbed tips, but also Xe, D_2, CO and CH_4 tips are useful for STM force sensors to resolve the chemical structure of organic molecules by the short-range Pauli repulsion [6]. On the other side, not only single CO inert (or inactive) tips, but also Br, Cl, Xe tips are useful for AFM to resolve the chemical structure of molecules by the Pauli repulsive force [5, 7]. Recently the Br tip was found to be particularly useful for AFM

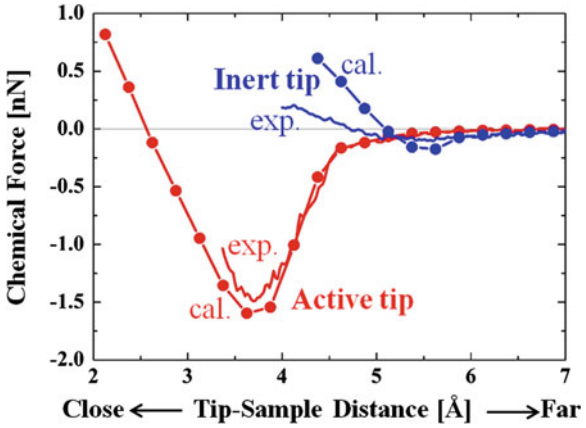

Fig. 1.1 Tip-to-sample distance curves of chemical force acquired over a Si adatom of the partly hydrogenated Si(111)-(7×7) surface with an active tip (*red*) and an inert tip (*blue*) measured at RT. DFT calculations identified the active tip as the dimer-terminated Si tip (*red circles*) and the inert tip as an oxidized Si dimer tip (*blue circles*) that bears a hydroxyl group on its apex [11]

and lateral manipulation, whereas the Xe tip excelled in STM and Kelvin probe force microscopy (KPFM) [5].

At RT defined functionalized tips are of great practical importance for nanoscience and nanotechnology to fabricate nanodevices and to investigate chemical activities. However at RT still we cannot fabricate defined functionalized AFM tips so much freely by picking up single atom/molecule from the sample surface, because of thermal desorption and/or diffusion of atom/molecules both at the tip apex and on the sample surface, except for a few special cases [8–10]. Nevertheless, even at RT, now it is possible to discover not only active (reactive) but also inert (non-reactive) AFM tips as shown in Fig. 1.1 and finally to identify tip termination in corroboration with DFT calculations performed for various tip models such as an H_3–Si(111), Si(001) dimer, hydrogen-terminated H_3–Si, hydrogen-terminated Si dimer, double-bonded O-terminated Si dimer, OH-terminated Si dimer, and double-bonded OH-terminated Si dimer tips [11].

1.1.2 Control of Atomic Force

To control atomic forces, measure mechanical response, and mechanically manipulate individual atoms, we have to carefully decrease and also precisely control the tip–sample distance by varying the tip-to-sample distance from noncontact regime toward nearcontact regime of active tip as shown in Fig. 1.2. In the noncontact regime (I) where a weak but finite attractive chemical force appears, AFM has successfully achieved atomically resolved imaging of various surfaces at the early stage in the

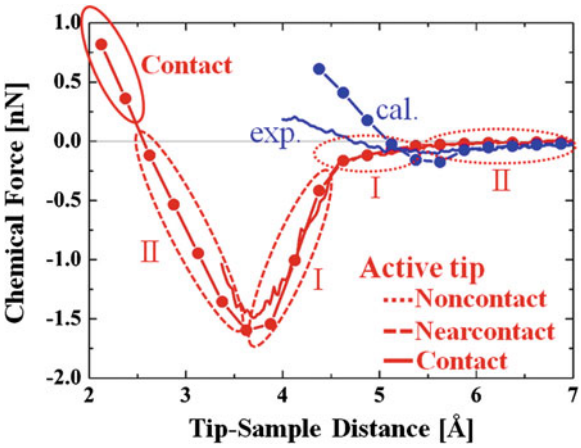

Fig. 1.2 Various regimes of chemical force curves in the case of active (reactive) tip. Those are noncontact regimes (I) and (II), nearcontact regimes (I) and (II), and contact regime

Vol. 1 age [1]. It should be noted that in these experiments clean and hence active Si tips with a relatively strong chemical forces have been used as shown in Fig. 1.2. The weak but finite attractive force enables nondestructive observations of the surface at the atomic scale. Here, deformation of the tip apex and the surface is negligibly small and the chemical potential is conservative.

Then sophisticated techniques allowing fine control over the tip–sample distance and the lateral tip position enabled AFM to achieve site-specific single atom pseudo-contact and expanded its applications to strictly controlled near-contact experiments. As shown in Fig. 1.2, the nearcontact regime includes not only the strong attractive chemical force regime (I), but also the relatively weak Pauli repulsive force regime (II), which does not significantly exceed the attractive bonding force. It should be noted that the short-range force in the two kinds of nearcontact regimes [(I) and (II)] depends oppositely on the tip–sample distance. Besides, under the nearcontact regime, the tip apex and surface atoms remarkably relax [12]. In the Vol. 1 age (1995–2002) [1] it was not easy to accurately control the closest tip-sample distance within the allowable limit of a few picometers error, needed for controlled atom manipulation using a large oscillation amplitude (typically from several nanometers up to several tens of nanometers). Now nearcontact AFM can be used not only to manipulate single atoms/molecules [13–15], but also to interchange embedded heterogeneous atoms at RT vertically and laterally, leading to atom-by-atom mechanical creation of composite nanoletters [8, 16] and nanostructures [10, 17]. Further it can be used for identification of the chemical species of intermixed semiconductor atoms using covalent bonding forces [18], imaging of individual chemical bonds using the Pauli repulsive force [7, 19, 20] and, in conjunction with STM in a combined AFM/STM system, the detection of energy gap openings due to covalent bond formation [21, 22]. Thus, the nearcontact regime is the current frontier and the rapidly growing hub of atomically resolved force microscopy.

As a consequence of precise control over both the tip–sample distance and the lateral tip position, site-specific force spectroscopy and force mapping [23] expanded to insulator surfaces [24], atom manipulation region [14] and the Pauli repulsive force region [nearcontact regime (II)] [25]. It should be noted that, in noncontact regime (II) of Fig. 1.2 where only STM can obtain atomically resolved image but not for AFM [26] because of too small attractive force, still precise site-specific force/current curves can be simultaneously obtained. As a consequence, the effects of electron energy level degeneracy on the conductance and the chemical force between two bodies at the atomic scale can be clarified [27, 28]. On the other hand, in the contact regime in Fig.1.2, the repulsive force dominates. This strong repulsive force results in uncontrolled nanoscale plastic deformation of the tip apex and sample surface.

1.1.3 Pauli Repulsive Force Imaging

During the last decade, the qPlus sensor (a kind of self-sensing cantilever based on a quartz tuning fork) has achieved remarkable progress and developed extensively in the low temperature (LT)-AFM field [1, 2]. The high stiffness of the quartz tuning fork allows stable operation at oscillation amplitudes enough small compared to the range of the short-range interaction. The thermal noise of a cantilever is roughly proportional to the square root of temperature. Consequently single pm resolution has been demonstrated at Liquid He temperature (LT) [14]. Operation in UHV at LT and low noise electrical detection of the qPlus deflection by Low Temperature amplifiers gave an opportunity to modify conventional high resolution LT-STM systems to the latest high resolution LT-AFM/STM systems immediately [14]. It should be noted that the tunneling current (STM) is sensitive to the local electron density of states close to the Fermi level, whereas the atomic force (AFM) probes the short-range chemical forces.

The qPlus and quartz tuning fork sensor LT-AFM has accomplished various outstanding results at LT. Pauli repulsive force imaging on the chemical structure of a molecule by a qPlus sensor is especially noteworthy topics and is described later. Local atomic structure imaging of a silica bilayer film grown on a Ru(0001) by a quartz tuning fork sensor is another topics that resolves the atomic arrangement in the crystalline and vitreous structures of silica. It clarified that AFM images Si atoms whereas STM reveals O atoms of silica glass [29]. It should be commented that the AFM z-corrugation during constant frequency shift imaging is roughly twice bigger on the repulsive branch [nearcontact regime (II)] than on the attractive branch [noncontact regime (I)] [30].

Pauli repulsive force measurements between the tip atom/molecule and the imaged molecule have been executed in nearcontact regime (II) and revealed the inner chemical structure of a molecule [7]. However during the tip approach, molecules will be manipulated due to a strong attractive chemical force in case of active (reactive) tips [7, 31]. Consequently, to keep away AFM tips from the strong attractive chemical force in nearcontact regime (I), inert (inactive) tips such as defined functionalized

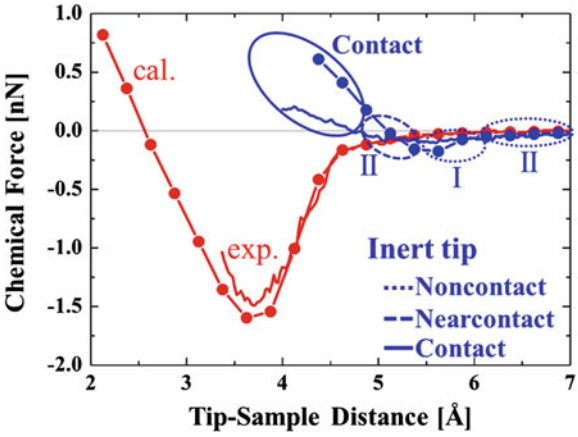

Fig. 1.3 Various regimes of chemical force curves in the case of inert (inactive) tip. Those are noncontact regimes (I) and (II), nearcontact regime (II), and contact regime. It should be noted that, in case of the ideal inert (inactive) tip, nearcontact regime (I) is missing because of a weak tip-to-sample surface interaction

CO tip [7] have been used. Ideal inert tips have no nearcontact regime (I) as shown in Fig. 1.3 [11] and hence do not induce atom/molecule manipulations [31] because of disappearance of strong attractive force. Nevertheless, by decreasing the tip-sample distance close to contact regime, AFM resulted in unstable imaging conditions. Here molecule manipulations will occur usually leading to the molecule being laterally displaced or picked up by the tip. Therefore, Pauli repulsive force imaging has been conducted just before the unstable imaging distance [7]. Recently, different tip functionalizations for AFM, STM, and KPFM of organic molecules on thin insulating films have been investigated at LT [5].

1.1.4 Atomic/Submolecular Imaging in Liquids

In the Vol.1 age (1995–2002), true atomic resolution was possible only under ultrahigh vacuum (UHV) environment. In air and liquid environments, Q-factor of mechanical resonant oscillation of cantilever drastically reduces and the small Q-factor gets disturbed to obtain atomic resolution. In 2005, by improving frequency noise in frequency modulation (FM) detection method and using small oscillation amplitude of cantilever, vertical and lateral resolutions of 2–6 and 300 pm were achieved, respectively, even with a low Q-factor in water [2, 32]. Now latest technique enables the three dimensional imaging and mapping of the hydration layers and forces on mica and protein GroEL surfaces with 10 pN, 2 Å and 40 s resolutions [33]. Besides, high performance liquid AFM revealed immunoactive two-dimensional self-assembly of monoclonal antibodies in aqueous solution [34].

Unfortunately, in general, high spatial resolution and high speed imaging are not compatible, because high spatial resolution requires high signal to noise ratio (SNR) but high speed imaging reduces SNR. Nonetheless, tremendous strides were recently accomplished in developing biocompatible high speed-AFM providing high

spatial and temporal resolution, and low-invasiveness in liquid environment [35]. As a result, high-speed AFM succeeded to visualize dynamics of proteins and live cells on a submolecular resolution [35].

1.2 Summary

Remarkable technical progresses such as tip modification and control of atomic force have expanded the AFM fields further as introduced in the following chapters in detail. Those include force spectroscopy and force-mapping with atomic resolution, repulsive force imaging, AFM/STM combined measurements, atomic/molecular manipulation and atomic/submolecular imaging in liquids. Consequently, the performance of NC-AFM functions has advanced furthermore exceeding the Vol. 2 (2009) extent as introduced in this book.

References

1. S. Morita, R. Wiesendanger, E. Meyer, *Noncontact Atomic Force Microscopy* (Springer, Berlin, 2002)
2. S. Morita, F.J. Giessibl, R. Wiesendanger, *Noncontact Atomic Force Microscopy*, vol. 2 (Springer, Berlin, 2009)
3. M. Abe, Y. Sugimoto, O. Custance, S. Morita, Appl. Phys. Lett. **87**, 173503 (2005)
4. M. Abe, Y. Sugimoto, T. Namikawa, K. Morita, N. Oyabu, S. Morita, Appl. Phys. Lett. **90**, 203103 (2007)
5. F. Mohn, B. Schuler, L. Gross, G. Meyer, Appl. Phys. Lett. **102**, 073109 (2013)
6. G. Kichin, C. Weiss, C. Wagner, F.S. Tautz, R. Temirov, J. Am. Chem. Soc. **133**, 16847 (2011)
7. L. Gross, F. Mohn, N. Moll, P. Liljeroth, G. Meyer, Science **325**, 1110 (2009)
8. Y. Sugimoto, P. Pou, O. Custance, P. Jelinek, M. Abe, R. Pérez et al., Science **322**, 413 (2008)
9. F. Ming, K. Wang, S. Pan, J. Liu, X. Zhang, J. Yang et al., ACS nano **5**, 7608 (2011)
10. S. Kawai, A.S. Foster, F.F. Canova, H. Onodera, S. Kitamura, E. Meyer, Nat. Commun. **5**, 4403 (2014)
11. A. Yurtsever, Y. Sugimoto, H. Tanaka, M. Abe, S. Morita, M. Ondráček et al., Phys. Rev. B **87**, 155403 (2013)
12. Y. Sugimoto, P. Pou, O. Custance, P. Jelinek, S. Morita, R. Pérez et al., Phys. Rev. B **73**, 205329 (2006)
13. N. Oyabu, O. Custance, I. Yi, Y. Sugawara, S. Morita, Phys. Rev. Lett. **90**, 176102 (2003)
14. M. Ternes, C.P. Lutz, C.F. Hirjibehedin, F.J. Giessibl, A.J. Heinrich, Science **319**, 1066 (2008)
15. S. Torbrügge, O. Custance, S. Morita, M. Reichling, J. Phys.: Condens. Matter **24**, 084010 (2012)
16. Y. Sugimoto, M. Abe, S. Hirayama, N. Oyabu, O. Custance, S. Morita, Nat. Mater. **4**, 156 (2005)
17. Y. Sugimoto, A. Yurtsever, N. Hirayama, M. Abe, S. Morita, Nat. Commun. **5**, 4360 (2014)
18. Y. Sugimoto, P. Pou, M. Abe, P. Jelinek, R. Pérez, S. Morita et al., Nature **446**, 64 (2007)
19. L. Gross, F. Mohn, N. Moll, G. Meyer, R. Ebel, W.M. Abdel-Mageed et al., Nat. Chem. **2**, 821 (2010)
20. D.G. de Oteyza, P. Gorman, Y. Chen, S. Wickenburg, A. Riss, D.J. Mowbray et al., Science **340**, 1434 (2013)

21. P. Jelinek, M. Švec, P. Pou, R. Perez, V. Cháb, Phys. Rev. Lett. **101**, 176101 (2008)
22. D. Sawada, Y. Sugimoto, K. Morita, M. Abe, S. Morita, Appl. Phys. Lett. **94**, 173117 (2009)
23. B.J. Albers, T.C. Schwendemann, M.Z. Baykara, N. Pilet, M. Liebmann, E.I. Altman et al., Nat. Nanotechnol. **4**, 307 (2009)
24. S. Fremy, S. Kawai, R. Pawlak, T. Glatzel, A. Baratoff, E. Meyer, Nanotechnology **23**, 055401 (2012)
25. F. Mohn, L. Gross, G. Meyer, Appl. Phys. Lett. **99**, 053106 (2011)
26. Y. Sugimoto, Y. Nakajima, D. Sawada, K. Morita, M. Abe, S. Morita, Phys. Rev. B **81**, 245322 (2010)
27. M. Ternes, C. González, C.P. Lutz, P. Hapala, F.J. Giessibl, P. Jelinek, A.J. Heinrich, Phys. Rev. Lett. **106**, 016802 (2011)
28. Y. Sugimoto, M. Ondráček, M. Abe, P. Pou, S. Morita, R. Perez et al., Phys. Rev. Lett. **111**, 106803 (2013)
29. L. Lichtenstein, M. Heyde, H.-J. Freund, Angew. J. Phys. Chem. C **116**, 20426 (2012)
30. L. Lichtenstein, C. Büchner, S. Stuckenholz, M. Heyde, H.-J. Freund, Appl. Phys. Lett. **100**, 123105 (2012)
31. Y. Sugimoto, A. Yurtsever, M. Abe, S. Morita, M. Ondráček, P. Pou, R. Pérez, P. Jelínek, ACS Nano **7**, 7370 (2013)
32. T. Fukuma, K. Kobayashi, K. Matsushige, H. Yamada, Appl. Phys. Lett. **86**, 193108 (2005)
33. E.T. Herruzo, H. Asakawa, T. Fukuma, R. Garcia, Nanoscale **5**, 2678 (2013)
34. S. Ido, H. Kimiya, K. Kobayashi, H. Kominami, K. Matsushige, H. Yamada, Nat. Mater. **13**, 264 (2014)
35. T. Ando, T. Uchihashi, S. Scheuring, Chem. Rev. **114**, 3120 (2014)

Chapter 2
3D Force Field Spectroscopy

Mehmet Z. Baykara and Udo D. Schwarz

Abstract With recent advances in instrumentation and experimental methodology, noncontact atomic force microscopy is now being frequently used to measure the atomic-scale interactions acting between a sharp probe tip and surfaces of interest as a function of three spatial dimensions, via the method of *three-dimensional atomic force microscopy* (3D-AFM). In this chapter, we discuss the different data collection and processing approaches taken towards this goal while highlighting the associated advantages and disadvantages in terms of correct interpretation of results. Additionally, common sources of artifacts in 3D-AFM measurements, including thermal drift, piezo nonlinearities, and tip-related issues such as asymmetry and elasticity are considered. Finally, the combination of 3D-AFM with simultaneous scanning tunneling microscopy (STM) is illustrated on surface-oxidized Cu(100). We conclude the chapter by an outlook regarding the future development of the 3D-AFM method.

2.1 Introduction

A complete and accurate understanding of the atomic structure of solids as well as their physical properties related to interatomic interactions and bonding are required for the successful development of new applications based on emerging phenomena such as superconductivity and molecular electronics. In this context, the physical properties of solid surfaces on the atomic scale are of primary concern due to the fact that the interaction of materials with other atoms and molecules in their vicinity via surfaces define their functionality for various applications from wear-resistant and low-friction coatings to microelectronics. The capability of imaging solid surfaces in

M.Z. Baykara (✉)
Department of Mechanical Engineering and UNAM-Institute of Materials Science and Nanotechnology, Bilkent University, 06800 Ankara, Turkey
e-mail: mehmet.baykara@bilkent.edu.tr

U.D. Schwarz
Center for Research on Interface Structures and Phenomena (CRISP), Department of Mechanical Engineering and Materials Science, Department of Chemical and Environmental Engineering, Yale University, New Haven 06520, USA
e-mail: udo.schwarz@yale.edu

© Springer International Publishing Switzerland 2015

S. Morita et al. (eds.), *Noncontact Atomic Force Microscopy*,
NanoScience and Technology, DOI 10.1007/978-3-319-15588-3_2

real space with atomic resolution was established with the invention of the scanning tunneling microscope (STM) in the early 1980s [1], and the subsequent development of the atomic force microscope [2] allowed nanometer-scale imaging of surfaces without limitations regarding conductivity [3]. Eventually, thanks to the development of the *noncontact* operation mode of AFM (NC-AFM) [4–7] based on a frequency-modulation approach involving oscillating cantilevers [8], true atomic-resolution imaging was achieved over the last two decades on a large array of material surfaces, ranging from ionic crystals [9–11], metals [12–14] and metal oxides [15] to the new class of *two-dimensional* materials, including graphene [16, 17] and silicene [18].

Atomic-resolution imaging of materials has initially been the primary focus of NC-AFM; shortly after its successful demonstration, however, scientists already started to direct parts of their efforts to the measurement of site-specific interactions using the method of *dynamic force spectroscopy* (DFS) [19–21]. Based on the idea of collecting *frequency shift* (Δf) information—the main signal utilized for atomic-resolution imaging in NC-AFM—as a function of tip-sample separation on atomically defined sites of the material surface under investigation, DFS allows the conversion of the acquired data to *force-distance* as well as *energy-distance* curves via mathematical procedures performed post-data-acquisition [22]. While the DFS technique allows the acquisition of single interaction curves on defined lattice sites as indicated, converting the method into a comprehensive tool capable of collecting full *three-dimensional* (volumetric) maps of interaction forces and energies with atomic resolution took considerable effort due to limitations in terms of various experimental factors including tip and sample stability, as well as thermal drift. Eventually, thanks to advancements in instrumentation and experimental methodology such as low temperature operation [23] and atom-tracking/feedforward methods [24, 25], the method of *three-dimensional atomic force microscopy* (3D-AFM) was established, implementation of which has now successfully been demonstrated by various research groups on a variety of sample surfaces [26–37]. Originally developed for vacuum conditions, the method has recently been extended to operation under liquid environments, thereby opening up tremendous possibilities for high-resolution investigation of biological material under close-to-natural conditions [38–40]. Despite the exciting potential of 3D force field spectroscopy in liquids, a related discussion is beyond the scope of this chapter, as we will solely focus on atomic-resolution spectroscopy experiments performed under ultrahigh vacuum.

Despite the recent success of the 3D-AFM method in acquiring atomic-resolution, volumetric maps of interaction forces and energies on a steadily growing list of materials, the experimental approaches used to collect the related data have not been standardized. Moreover, the technique frequently suffers from various artifacts related to thermal drift and piezo nonlinearities, as well as tip-related issues involving elasticity and asymmetry [41, 42]. In this chapter, we will review the advantages and disadvantages of the particular methods proposed in the literature to perform 3D-AFM and analyze the effect of different artifacts on the measurements. Moreover, the extension of the capabilities of the 3D-AFM method in terms of the collected physical information will be demonstrated via simultaneous 3D-AFM/STM measurements performed on surface-oxidized Cu(100) [36].

2.2 Experimental Methodology

The essential goal of any scanning probe microscopy (SPM) method (including AFM and STM) is to collect accurate information about the physical properties of the investigated surface. On the other hand, the information collected via such an approach will, to a certain extent, be always influenced by the specifics of the experimental methodology utilized to perform data acquisition as well as the physical properties of the probe itself. Within that context, we will review in this section the common methods reported in the literature to perform atomic-resolution 3D-AFM. The following section will then deal with the effect of various artifact sources on collected information. Finally, the methods reported here to perform 3D-AFM will be compared and contrasted with respect to the extent to which they are influenced by the discussed artifacts.

The most commonly reported methods in the literature to perform 3D-AFM may be considered under two general categories (Fig. 2.1):

(a) The *curve-by-curve* method, involving the recording of individual curves of frequency shift as a function of tip-sample distance ($\Delta f(z)$) at a number of lateral (x, y) locations on the sample surface [30, 31, 33–35, 37]. The curves are then

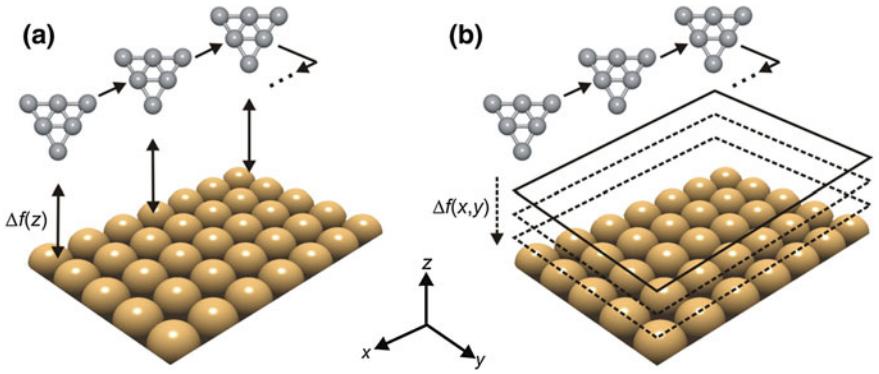

Fig. 2.1 Schematic illustrations describing the *curve-by-curve* (**a**) and the *layer-by-layer* (**b**) approaches taken towards 3D force field spectroscopy. While individual $\Delta f(z)$ curves are recorded in (**a**), consecutive NC-AFM images at fixed setpoints above the surface are collected in (**b**). Image reproduced from [41]

combined such that full three-dimensional maps of frequency shift ($\Delta f(x, y, z)$) are formed that are subsequently converted to interaction force ($F(x, y, z)$) and energy ($E(x, y, z)$) maps [22].

(b) Utilizing an alternative approach, the volumetric $\Delta f(x, y, z)$ data may be recorded in a *layer-by-layer* fashion, by combining a group of *topographical* NC-AFM images that contain $\Delta f(x, y)$ data for set tip-sample distances z [26, 29, 31, 32, 36]. Volumetric maps of interaction force ($F(x, y, z)$) and energy ($E(x, y, z)$) are then obtained via the same procedures employed for the *curve-by-curve* approach [22].

While the *curve-by-curve* method relies on conventional procedures established for dynamic force spectroscopy (DFS) to collect individual $\Delta f(z)$ curves, the *layer-by-layer* method necessitates a more involved data acquisition and processing procedure (Fig. 2.2), which will be briefly reviewed here (for details, see [43]).

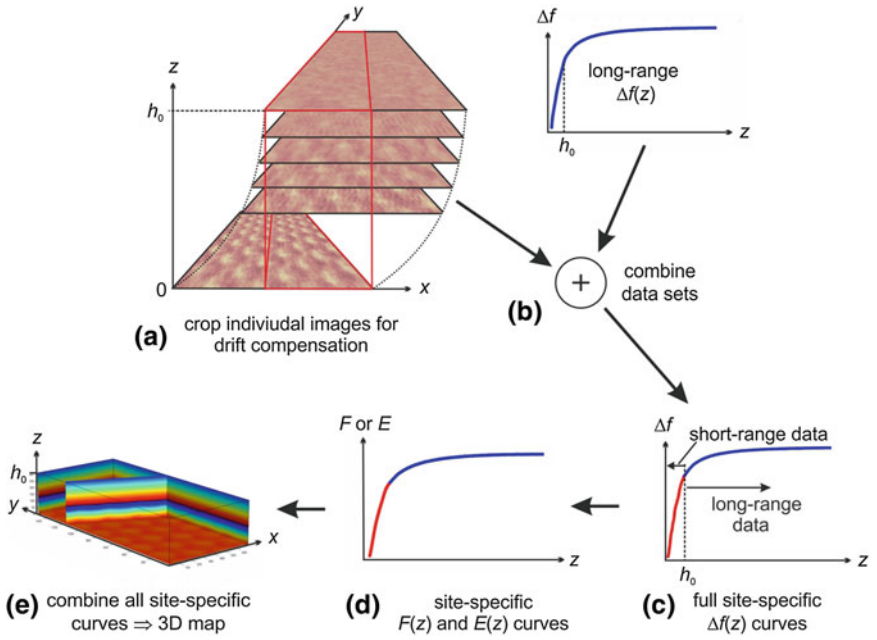

Fig. 2.2 Overview of the data processing steps involved in 3D force field spectroscopy via the *layer-by-layer* approach. **a** After slight Fourier filtering to remove high frequency noise, the individual images are laterally adjusted with respect to each other to correct for drift. Data outside the area where all recorded images overlap (indicated by the *red lines*) are cropped. **b** Long-range data from an individually collected $\Delta f(z)$ curve (i.e., data covering tip–sample separations $> h_0$) are added to the site-specific short-range curves for each lateral position (x, y) recovered from the images. The full $\Delta f(z)$ curves obtained in this fashion (**c**) are converted into $F(z)$ or $E(z)$ *curves* (**d**). Finally, all $F(z)$ and $E(z)$ curves are combined to form three-dimensional maps of $F(x, y, z)$ or $E(x, y, z)$, respectively (**e**). Image reproduced from [43]

The data acquisition procedure for 3D force field spectroscopy via the *layer-by-layer* approach involves the following steps:

- The sample surface is first imaged via regular (*topographical*) NC-AFM at a fixed frequency shift setpoint Δf. During imaging, the topography feedback is kept on to prevent sudden crashes of the tip with the sample surface. While imaging the surface, topography z as well as frequency shift Δf data for each lateral position (x, y) (which frequently vary to a small extent from the fixed setpoint due to non-perfect operation of the feedback loop) are recorded. Additional data channels recorded during imaging may include the oscillation amplitude A, the excitation amplitude A_{exc}, as well as tunneling current I in case of a (semi-)conducting sample.
- Following the recording of a given image as indicated above, the imaging setpoint for Δf is decreased, the tip-sample distance consequently increases, and a new image is recorded at the new setpoint.
- New images are recorded at subsequent setpoints until atomic-scale contrast vanishes (at a given height h_0), as following images at even lower setpoints will then contain the same, non-site-specific information.
- Additionally, individual $\Delta f(z)$ curves are recorded before and after data acquisition to (i) re-confirm that no tip changes have occurred during data collection and (ii) to calculate the non-site-specific (*long-range*) part of the tip-sample interaction, as explained in the following parts of the present section.

A couple of aspects that need to be mentioned in terms of data acquisition include (i) that the vertical distance between consecutive images is not constant and changes with the local slope of $\Delta f(z)$ and (ii) that the specific performance of the topography feedback loop (and associated deviations from the setpoint Δf during imaging) does not have a significant effect on the measurement since the Δf and z data for each lateral position (x, y) are later combined.

Once data collection is performed as indicated above, the collected information is subjected to several processing steps to eventually obtain three-dimensional $F(x, y, z)$ and $E(x, y, z)$ maps. The individual data processing steps may be summed up as:

- *Low-Pass Fourier Filtering*: The topographical (z) and frequency shift (Δf) maps collected are slightly low-pass filtered to remove any high-frequency noise in the data. Care is taken to ensure that the cut-off wavelength is significantly smaller than the interatomic spacing on the surface.
- *Removing Lateral Drift*: The lateral shift between subsequent images due to thermal drift (significantly reduced but not completely removed even for low-temperature measurements due to the long data acquisition times associated with the technique on the order of multiple hours) is determined by inspection and manually removed by shifting all individual images (of z and Δf) laterally in the xy plane. Only the pixels that overlap for all images are kept, and the rest of the images are then cropped accordingly (Fig. 2.2a).

- *Combining Short-Range and Long-Range Interactions*: To recover interaction force/energy information from frequency shift data, $\Delta f(z)$ information needs to be available, from the tip–sample distance that one is interested in, all the way back to where interactions are negligible [22]. As such, the short-range $\Delta f(z)$ information collected for each lateral position (x, y) in the previous steps needs to be combined with the long-range, non-site specific part of the interaction, that is the same for all lateral positions (x, y) in the data set above h_0. Towards this purpose, the tail of the long-range $\Delta f(z)$ curves (at $z > h_0$) recorded before and after *layer-by-layer* data acquisition is added on to the site-specific short-range $\Delta f(z)$ information recorded for each lateral position via the steps discussed above (Fig. 2.2b, c).
- *Calculation of 3D Force/Energy Maps*: In the final step of data processing for the *layer-by-layer* method, complete $\Delta f(z)$ curves calculated in the previous step are converted to $F(z)$ and $E(z)$ curves via the mathematical procedures established in the literature [22] and the individual curves for each (x, y) position (Fig. 2.2d) are combined to form full 3D maps of interaction force ($F(x, y, z)$) and energy ($E(x, y, z)$) (Fig. 2.2e).

It should be noted here that for the *layer-by-layer* approach to be applied in a feasible manner, the lateral as well as vertical drifts acting between the tip and sample need to be minimized. As such, the technique requires either low temperature operation [23] or the utilization of atom-tracking/feedforward methodologies [24, 25] for proper execution.

2.3 Sources of Artifacts in 3D Force Field Spectroscopy

All SPM measurements are influenced to a certain extent by artifacts affecting imaging and spectroscopy. While some artifact sources are due to the specifics of the instrumentation used in the measurements (such as thermal drift, piezo nonlinearities, etc.), others are intimately related to the physical properties of the probe itself (such as asymmetry, elasticity as well as chemical identity of the apex). In this section, we will review each source of artifact relevant for 3D force field spectroscopy measurements and evaluate its effect on acquired data.

2.3.1 Thermal Drift

As all scanning probe microscopes ultimately feature components that are made of different materials with varying thermal expansion coefficients, relative motion of the sample with respect to the probe tip due to changes in temperature (the phenomenon of *thermal drift*) are inevitable. Taking into account that performing 3D force field spectroscopy typically involves data acquisition over multiple hours, artifacts related to thermal drift become significant. Specifically, measurements performed at room

temperature as opposed to low temperatures (corresponding to liquid nitrogen or helium temperatures) may typically feature drift rates of several Å per minute. On the other hand, operation at, e.g., liquid helium temperatures may severely reduce drift rates (as low as a few Å per day, [23]).

Despite the impractically large drift rates typically experienced by scanning probe microscopes operating at room temperature, the associated problems have been largely overcome in recent years by the introduction of atom-tracking and feedforward positioning methods. Atom tracking [24] involves the determination of the three-dimensional drift vector by considering the shift in the position of an individual maximum in subsequently recorded SPM images followed by an appropriate correction of the tip location that compensates for this drift. In contrast, the feedforward procedure [25] is based on the real-time correction of drift during data acquisition by applying appropriate voltages to the scan piezo, which are predicted by relying on the assumption that the drift vector can be adequately determined in prior measurements. Both approaches have been successfully implemented in the past to perform 3D force field spectroscopy at room temperature and low temperatures on various sample surfaces [30, 31, 33–35, 37]. One potential shortcoming of the method is the fact that the drift vector may need to be frequently updated during actual measurements based on the unpredictability of thermal fluctuations and associated drift rates. Lateral thermal drift rates of more than one unit cell in the time required to collect a single image also prove to be problematic, limiting *layer-by-layer* data acquisition to low temperatures [31].

As explained in Sect. 2.2 of this chapter, lateral drift correction may be performed post-data-acquisition via manual lateral shifting of subsequent images with respect to each other, as part of the *layer-by-layer* 3D force field spectroscopy approach [26, 36, 43]. With a sufficiently dense dataset consisting of images separated by only a few picometer in the z direction, gradual lateral shifts between subsequent images due to thermal drift may be precisely monitored and corrected for provided that lateral drifts between images are significantly lower than one unit cell.

It should be noted that thermal drift is not limited to lateral dimensions, but also affects the tip-sample separation in the vertical direction. Fortunately, certain basic procedures can be employed to eliminate the effect of z drift on force field spectroscopy. For volumetric maps obtained using the *curve-by-curve* method, such drift-induced distortions can be corrected via standard algorithms involving line-fitting etc. When the *layer-by-layer* approach is utilized, the necessary adjustments can be carried out by comparison with site-specific $\Delta f(z)$ calibration curves recorded directly before and/or after the individual layers needed to assemble the actual data array.

2.3.2 Piezo Nonlinearities

Modern scanning probe microscopes rely on components made out of piezoelectric materials for precise (picometer-scale) positioning of the probe tip with respect to

the sample surface in the three spatial dimensions [44]. Despite their widespread use in almost every SPM system, piezoelectric positioning systems suffer from a number of material-related complications including piezo nonlinearities leading to problems associated with *hysteresis* and *creep*, which ultimately may affect 3D force field measurements in the form of distorted images [3].

Solutions aimed at the correction/prevention of artifacts associated with piezo nonlinearities include tracking the actual position of tip/sample with external deflection sensors in real time or the application of voltages in the form of distorted waveforms so that the resulting motion is linear with respect to voltage [44, 45]. Atom-tracking and feedforward techniques, successful in correcting the effects of thermal drift, also help alleviate artifacts associated with piezo nonlinearities. Alternative strategies include: (i) post-data-acquisition correction of lattice distortions in atomic-resolution images using the known size and symmetry of surface unit cells [46], (ii) waiting a certain amount of time between the recording of each curve/image to reduce piezo creep, and (iii) operation at low temperatures, which is known to reduce the extent of piezo nonlinearities [47].

Despite the fact that artifacts related to the nonlinear behavior of piezoelectric positioning elements may not be completely suppressed using a straightforward approach, operation at low temperatures emerges as an ideal strategy with regards to 3D force field spectroscopy when the additional effect of reduced thermal drift is considered [23].

2.3.3 Tip Asymmetry

Despite the remarkable success of NC-AFM in measuring the atomic-scale structure of surfaces as well as associated interaction forces/energies via 3D force field spectroscopy, an important but often overlooked shortcoming of the technique is the inadvertent effect of structural and chemical properties of the tip apex (such as tip asymmetry, elasticity or elemental composition) on acquired data [36, 41, 42, 48–51]. Since most tip apices used in 3D force field spectroscopy feature a certain degree of atomic-scale asymmetry at the very apex with respect to the surface due to the methods by which they are obtained, significant inconsistencies arise between different experiments performed on the same sample system by different research groups or even by the same research group on different occasions. As such, a comprehensive understanding of tip asymmetry and its effect on 3D force field spectroscopy is a prerequisite for correct interpretation of obtained results.

Motivated by the discussion above, we will present in this part of the chapter an investigation of the effect of *tip apex asymmetry* on 3D force field spectroscopy via numerical simulations using the model sample surface of Cu(001) (Fig. 2.3a) and model, two-dimensional tip apices consisting of six Pt atoms arranged in a close-packed configuration (Fig. 2.3b, c). Significant asymmetry in the tip apex structure is obtained by rotating the apex by an angle θ around the frontmost atom (Fig. 2.3c). Force interactions between each tip and sample atom for the symmetric

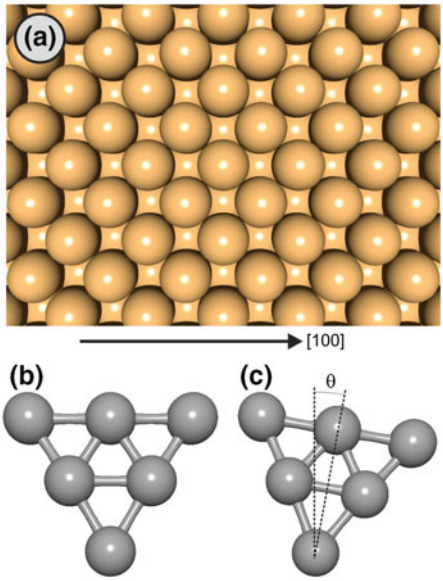

Fig. 2.3 (**a**) The *hard sphere* model of the Cu(001) surface employed in the numerical simulations regarding the effect of tip asymmetry on 3D force field spectroscopy. Symmetric (**b**) and asymmetric (**c**) tip apex models consisting of 6 Pt atoms in close-packed configuration are depicted, as well. Note that varying degrees of asymmetry in the tip apex are induced by rotating the symmetric apex model by an angle θ around the frontmost atom. Image reproduced from [41]

and asymmetric tip apices are calculated using a 12-6 Lennard-Jones (L-J) model with appropriate parameters for Cu and Pt atoms as well as Lorentz-Berthelot mixing rules [41]. Finally, the total normal force interaction experienced by the tip is plotted as a function of lateral position and tip-sample distance along the [100] crystallographic direction via 2D maps of force on the (x, z) plane (Fig. 2.4).

For a symmetric tip apex (i.e., $\theta = 0°$), force maxima are directly located above Cu atoms and evolve in a symmetric fashion as the tip-sample distance is increased (Fig. 2.4a). Please note that at very close separations, force maxima switch from atomic positions to hollow sites between the atoms, essentially pointing to a crossing of the $\Delta f(z)$ curves recorded above the atomic and hollow sites at small tip-sample separations, similar to the one previously observed in simulations carried out for a xenon (111) surface [52]. On the other hand, when asymmetric tips ($\theta = 45°$ and $\theta = 58°$) are used to simulate force field spectroscopy on the surface (Fig. 2.4b, c), force field maxima associated with the surface become increasingly *lopsided* (much like the data acquired on graphite and presented in [53]) and a significant offset between the locations of perceived force maxima and the (x, y) positions of the surface copper atoms develops with decreasing tip-sample distance.

Consequently, let us note that when the *layer-by-layer* approach is employed to perform 3D force field spectroscopy in conjunction with manual post-data-acquisition drift correction, the fact that the location of the maximum attractive force smoothly moves from the atomic to the hollow sites upon decreasing the tip-sample distance

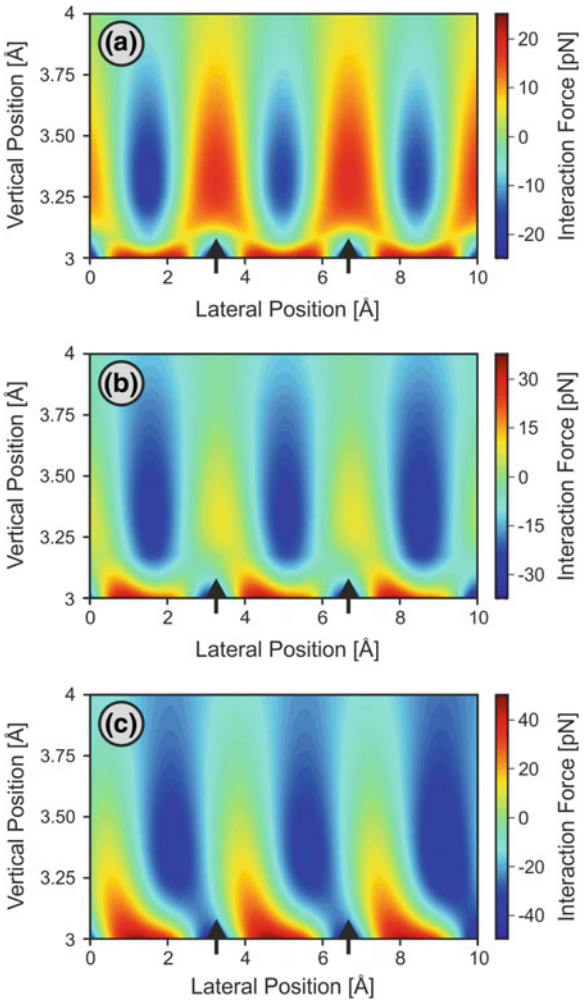

Fig. 2.4 2D maps of normal interaction forces simulated over the model Cu(001) surface along the [100] direction for symmetric (**a** $\theta = 0°$) and asymmetric (**b** $\theta = 45°$; **c** $\theta = 58°$) tip apices illustrated in Fig. 2.3b, c. The difference between the interaction force at each point and the mean interaction force at that height is displayed for better contrast visibility. The vertical axis indicates the distance in z direction between the center of the front-most tip atom and the centers of the surface copper atoms. *Black arrows* mark the lateral positions of surface Cu atoms. Image reproduced from [41]

for the sample surface of Cu(001) can be particularly problematic, as the associated effect cannot readily be distinguished from thermal drift or lateral shifting due to overall elastic bending of the probe tip. On the other hand, similar simulations performed on NaCl(001) have revealed that such effects are not observed when the dominant interactions between the probe and sample atoms are electrostatic (i.e., long-range) in character [41]. As such, the *layer-by-layer* method in conjunction with post-data-acquisition drift correction should be, to a first approximation, safely applicable to sample systems such as ionic crystals and metal oxides.

2.3.4 Tip Elasticity

In addition to tip asymmetry, an important factor affecting NC-AFM measurements in general and 3D force field spectroscopy experiments in particular is tip elasticity and associated elastic deformations of the tip apex under the influence of external forces as it is scanned over the sample surface. Elastic deformations of the tip apex may manifest in three distinct ways:

(a) Normal (i.e., vertical) forces acting on the tip apex in the attractive interaction regime will lead to an extension of the probe in the vertical direction as well as a bending and an effective overall lateral movement of the tip apex in a particular direction, if the tip used to probe the sample surface is asymmetric.

(b) Site-specific lateral forces acting on the tip apex will cause lateral shifts in its position as the tip is scanned over the surface. While such shifts are reversible and should average out while scanning along a periodic array of atoms for a given crystallographic direction, their local effect on 3D force field spectroscopy should be detectable if tips with low lateral stiffness values (k_{lateral}) are employed.

(c) Finally, lateral forces acting on the probe tip may lead to reversible (or irreversible) atomic-scale displacements at the very apex, leading to sudden changes in local tip-sample interactions.

It is important to point out here that the effect due to part (a) should be indistinguishable from that of thermal drift in the *layer-by-layer* approach since the bending of the tip towards a preferred direction at increasing setpoints would lead to a lateral shift of features with respect to each other in subsequent images. As such, the combined effects of thermal drift and (a) can be both eliminated via post-data-acquisition drift correction, highlighting a particular advantage of the *layer-by-layer* strategy for 3D force field spectroscopy.

On the other hand, the extent of (c) on 3D force field spectroscopy ultimately depends on the atomic-scale structure of the tip apex and whether atoms at particularly instable locations are to be found in a given experiment. While a discussion of associated artifacts are beyond the scope of this chapter, we will direct our attention to (b) and try to quantify the effect of site-specific lateral forces on force field spectroscopy using numerical simulations similar to those reported previously for tip asymmetry. Towards this purpose, the interactions between the model sample surface of NaCl(001) and a symmetric Pt tip apex are calculated, using a combination of L-J as well as ionic repulsion and attraction forces. Moreover, the Pt atom at the very end of the tip apex model is taken to carry a positive unit charge and the apex is considered to be connected to the rest of the microscope via a probe tip with a lateral stiffness of k_{lateral} [42].

2D maps of normal interaction forces calculated along the [100] crystallographic direction on NaCl(001) with tips having lateral stiffness values of ∞ (corresponding to a rigid tip), 25, 15, and 5 N/m are depicted in Fig. 2.5. It is clearly observed that elastic lateral deformations undergone by the probe tip lead to observable distortions in force maps, the extent of which increases with decreasing lateral stiffness. In

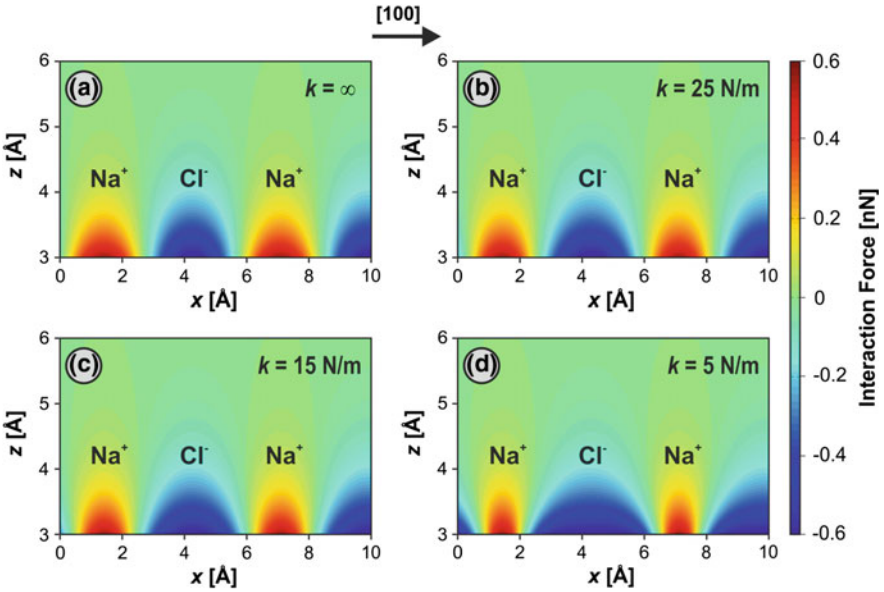

Fig. 2.5 2D maps of normal interaction forces on NaCl(001) calculated along the [100] direction for model Pt tip apices with lateral tip stiffness (k_{lateral}) values of ∞ (rigid tip), 25, 15, and 5 N/m. The distortions associated with the local force fields on Cl^- and Na^+ ions with decreasing tip stiffness can be clearly observed. Image reproduced from [42]

particular, repulsive force maxima situated on Na^+ ions become increasingly narrow with decreasing lateral stiffness and attractive force maxima on top of Cl^- ions become significantly wider. Taking into account that atomic-scale force spectroscopy and imaging experiments performed on ionic crystals often feature varying size and shape for the observed force maxima, the relevance of the results presented here in terms of the effect of tip elasticity on 3D force field spectroscopy becomes apparent.

2.4 Comparison of Data Acquisition and Processing Strategies for 3D Force Field Spectroscopy

Based on the information presented in this chapter so far, the various advantages and disadvantages of the methods established in the literature to perform 3D force field spectroscopy will be compared in this section. Towards this purpose, let us note that the main characteristics of the most commonly employed experimental methodologies for 3D force field spectroscopy can be summarized as:

- **Method A**: *Layer-by-layer* acquisition of data, post-data-acquisition drift correction, operation at low temperatures [26, 36]

- **Method B**: *Curve-by-curve* acquisition of data, atom-tracking/feedforward procedures, operation mostly at room temperature [30, 31, 33–35, 37]
- **Method C**: *Curve-by-curve* or *line-by-line* acquisition of data, use of a *reference image* for drift correction at fixed intervals during data acquisition, operation at low temperatures [27]

It should be noted though, that the three methods listed above represent a generalization at best and different combinations of approaches can be utilized in different experiments to address specific issues.

Using Table 2.1,

- All three methods satisfactorily address the effects of *thermal drift* and *piezo nonlinearities* on 3D force field spectroscopy.
- As *tip asymmetry* is an inherent issue associated with the probe tip itself, none of the presented methods are immune to its effects. Moreover, in the case of tip-sample interactions being predominantly short-range (see, e.g., the numerical simulation performed on Cu(001) and presented in Sect. 2.3.3), the post-data-acquisition correction of drift in the *layer-by-layer* approach becomes problematic as certain artifacts associated with tip asymmetry become indistinguishable from those related to thermal drift and elastic bending of the tip apex.

Table 2.1 Comparison of data acquisition and processing strategies for 3D force field spectroscopy

	Method A	Method B	Method C
Thermal drift	✓ Low thermal drift corrected post-acquisition	✓ Data acquisition has to be interrupted frequently to correct drift	✓ Data acquisition has to be interrupted to correct drift
Piezo nonlinearities	✓ Reduced piezo effects can be corrected post-acquisition	✓ Remaining piezo effects can be corrected post-acquisition	✓ Reduced piezo effects can be corrected post-acquisition
Tip elasticity	✓ Certain tip elasticity effects can be eliminated post-acquisition	×	×
Tip asymmetry	× May cause problems for post-acquisition drift correction on certain surfaces	×	×
Additional notes	Contrast distortions readily detectable during data acquisition	Irreversible tip changes much more likely at room temperature	–

- However, Method A holds a significant advantage over the other methods in case tip-sample interactions are predominantly long-range (as would be the case for most measurements performed on ionic crystals and metal oxides), since the post-data-acquisition correction procedures employed address both artifacts related to thermal drift as well as *elastic bending* of the tip apex towards a preferred direction due to normal forces (effect (a) discussed in Sect. 2.3.4, [43]).
- Another advantage of Method A over the other methods is the fact that irreversible changes in the tip apex are readily detectable during data acquisition in terms of changing image contrast whereas such observations cannot always be done in a straightforward fashion while data is collected *curve-by-curve*. Additionally, contrast changes with respect to changing tip-sample distance (such as those in [26, 32]) are directly observed during data acquisition, while such information only becomes observable after data processing in the case of *curve-by-curve* data acquisition.
- Despite the several advantages of Method A listed above when compared with the other data acquisition methods for 3D force field spectroscopy, it should be noted that the technique should not be employed when either (i) lateral drift between images is more than the lattice constant of the sample surface under investigation (unless a specific defect can be used as a *marker* of lateral position) and/or (ii) contrast patterns exhibit frequent changes with changing tip-sample distance such that alignment of features in subsequent images becomes problematic.

2.5 Combination of 3D Force Field Spectroscopy with Scanning Tunneling Microscopy: 3D-AFM/STM

A significant extension can be imparted on 3D force field spectroscopy via the recording of additional data channels such as energy dissipation and tunneling current during data acquisition [28]. While the recording of atomic-scale energy dissipation data during 3D force field spectroscopy has previously facilitated the identification of lattice sites on highly oriented pyrolytic graphite (HOPG) [26], the novel information that can be gathered regarding both the sample surface and the probe via the simultaneous recording of tunneling currents and interaction forces during 3D force field spectroscopy will be demonstrated in this section [36].

Simultaneous recording of interaction forces and tunneling currents is particularly interesting since information about atomic-scale reactivity of the surface and, at the same time, its electronic properties are collected to be contrasted and compared. Additionally, the data in the two channels can be utilized (i) to identify lattice sites on surfaces composed of multiple chemical species where symmetry arguments cannot be used in a straightforward fashion towards the same purpose and (ii) to uncover the structural and chemical characteristics of the probe tip apex, especially when the experimental data is interpreted in conjunction with ab initio simulations of interaction forces and tunneling currents.

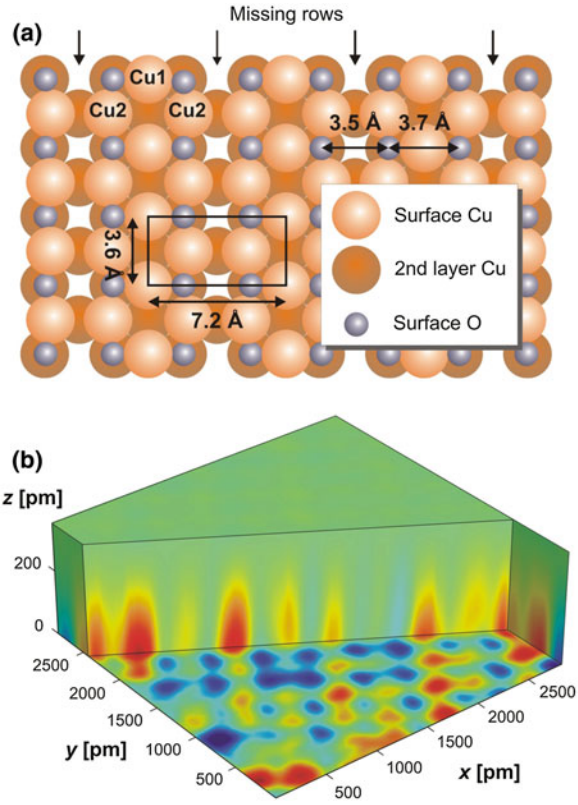

Fig. 2.6 **a** Reconstructed missing-row model of the surface oxide layer on Cu(100). Cu1 atoms are located at the centers of filled rows while Cu2 atoms are at the edges of troughs. **b** Three-dimensional representation of interaction forces measured on the sample surface using 3D force field spectroscopy. Atomic-scale features are clearly observed on the bottom plane. Image reproduced from [36]

To demonstrate the two points described above, a simultaneously recorded data set of interaction forces and tunneling currents on surface-oxidized Cu (100) is presented here [36]. The monolayer-thick surface oxide layer investigated in the experiments features a missing-row reconstruction where one in every four copper rows of the underlying substrate forms a trough, with filled rows between the troughs consisting of nearly co-planar Cu and O atoms in an alternating configuration (Fig. 2.6a). The combined 3D force field and tunneling current spectroscopy (3D-AFM/STM) experiments have been performed using a home-built, low temperature, ultrahigh vacuum instrument [23] equipped with a quartz tuning fork and an etched/field-ion beam treated Pt/Ir tip as the force sensor ($f_0 = 29{,}177\,\text{Hz}$, $A = 1.0\,\text{nm}$, $T = 5\,\text{K}$, bias voltage $U = -0.4\,\text{V}$, measurement time: 10 h). After drift correction performed according to *Method A* discussed in Sect. 2.4, the region of the surface over which the spectroscopy data is displayed comprises $2.89\,\text{nm} \times 2.89\,\text{nm}$.

The corresponding 3D force field spectroscopy data is displayed in Fig. 2.6b, where individual atomic-scale maxima can be observed in the bottom plane. Using the dense 3D information provided, the decay of interaction forces with increasing tip-sample distance as well as differences in interaction exhibited by different lattice

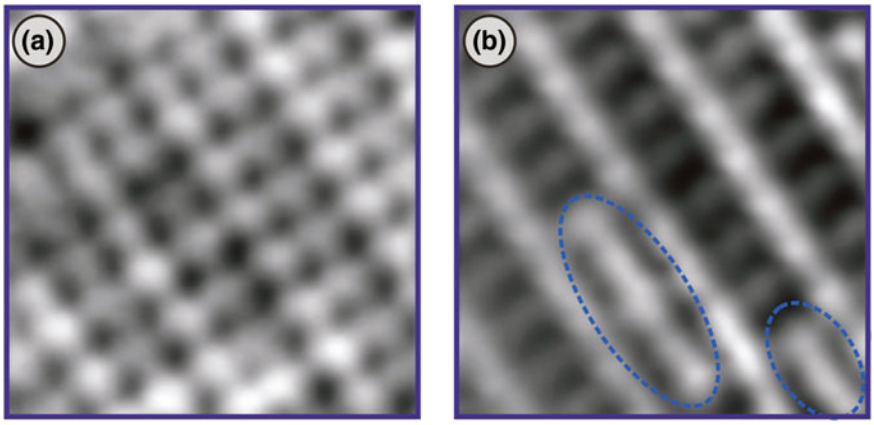

Fig. 2.7 **a** 2D map of interaction forces (2.89 nm × 2.89 nm) extracted from the 3D spectroscopy data in Fig. 2.6b at the bottom plane. Force maxima coincide with the O atoms on the surface. **b** 2D map of tunneling currents simultaneously acquired with interaction forces on the same plane. A *ladder-type* contrast is observed, coinciding with the copper atom arrangement on the surface. Surface defects in the form of partially filled troughs are highlighted. Image reproduced from [36]

sites can be studied with very high resolution. The magnitude of the maximum interaction force measured in the bottom plane is ∼1.34 nN whereas the contrast between atomically defined positions is ∼23 pN.

Employing a 2D map of interaction forces extracted from the 3D data set presented in Fig. 2.6b, force maxima can be unambiguously identified as the O atoms on the surface based on the symmetry of their arrangement (Fig. 2.7a). Surprisingly, the interaction force recorded for each O atom is different, with the values measured for different O atoms changing by as much as 40 % of the total force contrast on that plane. On the other hand, the map of tunneling currents simultaneously recorded at the same tip-sample separation features a very different, *ladder-like* symmetry, together with occasional linear defects imaged as partially *filled rows* on the troughs of the missing-row reconstruction (Fig. 2.7b).

To demonstrate the capability of identifying the structure and chemistry of the tip apex employed in the present 3D-AFM/STM experiment by a combination of experimental data with ab initio density functional theory simulations, force interactions of model tip apices involving Cu and O atoms with the sample surface as well as the associated tunneling currents are calculated. In the simulations, model tip apices consisting of Cu and O atoms are chosen due to the fact that tips have been treated by gentle crashes into the sample surface prior to data acquisition to improve imaging resolution in the experiments. A comparison of simulation results with experimental data then allows to determine that the tip apex used in the experiments is more than likely terminated by a Cu atom with an O atom adsorbed on the side (see inset in Fig. 2.8b), as this model apex successfully reproduces the experimentally obtained contrast in the tunneling current channel (where Cu1 atoms located at the centers of filled rows are imaged as bright protrusions and faint bridges of tunneling current are

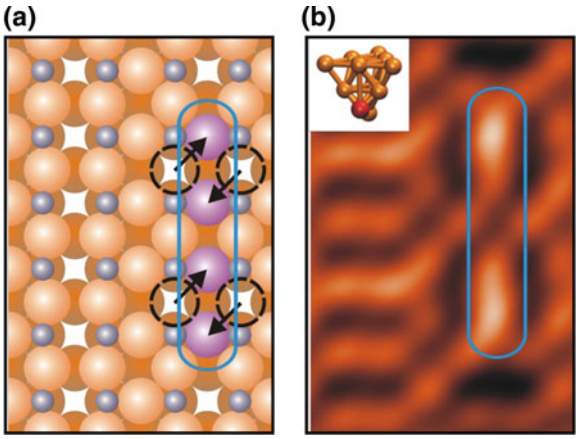

Fig. 2.8 **a** A surface defect model involving the displacement of two pairs of Cu2 atoms into the missing row. **b** The surface defect model presented in (**a**) is predicted to result in the observation of a linear defect in the tunneling current channel via ab initio simulations, in alignment with experimental data displayed in Fig. 2.7b. The *inset* in (**b**) represents the structural model of the tip apex used in the simulations. Image reproduced from [36]

formed by Cu2 atoms on both sides of the missing rows) and interacts most favorably with O atoms in the tip-sample distance regime of interest. *Simultaneous imaging of two different chemical species* via a combination of 3D force field spectroscopy and STM is demonstrated in this fashion.

Another aspect where the combined recording of interaction force and tunneling current data proves advantageous is the observation and identification of atomic-scale surface defects. In fact, the linear defect in the form of partially filled troughs observed in Fig. 2.7b would not have been detected if 3D force spectroscopy was being performed without simultaneous recording of the tunneling current channel, as the tip-sample interaction for the particular tip apex under consideration is dominated by O atoms. To identify the structural character of the defect under question, a number of defect models and the resulting simulations of tunneling current contrast were considered [36]. From the respective calculations, the atomic-scale origin of the linear defect observed in the current channel was established to involve the displacement of two pairs of Cu2 atoms into the missing rows (Fig. 2.8a). Based on this finding, it can be concluded that the variation of interaction force observed on each O atom is due to the variability in the chemical and electronic environment induced by the existence of surface defects, thereby providing direct, real-space evidence that surface defects affect chemical reactivity on the atomic scale [36].

As seen by the representative experiment discussed here, the combination of 3D force field spectroscopy with simultaneous recording of tunneling current (3D-AFM/STM) exhibits a tremendous potential for atomic-scale characterization of surfaces featuring multiple chemical species and even defects.

2.6 Conclusions and Outlook

The emerging method of 3D force field spectroscopy has been studied in this chapter, with particular attention paid to the different experimental methodologies proposed for data acquisition and processing. A discussion of common sources of artifacts in such measurements and the extent to which the proposed experimental methodologies address the related issues has been presented. The role that the probe itself plays on the acquired data, in terms of artifacts induced via asymmetry and elastic deformations has been investigated via numerical simulations involving basic pairwise potentials. Moreover, the combination of 3D force field spectroscopy with simultaneous recording of tunneling current has been demonstrated using experiments performed on surface-oxidized Cu(100). In particular, the advantages provided by such an approach in terms of the structural and chemical characterization of the tip apex, as well as the identification of individual lattice sites and even defects on the sample surface have been considered. Thereby, an interplay of experimental results and ab initio calculations proved crucial to achieve the indicated goals.

As the results presented in this chapter demonstrate, the data collected by 3D force field spectroscopy (and for that matter, any SPM technique) ultimately reflect a convolution of the physical properties of the surface with those of the probe tip. Since the aim of the 3D force field spectroscopy method is to uncover the atomic-scale properties of the surface itself, efforts towards standardization of probe tips are of utmost importance. While a significant amount of success has recently been achieved towards this goal via the deliberate functionalization of probe tips with molecules such as CO [27, 54], the next step in the development of the method towards increased functionality could involve functionalization of probe tips with molecules more relevant for practical processes such as catalysis and thin film growth. Despite the fact that such molecules are structurally more *complex* than CO and may, therefore potentially lead to certain other complications during experiments due to reduced structural rigidity, the results provided would open a new window to the world of chemical reactions on surfaces, as the actual force and energy landscapes that would be experienced by particular molecules relevant for practical processes can be visualized with unprecedented resolution via such an approach.

Acknowledgments The authors would like to thank Eric I. Altman, Omur E. Dagdeviren, Harry Mönig, Rubén Pérez, Lucia Rodrigo, Todd C. Schwendemann, Milica Todorović, Berkin Uluutku and Özhan Ünverdi for their invaluable contributions to the experimental and numerical studies presented in this chapter. Financial support from the National Science Foundation through the Yale Materials Research Science and Engineering Center (grant No. MRSEC DMR-1119826) and the Materials World Network program (grant No. MWN DMR-0806893) as well as the US Department of Energy (Basic Energy Sciences grant No. DE-FG02-06ER15834) are gratefully acknowledged. M.Z.B gratefully acknowledges support from the Turkish Academy of Sciences via the TÜBA-GEBİP program and the Marie Curie Actions of the European Commission's FP7 Program in the form of a Career Integration Grant (grant No. PCIG12-GA-2012-333843).

References

1. G. Binnig, H. Rohrer, Helvetica Physica Acta **55**, 726 (1982)
2. G. Binnig, C.F. Quate, C. Gerber, Phys. Rev. Lett. **56**, 930 (1986)
3. P.J. Eaton, P. West, *Atomic Force Microscopy* (Oxford University Press, Oxford, 2010)
4. F.J. Giessibl, Science **267**, 68 (1995)
5. Y. Sugawara, M. Ohta, H. Ueyama, S. Morita, Science **270**, 1646 (1995)
6. S. Morita, R. Wiesendanger, E. Meyer, *Noncontact Atomic Force Microscopy* (Springer, Berlin, 2002)
7. S. Morita, F.J. Giessibl, R. Wiesendanger, *Noncontact Atomic Force Microscopy* (Springer, Berlin, 2009)
8. T.R. Albrecht, P. Grutter, D. Horne, D. Rugar, J. Appl. Phys. **69**, 668 (1991)
9. M. Bammerlin, R. Luthi, E. Meyer, A. Baratoff, J. Lu, M. Guggisberg et al., Appl. Phys. A **66**, S293 (1998)
10. M. Reichling, C. Barth, Phys. Rev. Lett. **83**, 768 (1999)
11. R. Hoffmann, D. Weiner, A. Schirmeisen, A.S. Foster, Phys. Rev. B **80**, 115426 (2009)
12. C. Loppacher, M. Bammerlin, M. Guggisberg, S. Schar, R. Bennewitz, A. Baratoff et al., Phys. Rev. B **62**, 16944 (2000)
13. V. Caciuc, H. Hölscher, D. Weiner, H. Fuchs, A. Schirmeisen, Phys. Rev. B **77**, 045411 (2008)
14. T. Konig, G.H. Simon, H.P. Rust, M. Heyde, Appl. Phys. Lett. **95**, 083116 (2009)
15. J.V. Lauritsen, M. Reichling, J Phys.: Condens. Matter **22**, 263001 (2010)
16. M.P. Boneschanscher, J. van der Lit, Z.X. Sun, I. Swart, P. Liljeroth, D. Vanmaekelbergh, ACS Nano **6**, 10216 (2012)
17. Y. Dedkov, E. Voloshina, Phys. Chem. Chem. Phys. **16**, 3894 (2014)
18. Z. Majzik et al., J. Phys. Condens. Matter **25**, 225301 (2013)
19. H. Hölscher, A. Schwarz, W. Allers, U.D. Schwarz, R. Wiesendanger, Phys. Rev. B **61**, 12678 (2000)
20. M.A. Lantz, H.J. Hug, R. Hoffmann, P.J.A. van Schendel, P. Kappenberger, S. Martin et al., Science **291**, 2580 (2001)
21. Y. Sugimoto, P. Pou, M. Abe, P. Jelinek, R. Perez, S. Morita et al., Nature **446**, 64 (2007)
22. J.E. Sader, S.P. Jarvis, Appl. Phys. Lett. **84**, 1801 (2004)
23. B.J. Albers, M. Liebmann, T.C. Schwendemann, M.Z. Baykara, M. Heyde, M. Salmeron et al., Rev. Sci. Instrum. **79**, 033704 (2008)
24. M. Abe, Y. Sugimoto, O. Custance, S. Morita, Appl. Phys. Lett. **87**, 173503 (2005)
25. M. Abe, Y. Sugimoto, T. Namikawa, K. Morita, N. Oyabu, S. Morita, Appl. Phys. Lett. **90**, 203103 (2007)
26. B.J. Albers, T.C. Schwendemann, M.Z. Baykara, N. Pilet, M. Liebmann, E.I. Altman et al., Nat. Nanotechnol. **4**, 307 (2009)
27. L. Gross, F. Mohn, N. Moll, P. Liljeroth, G. Meyer, Science **325**, 1110 (2009)
28. M.Z. Baykara, T.C. Schwendemann, E.I. Altman, U.D. Schwarz, Adv. Mater. **22**, 2838 (2010)
29. B. Such, T. Glatzel, S. Kawai, S. Koch, E. Meyer, J. Vacuum Sci. Technol. B **28**, C4B1–C4B5 (2010)
30. S. Kawai, T. Glatzel, S. Koch, A. Baratoff, E. Meyer, Phys. Rev. B **83**, 035421 (2011)
31. S. Fremy, S. Kawai, R. Pawlak, T. Glatzel, A. Baratoff, E. Meyer, Nanotechnology **23**, 055401 (2012)
32. B. Such, T. Glatzel, S. Kawai, E. Meyer, R. Turansky, J. Brndiar et al., Nanotechnology **23**, 045705 (2012)
33. R. Pawlak, S. Kawai, S. Fremy, T. Glatzel, E. Meyer, ACS Nano **5**, 6349 (2011)
34. Y. Sugimoto, K. Ueda, M. Abe, S. Morita, J. Phys.: Condens. Matter **24**, 084008 (2012)
35. R. Pawlak, S. Kawai, S. Fremy, T. Glatzel, E. Meyer, J. Phys.: Condens. Matter **24**(8), 084005 (2012)
36. M.Z. Baykara, M. Todorovic, H. Monig, T.C. Schwendemann, O. Unverdi, L. Rodrigo et al., Phys. Rev. B **87**, 155414 (2013)

37. A.M. Sweetman et al., Nat. Commun. **5**, 7 (2014)
38. T. Fukuma, Y. Ueda, S. Yoshioka, H. Asakawa, Phys. Rev. Lett. **104**, 016101 (2010)
39. H. Asakawa, S. Yoshioka, K. Nishimura, T. Fukuma, ACS Nano **6**, 9013 (2012)
40. E.T. Herruzo, H. Asakawa, T. Fukuma, R. Garcia, Nanoscale **5**, 2678 (2013)
41. M.Z. Baykara, O.E. Dagdeviren, T.C. Schwendemann, H. Monig, E.I. Altman, U.D. Schwarz, Beilstein J. Nanotechnol. **3**, 637 (2012)
42. B. Uluutku, M.Z. Baykara, J. Vacuum Sci. Technol. B **31**, 041801 (2013)
43. B.J. Albers, T.C. Schwendemann, M.Z. Baykara, N. Pilet, M. Liebmann, E.I. Altman et al., Nanotechnology **20**, 264002 (2009)
44. S.O.R. Moheimani, Rev. Sci. Instrum. **79**, 071101 (2008)
45. H.J. Hug, B. Stiefel, P.J.A. van Schendel, A. Moser, S. Martin, H.J. Guntherodt, Rev. Sci. Instrum. **70**, 3625 (1999)
46. C.Z. Cai, X.Y. Chen, Q.Q. Shu, X.L. Zheng, Rev. Sci. Instrum. **63**, 5649 (1992)
47. W. Allers, A. Schwarz, U.D. Schwarz, R. Wiesendanger, Rev. Sci. Instrum. **69**, 221 (1998)
48. W.A. Hofer, A.S. Foster, A.L. Shluger, Rev. Mod. Phys. **75**, 1287 (2003)
49. N. Oyabu, P. Pou, Y. Sugimoto, P. Jelinek, M. Abe, S. Morita et al., Phys. Rev. Lett. **96**, 106101 (2006)
50. G.H. Enevoldsen, H.P. Pinto, A.S. Foster, M.C.R. Jensen, A. Kuhnle, M. Reichling et al., Phys. Rev. B **78**, 045416 (2008)
51. P. Pou, S.A. Ghasemi, P. Jelinek, T. Lenosky, S. Goedecker, R. Perez, Nanotechnology **20**, 264015 (2009)
52. H. Hölscher, W. Allers, U.D. Schwarz, A. Schwarz, R. Wiesendanger, Appl. Phys. A **72**, S35 (2001)
53. S. Kawai, T. Glatzel, S. Koch, B. Such, A. Baratoff, E. Meyer, Phys. Rev. B **81**, 085420 (2010)
54. J. Welker, A.J. Weymouth, F.J. Giessibl, ACS Nano **7**, 7377 (2013)

Chapter 3
Simultaneous nc-AFM/STM Measurements with Atomic Resolution

P. Hapala, M. Ondráček, O. Stetsovych, M. Švec and P. Jelínek

Abstract We discuss the history and recent progress of simultaneous AFM/STM measurements with atomic resolution. We demonstrate, that the technique can provide complex information about chemical and physical processes at atomic scale as well as about material properties of surfaces and nanostructures. We briefly overview one of the most fascinating achievements, high-resolution imaging with functionalized tips. The complexity of this technique calls for a new theoretical approach where relaxation of functionalized probe is considered in both AFM and STM modes. We describe mechanisms responsible for the high-resolution contrast introducing a numerical model, which provides deeper understanding of the AFM/STM measurements.

3.1 Introduction

The invention of Scanning Tunneling Microscopy (STM) [1] and Atomic Force Microscopy (AFM) [2] opened completely new horizons in characterization and modification of surfaces and nanostructures at the atomic scale. In STM, the tunneling current between a probe and the sample is used as the detection signal being the function of probe position. Due to its relatively simple design compared to AFM, it became a widely used surface science technique. However, the need to detect the tunneling current represents a significant deficiency, which limits the STM technique for potential applications on non-conductive surfaces, such as technologically important oxide materials.

This deficiency overcomes the AFM technique, which senses atomic forces acting between the frontend atoms of probe and sample. The first design of AFM, operating in the so-called static mode, was able to achieve atomic contrast on both conducting and insulating surfaces [2]. However, the presence of strong tip-sample interaction prevents a reliable interpretation of the experimental data.

P. Hapala · M. Ondráček · O. Stetsovych · M. Švec · P. Jelínek (✉)
Institute of Physics, Academy of Sciences of the Czech Republic, Cukrovarnická 10,
16200 Prague, Czech Republic
e-mail: jelinekp@fzu.cz

© Springer International Publishing Switzerland 2015

S. Morita et al. (eds.), *Noncontact Atomic Force Microscopy*,
NanoScience and Technology, DOI 10.1007/978-3-319-15588-3_3

The introduction of dynamically oscillating cantilever with frequency modulation (FM) by Albrecht and coworkers [3] represents the next milestone in the history of AFM. It allowed achieving true atomic resolution on the prototypical Si(111)-7 × 7 surface [4]. Among others, this seminal work stimulated the fast development of FM-AFM technique in the last decade [5, 6].

An idea to combine AFM and STM techniques appeared at the very beginning of the Scanning Probe Microscopy (SPM) history. Already in 1986, Dürig et al. [7] presented the first simultaneous measurements of the forces and current between a metallic tip and the sample. Using this experimental setup, they identified for the first time two different interaction regimes in atomic-sized metallic contacts [8]. In far distance regime, the force follows the power law $\sim z^3$ with the tip-sample distance z, revealing dominance of van der Waals interaction. In short distances, the exponential behavior emerges, which points to the formation of the chemical bond between frontier atoms on the tip and sample. At the same time, they found that the tunneling current scales exponentially, as expected.

Further instrumental development facilitated more precise AFM/STM measurements using dynamical FM-AFM approach. In 2000, Loppacher et al. [9] achieved atomically resolved images of Cu surfaces with simultaneous AFM/STM measurements using Si cantilever and tip. Silicon-based cantilevers oscillate typically with amplitudes of tens of nanometers. Consequently, the oscillating tip spends most of the time out of the tunneling regime, which reduces significantly the sensitivity of the tunneling current detection. In addition, the oscillation amplitude comparable to the characteristic decay length of the short-range force responsible for imaging provides the optimal signal-to-noise ratio [10]. Thus, the optimal oscillation amplitude should be in the order of few Å or even less, reducing the sensitivity to the long-range force contributions. Therefore it is evident that small amplitudes provide large benefits for simultaneous AFM/STM experiments. From this perspective, piezoelectric quartz sensors, with large stiffness compared to the traditional Si-based cantilevers, seem to be the proper choice.

In 1998, F.J. Giessibl introduced a new revolutionary type of sensor, called qPlus [11]. The qPlus sensor is based on the concept of piezoelectric quartz tuning forks similar to those used for example as frequency etalons in electronic watches. The configuration consists of one prong rigidly attached to a solid substrate while the second, oscillating prong with metallic tip acts as a probe with the capability of self-sensing. Presence of the metallic wire placed at the end of the oscillating prong allows simultaneous acquisition of the frequency shift (force) and the tunneling current [12]. Note that the proper wiring scheme is necessary to avoid a spurious cross-talk between the tunneling current and frequency shift channels [13]. Nowadays, the qPlus sensor and driving electronics is integrated in several commercially available instruments. This enlarged significantly the number of its applications that appeared in the last years (see e.g. [14–28]).

Another interesting alternative of self-sensing piezoelectric quartz sensor is the length extensional resonator [29] or the so-called Kolibri sensor [30]. The Kolibri sensor possesses much higher stiffness than qPlus sensors and thus it operates at much higher frequencies about MHz, compared to the qPlus sensor oscillating at

tens of kHz. From this perspective, the Kolibri sensor allows relatively fast scanning with a small amplitude. The performance comparison between qPlus and Kolibri sensors is still under debate in the community [31].

The simultaneous AFM/STM measurements already opened new horizons in the SPM field. In principle, the technique can provide more information than STM or AFM alone. One of the first successful applications of the combined AFM/STM measurements with qPlus sensor was detection of the single electron charge states of individual atoms. Namely, Gross et al. succeeded in distinguishing single neutral gold atoms deposited on an insulating layer from positively or negatively charged ones [15]. Measurements with the precision of a single electron charge and nanometer lateral resolution represents a milestone in the exploration of nanostructures and devices at the atomic and molecular limits. A second example, where the simultaneous AFM/STM measurements helped significantly to solve a long-standing debate, is the relationship between the tunneling current and the chemical force in atomic-sized contacts [9, 19, 32–40]. The simultaneous measurements of both tunneling current and force with high precision combined with first principles simulations provided a detailed insight into the fundamental relationship existing between the strength of the chemical bond and the charge transport through the established bond [19, 40]. The analysis showed that the relationship is directly controlled by the quantum degeneracy of frontier orbitals overlapping in a tunnel junction [40]. This relation holds for the region of relatively far tip-sample separations, where both the tunneling current and the chemical force scale exponentially with the tip-sample distance. For smaller distances, close to the atomic point contact, we can also observe correlated changes on both the force and current distance curve [19]. When a covalent or metallic bond is formed around distances, at which the attractive short-range force reaches its maximum, the current saturates at a value corresponding to approximately one conductance quantum [39]. At the same time, the formation of the covalent force induces accumulation of electron density inside the tunneling gap. Consequently, the tunneling barrier, which prevents electrons from passing between the tip and the sample, collapses and the character of the transport regime changes from tunneling to ballistic [19].

We should note that the scenario is different when the force acting between tip and sample has a weak character (e.g. interaction between CO-functionalized tip and a molecule deposited on surface). Here, the weak electrostatic force and/or van der Waals interaction takes place. We only observe polarization of the electron density due to an external field (e.g. proximity of charged tip or applied bias) but the accumulation of the charge in the middle of the tunneling gap is missing due to the lack of the chemical bonding. Thus the tunneling barrier does not collapse and the tunneling regime is preserved even when the mechanical contact between tip and sample is established. Nevertheless an abrupt change in the current-on-distance dependence can appear at the onset of the repulsive short-range force (i.e. for distances in which the Pauli repulsive force starts to dominate over the attractive bonding force). The cause of such change is that the system tends to relax the repulsive force by changes in the atomic configuration. Especially a tip functionalized by a molecule or an inert atom attached to its apex would be volatile to such geometry changes induced by the repulsive force.

Weymouth et al. pointed out a striking relation between the tunneling current passing through an atomic contact and force acting between tip and sample [18]. They detected the presence of repulsive force, which can dominate the atomic contrast of an AFM image when a tunneling current is present. The phenomenon can be ascribed to charge localization at the surface area just beneath the tip due to high resistivity of the sample. In other words, the tunneling current modifies a voltage drop in the tunneling junction. This effect affects directly the electrostatic attraction between the tip and sample, as the electrostatic force is voltage dependent. It gives rise to so-called phantom force [18]. Consequently the tunneling current signal in STM channel may also become correlated with the force signal in AFM or KPFM channels.

The combined AFM/STM measurement also provided important implications for the study of chemical processes on surfaces. Typically, small organic molecules deposited on semiconductor surfaces, such as the Si(111)-7 $\times$ 7 reconstruction, cannot be seen by STM at moderate bias due to their large band gap. Consequently, they appear as dark protrusions in the STM signal, indistinguishable from surface vacancies. Here, the force response allows discrimination of small organic molecules from common defects, such as vacancies, while the simultaneously acquired STM channel determines the molecular registry with the surface [24]. Baykara et al. investigated the influence of surface defects on the local structural, electronic, and chemical properties of a surface oxide on Cu(100) using atomically resolved 3D force mapping combined with STM measurements and density functional theory (DFT) calculations [28]. The complex analysis demonstrated the potential to directly probe local chemical activity of a surface influenced by the presence of defects.

3.2 High-Resolution AFM/STM Images with Functionalized Tips

One of the most remarkable and exciting achievements in the field of SPM in the last years is the unprecedented sub-molecular resolution of both atomic and electronic structures of single molecules deposited on surfaces. In 2005, Repp et al. reported STM measurements imaging molecular orbitals in real space [41]. Later, Temirov et al. [42, 43] discovered that proper functionalization of tip by admission of H_2 molecules into the UHV chamber enhances significantly the atomic contrast observed in STM images. Afterwards, they demonstrate that variety of other tips decorated by atomic and molecular particles (Xe, CH_4, CO) allows the STM to resolve the chemical structures of large organic molecules deposited on metallic surfaces [44]. This gave rise to a new technique, called scanning tunneling hydrogen microscopy (STHM).

In parallel, Gross et al. achieved high-resolution images of pentacene molecule deposited on an insulating thin film by means of AFM [45]. Here, the key is proper

functionalization of the tip with a single carbon monoxide (CO) molecule [46]. They attributed the origin of high-resolution AFM images to Pauli repulsion [45, 47] and later to the bending of the functionalized tip apex [48]. On the other hand, the precise origin of the STHM imaging mechanism was under debate [44, 49]. Recently, Hapala et al. introduced a numerical model [50] that provides a unified insight into the detailed mechanism of the high-resolution imaging with functionalized tips in both AFM and STM techniques.

Figure 3.1 shows a series of high-resolution AFM/STM images of herringbone monolayer of 3,4,9,10-perylene tetracarboxylic dianhydride (PTCDA) molecules deposited on the Ag(111) surface recorded with a Xe-functionalized tip at different distances. The images were acquired with SPECS low-temperature (LT) Joule-Thomson AFM/STM microscope operating at 1.2 K and equipped with the Kolibri sensor [30]. The sensor was oscillating with amplitude 70 pm, stiffness 540 kN/m, eigen-frequency 0.98 MHz and Q $\sim$ 200,000. The scan was performed at constant height mode with bias voltage -2 mV. Each frame, which covers an area of $4 \times 4\,\text{nm}^2$ sampled with 256×256 points, was recorded in 14 min. In total, we recorded 41 frames spaced by 5 pm in vertical direction with acquisition time $\sim$10 h.

In far distances (see panel a of Fig. 3.1), there is no atomically resolved contrast in the AFM channel. Individual molecules only appear as dark depressions due to attractive van der Waals interaction. On the other hand, the STM contrast concurs with real-space distribution of the LUMO orbital of PTCDA. The orbital is located 0.3 eV below the Fermi level in a PTCDA molecule on the Ag(111) surface. Therefore we can conclude that the tunneling through the tail of the LUMO orbital mediates the electron transport from the tip to surface. The situation changes when the tip approaches closer towards the surface. Internal benzene rings start to be resolved in the AFM image, see panel b of Fig. 3.1. On the other hand, oxygen atoms on the periphery are still invisible. The image contrast reflects repulsive interaction over atoms and bond edges and attractive interaction over centers of the benzene rings and intermolecular voids. At the same time, the STM contrast has changed slightly; on top of the LUMO contrast, new features are developing and the resolution is enhanced. In very close distances, the STM resolution changes completely as shown on panel c of Fig. 3.1. Very sharp features are clearly resolved, suppressing completely the LUMO contrast, which dominated the STM image in far distance. A clear sub-molecular contrast is achieved, showing both internal benzene rings and the peripheral rings including oxygen atoms. Both STM and AFM contrasts show very similar sharp features. In AFM images, we observe a contrast inversion between benzene rings and atoms/bonds. Now, the centers of benzene rings show larger repulsion than atoms/bonds. Sharp lines emerge in intermolecular regions, connecting hydrogen and oxygen atoms of neighboring molecules. Therefore it is tempting to connect these intermolecular features to hydrogen bonds [51, 52]. However, the true origin of these sharp features has been extensively discussed here [50, 53].

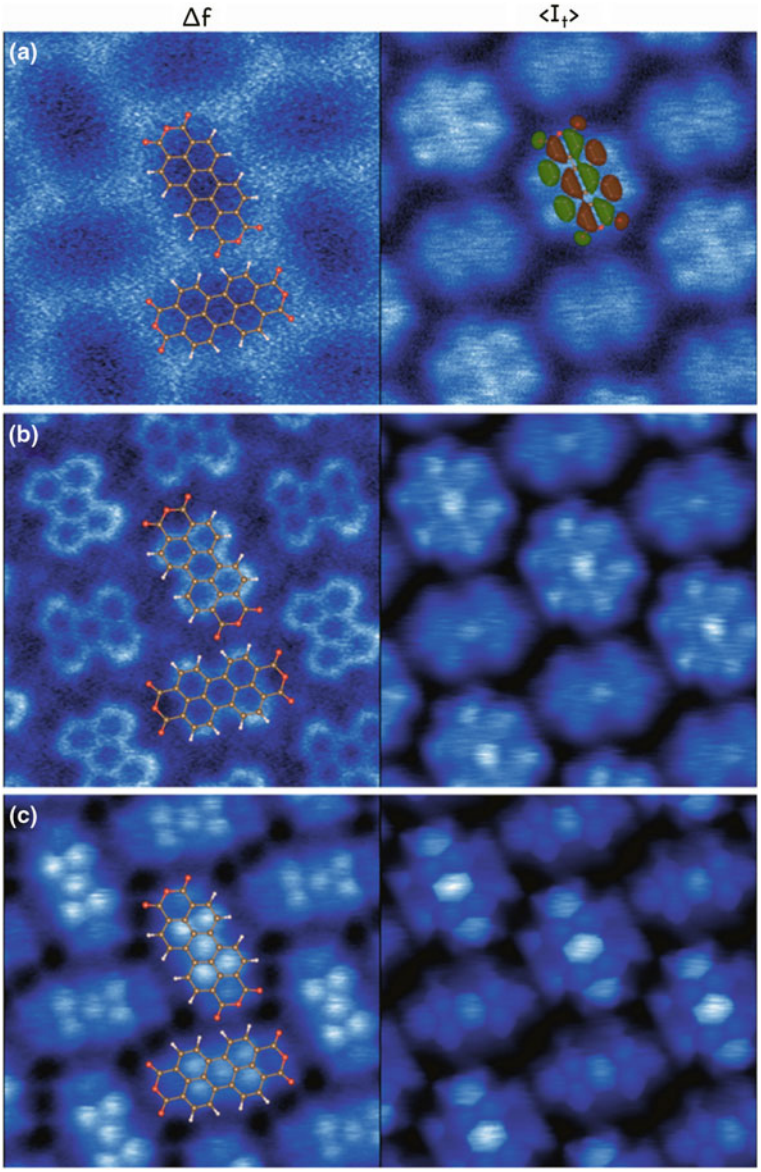

Fig. 3.1 Simultaneous AFM/STM images obtained with Xe-functionalized probe of herringbone monolayer of PTCDA molecules deposited on Ag(111) surface acquired with Kolibri sensor at 1.2 K in different tip-sample distances. Figures show the evolution of the frequency shift (*left*) and average tunneling current (*right*) while decreasing the tip-sample distance. Skeleton of PTCDA molecule is superimposed over AFM images to facilitate recognition of the high-resolution contrast. In the *right top figure*, real-space distribution of the LUMO orbital obtained from DFT calculations is shown in order to underline its good agreement with the STM contrast at this distance

3.3 Numerical Modeling of High-Resolution AFM/STM Images with Functionalized Tips

From the previous discussion, it is evident that the variation of the high-resolution AFM/STM contrast with tip-sample distance in experiments (see Fig. 3.1) is quite complex. Thus a theoretical tool, which is able to simulate both AFM and STM images at different distances, is required. Unfortunately, traditional theoretical approaches to AFM and STM simulations (see e.g. [54–59]) based on density functional theory (DFT) are numerically too expensive to carry out such a task. On the other hand, it has been pointed out that the enhanced contrast observed in high-resolution AFM/STM images [48, 50] is strongly related to the relaxation of the front atom/molecule placed on the apex of a functionalized tip. This means that any theoretical simulation must take into account relaxation of atomic positions due to the tip-sample interaction. Until now, this condition has been mostly neglected in the STM calculations. Note that formation of the chemical bond between frontier atoms of tip and sample can have fundamental impact on the tunneling current [60, 61] and local surface dipole [62].

In summary, there is a strong demand for a new simulation tool, which could mimic high-resolution AFM and STM acquired with functionalized tips in close distances. To meet these criteria, we have developed a numerical model, which despite its simplicity is able to reproduce high-resolution AFM and STM images of molecules very well [50, 63].

Here we provide a brief overview of the numerical model [50, 63], which is based on simple mechanics of a molecule attached to the tip apex in presence of surface potential. Schematic representation of the model is shown in Fig. 3.2. In the model, a single atom or a small molecule decorating the apex of a metal tip is modeled by a single atom (probe particle), which experiences van der Waals attraction and Pauli repulsion from surface atoms and front end tip atom. We use an empirical pairwise Lenard-Jones (L-J) potential, where the repulsive branch of the L-J potential mimicks the Pauli repulsion responsible for the high-resolution imaging. In addition, we restrict the lateral movement of the probe particle under the metallic tip apex by applying a harmonic potential. The harmonic potential determines the lateral ("bending") stiffness of the probe particle. Later [63], we also included the electrostatic force, which describes the Coulombic interaction between the charge density on a surface/molecule and a charge cloud localized on the probe particle (see Fig. 3.2).

On top of the mechanical model, we perform STM simulations calculating the tunneling current between the tip and sample as a two-step tunneling process: electron hopping (i) from the base-tip atom to the probe particle and (ii) between the probe particle and surface atoms. We consider the tunneling hopping to depend exponentially on the distances between the atoms. Despite its simplicity, this AFM/STM model is able to reproduce numerous features observed in the experimental high-resolution AFM/STM images. In addition, we extended the model by an analysis of the vibrational modes of the probe particle [63], which allows us to simulate the

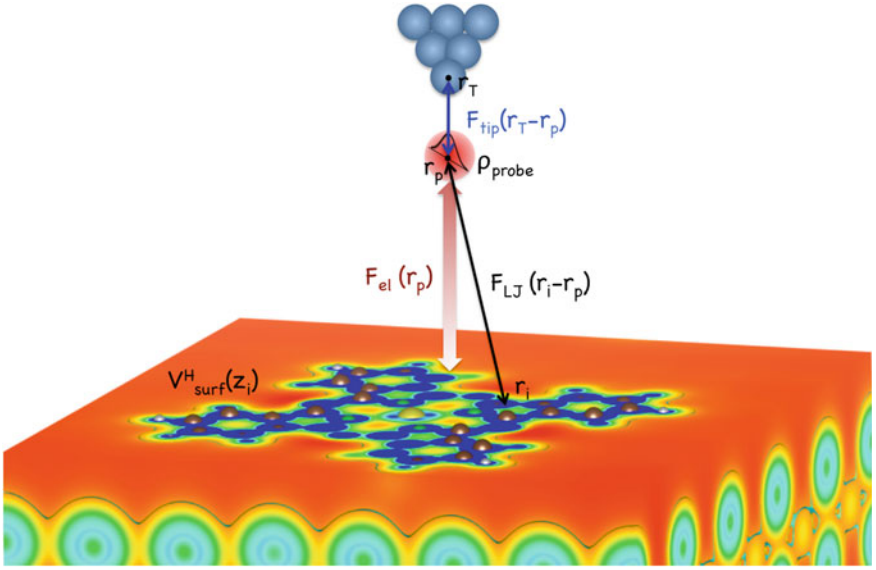

Fig. 3.2 Schematic view of the numerical model, which shows the geometry setup of CuPc molecule deposited on Ag(110) surface including the probe particle, tip base and the surface. Movement of the probe particle is driven by its interaction with the tip base (*blue* apex atom) F_{TIP} and with molecules deposited on the surface. The interaction between the tip and the surface consists of (i) the short range Lenard-Jones pair wise interaction F_{L-J} and (ii) the electrostatic interaction between charge density ρ_{PROBE} localized on the probe particle and the surface Hartree potential $V^H{}_{SURF}$. Typically, the surface Hartree potential is obtained from fully relaxed DFT calculations of a molecule deposited on a surface (for more details see [49, 62])

recently introduced inelastic electron tunneling (IETS)-STM technique [64]. This new technique images the inner structure of organic molecules with high resolution by mapping the vibrational energy of the frustrated translational mode of a single CO molecule positioned at the apex of a STM tip.

Figure 3.3 shows simulated AFM and STM images of the herringbone monolayer of PTCDA molecules deposited on the Au(111) surface for different distances obtained with the numerical model. Overall agreement with the experimental evidence is very good. We can see that in intermediated distances, $z = 7.9$ Å, where the probe position relaxation is negligible, the AFM contrast corresponds to the true shape of the electron density envelope, i.e. to the molecular skeleton. The atom and bonds appear brighter than intermolecular voids and the central parts of benzene rings due to higher repulsion experienced by the particle probe. When the tip approaches closer, $z = 7.4$ Å, the relaxation is no longer negligible and the sharp contrast emerges. In particular, the bonds are visible as sharp edges. Approaching the tip further, $z = 7.1$ Å, the atomic contrast over the molecule is inverted. The central parts of benzene rings become brighter than bond edges, in good agreement with the experimental observations. More details about the comparison between the theory and experiment can be found in [50].

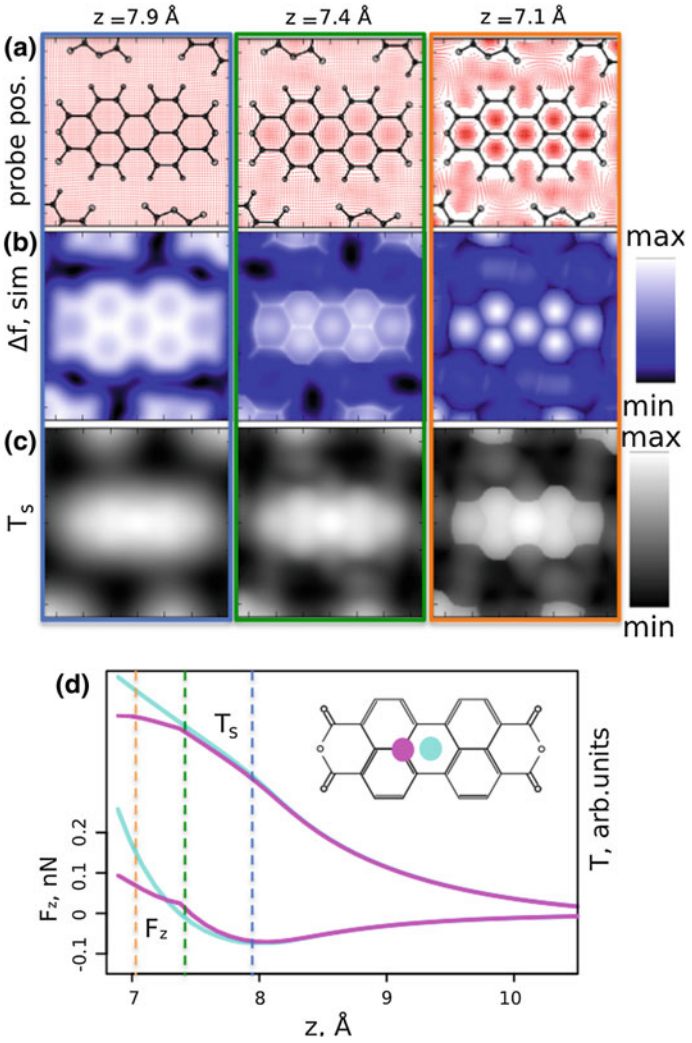

Fig. 3.3 Calculated high-resolution AFM/STM images at different distances of herringbone monolayer of PTCDA molecules deposited on Au(111) surface [49]; **a** shows the lateral particle probe relaxation; **b** AFM (frequency shift) images and; **c** STM images along tip approach. Figure **d** displays calculated force F_Z (*left*) and tunneling current T_S (*right*) as a function of the tip-sample distance *z* measured over a carbon atom (*pink*) and the *center* of a benzene ring (turquoise; see *inset* of Figure **d**) *Vertical color dashed lines* denote the distances where the images where calculated

The simulated STM image calculated at the far distance, z = 7.9 Å, shows only a faint contrast over the molecule (see Fig. 3.3). This is in contradiction to the experimental observation, where the LUMO orbital is clearly resolved (see Fig. 3.1). In the far distances, the tunneling process is completely dominated by the electronic

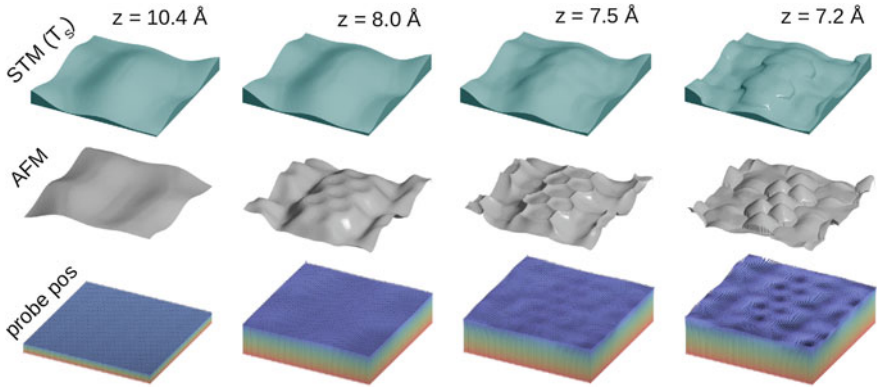

Fig. 3.4 3D perspective view of calculated high-resolution AFM/STM images at different distances of herringbone monolayer of PTCDA molecules deposited on Au(111) surface [49] at different distances. The figure shows STM and AFM images and the lateral probe-particle relaxation. The evolution of the sub-molecular contrast reveals strong correlation between onset of the probe-particle relaxation and the appearance of the sharp contours in both AFM and STM images

structure [54–56], which is not explicitly considered in our STM model (see the discussion in [50] for more details). However, when the tip comes closer to the surface, the repulsive interaction between the probe particle and the molecule on the surface induces a relaxation of the particle probe. At the same time, the sharp sub-molecular contrast appears.

Therefore we can conclude that the appearance of sharply resolved molecular structure is directly related to strong lateral relaxations of the atomic or molecular probe (CO, Xe, H_2 etc.) attached to the metallic tip apex. Figure 3.4 displays the variation of AFM and STM contrast together with the lateral probe particle distortion in 3D perspective to highlight the discussed effects. At close tip-sample distances, the probe particle relaxes into distinct potential energy basins separated by the enhanced Pauli repulsion over bonds and atoms. Thus we can always identify the sharp features with borders between neighboring basins, i.e. the cups where the magnitude and the direction of the lateral relaxation of the probe particle change strongly upon small variations of the tip position. This effect produces the sharp image features in both AFM and STM images. Notably, we found that the same effect also plays an important role in the IETS-STM mechanism [63, 64].

Sometimes the molecular contrast in the experimental images acquired in close distances shows significant asymmetrical shapes or pronounced shadows visible on benzene rings, see [50]. Figure 3.5 displays comparison of calculated AFM images of the PTCDA molecule in close distance with different symmetries of the probe particle. In the symmetric configuration, the probe particle is oriented perpendicularly to the surface, while in the asymmetric configuration the original position of the probe particle is slightly tilted to the side (the equilibrium position of the probe particle is displaced by 1 Å along the y-axis away from the lateral position of the tip base).

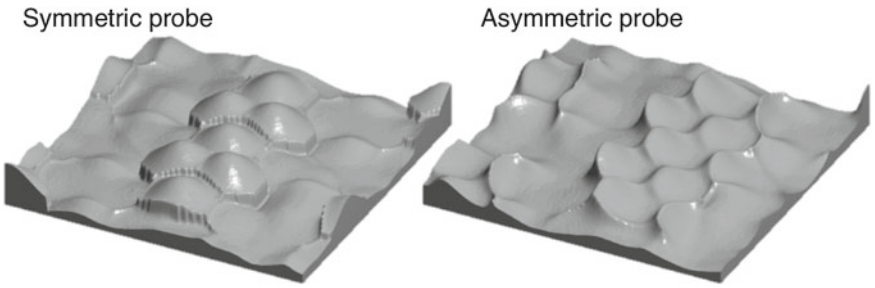

Fig. 3.5 3D images of calculated AFM images at the distances z = 7.2 Å of herringbone monolayer of PTCDA molecules deposited on Au(111) surface [49] with a symmetric and an asymmetric probe. The asymmetry of the probe causes a significant distortion of AFM images in close distances

The AFM image with the asymmetric probe shows a sloped contrast on benzene rings and in intermolecular features, similarly to the experimental findings. Therefore we can attribute the asymmetries and shadows observed in the high-resolution AFM/STM images to the asymmetric position of the molecular probe.

Let us now analyze the effect of the lateral stiffness k of the probe particle on apparent bond length in AFM images. Note that similar trends discussed below hold also for the STM or IETS-STM imaging. We calculated AFM images of a freestanding C_{60} molecule using different stiffness k of the particle probe at various tip sample distances. The results are shown in Fig. 3.6a. We can immediately recognize two striking effects directly related to the higher flexibility (i.e. lower lateral stiffness) of the particle probe: (i) apparent bond lengths increase; and (ii) the contrast inversion occurs at far tip-sample distances.

Our DFT calculation of the freestanding C_{60} molecule gives lengths of characteristic C–C bonds adjacent to hexagon edges (h-bond) and pentagon edges (p-bond) to be 1.38 and 1.45 Å, respectively. From simulated AFM images we can estimate the apparent bond length. Table 3.1 summarizes different apparent h and p-bond lengths for three different stiffness values ($k = 0.16$, 0.48 and 0.80 N/m) at the tip-sample distance $z = 7.7$ Å. First, the p-bond has larger apparent length than h-bonds in good agreement with experimental evidence [48]. This effect is simply caused by geometric effect, i.e. caused by bigger overlap of spherically symmetric Lenard-Jones potentials of the two adjacent carbon atoms in case of the h-bond. Second, we also observe that the increase of the apparent bond lengths is directly proportional to the flexibility of the particle probe. Third, the difference between apparent h and p-bond length reduces slightly with increase of the lateral stiffness. We find from the analysis of the calculated image that the p-bond is about 10–15 % larger than h-bond. However Gross et al. found experimentally the difference about ∼35 % ($d_p = 2.7$ Å, $d_p = 2.0$ Å), for more details see [48]. We will rationalize this discrepancy later, when discussing the influence of the electrostatic force on the high-resolution images.

In summary, we see that the relatively simple mechanical model, combined with a generic model of the electron tunneling through the tip-sample junction, successfully

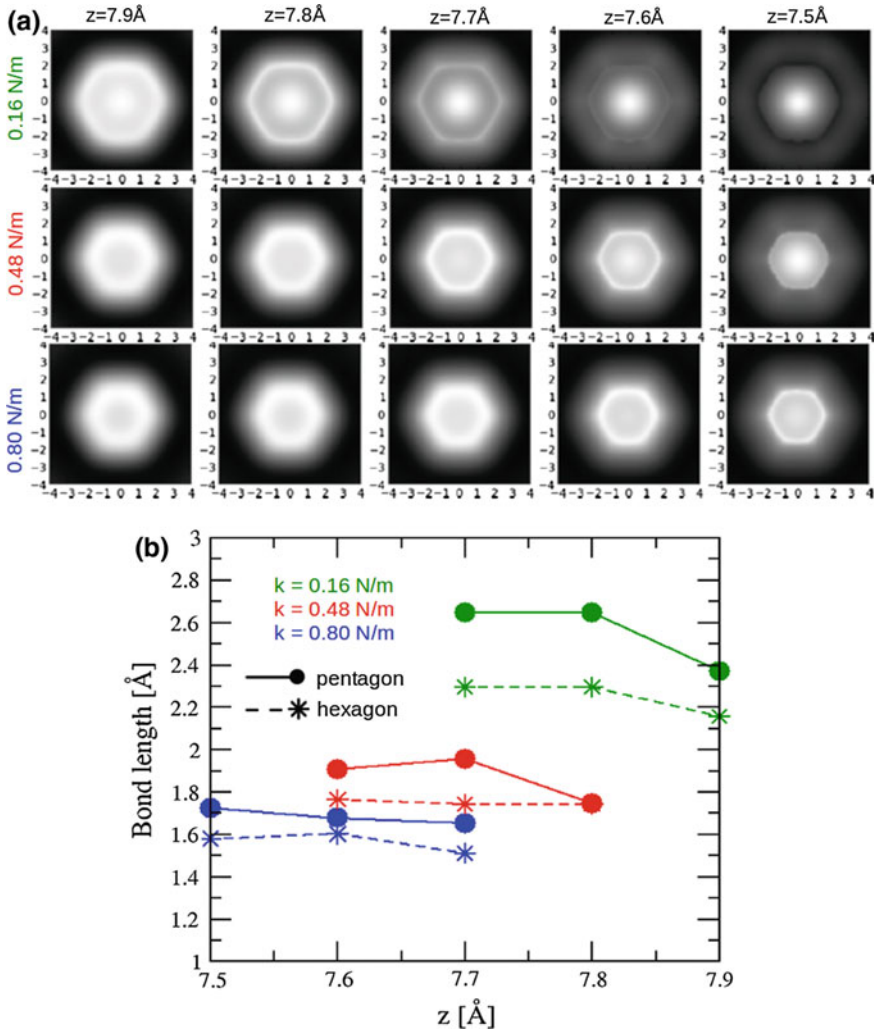

Fig. 3.6 Calculated AFM images of C_{60} molecule using functionalized tips with different stiffness k neglecting the electrostatic interaction for different tip-sample distances. **b** Variation of h-bond (*dashed lines*) and p-bond (*solid lines*) of a C_{60} with the tip-sample distance and the stiffness of the probing particle

Table 3.1 Estimated apparent lengths of p and h-bond lengths from calculated AFM images of C_{60} molecule at the distance $z = 7.7$ Å

	$k = 0.16$ (N/m)	$k = 0.48$ (N/m)	$k = 0.80$ (N/m)
d_h (Å)	2.30	1.74	1.51
d_p (Å)	2.65	1.95	1.65
d_p / d_h	1.15	1.12	1.08

explains the features of the high-resolution AFM/STM atomic contrast. Following remarks can be drawn from the numerical models:

(1) Relatively simple mechanistic model can capture the main ingredients of the high-resolution AFM, STM and IETS-STM imaging mechanism. The model represents not only very efficient but also sufficiently precise way to simulate the high-resolution images obtained with functionalized tips.
(2) The sharp contrast observed in both AFM and STM images is directly related to the abrupt changes in the relaxation of the probe particle, which occur when the junction crosses boundaries between neighboring basins of the repulsive tip-sample potential.
(3) The sharp edges observed in the high-resolution STM/AFM images acquired with functionalized tips do not necessarily represent interatomic or intermolecular bonds. Instead, they map the sharp boundaries between the energy basins separated by the short-range repulsive potential produced by atoms residing close to each other.
(4) The flexibility of the probe particle affects the apparent bond lengths observed in the high-resolution images. The apparent bond length increases with smaller lateral stiffness of the probe particle.
(5) The probe particle acts as a combined sensor and transducer [43, 44]. Here, the probe particle senses the repulsive force in close tip-sample distances, which causes its lateral relaxation. The relaxation transduces the exerted mechanical force into the tunneling conductance, frequency shift or IETS signal respectively, directly projected into the high-resolution images.

We should also note that the high-resolution imaging mechanism discussed above has a direct connection to the point contact microscopy [65–67] and force friction microscopy [68, 69]. In these cases, atomically resolved images also display sharp features very similar to those observed in the high-resolution AFM/STM images obtained with the functionalized tips. We believe that all mechanisms originate from relaxation of central part of the junction. However, in the case of the high-resolution AFM/STM images there is no hysteresis in the position of the probe particle as the tip is being scanned across the surface. Consequently, the AFM/STM imaging with functionalized tips does not depend on scanning direction or speed, contrary to the friction force microscopy.

3.4 Effect of Intra-molecular Charge on High-Resolution Images

The high-resolution SPM imaging techniques with functionalized tips have achieved unprecedented resolution of chemical structure of molecules deposited on surface. There is an ongoing debate what can be the ultimate resolution of the technique. Or what new information can we learn from the high-resolution imaging, apart from

the unprecedented resolution of the molecular structures [71, 72]? Very soon, it was recognized that the (apparent) bond lengths and angles tend to be slightly distorted. This can hamper precise determination of atomic positions for unknown structures or adsorption sites on surfaces. It has been extensively discussed that the bending of the molecular probe decorated at the tip apex causes the image distortion due to Pauli repulsion [15, 47, 48]. Pauli repulsion, however, is not the only force, which can cause bending of the tip leading to image distortion. If the atomic or molecular probe carries a charge, it will be deflected by electrostatic fields, which exist over the sample because of an internal charge transfer in the material under study.

In the seminal work, Gross et al. [48] pushed further the limit of the ultimate submolecular resolution. Deliberately, they selected the C_{60} molecule, so as to exclude any possible effect of different atomic species and the presence of polar bonds. By careful analysis of the high-resolution AFM images supported further by DFT calculation, they were able to determine the bond order of different C–C bonds in the C_{60} molecule. They found that bonds with higher bond order (hexagon edges, *h*-bond) appear to be shorter than bonds with lower bond order (pentagon edges, *p*-bond), in qualitative agreement with true bond length. However, quantitatively the differences of bond lengths determined experimentally were much bigger (35 %) than differences of true bond lengths (5 %) and all bonds were apparently longer than the real values (2.0 Å *h*-bond and 2.7 Å *p*-bond, in contrast to 1.38 and 1.45 Å, respectively). Gross et al. attributed the distortion to deviation of the CO molecule on the tip by Pauli repulsion. The Pauli repulsion is stronger over bonds with higher bond order due to increased electron density.

In the previous Section, we have analyzed the impact of the particle probe bending on the apparent bond length using the numerical model without inclusion of the electrostatic interaction. Namely, we found that the calculated difference between the apparent *p* and *h*-bond length ($\sim$10–15%) is smaller than the experimental one $\sim$35 % [48]. To overcome this discrepancy, we investigate the influence of electrostatic field caused by the variation of electron density due to different bond order. Is it possible that the electrostatic field also causes an additional deflection of CO molecule, which affects the apparent bond length?

To understand the influence of the electrostatic interaction determined by the subtle charge density variation over bonds with different bond order, we calculated the AFM images using our numerical model, supplemented by the electrostatic interaction [63]. The force-field was constructed from the Hartree potential obtained from a DFT calculation of a freestanding C_{60} molecule. In addition, we also calculated AFM images of the C_{60} molecule without the presence of the electrostatic interaction for better comparison (see Fig. 3.7a). This allows us to identify directly the effect of the electrostatic interaction on the image distortion. According to the previous discussion we found only small difference between C–C bonds adjacent to pentagons and hexagons. On the other hand, Fig. 3.7b displays the AFM images calculated with negatively charged probe particle $Q = -0.4\,e$. The AFM contrast reveals a significant difference between *h* and *p* C–C bonds.

Dependence of the apparent bond lengths on the probe particle charge (i.e. oxygen of CO) for the given stiffness $k = 0.48$ N/m simulated at $z = 7.7$ Å is

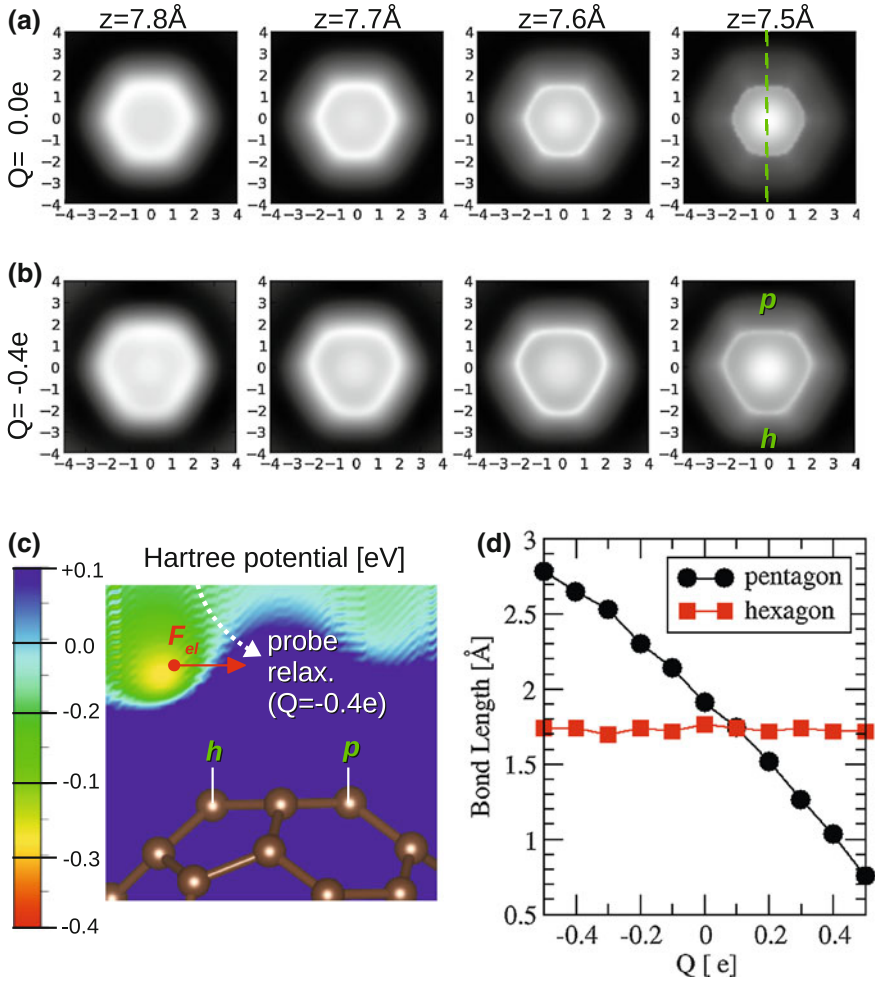

Fig. 3.7 Calculated AFM images of C_{60} molecule using functionalized tip **a** without (Q = 0.0 e) and **b** with (Q = − 0.4 e) the electrostatic interaction acting between the particle probe and C_{60} molecule. **c** Cut-plane of Hartree potential through the centers of a C_{60} *hexagonal* face showing different distribution over *h*-bond and *p*-bond. *Dashed white line* depicts schematically relaxation of the probe particle due to the presence of the electrostatic force. **d** Bond length dependence of *h*-bond and *p*-bond on the effective charge on the probing particle

plotted in Fig. 3.7d. We found the electrostatic force for a moderate charge on the probe particle, Q = −0.2 e, enhances the difference in the apparent *p* and *h*-bond lengths up to ∼32 %. Thus we see that the inclusion of the short-range electrostatic force can reproduce very well the experimentally observed difference between *p* and *h*-bonds (35 %) [48]. The reason why the *p*-bond is apparently elongated by distortions caused by electrostatic force while the length of the *h*-bond remains almost

constant can be rationalized by exploration of electrostatic potential as depicted in Fig.3.7c. The increased electron density in *h*-bonds creates a pocket of negative potential above this area. If the C_{60} molecule is oriented with the hexagonal ring upwards, the pocket is positioned slightly sideways, further from the center of the benzene ring than the *h*-bond itself, due to the curvature of the C_{60} surface (see Fig.3.7c). If the negatively charged probe particle approaches from top over an *h*-bond, it is repelled by the negative potential. Consequently, it is deflected inwards to the center of the ring. This leads to the image distortion, apparently shifting positions of the *h*-bond outwards and, as a result, elongating the *p*-bonds.

In our numerical model, the Pauli repulsion is described only effectively by the repulsive part of spherically symmetric atomic-wise Lenard-Jones potential. This description of Pauli repulsion does not account for the increased charge density in double bonds over the hexagon edge or any other variation of the electron density. The fact that the model including the electrostatic interaction can reproduce apparent bond length distortions experimentally observed on the C_{60} molecule indicates that the electrostatic interaction is probably the important factor leading to enhanced discrimination of the bond order with CO functionalized tips. However, we cannot completely rule out the role of the extra Pauli repulsion due to the enhanced electron density, which is omitted in our model.

There is another example, in which the presence of internal molecular charge transfer is projected into the sub-molecular contrast. The high-resolution IETS-STM images of a single Cobalto-Phtalocyanine (CoPc) molecule deposited on a metal surface show the sharply resolved molecular structure (i.e. positions of atoms and bonds). However, a detailed inspection of the sub-molecular contrast reveals notable distortion of the central part of the CoPc molecule, which cannot be attributed to changes of molecular conformation due to interaction with the substrate.

Namely, the images show an extension of the pyrrole rings accompanied with a diminution of the area corresponding to imine nitrogen in the central part of the molecule (see Fig. 3.3 in [63]). Total energy DFT calculation of the CoPc molecule reveals significant intramolecular charge transfer in the central part [62]. Moreover, calculated constant-height IETS-STM images show significant variation of the sub-molecular contrast in the central part, according to the amount of the charge localized on the probe particle. We note that the calculated IETS-STM image for the negative charge $Q = -0.4\,e$ matches very well the experimental evidence (for detailed discussion see [62]). This demonstrates that the decorated tip is senstive enough to map out the electrostatic polarization driven by intramolecular charge transfer. This opens a possibility for the development of imaging techniques yielding better spatial resolution than the traditional AFM-based Kelvin probe force microscopy (KPFM) [69].

3.5 Conclusions and Outlook

In conclusion, simultaneous AFM/STM measurement is well-established and powerful technique, which provides complex information about chemical and physical processes at atomic scale as well as about material properties of surfaces and nanostructures. The simultaneous application of force and current will soon open new possibilities and challenges in different fields. For example the AFM/STM measurements can lead to different atomic manipulation mechanisms, which can compete or cooperate on the same object. Also, simultaneous AFM/STM measurements on single molecular junctions can extend our knowledge about the relation between mechanical and transport properties [74], the nature of current-induced forces [75] or molecular switches driven by charge and mechanical action [76].

The whole family of SPM techniques (AFM, STM and IETS-STM) for high-resolution imaging becomes widely used by many research groups. The basic mechanism (Pauli repulsion, molecular probe relaxation) of the sharp molecular contrast is well established [45, 47, 48, 50, 53, 63]. The analysis reveals that a molecule deposited on the tip apex acts as an atomistic force sensor transducing its mechanical response to the tip-sample interaction potential into variation of the frequency shift (AFM) or the tunneling current (STM). Namely, the relaxations of the molecular probe cause discontinuities in both the frequency shift and the tunneling current signals, the sharp contrast features in AFM as well as in STM images. One of the important lessons we learned from the numerical model [50, 53] is the fact that the sharp edges observed in the high-resolution STM/AFM images do not necessarily correspond to bonds. Instead, they trace the sharp boundaries between neighbor basins of the tip-surface potential energy landscape.

The high-resolution imaging mechanism reported in this chapter has also direct connection to point contact microscopy [65, 67] and contact force microscopy [77, 78], where sharp features appear as consequence of atomic relaxation of the junction. However, in the present case the atomic contrast does not depend on the scanning direction and speed. This is due to lack of *hysteresis* in the position of the probe particle as the tip is scanned across the surface.

Recent trends go beyond the high-resolution to unveil what more information apart of the chemical structure of molecules we can obtain from the high-resolution images. The recent experimental and theoretical findings [63] suggest that information about internal charge distribution is included in these images and can be used as an alternative approach to the KPFM technique. This opens a new alternative way for mapping the charge with sub-molecular resolution.

Acknowledgments Our research was performed within the GAČR project no. 14-02079S and EMRP joint research project CRYSTAL. The EMRP is jointly funded by the EMRP participating countries within EURAMET and the European Union. We would like to acknowledge very fruitful discussion with R. Temirov, S. Tautz. R. Pérez, P. Pou, F. Flores, N. Moll, O. Custance, Y. Sugimoto, J. Repp, L. Gross, M. Ternes, F.J. Giessibl, P. Grutter, P. Moriarty and many others.

References

1. G. Binning, H. Rohrer, Ch. Gerber, E. Weibel, Surface studies by scanning tunneling microscopy. Phys. Rev. Lett. **49**, 57–61 (1982)
2. G. Binning, C.F. Quate, Ch. Gerber, Atomic force microscopy. Phys. Rev. Lett. **56**, 930–933 (1986)
3. T.R. Albrecht, P. Grütter, D. Horne, D. Rugar, Frequency modulation detection using high-Q cantilevers for enhanced force microscope sensitivity. J. Appl. Phys. **69**, 668 (1991)
4. F.J. Giessibl, Atomic resolution of the silicon (111)-(7x7) surface by atomic force microscopy. Science **267**, 68–72 (1995)
5. S. Morita, R. Wiesendanger, E. Meyer, *Noncontact Atomic Force Microscopy*, vol. 1 (Springer, Berlin, 2002)
6. S. Morita, F.J. Giessibl, R. Wiesendanger, *Noncontact Atomic Force Microscopy* (Springer, Berlin, 2009)
7. U. Durig, J.K. Gimzewski, D.W. Pohl, Experimental-observation of forces acting during scanning tunneling microscopy phys. Rev. Lett. **57**, 2403–2406 (1986)
8. U. Durig, J.K. Gimzewski, D.W. Pohl, Observation of metallic adhesion using the scanning tunneling microscope. Phys. Rev. Lett. **65**, 349–352 (1990)
9. Ch. Loppacher, M. Bammerlin, M. Guggisberg, S. Schol, R. Bennewitz, A. Baratoff et al., Dynamic force microscopy of copper surfaces- atomic resolution and distance dependence of tip-sample interaction and tunneling current. Phys. Rev. B **62**, 16944 (2000)
10. F.J. Giessibl, Advances in atomic force microscopy. Rev. Mod. Phys. **75**, 949–983 (2003)
11. F.J. Giessibl, High-speed force sensor for force microscopy and profilometry utilizing a quartz tuning fork. Appl. Phys. Lett. **73**, 3956–3958 (1998)
12. H. Herz, Ch. Schiller, F.J. Giessibl, J. Mannhart, Simultaneous current-, force-, and work-function measurement with atomic resolution. Appl. Phys. Lett. **86**, 153101 (2005)
13. Z. Majzik, M. Setvín, A. Bettac, A. Feltz, V. Cháb, P. Jelínek, Simultaneous current, force and dissipation measurements on the Si(111) 7×7 surface with an optimized qPlus AFM/STM technique. Beilstein J. Nanotechnol. **3**, 249 (2012)
14. M. Ternes, C.P. Lutz, C.F. Hirjibehedin, F.J. Giessibl, A.J. Heinrich, The force needed to move an atom on a surface. Surf. Sci. **319**, 1066–1069 (2008)
15. L. Gross, F. Mohn, P. Liljeroth, J. Repp, F.J. Giessibl, G. Meyer, Measuring the charge state of an adatom with noncontact atomic force microscopy. Science **324**, 1428 (2009)
16. A. Sweetman, S. Jarvis, R. Danza, J. Bamidele, L. Kantorovich, P. Moriarty, Manipulating Si(100) at 5 K using qPlus frequency modulated atomic force microscopy: role of defects and dynamics in the mechanical switching of atoms. Phys. Rev. B **84**, 085426 (2011)
17. Zh Sun, M. Boneschanscher, I. Swart, D. Vanmaekelbergh, P. Liljeroth, Quantitative atomic force microscopy with carbon monoxide terminated tips. Phys. Rev. Lett. **106**, 046104 (2011)
18. A.J. Weymouth, T. Wutscher, J. Welker, T. Hofmann, F.J. Giessibl, A phantom force induced by the tunneling current, characterized on Si(111). Phys. Rev. Lett. **106**, 226801 (2011)
19. M. Ternes, C. Gonzalez, ChP Lutz, P. Hapala, F.J. Giessibl, P. Jelinek et al., Interplay of conductance, force and structural change in metallic point contacts. Phys. Rev. Lett. **106**, 016802 (2011)
20. C. Chiutu, A.M. Sweetman, A.J. Lakin, A. Stannard, S. Jarvis, L. Kantorovich et al., Precise orientation of a single C60 molecule on the tip of a scanning probe microscope Phys. Rev. Lett. **108**, 268302 (2012)
21. B. Such, Th Glatzel, Sh Kawai, E. Meyer, R. Turanský, J. Brndiar et al., Interplay of the tip-sample junction stability and image contrast reversal on a Cu(111) surface revealed by the 3D force field. Nanotechnology **23**, 045705 (2012)
22. R. Pawlak, Th Glatzel, V. Pichot, L. Schmidlin, Sh Kawai, S. Fremy et al., Local detection of nitrogen-vacancy centers in a nanodiamond monolayer. Nano Lett. **13**, 5803 (2013)
23. T. König, G.H. Simon, H.P. Rust, M. Heyde, Atomic resolution on a metal single crystal with dynamic force microscopy. Appl. Phys. Lett. **95**, 083116 (2009)

24. Z. Majzik, B. Drevniok, W. Kamiński, M. Ondracek, A.B. McLean, P. Jelinek, Room temperature discrimination of adsorbed molecules and attachment sites on the Si(111)-7 × 7 surface using a qPlus sensor. ACS Nano **7**, 2686 (2013)
25. O. Guillermet, S. Gauthier, Ch. Joachim, P. de Mendoza, T. Lauterbach, A. Echavarren, STM and AFM high resolution intramolecular imaging of a single decastarphene molecule. Chem. Phys. Lett. **511**, 482–485 (2011)
26. N. Hauptmann, F. Mohn, L. Gross, G. Meyer, T. Frederiksen, R. Berndt, Force and conductance during contact formation to a C60 molecule. New J. Phys. **14**, 073032 (2012)
27. T. Herden, M. Ternes, K. Kern, The lateral and vertical stiffness of the epitaxial h-BN monolayer on Rh(111). Nano Lett. **14**, 3623 (2014)
28. M.Z. Baykara, M. Todorović, H. Mönig, T.C. Schwendemann, Ö. Ünverdi, L. Rodrigo et al., Atom-specific forces and defect identification on surface-oxidized Cu(100) with combined 3D-AFM and STM measurements. Phys. Rev. B **87**, 155414 (2013)
29. K. Bartzke, T. Antrack, K.H. Schmidt, E. Dammann, C.H. Schatterny, The needle sensor a micromechanical detector for atomic force microscopy. Int. J. Optoelectron **8**, 669 (1993)
30. S. Torbrügge, O. Schaff, J. Rychen, Application of the KolibriSensor to combined atomic-resolution scanning tunneling microscopy and noncontact atomic-force microscopy imaging. J. Vac. Sci. Technol. B **28**, C4E12 (2010)
31. F.J. Giessibl, F. Pielmeier, T. Eguchi, T. An, Y. Hasegawa, Comparison of force sensors for atomic force microscopy based on quartz tuning forks and length-extensional resonators. Phys. Rev. B **84**, 125409 (2011)
32. C.J. Chen, *Introduction to Scanning Tunneling Microscopy* (Oxford University Press, Oxford, 2008)
33. W.A. Hofer, A.J. Fisher, Signature of a chemical bond in the conductance between two metal surfaces. Phys. Rev. Lett. **91**, 036803 (2003)
34. C.J. Chen, Comment on signature of a chemical bond in the conductance between two metal surfaces. Phys. Rev. Lett. **96**, 069701 (2006)
35. W.A. Hofer, A.J. Fisher, Hofer and fisher reply. Phys. Rev. Lett. **96**, 069702 (2006)
36. S. Hembacher, F.J. Giessibl, J. Mannhart, C.F. Quate, Revealing the hidden atom in graphite by low-temperature atomic force microscopy. Proc. Natl. Acad. Sci. USA **100**, 12539 (2003)
37. A. Schirmeisen, G. Cross, A. Stalder, P. Grütter, U. Dürig, Metallic adhesion and tunnelling at the atomic scale. New. J. Phys. **2**, 29 (2000)
38. Y. Sun, H. Mortensen, S. Schär, A. Lucier, Y. Miyahara, P. Grütter et al., From tunneling to point contact: correlation between forces and current. Phys. Rev. B **71**, 193407 (2005)
39. P. Jelínek, M. Ondráček, F. Flores, Relation between the chemical force and the tunnelling current in atomic point contacts: a simple model. J. Phys. Condens. Matter **24**, 084001 (2012)
40. Y. Sugimoto, M. Ondráček, M. Abe, P. Pou, S. Morita, R. Pérez et al., Quantum degeneracy in atomic point contacts revealed by chemical force and conductance. Phys. Rev. Lett. **111**, 106803 (2013)
41. J. Repp, G. Meyer, S.M. Stojkovic, G. Gourdon, C. Joachim, Molecules on insulating films: scanning-tunneling microscopy imaging of individual molecular orbitals. Phys. Rev. Lett. **94**, 026803 (2005)
42. R. Temirov, S. Soubatch, O. Neucheva, A.C. Lassise, F.S. Tautz, A novel method achieving ultra-high geometrical resolution in scanning tunnelling microscopy. New J. Phys. **10**, 053012 (2008)
43. C. Weiss, C. Wagner, C. Kleimann, M. Rohlfing, F.S. Tautz, R. Temirov, Imaging Pauli Repulsion in scanning tunneling microscopy. Phys. Rev. Lett. **105**, 086103 (2010)
44. G. Kichin, C. Weiss, C. Wagner, F.S. Tautz, R. Temirov, Single molecule and single atom sensors for atomic resolution imaging of chemically complex surfaces. J. Am. Chem. Soc. **133**, 16847 (2011)
45. L. Gross, F. Mohn, N. Moll, P. Liljeroth, G. Meyer, The chemical structure of a molecule resolved by atomic force microscopy. Science **325**, 1110 (2009)
46. L. Bartels, G. Meyer, K.-H. Rieder, D. Velic, E. Knoesel, A. Hotzel et al., Dynamics of electron-induced manipulation of individual CO molecules on Cu(111). Phys. Rev. Lett. **80**, 2004 (1998)

47. N. Moll, L. Gross, F. Mohn, A. Curioni, G. Meyer, The mechanisms underlying the enhanced resolution of atomic force microscopy with functionalized tips. New J. Phys. **12**, 125020 (2010)
48. M.F. Gross, N. Moll, B. Schuler, A. Criado, E. Guitian, D. Pena, A. Gourdon, G. Meyer, Bond-order discrimination by atomic force microscopy. Science **337**, 1326 (2012)
49. J.I. Martínez, E. Abad, C. González, F. Flores, J. Ortega, Improvement of scanning tunneling microscopy resolution with H-sensitized tips. Phys. Rev. Lett. **108**, 246102 (2012)
50. P. Hapala, G. Kichin, Ch. Wagner, S.F. Tautz, R. Temirov, P. Jelínek, Mechanism of high-resolution STM/AFM imaging with functionalized tips. Phys. Rev. B **90**, 085421 (2014)
51. J. Zhang, P. Chen, B. Yuan, W. Ji, Z. Cheng, X. Qiu, Real-space identification of intermolecular bonding with atomic force microscopy. Science **342**, 611 (2013)
52. A.M. Sweetman, S.P. Jarvis, H. Sang, I. Lekkas, P. Rahe, Y. Wang et al., Mapping the force field of a hydrogen-bonded assembly. Nat. Commun. **5**, 3931 (2014)
53. Hamalainen S.K., van der Heijden N., van der Lit J., den Hartog S., Liljeroth P., Swart I., Intermolecular contrast in atomic force microscopy without intermolecular bonds, (submitted)
54. J. Tersoff, D.R. Hamann, Theory and application for the scanning tunneling microscope. Phys. Rev. Lett. **50**, 1998–2001 (1983)
55. J. Bardeen, Tunneling from a many-particle point of view. Phys. Rev. Lett. **6**(2), 57–59 (1961)
56. C.J. Chen, Tunneling matrix elements in three dimensional space: the derivative rule and the sum rule. Phys. Rev. B **42**, 8841–8857 (1990)
57. W.A. Hofer, A.S. Foster, A.L. Shluger, Theories of scanning probe microscopes at the atomic scale. Rev. Mod. Phys. **75**, 1287 (2003)
58. K. Palotás, G. Mándi, L. Szunyogh, Orbital-dependent electron tunneling within the atom superposition approach: theory and application to W(110). Phys. Rev. B **86**, 235415 (2012)
59. J.M. Blanco, F. Flores, R. Perez, STM-theory: image potential, chemistry and surface relaxation. Prog. Surf. Sci. **81**, 403 (2006)
60. P. Jelinek, M. Svec, P. Pou, R. Perez, V. Chab, Tip-induced reduction of the resonant tunneling current on semiconductor surfaces. Phys. Rev. Lett. **101**, 176101 (2008)
61. D. Sawada, Y. Sugimoto, K. Morita, M. Abe, S. Morita, Simultaneous measurement of force and tunneling current at room temperature. Appl. Phys. Lett. **94**, 173117 (2009)
62. S. Sadewasser, P. Jelinek, C. Fang, O. Custance, Y. Yamada, Y. Sugimoto, S. Morita et al., New insights on atomic-resolution frequency-modulation kelvin probe force microscopy imaging on semiconductors. Phys. Rev. Lett. **103**, 266103 (2009)
63. P. Hapala, F.S. Tautz, R. Temirov, P. Jelinek, Origin of high-resolution IETS-STM images of organic molecules with functionalized tips. Phys. Rev. Lett. **113**, 226101 (2014)
64. Ch. Chiang, Ch. Xu, Z. Han, W. Ho, Real-space imaging of molecular structure and chemical bonding by single-molecule inelastic tunneling probe. Science **344**, 885 (2014)
65. J.A. Stroscio, R.J. Celotta, Controlling the dynamics of a single atom in lateral atom manipulation. Science **306**, 242 (2004)
66. Y.-H. Zhang, P. Wahl, K. Kern, Quantum point contact microscopy. Nano Lett. **11**, 3838 (2011)
67. G. Schull, Y.J. Dappe, C. Gonzalez, H. Bulou, R. Berndt, Charge injection through single and double carbon bonds. Nano Lett. **11**, 3142 (2011)
68. H. Holscher, U.D. Schwarz, O. Zworner, R. Wiesendanger, Consequences of the stick-slip movement for the scanning force microscopy imaging of graphite. Phys. Rev. B **57**, 2477 (1998)
69. H. Holscher, U.D. Schwarz, R. Wiesendanger, Simulation of a scanned tip on a NaF(001) surface in friction force microscopy. Europhys. Lett. **36**, 19 (1996)
70. F. Mohn, L. Gross, N. Moll, G. Meyer, Imaging the charge distribution within a single molecule. Nat. Nanotechnol. **7**, 227 (2012)
71. D.G. de Oteyza, P. Gorman, Y.-C. Chen, S. Wickenburg, A. Riss, D.J. Mowbray et al., Direct imaging of covalent bond structure in single-molecule chemical reactions. Science **340**, 1434 (2013)
72. L. Gross, F. Mohn, N. Moll, G. Meyer, R. Ebel, W.M. Abdel-Mageed et al., Organic structure determination using atomic-resolution scanning probe microscopy. Nat. Chem. **2**, 821 (2010)

73. N. Neu, N. Moll, L. Gross, G. Meyer, F.J. Giessibl, J. Repp, Image correction for atomic force microscopy images with functionalized tips. Phys. Rev. B **89**, 205407 (2014)
74. S. Aradhya, L. Venkataraman, Single-molecule junctions beyond electronic transport. Nat. Nanotechnol. **8**, 399 (2013)
75. D. Dundas, E.J. McEniry, N. Todorov, Current-driven atomic waterwheels. Nat. Nanotechnol. **4**, 99 (2009)
76. S.J. van der Molen, P. Liljeroth, Charge transport through molecular switches. J. Phys. Condens. Matter **22**(13), 133001 (2010)
77. H. Holscher, U.D. Schwarz, O. Zworner, R. Wiesendanger, Consequences of the stick-slip movement for the scanning force microscopy imaging of graphite. Phys. Rev. B **57**, 2477 (1998)
78. S. Fujisawa, E. Kishi, Y. Sugawara, S. Morita, Atomic-scale friction observed with a two-dimensional frictional-force microscope. Phys. Rev. B **51**, 7849 (1995)

Chapter 4
Manipulation and Spectroscopy Using AFM/STM at Room Temperature

Masayuki Abe, Yoshiaki Sugimoto and Seizo Morita

Abstract In the atom manipulation process with atomic force microscopy (AFM) at room temperature, reduction of the local energy barrier induced by interaction forces between atoms of a tip and a surface plays a key role. This means that the force value depending on the tip-apex condition determines the success of manipulation. In the first part of this chapter, the probability of the AFM atom manipulation is discussed. It is found that the value of the maximum attractive force, i.e. the tip reactivity, determines the manipulation capability. In addition, the potential barrier reduction can be used for various purposes such as local chemical reactions, barrier height control of the potential of nanospace, and fabrication of atomic-sized materials (i.e., nanoclusters). In the second part of the chapter, nanoclusters are fabricated as an application of the AFM atom manipulation. Half-unit cells of the Si(111)-(7 × 7) are used as a nanospace for structuring the atomic-sized clusters.

4.1 Introduction

Atomic force microscopy (AFM) is an important tool for characterizing various nanostructures and sample surfaces, including insulators. Stable acquisition of atomic resolution images can now be achieved using the frequency modulation technique [1],

M. Abe (✉)
Center for Science and Technology Under Extreme Conditions,
Graduate School of Engineering Science, Osaka University,
1-3, Machikaneyama-Cho, Toyonaka, Osaka 560-8531, Japan
e-mail: abe@stec.es.osaka-u.ac.jp

Y. Sugimoto
Department of Electrical, Electronic and Information Engineering,
Graduate School of Engineering, Osaka University, Yamada-Oka 2-1,
Suita 565-0871, Japan
e-mail: sugimoto@afm.eei.eng.osaka-u.ac.jp

S. Morita
Nanoscience and Nanotechnology Center, The Institute of Scientific and Industrial Research,
Osaka University, 8-1 Mihogaoka, Ibaraki, Osaka 567-0047, Japan
e-mail: smorita@eei.eng.osaka-u.ac.jp

© Springer International Publishing Switzerland 2015

S. Morita et al. (eds.), *Noncontact Atomic Force Microscopy*,
NanoScience and Technology, DOI 10.1007/978-3-319-15588-3_4

wherein a cantilever is oscillated at its resonance frequency (f_0), and the frequency shift (Δf) caused by the tip-surface interaction force is detected [2, 3]. As an application of the frequency modulation AFM, measurement of the tip-surface distance dependence of the Δf (so-called force spectroscopy) [4] enables analysis of single-atom chemical properties [5, 6].

Atom manipulation using AFM [7–17] has recently become a fascinating area of research, since the AFM manipulation experiments can be performed not only at low temperature but also at room temperature. Another attractive feature of the AFM atom manipulation is that the AFM can measure the driving forces involved in the atom manipulation process at the same time. Ternes et al. manipulated metal adsorbates on a metal surface at low temperature, and concluded that the lateral force acting on the AFM tip determined the manipulation process [9]. Conversely, on semiconductor surfaces at room temperature, the vertical force plays a dominant role [8]. This striking difference was attributed to the presence of highly directional covalent bonds on semiconductor surfaces. The measurements of forces during the manipulation process have provided the signatures of specific mechanical atom manipulation processes [8, 9, 14, 18]. In the attractive tip-sample interaction regime, reduction of the local energy barrier between atoms induced by interaction forces between the tip and surface atoms was found to be a key in the manipulation process (Fig. 4.1) [8, 18–20]. Surface atoms do not move to a neighboring site unless the tip reduces the surface potential barrier sufficiently for the surface atom to "hop".

From a slightly different perspective, reduction of the potential barrier can be used for various purposes, such as local chemical reactions and height control of the potential of nanospaces, and fabrication of atomic-sized materials (i.e., nanoclusters). Scanning tunneling microscopy (STM) has been used to create atomic-sized structures [21] at low temperature. This method has also been applied for the creation of various artificial nanostructures in an atom-by-atom fashion [22–25]. It has been proven that AFM could be used for the atomic-size creation even at room temperature [26]. Despite these achievements, the assembly of well-defined clusters exhibiting high thermal stability at room temperature and precise determination of the cluster size remain challenging tasks [27]. More importantly, the assembly of nanoclusters

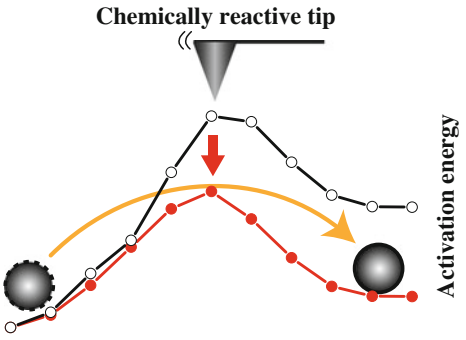

Fig. 4.1 Principle model for explaining the atom manipulation using atomic force microscopy (AFM) at room temperature

from multi-elements at room temperature has not been demonstrated, despite the wide potential range of technical applications for such assembly.

In the first part of this chapter, the probability of atom manipulation is discussed. Attractive force maxima over the Si adatoms are measured using a large variety of tips, and their relations to the manipulation probability at room-temperature are investigated. We found that the atom manipulation capability and its efficiency in the manipulation process are strongly dependent on the maximal force of a tip acting on the Si adatom. It is also found that the tip reactivity determines not only the manipulation capability but also the spatial resolution of AFM. In the second part of this chapter, as an application of the AFM atom manipulation, we propose a novel technique to assemble various atom clusters composed of a defined number of atoms at room temperature. Half-unit cells of the Si(111)-(7 × 7) are used as nanospaces for structuring the atomic-sized clusters. By reducing the height of the potential barrier of the nanospace (i.e., the boundary of the Si(111)-(7 × 7) half-unit cell) in the attractive region, AFM tip opens the "gate" for an atom to move to a neighboring nanospace.

4.2 Relation Between Manipulation Probability and Tip Reactivity

In the AFM manipulation process, the tip-apex structure, orientation, and chemical nature influence the success rate [18]. For example, tip reactivities (i.e., the maximum attractive force of the AFM tip) are different even if same type cantilevers are used [5]. In order to increase the efficiency of the atomic manipulation process, a detailed understanding of the tips exhibiting different interaction characteristics is therefore required.

Here we will show the probability of displacing a Si adatom to a vacancy site on the Si(111)-(7 × 7) surface as a function of the tip-sample distance. The statistics of the lateral manipulation of Si adatoms for various processes are produced using many tips that span a broad range of attractive force maxima over the Si adatoms. It is shown that the atom manipulation capability and its efficiency in this particular manipulation process are strongly dependent on the maximal force of a tip acting on the Si adatom.

4.2.1 AFM Setup

The experiments were performed using a home-built ultrahigh-vacuum AFM operated at room temperature. The AFM operation mode used here was the frequency modulation (FM) detection [1], which we have previously used to perform atom manipulation experiments [8, 10, 26, 28]. Commercial Si cantilevers were cleaned

by Ar ion sputtering prior to the imaging and manipulation experiments to remove native oxide layers and other contaminants. A sample bias voltage (V_s) was applied so that the electrostatic force was minimized. Undesired tip-sample motion due to the thermal drift was compensated during the experiment at the appropriate time point: measurement of the drift velocity [29] and its use as a feedforward [30] parameter were performed. The thermal drift compensation enables us to perform room-temperature experiments of atom-manipulation and site-specific force spectroscopy with a lateral precision of 0.1 Å.

4.2.2 Vacancy Formation on the Si(111)-(7 × 7) Surface

For suitable atom manipulation experiments, we selected a center of terrace of the Si(111)-(7 × 7) surface. Since we need a vacancy to perform the experiment, as indicated by the drawing in Fig. 4.2a, we created a vacancy site by mechanical indentation [31]. The process for the vacancy creation is outlined below: we positioned the AFM tip over a Si adatom to be removed, and then opened the z feedback to close and retract the AFM tip from the Si surface by a certain displacement that was preliminarily input. If a vacancy was not created in the AFM image obtained just after the z displacement of the AFM tip, we repeated the same process with a gradual increment of the displacement until we found the vacancy. After repeated indentations, the tip apex may become unstable or a clear atomic resolution image may not been obtained. We moved the AFM tip position 10 nm laterally away from the vacancy site, and scanned it vertically until it became stable.

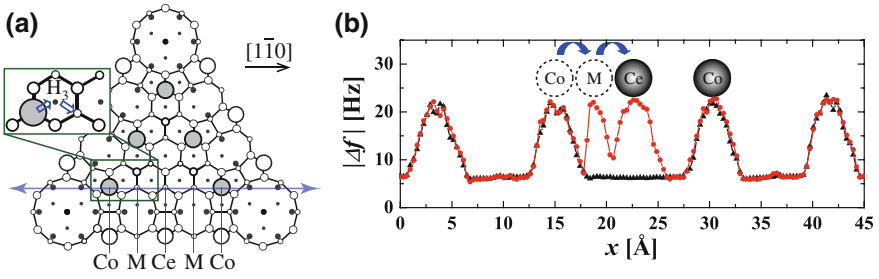

Fig. 4.2 **a** A schematic model of a half-unit cell of a Si(111)-(7 × 7) surface. *Gray circles* are Si adatoms, and a vacancy exists at the center (Ce) adatom site. The *zoom out* indicates the detail of the most favorable adatom hopping path from a corner (Co) adatom → a hollow site (H_3) → a meta stable (M) site. Successive forward and backward tip scans above the line connecting the two Co sites including the vacancy Ce site are carried out. **b** Two examples of Δf line profiles reveal the dynamics of the Si adatom during the manipulation process acquired with the same scan parameters. The *line profile* indicated with *triangles* does not show the atom hopping signature while the profile with *circles* shows atom hopping from a Co to a Ce site *via* the M site

4.2.3 Confirmation of Tip Reactivity

Since we know that, in previous studies, the tip approach reduced the potential barrier between two atomic sites in the room-temperature manipulation, the tip-apex condition determines the performance of the atom manipulation experiment. This is why, prior to the manipulation experiments, we performed force spectroscopic measurements above a Si adatom. The obtained distance-dependence curve of the frequency shift ($\Delta f - z$ curve) was inverted to force distance curve ($F - z$ curve) using Sader's method [32]. We eliminated long-range component from the inverted $F - z$ curve to obtain a short-range force (F_{SR}) having a high correlation with atomic resolution imaging. The maximum attractive value of F_{SR} varies even if the same commercial AFM tips are used [5]. This means that the chemical reactivity of the AFM tip is not the same.

4.2.4 Atom Manipulation Procedures

Atom manipulation requires precise adjustment of the scan line above the center of a vacancy and a target adatom. While the compensation of the thermal drift is activating, in order to manipulate a Si adatom to the vacancy site, we carried successive line scans above the line connecting the vacancy and the target adatom (in the $[1\bar{1}0]$ direction). Constant height scans where the tip-surface feedback was turned off were used to obtain reliable statistics on the atom manipulation procedure at well-defined distances. The Δf signal was recorded simultaneously during the scan. For control of the scan direction, we used a versatile scan controller [33]. Since the probability of adatom hopping to the adjacent vacancy side depends on the interaction force [8], we performed the manipulation line scan at different tip-sample distances to investigate the change of the manipulation probability. For example, when the line scan was performed as shown in Fig. 4.2a, we obtained two types of Δf line profiles in Fig. 4.2b. From these line profiles, we found two different outcomes starting from the same initial atom configuration. Even under the same scan conditions, there was a case that atom hopping occurred or not. In Fig. 4.2b, the profile with triangles does not show Δf at the Ce site, which means the Ce site is the vacancy. On the other hand, Δf with circles shows the existence of an adatom not only at the Ce site but also at the M site. This indicates that the Co adatom at the left side hops to the Ce site via the M site during the scan. After this process, the vacancy was located on the left Co site.

Figure 4.3(a_1–f_2) shows changes over time in the constant height Δf line profile. Successive line scans above the same line on the Si(111)-(7 × 7) surface along the $[1\bar{1}0]$ direction visualize the atom manipulation processes as images. We got the AFM tip closer to the surface in order to obtain the images $a_{1,2}$ to $f_{1,2}$. The subscript notation indicates the fast scan direction: the scan passes through from left to right (a_1–f_1) and right to left (a_2–f_2) along the $[1\bar{1}0]$ line. We emphasize that the tip apex did

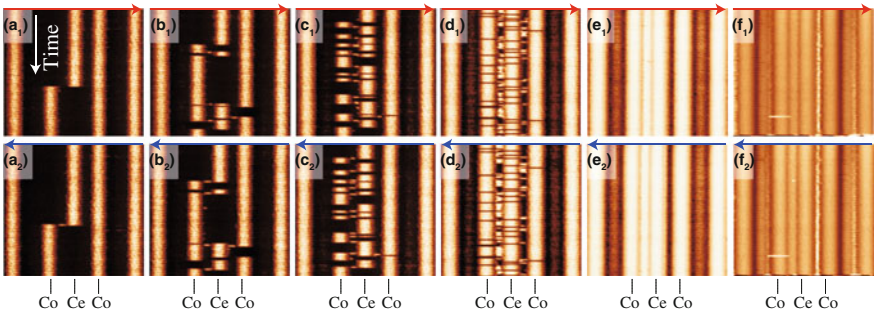

Fig. 4.3 Atom manipulation images composed by the successive line scan profiles (the constant height Δf) at different tip-sample distances. The *subscript notation* indicates the fast scan direction from *left* to *right* (a_1–f_1), and *right* to *left* (a_2–f_2). The tip-sample distances for data acquisition were $z = 0.21$ Å (a_1, a_2), $z = 0.12$ Å(b_1, b_2), $z = 0.02$ Å (c_1, c_2), $z = -0.17$ Å (d_1, d_2), $z = -0.31$ Å (e_1, e_2), and $z = -1.16$ Å (f_1, f_2). The z values were determined from the force curves acquired before the experiments shown here. $z = 0.0$ Å is defined at the distance where the force takes the minimum value

not change during this series of experiments. In the images, the bright and continuous stripes as well as the intermittent stripes in the Δf images indicate the position of the Si adatom during the manipulation processes. The success of the manipulation process could be inferred from the pattern of Δf images and from the line profiles.

The Si adatoms happened to change their adsorption locations among the corner adatom (Co), meta-stable (M), and center adatom (Ce) sites by interaction with the tip when the tip was repeatedly scanned at sufficiently small tip-surface distances along the same line. The probability of a change in the induced site due to the tip-sample interaction depends on the tip-sample distance under the same tip-apex condition. In Fig. 4.3, we observed various types of line profiles corresponding to different atom-hopping processes, meaning the stochastic nature of the hopping processes at room temperature [11]. Since a continuous stripe means that the tip manipulates the Si adatom at a high rate, a closer tip-sample distance has higher probability for the atom move.

4.2.5 Relation Between Measured Force and Atom Manipulation Probability

Analyses of the line profiles in Fig. 4.3 reveal the relation between the atom manipulation probability and the force acting on the tip apex. We analyzed more than 3000 line profiles to find the distance dependence of the probability, as shown in Fig. 4.4. Here, the probability is defined as the ratio of the number of successful atom movements to the total number of line scans (i.e., manipulation attempts), which are represented as a percentage. In Fig. 4.4, solid circles, open circles, and open triangles give atom

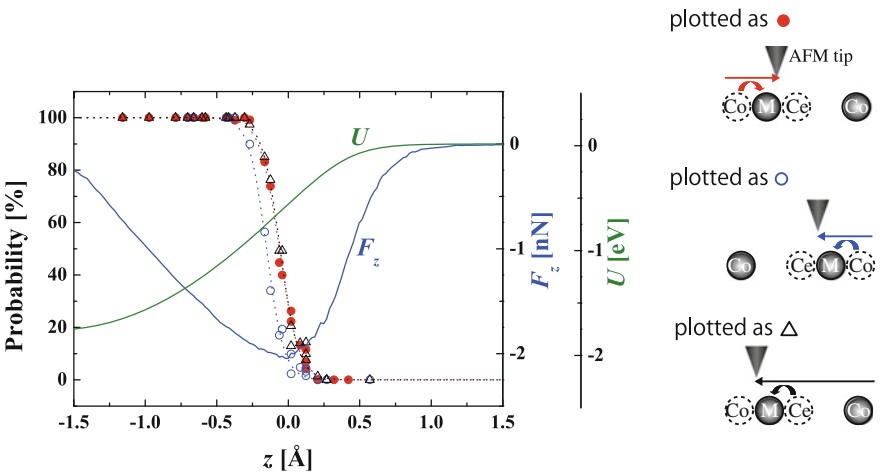

Fig. 4.4 Relation between atom manipulation probabilities and tip-sample distance from the *left* Co to the M site (*solid circles*), from the *right* Co to the M site (*open circles*), and from the Ce to the M site (*open triangles*). The plots are fitted to an empirical step function, $P(z) = 100/[1 + \exp[\alpha (z - z_0)]]$, where α is the thermal broadening coefficient and z_0 is defined as the distance for $P = 50\,\%$. $F_z(z)$ and $U(z)$ curves obtained above the Co adatom using the same tip are also shown. *Right side* figures indicate three types of the Si adatom hopping by tip scan

manipulation probabilities from the left Co to the M site, from the right Co to the M site, and from the Ce to the M site, respectively.

Each of these processes is illustrated schematically on the right side of Fig. 4.4. The short-range force curve $[F_z(z)]$ together with the potential energy curve $[U(z)]$ which are inverted from the $\Delta f(z)$ curve on a Co adatom are also indicated in Fig. 4.4. The $F_z(z)$ and $U(z)$ curves acquired over the Co adatom site are used as a reference for estimation of the tip-sample distances. Even in the attractive force region, the hopping probability is almost zero, but it drastically increases from 0 to 100 % at around the distance of the maximum attractive F_z region.

A comparison of the probability difference of the scan direction (solid plot as left-to-right tip scan, and open plots as right-to-left scan) revealed that the probability was also dependent on the scan direction, as shown in Fig. 4.4. The probability of atom movement from left to right along the Co to the M site is higher than the probability of movement from the right to the left. Since the manipulation pathways of both directions are symmetrical, the difference in probability should come from the tip asymmetry and/or the orientation of the tip-apex dangling bond with respect to the surface adatoms. The ability to vertically manipulate atoms on semiconductors depends strongly on the orientation of the dangling bonds at the tip apex with respect to the target atom [34]. This means that the directional difference in the dangling bond alignment with respect to the target atom leads to a variation of the manipulation probability.

By comparing the site difference with the same scan direction, it is found that the probability for adatom hopping from the Ce to the M site (triangles) is higher than that from the Co to the M site (open circles) at the same tip-surface distances. This difference results from the difference in the diffusion energy barrier. The results do not contradict previous experimental investigations based on adatom extraction [35] and displacement [36] acquired by applying a voltage pulse to the Si(111)-(7 × 7) surface. The above-described results, including those of the AFM manipulation in this chapter, suggest that a higher energy barrier is associated with the transition from the Co to the M site.

4.2.6 Tip Reactivity and Manipulation Capability

Although the probability of AFM atom manipulation depends on the tip-sample distance, there are AFM tips that can not move Si adatoms even at closer tip-sample distance. As shown in Fig. 4.5a, the probability of atom manipulation (solid circle) with this type of AFM tip continues to be zero even when the tip approaches the surface beyond the maximum attractive force region. But tip-apex modification due to gentle contact between the tip and sample does result in the probability change. Figure 4.5b shows the distance dependence of the manipulation probability after the gentle contact of the AFM tip of Fig. 4.5a. Although the same tip was used, the probability began to increase at the distance of the maximum attractive force due to the tip-apex change. It was found that the difference between before and after the gentle contact was the difference between the maximum attractive forces, which were ≈1.2 nN and ≈1.7 nN, respectively.

In order to investigate the relation between the manipulation capability and the maximum attractive force values, we performed the same experiment with 15 different states of the AFM tip apex using 10 cantilevers, where gentle tip contact with the sample surface enabled the tip apex to be in a different state. Figure 4.6 is a histogram of the maximum attractive forces measured above Si adatoms using 15 different tip

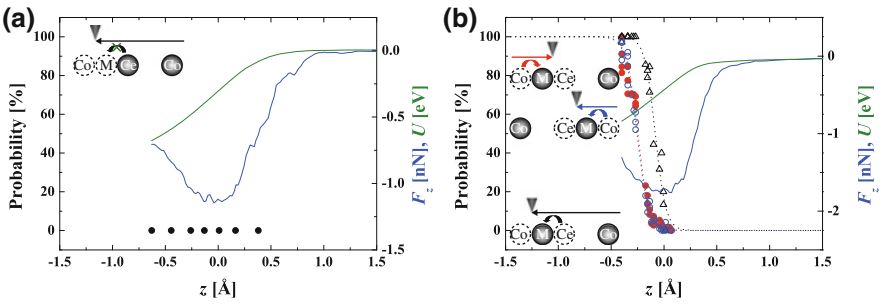

Fig. 4.5 **a** A case zero with manipulation probability in the whole measured region (*solid circle*). $F_z(z)$ and $U(z)$ are shown together to refer the tip-sample distance. The distance of the maximum attractive force is defined as $z = 0$ Å. **b** The same data set after the tip-apex modification done by gentle tip-sample contacts

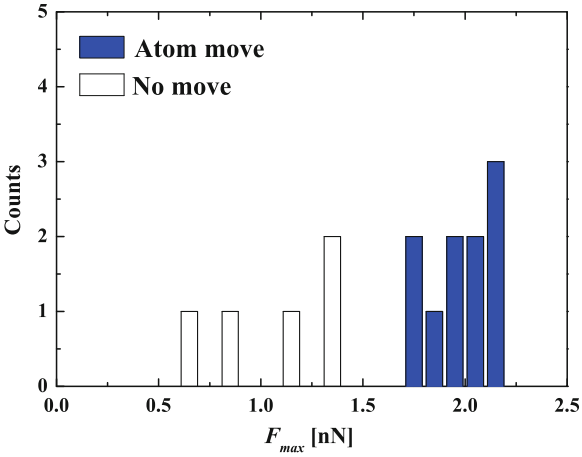

Fig. 4.6 Histogram of the maximum attractive forces measured above Si adatoms; the histogram was obtained using 15 different tips, and reveals the relationship between the magnitude of the maximum attractive force and the capability of atom manipulation

apexes. In the histogram, the solid and the white counted on each force values indicate whether or not the manipulation occurred, respectively. The histogram has wide distribution, but the capability of the atom manipulation separate distinctly at around ≈1.5 nN.[1] This means that the tip reactivity determines whether the tip can induce the manipulation: the Si adatoms can be manipulated with the reactive tips, but not with less-reactive tips.

4.2.7 Tip Reactivity and Spatial Resolution

The signatures attributed to the atom manipulation capabilities of the tips also appear in the AFM topographic images. Figure 4.7a, b shows AFM topographic images using the tips that can move the atom and those that can not, respectively. The tips of Fig. 4.7a, b have maximum attractive forces of ≈2.0 nN and ≈1.2 nN. The tip of Fig. 4.7b, which has no ability to manipulate Si adatoms, resolves the Si rest atoms together with adatoms.

4.3 Inter-nanospace Atom Manipulation for Structuring Nanoclusters

As a application field of the atom manipulation experiments, nanoclusters are of great importance in physics and chemistry as well as in technical applications, such as single electron transistors [39, 40], nanocatalysts [41–43], and quantum

[1] Such a broad dispersion of F_{max} can be attributed to the varying degrees of tip-apex chemical reactivity [37, 38].

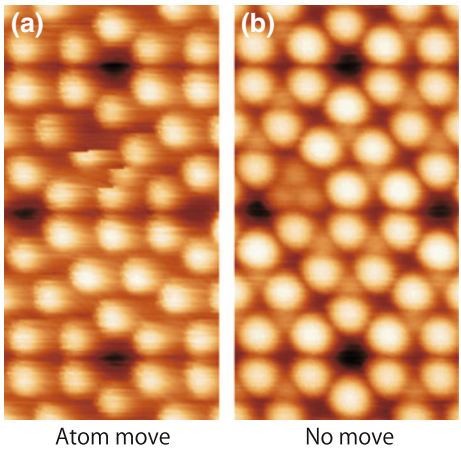

Fig. 4.7 AFM topographic images of Si(111)-(7 × 7) showing different spatial resolutions with different types of tip apex. In the experiment of **a** the AFM tip has a larger maximum attractive force (≈2.0 nN) and reduced the potential barrier until the atom manipulation occurred. With the AFM tip of **b** the Si adatom could not be moved, but rest atoms were resolved in imaging. The AFM tip has a smaller maximum attractive force (≈1.2 nN)

computing devices [44]. The properties of nanoclusters are highly sensitive to size and chemical composition. For example, Au clusters of nm-scale show size effects on catalytic behavior [41, 43]. For a fundamental understanding of atomically well-defined clusters, it is essential to control number of atoms. Although the cluster formation method allows us to obtain uniform cluster arrays [45, 46], one cannot determine the number of atoms involved in a cluster structure once they are deposited on surfaces.

Recently, we have demonstrated an alternative approach to fabrication of single nanoclusters using the same principle as used for AFM atom manipulation at room temperature (Inter-nanospace Atom Manipulation; INSAM) [47]. This method allows us to create nanoclusters with different chemical compositions and to evaluate their chemical stabilities. In this section, the assembly of various nanoclusters in an atom-by-atom fashion using the AFM at room temperature is shown. The method is based on the transfer of single diffusing atoms among nanospaces governed by "atomic gates," in which potential barriers are reduced by the AFM tip.

4.3.1 Method for Inter-nanospace Atom Manipulation

Figure 4.8 shows the concept of the INSAM process for fabricating a nanocluster. We consider that a small area is surrounded by a potential barrier, which is called a "nanospace" in this chapter. An adsorbate atom in the nanospace would move due to the thermal diffusion, but would not go over the barrier. In the INSAM operation, the approach of the AFM tip near the surface causes a decrease in the potential barrier,

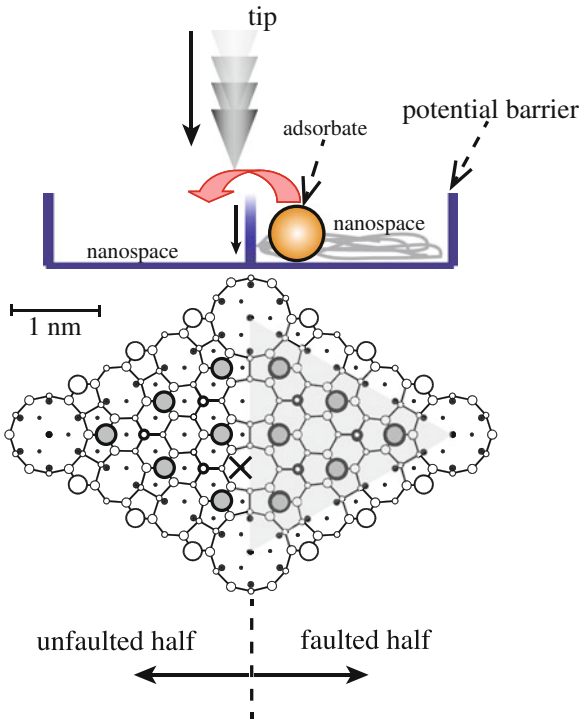

Fig. 4.8 Concept of Inter-nanospace Atom Manipulation (INSAM). The approach of the AFM tip near the surface reduces the potential barrier, allowing the adsorbed atom to "hop" to a neighboring nanospace. Here, we use half-unit cells of Si(111)-(7 × 7) as the nanospace

and thereby induces movement of the adsorbed atom to a neighboring nanospace. In the experiment described here, we used a half-unit cell in the Si(111)-(7 × 7) surface works as a nanospace of an equilateral triangle with side lengths of 2.7 nm. The adsorbate atom travels among the various potential minima in a nanospace. These minima are known to be multi-coordinate sites rather than the tops of Si adatoms and rest atom sites [48]. The successive INSAM operations allow us to assemble single atoms to the predetermined nanospace: we can control the number of atoms to configure nanoclusters. Further, various elements can be moved, and the relation between electronic and geometrical properties of nanoclusters can be investigated just after the fabrication using AFM/STM and other scanning probe techniques.

Given the fact that nanoclusters on surfaces have a wide range of applications, it becomes important to construct ordered and well-defined cluster arrays with a defined number of atoms. We expect that nanoclusters constructed from a well-determined number of atoms would provide evidence of the unique size-dependent properties.

4.3.2 AFM/STM Setup for the INSAM Operation

We performed the experiments for the INSAM method not only with AFM but also with STM and AFM/STM with metallic cantilever. The experiments were carried

out using an ultrahigh-vacuum AFM as mentioned in Sect. 4.2.1. Commercial Pt-Ir-coated Si cantilevers (NCLPt, NanoWorld) were used for the STM measurements. Metallic cantilevers can demonstrate conventional (static) STM measurement without cantilever oscillation. In the AFM/STM mode, the cantilevers need to be oscillated for AFM operation, so STM is operated in the dynamic mode. In the dynamic STM, the tunneling current flows instantaneously at a close tip-surface distance during cantilever oscillation. The time-averaged tunneling current ($\langle I_t \rangle$) is then detected, since the bandwidth of the current-to-voltage converter is usually much smaller than the resonance frequency of the cantilever [49]. A bias voltage (V_s) was applied to the sample with respect to the tip, which was virtually grounded using an operational amplifier. The tunneling current I_t signal was measured from the tip. Elements of Si, Sn, Pb, Ag, and Au were deposited onto the Si(111)-(7 × 7) surface to form the nanoclusters. The element deposition was performed by using a Joule heating evaporator in an ultra-high vacuum, while the Si sample temperature was kept at room temperature.

4.3.3 Inter-nanospace Atom Manipulation of Various Elements

Figure 4.9 shows STM (a–f) and AFM (g, h) images before and after the INSAM operation to various elements on the Si(111)-(7 × 7). Single atoms of Au (a → b), Ag (c → d), Pb (e → f), Sn (g → h) deposited on the Si(111)-(7 × 7) surface are imaged. In Fig. 4.9a, three single Au atoms are imaged: two of them are in the faulted half-unit cells and one is in the unfaulted half-unit cell. Three half-unit cells with Au atoms appear brighter than the half-unit cells without Au atoms. The contrast of the STM image of the two different half-unit cells (faulted and unfaulted) occupied by single Au atoms appears to be different. Corner (center) adatoms were imaged more brightly than center (corner) adatoms in the faulted half-unit cell (unfaulted half-unit cell) in the filled-state STM images. The results are consistent with the results of the previous studies [50, 51]. In the case of the other elements, the contrast of the faulted sites is different from that of the unfaulted sites. This difference in contrast is attributed to the electronic structure modifications and the topographic differences between the faulted and unfaulted sites. As is the case in Au atoms, the diffusion rate of the adsorbates in the nanospace is so large that an STM image cannot resolve the specific adsorption sites offered by the surface at room temperature [52]. And the different adsorbate atoms on the Si(111)-(7 × 7) appear differently in the STM images due to differences in the diffusion properties.

As the tip gradually approaches the position indicated by a cross in the Si(111)-(7 × 7) unit (a, c, e, g), the adsorbate atom moves to the neighboring half-unit cell (b, d, f, h). The approach was repeated until the diffusing atom was successfully transferred into the desired nanospace.

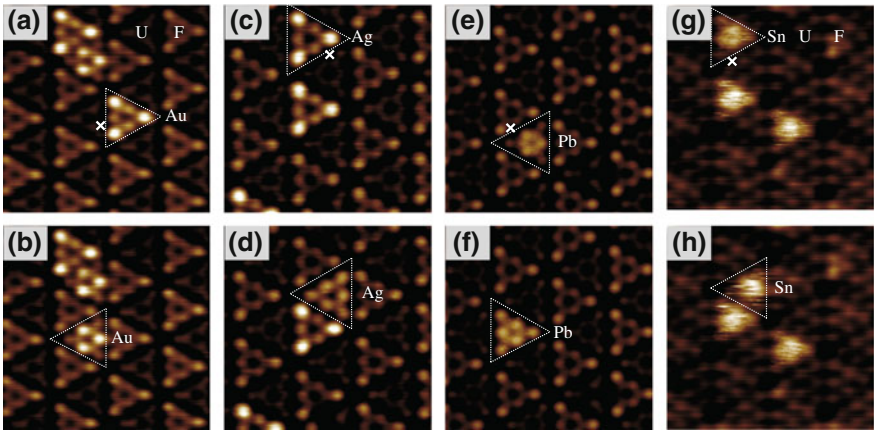

Fig. 4.9 STM (**a**–**f**) and AFM (**g**, **h**) images before and after the INSAM of various elements on the Si(111)-(7 × 7). The tip gradually approaches the position indicated by a cross in the Si(111)-(7 × 7) unit cell to move single atoms of Au (a → b), Ag (c → d), Pb (e → f), Sn (g → h). F and U denote faulted and unfaulted half unit cell, respectively. The bias voltage and the tunneling current set points for STM imaging are $V_s = -1000\,\mathrm{mV}$ and $I_t = 30\,\mathrm{pA}$ (**a**, **b**), 50 pA (**c**, **d**), and 40 pA (**e**, **f**), respectively. The bias voltage in the INSAM for Sn was $V_s = 0\,\mathrm{V}$. The acquisition parameters for AFM imaging were $f_0 = 153972.5\,\mathrm{Hz}$, $k = 25.2\,\mathrm{N/m}$, $A = 198\,\text{Å}$, and $\Delta f = -2.1\,\mathrm{Hz}$

The INSAM operations of g–h are performed with the 0 V bias voltage. The Sn atom can be successfully relocated into the predetermined nanospace using an AFM tip. This is strong evidence that the INSAM is caused by the mechanical (force) effects and not by tunneling current.

4.3.4 Fabrication of Nanocluster Using Inter-nanospace Atom Manipulation

Complex nanoclusters can be fabricated by repeating the INSAM operation. As an example, the assembly of Au_N clusters (N = 1–17) is demonstrated in Fig. 4.10. We fabricated these clusters by bringing single Au atoms into the predetermined nanospace one-by-one using the INSAM method. Atom-by-atom assembly allows us to study the dependence of the cluster stability on the size of clusters or the number of atoms that compose them. While Au_1–Au_3 clusters show quick thermal diffusion, Au_4 and Au_7–Au_{12} clusters retain stable structures, and no changes were observed in their appearance over several hours. The Au_5 and Au_6 clusters were relatively stable within the scanning time scale, but we confirmed the structure changes of Au_5 and Au_6. These changes occurred unexpectedly every several minutes to be conformations among equivalent forms by following the threefold and/or the mirror symmetry of the surface. A threefold symmetry contrast was obtained in STM images on Au_7–Au_{11} clusters. These clusters are similar to the self-assembled

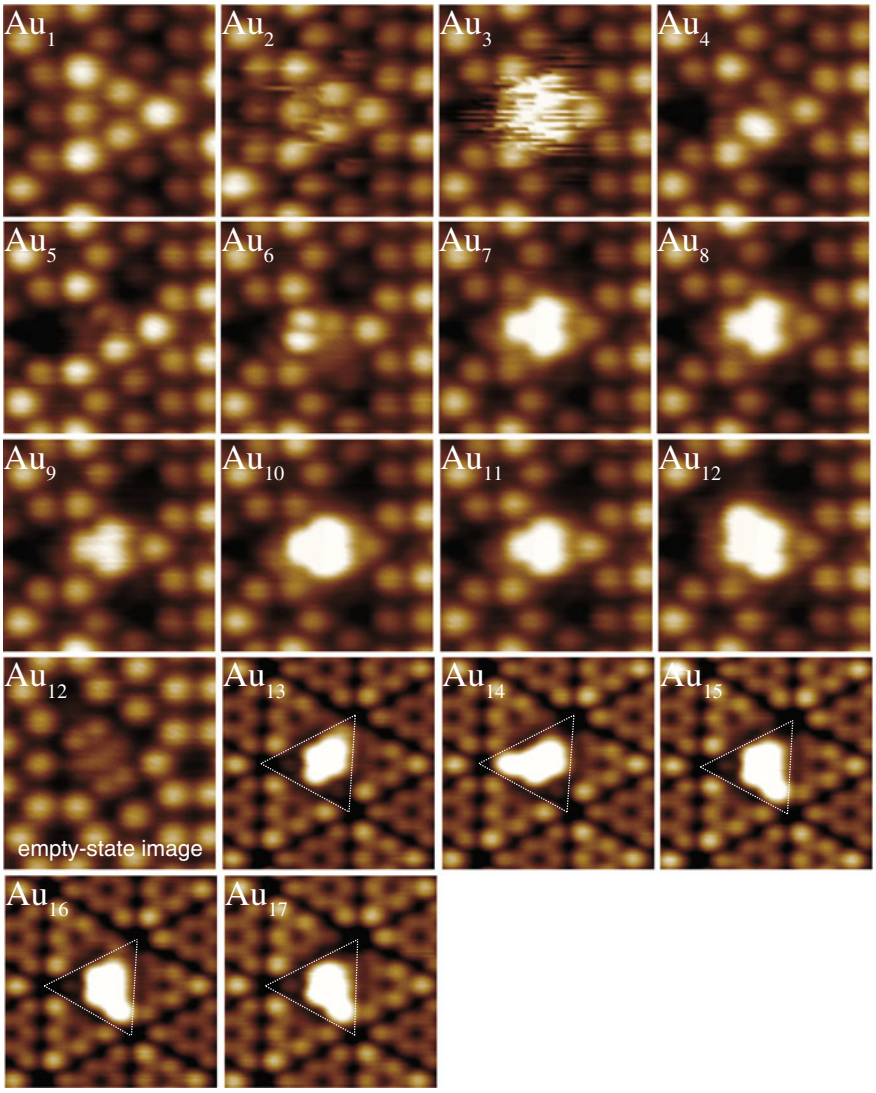

Fig. 4.10 Fabrication of Au atom clusters (Au_1–Au_{17}) using the INSAM method on the half unit cell of the Si(111)-(7 × 7) surface. The imaging parameters were $V_s = -500\,mV$ and $I_t = 30\,pA$ for Au_1–Au_{12} and $V_s = -1000\,mV$ and $I_t = 30\,pA$ for Au_{13}–Au_{17}. One of the Au_{12} STM images is acquired in the empty-state mode ($V_s = 1000\,mV$ and $I_t = 40\,pA$)

clusters observed previously [53, 54]. In contrast, the structure of Au_{12} did not retain the threefold symmetry. From both the filled- and empty-state STM images, we find that the Au_{12} structure has a mirror symmetry. By repeating it further, we finally succeeded in fabricating the Au_{17} cluster.

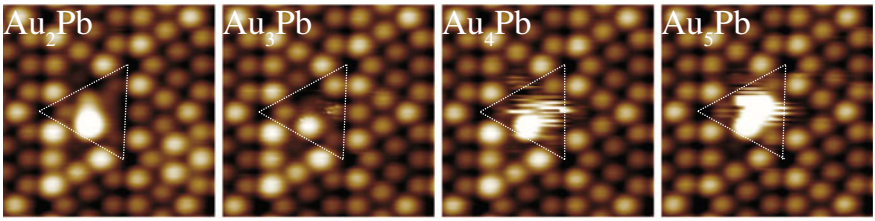

Fig. 4.11 STM images of multi-element atom clusters showing the influence of a single Pb atom on the stability of Au_2–Au_5 clusters assembled by atom gating control. The acquisition parameters were $V_s = -1000\,\mathrm{mV}$ and $I_t = 30\,\mathrm{pA}$

The INSAM operation can also be used to assemble multi-element clusters. The composition can be designed and controlled in the cluster in an atom-by-atom fashion. The images in Fig. 4.11 are bimetallic clusters involving metal atoms of two different species assembled using the INSAM operations. The presence of the single Pb atom in Au_2 can stabilize the Au_2Pb cluster, although Au_2 and Au_3 are mobile at room temperature. In contrast, the Au_4Pb and Au_5Pb clusters exhibit two distinct features separated by partially stable round and fuzzy features in the STM images, whereas Au_4–Au_6 are relatively stable (see Fig. 4.10). Details of the characteristics of clusters are described in [47].

4.3.5 Distance Spectroscopic Measurement During INSAM Operation

To understand the mechanisms underlying the INSAM operation, we performed force-distance spectroscopy acquired together with the INSAM operation using AFM/STM. Since the tip is closed to the surface to reduce the potential barrier in the INSAM operation, one can measure the distance dependence at the same time. The simultaneously measured distance dependence of the tunneling current (I_t), the energy dissipation, and the force during the INSAM operation of the Au atom are shown in Fig. 4.12. During the decrease in the tip-sample distance for the INSAM operation, I_t varies exponentially with distances (see the "Approach" curve in Fig. 4.12a). Then, discontinuous jumps are observed at $z = 0.3\,\text{Å}$ in all signals. This comes from an Au atom hop from the original nanospace to the neighboring nanospace located below the tip. Once the Au atom is transferred to the nanospace below the tip, trapping and release of the Au atom occurs repeatedly due to the large cantilever oscillation amplitude used in our experiments. The trap and release cycles of the Au atom should not happen when the closest tip-sample distance is out of the interaction region.

There are three distance regions in the distance curves, which are determined by the observed differences in their slopes: the trapping and release region ((i) $z \leq 1.2\,\text{Å}$),

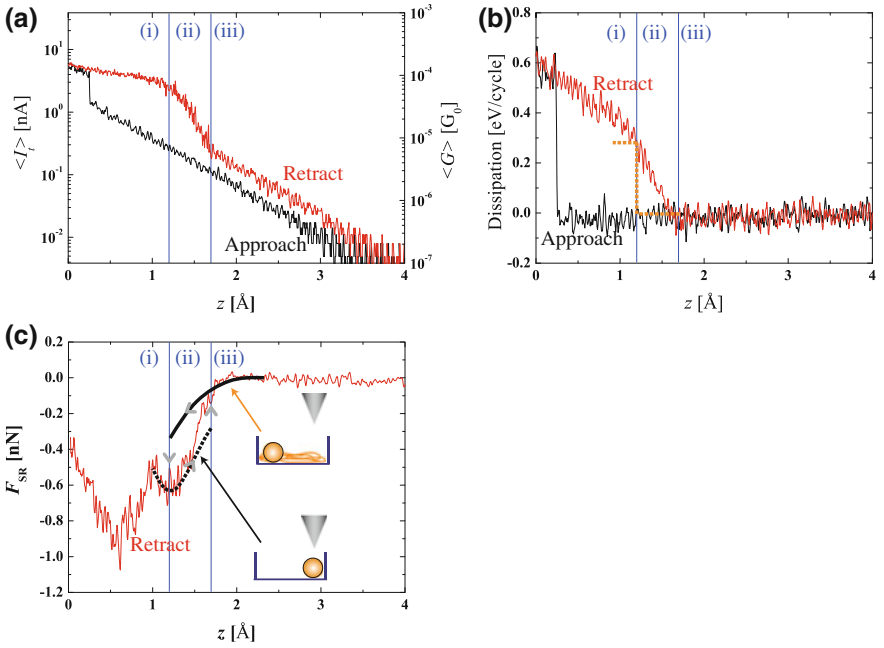

Fig. 4.12 Simultaneous measurements of **a** $\langle I_t(z) \rangle$ and **b** energy dissipation and **c** short-range force curves (F_{SR}) as a function of the tip-sample distance during the INSAM operation for the Au atom on the Si(111)-(7 × 7). The sample bias is $V_s = -500$ mV during the data acquisition. The short-range force was inverted from $\Delta f(z)$ [32] and the background long-range force was subtracted

the region of transition from contact to tunneling ((ii) $1.2 \leq z \leq 1.7$ Å), and the free diffusion region ((iii) $z \geq 1.7$ Å). In region (i), I_t decreases with smaller slope by increasing tip-sample distance. In this regime, the formation and collapse of the tip-Au-surface atomic junction are repeated for every tip oscillation cycle, and the ballistic current would flow through the junction at around the lowest tip point. In region (ii), the slope of the $I_t(z)$ curve is larger than that of region (i), and more importantly, the Au atom is not trapped in every cantilever oscillation cycle. The Au atom-trapping rate varies from 100 % at $z = 1.2$ Å to 0 % at $z = 1.7$ Å as the tip-sample distance increases. In regime (iii), there is no chemical bonding between the Au atom and the tip-apex atom, and the tip cannot trap the Au atom. Since the Au atom is not trapped, it thermally diffuses within the nanospace. In this region, I_t decreases exponentially by following the basic tunneling law. It is worth mentioning that, in this region, the $I_t(z)$ curves of approach and retraction do not match. The existence of the diffusing Au causes the difference: the topographic and electronic structure modifications induced by the Au atom diffusion on the surface enhance the tunneling current upon retraction.

The simultaneously measured energy dissipation also contains information on the dynamic evolution of the atomic junction during Au atom trapping and release.

Trapping and release during the INSAM in region (i) enhances the dissipation energy of the 0.6 eV/cycle (see Fig. 4.12b). The observed behavior can be attributed to the adhesion mechanism of dissipation, as previously proposed in [10, 55–58], where a double-well potential energy surface caused energy dissipation. In our studies, a hysteresis caused by the trapping and the release of the Au atom produces the dissipation signal. Since the atomic scale dissipation as observed in dynamic AFM is usually associated with instabilities at the tip-surface interface at close proximity [10, 57, 58], it is clear that the dissipation is caused by the trapping and release of the Au atom by the tip. This means that the observed enhancement of the dissipation signal is due to such structural rearrangements, and the triggering mechanism of the INSAM is a purely mechanical effect.

One can estimate, from short-range force (F_{SR}), the threshold force associated with the atom trapping and the chemical bonding force that can stabilize the atomic junction formed between the tip and surface. In region (iii), the Au atom diffuses freely without any tip trapping (see the inset in this region). At the boundary of regions (ii) and (iii), where the Au atom begins to diffuse (i.e., $z = 1.7$ Å), we were able to obtain this force value required to trap a single diffusing Au atom by the tip of -0.1 nN. And as the tip starts to trap/diffuse the Au atom, the dependence of the force distance begins to change. This force change is due to the existence of the Au atom trap. While the solid curve represents the force curve that is expected for the diffusing Au atom within a half-unit cell, the dashed curve represents the force expected on the Au atom trapped by the tip. This means that the tip-Au-surface junction is in region (ii), and this force is more attractive than the non-conservative force in region (iii). It is specious to relate the force minima at $z = 1.2$ Å to the force needed to maintain the atomic junction. In addition, the chemical bonding force between the tip and the Au atom which stably maintains the atomic junction at $z = 1.2$ Å is close to -0.6 nN. Since this value is comparable to a chemical bonding force [37], the INSAM mechanism can be attributed to a purely mechanical effect. At smaller tip-surface distances (in region (i)), the second force minimum appears in the short-range force curve. Atomic relaxations induced by the tip-Au-surface interaction should occur in this region. The configuration change caused the force minimum. As the tip is closer to the surface, second-layer atoms on the tip-apex contribute to the interaction, resulting in a more attractive force. The further increase of the dissipation signal at $z < 1.2$ Å is related to the onset of an additional dissipation channel, which stems from the tip apex or surface atom modifications [10, 57, 58]. This atomic junction is less stable than the junction formed in region (ii) because the repulsive force starts to act in region (i).

Acknowledgments This work was supported by a Grant-in-Aid for Scientific Research from the Ministry of Education, Culture, Sports, Science and Technology of Japan (MEXT), and by the Funding Program for Next Generation World-Leading Researchers.

References

1. T.R. Albrecht, P. Grütter, D. Horne, D. Rugar, J. Appl. Phys. **69**, 668 (1991)
2. S. Morita, R. Wiesendanger, E. Meyer (eds.), *Noncontact Atomic Force Microscopy* (Springer, Berlin, 2002)
3. F.J. Giessibl, Rev. Mod. Phys. **75**, 949 (2003)
4. M.A. Lantz, H.J. Hug, R. Hoffmann, P.J.A. van Schendel, P. Kappenberger, S. Martin, A. Baratoff, H.-J. Guntherodt, Science **291**, 2580 (2001)
5. Y. Sugimoto, P. Pou, M. Abe, P. Jelínek, R. Pérez, S. Morita, O. Custance, Nature **446**, 64 (2007)
6. M. Setvín, P. Mutombo, M. Ondráček, Z. Majzik, M. Švec, V. Cháb, I. Ošt'ádal, P. Sobotík, P. Jelínek, ACS Nano **6**, 6969 (2012)
7. S. Hirth, F. Ostendorf, M. Reichling, Nanotechnology **17**, S148 (2006)
8. Y. Sugimoto, P. Jelínek, P. Pou, M. Abe, S. Morita, R. Pérez, O. Custance, Phys. Rev. Lett. **98**, 106104 (2007)
9. M. Ternes, C.P. Lutz, C.F. Hirjibehedin, F.J. Giessibl, A.J. Heinrich, Science **319**, 1066 (2008)
10. Y. Sugimoto, P. Pou, O. Custance, P. Jelinek, M. Abe, R. Perez, S. Morita, Science **322**, 413 (2008)
11. Y. Sugimoto, K. Miki, M. Abe, S. Morita, Phys. Rev. B **78**, 205305 (2008)
12. O. Custance, R. Perez, S. Morita, Nat. Nanotechnol. **4**, 803 (2009)
13. A. Yurtsever, Y. Sugimoto, M. Abe, K. Matsunaga, I. Tanaka, S. Morita, Phys. Rev. B **84**, 085413 (2011)
14. A. Sweetman, S. Jarvis, R. Danza, J. Bamidele, S. Gangopadhyay, G.A. Shaw, L. Kantorovich, P. Moriarty, Phys. Rev. Lett. **106**, 136101 (2011)
15. H.Q. Mao, N. Li, X. Chen, Q.K. Xue, J. Phys. Condens. Matter **24**, 084004 (2012)
16. R. Pawlak, S. Fremy, S. Kawai, T. Glatzel, H. Fang, L.A. Fendt, F. Diederich, E. Meyer, ACS Nano **6**, 6318 (2012)
17. G. Langewisch, J. Falter, H. Fuchs, A. Schirmeisen, Phys. Rev. Lett. **110**, 036101 (2013)
18. L. Pizzagalli, A. Baratoff, Phys. Rev. B **68**, 115427 (2003)
19. U. Kurpick, T.S. Rahman, Phys. Rev. Lett. **83**, 2765 (1999)
20. A. Kuhnle, G. Meyer, S.W. Hla, K.H. Rieder, Surf. Sci. **499**, 15 (2002)
21. D.M. Eigler, E.K. Schweizer, Nature (London) **344**, 524 (1990)
22. N. Nilius, T.M. Wallis, W. Ho, Science **297**, 1853 (2002)
23. J.A. Stroscio, F. Tavazza, J.N. Crain, R.J. Celotta, A.M. Chaka, Science **313**, 948 (2006)
24. S. Loth, S. Baumann, C.P. Lutz, D.M. Eigler, A.J. Heinrich, Science **335**, 2012 (2012)
25. A.A. Khajetoorians, B. Baxevanis, C. Hübner, T. Schlenk, S. Krause, T.O. Wehling, S. Lounis, A. Lichtenstein, D. Pfannkuche, J. Wiebe, R. Wiesendanger, Science **339**, 55 (2013)
26. Y. Sugimoto, M. Abe, S. Hirayama, N. Oyabu, O. Custance, S. Morita, Nat. Mater. **4**, 156 (2005)
27. F. Ming, K. Wang, S. Pan, J. Liu, X. Zhang, J. Yang, X. Xiao, ACS Nano **5**, 7608 (2011)
28. Y. Sugimoto, A. Yurtsever, M. Abe, S. Morita, M. Ondráček, R. Pérez, P. Jelínek, ACS Nano **7**, 7370 (2013)
29. M. Abe, Y. Sugimoto, O. Custance, S. Morita, Appl. Phys. Lett. **87**, 173503 (2005)
30. M. Abe, Y. Sugimoto, T. Namikawa, K. Morita, N. Oyabu, S. Morita, Appl. Phys. Lett. **90**, 203103 (2007)
31. N. Oyabu, O. Custance, I. Yi, Y. Sugawara, S. Morita, Phys. Rev. Lett. **90**, 176102 (2003)
32. J.E. Sader, S.P. Jarvis, Appl. Phys. Lett. **84**, 1801 (2004)
33. I. Horcas, R. Fernandez, J.M. Gomez-Rodriguez, J. Colchero, J. Gomez-Herrero, A.M. Baro, Rev. Sci. Instrum. **78**, 013705 (2007)
34. S. Jarvis, A. Sweetman, J. Bamidele, L. Kantorovich, P. Moriarty, Phys. Rev. B **85**, 235305 (2012)
35. H. Uchida, D. Huang, F.m c Grey, M. Aono, Phys. Rev. Lett. **70**, 2040 (1993)
36. B.C. Stipe, M.A. Rezaei, W. Ho, Phys. Rev. Lett. **79**, 4397 (1997)

37. A. Yurtsever, Y. Sugimoto, H. Tanaka, M. Abe, S. Morita, M. Ondracek, P. Pou, R. Perez, P. Jelinek, Phys. Rev. B **87**, 155403 (2013)
38. P. Sharp, S. Jarvis, R. Woolley, A. Sweetman, L. Kantorovich, C. Pakes, P. Moriarty, Appl. Phys. Lett. **100**, 233120 (2012)
39. D.L. Klein, R. Roth, A.K.L. Lim, A.P. Alivisatos, P.L. McEuen, Nature **389**, 699 (1997)
40. V. Ray, R. Subramanian, P. Bhadrachalam, L.C. Ma, C.U. Kim, S.J. Koh, Nat. Nanotechnol. **3**, 603 (2008)
41. M. Haruta, N. Yamada, T. Kobayashi, S. Iijima, J. Catal. **115**, 301 (1989)
42. M. Haruta, Catal. Today **36**, 153 (1997)
43. M. Valden, X. Lai, D.W. Goodman, Science **281**, 1647 (1998)
44. T.D. Ladd, F. Jelezko, R. Laflamme, Y. Nakamura, C. Monroe, J.L. O'Brien, Nature **464**, 45 (2010)
45. J.-L. Li, J.-F. Jia, X.-J. Liang, X. Liu, J.-Z. Wang, Q.-K. Xue, Z.-Q. Li, J.S. Tse, Z. Zhang, S.B. Zhang, Phys. Rev. Lett. **88**, 066101 (2002)
46. S.-C. Li, J.-F. Jia, R.-F. Dou, Q.-K. Xue, I.G. Batyrev, S.B. Zhang, Phys. Rev. Lett. **93**, 116103 (2004)
47. Y. Sugimoto, A. Yurtsever, N. Hirayama, M. Abe, S. Morita, Nat. Commun. **5**, 4360 (2014)
48. C. Zhang, G. Chen, K. Wang, H. Yang, T. Su, C.T. Chan, M.M.T. Loy, X. Xiao, Phys. Rev. Lett. **94**, 176104 (2005)
49. Y. Sugimoto, Y. Nakajima, D. Sawada, K. Morita, M. Abe, S. Morita, Phys. Rev. B **81**, 245322 (2010)
50. K. Wang, C. Zhang, M.M.T. Loy, X. Xiao, Phys. Rev. Lett. **94**, 036103 (2005)
51. Y. Zhou, Q.H. Wu, H.Z.H. Zhou, C. Zhan, J. Kang, Surf. Sci. **602**, 638 (2008)
52. J.M. Gómez-Rodríguez, J.J. Sáenz, A.M. Baró, J.-Y. Veuillen, R.C. Cinti, Phys. Rev. Lett. **76**, 799 (1996)
53. G. Chizhov, I. Lee, R.F. Willis, Phys. Rev. B **56**, 12316 (1997)
54. Y. Wu, Y. Zhou, C. Zhou, H. Zhan, J. Kang, J. Chem. Phys. **133**, 124706 (2010)
55. N. Sasaki, M. Tsukada, Jpn. J. Appl. Phys. **39**, L1334–L1337 (2000)
56. L.N. Kantorovich, T. Trevethan, Phys. Rev. Lett. **93**, 236102 (2004)
57. N. Oyabu, P. Pou, T. Sugimoto, P. Jelinek, M. Abe, S. Morita, R. Perez, O. Custance, Phys. Rev. Lett. **96**, 106101 (2006)
58. A. Schirmeisen, D. Weiner, H. Fuchs, Phys. Rev. Lett. **97**, 136101 (2006)

Chapter 5
The Phantom Force

Alfred John Weymouth and Franz J. Giessibl

Abstract While atomic resolution in an AFM image is usually assumed to originate from the formation of a chemical bond or Pauli repulsion, it can also be caused by a phenomenon we called the phantom force. When there is an electric potential difference between tip and sample, they will be attracted to one another. It is quite common in AFM experiments to apply a voltage between the tip and the sample. At distances required for atomic resolution, this can result in a tunneling current. If there is a tunneling current, then there will also be a potential difference within the sample (as charge carriers do not accumulate after they have tunnelled). The magnitude of this potential difference within the sample is related to the resistivity of the sample. The total potential difference between the sample bulk and the tip is fixed by the applied voltage, so any potential difference within the sample reduces the potential drop in the junction between the tip and sample. This phantom force is an apparently repulsive force caused by a decrease in the electrostatic attraction between tip and sample. If the total resistance within the tip or sample is high enough, then the phantom force can be the dominant contrast mechanism in AFM images. It can also dominate features in bias and distance spectroscopy. This chapter includes a comprehensive description of our theory of the phantom force and data which demonstrate this effect.

5.1 Introduction and Background

The most exciting aspect of scanning tunneling microscopy (STM) is that images can be acquired with spatial resolution on the atomic scale [1]. STM is not a microscopy technique in the typical sense, with lenses used to optically focus a beam, but rather uses a sharp tip to locally probe surfaces and adsorbates [2]. A voltage difference is applied between the atomically-sharp tip and the surface, and although they are not

A.J. Weymouth (✉) · F.J. Giessibl
University of Regensburg, 31 Universitaetsstrasse, 93053 Regensburg, Germany
e-mail: jay.weymouth@ur.de

F.J. Giessibl
e-mail: Franz.Giessibl@physik.uni-regensburg.de

© Springer International Publishing Switzerland 2015

S. Morita et al. (eds.), *Noncontact Atomic Force Microscopy*,
NanoScience and Technology, DOI 10.1007/978-3-319-15588-3_5

touching (the tip is up to a few atomic diameters away from the surface), electrons tunnel through the vacuum gap. Because tunneling occurs mainly through the apex atom of the tip, the STM can achieve spatial resolution on the atomic scale.

In a tunneling event, an electron (either to or from the tip) tunnels across the vacuum gap into an unoccupied state. It is this process that is most often considered in the STM community, and theoretical techniques based upon this consideration are the groundwork for understanding STM data [3, 4]. However, two other processes also occur: The electron will not remain localized where it first arrived but will rather conduct to the bulk, as will the corresponding hole.

Because of the high local concentration of the tunneling current around the front atom of the tip, the areal current density is very large [5]. Ohm's law directly relates the current density to the electrical field via the resistivity of the conductive material. If the tip or the sample has substantial resistivity, then a significant electric field will be present within it. This electric field can equivalently be described by a voltage difference between the surface and the bulk. While it is difficult for STM alone to be sensitive to this, atomic force microscopy (AFM) is.

AFM is sensitive to the total force interaction between the tip and the sample including those contributions resulting from electrostatic interactions. When a substantial fraction of the applied voltage drops within the sample, a smaller fracton thereof drops between the tip and sample. This decreases the electrostatic attraction which can be observed in AFM. We call this effect the phantom force.

The remainder of this section begins with a short description of atomic force microscopy. The forces that dominate AFM measurements at the atomic scale include the chemical binding force, van der Waals force and electrostatic forces. As the phantom force is caused by changes in the electrostatic force, the electrostatic force is discussed in more detail. A key ingredient to our theory is a potential drop within the sample, from the surface below the tip to the bulk. Finally, these ingredients are combined to present the theoretical picture of the phantom force.

5.1.1 Frequency-Modulation Atomic Force Microscopy

Frequency-modulation atomic force microscopy (FM-AFM) is a non-contact AFM technique that is highly sensitive to short-range forces. One advantage of FM-AFM is that frequency is a value that we are able to measure with high precision. Short-range forces, by definition, decay very quickly as a function of distance. Instead of being directly sensitive to the vertical force component F_{ts} between the tip and the sample, FM-AFM is sensitive to the force gradient $k_{ts} = -\mathrm{d}F_{ts}/\mathrm{d}z$.

Throughout this chapter z and vertical refer to distances along the surface normal. Increasing z refers to a greater distance from the surface. Lateral motion refers to motion along the surface, that is, perpendicular to the surface normal.

The tip is attached to a cantilever that can be characterized by an effective spring constant k. The forces acting on the tip are a superposition of the cantilever and the tip-sample interaction:

$$F_{ts} = -kz + -k_{ts}z = -(k + k_{ts})z \tag{5.1}$$

The assumption here is that k_{ts} is constant over the oscillation of the cantilever, referred to as the small-amplitude approximation. The cantilever is oscillated in the z-direction at its resonance frequency f_0. The influence of k_{ts} is detected via a frequency shift $\Delta f = f - f_0$, where f is the actual oscillation frequency. If we consider the tip to have some mass m and the cantilever to be massless, then the frequency

$$f = \frac{1}{2\pi}\sqrt{\frac{k + k_{ts}}{m}}. \tag{5.2}$$

This is also acceptable to the situation where the cantilever has mass, and in this case m is replaced by an effective mass term plus the mass of the tip. Expanding f around $k_{ts} = 0$ in terms of k_{ts}:

$$f = f_0 + \frac{f_0}{2k}k_{ts} + O \tag{5.3}$$

Here O represents the higher-order terms (those with k_{ts}^2 terms and above). If the force gradient is constant over the cantilever oscillation, one can write:

$$\Delta f = \frac{f_0}{2k}k_{ts} \tag{5.4}$$

This approximation is the small-amplitude approximation. In order to convert the frequency shift into the force between tip and sample, k_{ts} must be calculated from Δf, and then integrated from a point far from the surface (that is, where the tip-sample interaction can be assumed to be zero) to the point of interest. In the case of a conservative force field, the force can be integrated to yield the potential energy.

If the force gradient cannot be assumed to be constant over one tip oscillation, then the relation between Δf and k_{ts} includes a weighting of k_{ts} over the cantilever oscillation. Δf is then written as

$$\Delta f = \frac{f_0}{2k}\langle k_{ts}\rangle, \tag{5.5}$$

where the angled brackets represent a weighted average, described in more detail in [6]. In this case, evaluation of F_{ts} requires a deconvolution of Δf followed by an integration step. Two methods for this deconvolution and integration include the Sader-Jarvis deconvolution method [7] and Giessibl's matrix method [8]. For a comparison of the two methods, the reader is directed to [9].

In general, the frequency shift Δf can be interpreted as follows: an increase in Δf indicates a repulsive contribution to the force, whereas a decrease in Δf indicates an attractive contribution.

5.1.2 The Forces at Play at the Atomic Scale

Many forces can play a significant role in atomic-scale AFM, but we focus on the chemical interaction of the apex atom with the sample, the van der Waals interaction and electrostatic interactions.

Historically, it is the chemical interaction between tip and sample that was first believed to be responsible for atomic resolution in AFM images [10, 11]. A complete description of chemical bonds is quite complex, including overlapping orbitals and rehybridization. An approximation of the interaction between single atoms is given by the Morse potential, which describes attraction between two atoms up to an equilibrium distance, and then the subsequent repulsion. This overall behavior can also be modelled by a Lennard-Jones potential. Recently high-resolution AFM results have shown that both can very accurately model certain tip-sample interactions [12, 13].

The van der Waals force describes the interaction between two induced dipoles. This interaction is surprisingly well-described by the Hamaker approximation, in which all interacting particles are assumed to interact independently. The van der Waals interaction can dominate at the nanometer-scale. The force-distance relationship of the van der Waals interactions have been explicitly calculated for a number of high-symmetry AFM tips [14].

The description of the long-range electrostatic force comes from considering the tip-sample junction as a capacitor, where the presence of a potential difference causes attractive interaction. This model is appropriate for metallic surfaces. In a macroscopic picture, this results from both the work function differences of the two materials (discussed in the next section) and any applied voltage. Semiconductors are more challenging, in that the electric field cannot be assumed to fully drop over the junction, but rather penetrates significantly into the sample. This effect has been well-studied in the framework of STM and is known as Tip Induced Band-Bending (TIBB) [15]. For all sample systems, even insulators, it is common to apply a voltage to minimize this macroscopic electrostatic force.

These three forces are a good foundation for interpreting most AFM data. The electrostatic and van der Waals forces are expected to increase in magnitude and stay attractive as the tip approaches the surface. The chemical interaction is expected to dominate at short-range with an attractive bond followed by repulsion caused by Pauli repulsion. This picture is what makes the phantom force so confusing: one expects repulsive contrast only at very small tip-sample distances that are closer than the chemical bonding distance. However this phantom force, as presented in more detail in Sect. 5.1.6, can also appear to be a repulsive force that can be mistaken for Pauli repulsion.

5.1.3 Electrostatic Attraction Between Metal Surfaces

The electrostatic attraction between two flat metal surfaces depends upon the potential between them. This is a function of the applied voltage, as well as the differences in their work functions. The energy necessary to remove an electron from a solid at 0 K is the work function, Φ. Two materials far from each other will share vacuum levels, however there is no requirement that their Fermi levels align. This occurs when they are put in electrical contact with each other. If they do not have the same work function, then a potential difference will exist between the two metal surfaces.

Different crystal facets have different values of Φ, and we understand these differences in terms of surface dipoles, p_s, that cover a surface with an areal density n_p. Considering the potential in the vertical dimension,

$$\Phi = E_F + \frac{q_e}{\varepsilon_0} p_s n_p \tag{5.6}$$

where q_e is the elementary charge and E_F is the Fermi level.

Writing the total potential difference within the tip-sample junction as the sum of the differences in work function and of any applied voltage:

$$V_J = V_B + \Delta\Phi \tag{5.7}$$

To consider the effect of this to a FM-AFM setup, we can consider a geometrically simple arrangement, in which both tip and surface are two parallel plates, with area A. The magnitude of the electric field between the two is given as

$$|\mathbf{E}| = E = V_J/z \tag{5.8}$$

where the distance between the plates is z. The potential energy, U_{PE}, stored in the electric field can be calculated by the total work, W, required to create the charge distribution. In a conservative field, this yields the following:

$$-U_{PE} = W = \frac{\varepsilon_0}{2}\int_V |E|^2 dV = \frac{\varepsilon_0}{2}\left(\frac{V_J}{z}\right)^2 zA = \frac{\varepsilon_0}{2} V_J^2 \frac{A}{z} \tag{5.9}$$

If we have a purely conservative force, then the interaction force between the two plates would be given by the negative gradient of the energy. The $z-$component of the electrostatic force can be written:

$$F_{es} = -\frac{\mathrm{d}U_{PE}}{\mathrm{d}z} = -\frac{\varepsilon_0}{2} V_J^2 \frac{A}{z^2} \tag{5.10}$$

That is, there will be an attractive force that is proportional to the potential difference squared. Capacitance C is as a measure of the charge on each surface Q as a function of the potential difference, $C = Q/V_J$. For a general case, the attractive force can

be rewritten as a function of capacitance:

$$F_{es} = \frac{1}{2}\frac{\mathrm{d}C}{\mathrm{d}z}V_J^2 \tag{5.11}$$

In the typical picture of long-range electrostatic interactions, this interaction does not vary over the surface. In Kelvin Probe Force Microscopy (KPFM), one measures the electrostatic interactions locally by varying the applied voltage:

$$F_{es} = \frac{1}{2}\frac{\mathrm{d}C}{\mathrm{d}z}(V_B + \Delta\Phi)^2 \tag{5.12}$$

This picture, while widely used, does not include the effect of the phantom force, which is discussed in the next section.

5.1.4 Conductance in an Atomic-Scale Junction

To consider the conductance within the sample, we started with an Ohmic model [16]. Under this model, there is a linear relationship between current density, $\mathbf{j}$, and electric field, characterized by the resistivity ρ:

$$\mathbf{E} = \rho\mathbf{j} \tag{5.13}$$

Given that there is a current from the point of the surface where the electrons tunnel either to or from the tip, $\mathbf{r}_0$, and the bulk, $\mathbf{r}_1$, there must be an electric field present (as there must be a force upon the charge carriers) and therefore a potential as well. The potential

$$\phi = -\int_{\mathbf{r}_0}^{\mathbf{r}_1}\mathbf{E}\cdot\mathrm{d}\mathbf{r} = -\int_{\mathbf{r}_0}^{\mathbf{r}_1}\rho\mathbf{j}\cdot\mathrm{d}\mathbf{r} = -\int_{\mathbf{r}_0}^{\mathbf{r}_1}\rho\frac{\mathbf{I}}{A}\cdot\mathrm{d}\mathbf{r} \tag{5.14}$$

If we assume nothing other than a radial current flow, then the vectors can be omitted and

$$\phi = -\int_{r_0}^{r_1}\rho\frac{I}{A}\mathrm{d}r = -\int_{r_0}^{r_1}\rho\frac{I}{2\pi r^2}\mathrm{d}r = -\rho I\left(\frac{1}{2\pi r_1} - \frac{1}{2\pi r_0}\right) \tag{5.15}$$

For the case where $r_1 = \infty$ is the bulk, and r_0 is the radius of the tunneling current, ϕ can be simplified:

$$\phi = -\frac{\rho I}{2\pi r_0} \tag{5.16}$$

We will consider a piece of silicon, doped to have a resistivity of $\rho_{Si} = 10\,\Omega\,\mathrm{cm}$. We assume that the tunneling current is a cylindrical stream with a radius of $r_0 = 100$

pm. The effective sample resistance is then

$$R_S = \frac{\phi}{I} = \frac{1\,\Omega\,\mathrm{cm}}{2\pi \cdot 100\,\mathrm{pm}} = 159\,\mathrm{M}\Omega. \tag{5.17}$$

The Ohmic model is usually accepted as a model for bulk transport, so one would naturally ask how relevant it is to atomic-scale transport. Recent work from the Simmons group indicates that for Si wires doped with P, this law does hold down to the atomic scale [17].

One failure of the Ohmic model is that it does not represent the electronic band structure. In the case of Si(111)−7×7, for example, the surface has a metallic surface state within the band gap of the bulk Si crystal [18]. Transport from the surface to the bulk has been extensively studied [19, 20] and is neither Ohmic nor constant over the surface [21]. While this is correct, the Ohmic model nevertheless explains the majority of our observations, and we expect inclusion of the electronic structure to simply increase the accuracy of the phantom force model.

This model provides an understanding of the systems where we expect non-negligable phantom force effects to be observed. A tunneling current of $I = 1\,\mathrm{nA}$ through low-doped Si will result in a voltage difference of 0.159 V between the tip-sample junction and the bulk. This is a significant fraction of the voltage that is normally applied while scanning this surface. On the other hand, metallic surfaces like Cu have a resistivity of $\rho_{Cu} \approx 2 \times 10^{-8}\,\Omega\,\mathrm{m}$. This would result in a sample resistance of $R_S = 0.32\,\Omega$, and a negligible voltage drop within the sample.

5.1.5 *Including Resistance in Our Overall Picture of Tunneling*

The sample resistance describes the effect of the sample on the current within it. The total current, therefore, will no longer be a function just of the applied bias voltage and the effective resistive drop in the tunneling junction,[1] but rather include the resistive sample component described by the phantom force:

$$I = \frac{V_B}{R_J + R_S} \tag{5.18}$$

This sample resistance will also act as a voltage divider. That is, the potential difference between tip and sample does not simply include contributions from the applied bias voltage V_B and the difference in work functions:

$$V_J = V_B + \Delta\Phi - I R_S = V_B \frac{R_J}{R_J + R_S} + \Delta\Phi \tag{5.19}$$

[1] Tunneling is an elastic process but the effect of tunneling and then a quick energetic relaxation is often modelled by a resistor.

The effect of sample resistance on an AFM image is via the electrostatic force:

$$F_{es} = \frac{1}{2}\frac{\mathrm{d}C}{\mathrm{d}z}V_J^2 \tag{5.20}$$

And so, in terms of the junction resistance:

$$F_{es} = \frac{1}{2}\frac{\mathrm{d}C}{\mathrm{d}z}\left(V_B\frac{R_J}{R_J + R_S} + \Delta\Phi\right)^2 \tag{5.21}$$

And as a function of the current:

$$F_{es} = \frac{1}{2}\frac{\mathrm{d}C}{\mathrm{d}z}(V_B + \Delta\Phi - IR_S)^2 \tag{5.22}$$

In order to determine the regime in which the phantom force is significant, we rewrite the tunneling current junction resistance depending exponentially upon the tip-sample distance:

$$R_J = R_0 \exp[2\kappa z] \tag{5.23}$$

κ is the decay constant of the tunneling current, which is usually around $1\,\text{Å}^{-1}$ [2]. If $z = 0\,\text{m}$ denotes the position where the tip and sample are in chemical contact, then R_0 is the resistance at point contact. This has been very well measured for the case of metal-metal single-atom contacts in break-junction measurements [22] and is known to be $1/G_0$, where G_0 is the quantum-point conductance. The phantom force starts to play a noticeable role when the sample (or tip) resistivity R_S becomes comparable to the junction resistance R_J. For example, if the junction resistance is $1\,\text{G}\Omega$ (1 V and 1 nA), then a sample resistance of $R_S = 159\,\text{M}\Omega$ cannot be ignored. From (5.23), we expect this to happen at tip-sample distances of $z < 0.6\,\text{nm}$, which is a typical distance for AFM images.

5.1.6 Summary

The phantom force is an effect that can be observed when a tunneling current is present in force measurements, and there is a substantial resistance for the current from the point of tunneling to the bulk. It can be represented by an internal sample resistance, as sketched in Fig. 5.1. For low-doped Si samples, this resistance can be on the order of $100\,\text{M}\Omega$.

An internal resistance can also be present in the tip. Morita et al. reported measurements of the tunneling current while using Δf to regulate tip height [23]. Before poking a clean W tip into a Si surface, they recorded a current of 16 nA at 0.2 V. After a tip poke, with the same feedback parameters, the current was less than the noise floor of 5 pA at a voltage of 0.1 V. This indicates an additional resistance of $20\,\text{G}\Omega$.

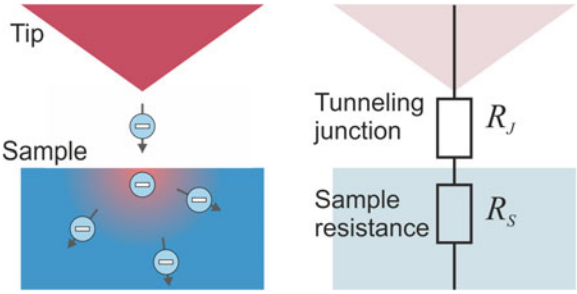

Fig. 5.1 A net tunneling current flows because there is a potential difference between the tip and sample. In this drawing, the tip has a higher potential for electrons and they tunnel to the sample. Electrons then disperse from the point of entry to the bulk. A similar process occurs in the tip (not shown). The overall effect depends strongly on the material's ability to conduct electrons from this point to the bulk. This can be modelled by the addition of a sample resistance R_S

In order to demonstrate the effect of the phantom force, we can explicitly model three contributions to the overall force: the van der Waals force, the electrostatic force, and the chemical interaction. The van der Waals contribution is modelled as suggested by Giessibl [14] with a conic tip that has an opening angle of $\alpha = 70°$, using a Hamaker coefficient of $A_H = 0.1865\,\text{aJ}$. The chemical interaction was modelled with a Morse potential having a bonding energy of $E_B = 4\,\text{eV}$, an equilibrium distance of $z_0 = 200\,\text{pm}$, and a decay constant of $\lambda = 100\,\text{pm}$[2]:

$$E_{\text{Morse}} = E_B \left(\exp -\frac{2(z - z_0)}{\lambda} - 2\exp -\frac{(z - z_0)}{\lambda} \right) \tag{5.24}$$

The electrostatic force is modelled as suggested by Guggisberg et al. [25], with an opening angle of $\alpha = 70°$, a final tip radius of $r_{tip} = 4\,\text{nm}$, a tip length of 1 mm, and an offset distance between the final apex atom and the part of the tip that contributes significantly to the electrostatic force of $z_{off} = 1\,\text{nm}$. A sketch of this tip model is shown in Fig. 5.4. The voltage is the junction voltage, as described by (5.19), with a bias of $V_B = 1\,\text{V}$ and a contact potential difference of $\Delta\Phi = -0.2\,\text{V}$.

Each of these contributions is individually shown in Fig. 5.2a. The van der Waals contribution is attractive over the entire range. The chemical bond contribution only becomes significant with distances $z < 1\,\text{nm}$. The electrostatic contribution, although at further distances is simply attractive, also changes suddenly at $z < 1\,\text{nm}$. At this point, $R_J \approx R_S$.

The effect of the phantom force is also evident in the total force interaction, shown in Fig. 5.2b, and in the force gradient, shown in Fig. 5.2c. Although the total force gradient decreases with decreasing tip-sample distance, the phantom force causes a first minimum followed by a zero-crossing. This first minimum can therefore be

[2]These parameters were chosen as representative. Bond lengths from 100 to 300 pm are common, as are dissociation energies on the order of a few eV [24].

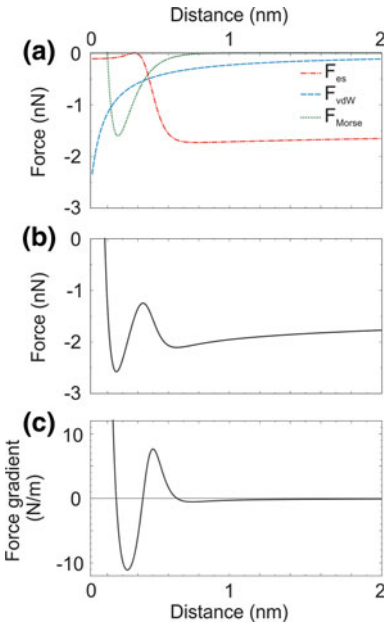

Fig. 5.2 Out of the three forces discussed in Sect. 5.1.2, the electrostatic force changes the strongest when the phantom force is present. **a** A model of the z dependance of the electrostatic force, van der Waals force, and chemical interaction (represented by a Morse potential). **b** The total force *curve*. Note the two local minima, in contrast to what is normally expected. **b** A corresponding plot of the force gradient, calculated from the *curve* in **b**. Again there is a second local minimum

incorrectly attributed to the equilibrium distance of the chemical interaction, although it is several hundred picometers further.

It is therefore easy to mistake an effect of the phantom force as an observation of chemical interaction, especially as tunneling is usually localized over atomic sites.

5.2 Observations

Silicon was the first material upon which we observed the phantom force. We were imaging at room temperature and noticed when we collected constant-height data that the adatoms appeared repulsive. This on its own was surprising, as the reactive nature of the surface also makes it ideal to investigate adsorbates [26, 27].[3] While we expected differences in the adatom types [29, 30], the contrast we observed very closely resembled the contrast in our STM images.

Since these initial observations, we have recorded observations at both liquid He-temperature (with an Omicron low-temperature SPM system, operating nominally at 4.5 K) and at room temperature (with a homebuilt microscope, modelled after the Park Scientific Instruments UHV system [31]). We used two types of Si samples: a highly doped sample with a resistivity of 0.010–0.012 Ω cm at 300 K, and a lower doped sample with a resistivity of 6–9 Ω cm at 300 K.

[3]It should be noted that Sweetman et al. have reported repulsive contrast over the Si(111)−7×7 surface, which can occur with non-reactive tip apexes [28].

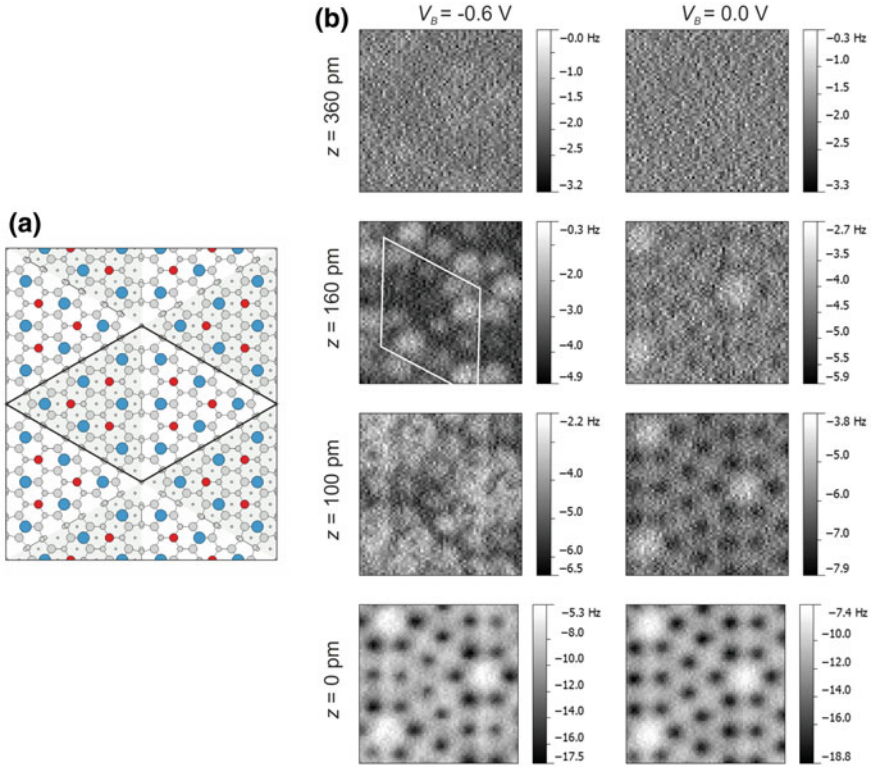

Fig. 5.3 **a** Schematic of the Si(111)−7×7 surface. Nominally, only the Si adatoms (*blue*) are observable by AFM and STM. **b** Constant-height FM-AFM data taken with and without an applied bias voltage at various heights z. $z = 0$ pm is the point of closest approach

Figure 5.3 shows two series' of AFM images at various tip-sample distances, one with an applied voltage of −0.6 V and the second with an applied voltage of 0.0 V. At $z = 160$ pm, contrast can be seen in both datasets. In the dataset with $V_B = -0.6$ V, the adatoms appear repulsive. In the dataset with $V_B = -0.0$, the area over the adatoms appears more attractive than the area over the corner holes. The repulsive contrast is attributed to the phantom force, whereas the attractive contrast is attributed to the chemical interaction. This trend continues with closer approach, as the chemical interaction stars to dominate. At $z = 0$ m, the images appear similar.

A second experiment (also at liquid-He temperature) demonstrates the effect of the phantom force, shown in Fig. 5.4. At standard STM conditions of a voltage of 1.5 V and a current of 2 nA, contrast can be observed in the AFM channel in constant-height mode. This is again due to the phantom force. When the voltage is decreased to 0 V, the contrast disappears. In order to observe the expected attractive contrast, we need to approach the tip 340 pm closer to the surface.

Several questions naturally arise with this data. We have presented a theory based upon the internal sample resistance, however there are other phenomena at play

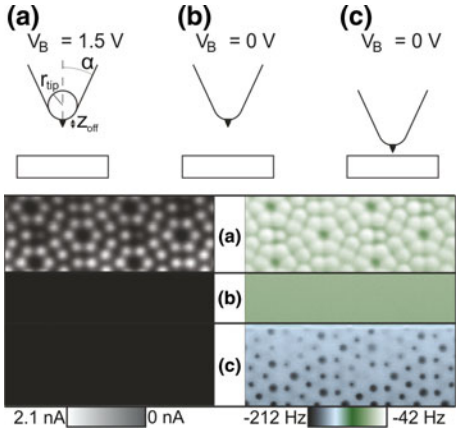

Fig. 5.4 Constant-height FM-AFM data. The *top third* was acquired with a voltage $V = 1.5\,\mathrm{V}$ at a relative tip height of $z = 340\,\mathrm{pm}$. The *middle third* was acquired with no applied voltage at $z = 340\,\mathrm{pm}$. The *lower third* was acquired with no applied voltage at $z = 0\,\mathrm{m}$. Adapted from [16]

that could cause contrast inversion or, at the least, a strong bias dependance: 1. We could be changing the tip-sample distance by changing the bias and probing repulsive interaction due to a chemical bond. 2. This effect could be related to tip-induced band bending. 3. This could all be an artifact from a poorly-chosen STM preamplifier. None of these three are acceptable explanations, for the following reasons.

1. In Fig. 5.4, the tip must be approached to the surface 340 pm before attractive chemical interaction can be observed. If the contrast in the upper third of the image was caused by repulsive chemical interaction, then removal of the bias voltage must result in the average cantilever height being increased by over 340 pm. We used a qPlus sensor with a spring constant of $k = 1800\,\mathrm{N/m}$, meaning that a force difference of 612 nN is required. With the calculations presented in Sect. 5.1.6, the electrostatic forces are one hundred times too low for this to be feasible.

2. Tip-induced band bending is a description of the field effect of the tip when probing a semiconducting surface [32, 33]. However, in the case of Si(111)−7×7, it is weakly present [34]. The surface reconstruction presents a metallic surface state, and therefore the field effect of the tip is greatly reduced. Of course, this means that we must now demonstrate that the phantom force is not unique to this special case, which we present later for the case of H-terminated Si(100).

3. If the STM preamplifier was poorly selected, then the virtual ground would be insufficient. In that case, a current could result in a significant deviation from 0 V, and also reduce the attractive electrostatic force. The simplest test for this was to install a switch where we could change from using the virtual ground to using a real ground. The result is presented in [35], but to summarize, we observed no difference in the two. This does not mean that the virtual ground cannot affect AFM measurements, it simply means that the deviation of the virtual ground provided by the STM preamplifier from an ideal ground is not responsible for the phantom force.

In the rest of this section, the data collected on Si(111)−7×7 is used to quantitatively extract values of R_S. The effect of the phantom force on Kelvin probe force microscopy is demonstrated and discussed. Data is shown of the phantom force on the

H-terminated Si(100) surface. Finally, we show data that indicate that the phantom force is present even on molecular adsorbates that lie on highly conductive surfaces.

5.2.1 Characterizing the Phantom Force

While the previous two examples demonstrate qualitatively the effect of the phantom force, they do not provide a quantitative measurement of the phantom force. One method to do this is by investigating the relationship between the recorded current $\langle I \rangle$ and Δf. We published these results in [16]; here we review them. The recorded current is written $\langle I \rangle$ because it is the average current over the oscillation of the cantilever. All data taken in this subsection were acquired at room temperature.

In Fig. 5.5, constant-height data of low-doped Si(111)−7×7 are shown at both bias polarities: In (a) and (b), $V_B = +1.5\,\mathrm{V}$ and in (c) and (d), $V_B = -1.5\,\mathrm{V}$. The AFM images show an increase in Δf above the adatoms in the unit cell, irrespective of the polarity of the bias voltage. The data show strong similarity to the STM data, with adatoms of the faulted half of the unit cell appearing brighter when probing filled-state images. While this is expected in STM data [21], it is surprising that the contrast in the AFM image would also be so dependent upon V_B.

As we simultaneously measure $\langle I \rangle$ and Δf, we can directly compare the two, pixel-by-pixel. One technical detail is that the relative bandwidths of the two measurements must be taken into account. Even with a relatively high bandwidth of the phase-locked loop (AFM controller) of $B = 120\,\mathrm{Hz}$, it is much lower than the

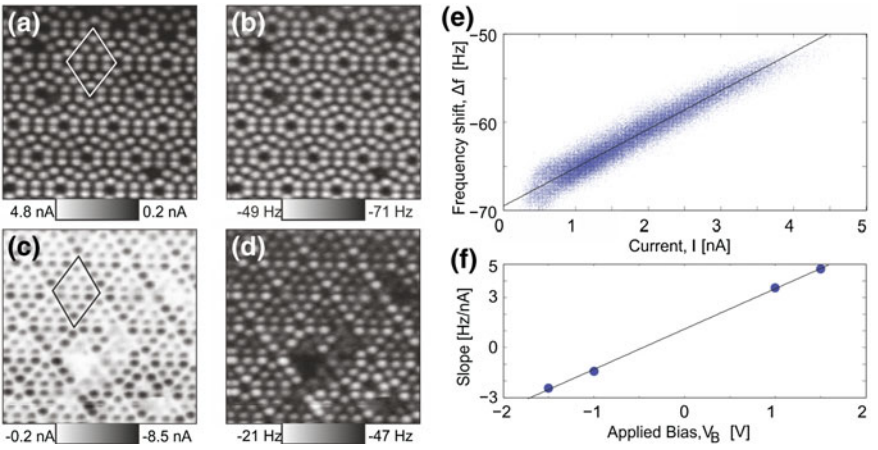

Fig. 5.5 Constant-height data taken at room temperature with simultaneous $\langle I \rangle$ and Δf. **a** and **b** taken at $V_B = +1.5\,\mathrm{V}$, **c** and **d** taken at $V_B = -1.5\,\mathrm{V}$. **e** Pixel-by-pixel plot of Δf as a function of $\langle I \rangle$ from data in **a** and **b** with a linear fit. **f** Slopes of the linear fits as a function of the bias voltage follow themselves a linear relation. Adapted from [16]

STM measurements, which can be assumed to be instantaneous in comparison.[4] This will result in a pixel shift between the STM and AFM images. At a scan speed of $v = 20\,\text{nm/s}$, the offset is $\Delta x = v/B = 166\,\text{pm}$.

The corresponding points are shown in Fig. 5.5e. The trend is linear and a fit line is shown. We can understand this linear relation in terms of the Phantom force, within a small amplitude approximation. As we consider only the contrast mechanism, we consider only the contribution to k_{ts} from the electrostatic force[5]:

$$k_{ts} = -\frac{\mathrm{d}F_{es}}{\mathrm{d}z} = -\frac{\mathrm{d}}{\mathrm{d}z}\frac{1}{2}\frac{\mathrm{d}C}{\mathrm{d}z}(V_B + \Delta\Phi - I R_S)^2 \tag{5.25}$$

$$k_{ts} = -\frac{1}{2}\frac{\mathrm{d}^2C}{\mathrm{d}z^2}(V_B + \Delta\Phi - IR_S)^2 + \frac{\mathrm{d}C}{\mathrm{d}z}(V_B + \Delta\Phi - I R_S)\left(R_S\frac{\mathrm{d}I}{\mathrm{d}z}\right) \tag{5.26}$$

In order to write k_{ts} as a polynomial in terms of I, we must rewrite the last term as a polynomial in terms of I. Substituting (5.18) into $\frac{\mathrm{d}I}{\mathrm{d}z}$:

$$\frac{\mathrm{d}I}{\mathrm{d}z} = \frac{\mathrm{d}}{\mathrm{d}z}\frac{V_B}{R_J + R_S} = \frac{\mathrm{d}}{\mathrm{d}z}\frac{V_B}{R_0\exp[2\kappa z] + R_S} \tag{5.27}$$

$$\frac{\mathrm{d}I}{\mathrm{d}z} = -\frac{V_B}{R_0\exp[2\kappa z] + R_S}\frac{R_0\exp[2\kappa z]}{R_0\exp[2\kappa z] + R_S} \tag{5.28}$$

$$\frac{\mathrm{d}I}{\mathrm{d}z} = -2\kappa I\frac{R_J}{R_J + R_S} \tag{5.29}$$

Rewriting k_{ts} as a polynomial of current:

$$\begin{aligned} k_{ts} = &-\frac{1}{2}\frac{\mathrm{d}^2C}{\mathrm{d}z^2}(V_B + \Delta\Phi)^2 + \\ &+\left[\frac{\mathrm{d}^2C}{\mathrm{d}z^2} - 2\kappa\frac{R_J}{R_J + R_S}\frac{\mathrm{d}C}{\mathrm{d}z}\right](V_B + \Delta\Phi)\,R_S\,I + \\ &+\left[-\frac{1}{2}\frac{\mathrm{d}^2C}{\mathrm{d}z^2} + 2\kappa\frac{R_J}{R_J + R_S}\frac{\mathrm{d}C}{\mathrm{d}z}\right]R_S^2\,I^2 \end{aligned} \tag{5.30}$$

[4] Our STM signal is recorded at 500 Hz.

[5] A complete description of the forces would require consideration of the van der Waals and chemical interactions as well. But, as shown in Fig. 5.4, these do not contribute to the contrast in the AFM image. Therefore it suffices to consider only the electrostatic interaction.

If we assume that the tip is relatively far from the surface and $R_J \gg R_S$:

$$\frac{R_J}{R_J + R_S} \approx 1 \tag{5.31}$$

k_{ts} can then be simplified:

$$\begin{aligned} k_{ts} = &- \frac{1}{2}\frac{\mathrm{d}^2 C}{\mathrm{d}z^2}(V_B + \Delta\Phi)^2 + \\ &+ \left[\frac{\mathrm{d}^2 C}{\mathrm{d}z^2} - 2\kappa\frac{\mathrm{d}C}{\mathrm{d}z}\right](V_B + \Delta\Phi)\, R_S\, I + \\ &+ \left[-\frac{1}{2}\frac{\mathrm{d}^2 C}{\mathrm{d}z^2} + 2\kappa\frac{\mathrm{d}C}{\mathrm{d}z}\right] R_S^2\, I^2 \end{aligned} \tag{5.32}$$

Finally, arguing that $R_S I < 1$, which is valid for $R_S \approx 100\,\mathrm{M\Omega}$ and $I = 1\,\mathrm{nA}$, then $R_S I \gg R_S^2 I^2$:

$$\begin{aligned} k_{ts} &\approx -\frac{1}{2}\frac{\mathrm{d}^2 C}{\mathrm{d}z^2}(V_B + \Delta\Phi)^2 + \left[\frac{\mathrm{d}^2 C}{\mathrm{d}z^2} - 2\kappa\frac{\mathrm{d}C}{\mathrm{d}z}\right](V_B + \Delta\Phi)\, R_S\, I \\ k_{ts} &\approx b + m\, R_S\, I \end{aligned} \tag{5.33}$$

where b and m represent terms independant of R_S and I. The slope $m R_S$ is plotted in Fig. 5.5f. In agreement with (5.33), this term varies linearly with V_B.

In order to extract a value for R_S, we added additional external resistances, R_{ext}, to the circuit. While the phantom force is a physical effect caused by the local conductance, addition of an external resistor will cause the same effect, and from (5.33), k_{ts} now can be rewritten:

$$k_{ts} \approx b + m\,(R_S + R_{ext})\, I \tag{5.34}$$

We collected simultaneous $\langle I \rangle$ and Δf data for three values of external resistors: $R_{ext} = 0\,\Omega$, $10\,\mathrm{M\Omega}$ and $30\,\mathrm{M\Omega}$, shown in Fig. 5.6.

A linear fit at $R_{ext} = 0\,\Omega$ and $10\,\mathrm{M\Omega}$ yielded a predicted value of $m(R_S + 30\,\mathrm{M\Omega}) = -0.99\,\mathrm{Hz/nA}$.

The observed slope was $-1.03\,\mathrm{Hz/nA}$. This outstanding agreement is a statement to the accuracy of this simple model. In it, we have neglected the weighted average $\langle k_{ts} \rangle$ and used simply a small amplitude approximation $\Delta f \propto k_{ts}$. For the amplitudes used in imaging, $A = 400\,\mathrm{pm}$, this is rarely accurate when probing chemical interactions. However, the electrostatic force has a much weaker distance dependance. We have also approximated $\langle I \rangle \approx I$. This is slighty inaccurate, as $\langle I \rangle$ is 14 % of the peak tunneling current [6].

From the fit, we can extract a value for R_S of $164\,\mathrm{M\Omega}$. This also agrees very well with our predicted value of $159\,\mathrm{M\Omega}$, derived in (5.17).

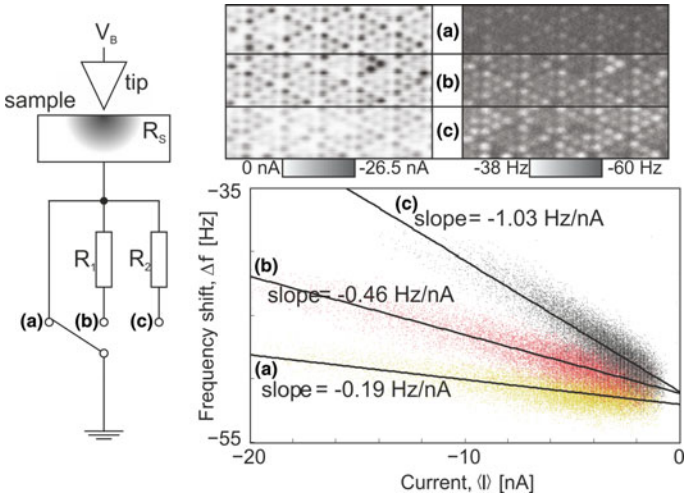

Fig. 5.6 Adding additional external resistors, R_1 and R_2, allows us to characterize R_S. Simultaneous $\langle I \rangle$ and Δf data collected at $V_B = -1.5\,\mathrm{V}$ with **a** $R_{ext} = 0\,\Omega$ **b** $R_{ext} = R_1 = 10\,\mathrm{M\Omega}$, and **c** $R_{ext} = R_2 = 30\,\mathrm{M\Omega}$. Adapted from [16]

It is important that the contrast in these images was due only to the electrostatic interaction. This was verified by the observation that under normal STM imaging conditions, only the phantom force produces contrast in constant-height images, as discussed in the previous subsection. That the images were taken at constant height also confirms that the contrast is not due to the long-range van der Waals component.

5.2.2 Kelvin Probe Force Microscopy

Kelvin Probe Force Microscopy (KPFM) is based on the idea that the difference in the work functions of two metals, $\Delta\Phi$, can be determined by measuring the force between the two as a function of an applied bias voltage, as described in (5.12).

Practically, it is performed in one of two ways. In the conceptually simplest approach, Δf is recorded at a fixed tip position as a function of V_B. The apex of the resulting parabola is a measure of the local work function, $\Delta\Phi_L$. An alternate method, inspired by the so-called vibrating capacitor method, was introduced by Nonnenmacher and coworkers [36], in which the system is excited with an AC voltage at a frequency f_0 and the response is measured at $2f_0$. We will focus on the first method because it contains all relevant physics and is the technique that we performed in this set of experiments.

Similar to AFM imaging, KPFM data can be very susceptible to phantom force effects. Starting from (5.21), the extremum of the parabola will not be $\Delta\Phi_L$, but rather dependant upon R_S:

$$-V_B = \Delta\Phi_L \frac{R_J + R_S}{R_J} \tag{5.35}$$

The danger, of course, is that this is not simply a sample property $\Delta\Phi_L$ but also contains a distance dependant term, R_J. As the tip approaches the sample, R_J decreases and $\Delta\Phi_L$ appears to increase in magnitude.

There is a further complication because we are sensitive not to forces but to force gradients. Equation (5.26) describes the electrostatic component of the force gradient, and consists of two terms. The first term includes $\frac{\mathrm{d}^2C}{\mathrm{d}z^2}$, which is positive,[6] and a quadratic term which is positive. Therefore

$$-\frac{1}{2}\frac{\mathrm{d}^2C}{\mathrm{d}z^2}(V_B + \Delta\Phi - IR_S)^2 \leq 0 \tag{5.36}$$

Normally this is the only term that is considered in KPFM. However, there is a second term of opposite sign. Because both $\frac{\mathrm{d}C}{\mathrm{d}z}$ and $\frac{\mathrm{d}I}{\mathrm{d}z}$ (as discussed in (5.29)) are negative,

$$\frac{\mathrm{d}C}{\mathrm{d}z}(V_B + \Delta\Phi - IR_S)\left(R_S\frac{\mathrm{d}I}{\mathrm{d}z}\right) \geq 0 \tag{5.37}$$

When performing KPFM with low resistance samples, this term can be ignored, as $R_S \approx 0\,\Omega$.

We performed bias-spectroscopy at low temperature on the Si(111)−7×7 surface. Figure 5.7 shows the simultaneously-collected $\langle I\rangle$ and Δf images, as well as $\langle k_{ts}\rangle$ spectra for various tip-sample distances. The z distances are relative to the imaging height. Curves were offset to show the shape easier. The strong z-dependance of the curvature of the parabolae is due to the $\frac{\mathrm{d}I}{\mathrm{d}z}$ term, which increases with decreasing tip-sample height, dominating the $\langle k_{ts}\rangle$ data with positive curvature.

We applied a model of the tip as a sphere as described by Hudlet et al. [37]. Similar to the model described in Sect. 5.1.6, we added a $z-$offset term that accounts for the fact that the electrostatic interaction is dominated by a component several atomic layers higher than the imaging apex. The results of the model are shown as dashed lines in Fig. 5.7c, with a tip radius of 4.0 nm, a $z-$offset value of 0.7 nm, and a tunnel current decay constant of $\kappa = 0.9 \times 10^{10}\,\mathrm{m}^{-1}$.

This model very accurately describes the significant feature in the data, that is, the upward-turning of the parabolae at smaller tip-sample distances. The accuracy, especially at larger tip-sample distances, could probably be increased with a more complex geometric model of the tip. At $z = 200$ pm, the shape of the curve seems to deviate from a parabola. This could be due to the electronic structure discussed earlier; in other words, a limitation of the simple Ohmic model.

[6] If this is not clear, consider a parallel plate capacitor with $C = \varepsilon A z^{-1}$. The first derivative with z is negative, and the second is positive.

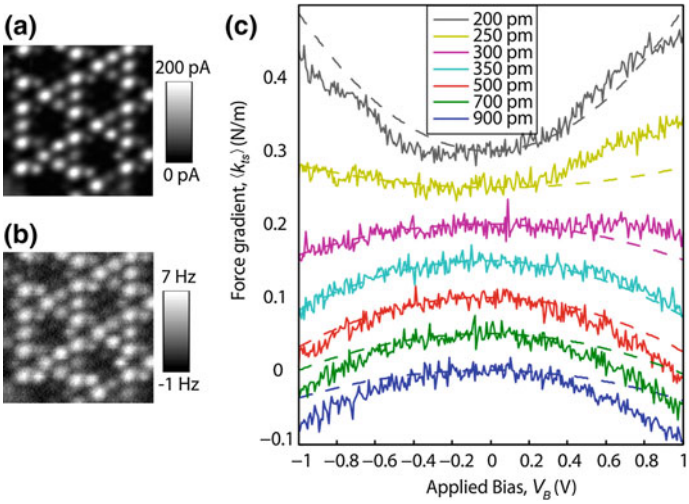

Fig. 5.7 Constant-height **a** $\langle I \rangle$ and **b** Δf images. **c** Kelvin parabolae taken over an adatom at various z distances. Reprinted with permission from A.J. Weymouth and F.J. Giessibl, Appl. Phys. Lett. 101, 213105 (2012), Copyright 2012, AIP Publishing LLC

5.2.3 Observations on H-Terminated Si(100)

The unsaturated Si(100) surface, when prepared in vacuum, reconstructs into rows of Si dimers [39]. This surface is quite reactive, making it experimentally difficult to work with, especially at room temperature. Exposing Si(100) to hydrogen saturates the unsaturated dangling bonds [40]. The electronic states of the hydrogenated dimers have been shown to lie outside the bandgap of bulk Si [41], meaning that in contrast to Si(111)−7×7, the surface is semiconducting. Under normal preparation, not all Si atoms are saturated but a few unsaturated reactive dangling bonds are left.

We compare data taken in which it is the dominant imaging mechanism, shown schematically in Fig. 5.8a, to AFM data collected at low bias, shown in Fig. 5.8d. Figure 5.8b and c show simultaneous AFM and STM data collected with a bias of 1.5 V. In them, the dimer rows can be seen running from upper left to lower right. The low contrast is due to the fact that we did not want to encounter a tunneling current that was too high when scanning over the defect area, circled in red. This is a dangling bond, which we would expect to observe in AFM data as attractive. However due to the increase of the tunneling current over it, the phantom force effect causes an increase in Δf that makes it appear repulsive. This attractive interaction is clearly observed in AFM data collected at low bias, as shown in Fig. 5.8e. (The red circle has been laterally offset to account for drift.) Not only is the atomic structure of the surface visible, as shown by the spacefill model overlaid in the lower third of the image, but the defect now appears as attractive.

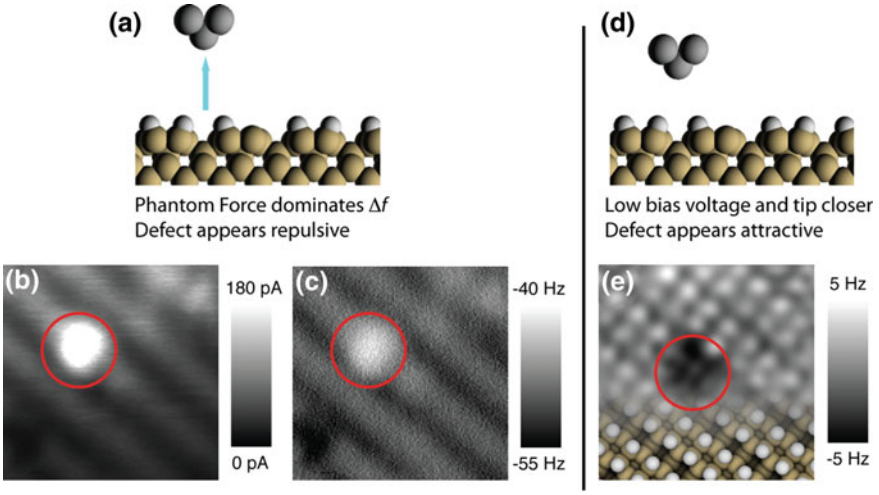

Fig. 5.8 When the tip is far from the surface with an applied bias of 1.5 V, (**a**) atomic contrast can be observed in STM, (**b**) and AFM data, (**c**). The defect outlined in *red* appears repulsive. However, at close tip-sample distances, (**d**) and low bias, in this case 200 mV, it appears attractive, (**e**). (Plane subtraction and low-pass filtering have been applied to **e** for clarity.) Images are 3 nm × 3 nm [38]

5.2.4 Molecular Adsorbate on Graphene

The R_S term in our theory describes the sample resistance that is internal and therefore decreases the voltage in the junction. This resistance can be due to resistivity of a bulk sample, and it can also be due to a smaller resistive element on the surface.

Graphene has one of the highest electron mobilities of any material. We have investigated graphene grown on SiC, supplied by Th. Seyller's workgroup [42], with low temperature AFM and STM. On some samples, we come across adsorbates that we can manipulate with the tip. We propose that these adsorbates are hydrocarbon molecules that are either a biproduct of the manufacturing or a natural contaminant that is introduced when we fix the graphene samples to appropriate holders.

Figure 5.9 shows constant-height Δf data of one of these adsorbates, both (a) with and (b) without an applied bias voltage. This dataset was collected by moving the tip over each line first with an applied bias and then without. Most of the image shows very similar contrast, however, there is a lobe on the lower left that appears brighter in Fig. 5.9a. We compared a line scan over this lobe from the two images, as shown in Fig. 5.9c.

The area with greater Δf corresponds to a region where the current was greater. Because these adsorbates are easy to manipulate with the tip, they are likely not strongly coupled to the surface. This weak coupling could be the physical explanation of the potential drop from the point on the molecule into which electrons tunnel, and the rest of the surface, where the electrons can rapidly move into equilibrium.

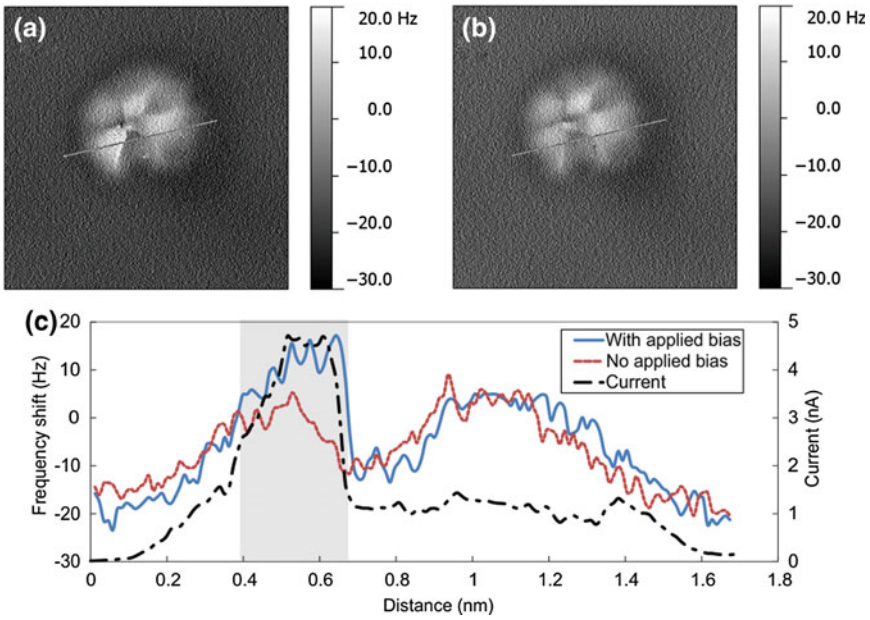

Fig. 5.9 Constant height measurements reveal a difference in $\langle k \rangle_{ts}$ images as a function of bias voltage. **a** With an applied bias of 0.4 V. **b** 0 V. **c** A linescan comparing the two $\langle k \rangle_{ts}$ data and the corresponding current

5.3 Concluding Remarks and Outlook

There are several mentions in literature of AFM contrast inversion as a function of the applied bias voltage, and therefore, of the current. The three reviewed here are investigations of the Si(111)−7×7 surface. Molitor et al. reported contrast inversion depending upon scan parameters [43]. While scanning in STM mode (with an undriven thermal amplitude of $A = 30\,\text{pm}$ and an applied bias of 1.1 V) they report a decrease of Δf over the adatoms. When scanning in AFM mode, using Δf to regulate the tip height (and a driven amplitude of $A = 20\,\text{nm}$, and a voltage of 1.9 V), they observe contrast inversion in the Δf image. Arai and Tomitori compared data taken with and without an applied voltage [44]. They note that differences between the adatom species can be seen with the applied voltage, but not without. At higher applied voltages, the authors observe contrast inversion of the AFM signal. Guggisberg et al. also reported inverted AFM contrast as a function of the applied voltage [45]. They note that at a sample bias of 2 V, the AFM signal is inverted and moreover, that the features correlate very well with the recorded tunneling current data. They compare this image to one taken at −1 V, where the contrast is not inverted.

One explanation for all these observations is the phantom force. In Sect. 5.2.1, we present data in which the Δf images appear similar to STM data as a function of bias voltage. This similar contrast is because when probing the filled states

of Si(111)−7×7, the tunnelling current is higher over the faulted half. Therefore, differences in the adatoms can be observed that is equivalent to that seen in STM images.

It is important to note that the occurrence of the phantom force does not require that the tunneling current is measured. Rather, it is due to an additional resistance outside the tip-sample junction. By adding external resistors, as discussed in Sect. 5.2.1, we were able to quantify this additional resistive element.

We present a model based upon a Ohmic mechanism of conductance that explains our observed images and spectra. It's likely that this can also explain previous reports of contrast inversion in AFM as a function of voltage. While most of our observations have demonstrated the phantom force on surfaces of semiconductors, we also presented data where it appears to be present on a molecular adsorbate. As AFM studies continue, and are coupled with a drive to understand the electronic structure of surface and adsorbates, the phantom force is an effect which must be taken into account.

Acknowledgments A.J.W. thanks J. Repp and T. Arai for helpful discussions, as well as B. Drevniok for his helpful comments of the manuscript. The authors acknowledge T. Wutscher for his great contributions to the phantom force work.

References

1. G. Binnig, H. Rohrer, C. Gerber, E. Weibel, Phys. Rev. Lett. **50**(2), 120 (1983)
2. G. Binnig, H. Rohrer, Rev. Mod. Phys. **71**(2), S324 (1999)
3. J. Tersoff, D. Hamann, Phys. Rev. B **31**, 805 (1985)
4. J.M. Blanco, F. Flores, R. Pérez, Prog. Surf. Sci. **81**(10–12), 403 (2006)
5. G. Binnig, H. Rohrer, C. Gerber, E. Weibel, Phys. Rev. Lett. **49**(1), 57 (1982)
6. F.J. Giessibl, Rev. Mod. Phys. **75**(3), 949 (2003)
7. J.E. Sader, S.P. Jarvis, Appl. Phys. Lett. **84**(10), 1801 (2004)
8. F.J. Giessibl, Appl. Phys. Lett. **78**, 123 (2001)
9. J. Welker, E. Illek, F.J. Giessibl, Beilstein J. Nanotechnol. **3**, 238 (2012)
10. F.J. Giessibl, Science **267**(5194), 68 (1995)
11. R. Pérez, I. Štich, M. Payne, K. Terakura, Phys. Rev. B **58**(16), 10835 (1998)
12. N. Moll, L. Gross, F. Mohn, A. Curioni, G. Meyer, New J. Phys. **12**(12), 125020 (2010)
13. A.J. Weymouth, T. Hofmann, F.J. Giessibl, Science **343**, 1120 (2014)
14. F.J. Giessibl, Phys. Rev. B **56**(24), 16010 (1997)
15. R.M. Feenstra, Y. Dong, M.P. Semtsiv, W.T. Masselink, Nanotechnology **18**(4), 044015 (2007)
16. A.J. Weymouth, T. Wutscher, J. Welker, T. Hofmann, F.J. Giessibl, Phys. Rev. Lett. **106**(22), 226801 (2011)
17. B. Weber, S. Mahapatra, H. Ryu, S. Lee, A. Fuhrer, T.C.G. Reusch, D.L. Thompson, W.C.T. Lee, G. Klimeck, L.C.L. Hollenberg, M.Y. Simmons, Science **335**(6064), 64 (2012)
18. R. Losio, K.N. Altmann, F.J. Himpsel, Phys. Rev. B **61**, 10845 (2000)
19. J. Mysliveček, A. Stróecka, J. Steffl, P. Sobotík, I. Oštádal, B. Voigtländer, Phys. Rev. B **73**, 161302(R) (2006)
20. P. Jelínek, M. Švec, P. Pou, R. Perez, V. Cháb, Phys. Rev. Lett. **101**(17), 176101 (2008)
21. R.J. Hamers, R.M. Tromp, J.E. Demuth, Phys. Rev. Lett. **56**(18), 1972 (1986)
22. N. Agrait, J. Rodrigo, S. Vieira, Phys. Rev. B **47**(18), 12345 (1993)
23. K.I. Morita, Y. Sugimoto, M. Abe, S. Morita, Appl. Phys. Express **4**(11), 115201 (2011)

24. D.R. Lide (ed.), *CRC Handbook of Chemistry and Physics, Internet Version 2005* (CRC Press, Boca Raton, 2005)
25. M. Guggisberg, M. Bammerlin, C. Loppacher, O. Pfeiffer, A. Abdurixit, V. Barwich, R. Bennewitz, A. Baratoff, E. Meyer, H.J. Güntherodt, Phys. Rev. B **61**(16), 11151 (2000)
26. R.A. Wolkow, P. Avouris, Phys. Rev. Lett. **60**(11), 1049 (1988)
27. A.J. Weymouth, R.H. Miwa, G.J.A. Edge, G.P. Srivastava, A.B. McLean, Chemical Communications (Cambridge, England) **47**(28), 8031 (2011)
28. A. Sweetman, P. Rahe, P. Moriarty, Nano Lett. **14**(5), 2265 (2014)
29. M.A. Lantz, H.J. Hug, R. Hoffmann, P.J. van Schendel, P. Kappenberger, S. Martin, A. Baratoff, H.J. Güntherodt, Science **291**(5513), 2580 (2001)
30. J. Welker, A.J. Weymouth, F.J. Giessibl, ACS Nano **7**(8), 7377 (2013)
31. F.J. Giessibl, B.M. Trafas, Rev. Sci. Instrum. **65**(6), 1923 (1994)
32. R. Feenstra, G. Meyer, K. Rieder, Phys. Rev. B **69**(8), 081309(R) (2004)
33. V. Ramachandran, R.M. Feenstra, Phys. Rev. Lett. **82**, 1000 (1999)
34. M. McEllistrem, G. Haase, D. Chen, R.J. Hamers, Phys. Rev. Lett. **70**(16), 2471 (1993)
35. T. Wutscher, A.J. Weymouth, F.J. Giessibl, Phys. Rev. B **85**(19), 195426 (2012)
36. M. Nonnenmacher, M.P. OBoyle, H.K. Wickramasinghe. Appl. Phys. Lett. **58**(25), 2921 (1991)
37. S. Hudlet, M. Saint Jean, C. Guthmann, J. Berger, Eur. Phys. J. B **2**(1), 5 (1998)
38. T. Wutscher, Untersuchung der Kopplung von atomaren Strömen und atomaren Kräften durch die Rastersondenmikroskopie. Ph.D. thesis, Universität Regensburg (2012)
39. D.J. Chadi, Phys. Rev. Lett. **43**(1), 43 (1979)
40. J.J. Boland, Phys. Rev. Lett. **65**(26), 3325 (1990)
41. H. Raza, Phys. Rev. B **76**(4), 045308 (2007)
42. K.V. Emtsev, A. Bostwick, K. Horn, J. Jobst, G.L. Kellogg, L. Ley, J.L. McChesney, T. Ohta, S.A. Reshanov, J. Röhrl, E. Rotenberg, A.K. Schmid, D. Waldmann, H.B. Weber, T. Seyller, Nat. Mater. **8**(3), 203 (2009)
43. S. Molitor, P. Güthner, T. Berghaus, App. Surf. Sci. **140**(3–4), 276 (1999)
44. T. Arai, M. Tomitori, Appl. Surf. Sci. **157**(4), 207 (2000)
45. M. Guggisberg, O. Pfeiffer, S. Schär, V. Barwich, M. Bammerlin, C. Loppacher, R. Bennewitz, A. Baratoff, E. Meyer, App. Phys. A Mater. Sci. Proc. **72**(S1), S19 (2001)

Chapter 6
Non-contact Friction

Marcin Kisiel, Markus Samadashvili, Urs Gysin and Ernst Meyer

Abstract Our understanding of friction and mechanism of energy dissipation has undoubtedly experienced a tremendous profit after the introduction of scanning probe microscopy. Nowadays the tribological response of a sliding asperity can be easily traced down to the atomic scale. Still, many important aspects of friction on the nanoscale are scarcely studied. Among them we can easily recognize the dissipation accompanying the motion of a nano-object in close proximity to a solid surface. An example, which is quite suitable for experimental investigations, is given by the oscillations of a tiny pendulum. Here we report on different mechanisms of energy loss—for instance probably the most common Joule dissipation. Next we demonstrate that pendulum oscillations are expected to induce both phononic and electronic excitations in the underlying surface and the clear distinction between them is possible while working over metal/superconductor phase transition. Finally, we describe an example of coupling of mechanical oscillator to the charge-density-wave phase, an exquisitely subtle long-range order property of matter.

6.1 Introduction: Dissipation at Large Separation

Friction force has a pivotal role in nature and our everyday life is full of examples of frictional processes. When two macroscopic bodies slide in contact energy is dissipated due to friction [1, 2]. Sometimes it is desired, like in case of brakes in the bicycle, sometimes unwelcome—when you ask yourself why your automated coffee machine broke for the third time. In nanoscale, a tiny friction force is present

M. Kisiel (✉) · M. Samadashvili · U. Gysin · E. Meyer
Department of Physics, Univeristy of Basel, Klingelberstrasse 82,
4056 Basel, Switzerland
e-mail: marcin.kisiel@unibas.ch

M. Samadashvili
e-mail: Markus.Langer@unibas.ch

U. Gysin
e-mail: urs.gysin@unibas.ch

E. Meyer
e-mail: ernst.meyer@unibas.ch

© Springer International Publishing Switzerland 2015

S. Morita et al. (eds.), *Noncontact Atomic Force Microscopy*,
NanoScience and Technology, DOI 10.1007/978-3-319-15588-3_6

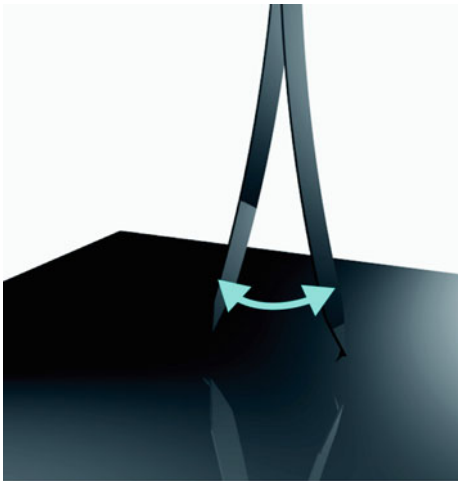

Fig. 6.1 Schematic view of the oscillating cantilever in the pendulum geometry

when bodies in relative motion are separated by few nanometer gap [3–5]. This non-contact form of friction might be successfully measured by highly sensitive cantilever oscillating like a tiny pendulum over the surface as it is shown in Fig. 6.1 [5–8]. The elusive non-contact friction might by due to vdW interaction, which is mediated by the long-range electromagnetic fields or in many cases by fluctuations of static surface charges arising from material inhomogeneities [9]. It also strongly depends on the bias voltage between tip and sample. The non-contact friction or we should rather say energy dissipation is a non-reversible process, where the kinetic energy of the damped oscillator is transferred into heat, which is observed as a decay in time of the cantilever amplitude. The amplitude drops until the thermal equilibrium is reached. Both decay time τ and equilibrium fluctuations $x(t)$ contain information about the dissipative process. The quality factor Q is equal to:

$$Q = \frac{\tau \omega_0}{2} \tag{6.1}$$

and the corresponding damping coefficient is given by:

$$\Gamma = \frac{k}{\omega_0 Q} \tag{6.2}$$

where k is the spring constant and ω_0 is oscillation frequency of the cantilever. It is obvious (6.2), that the smallest spring constant k and the highest quality factor Q imply higher non-contact friction sensitivity. Cantilevers with these features are also very force sensitive. The minimal detectable force $F_{\min}$ is given by the formula:

$$F_{\min} = \sqrt{\frac{2k_B T \Gamma \Delta\omega}{\pi}} \tag{6.3}$$

where k_B is the Boltzmann constant, T and $\Delta\omega$ are the temperature and the bandwidth of the measurement. Any change of the friction coefficient Γ is always accompanied by a change of the minimal detectable force.

In case of an extremely soft cantilever characterised by spring constant $k = 130\,\mu$N/m, the quality factor $Q = 250{,}000$ and the resonance frequency $f_0 = 6\,$kHz the non-contact friction is in the order of $\Gamma = 10^{-14}\,$kg/s.

Approaching soft cantilever to the surface will open new dissipation channels, however the tip-surface interaction will immediately provoke cantilever snap into contact. That will happen on every surface when the attractive force gradient is larger then cantilever spring constant. An easy way to overcome this obstacle is to oscillate the cantilever in a pendulum geometry. This way the cantilever is oriented perpendicularly to the surface and oscillates like a tiny pendulum over it.

In this chapter several experiments reporting on non-contact friction are discussed. Next section concerns the experimental tool designed to study non-contact friction—the Atomic Force Microscope (AFM) operating in pendulum geometry. We next discuss the mechanisms influencing internal dissipation of the sensor, as they strongly limit our measurement sensitivity. In order to introduce non-contact friction itself, few mechanisms leading to this phenomena are discussed in the following section. Finally three experiments dealing with non-contact friction are reported. This part is structured as follows: first, experiment on γ-irradiated quartz sample is discussed. It was found that non-contact friction increases at separations of 30 nm. In this case long-range dissipation is related to the long-range electrostatic forces and distance dependence of the contact potential was found to influence the non-contact friction. Next we discuss the experiment on superconducting Nb surface which allowed to distinguish between electronic and phononic dissipation channels. The last part reports on experiment on $NbSe_2$ surface, where the non-contact friction is caused by the hysteretic switching of the charge density wave provoked by the oscillating tip.

6.2 The Pendulum AFM System

6.2.1 The Microscope

The results reported in this chapter were obtained by means of pendulum AFM located at University of Basel with the capability of working under Ultra High Vacuum (UHV) ($p < 10^{-10}\,$mbar) as well as cryogenic conditions ($T = 5\,$K). The setup of the microscope is shown in Fig. 6.2 and is described in details elsewhere [10].

It is worth to mention that the beam deflection detection technique [11] was chosen to measure the cantilever oscillations. The technique does not rely on a laser light source with a long coherence length. Instead superluminescent diodes (e.g. Superlum SLD-381-MP3 or Hamamatsu SLD) with lower noise levels are used as a light source. The cantilever motion is controlled by means of standard Phase-Lock-Loop (PLL) electronics where the detection of the frequency, amplitude and phase are performed.

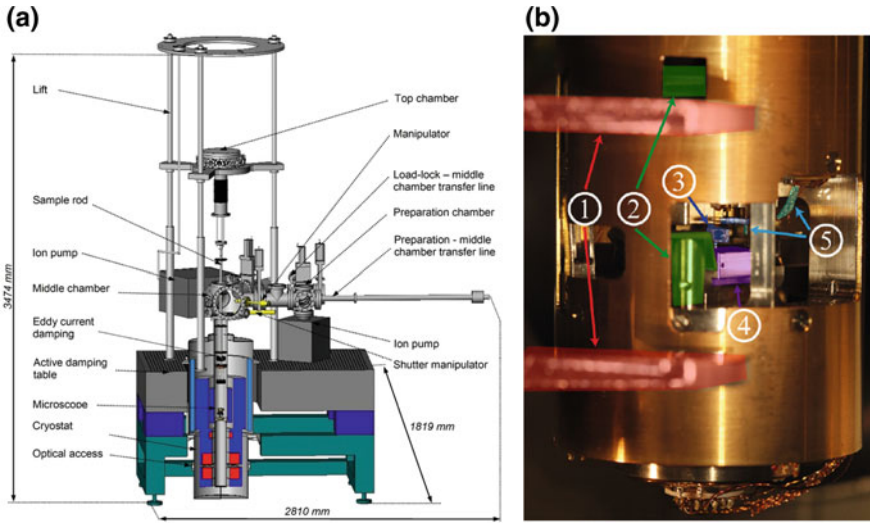

Fig. 6.2 The UHV system is shown in figure (**a**) with the top loaded cryostat. The microscope itself is shown in (**b**), where *1* (*red*) is the microscope holder, *2* (*green*) the mirrors of the beam deflection detection system, *3* (*dark blue*) the cantilever itself, *4* (*violet*) the sample holder and *5* (*light blue*) the STM shielded current line

In order to maintain the amplitude of oscillation constant the excitation voltage is brought back to the shaking piezo.

The pendulum AFM is not an overwhelming imaging tool and the atomic resolution is hard to reach. The capability to acquire a topography information is limited due to the lateral oscillation and the spacial averaging is performed in every topographic pixel. The strength of the pendulum geometry lays in the spectroscopy.

6.2.2 Internal Friction of the Cantilever

The experimentally determined cantilever damping Γ is a superposition of different ingredients:

$$\Gamma(T, p, E, B, d, ...) = \Gamma_0 + \Gamma_{TS} \tag{6.4}$$

and depends in general on temperature T, pressure p and external electric E and magnetic B fields. The influence of the electromagnetic field plays a role in case of tip-sample proximity. This effect leads to a distance dependent friction coefficient $\Gamma_{TS}(d)$ at small tip sample separations [5–7, 12–14]. The internal friction of the cantilever Γ_0 describes the friction losses which occur while bending of the cantilever and several components might be distinguished:

1. Viscous damping due to the presence of gases,
2. Energy losses due to clamping of the cantilever,

3. Thermoelastic damping,
4. Bulk and surface energy looses.

To minimize the viscous damping which occurs due to inelastic scattering between the vibrating cantilever and gas molecules cantilever has to be operated under vacuum conditions. At pressures below $p < 10^6$ mbar viscous damping is negligible [15]. The second effect might be partly eliminated by means of rigid clamping and avoiding of glues with high damping rates [16].

Periodic compression and expansion of oscillating cantilever causes heat flow between compressed and expanded areas. The energy loss due to local heating of the cantilever is known as a thermoelastic damping. The thermoelastic damping is the dominant loss mechanism at room temperature [17]. At temperatures below $T < 200$ K other mechanisms start to dominate such as bulk or surface losses.

Bulk and surface losses due to scattering of elastic waves on defects present on the surface or in the bulk are dominant loss mechanisms at low temperatures. The time dependent stress field changes the energy landscape of the defects and the instabilities of those might occur. The effect is related to jumps of the atoms between different equilibrium positions. This effect is temperature dependent and dissipation versus temperature curves show Debye activation peaks. In case of Silicon cantilever Debye peak is observed often at $T = 30$ K [18]. Another peak positioned at $T = 160$ K cannot be related to such an activation peak because of too high activation barrier. It is also observed that the peak does not shift with the resonance frequency, which is not in agreement with the simple activation energy model. It has been observed that the 160 K peak is reduced after annealing the cantilever under vacuum conditions and the authors suggest that it is related to an existence of adsorbate layer [18]. In fact coating of cantilevers leads to a strong increase of dissipation. The rise of Γ_0 is owing to the phonon scattering on grain boundaries because of polycrystalline nature of the coating layer. The presence of adsorbates (H_2O or hydrocarbons) also have a negative impact on the internal friction. It has been shown that annealing at temperatures up to about 700 °C under ultra high vacuum conditions leads to substantial reduction of dissipation [19, 20]. Figure 6.3 demonstrates the improvement of pristine quality

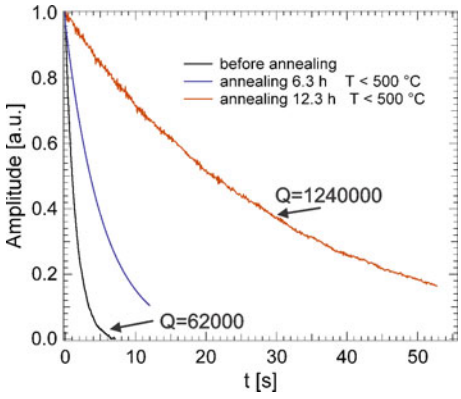

Fig. 6.3 Ring down measurement of a cantilever before and after annealing under UHV-conditions and at the temperature $T = 77$ K. The initial quality factor of 62,000 is improved by an order of magnitude after 6 h annealing. Further annealing improved the quality factor to 1,240,000. Data from [20]

factor of 62,000 by an order of magnitude after 6 h annealing at temperatures below at 500 °C. Further annealing improved the quality factor to 1,200,000 as measured in $T = 77$ K. The increase of sensitivity is mainly due to removal of weakly bounded molecules from the cantilever surface or alternatively the amount of surface/bulk defects is reduced. It is also known that long term annealing leads to negligible amount of localized charges at the end of the probing tip.

6.3 Non-contact Friction Due to Tip-Sample Interaction

Approaching the cantilever close to a surface leads to distance d dependent dissipation $\Gamma_{TS}(d)$. Experimentally there are three methods to determine the non-contact friction: ring-down measurements, the measurement of the excitation voltage A_{exc} which is needed to maintain constant amplitude of oscillation and the measurement of the power spectral density $S(\omega)$ of the cantilever fluctuations [6, 21].

In the first method the Γ is determined from the decay time τ of the cantilever oscillations using the relations (6.1) and (6.2). In this method, the cantilever is oscillating at its resonant frequency with a constant amplitude until the driving voltage A_{exc} is suddenly switched off and the oscillations decay towards thermal equilibrium with a characteristic time τ (see Fig. 6.3). This method apply to the sensors with relatively large quality factors Q.

Usually the cantilever oscillations are controlled by means of phase-locked loop (PLL) feedback system, where the phase between constant amplitude cantilever oscillation signal and cantilever excitation A_{exc} is locked. This way the frequency shift Δf caused by the tip sample interaction is measured. The friction coefficient is calculated according to a formula:

$$\Gamma = \Gamma_0 \left(\frac{A_{\mathrm{exc}}(d)}{A_{\mathrm{exc},0}} - \frac{f(d)}{f_0} \right) , \tag{6.5}$$

where Γ_0 is the internal cantilever dissipation, measured at large tip-sample separation, $A_{\mathrm{exc}}(d)$ and $f(d)$ are the distance dependent excitation amplitude (as measured by the excitation voltage needed to excite the cantilever at constant oscillation amplitude A) and frequency of the cantilever and the suffix zero refers to the free cantilever. Both methods are complementary as it is demonstrated in Fig. 6.4.

Quantities like the frequency noise $\delta\omega$ of cantilever which oscillates with an amplitude x_0 at its resonance frequency ω_0 depend on the dissipation Γ [21]:

$$\delta\omega = \frac{\omega}{x_0 k} \sqrt{\frac{2 k_B T \Gamma \Delta\omega}{\pi^3}} \tag{6.6}$$

The oscillator frequency noise $\delta\omega$ is influenced by Γ and the temperature T. It is therefore possible to quantitatively measure the non-contact friction based on power

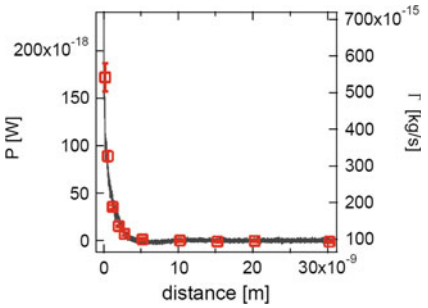

Fig. 6.4 The non-contact friction coefficient Γ and dissipated power P as a function of distance from Cu(110) surface measured by means of ring down method (*red squares*) and by measurement of the excitation voltage A_{exc} (*gray line*), (6.5). Cantilever and sample temperature was equal $T = 77\,\mathrm{K}$

spectral density of the $\delta\omega$. The power spectral noise density $S(\omega)^2\Delta\omega = \delta\omega^2$ can be estimated in a narrow bandwidth as follows:

$$S(\omega)^2 = \frac{2k_bT\omega_0^2\Gamma}{\pi^3k^2x_0^2} \tag{6.7}$$

6.4 Origins of Non-contact Friction

When contact friction deals with two bodies being close enough to interact chemically, the non-contact energy dissipation appears at any distance larger than chemical interaction range. The range of the interacting force determines the distance dependency of the friction coefficient Γ_{TS} and thus it is possible to distinguish between long-range and short-range friction forces. The non-contact friction mechanisms are still the subject of ongoing discussion, since the theoretically predicted values [3, 4] might be sometimes orders of magnitude smaller than experimentally observed ones [5, 6, 14, 22]. An overview of main dissipation mechanisms is presented below.

6.4.1 Phononic Friction

The non-contact friction by phonon creation of two interacting surfaces is only observed for realtively small tip sample separations, when the force acting on the surface is large. It implies the existence of tiny deformation of the surfaces induced by attractive van der Waals or electrostatic interaction. The oscillating cantilever tip over the surface of an elastic body might create the the time dependent stress field and thus excites acoustic waves parallel to the surface. In this case the energy is dissipated into emission of acoustic phonons. The situation is schematically sketched in Fig. 6.5a [23].

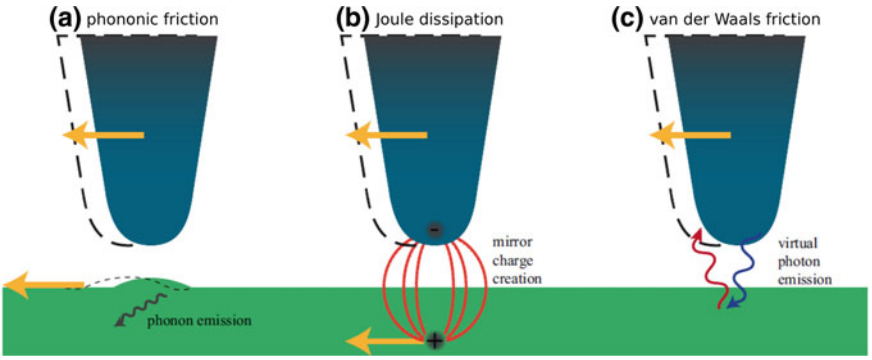

Fig. 6.5 Phononic friction appears at small tip sample separation. A surface deformation occurs and is dragged along with the tip movement. Upon the spatial variation of this deformation phonons are created and energy loss occurs (**a**). Joule dissipation takes place if non compensated charges situated on the surface or on the tip move through resistive media. The spatial variation creates a displacement current in tip/sample and the energy is lost to Joule heating (**b**). The van der Waals friction arises from the van der Waals force owing to dipole fluctuations or random currents. This is equivalent to emission of real/virtual photon to the surface. The re-emitted photon is absorbed back in the tip. The friction arises due to the fact, that the initial photon compared the the reabsorbed one are Doppler shifted (**c**)

6.4.2 Joule Dissipation

The Joule dissipation is present due to electrostatic forces which arise from permanent or fluctuating charges situated on the tip or/and the surface. The charge induced on the other surface follows the tip motion and experiences a resistive loss [13]. The charge interaction is strongly enhanced by biasing a tip. If a voltage U is applied between tip and sample, the system acts as a distance dependent capacitance. Due to the amplitude x_0 of the driven oscillator, the capacitance varies accordingly. The change of capacitance generates an alternating displacement current in the tip or sample upon the oscillation at the driving frequency ω_0. The dynamic distance is then given by $z(t) = z_0 + x_0 \cos(\omega_0 t)$. Further, we can write the displacement current D as:

$$D(t) = \frac{\partial C}{\partial t} U = \frac{\partial C}{\partial z} \frac{\partial z}{\partial t} U \tag{6.8}$$

and the dissipated power:

$$P_{\text{Joule}} = R_{t-s} D^2(t) = R_{t-s} \left(\frac{\partial C}{\partial z} \right)^2 U^2 x_0^2 \omega_0^2 \sin^2(\omega_0 t) \tag{6.9}$$

where R_{t-s} is the electrical resistance of the tip and sample. The average power dissipated $\langle P_{\text{Joule}} \rangle$ in one single oscillation cycle is equal:

$$\langle P_{\text{Joule}} \rangle = \pi R_{t-s} \left(\frac{\partial C}{\partial z} \right)^2 U^2 x_0^2 \omega_0^2 \tag{6.10}$$

6.4.3 van der Waals Friction

The van der Waals friction is a dissipative analogue of the conservative van der Waals force. Both mechanisms rely on the same physics. The force arises from the quantum fluctuation of the electron density, when a spontaneous dipole is created. The short lived dipole interacts with a nearby surface via a photon exchange and induces a dipole moment. The induced dipole re-emits a photon to the original one and a force arises between the two dipoles. When two bodies are in relative motion with respect to each other the friction force occurs owing to the Doppler shift of the exchanged photon. The situation is shown in Fig. 6.5c. The calculation of the van der Waals friction is more complex than the force, since it originates from the electromagnetic field fluctuations with moving boundary conditions. The literature approaches the solution by regarding each surface in its reference frame. The relation between the two electromagnetic fields of each reference frame is determined by the Lorentz transformation [3, 4]. Since, Γ originates from the stochastic electromagnetic field fluctuations, the energy loss might be calculated by means of fluctuation-dissipation theorem [24, 25]. For non-contact friction coefficient we obtain:

$$\Gamma \propto \frac{1}{k_B T} \int_0^\infty \langle \mathbf{f}(t_0) \mathbf{f}(t_1) \rangle \tag{6.11}$$

where $\mathbf{f}(t)$ is random force which obeys $\langle \mathbf{f}(t) \rangle = 0$ and $\langle \mathbf{f}(t_0) \mathbf{f}(t_1) \rangle$ is the autocorrelation function of the random force. The theory of van der Waals friction is more complex than conservative van der Waals force and up to now there is no unified understanding of it. Many theories [3, 26–28] lead to different scaling laws and large differences in the magnitude of the friction force. Experimentally, the problem is challenging, as well. Stipe and co-workers probably came closest to measuring the tiny vdW friction [5].

6.5 Dissipation at Large Separation

Dissipation due to electromagnetic interaction was first observed by Denk and Pohl [13]. Subsequent measurements [5] showed substantial electrostatic dissipation at separations of 1–200 nm measured by means of ultrasensitve force sensors oscillating in pendulum geometry. Friction coefficients of the order of 10^{-13} kg/s between gold coated tip and metal substrate were reported. The distance dependence of the friction coefficient scales with a power law $\Gamma \propto d^{-n}$ with an exponent $n = 1.3$. Volokitin et al. [3, 4] have found those data consistent with dissipation between a spherical

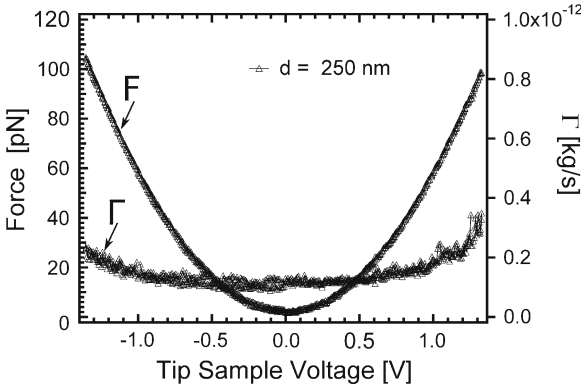

Fig. 6.6 Voltage-dependence of the normal force (F) and friction coefficient (Γ) at tip distance of d = 250 nm from 20 nm thick gold film. The quadratic behaviour of the normal force and the friction coefficient with respect to bias voltage indicate that non-contact friction has electrostatic origin. Data from [20]

tip and the clean metal surface. Their calculation showed that dissipation caused by fluctuations of the contact potential scales with the exponent $n = 1.5$.

Rast and collaborators performed similar experiment under ultra high vacuum conditions and at temperature $T = 7$ K [20]. They used a magnetic Co-Sm tip oscillating in proximity of γ-irradiated quartz substrate coated subsequently with 20 nm of gold. As it is shown in Fig. 6.6 both conservative and dissipative forces increase and obey the parabolic behaviour when the bias voltage is applied. The quadratic behaviour of Γ versus bias voltage is direct evidence of the electronic origin of friction [3–5]. In this particular case the time dependent electric field induces local electric currents in the sample and/or the cantilever. Moreover, the authors noticed strong dependence of contact potential on distance, presumably due to tip averaging over areas with different work functions. Both non-contact friction and force have a minimum exactly when the contact potential between tip and sample is compensated i.e. $V = +20$ mV, therefore it is important to compensate the contact potential in order to establish the minimum friction coefficients.

Compensating the contact potential allows us to investigate the friction force which is not dominated by Joule losses. Figure 6.7 shows the distance d dependence of the friction coefficient as a function of distance with compensated contact potential. Absolute values are between 1×10^{-13} kg/s down to 5×10^{-14} kg/s at $d > 30$ nm where the dissipation is mainly governed by internal friction. At separations below 30 nm the friction coefficient is larger than the internal friction of the cantilever and non-reversible energy flow between tip and sample is observed. Volokitin et al. [3, 4] calculated the friction coefficient of a tip separated by a distance d generated by a van der Waals friction force in dielectrics. For a cylindrical tip with radius R and width w the calculated friction coefficient scales with $d^{-1/2}$, which is in good agreement with the data. The friction might then occur due to fluctuating defects

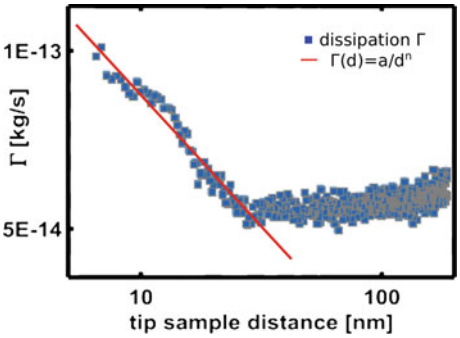

Fig. 6.7 Distance dependence of the non-contact friction coefficient for compensated contact potential at separations between 1–100 nm. At distance up to 30 nm friction scales with inverse power law $\Gamma \propto d^{-n}$. At a separation larger than 30 nm the friction is governed by the internal friction Γ_0 of the cantilever. Temperature of the measurement $T = 7$ K. Data from [20]

in the quartz crystal. The higher the defect concentration the higher the value of distance dependent friction coefficient. However, the 20 nm thick gold film prevents a penetrating of the electrical field into the nonconducting substrate, so that damping effects by this mechanism are minimized. A metal film always consists of a number of crystallites whose work function depend of the crystal orientation. The magnet tip also consists of numerous of crystals. Electrical fields always exist between the crystal boundaries with different work function. and the external bias voltage never compensates globally the electrical field. The non compensated electrical fields are decisive for the friction losses.

6.6 Suppression of Electronic Friction in the Superconducting State

The pendulum AFM tip oscillating in close proximity to a substrate might induce phononic excitations. An easy way to distinguish between electronic and phononic contribution to non-contact friction is to work across the metal/superconductor transition. In order to estimate the phononic and electronic contributions, Kisiel et al. [6] oscillate the pendulum cantilever over a 150 nm thick Nb film. The ultrasensitive cantilever with spring constant $k = 30$ mN/m and resonance frequency $f = 5.3$ kHz was used. After long term annealing under UHV condition the internal dissipation was improved and equal to $\Gamma_0 = 2.0 \times 10^{-12}$ kg/s at temperature $T = 6$ K. The cantilever end was exposed to focus ion beam (FIB) to form a sharp tip with spherical apex, approximately 50 nm in diameter (inset in Fig. 6.8). The oscillation amplitude $A = 5$ nm was kept constant during the measurement.

The dependence of the friction coefficient on the temperature is shown in Fig. 6.8. During the measurement the tip sample distance d = 0.5 nm was kept constant and

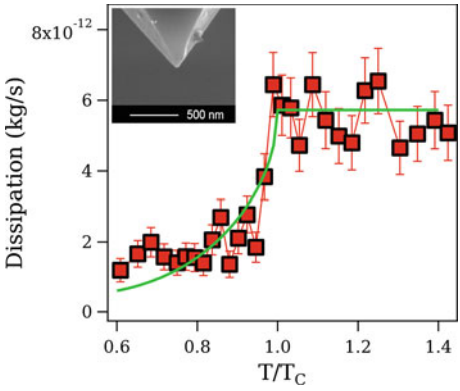

Fig. 6.8 Temperature variation of the non-contact friction coefficient across $T_c = 9.2\,\mathrm{K}$ of Nb surface. The *green line* is a fit of (6.12) to the measured data. *Inset* the focused ion beam (FIB) shaped tip used in experiment

the contact potential between tip and sample was compensated. The non-contact friction was measured by means of ring down method (see Fig. 6.3). The non-contact friction coefficient rises by a factor of three when the critical temperature T_c is approached from below and levels off in the normal state. It is equal to 25 μeV/cycle in superconducting phase and rises to 80 μeV/cycle in a metallic phase. The character of the friction coefficient in the vicinity of $T_c = 9.2\,\mathrm{K}$ is smooth as predicted by BCS (Bardeen-Cooper-Schrieffer) theory of superconductivity [29]. Persson [30, 31] realized that friction over superconducting phase transition is owing to the acoustic attenuation of the longitudinal acoustic phonons known from BCS theory. The surface contribution to the friction is given by temperature dependent formula:

$$\frac{\Gamma_{\mathrm{surf}}(T)}{\Gamma_{\mathrm{surf}}(T_c)} \simeq \frac{2}{\exp\left(\Delta(T)/k_B T\right) + 1} \tag{6.12}$$

where $\Delta(T)$ is the temperature dependent energy band gap:

$$\Delta(T) = C \cdot \frac{k_B T_c}{\sqrt{1 - (T/T_c)}} \tag{6.13}$$

The data shown in Fig. 6.8 agree with (6.12) and the fit parameter is $C = 3.8 \pm 0.7$. That is in relatively good agreement with BCS theory established value—$C = 3.5$. Based on those data the simplified mechanism might be sketched. In the superconducting phase, the electrons lose their identity and form Cooper pairs. Therefore, the energy is lost only to the emission of phonons. The acoustic wave created by oscillating tip interacts only with the normal electrons near the Fermi surface. Close to T_C the normal electron population is gradually growing and the acoustic wave attenuation rises due to electron-phonon scattering, which causes an onset of dissipation.

Further measurements of voltage V and distance d dependent friction support the hypothesis of separation of phononic and electronic channels. In Fig. 6.9 the $\Gamma(V)$ is shown in metallic state ($T = 13\,\mathrm{K}$) and in superconducting state ($T = 5.8\,\mathrm{K}$), both acquired at the same tip sample distance $d = 0.5\,\mathrm{nm}$. In the normal state data follow a quadratic dependence $\Gamma(V) \propto V^2$, as expected for dissipation due to ohmic

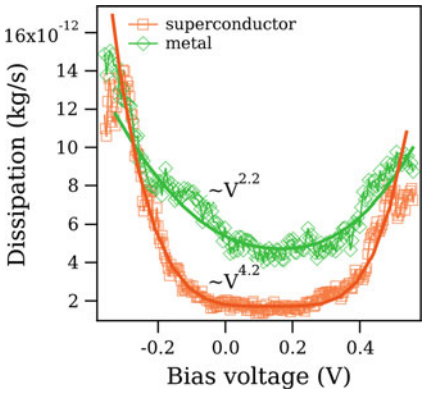

Fig. 6.9 The non-contact friction as a function of the bias voltage. The data were acquired in superconducting (*red*) and normal (*green*) state. The dissipation has a parabolic dependence in metallic state, while $\Gamma \propto \mathrm{V}^4$ for superconducting state of Nb. The tip sample distance is constant and equal $d = 0.5\,\mathrm{nm}$

looses [3, 4], In contrary to that in the superconducting state the friction depends on the fourth power of voltage—$\Gamma(V) \propto V^4$. Volokitin et al. [3, 4] calculated the non-contact friction between spherical tip oscillating laterally above the elastic surface. The friction is proportional to the second power of the static force—$\Gamma \propto F^2$. Since $F \propto V^2$, the friction coefficient has to vary as a fourth power of the voltage, which is in very good agreement with the measurement.

Dependence of the friction coefficient Γ on distance d for metallic and superconducting phase is shown in Fig. 6.10. The distance changes in between $0 < d < 3\,\mathrm{nm}$ and the contact potential is compensated. In normal state clear rise of dissipation is visible few nanometers away from the surface, otherwise as in the case of superconducting Nb state. The fit of the inverse power low function $\Gamma \propto d^{-n}$ to the experimental data gives $n = 1.0 \pm 0.1$ and $n = 3.8 \pm 0.3$, respectively for normal and superconducting state. In normal state the distance dependence is in good agreement with the results obtained by Stipe et.al ($n = 1.3$) [5]. In the case of phononic friction, Lifshitz theory of van der Waals interaction [32] predicts that elastic stress leads to a vdW force $F(d) \propto d^{-2}$. Thus the phononic friction should vary as $\Gamma_{ph} \propto d^{-4}$ and the experimental value is in excellent agreement with this prediction.

6.7 The Non-contact Friction Due to Phase Slips of the Charge Density Wave (CDW) in $NbSe_2$ Sample

So far we reported on dissipation due to linear response of the system under study. The non-contact friction in that case has a form of viscous drag. It this section we report on experiment when dissipation is produced by cycle of hysteretic processes induced in the sample by oscillating cantilever tip [7]. The measured sample is $NbSe_2$—an intercalated dichalcogenide compound with bulk charge density wave (CDW) state

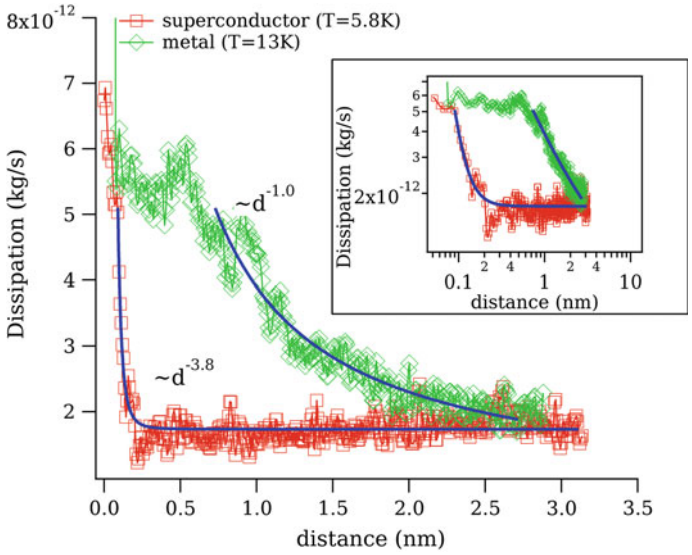

Fig. 6.10 Distance dependence of the non-contact friction coefficient for Nb superconductor (*red*) and Nb normal metal (*green*) state. The data are well fitted by inverse power law dependence $\Gamma \propto d^{-n}$ with $n = 1.0$ and $n = 3.8$, respectively for metal and superconducting state

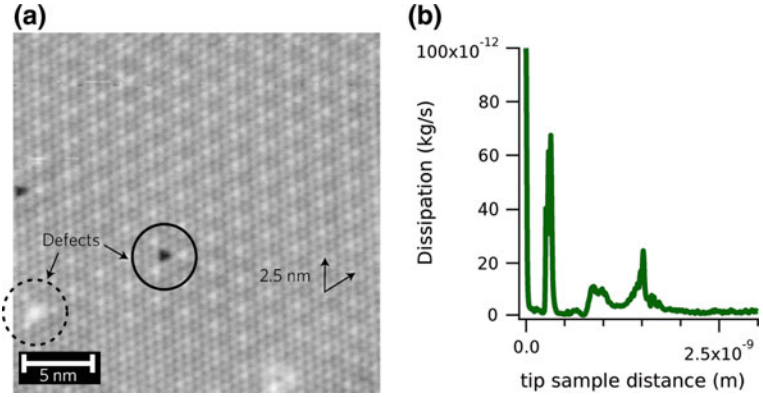

Fig. 6.11 **a** STM image of $NbSe_2$ surface obtained at $T = 6$ K. **b** The energy dissipation as a function of tip $NbSe_2$ sample distance for compensated contact potential difference. Three dissipation spikes positioned few nanometers above the surface are clearly visible

accompanied by periodic lattice distortion (PLD). Figure 6.11a shows the atomically resolved surface topography with the additional CDW induced Moirè pattern, which is incommensurate with underlying lattice. Layered dichalchogenides have long been known for their phase transitions leading to picometre-sized superstructure lattice distortions and corresponding new electronic periodicities in their low-temperature

ground state [33]. Lots of their properties, namely nonlinear conductivity, Shapiro steps are related to the CDW motion under the external voltage.

The probe consisted of a soft cantilever (ATEC-CONT from Nanosensors) with spring constant k = 120 mN/m, the resonance frequency f = 12 kHz, quality factor Q = 9×10^5 and a friction coefficient $\Gamma_0 = 1.7 \times 10^{-12}$ kg/s (at 6 K). Due to the asymmetric tip design the cantilever lateral oscillatory motion also implies a normal action. The lateral oscillation and the corresponding normal oscillation amplitudes were equal to A = 5 nm and A_{norm} = 180 pm, respectively. The dissipated energy was calculated according to (6.5), meaning the recorded signal was the excitation voltage needed to maintain constant oscillation amplitude. The distance dependence of friction coefficient $\Gamma(d)$ shows striking multiple of dissipation peaks arising at few nanometer distance from the surface, as shown in Fig. 6.11b. The data are contrary to most non-contact friction experiments, where the energy dissipation increases smoothly as the tip approaches the surface [5, 6]. Here however, the train of peaks on $NbSe_2$ surface is perfectly reproducible over well ordered surfaces. Moreover, the temperature evolution of the peaks suggests a strong connection with the CDW.

The dissipated power $P(z, V)$ versus tip sample distance z and tip sample bias voltage V is shown in Fig. 6.12. The bright features correspond to high dissipation maxima up to P = 2 meV/cycle. Within each dissipation branch the amount of energy loss stays constant, independently on bias voltage V. The giant non-contact friction maxima remain even after careful compensation of the contact potential difference

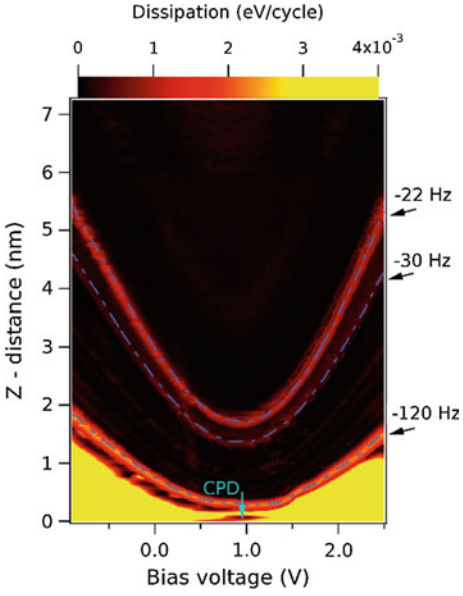

Fig. 6.12 Energy dissipation between $NbSe_2$ surface and oscillating pendulum AFM cantilever tip versus tip sample voltage and tip sample distance. Bright features correspond to high dissipation peaks. The peaks always follow the tip-sample interaction force (constant frequency shift contours $\Delta f = -22$ Hz, $\Delta f = -30$ Hz, $\Delta f = -120$ Hz are indicated with *dashed lines*)

(CPD) between the tip and the sample. In other words no matter the character of the interaction force is van der Waals ($V = V_{\mathrm{CPD}}$) or electrostatic ($V \neq V_{\mathrm{CPD}}$). Moreover, $z(V)$ dependence of the particular dissipation branch has a parabolic behaviour. For capacitively coupled conical tip and sample the force varies as $F \propto V^2/z$, meaning that the each dissipation peak always follow the same tip-sample interaction force. Indeed, the three dominant frictional maxima might be nicely superimposed with dashed lines which correspond to contours of constant cantilever frequency shift (constant conservative force)—$\Delta f = -22\,\mathrm{Hz}$, $\Delta f = -30\,\mathrm{Hz}$ and $\Delta f = -120\,\mathrm{Hz}$—as tip approaches the sample's surface. The above observations mean that the effect is force controlled rather than voltage controlled.

In order to understand the origin of dissipation spikes a theoretical model was proposed, where the CDW is considered to be an elastic medium, perturbed locally by the attractive potential of the cantilever tip [34, 35]. The CDW is described through phase $\phi(x)$ and amplitude $\rho(x)$ order parameters and the latter is assumed to be constant in case of small perturbations. Thus only phase degree of freedom is considered. The total energy is estimated according to equation:

$$E[\phi(x)] = \int [(\nabla\phi(x))^2 + V(x)\rho(x)]\mathrm{d}x. \tag{6.14}$$

Where first term is an elastic energy and the second stands for perturbation. The energy given by (6.14) is next minimized in order to find the preferential shape of the phase. This is shown in Fig. 6.13. For a given perturbation the charge peak below the tip displaces (red solid line) and the resulting CDW phase is getting distorted

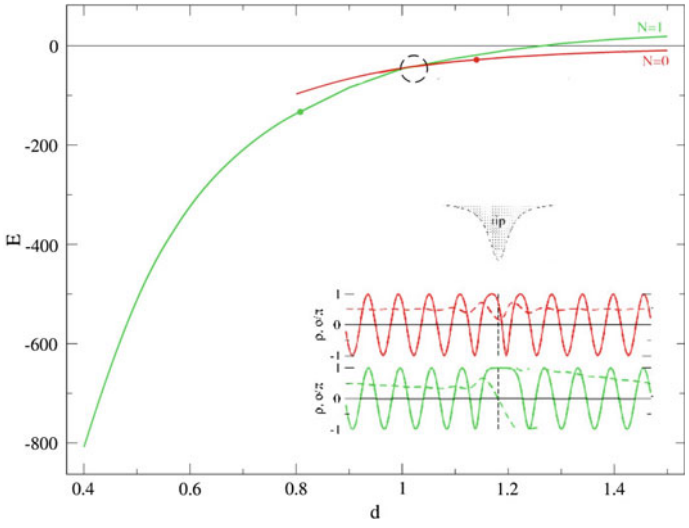

Fig. 6.13 The calculated energy E as a function of distance d for locally perturbed elastic charge density wave. The tip oscillation around crossover point (marked by a *circle*) causes hysteresis in tip dynamics. *Inset* shows the charge density (*solid lines*) and phase (*dashed lines*) of the CDW under the tip perturbation respectively for two different energy-distance curves

(red dashed line). As the force reaches critical value the central peak disappears and an extra 2π phase is pumped locally below the cantilever tip (green dashed line). The energies for the two discussed phase deformations are shown in Fig. 6.13 and a crossover energy is marked by a circle. Oscillations close to a crossover point will cause pumping *in* and *out* an extra 2π phase and thus be accompanied by a hysteresis cycle in the tip mechanics. The hysteresis explains the giant size of dissipation peaks despite the extremely low tip oscillation frequency. Approaching the tip further down, there can be another phase slip explaining multiple dissipation peaks.

More sophisticated theoretical model taking into account the other dimensions, namely y-intersurfaceplane, and z-intounderlying is presented elsewhere [36].

6.8 Conclusion

The contribution of non-contact friction to the friction force of a typical sliding contact is about one billionth. Very soft silicon sensors with high quality factors operated in pendulum geometry let us to measure those elusive friction forces. Cantilever annealing under ultra high vacuum conditions improves the force sensitivity by at least an order of magnitude. The effect is mainly due to removal of adsorbates from the cantilever surface. Cooling to cryogenic temperatures reduces the thermal fluctuations and lowers the internal friction further down. Approaching the cantilever to the surface opens new dissipation channels. At large tip-sample separations the long range Joule dissipation is dominant frictional process. Compensation of the contact potential minimizes the contribution of Joule dissipation into non-contact friction. A direct way to distinguish between electronic and phononic contribution to friction is to work across the superconducting phase transition. It was demonstrated that the non-contact friction coefficient is reduced by a factor of three when the sample enters the superconducting state. The temperature behaviour of Γ was found to be in good agreement with BCS theory of superconductivity. Thus friction has an electronic character in normal metal state, whereas the phononic friction dominates in the superconducting phase. The experiment on $NbSe_2$ surface reports on dissipation being a result of hysteresis switching induced in the sample. It was demonstrated that noncontact AFM dissipation dramatically peaks when an extra 2π phase is locally "pumped" into the phase of a charge-density-wave material surface, by the mechanical oscillation of a tip hovering above the surface at a large distance of one nanometer or more. Because states with and without the local 2π shift behave as different branches of the energy in a simple phase-only model, their crossing is expected to give rise to mechanical hysteresis, explaining the large dissipation of the peaks even at extremely low oscillation frequencies.

Acknowledgments We express our gratitude to E. Gnecco, S. Rast, L. Marot, R. Pawlak, F. Pellegrini, G.E. Santoro, R. Buzio, A. Gerbi, G. Balakrishnan, A. Baratoff and E. Tosatti for collaboration and helpful discussions. This work was supported by the Swiss National Science Foundation.

References

1. B. Gottsmann, H. Fuchs, Phys. Rev. Lett. **86**, 2597 (2001)
2. A. Vanossi, N. Manini, M. Urbakh, S. Zapperi, E. Tosatti, Rev. Mod. Phys. **85**, 529–552 (2013)
3. A. Volokitin, B. Persson, Phys. Rev. Lett. **94**, 086104 (2005)
4. A.I. Volokitin, B.N.J. Persson, H. Ueba, Phys. Rev. B **73**, 165423 (2006)
5. B.C. Stipe, H.J. Mamin, T.D. Stowe, T.W. Kenny, D. Rugar, Phys. Rev. Lett. **87**, 096801–1 (2001)
6. M. Kisiel, E. Gnecco, U. Gysin, L. Marot, S. Rast, E. Meyer, Nat. Mater. **10**, 119 (2011)
7. M. Langer, M. Kisiel, R. Pawlak, F. Pellegrini, G.E. Santoro, R. Buzio et al., Nat. Mater. **13**, 173 (2013). doi:10.1038/NMAT3836
8. G. Binnig, H. Roher, Ch. Gerber, E. Weibel, Phys. Rev. Lett. **49**, 57 (1982)
9. R. Perez, Nat. Mater. **13**, 118 (2014)
10. U. Gysin, S. Rast, M. Kisiel, C. Werle, E. Meyer, Rev. Sci. Instrum. **82**, 023705 (2011)
11. G. Meyer, N.M. Amer, Appl. Phys. Lett. **53**, 2400 (1988)
12. I. Dorofeyef, H. Fuchs, G. Wenning, B. Gotsmann, Phys. Rev. Lett. **83**, 2402 (1999)
13. W. Denk, D.W. Pohl, Appl. Phys. Lett. **59**, 2173 (1991)
14. B.C. Stipe, H.J. Mamin, T.D. Stowe, T.W. Kenny, D. Rugar, Phys. Rev. Lett. **86**, 2874 (2001)
15. S. Rast, Sensoren mit geringer Dissipation zur Messung kleiner Krafte, Diss. Phil.-naturwiss. Fak., Basel, 1999
16. J. Lübbe, L. Tröger, S. Torbrügge, R. Bechstein, C. Richter, A. Kühnle et al., Meas. Sci. Technol. **21**, 125501 (2010)
17. K.G. Lyon, G.L. Salinger, C.A. Swenson, G.K. White, J. Appl. Phys. **48**, 865 (1977)
18. H. Haucke, X. Liu, J.F. Vignola, B.H. Houston, M.H. Marcus, J.W. Baldwin, Appl. Phys. Lett. **86**, 191903 (2005)
19. J. Yang, T. Ono, M. Esashi, Appl. Phys. Lett. **77**, 3860 (2000)
20. S. Rast, U. Gysin, P. Ruff, Ch. Gerber, E. Meyer, D.W. Lee, Nanotechnology **17**, 189 (2006)
21. T. Albrecht, T.R. Albrecht, P. Grutter, H.K. Horne, D. Rugar, J. Appl. Phys. **69**, 668 (1991)
22. K. Saitoh, K. Hayashi, Y. Shibayama, K. Shirahama, Phys. Rev. Lett. **105**, 236103 (2010)
23. B. Gotsmann, Nat. Mater. **10**, 8788 (2011)
24. R. Kubo, Rep. Prog. Theor. Phys. **29**, 255 (1966)
25. R. Kubo, M. Toda, N. Hashitsume, *Statistical Physics Vol. II, Nonequlibrium Statistical Mechanics* (Springer, Berlin, 1995)
26. A.I. Volokitin, B.N.J. Persson, Solid State Commun. **115**, 145 (2008)
27. J.B. Pendry, J. Phys. Condens. Matter **9**, 10301 (1997)
28. G.V. Dedkov, Wear **232**, 145 (1999)
29. J. Bardeen, L.N. Cooper, J.R. Schrieffer, Phys. Rev. **108**, 1175 (1957)
30. B.N.J. Persson, *Sliding Friction* (Springer, Berlin, 2000)
31. B.N.J. Persson, Solid State Commun. **115**, 145 (2000)
32. R. Lifshitz, M. Roukes, Phys. Rev. B **61**, 5600 (2000)
33. C. Schlenker, *Physics and Chemistry of Low-Dimensional Inorganic Conductors*. North Atlantic Treaty Organization, & NATO Advanced Study Institute on Physics and Chemistry of Low-Dimensional Inorganic Conductors (Plenum Press, New York, 1996)
34. H. Fukuyama, P.A. Lee, Dynamics of the charge-density wave. I. Impurity pinning in a single chain. Phys. Rev. B **17**, 535–541 (1978)
35. P.A. Lee, T.M. Rice, Electric field depinning of charge density waves. Phys. Rev. B **19**, 3970–3980 (1979)
36. F. Pellegrini, G.E. Santoro, E. Tosatti, Phys. Rev. B **89**, 245416 (2014)

Chapter 7
Magnetic Exchange Force Spectroscopy

Alexander Schwarz and Stefan Heinze

Abstract Magnetic exchange force spectroscopy is an elegant experimental method to extract the short-range magnetic contribution to the total interatomic interaction energy between the tip apex atom and the sample atoms across a vacuum gap. If the tip does not exhibit a spin-dependent reversible hysteretic reconfiguration of its atomic structure, experimental data can be directly compared quantitatively with *first principles* electronic structure calculations. Moreover, knowing the distance dependence and magnitude of the magnetic exchange interaction opens a new route to induce magnetization reversal events.

7.1 Introduction

Force spectroscopy is a very powerful tool to determine magnitude and distance dependence of tip-sample interactions. It has been used to quantify short-ranged chemical interactions [1] and to identify atomic species [2]. Recording three-dimensional spectroscopy maps [3] are nowadays common practice to determine the tip-sample interaction energy as well as vertical and lateral force fields (see Chap. 2 of this book). After it became possible to image magnetic structures with atomic resolution on insulators [4, 18] as well as on metals [5], this technique was also employed to obtain more quantitative information about the short range magnetic tip-sample interaction [6, 18]. Noteworthy, such quantitative data can become also relevant for spin-polarized scanning tunneling microscopy (SP-STM) and spectroscopy (SP-STS) experiments, if the tip gets very close to the sample, i.e., during conductance [7] or spin-friction experiments [8]. Moreover, the onset of a Kondo peak splitting has been attributed to the magnetic exchange interaction between a magnetic STM

A. Schwarz (✉)
Department of Physics, University of Hamburg, Jungiusstrasse 11, 20355 Hamburg, Germany
e-mail: aschwarz@physnet.uni-hamburg.de

S. Heinze
Institute of Theoretical Physics and Astrophysics, University of Kiel, Leibnizstrasse 15, 24098 Kiel, Germany
e-mail: heinze@physik.uni-kiel.de

© Springer International Publishing Switzerland 2015

S. Morita et al. (eds.), *Noncontact Atomic Force Microscopy*,
NanoScience and Technology, DOI 10.1007/978-3-319-15588-3_7

tip and a Kondo atom on a surface [9]. Finally, it has been demonstrated that the strong distance dependence of the magnetic exchange interaction can be utilized to alter the magnetic configuration locally [10].

Determining the magnetic exchange interaction between atoms experimentally is not an easy task. Nonetheless, SP-STM was used recently to study the magnetic coupling between neighboring atoms on a non-magnetic substrate, which exhibits an oscillatory distance dependence characteristic for an RKKY-type magnetic exchange mechanism [11]. Here, the interaction is mediated via conduction electrons of the host material. Magnetic exchange interactions across a vacuum gap were calculated utilizing density functional theory (DFT) [12–17, 20], and, as we will discuss in the following, they can be indeed measured by magnetic exchange force spectroscopy (MExFS) [6, 18]. Although the experiment described here has been performed on a metallic system, this force microscopy based technique can of course also be applied to insulating systems, as it was demonstrated recently [18].

7.2 The Tip-Sample System

The first successful MExFM experiments were realized on NiO(001) [4]. However, as a system with strongly correlated electrons, it is rather difficult to treat theoretically. Hence, DFT calculations of the complete tip-sample system are challenging and very time consuming. Note that early DFT calculations have been published for NiO(001), but either without a tip at all [19] (only the spin-resolved local density of states was calculated, which is often sufficient to interpret STM experiments), or with a single atom tip [13]. In the latter case, relaxation effects in the tip, which are indeed relevant [14], cannot be included. Just lately, a DFT calculation for NiO(001) including a five atom tip has been conducted [20].

For our investigation we selected an itinerant metallic system that can be treated with high accuracy, i.e., the pseudomorphically grown Fe monolayer on W(001). Its substrate induced (via spin-orbit coupling) antiferromagnetic checkerboard structure with out-of-plane anisotropy is well known [21] and we observed a three times larger magnetic signal than on NiO(001). Moreover, this metallic system is also experimentally easier to handle than the bulk insulator NiO: no charging problems and tip preparation *on the fly*, i.e., inducing tip changes to obtain a *good* tip, have a significantly higher success rate.

7.2.1 Sample Preparation

A clean W(001) substrate is prepared in-situ by annealing at 1600 °C in oxygen ($p_{O_2} \approx 1 \times 10^{-6}$ hPa). Thereby, carbon segregates to the surface, where is reacts with oxygen into CO that desorbs. A final high temperature flash (10 s at 2000 °C) removes the excess oxygen from the surface. This procedure avoids the formation

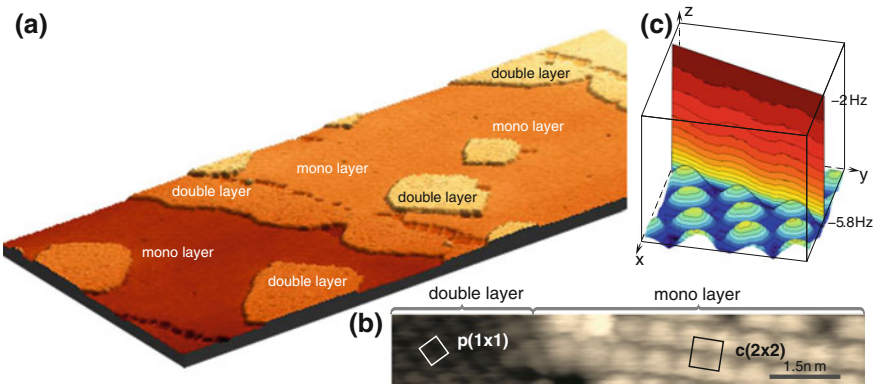

Fig. 7.1 **a** Topography of 1.3 atomic layers of Fe deposited on W(001). **b** Atomically resolved image across a step between the ferromagnetic double layer and the antiferromagnetic monolayer. The c(2 × 2) pattern on the monolayer shows that the tip is magnetically sensitive [5]. **c** Atomically resolved 3D-MExFS data recorded on the Fe monolayer with such a tip. Sites with opposite spin orientations can be identified as maxima and minima in the topographic data at the *bottom*. The *color coded* slice through the $\Delta f(x, y, z)$ data set along the [100]-direction reflects the site and distance dependence of the magnetic exchange interaction

of tungsten carbide, which cannot be removed by heating. Subsequently, about 1.3 atomic layers of Fe are deposited at a background pressure below 2×10^{-10} hPa onto the substrate, which is kept at a temperature of about 200 °C. As a result a closed p(1 × 1) Fe monolayer (wetting layer) grows pseudomorphically, while the additional Fe forms second layer stripes attached to the step edges (step flow growth) and small islands; cf. Fig. 7.1a. Note that the two atomic layer high Fe areas grow still pseudomorphically, but the spins are ferromagnetically ordered and exhibit an in-plane anisotropy [21].

The sample is then transferred into a homebuilt microscope located in a UHV cryostat with a base temperature of about 8 K and a magnetic field that can be applied perpendicular to the sample surface of up to 5 T [22]. Data were acquired using the frequency modulation technique while keeping the amplitude A constant [23].

7.2.2 Tip Preparation

To obtain magnetically sensitive tips, Si cantilevers ($k \approx 150$ N/m, $f_0 \approx 190$ KHz, $A \approx 4$ nm) were coated in-situ with a few nm Cr. Previously, we used Fe to image the antiferromagnetic spin structure of the Fe monolayer on W(001), because even after tip changes we could be sure that a magnetic sensitive tip stems from a Fe tip apex. Hence, only Fe tips needed to be considered for theoretical calculations. However, Cr is stronger attached to the oxidized Si tip and is thus better suited to perform long term spectroscopy experiments without tip changes. Since we usually had to provoke tip

changes before atomic resolution with magnetic sensitivity became possible, surface material, i.e., Fe, could be transferred to the tip apex.

Figure 7.1b displays an image recorded with a magnetically sensitive tip across a small step that separates the Fe double layer from the Fe monolayer. On the ferromagnetic doublelayer all surface Fe atoms are imaged as protrusion (p(1 × 1) pattern), while on the antiferromagnetic monolayer only every second Fe atoms appears as protrusion (c(2 × 2) pattern).

7.3 Determining the Magnetic Exchange Interaction

In the following we describe the experimental and theoretical procedures to obtain magnitude and distance dependence of the magnetic exchange interaction between tip and sample. The results are then compared qualitatively and quantitatively with each other.

7.3.1 Data Acquisition Procedure

The experimental way to determine the magnetic exchange interaction between tip and sample is performed in the following manner: First, an atomically sharp and magnetically sensitive tip is prepared. It can be readily distinguished from non-magnetic tips by the characteristic c(2 × 2) contrast pattern as visible on the Fe monolayer in Fig. 7.1b. Note that a magnetic sensitive tip still exhibits the p(1 × 1) contrast pattern on areas which are two atomic layers high, because they are ferromagnetically ordered. If an as prepared tip does not display magnetic sensitivity, intentionally provoked tip changes, e.g., induced by collisions with the surface, usually produces an atomically sharp and magnetically sensitive tip after some tries. As a result of this *on the fly* preparation procedure the initially pure Cr tip could have picked up Fe from the surface—a fact that has to be considered, if experimental data are compared with theoretical calculations (see Sect. 7.3.2).

To record a spectroscopy field, the tip should exhibit a sufficient long-term stability, i.e., tip changes should be absent during data acquisition. With such tips a $\Delta f(z)$-curve is recorded above every image point together with the z-position z_{start} at Δf set-point Δf_{stab}, at which the tip is stabilized. For the data presented here a Δf_{stab} was selected to be so close to the sample that atomic resolution with magnetic contrast was achieved. Subsequently, the z-feedback was switched off and $\Delta f(z)$ data were recorded while the tip-sample distance was increased up to a height h above z_{start} with an increment of Δz.

Simultaneously, the excitation amplitude $a_{\mathrm{exc}}(z)$ required to keep A constant was saved and used to calculate the dissipated energy per oscillation cycle $E_{\mathrm{D}}(z)$ [25]. Note that the zero line corresponds to the intrinsically dissipated energy in the absence of any tip-sample interaction, i.e., at large tip-sample separations. The

reapproach curve was recorded as well, but not evaluated further, because the final tip-sample separation is systematically larger than initially due to piezo creep. After restabilization at Δf_{stab} with activated z-feedback, the tip was moved to the next (x, y)-position, where the whole procedure was repeated. This method is known as 3D-force field spectroscopy (3D-FFS) [3]. A 3-dimensional $\Delta f(x, y, z)$ data set acquired in this way is shown in Fig. 7.2a: The bottom displays $z_{\mathrm{start}}(x, y)$ showing the c(2×2) antiferromagnetic structure. On top a slice along the [110] direction is displayed with the $\Delta f(z)$ values color-coded.

The complete $\Delta f(x, y, z)$ data-set could be converted into the 3D energy landscape $E(x, y, z)$ or, by differentiation, into the vertical force field $F_z(x, y, z)$. However, for direct comparison with our theoretical calculations discussed in the next Sect. 7.3.2, we selected individual curves taken on top of Fe atoms with opposite spins meaning that both spin configurations, i.e., parallel (p-configuration) and antiparallel (ap-configuration), are probed. Note that the experimental data alone does not allow for an unambiguous assignment of minima and maxima to p- and ap-sites, respectively.

Two such individual curves recorded on a minimum ($\Delta f_{\mathrm{min}}(z)$ in blue) and on a maximum ($\Delta f_{\mathrm{max}}(z)$ in red) taken from such a 3D data set are plotted in Fig. 7.2 (the positions are indicated in the inset showing the atomically resolved data). The two $\Delta f(z)$-curves in Fig. 7.2a are smooth and indistinguishable at larger distances, but split into two branches at smaller distances. The dissipation signal is constant and identical for both curves ($E_{\mathrm{D}}(z) = \mathrm{const.}$; non-dissipative tip). Both $\Delta f(z)$-curves represent the total tip-sample interaction. Since all non-magnetic contributions, such as the long-range van der Waals interaction as well as the short-range chemical

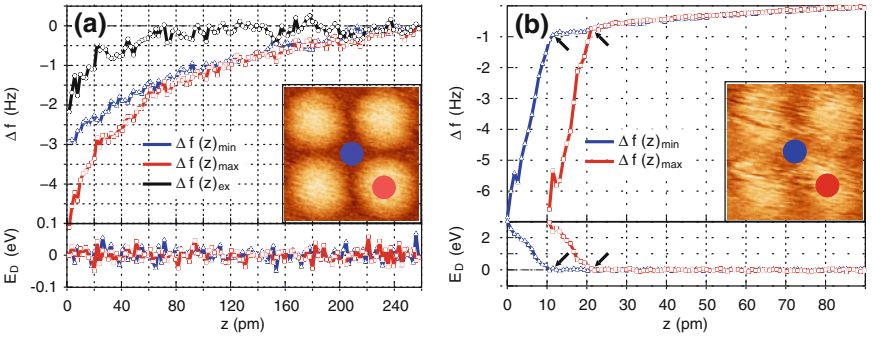

Fig. 7.2 **a** Two individual $\Delta f(z)$-curves recorded with a non-dissipative (cf., *bottom curve*) and hence stable tip on Fe atoms with opposite spins (see *inset*). The difference between both curves (*black circles*) can be converted into $E_{\mathrm{ex}}(z)$ (see Fig. 7.5). **b** A data set recorded with a dissipative tip (cf., *bottom curve*). Both $\Delta f(z)$-curves exhibit a sudden steep decrease at a certain tip-sample distance separated by about 12 pm that coincides with a sudden increase in dissipated energy (see *arrows*). Such features suggest atomic reconfigurations at the tip apex due to a spin-dependent adhesion hysteresis [24]. Hence, $E_{\mathrm{ex}}(z)$ cannot be extracted by subtracting both curves from each other. Note that the MExFM image recorded with that tip exhibits a larger noise level than the MExFM image in (**a**)

interaction, are identical on sites with opposite spin orientations, the frequency shift $\Delta f_{\mathrm{ex}}(z)$ representing the magnetic exchange interaction can be extracted simply by subtracting both curves from each other, i.e., $\Delta f_{\mathrm{ex}}(z) = \Delta f_{\mathrm{max}}(z) - \Delta f_{\mathrm{min}}(z)$ (black circles). Note that the relative spin orientation is not known a priori, but choosing the sign definition $\Delta f_{\mathrm{ex}}(z) = \Delta f_{\mathrm{max}}(z) - \Delta f_{\mathrm{min}}(z)$ is justified by comparison with theory (see below). For further quantitative comparison with theory, $\Delta f_{\mathrm{ex}}(z)$ can be converted into $E_{\mathrm{ex}}(z)$ using established algorithms [26–29] (cf. Fig. 7.3). The simultaneously recorded dissipation signal $E_{\mathrm{D}}(z)$ is featureless, indicating a stable tip without any adhesion hysteresis [30–32].

We also could observe another type of $\Delta f(z)$-curves, which exhibit distinctively different features. Figure 7.2b shows such a set, again recorded on a minimum (blue) and maximum (red). Peculiarly, both curves display a sudden steep decrease of the $\Delta f(z)$-curve at z-positions separated by about 12 pm. At exactly the same positions the dissipation E_{D} increases drastically to about 3 eV/cycle at the smallest separation, indicating a spin-dependent dissipation mechanism [24]. Noteworthy, the atomically resolved MExFM image recorded with this dissipative tip appears much noisier compared to the image recorded with a non-dissipative tip (cf. insets).

7.3.2 First-Principles Calculations

In order to interpret the experimentally obtained $E_{\mathrm{ex}}(z)$-curves, we have performed DFT based first-principles calculations within the generalized gradient approximation (GGA) [33] to the exchange-correlation potential. We apply the full-potential linearized augmented plane wave method as implemented in the WIEN2K [34] code.

The coupled system of tip and sample was calculated in a supercell geometry as described in [16]. The tip-sample geometry used for the calculation is illustrated in Fig. 7.3a: The Fe monolayer on W(001) was modeled by a symmetric slab with five W layers and one Fe layer on each side.

Since the tip preparation could lead to a material transfer from the surface to the tip apex not only pure Cr nanotips but also pure Fe nanotips and mixed Fe-Cr nanotips were considered. In our calculation they all possess a pyramidal geometry containing 14 atoms in three layers (see sketches in Fig. 7.3b): (i) a Cr-base with an Fe termination, (ii) a pure Fe tip, (iii) a pure Cr tip, and (iv) an Fe-base with a Cr termination. Adjacent Cr layers as well as adjacent Fe and Cr layers are coupled antiferromagnetically, while coupling in the pure Fe tip is ferromagnetic. Note that these nanotips represent the tip apex, i.e., the part of the tip that is relevant for the short-range interaction. The tip-sample interaction stemming from the rest of the tip need not be considered, because they cancel out by performing the subtraction procedure.

Tips and surface were relaxed independently before considering the coupled system. Each tip was then approached to the surface along a trajectory of discrete points. For every distance we carried out a DFT calculation including structural relaxations of the tip atoms and the Fe monolayer and uppermost W layer. As in the experimental

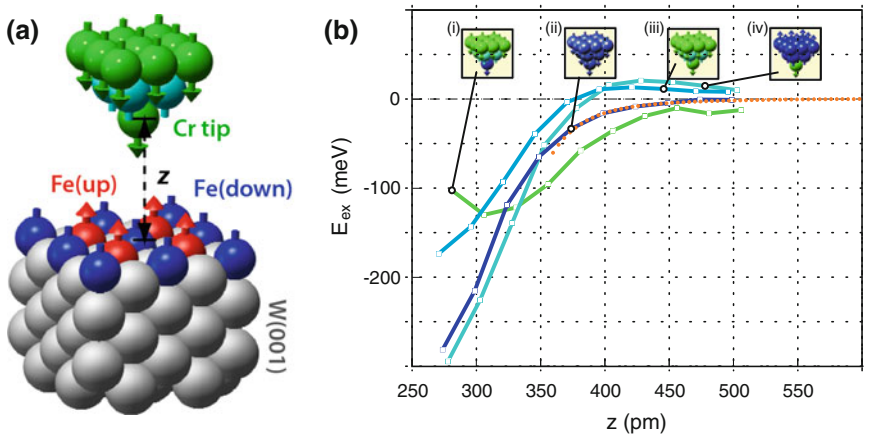

Fig. 7.3 **a** Tip-sample geometry used to calculate the distance dependent total energy above ap- and p-site, i.e., $E_{\mathrm{ap}}(z)$ and $E_{\mathrm{p}}(z)$, respectively. The contribution stemming from the magnetic exchange interaction is obtained by subtraction, i.e., $E_{\mathrm{ex}}(z) = E_{\mathrm{ap}}(z) - E_{\mathrm{p}}(z)$. **b** Comparison between theoretical and experimental $E_{\mathrm{ex}}(z)$-curves. $E_{\mathrm{ex}}(z)$ was calculated using DFT for four different tips. Chemical composition (*blue* Fe; *green/cyan* Cr) and spin structure are indicated for each curve. $E_{\mathrm{ex}} > 0$ ($E_{\mathrm{ex}} < 0$) indicates a ferromagnetic (antiferromagnetic) coupling. Note the transition from preferred ferromagnetic to a preferred antiferromagnetic coupling for the two Cr-terminated tip pyramids. $E_{\mathrm{ex}}(z)$ obtained after conversion of the $\Delta f_{\mathrm{ex}}(z)$ curves with the non-dissipative tip (cf. Fig. 7.2a) is plotted as well (*orange curve*). It fits excellently with the theoretical result for a pure Fe tip apex

situation the separation z in the coupled system is defined as the distance between the tip apex atom and the Fe surface atom before considering relaxations.

For every tip we considered a parallel (p) and an antiparallel (ap) alignment of the magnetic moments of the tip apex atom and the surface atom underneath. Relaxations on the order of 10 pm were observed for all tips [16], but no hysteretic reconfigurations or instabilities. Thus, our tip models reflect stable tips.

The magnetic exchange energy is obtained by subtracting the total energies in the ap- and p-alignment, i.e., $E_{\mathrm{ex}}(z) = E_{\mathrm{ap}}(z) - E_{\mathrm{p}}(z)$. $E_{\mathrm{ex}}(z) > 0$ (< 0) indicates ferromagnetic (antiferromagnetic) coupling. This approach is equivalent to subtracting the experimental data obtained on minima and maxima as performed for the stable non-dissipative tip. Note that the tips used for the calculations are much smaller than real tips and long-range interactions are not accounted for. However, after subtraction all non-magnetic contributions to the total tip-sample interaction cancel out.

The calculated $E_{\mathrm{ex}}(z)$ data points are displayed in Fig. 7.3b. The solid line (a spline fit) are guides for the eye. At small tip-sample distances E_{ex} is negative indicating the favorable antiferromagnetic exchange interaction. This finding justifies the sign definition of $\Delta f_{\mathrm{ex}}(z)$ used for the experimental data. The magnitude at a distance of 300 pm is on the order of 100 meV. Interestingly, Cr-terminated tips show a characteristic change of sign, i.e., a transition from preferred ferromagnetic

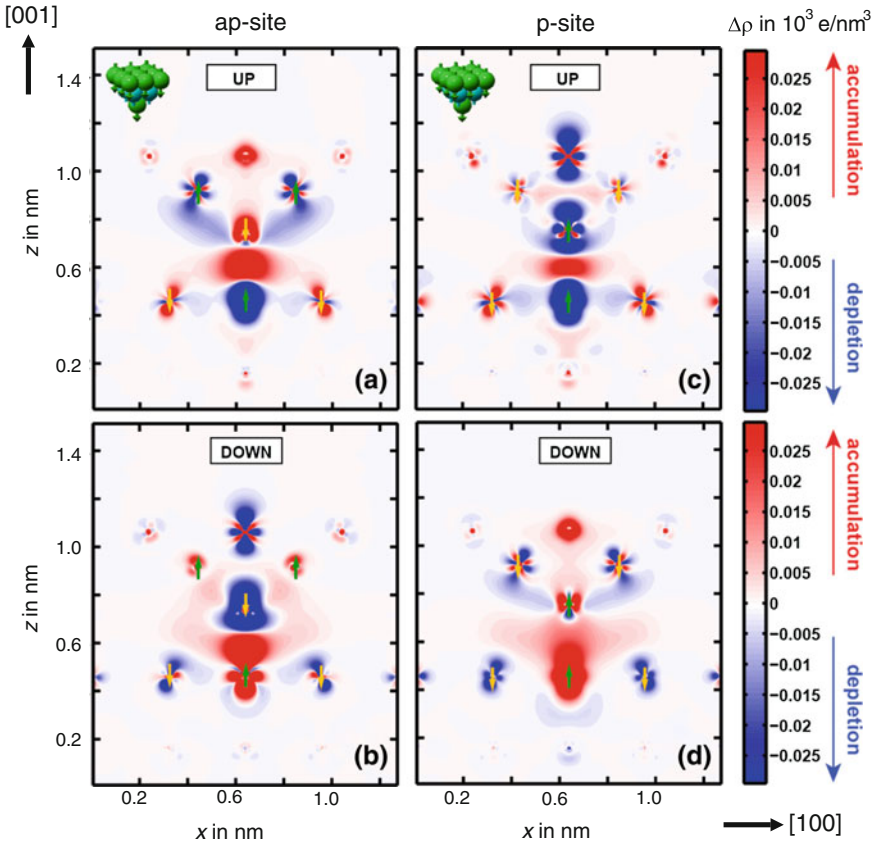

Fig. 7.4 Spin-resolved cross-sectional charge-density difference plots along the [100] direction for the interaction of the Cr tip with the Fe monolayer on W(001) at a tip-sample separation of $z = 290$ pm. The configurations of antiparallel (ap) and parallel (p) alignment between the magnetic moments of apex and surface atom are displayed as indicated at the *top*. The plots are obtained from the difference of charge densities of isolated and interacting tip and sample for the spin-up and spin-down channel (indicated at the *top* of each panel). The directions of the magnetic moments (spins) are given by *arrows* for the apex tip and surface Fe atoms. *Red* and *blue color* denote charge accumulation and depletion, respectively. The results presented here correspond to relaxed geometries for tip and sample due to their interaction

alignment (p-configuration) at large distances to a preferred antiferromagnetic alignment (ap-configuration) at smaller distances.

The origin of the exchange interaction and the sign reversal can be understood based on spin-resolved charge density difference plots shown in Fig. 7.4. These plots are obtained by subtracting from the charge density of the interacting system comprising tip and sample, both the charge density from the isolated tip and the isolated sample using the structural relaxations of the coupled system. In this way, we can

study the spin- and spatially-resolved change of electron density due to the interaction, i.e. charge accumulation or depletion.

We focus on the Cr tip to discuss the exchange interaction between tip and sample. At the chosen distance of $z = 290$ pm the sign of the exchange interaction is negative, i.e., the ap configuration is energetically favorable (see Fig. 7.3). In this configuration, cf. Fig. 7.4a, b, we notice that the charge redistribution at the apex and probed surface atom are very similar for the spin-up and spin-down channels. However, there is an inversion of charge accumulation and depletion at the interacting atoms, i.e., in the spin-up channel charge is accumulated at the apex atom and depleted at the probed surface atom and vice versa in the spin-down channel. This spin-resolved charge redistribution is characteristic for a direct antiferromagnetic exchange mechanism between the d-orbitals due to the formation of spin-dependent covalent bonds [35].

In the p configuration, cf. Fig. 7.4c, d, the spin-resolved plots are distinctively different. In the spin-up channel we notice a charge depletion at the apex and the surface atom and an accumulation between them. This charge redistribution can be explained based on the indirect Zener double exchange mechanism [36, 37], which leads to a ferromagnetic exchange coupling between tip and sample [15]. The origin of the energy gain is the delocalization of the sp-conduction electrons, which are coupled to the d-states and can wander between apex and surface atom only for a parallel spin alignment of the magnetic moments resulting from the localized d-electrons. This double exchange mechanism is weaker than the direct antiferromagnetic exchange mechanism via overlapping tip and sample d-states. As a result, the total exchange interaction is antiferromagnetic at close tip-sample separations. However, the indirect double exchange mechanism, which favors ferromagnetic alignment, is of longer range as it is mediated by the delocalized electrons. Hence, we find a change to ferromagnetic exchange interaction at larger tip-sample separations as visible in Fig. 7.3. Since the indirect exchange mechanism scales with the coupling of sp-electrons and d-electrons, which is weaker for Fe atoms than for Cr [15], we do not observe such a transition for Fe-terminated tips. Thus, for tips with an Fe atom apex the direct coupling of adjacent d shells is the dominant exchange mechanism in the whole interaction range, which prefers an antiferromagnetic alignment in accordance with Moriya's theory [38].

7.3.3 Comparison Between Theory and Experiment

For a direct comparison between theoretical predictions and experimental data, the $E_{\mathrm{ex}}(z)$-curve calculated from the $\Delta f_{\mathrm{ex}}(z)$-curve obtained with the non-dissipative stable tip is displayed together with the calculated $E_{\mathrm{ex}}(z)$-curves in Fig. 7.3b (orange curve). Since no sign change is observed in the experimental data, we can infer that the tip is Fe-terminated (only Cr-terminated tips exhibit a sign change), most probably because the Cr-coated tip picks up surface Fe atoms during our *on the fly* tip-preparation procedure. Since we never observed a sign reversal up to now, our

tip preparation procedure (intended collisions between the Cr-coated tip and the Fe surface) seems to favor Fe-terminated tip apices.

In the experiment, the absolute z-position is not known. Therefore, we shifted the experimental curve in z-direction with respect to the theoretical curves. Best agreement between theory and experiment is found for the pure Fe tip apex, for which magnitude as well as distance dependence of the magnetic exchange energy fits very well. The minimal tip-sample separation adjusted in the experiment is much larger than in the calculation, because otherwise tip changes are more likely to occur, which would compromise the 3D-MExFS data acquisition and evaluation procedure.

Tips, which show a increased dissipation in the distance regime where a magnetic contrast is observed (see Fig. 7.2b) cannot be evaluated in this manner. A strong increase of the dissipation signal indicates a reversible but hysteretic reconfiguration of atoms at the tip apex, which occur at different tip-sample distances during approach and retrace of an oscillation cycle [30–32]. That such an adhesion hysteresis can depend on the relative orientation between the spins in tip and sample has been observed on NiO(001) [24]. Since the tip apex structure is different before and after the onset of dissipation, $\Delta f_{\mathrm{ex}}(z)$, and hence $E_{\mathrm{ex}}(z)$, cannot be extracted by subtracting ap- and p-curves from each other.

That such dissipative tips are structurally less stable is also suggested by the larger noise visible in MExFM images recorded with such tips (see insets in Fig. 7.2). Indeed, a behavior consistent with such an assertion has been found in six 3D-MExFS data sets and more than 20 MExFM images.

7.4 Magnetic Exchange Induced Switching

According to the theoretical and experimental data presented in Fig. 7.3b the magnetic exchange interaction can be quite large, i.e., at least several 10 meV. Hence, it should be possible to modify the magnetization locally at the position of the tip. Note the difference compared to other magnetization reversal mechanisms induced with scanning probe methods: With magnetic force microscopy (MFM), the magnetization direction of individual nanodots could be selectively reversed using the stray field emanating from a ferromagnetic tip [39]. This approach is very similar to the *conventional* strategy, i.e., applying an external magnetic field to enforce a magnetization reversal. With SP-STM it was possible to switch even smaller magnetic nanoislands employing the spin-torque effect [40].

7.4.1 Experimental Observation

Figure 7.5a shows an image scanned from bottom to top with a magnetically sensitive tip on the antiferromagnetic Fe monolayer on W(001) with the characteristic c(2×2) spin texture. The overlaid grid shows the position of Fe atoms, i.e., the p(1×1)

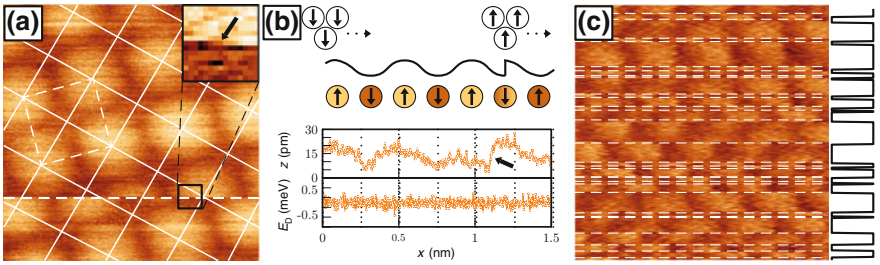

Fig. 7.5 **a** $(1.5 \times 1.5)\,\mathrm{nm}^2$ MExFM image ($B = 4.5$ T) of the Fe monolayer on W(001) scanned from *bottom* to *top*. The grid marks the position of Fe atoms with minima and maxima corresponding to p- and ap-configurations. On the *dashed line* within the marked area (see *inset*) the p to ap switching event took place. **b** Sketch of the contrast reversal after switching of the magnetization direction at the tip apex and actual scan line, on which the switching occurred. The featureless dissipation signal is also shown. **c** $(2 \times 2)\,\mathrm{nm}^2$ MExFM image ($B = 0$ T) exhibiting many switching events. Only p to ap transitions occur. On the right the corresponding telegraph signal is depicted, which can be used to determine the two lifetimes $\tau_{\langle 0\rangle}$ and $\tau_{\langle 1\rangle}$ characterizing tip spins pointing in opposite directions

chemical surface unit cell. In the surface area marked by the frame, a switching event occurred (see inset), whereafter the minima appear as maxima and vice versa. Here, the spins at the tip apex (not in the sample) are reversed and this reversal is detected via their interaction with the unchanged surface spins. Note that the registry is kept. The scan line with the switching event and an illustrating sketch is displayed together with the dissipation signal in Fig. 7.5b. The latter is featureless.

The number of switching events increases drastically, if the tip-sample separation is reduced [10]. If many switching events can be observed, as in Fig. 7.5c, the lifetime of the two tip states $\tau_{\langle 0\rangle}$ and $\tau_{\langle 1\rangle}$ with opposite spin direction, given by the time span between two switching events, can be statistically evaluated. It is instructive to generate a telegraph noise signal from the image data as sketched on the right by plotting average line section along parallel to the slow scan axis. For this particular data set recorded in zero field we find $\tau_{\langle 0\rangle} = 27$ s and $\tau_{\langle 1\rangle} = 17$ s, respectively. Surprisingly, $\tau_{\langle 0\rangle} \neq \tau_{\langle 1\rangle}$ for $B = 0$ T, but the difference is significantly smaller than for $B \neq 0$ T [10].

From the featureless dissipation signal, the absence of any z-offset and since the registry between the overlaid grid and positions of maxima and minima, respectively, remains perfect after the switching event, we can infer that the magnetization reversal is not accompanied by any structural change at the tip apex. As the transition occurs on a minimum, which becomes a maximum, the tip expectedly switches from a p- to the energetically preferred ap-configuration. We never observe the opposite. Since the magnetic corrugation before and after the switching event is identical, we can infer that the magnetization direction of the tip rotated by 180°.

7.4.2 Modified Néel-Brown Model

Qualitatively the field and distance dependence of the switching can be understood in terms of a slightly modified Néel-Brown model [41, 42]: The tip apex is assumed to behave like a superparamagnetic cluster with uniaxial anisotropy that can switch its magnetization direction across an energy barrier via thermal excitation (it is very unlikely that the whole tip switches its magnetization direction). Additionally, its magnetization direction is influenced by the presence of magnetic exchange interaction and, if applied, an external magnetic field. In this model larger lifetimes τ indicate a larger energy barrier E_b: $\tau = 1/\nu_0 \cdot \exp(-E_\mathrm{b}/k_\mathrm{B}T)$. Here, ν_0 is the attempt frequency, which is typically 1 GHz and related to the Larmor frequency, while $k_\mathrm{B}T$ is the available thermal energy.

In the *usual* Néel-Brown model, i.e., without any local probe the interacts with the sample via magnetic exchange, both states are energetically degenerate and an externally applied magnetic field would prefer parallel magnetization direction, i.e., one lifetime would become larger than the other. However, in our experiments the magnetic exchange interaction between tip and sample is the dominating energy term ($E_\mathrm{ex} \gg E_\mathrm{Z}$). Since we only observe switching from p- to ap-configurations, the energy barrier $E_\mathrm{b} = E_\mathrm{p/ap}$ can be calculated using the Néel-Brown formula. Interestingly, the data presented in Fig. 7.5c exhibits different life times and thus different corresponding energy barriers, i.e., 16.3 and 17.1 meV, respectively, although the measurements were performed in zero field. Apparently, an additionally anisotropy energy is present that favors one direction over the other. Note that the nanotip is not a free particle, but magnetically coupled to the rest of the tip, which, e.g., could possess a finite residual magnetic stray field. The existence of such a stray field is supported by our observation that a deliberately applied external magnetic field corresponding to a Zeeman energy E_Z of just a few 0.1 meV is sufficient to induce uneven life times.

That exclusively p to ap transitions are observed is related to the large magnetic exchange interaction: Compared to the energy barrier from the p- into the ap-configuration, i.e., $E_\mathrm{p/ap}$, the energy barrier in the other direction is larger by E_ex, i.e., $E_\mathrm{ap/p} = E_\mathrm{p/ap} + E_\mathrm{ex}$. Since $E_\mathrm{ex} = E_\mathrm{ap} - E_\mathrm{p}$ is on the order of a few 10 meV ($\gg E_\mathrm{Z}$), switching from the ap- into the p-configuration is extremely unlikely, even if favored by the Zeeman energy. The situation is illustrated in Fig. 7.6 for all four possible configurations between an external magnetic field (parallel or antiparallel to the tip apex spins) and the spin configuration between tip and sample (p- or ap-configuration).

7.4.3 Magnetic Stability of Tips

The analysis given above allows us to distinguish between magnetically stable and unstable tips by considering the energy barrier between p- and ap-configuration of

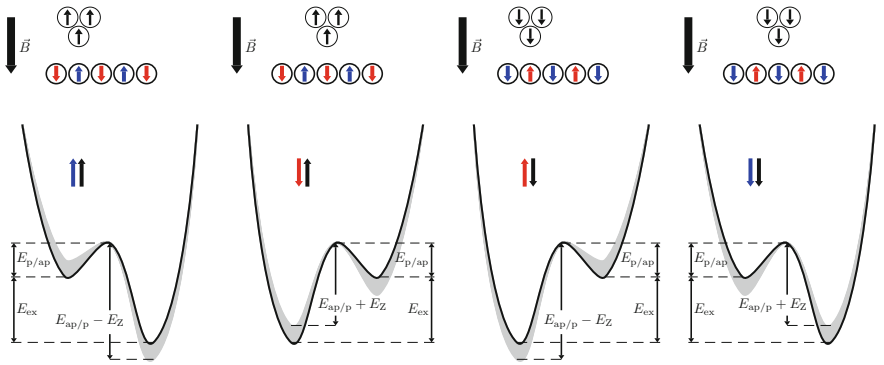

Fig. 7.6 Modified Néel-Brown model showing the effect of an external magnetic field and the magnetic exchange energy between tip and sample on the energy landscape. For large tip-sample separations and without external magnetic field the energy barrier between p- and ap-configuration is symmetric. The sketches illustrate the combined effect of the magnetic exchange interaction E_{ex} present at a smaller tip-sample separation and the Zeeman energy E_{Z} (*shaded area* with $E_{\mathrm{Z}} \ll E_{\mathrm{ex}}$), if an external magnetic field is applied, for all four possible configurations between tip and sample spin. Since E_{ex} is much larger than E_{Z}, only switching from the p- into the ap-configuration takes place. As explained in the text, but not depicted in the graphs, the increased switching rate at smaller tip-sample separations indicates that the energy barrier $E_{\mathrm{p/ap}}$ becomes smaller at smaller tip-sample separations due to the distance dependence of E_{ex})

tip apex spins. Its height depends on the local environment of the tip apex. If the magnetic coupling between the tip apex, i.e., the atomically sharp nanotip, and the rest of the tip is strong, the energy barrier is high and no switching will take place. Those tips can be regarded as magnetically stable. For example, at our measurement temperature of 8 K an energy barrier of about 22 meV would result in about one switching event per day. If the nanotip is only weakly coupled to the rest of the tip, e.g., due to structural irregularities or a kind of grain boundary, the energy barrier can be small enough to allow for thermally induced switching. Actually, if the energy barrier is less than 10 meV the switching time would be below 1 ms, i.e., faster than our data acquisition time. Such a tip would actually appear as a non-magnetic tip! Intermediate barrier heights would result in more or less frequent observable switching events as in Fig. 7.6c.

7.5 Conclusion

Our experimental data and the DFT calculations demonstrate that it is possible to quantitatively measure the distance dependence of the magnetic exchange interaction across a vacuum gap by subtracting force spectroscopy curves recorded above atoms with opposite spin. Noteworthy, some tips are magnetically sensitive but structurally unstable and thus unsuitable for the evaluation procedure presented here. Such tips

can be identified by a large increase of the dissipation signal, which indicates a spin-dependent adhesion hysteresis. Our experimental procedure can be universally applied to any combination of similar or dissimilar atomic species to measure the distance dependence of the magnetic exchange interaction across a vacuum gap with atomic resolution, even on insulating tip-sample systems.

The strength of the magnetic exchange energy can induce magnetization reversals. Interestingly, such reversal events can affect the tip apex, which can be regarded as a magnetic cluster. Its magnetic coupling to the rest of the tip determines the magnetic stability of the tip. Our findings suggest that it should be possible to utilize the distance dependence of the magnetic exchange interaction to switch the magnetization of clusters, molecules or atoms on surfaces. The short range magnetic exchange interaction can become also relevant for scanning tunneling microscopy experiments with magnetic tips, i.e., SP-STM, if the tip-sample distance becomes smaller than about 0.5 nm, e.g., in conductance measurements.

Acknowledgments We acknowledge financial support from the Deutsche Forschungsgemeinschaft (SFB 668-A5 and HE 3292/7-1), the ERC Advanced Grant FURORE, and from the Cluster of Excellence NANOSPINTRONICS

References

1. M. Lantz, H. Hug, P. Van Schendel, R. Hoffmann, S. Martin, A. Baratoff et al., Phys. Rev. Lett. **84**(12), 2642 (2000)
2. Y. Sugimoto, P. Pou, M. Abe, P. Jelinek, R. Pérez, S. Morita et al., Nature **446**(7131), 64 (2007)
3. H. Hölscher, S. Langkat, A. Schwarz, R. Wiesendanger, Appl. Phys. Lett. **81**(23), 4428 (2002)
4. U. Kaiser, A. Schwarz, R. Wiesendanger, Nature **446**(7135), 522 (2007)
5. R. Schmidt, C. Lazo, H. Holscher, U. Pi, V. Caciuc, A. Schwarz et al., Nano Lett. **9**(1), 200 (2009)
6. R. Schmidt, C. Lazo, U. Kaiser, A. Schwarz, S. Heinze, R. Wiesendanger, Phys. Rev. Lett. **106**(25), 257202 (2011)
7. C. Lazo, N. Néel, J. Kröger, R. Berndt, S. Heinze, Phys. Rev. B **86**, 180406 (2012). doi:10.1103/PhysRevB.86.180406. http://link.aps.org/doi/10.1103/PhysRevB.86.180406
8. B. Wolter, Y. Yoshida, A. Kubetzka, S.W. Hla, K. von Bergmann, R. Wiesendanger, Phys. Rev. Lett. **109**(11), 116102 (2012)
9. J. Bork, Y.h. Zhang, L. Diekhöner, L. Borda, P. Simon, J. Kroha, P. Wahl, K. Kern. Nat. Phys. **7**(11), 901 (2011)
10. R. Schmidt, A. Schwarz, R. Wiesendanger, Phys. Rev. B **86**(17), 174402 (2012)
11. L. Zhou, J. Wiebe, S. Lounis, E. Vedmedenko, F. Meier, S. Blögel et al., Nat. Phys. **6**(3), 187 (2010)
12. A. Foster, A. Shluger, Surf. Sci. **490**(1), 211 (2001)
13. H. Momida, T. Oguchi, Surf. Sci. **590**(1), 42 (2005). http://dx.doi.org/10.1016/j.susc.2005.06.006
14. C. Lazo, V. Caciuc, H. Hölscher, S. Heinze, Phys. Rev. B **78**, 214416 (2008). doi:10.1103/PhysRevB.78.214416. http://link.aps.org/doi/10.1103/PhysRevB.78.214416
15. K. Tao, V.S. Stepanyuk, W. Hergert, I. Rungger, S. Sanvito, P. Bruno, Phys. Rev. Lett. **103**, 057202 (2009). doi:10.1103/PhysRevLett.103.057202. http://link.aps.org/doi/10.1103/PhysRevLett.103.057202

16. C. Lazo, S. Heinze, Phys. Rev. B **84**, 144428 (2011). doi:10.1103/PhysRevB.84.144428. http://link.aps.org/doi/10.1103/PhysRevB.84.144428
17. M. Granovskij, A. Schrn, F. Bechstedt, New J. Phys. **16**(2), 023020 (2014). http://stacks.iop.org/1367-2630/16/i=2/a=023020
18. F. Pielmeier, F.J. Giessibl, Phys. Rev. Lett. **110**(26), 266101 (2013)
19. S.L. Dudarev, A.I. Liechtenstein, M.R. Castell, G.A.D. Briggs, A.P. Sutton, Phys. Rev. B **56**, 4900 (1997). doi:10.1103/PhysRevB.56.4900. http://link.aps.org/doi/10.1103/PhysRevB.56.4900
20. M. Granovskij, A. Schrn, F. Bechstedt, New J. Phys. **16**(2), 023020 (2014). http://stacks.iop.org/1367-2630/16/i=2/a=023020
21. A. Kubetzka, P. Ferriani, M. Bode, S. Heinze, G. Bihlmayer, K. Von Bergmann et al., Phys. Rev. Lett. **94**(8), 087204 (2005)
22. M. Liebmann, A. Schwarz, S. Langkat, R. Wiesendanger, Rev. Sci. Instrum. **73**(10), 3508 (2002)
23. T.R. Albrecht, P. Grütter, D. Horne, D. Rugar, J. Appl. Phys. **69**(2) (1991)
24. E. Vedmedenko, Q. Zhu, U. Kaiser, A. Schwarz, R. Wiesendanger, Phys. Rev. B **85**(17), 174410 (2012)
25. H. Hölscher, B. Gotsmann, A. Schirmeisen, Phys. Rev. B **68**, 153401 (2003). doi:10.1103/PhysRevB.68.153401. http://link.aps.org/doi/10.1103/PhysRevB.68.153401
26. U. Dürig, Appl. Phys. Lett. **75**(3), 433 (1999). doi:10.1063/1.124399. http://scitation.aip.org/content/aip/journal/apl/75/3/10.1063/1.124399
27. H. Hölscher, A. Schwarz, W. Allers, U. Schwarz, R. Wiesendanger, Phys. Rev. B **61**(19), 12678 (2000)
28. F.J. Giessibl, Appl. Phys. Lett. **78**(1), 123 (2001)
29. J.E. Sader, S.P. Jarvis, Phys. Rev. B **70**, 012303 (2004)
30. N. Sasaki, M. Tsukada, Jpn. J. Appl. Phys. **39**(12B), L1334 (2000). http://stacks.iop.org/1347-4065/39/i=12B/a=L1334
31. T. Trevethan, L. Kantorovich, Phys. Rev. B **70**, 115411 (2004). doi:10.1103/PhysRevB.70.115411. http://link.aps.org/doi/10.1103/PhysRevB.70.115411
32. S.A. Ghasemi, S. Goedecker, A. Baratoff, T. Lenosky, E. Meyer, H.J. Hug, Phys. Rev. Lett. **100**, 236106 (2008). doi:10.1103/PhysRevLett.100.236106. http://link.aps.org/doi/10.1103/PhysRevLett.100.236106
33. J.P. Perdew, K. Burke, M. Ernzerhof, Phys. Rev. Lett. **77**, 3865 (1996). doi:10.1103/PhysRevLett.77.3865. http://link.aps.org/doi/10.1103/PhysRevLett.77.3865
34. K. Schwarz, P. Blaha, G. Madsen, Comput. Phys. Commun. **147**(12), 71 (2002). doi:10.1016/S0010-4655(02)00206-0.http://www.sciencedirect.com/science/article/pii/S0010465502002060. (Proceedings of the Europhysics Conference on Computational Physics Computational Modeling and Simulation of Complex Systems.)
35. A.R. Williams, R. Zeller, V.L. Moruzzi, J.C.D. Gelatt, J. Kübler, J. Appl. Phys. **52**, 2067 (1981)
36. C. Zener, Phys. Rev. **81**, 440 (1951). doi:10.1103/PhysRev.81.440
37. C. Zener, Phys. Rev. **82**, 403 (1951). doi:10.1103/PhysRev.82.403
38. T. Moriya, Solid State Commun. **2**, 239 (1964)
39. G.A. Gibson, S. Schultz, J. Appl. Phys. **73**(9) (1993)
40. S. Krause, L. Berbil-Bautista, G. Herzog, M. Bode, R. Wiesendanger, Science **317**(5844), 1537 (2007). doi:10.1126/science.1145336. http://www.sciencemag.org/content/317/5844/1537.abstract
41. L. Neel, Ann. Géol. **5**, 99 (1949)
42. W.F. Brown, Phys. Rev. **130**, 1677 (1963). doi:10.1103/PhysRev.130.1677. http://link.aps.org/doi/10.1103/PhysRev.130.1677

Chapter 8
Revealing Subsurface Vibrational Modes by Atomic-Resolution Damping Force Spectroscopy

Makoto Ashino and Roland Wiesendanger

Abstract Damping of the oscillating cantilever in dynamic atomic force microscopy contains valuable information about the local vibrational structure and elastic compliance of the substrate. We review Damping Force Spectroscopy which has successfully visualized atomically-resolved damping in supramolecular assemblies, capable of identifying the location and packing of inner molecules as well as local excitations of vibrational modes, dependent on outer molecules with specific geometry. We introduce the physical origin of damping in a microscopic model and quantitative interpretation of the practical observations by calculating the vibrational spectrum and damping of inner metallofullerene Dy@C_{82} molecules inside carbon nanotubes with different diameters using ab initio total energy and molecular dynamics calculations.

8.1 Introduction

A daunting endeavor has been paid to achieve atomic-scale spatial resolution in detecting surface and subsurface vibrations by scanning probe methods. Inelastic Scanning Tunnelling Spectroscopy (IESTS) has been utilized so far for observing atomic-scale molecular vibrations but requires an electrically conducting substrate [1]. Atomic force microscopy (AFM) [2] has become one of the most versatile and powerful tools to determine the morphology of both insulating and conducting objects down to the atomic scale. Involving ultrasonic oscillations of elastically

M. Ashino (✉)
Kanazawa Institute of Technology, Kanazawa, Japan
e-mail: mashino@neptune.kanazawa-it.ac.jp

R. Wiesendanger
Interdisciplinary Nanoscience Center Hamburg (INCH), University of Hamburg,
Jungiusstrasse 11, 20355 Hamburg, Germany
e-mail: wiesendanger@physnet.uni-hamburg.de

© Springer International Publishing Switzerland 2015

S. Morita et al. (eds.), *Noncontact Atomic Force Microscopy*,
NanoScience and Technology, DOI 10.1007/978-3-319-15588-3_8

indented sample surfaces AFM can be used as a non-invasive tool to image subsurface structures even on electrically insulating systems [3, 4]. The technique based on the nonlinear detection of ultrasonic oscillation in elastically "indented" samples, however, yields subsurface images with nanometer-scale resolution at best. Building on the high spatial resolution and sensitivity of dynamic non-contact AFM, Damping Force Spectroscopy (DFS) [5] has been introduced as a non-invasive tool to study subsurface structure and vibrational modes in complex molecular systems at the atomic scale. Carbon nanotube peapods [6–8] consisting of linear chains of fullerenes enclosed in single-walled carbon nanotubes (SWNTs) [9] have been chosen as a prominent example of supramolecular compounds. Of particular interest are (M@C_n)@SWNT peapods containing M@C_n metallofullerenes, hollow cages of n carbon atoms surrounding the metal atom M, known for their unusual electronic transport behavior [10].

8.2 Damping Force Spectroscopy

8.2.1 Dynamic AFM Operation

Atomic Force Microscopy (AFM) is a real-space technique to image sample surfaces by sensing the interaction force acting between the AFM probe tip and sample surface. In the dynamic mode of operation (see Fig. 8.1) [11], a cantilever mounted on a piezo actuator is oscillated at its eigenfrequency f_0 by a self-excitation resonance loop. The actual resonance frequency f is shifted by Δf (i.e. $\Delta f = f - f_0$) due to the tip-sample interaction involving long- and short-range terms. Surface topography images are acquired by applying an active feedback control to maintain a constant Δf during the raster scan. The long-range terms originating from their van der Waals and electrostatic interactions are minimized respectively by using the AFM tip with a very sharp apex and by compensating the tip-sample contact potential differences. In that case, true atomic resolution can be achieved in surface topography imaging. In addition, careful adjustment of the operation within the non-contact regime makes it possible to decouple atomically-resolved topography features from effects caused by tip-induced elastic deformation of the sample [12].

8.2.2 The Damping Signals ΔE

By applying another feedback control to maintain a constant amplitude A of the cantilever oscillation instead (see Fig. 8.1), energy loss (or damping) images are acquired, identifying spatial variations of the energy loss ΔE per cycle of the cantilever oscillation. This quantity is given by

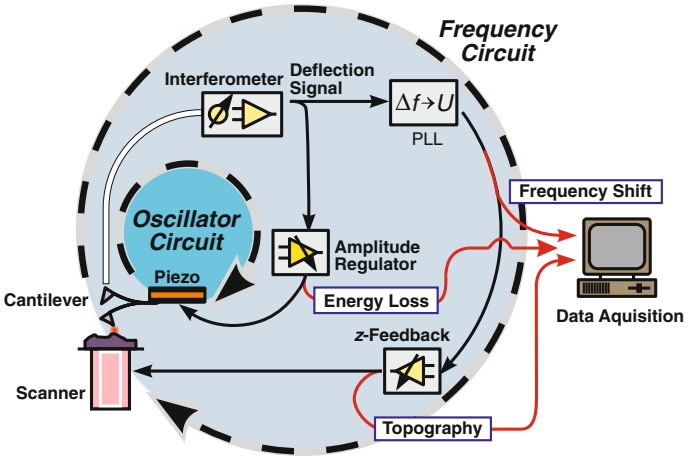

Fig. 8.1 Schematic operational diagram of a dynamic Atomic Force Microscope (AFM) system. Using two separate feedback control channels indicated by *large arrows*, surface topography and energy loss ΔE images are acquired simultaneously

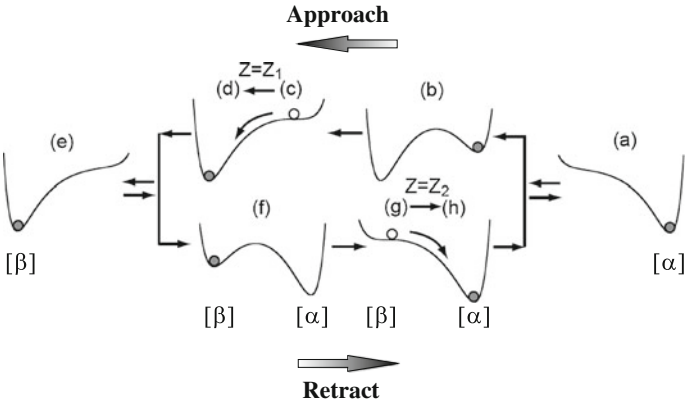

Fig. 8.2 Schematic diagrams of the non-conservative tip-sample interaction associated with the hysteretic behavior in (*a*)–(*h*) the approach-retraction cycle [13, 14]. The bistable states $E_\alpha(z)$ and $E_\beta(z)$ cross at $z = z_c$. Initially, as the tip is far from the surface, the system rests in state α. Then, at some value $z_1 < z_c$ of z, it jumps into state β when the barrier $\Delta E_{T\alpha}(z) = E_T(z) - E_{T\alpha}(z)$ becomes small enough, similarly, during retraction, the system falls back into state α at some $z_2 > z_c$.

$$\Delta E(x, y, z) = \pi \frac{c_L A^2}{Q_0} \left[\frac{G(x, y, z)}{G_0} - \frac{f(x, y, z)}{f_0} \right], \tag{8.1}$$

where c_L is the cantilever's spring constant, Q_0 the intrinsic quality factor, and G the gain factor to keep the constant oscillation amplitude. In the dynamic mode of AFM operation, the non-conservative tip-sample interaction associated with the hysteretic behavior in the approach-retraction cycle depicted in Fig. 8.2, which is likely due

to atomic instabilities, would be the main mechanism for the atomic-scale dissipation (i.e. energy losses or damping) [13, 14]. The quantity $\Delta E(x, y, z)$ is the signal probed by Damping Force Spectroscopy (DFS).

The fundamental concept of an AFM imaging an elastic sample is illustrated in Fig. 8.3. The position z_t of the tip apex atom depends on the position z_c of the cantilever mount and the deflection of the elastic cantilever, represented by a spring. Similarly, an elastic sample surface is represented by another spring, allowing the position z_a of the closest sample atom to differ from z_s of the sample substrate. The force exerted on the tip by the sample depends largely on the tip-sample distance $h = z_t - z_a$ (also represented by another spring).

The origin of energy dissipation in the non-contact regime is depicted in Fig. 8.4. At each value of the distance h between the tip and the closest sample atom, the tip-sample attraction is considered to be compensated by the restoring force caused by strain in the elastic sample and deflected cantilever. The force F_a exerted on an elastic sample atom by an approaching the AFM tip apex at height h is shown by the solid line in Fig. 8.4. For a given position z_c of the cantilever mount (see in Fig. 8.3), the instantaneous position of the tip apex z_t and the sample atom z_a depends not only on their mutual distance h, which determines the nonlinear interaction force shown

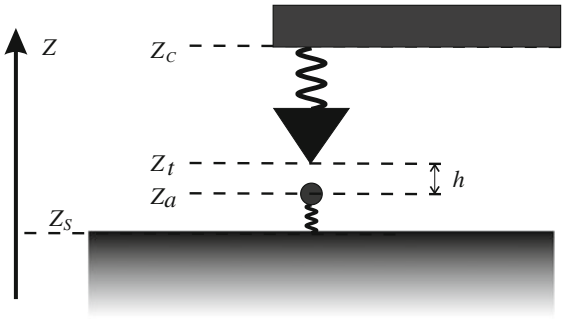

Fig. 8.3 Schematic of the coupling mechanism between a sharp AFM tip and a flexible substrate. The cantilever stiffness is represented by the spring connecting the tip and its suspension. The elastic substrate is represented by the spring connecting a representative atom to its surroundings

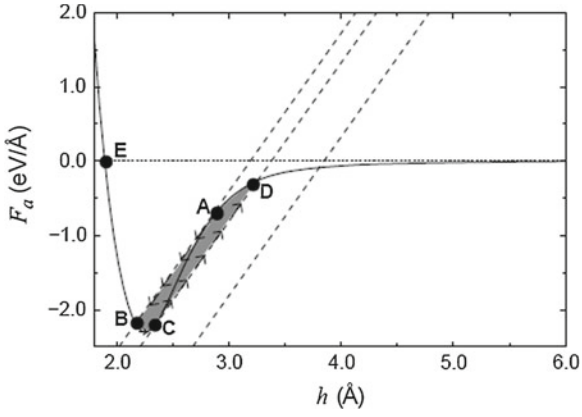

Fig. 8.4 Mechanism of energy dissipation during the dynamic AFM operation in noncontact regime

by the solid line, but also on the compensating forces of the strained cantilever and sample, shown by the dotted lines, as well as the history. As the tip approaches from infinity, it experiences a noticeable attraction from the sample near point D (see in Fig. 8.4). In the case of a soft sample (or cantilever), as the AFM tip approaches closer, the restoring force can no longer compensate the attraction from the sample and an instability occurs at point A, causing an abrupt decrease in the tip-sample distance to point B. No further instability occurs as the tip further approaches the sample towards point E, the equilibrium tip-substrate separation. After initiating the tip retraction by increasing h, a similar instability occurs at C. At this point, the restoring force equals the tip-sample attraction, causing an abrupt increase in the tip-sample distance to D. We note that even the closest-approach point B occurs in the non-contact regime, since h_B is beyond the equilibrium tip-sample separation h_E, characterized by $F_a = 0$. The approach-retraction relationship is reversible in the range $0 < h < h_B$ and $h_D < h < \infty$. The hysteresis corresponding to the shaded area in Fig. 8.4, delimited by A, B, C, and D, represents the energy dissipation in the sample during an ideal approach-retraction cycle, which is observed in the dynamic AFM.

8.3 DFS on Complex Molecular Systems

In Medicine, ultrasound is successfully used as a non-invasive tool to image an unborn baby in the mother's womb. The non-invasive technique of Damping Force Spectroscopy (DFS) has been introduced first as its counterpart in nanotechnology, which is capable of imaging subsurface structures on the atomic scale by observing the damping of an oscillating AFM tip in the "non-contact" regime. Here we review a representative example of complex molecular systems, in which the DFS resolution exceeds significantly that of a previously-used approach [3, 4] based on the nonlinear detection of ultrasonic oscillation in elastically "indented" samples with nanometer-scale resolution at best. The DFS technique builds upon and extends the high spatial resolution and sensitivity of the dynamic AFM as a powerful tool to probe damping and to reveal the subsurface structures.

8.3.1 Supramolecular Assembly

Molecular self-assembly can form a higher-order structure involving so-called supramolecular assembly, in which a well-defined complex of two molecules are held together by intermolecuar forces usually originating from noncovalent bonds. A well-known example in the interdisciplinary field of biology and materials science are self-assembling dendritic dipeptides, in which cyclindrical supramolecular assemblies with internal helical order are formed both in solution and in bulk [15]. Molecules and atoms are known to enter spontaneously the inner cavities of

larger molecules in a process called molecular encapsulation, which has stimulated activities in supramolecular chemistry [16, 17]. A well-known example of supramolecular host molecules in nanoscience and nanotechnology are single-walled carbon nanotubes (SWNTs) having a nanometer-size diameter and macroscale length [8]. Molecules encapsulated within these nanoscale containers have been reported to form one-dimensionally ordered chains [6, 7], called nanotube "peapods". The first DFS measurements has been performed for a metallofullerene $(M@C_n)@SWNT$ peapod. The $M@C_n$ metallofullerenes consist of hollow cages of n carbon atoms containing the metal atom M, filling carbon nanotubes and forming $(M@C_n)@SWNT$ peapods.

The molecular encapsulation follows thermodynamic processes influencing intermolecular interactions [18, 19]. The $M@C_n$ molecules can modify significantly mechanical, electrical and/or magnetic properties of the host nanotube, potentially causing unusual behaviour in $(M@C_n)@SWNT$ peapods [9, 20]. These hybrid structures have been investigated predominantly using electrons as a probe in electronic transport measurements [10, 21], transmission electron microscopy (TEM) [22, 23], and scanning tunnelling microscopy/spectroscopy (STM/STS) [24, 25] studies. Figure 8.5 shows TEM images of the $(Dy@C_{82})@SWNT$ sample used in [5], in which the fullerene cages are imaged as circles and the enclosed Dy atoms as dark spots positioned off the center, clearly representing the "quasi" one-dimensional crystal formation [26] of encapsulated $Dy@C_{82}$ endohedral metallofullerene molecules. In the process of sample preparation, the $Dy@C_{82}$ molecules were encapsulated into open-ended SWNTs with different diameters by heating their mixture in a platinum crucible under 10^{-6} Torr at 440 °C for 5 days [27]. The filling rate of the $Dy@C_{82}$ molecules into the empty SWNTs was confirmed to be approximately 60 % not only by TEM imaging but also by DFS measurements as mentioned below.

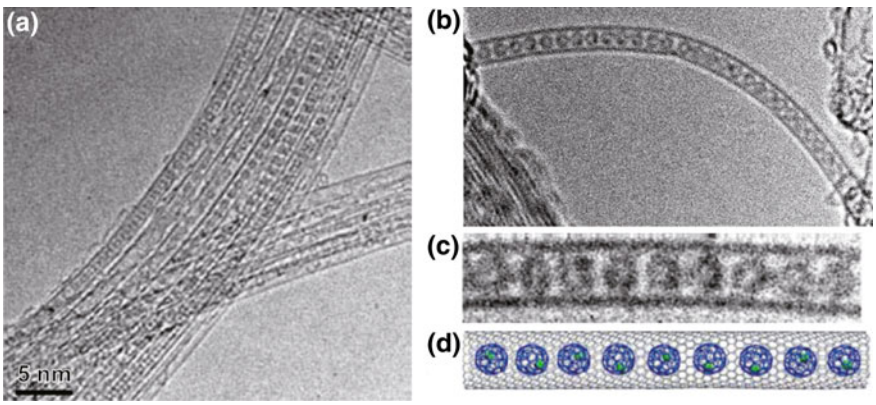

Fig. 8.5 **a**–**c** High-resolution transmission electron microscopy images and **d** a structural diagram of the $(Dy@C_{82})@SWNT$ endohedral metallofullerene peapod samples used in [5] (see [27])

8.3.2 Dynamic AFM Instrumentation

The (Dy@C_{82})@SWNT peapods were deposited at low coverage onto an insulating flat SiO_2 surface of a Si substrate and observed by dynamic AFM, as illustrated schematically in Fig. 8.6. The AFM was operated at constant oscillation amplitude of 2.1–2.3 nm maintained by the feedback loop (see Fig. 8.1) under ultra-high vacuum ($p < 1 \times 10^{-8}$ Pa) and low temperature ($T < 13$ K) conditions. The dynamic AFM imaging was carried out using a commercial Si cantilever (spring constant $c_L = 34.3$ N/m and eigenfrequency $f_0 = 159$ kHz) with a sharp tip of monocrystalline Si (nominal tip radius <2.5 nm). After transfer into the vacuum, the probe tips were cleaned by Ar^+ sputtering. To minimize the effect of long-range electrostatic forces, the average contact potential difference was compensated by applying a bias voltage U_{bias} to the cantilever [12].

Under the above-mentioned conditions atomic resolution images have been successfully obtained without any "ghost structures" (caused by double-tips etc.) and consistent with lattice parameters of graphitic carbon, as show in Fig. 8.7 [28]. In that case the AFM tip was reported to have an "atomically sharp" apex, whose radius R was estimated to be less than 0.5 nm [5]. The sharpness and the effective shape of the tip apex were deduced by deconvoluting AFM images of empty SWNTs, used for calibration. By taking into account the high Young's moduli Y = 180 GPa [29] of the Si tip and the effective value of 17 GPa [30] for the radial deformation of the nanotube, elastic deformations associated with the tip-nanotube interaction were calculated to be within the noise range for nominal forces below 250 pN. According to the numerical estimates based on the spring constant and oscillation amplitude, the damping energy as well as the tip-sample interaction were concluded to be too small in the operating range of the experiment to cause problems such as jump-to-contact and other instabilities of the cantilevers, mostly related to the hysteresis depicted in Fig. 8.4.

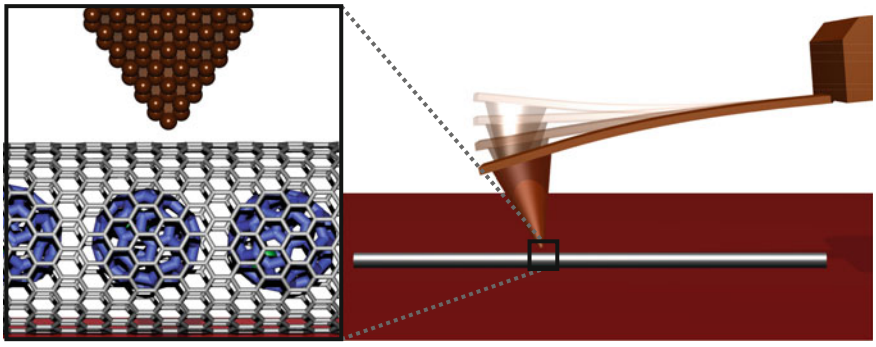

Fig. 8.6 Close-up view (*left*) and overview (*right*) illustrations of a sharp AFM tip, mounted on an oscillating silicon cantilever, as it probes a carbon nanotube peapod on an insulating flat SiO_2 surface of a Si substrate. Interaction between the tip apex atom and the peapod surface shifts the resonance frequency and dampens the oscillation. Topography images are obtained by scanning the peapod surface under feedback control to keep the frequency shift Δf constant

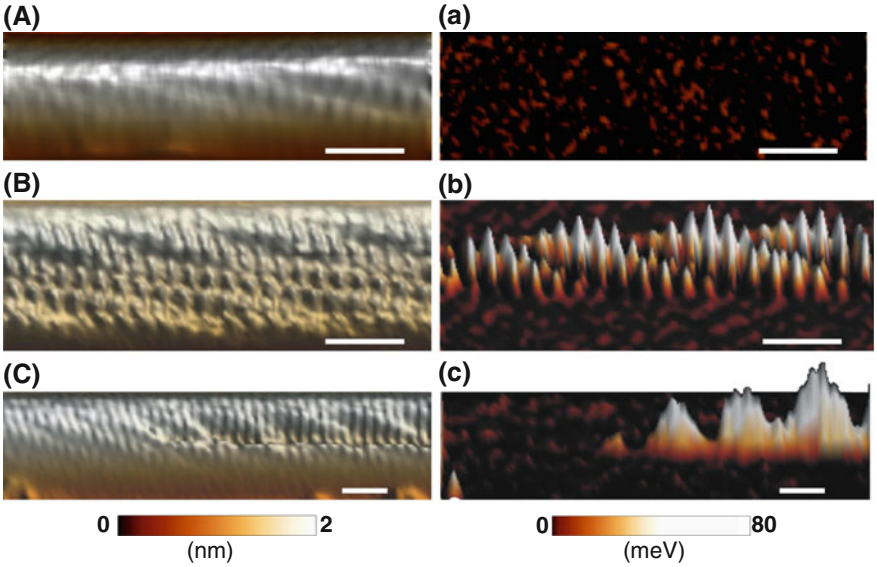

Fig. 8.7 Atomic-resolution AFM topography and damping images of individual nanotubes in the (Dy@C82)@SWNT sample in 3D views. The *scale bars* correspond to 1 nm. Atomic-resolution AFM topography images of an empty SWNT part (**A**), a peapod part (**B**) filled with Dy@C_{82}, and a boundary between the empty part (*left*) and the filled part (*right*) (**C**). **a**–**c** Damping images, simultaneously obtained with **A**–**C**, respectively. Damping signals in **c** have been generated at the boundary and become prominent following the sequence of the topographic undulation in **C**

8.3.3 Topography and Damping on Peapods

As already mentioned, the filling ratio of the Dy@C_{82} molecules in the empty SWNTs was confirmed to be approximately 60 % not only by TEM imaging but also by DFS measurements. The (Dy@C_{82})SWNT peapods were produced by heating the mixture of the Dy@C_{82} molecules and open-ended SWNTs [27]. TEM imaging shows that in the (Dy@C_{82})SWNT peapod sample some peapods include partially-unfilled (vacant SWNT) parts coexisting next to the parts densely filled by the Dy@C_{82} molecules [27] (see Fig. 8.8). Without any prior knowledge concerning which part is filled (peapod) and which is unfilled (SWNT), the partially-unfilled peapods were successively imaged by dynamic AFM [5]. In order to distinguish the filled (peapod) parts from the vacant (SWNT) parts on the basis of their image contrast, the sample of 100 % empty SWNTs deposited on another SiO_2 substrate was also imaged as a reference by dynamic AFM. By comparing the images obtained for the partially-unfilled peapods with those obtained for the empty SWNT sample, it was found that the topography images obtained over the partially-unfilled peapods represent not only the same atomic features (Fig. 8.7A) as obtained over the empty SWNT but also the obviously different atomic features (Fig. 8.7B) as well as their boundary (Fig. 8.7C). Furthermore, the atomic features in Fig. 8.7B were found to be superimposed and

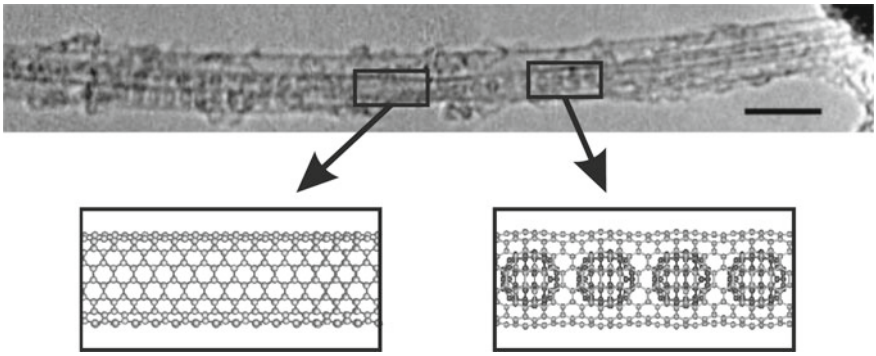

Fig. 8.8 A high-resolution transmission electron microscopy image of the (Dy@C_{82})@SWNT endohedral metallofullerene peapods, including partially-unfilled (vacant SWNT) parts, taken with a Philip CM200 TEM at 120 kV. *Scale bar* is 5 nm (see [27]). In a partially-unfilled peapod, the typical features corresponding to an unfilled (vacant SWNT) part is highlighted by the *left square* frame together with a filled (*peapod*) part, highlighted by the *right* one. Their structural diagrams are illustrated in the *left* and *right bottom insets*, respectively

amplified with respect to those over the empty SWNT in Fig. 8.7A. The contrast enhancement in topography images was expected to be attributed to local stiffening of the nanotube wall next to the enclosed Dy@C_{82} molecules [5].

More intriguing than the topography are the results for the spatial variation of the energy loss ΔE per cycle of the cantilever oscillation, defined as damping and monitored in DFS. The damping images, shown in Fig. 8.7a–c, have been recorded simultaneously with the topography images, shown in Fig. 8.7A–C. In case the topography images represent the same atomic features (Fig. 8.7A) as those over the empty SWNTs, almost no obvious features are observed in the damping channel (Fig. 8.7a), as shown in the 100 % empty SWNTs. On the other hand in case topography images represent the obviously different atomic features (Fig. 8.7B, C) the damping increases significantly (Fig. 8.7b, c). It should be noted that the scan direction was horizontal, i.e. parallel to the tube axis, in all images to prevent tip-induced nanotube displacement. In addition, the same atomic features as represented in Fig. 8.7b, c (also in Fig. 8.7B, C) were obtained in both forward and backward scan directions. Thereby the significant enhancement of the damping signals might be assigned to the instability originating unlikely from atomic conformation changes in the tip apex side but more likely from the existence of encapsulated molecules in the peapod sample [5, 28]. As mentioned furthermore below, the presence of significant damping shown in Fig. 8.7b, c would be a primary evidence of dealing with a peapod. Hence the AFM-based distinction between the filled peapod part and unfilled SWNT part was found to be consistent with the TEM finding that about 60 % of the nanotubes were filled.

As displayed by three-dimensional contour plots in Fig. 8.9, topography and damping images representing various atomic features were obtained successively over the partially-unfilled peapods having different diameters on the same substrate,

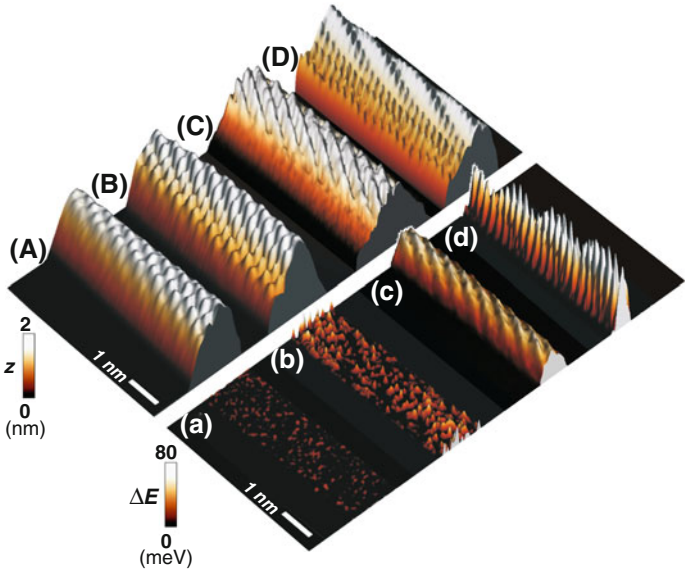

Fig. 8.9 AFM topography and damping in SWNTs and peapods with different diameter D. Atomically resolved dynamic AFM observations of the topography (**A**–**D**) and damping (**a**–**d**), defined as energy loss per cycle ΔE and represented by the *color codes*. Results of simultaneous scans for an empty SWNT with $D = 1.62 \pm 0.05$ nm are shown in (**A**, **a**), those for (Dy@C_{82})SWNT peapods with $D = 1.62 \pm 0.03$ nm in (**B**, **b**), with $D = 1.50 \pm 0.05$ nm in (**C**, **c**), and with $D = 1.30 \pm 0.05$ nm in (**D**, **d**). The way how to determine those diameters is described in the text

by their simultaneous measurements using the same Si tip [5]. Figure 8.9A, a show topography and damping images, respectively, over the unfilled (SWNT) part. Figure 8.9B, b show those over the filled (peapod) part, respectively. The tube diameters were determined by comparing the topographic heights obtained over the unfilled (SWNT) parts with those over the SWNTs with a well-defined diameter [12]. Thereby the diameter D of the partially-unfilled peapod in Fig. 8.9A, B was found to be $D = 1.62 \pm 0.05$ nm. In addition, the chiral index of their outer nanotube wall was derived to be (18, 5) from measuring its chiral angle for the arrangement of atomic features in Fig. 8.9A. In the same way, the diameters of other partially-unfilled peapods in Fig. 8.9C, D have been determined to be 1.50 ± 0.05 nm and 1.30 ± 0.05 nm, respectively, by the topographic heights over their unfilled parts.

As already mentioned above, more intriguing than the topography are the results for the spatial variation of the energy loss ΔE per cycle of the cantilever oscillation, defined as damping and monitored in DFS. The damping data, displayed in Fig. 8.9a–d, have been recorded simultaneously with the topography data in Fig. 8.9A–D, respectively. According to Fig. 8.9a, almost no damping is observed in an unfilled (SWNT) part. In comparison to these observations, Fig. 8.9b suggests that in the filled (peapod) part of the same nanotube damping increases significantly. The data displayed in Fig. 8.9b–d show that (i) ΔE increases, (ii) the atomic features

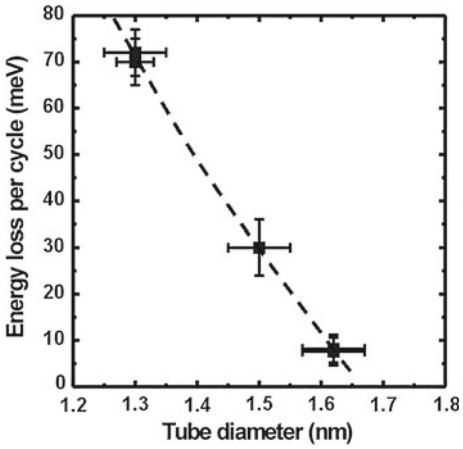

Fig. 8.10 Relationship of the maximum damping energy $\Delta E_{\max}$ with the outer nanotube diameter D. The data points are representative for tens of tube samples. The *dashed line* is a guide to the eye

within ΔE are amplified, and (iii) helical undulations in ΔE grow in magnitude with decreasing diameter of the enclosing nanotube. In Fig. 8.10, the maximum energy loss per cycle $\Delta E_{\max}$ observed during a DFS scan is plotted as a function of the host nanotube diameter D [5]. The data points in the diagram are presented for a (13, 6) and a (11, 8) nanotube of $D = 1.30 \pm 0.05$ nm, a (19, 0) nanotube of $D = 1.50 \pm 0.05$ nm, and (20, 1) and (18, 5) nanotubes of $D = 1.62 \pm 0.05$ nm. The results indicate a universal dependence of $\Delta E_{\max}$ on the diameter D. From the narrowest to the widest nanotube, as plotted in Fig. 8.10, the value of $\Delta E_{\max}$ is found to decrease from 71 ± 5 meV to 30 ± 6 meV and 7.9 ± 3.0 meV per cycle of the oscillating tip.

8.3.4 Packing and Optimum Geometry of Peapods

The formation energy and optimum geometry of peapods is determined by the diameters of the encapsulated fullerene molecules D_F and the enclosing nanotube D [7], as illustrated in Fig. 8.11. An optimum snug fit is expected to occur at $D \approx D_F + 0.64$ nm [18, 19], with the optimum distance $D_{F-F} \approx D_F + 0.32$ nm between the centers of neighboring fullerenes. As for the diameter $D_F \approx 0.8$ nm of $Dy@C_{82}$, an optimum fit is expected to occur in a $D \approx 1.42$ nm wide SWNT, with the encapsulated molecules separated by $D_{F-F} \approx 1.12$ nm. The diameter $D = 1.30 \pm 0.05$ nm of the narrowest peapod reported in [5], discussed in Fig. 8.9D, is smaller than optimum. In this case, the enclosed molecules distort elastically the nanotube wall, causing an undulation along the nanotube axis, as reported in [28] and as seen in Fig. 8.9D. As mentioned below, the observed undulation period of 1.15 ± 0.05 nm shows good agreement with the above estimated inter-fullerene distance D_{F-F} [5].

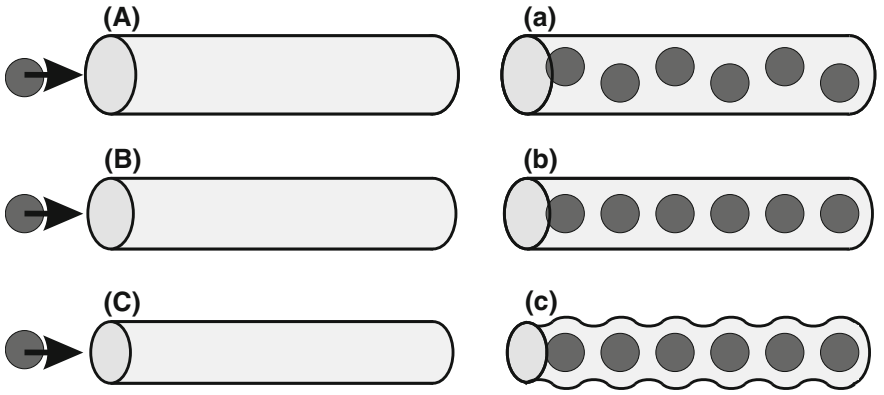

Fig. 8.11 Schematic illustrations of getting a fullerene molecule into the nanotubes with larger to smaller diameters (**A**–**C**) and of packing and optimum geometry of the peapods (**a**–**c**) after encapsulating fullerenes into the corresponding nanotubes of **A**–**C**. The *upper* section shows a loose fit, and the *middle* and *bottom* sections show an optimum and a tight fit, respectively (see text)

The overall features in the atomic-resolution topography images obtained over the empty SWNTs, such as that in Fig. 8.9A, were found to be symmetric with respect to the axis, indicating that the tip-apex shape would be symmetric [5]. On the other hand, some degree of asymmetries were observed in Fig. 8.9B–D, displaying topography images of the peapods. Even though extra precautions (e.g. slow scan in the axial direction) were taken to avoid artifacts caused by tip-induced lateral displacement of the nanotube and feedback lag, it might be impossible to exclude artifacts caused by tip asymmetry as the origin of the observed lateral asymmetry in topographic images of peapods. Possible reasons of those lateral asymmetries could be either a genuine Dy@C_{82} endohedral metallofullerene encapsulated inside the outer nanotube (which might be spontaneous or induced by the AFM tip), as depicted in Fig. 8.12, or an artifact of the measurement. It is conceivable that an ordered subsurface structure, in particular an off-axis location of the encapsulated metallofullerenes in wide nanotubes, as depicted in Fig. 8.11a, could cause a lateral asymmetry in the AFM signal. In that case, as shown in Fig. 8.12, the net charge on the Dy ion and the enclosing fullerene may cause an electric field with a non-axially symmetric distribution outside the peapod, which would exert an extra force on the tip. Since heavily-doped Si cantilevers were used [5], an asymmetric doping profile may evolve also on the Si tip with an otherwise symmetric morphology. Should this indeed be the case, an asymmetry in the charge distribution on the tip should not be noticeable when probing locally charge neutral SWNTs, but could play a more important role when probing (Dy@C_{82})@SWNT peapods with a significant charge re-distribution.

As shown in Fig. 8.9, atomic features in damping ΔE show a similar or possibly larger contrast than topography features in the case of a snug fit. Even though both are spatially correlated, the strongest damping was observed slightly off the center of

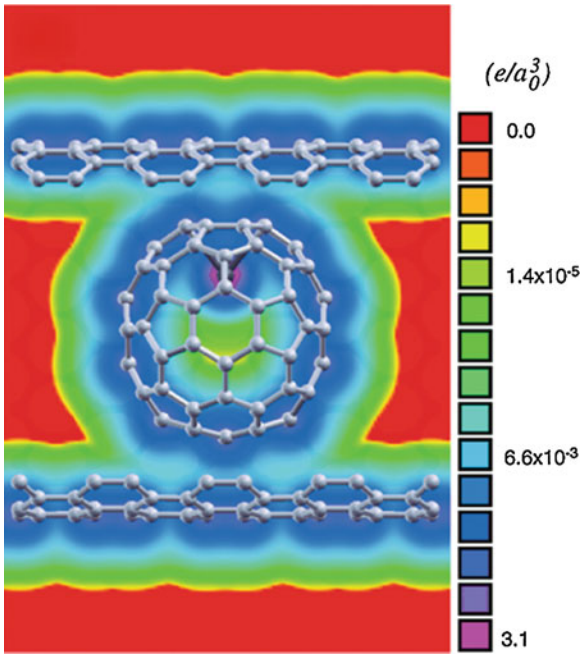

Fig. 8.12 Total charge density of the optimized Dy@C_{82} endohedral metallofullerene encapsulated in the (18, 0) nanotube, superposed with the skeletal structure of the peapod. It should be noted that the Dy ion is located at off-center position, causing asymmetry in the charge distribution

the largest topographic protrusions above the encapsulated fullerenes. Decreasing the diameter of the enclosing nanotube causes an increasingly snug fit of Dy@C_{82} in the peapod (see Fig. 8.11). For a detailed comparison between topography and damping observations, the atomic-scale asymmetric features obtained on the narrowest peapod are displayed and highlighted in Fig. 8.13 by 2D color-coded contour plots and by line sections along an individual scan. The topography (Fig. 8.13A) and damping signals (Fig. 8.13a) obtained over the narrowest peapod show an axial undulation with the axial periodicity of 1.15 ± 0.05 nm and amplitudes of 56 ± 5 pm in topographic height and 70 ± 5 meV in damping energy [28]. The profiles in the bottom panels, where the vertical scales are normalized, show that the atomic-scale contrast in damping (right panels) is generally larger than in topography (left panels). Positions of relative maxima in topography and damping along the same blue-dashed trajectory are indicated by the blue crosses. The results show that the position of relative maxima in damping shifts 0.2–0.3 nm perpendicularly to the nanotube axis with respect to the maxima in topography. The axial band with maximum contrast in damping, shown in Fig. 8.13a, is much narrower and positioned differently from the band of contrast maximum in topography (Fig. 8.13A) by the red dotted trajectory. The result is expected to be one more indication that the damping signal is a source of new, rich information surpassing that of pure topography measurements. It can be concluded that monitoring the damping of the oscillating tip provides superior information to topography imaging in discriminating between snug and loose packing of fullerenes inside the nanotube.

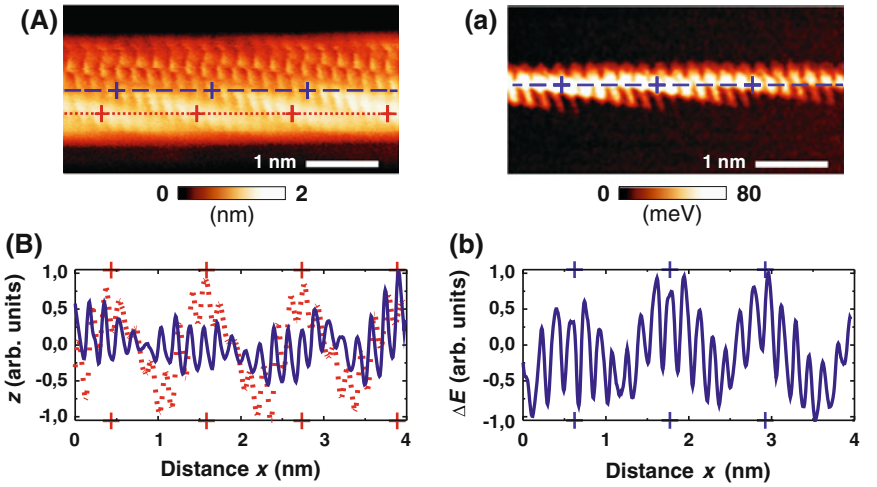

Fig. 8.13 Results of simultaneous topographic AFM (**A**) and damping measurements (**a**) of the nanotube peapod represented in Fig. 8.9D, d, respectively. In the atomic-resolution images, local maxima reflect the atomic positions in the chiral enclosing nanotube and those of the enclosed metallofullerenes. The scan data are represented as color-coded 2D images in (**B**). *Red-* and *blue-colored graphs* in **B** show original scan data along trajectories indicated by the *same color* and *dashed* or *dotted* pattern in (**b**)

8.3.5 Molecular Dynamics Simulations

In order to uncover the origin of damping in DFS, ab initio density functional calculations of the electronic structure, equilibrium geometry and elastic response of these systems, have been performed along with molecular dynamics (MD) simulations of the dynamical coupling between the AFM tip and the nanotube peapod [5]. Indeed detailed analysis of the calculations provides insight into the microscopic mechanism of damping in the complex system, including its dependence on tip apex atom position and outer nanotube wall diameter.

The total energy calculations indicate that the Dy@C_{82} metallofullerene isomer with C_{2v} symmetry and a nearly spherical shape would be energetically preferred by at least 0.5 eV over any other isomer including the C_2 isomer. While the C_2 isomer of C_{82} is generally most stable and abundant in absence of Dy, the near-spherical isomer of Dy@C_{82} with the C_{2v} symmetry likely abounds in the (Dy@C_{82})@SWNT peapods. This structural preference is due to the enclosed Dy atom, since the most stable C_{82} fullerene has the C_2 symmetry. The total charge distribution of Dy@C_{82} inside the (18, 0) nanotube, providing optimum enclosure, is shown in Fig. 8.12. Loose and snug peapod packing scenarios are shown schematically in Fig. 8.11.

A series of MD calculations have been performed to make a quantitative prediction of how the energy loss of an oscillating tip depends on its position and the host tube diameter. As illustrated in the inset of Fig. 8.14, an initial perturbation was induced by radially displacing a surface atom by 0.3 Å, corresponding to the distance $h_C - h_E$

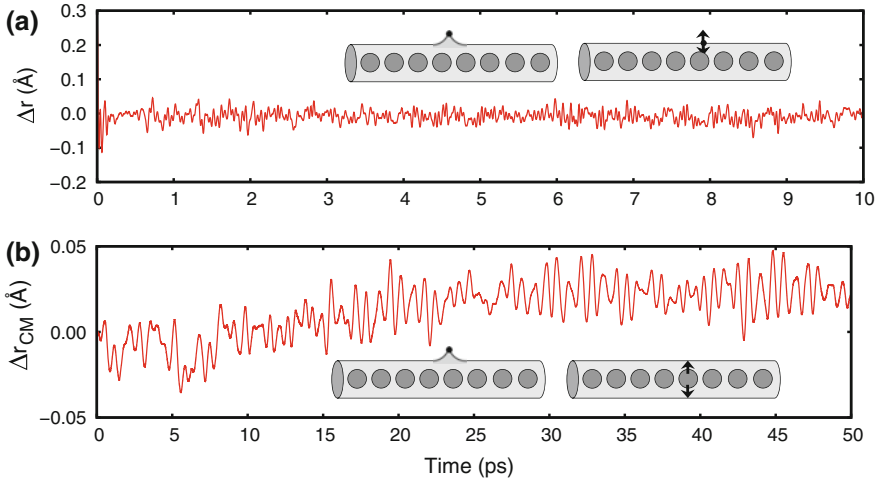

Fig. 8.14 Schematic illustrations and calculated dynamics and energy dissipation in the C_{82}@SWNT system following an initial "radial plucking" at the nanotube surface. Strongest damping occurs when plucking an atom located axially ≈1 Å off the center of the nearest C_{82}. **a** Radial displacement of the plucked atom as a function of time in C_{82}@(18, 0). **b** Radial displacement of the C_{82} center-of-mass as a function of time in C_{82}@(18, 0). The insets in **a** and **b** illustrate the initial distortion and the quantity monitored.

in Fig. 8.4, and abruptly releasing it. The energy released in this plucking process is transferred to energetically accessible vibration modes of the system. The observed energy loss per cycle ΔE depends on the frequency $h\nu$ of the individual modes and the likelihood of exciting them. This energy is thought to be then dissipated efficiently owing to the high thermal conductivity of nanotube systems [31]. Since the tip remains the same lateral positions, spatial contrast in $\Delta E_{\max}$ is found to be attributed only to the substrate.

The MD calculations also show that in empty SWNTs, plucking would excite solely the radial breathing mode (RBM), which occurs at frequencies ranging from $h\nu = 17.8 - 23.1$ meV in the systems considered in [5]. It was found that the energy required to excite the RBM is consistent with ΔE values observed in Fig. 8.9a. It is expected that stronger damping in peapods is attributed to additional modes introduced by the fullerenes. Ultra-soft vibrations of Dy within the C_{82} cage at $h\nu = 4.1 - 16.5$ meV would be attributed to the soft Dy$-C_{82}$ interaction and the large mass of Dy. Since those modes were thought to be decoupled from the remaining modes, the presence of Dy was ignored in the further discussion. Among the fullerene modes, librations about the center are certainly the softest, followed by axial and off-axis motion of the center of mass. Harder fullerene modes associated with fullerene deformation would include the RBM at $h\nu = 29$ meV, the quadrupolar deformation mode near $h\nu = 62.0$ meV, and higher multipolar modes. Especially in the case of a snug fit in the peapod, the nanotube and fullerene modes are expected to be strongly mixed.

For each of the nanotubes studied, the axial position of the surface atom plucked was changed from on-top a fullerene to in-between fullerenes, including a position half-way between the two as well. The simulation results indicate that the strongest damping is induced for the last position (axially $\approx$1 Å off the center of the nearest C_{82}), due to the possibility of exciting librations and axial vibrations of the fullerene underneath. This off-center position, indicated in the inset of Fig. 8.14a, certainly shows good agreement with the interpretation of the DFS results in Fig. 8.13.

Results of the MD simulation for $C_{82}@(18, 0)$ are displayed in Fig. 8.14. The radial trajectory of the plucked atom, $\Delta r(t)$ shown in Fig. 8.14a, and that of the closest fullerene molecule, $\Delta r_{CM}(t)$ shown in Fig. 8.14b, suggest that several modes are excited all at once. In order to elucidate which modes are dominant in damping, all trajectories were Fourier analyzed in the study. For zigzag nanotubes ranging from $(17, 0)$ to $(21, 0)$, the Fourier spectra of $\Delta r(t)$ and $\Delta r_{CM}(t)$ are displayed in Fig. 8.15a, b, respectively. Data for intermediate nanotube diameters have been obtained by interpolation.

The narrowest $C_{82}@(17, 0)$ peapod was expected to provide optimum coupling between the snugly fit fullerene and the enclosing nanotube. In the narrowest peapod, ΔE and its spatial modulation should be particularly enhanced. In contrast to an empty SWNT, the vibration spectrum of a surface atom in the $C_{82}@(17, 0)$ peapod indicates a variety of modes, as observed at the left side of Fig. 8.15a. Besides low-frequency modes with $h\nu < 20.7$ meV, it contains a series of modes with equally-spaced frequencies spanning the range $0 < h\nu < 90.9$ meV. In the wider $(18, 0)$ nanotube, the vibration spectrum is observed to be similar, but softer (i.e. red shifts). In the $(19, 0)$ and wider nanotubes, the fullerene-nanotube coupling is reduced drastically, as the inner fullerenes may be rearranged by little energy cost. As observed in Fig. 8.15a, decreased fullerene-nanotube (i.e. guest-host) coupling causes an obvious intensity drop of the high-frequency modes at $h\nu > 20$ meV. Especially in the narrowest nanotubes, the results for the off-center plucking position in Fig. 8.14a differ from those of other simulations, where the plucked atom is on top of a fullerene. Since plucking on top of a fullerene excites neither librations nor axial fullerene motion, energy dissipation in the on-top plucking position is very low. Comparing the results for those two plucking positions would explain the high spatial modulation of ΔE observed in Fig. 8.13.

The MD simulations also indicate that the vibration spectrum of the center-of-mass motion of an inner C_{82} fullerene inside the narrowest $(17, 0)$ nanotube, shown in Fig. 8.15b, is rather featureless and much softer than that in Fig. 8.15a. The $h\nu \approx 8$ meV off-axis vibration mode, which dominates the $(17, 0)$ spectrum, red shifts in wider nanotubes. Owing to the zigzag or helical arrangement of fullerenes in wider peapods, as depicted in Fig. 8.11a, the off-axis vibrations of the fullerenes may couple to soft axial vibrations and librations, which appear in the Fourier spectrum of Δr_{CM} in Fig. 8.15b. Those noticeable soft modes, without any effects on Δr_{CM}, modify the spectrum indirectly by coupling anharmonically to off-axis modes. Especially in the wider nanotubes, the center-of-mass vibrations of C_{82} was found to be rather insensitive to the axial position of the plucked atom, thus contributing very little to the spatial modulation of ΔE.

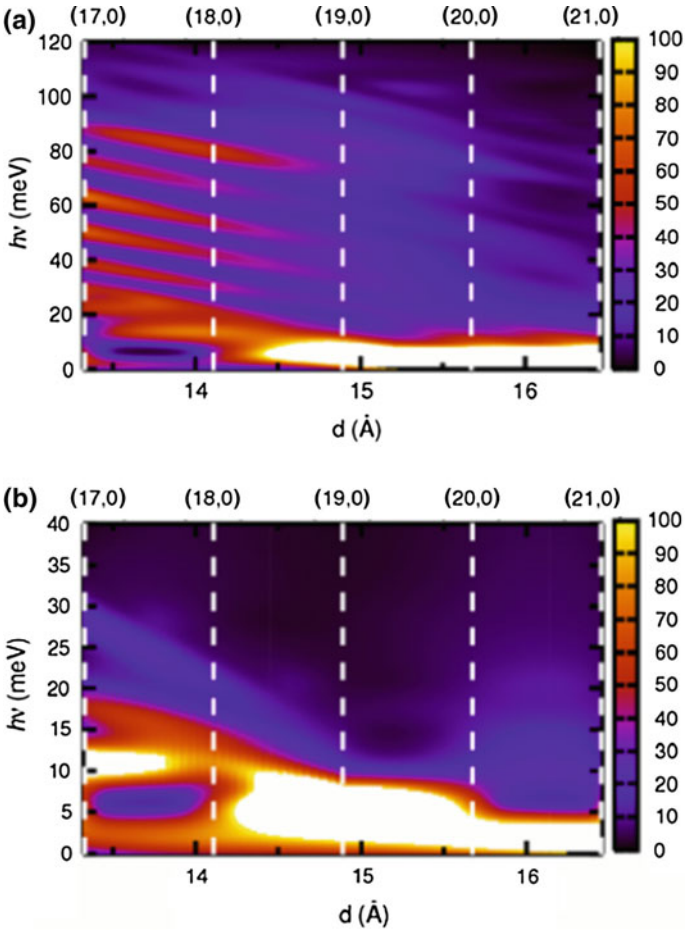

Fig. 8.15 For zigzag nanotubes ranging from (17, 0) to (21, 0): **a** Fourier spectrum of the radial displacement of the initially plucked atom as a function of the nanotube diameter d, and **b** Fourier spectrum of the C_{82} center-of-mass as a function of the nanotube diameter d.

8.3.6 Summary

For the (Dy@C_{82})@SWNT endohedral metallofullerene peapod, which is a representative example of supramolecular and complex systems, Damping Force Spectroscopy (DFS) has successfully demonstrated atomically-resolved maps of damping. The theoretical simulations based on ab initio total energy and molecular dynamics calculations have elucidated the physical origin of damping in a microscopic model and provided quantitative interpretation of the practical observations by calculating the vibrational spectrum and damping of Dy@C_{82} inside nanotubes with different diameters. Those results assist to conclude that damping of the oscillating cantilever

in dynamic atomic force microscopy contains valuable information about the local vibrational structure and elastic compliance of the sample, and that DFS is capable of identifying the location and packing of inner $Dy@C_{82}$ molecules as well as local excitations of vibrational modes inside nanotubes with different diameters. Thereby it should be prospective that further applications of DFS to variety of complex systems as well as to supramolecular systems could unveil their subsurface vibrational structures in addition to their geometric structures at the atomic scale.

Acknowledgments We appreciate Siegmar Roth and Dirk Obergfell for useful discussions and for sample preparation and David Tománek for theoretical support of our study.

References

1. B.C. Stipe, M.A. Rezaei, W. Ho, Science **280**, 1732–1735 (1998)
2. G. Binnig, C.F. Quate, C. Gerber, Phys. Rev. Lett. **56**, 930–933 (1986)
3. K. Yamanaka, H. Ogiso, O. Kolosov, Appl. Phys. Lett. **64**, 178–180 (1994)
4. O.V. Kolosov, M.R. Castell, C.D. Marsh, G.A.D. Briggs, T.I. Kamins, R.S. Williams, Phys. Rev. Lett. **81**, 1046–1049 (1998)
5. M. Ashino, R. Wiesendanger, A.N. Khlobystov, S. Berber, D. Tománek, Phys. Rev. Lett. **102**, 195503 (2009)
6. B.W. Smith, M. Monthioux, D.E. Luzzi, Nature **396**, 323–324 (1998)
7. D.A. Britz, A.N. Khlobystov, Chem. Soc. Rev. **35**, 637–659 (2006)
8. A. Jorio, G. Dresselhaus, M.S. Dresselhaus, *Carbon Nanotubes: Advanced Topics in the Synthesis, Structure, Properties and Applications, Topics in Applied Physics*, vol. 111 (Springer, Berlin, 1992)
9. R. Kitaura, H. Shinohara, Chem. Asian J. **1**, 646–655 (2006)
10. T. Shimada, T. Okazaki, R. Taniguchi, T. Sugai, H. Shinohara, K. Suenaga et al., Appl. Phys. Lett. **81**, 4067–4069 (2002)
11. T.R. Albrecht, P. Grütter, D. Horne, D. Rugar, J. Appl. Phys. **69**, 668–673 (1991)
12. M. Ashino, A. Schwarz, T. Behnke, R. Wiesendanger, Phys. Rev. Lett. **93**, 136101 (2004)
13. N. Sasaki, M. Tsukada, Jpn. J. Appl. Phys. **39**, L1334 (2000)
14. L.N. Kantorovich, T. Trevethan, Phys. Rev. Lett. **93**, 236102 (2004)
15. V. Percec, A.E. Dulcey, V.S.K. Balagarusamy, Y. Miura, J. Smidrkal, M. Peterca et al., Nature **430**, 764–768 (2004)
16. J.-M. Lehn, *Supramolecular Chemistry: Concepts and Perspectives* (VCH, Weinheim, Germany, 1995)
17. D. Fiedler, D.H. Leung, R.G. Bergman, K.N. Raymond, Acc. Chem. Res. **38**, 351–360 (2005)
18. M. Hodak, L.A. Girifalco, Chem. Phys. Lett. **350**, 450–411 (2001)
19. M. Yoon, S. Berber, D. Tománek, Phys. Rev. B **71**, 155406 (2005)
20. I.V. Krive, R.I. Shekhter, M. Jonson, Low Temp. Phys. **32**, 887–905 (2006)
21. P.W. Chiu, G. Gu, G.T. Kim, G. Philipp, S. Roth, S.F. Yang et al., Appl. Phys. Lett. **79**, 3845–3847 (2001)
22. K. Hirahara, K. Suenaga, S. Bandow, H. Kato, T. Okazaki, H. Shinohara et al., Phys. Rev. Lett. **85**, 5384–5387 (2000)
23. K. Suenaga, R. Taniguchi, T. Shimada, T. Okazaki, H. Shinohara, S. Iijima, Nano Lett. **3**, 1395–1398 (2003)
24. J. Lee, H. Kim, S.-J. Kahng, G. Kim, Y.-W. Son, J. Ihm et al., Nature **415**, 1005–1008 (2002)
25. K. Kimura, N. Ikeda, Y. Maruyama, T. Okazaki, H. Shinohara, S. Bandow et al., Chem. Phys. Lett. **379**, 340–344 (2003)

26. M. Hodak, L.A. Girifalco, Phys. Rev. B **64**, 035407 (2001)
27. D. Obergfell, J.C. Meyer, M. Haluska, A.N. Khlobystov, S. Yang, L. Fan et al., Phys. Stat. Sol. b **243**, 3430–3434 (2006)
28. M. Ashino, D. Obergfell, M. Haluska, S. Yang, A.N. Khlobystov, S. Roth et al., Nat. Nanotechnol. **3**, 337–341 (2008)
29. M.-F. Yu, T. Kowalewski, R.S. Ruoff, Phys. Rev. Lett. **85**, 1456–1459 (2000)
30. L. Shen, J. Li, Phys. Rev. B **69**, 045414 (2004)
31. S. Berber, Y.-K. Kwon, and David Tománek, Phys. Rev. Lett. **84**, 4613–4616 (2000)

Chapter 9
Self-assembly of Organic Molecules on Insulating Surfaces

Felix Kling, Ralf Bechstein, Philipp Rahe and Angelika Kühnle

Abstract Molecular self-assembly is known to provide a powerful tool for creating functional structures, with the ultimate structure and functionality encoded in the molecular building blocks. Upon molecule deposition onto surfaces, functional structures have been created ranging from defect-free, highly symmetric two-dimensional layers to complex assemblies with dedicated functionality. Especially organic molecules play a key role for molecular self-assembly due to their impressive structural flexibility and the high degree of control by chemical synthesis. Furthermore, the surface itself provides another exciting dimension: adjusting the subtle balance between intermolecular and molecule-surface interactions allows creating a broad variety of structures and explains the great success when confining molecular self-assembly to surfaces. While most of the structures realized so far have been fabricated on metallic substrates, comparatively little is known about molecular self-assembly on insulating surfaces. However, extending the materials basis to insulating substrates is of increasing interest to benefit from self-assembly strategies for emerging technologies such as molecular (opto)electronics. For the latter and further related applications, decoupling of the electronic structure from the underlying substrate is mandatory for the device functionality. Moreover, future applications will require the molecular structure to be stable at room temperature rather than at low temperatures. On insulating support surfaces, however, most attempts to create self-assembled molecular structures at room temperature have been hampered by the weak molecule-surface interactions. Thus, considerable effort has been made to establish means for increasing

F. Kling · R. Bechstein · A. Kühnle (✉)
Institut für Physikalische Chemie, Johannes Gutenberg Universität,
Duesbergweg 10-14, 55099 Mainz, Germany
e-mail: kuehnle@uni-mainz.de

F. Kling
e-mail: kling@uni-mainz.de

R. Bechstein
e-mail: ralf.bechstein@uni-mainz.de

P. Rahe
School of Physics and Astronomy, The University of Nottingham,
Nottingham NG7 2RD, UK
e-mail: rahe@uni-mainz.de

© Springer International Publishing Switzerland 2015

S. Morita et al. (eds.), *Noncontact Atomic Force Microscopy*,
NanoScience and Technology, DOI 10.1007/978-3-319-15588-3_9

the molecule-surface interaction and to provide strategies for tailoring the anchoring of the molecules towards the surface. Non-contact atomic force microscopy has been proven to provide an indispensable tool for direct imaging of molecular structures on electronically insulating surfaces with molecular resolution. Besides imaging, this technique also offers the potential to obtain complementary information, for example when performing Kelvin probe force microscopy or three-dimensional force mapping. In this chapter, we report the current status of molecular self-assembly on insulating surfaces in ultra-high vacuum with a special emphasis on structures stable at room temperature. Basic molecular self-assembly principles are reviewed and applied to the specific situation of prototypical insulating surfaces. Strategies for anchoring organic molecules towards insulating surfaces are discussed in the view of macroscopic as well as microscopic parameters such as the surface energy and detailed molecule-surface binding motifs. Based on structure optimization at the molecular level, the molecule-surface interaction can be tuned to adjust the final assembly, ranging from largely unperturbed molecular bulk crystals to strongly substrate-templated overlayers. Finally, current research topics are outlined, focusing on efforts directed towards steadily increasing the control of the resulting structures.

9.1 Introduction

The concept of self-assembly has been recognized as a most elegant tool for creating ordered, functional materials at all scales [1]. The most widespread use of this autonomous assembly process is probably found in solution chemistry, where supramolecular structures are formed from tailored molecular building blocks. Identified as a most powerful design principle, the development of this strategy has been honored with the Nobel Prize in chemistry in 1987. The prize has been awarded jointly to Donald J. Cram, Jean-Marie Lehn and Charles J. Pedersen for "their development and use of molecules with structure-specific interactions of high selectivity".

This chemists' concept of molecular self-assembly has been transferred into the surface science community, starting with the deposition of molecules onto single-crystal surfaces under well-controlled conditions of an ultra-high vacuum environment. In the early days, rather simple molecules have been deposited onto metal surfaces with little control over the intermolecular and molecule-surface interactions. In fact, most of these early studies have been performed with small molecules such as carbon monoxide or benzene [2] to establish a fundamental understanding about the interaction of individual molecules with the surface. From this single-molecule perspective, studies moved towards investigating molecular ensembles. Larger, mostly organic molecules have been explored [3], allowing for introducing intermolecular interactions in the structure formation, which marks the beginning of exploring molecular self-assembly on surfaces. It has soon been recognized that tuning the balance between molecule-surface and intermolecular interactions offers the potential for creating manifold structures on surfaces with dedicated functionality. Nowadays, molecular self-assembly is used in many applications, e.g., for surface

functionalization to provide specific and even switchable properties, fabrication of sensors or biocompatible surfaces, to name but a few [4, 5].

So far, however, most knowledge has been gathered on metallic substrates, as many surface science techniques require electrically conducting surfaces [6–11]. Especially scanning tunneling microscopy [12], providing the ability to directly image molecular structures with single-molecule and even sub-molecular resolution, has tremendously pushed these studies forward. The advent of non-contact atomic force microscopy [13, 14] and the constant improvements in resolution has now opened the option to extend these studies to non-conducting surfaces.

When studying molecular self-assembly on insulating surfaces, several design principles remain unaltered, while at the same time new challenges and possibilities arise from the fundamental difference in the molecule-surface interaction. Qualitatively different structures can be achieved due to the fundamental differences in the molecule-surface interactions. These aspects will surely further enhance the variability of molecular self-assembly on surfaces. Together with the greatly enlarged materials basis, this will provide flexibility for future applications, e.g., in the field of molecular electronics.

9.2 Self-assembly Principles

In the following section, we first review basic principles relevant for self-assembly before discussing the specific situation when turning to insulator surfaces.

9.2.1 General Considerations

Self-assembly describes the autonomous formation of ordered structures by predefined building blocks, controlled by the interaction between these constituting entities [15]. The impressive variety of organic synthesis offers an outstanding platform for providing a large variety of tailor-made organic molecules as building blocks with specific interactions both in terms of interaction strength and directionality [16, 17]. The latter two features are clearly both of high importance when aiming for controlled structure formation. Consequently, the ability of fine-tuning both strength and directionality is pivotal for enlarging the structural variety of molecular self-assembly.

An important aspect of molecular self-assembly is exploiting intermolecular interactions resulting in bond formation which is reversible at room temperature. This enables binding and unbinding of the molecular entities to eventually reach the thermodynamically most favorable structure.[1] Consequently, non-covalent bonds with

[1] In contrast, the term self-organization is typically used when discussing kinetically controlled structures such as diffusion-limited structures. However, the terms self-assembly and self-organisation are often used synonymously.

Table 9.1 Characteristics of intermolecular interactions used in molecular self-assembly

Type	Directionality	Selectivity	Binding partners
Hydrogen bond	Highly directional	Highly selective	X–H and Y, where X and Y are more electronegative than H [18]
Halogen bond			Electrophilic region at halogen atom in a molecule and nucleophilic region in another [19]
Pnicogen bond			P and N bonded to electron donors/acceptors [20]
Carbon bond			Alkyl carbon bonded to electronegative partners and negative centers in polar molecules [21]
π–π bond		Selective	Aromatic molecules [22]
Metal coordination bond	Directional		Metal atoms and ligands [23]
Van-der-Waals interaction		Poorly selective	Dipoles and/or polarizable species
Ion-ion interaction	Isotropic		Monopoles

This categorization is to some extend ambiguous. Note that a bond is per definition an overall attractive interaction while electrostatic interaction as such can be either attractive or repulsive

binding energies in the range of tenth of an eV are typically employed. In smart designs often several interactions of the same or of various type and/or attractive and repulsive interactions are combined to create a desired structure. To give an overview, Table 9.1 summarizes the relevant non-covalent interactions.

Categorizing interactions regarding their strength is not straightforward. For most bond types listed in Table 9.1, examples can be found with binding energies in the range of small fractions of an eV up to roughly one eV. The strength of a specific bond is, however, not sufficiently described by stating the binding energy, i.e., the depth of the pair potential at equilibrium distance. Bonds can be broken in many different ways, including the formation of transition states and possibly resulting in a new binding situation. For each process different parameters need consideration if the bond strength is to be characterized. For example, lifting a molecule from a surface via mechanical pulling requires applying a certain force determined by the maximum slope of the pair potential. For many processes it is necessary to consider how a potential decays with increasing distance between the binding partners. Fast decaying interactions of small binding energy might in some cases be stronger than slowly decaying interactions of large binding energy.

The relevant bond-breaking process for self-assembled structures is usually thermal excitation, which is a statistical process. Here it makes sense to analyze the stability of the bond, i.e., its average life time, which is the inverse of the dissociation rate. Whether a bond is considered stable depends on the binding strength but also on the temperature of the system and the time of observation. As simple model to describe thermally excited bond breaking, often an Arrhenius law is employed as described in the next chapter (9.1).

Classical electrostatic forces can be used to describe all intermolecular and molecule-substrate interactions that are relevant here once the electron density distribution in thermodynamic equilibrium is known [24]. The Coulomb force between charges is the physical origin of interactions such as hydrogen, halogen, pnicogen and carbon bonds, π–π bonds, metal coordination bonds, van-der-Waals and other electrostatic interactions[2] between monopoles, dipoles, quadrupoles and so on (see Table 9.1). The desire to classify electrostatic interactions into these somewhat ambiguous categories bears the risk to count the same force twice, but it allows grouping interactions regarding their directionality and selectivity [25]. The directionality of an interaction determines the geometry of the resulting assembly, while the selectivity decides how compatible accessible binding partners are. Especially hydrogen bonding motifs have been explored extensively, benefiting from the selectivity and strong directionality of this interaction. A clever design of the molecules allows for encoding the desired supramolecular structure in the molecular building blocks, explaining the tremendous success of supramolecular chemistry in the last decades [26, 27].

Molecular self-assembly has also been explored for creating functional molecular structures on surfaces. Upon deposition of molecules onto a surface, a new dimension is obtained for controlling the final structure of the molecular self-assembly process by the molecule-surface interaction. Tailoring the ratio between intermolecular and the molecule-surface interactions allows for tremendously enlarging the structural variety of the resulting patterns [7–11]. On metals, structures ranging from two-dimensional molecular films [28, 29] over one-dimensional wire-like structures [30–32] to complex patterns such as porous networks [33–35], bi-molecular assemblies [36, 37] or host-guest systems [38, 39] have been created (see Fig. 9.1).

A further interesting design principle is involving adsorbate-induced surface modifications such as surface restructuring. This has been employed for creating, e.g., uni-directional structures on an Au(110)-(1 × 2) surface [31], driven by lifting the (1 × 2) missing-row reconstruction. Further examples include structuring by charge density waves [40] and other substrate-mediated interactions [41].

Most single-crystal metal surfaces exhibit a pronounced influence on the self-assembly of organic molecules *via* the molecule-surface interaction. This *templating effect* often originates from two different factors. First, most single-crystal metal

[2]All electrostatic interactions that have been awarded with a proper name are characterized by charge-transfer bonding while "other electrostatic interactions" usually refers to interactions between permanent multipoles like ion-ion interaction. The latter can be either attractive or repulsive and is, therefore, a powerful instrument to develop structural complexity.

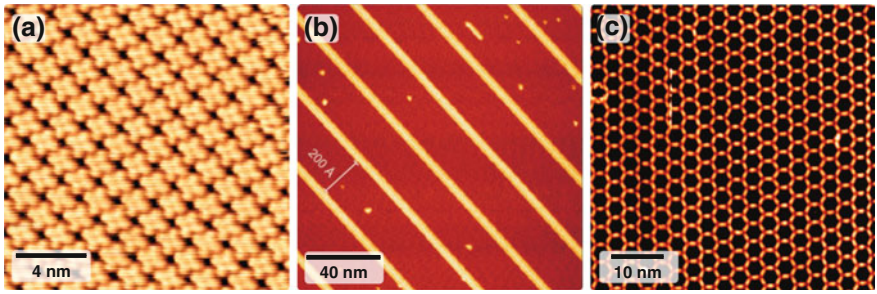

Fig. 9.1 Structural variety of self-assembled patterns ranging from **a** defect free two-dimensional layers (reprinted figure with permission from [28], copyright 2007 by the American Physical Society) to **b** one-dimensional wire-like structures (reprinted with permission from [32], copyright (2007) National Academy of Sciences, U.S.A.), eventually arriving at **c** complex patterns such as porous networks (reprinted with permission from [35], copyright 2007 American Chemical Society)

surfaces exhibit a diffusion barrier, G_{diff}, in the range of several tenth of an eV for a single, isolated molecule [42–44]. This range is favorable for molecular self-assembly at room temperature as outlined below. Second, single-crystal surfaces can provide anisotropic diffusion parallel and perpendicular to the close-packed metal rows, constituting a further option for influencing the final structure [45, 46].

In the following, a simplified picture is considered to provide an estimate for diffusion barriers that allow for molecular self-assembly. Diffusion is a statistical process which can be modelled using an Arrhenius law (9.1). Here, the diffusion rate ν_{diff} at a given temperature T is determined by the diffusion barrier G_{diff} and the attempt frequency ν_0 (k_B is the Boltzmann constant).

$$\nu_{diff} = \nu_0 \exp[-G_{diff}/k_B T] \tag{9.1}$$

In the following, we consider room temperature (T = 300 K) and an attempt frequency[3] [47] of $\nu_0 = 1 \times 10^{12}\,\mathrm{s}^{-1}$.

The diffusion barrier, G_{diff}, must be small enough to allow for diffusion with a reasonable rate. To arrive at a well-ordered self-assembly within a realistic time frame, the diffusion barrier cannot be larger than 0.8 eV. According to (9.1), this barrier corresponds to a diffusion rate of $3.6 \times 10^{-2}\,\mathrm{s}^{-1}$ and each molecule performs on average 1000 hops within 8 h. If the diffusion barrier is larger than that value, the molecules are practically immobile at room temperature (Fig. 9.2a), inhibiting the formation of a self-assembled structure. Thus, the value of 0.8 eV can be regarded

[3] For drawing a qualitative picture, we use a fixed attempt frequency of $\nu_0 = 1 \times 10^{12}\,\mathrm{s}^{-1}$. This value is motivated by the estimate of the phonon frequency of $k_B T/h = 6 \times 10^{12}\,\mathrm{s}^{-1}$. When aiming for quantitative statements for a specific molecule-substrate system, the correct values for the attempt frequency and the diffusion barrier must be considered since both parameters are equally important. For molecules at submonolayer coverage, attempt frequencies in the range of approximately $10^{10}\,\mathrm{s}^{-1}$ to $10^{14}\,\mathrm{s}^{-1}$ have been observed experimentally.

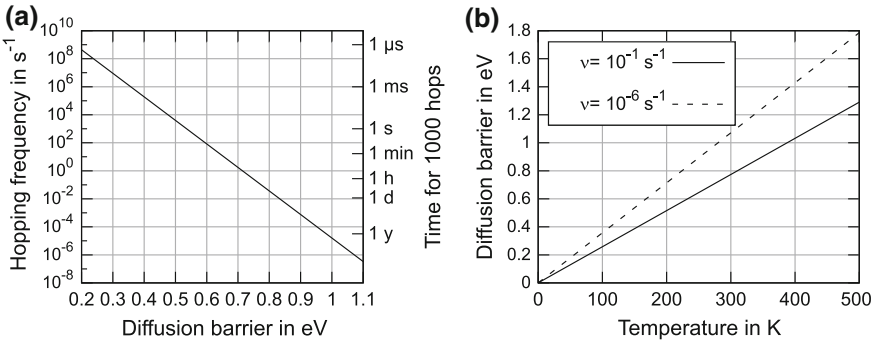

Fig. 9.2 **a** Hopping frequency (diffusion rate) as a function of diffusion barrier (at $T = 300$ K) and corresponding time required for a single molecule to perform on average 1000 hops. **b** Diffusion barriers typically accessible in AFM experiments as a function of temperature assuming a maximum observable hopping frequency of $0.1\,\mathrm{s}^{-1}$ (corresponding to 95 % of the molecules move within 30 s) and a minimum hopping frequency of $1 \times 10^{-6}\,\mathrm{s}^{-1}$ (corresponding to 10 % of the molecules move within 1 day) and $\nu_0 = 1 \times 10^{12}\,\mathrm{s}^{-1}$

as an upper bound for the diffusion barrier. (We refer to Fig. 9.2b for experimentally accessible diffusion barriers.)

At the same time, it is favorable to have a high diffusion barrier to ensure the surface having a templating effect on the final arrangement of the molecular ensemble. The mobility increases with lowering the diffusion barrier as shown in Fig. 9.2a. However, if the diffusion barrier gets too low—a situation often encountered for molecules on prototypical insulating surfaces—the molecules diffuse rapidly on the surface with little control of the surface over the resulting molecular structure. In such a situation, the structure formation is governed entirely by the intermolecular interactions, typically resulting in the same molecular structure regardless of the specific surface, namely the molecular bulk crystal [48]. Therefore, the diffusion barrier needs to be large enough to provide an influence of the substrate on the final structural arrangement. A simple estimate for a lower bound of the diffusion barrier will be obtained at the end of the following discussion.

The diffusion barrier is only one of the energies relevant for the self-assembly process. Self-assembly usually involves the deposition of the molecules from the gas phase as well as a transition from freely diffusing molecules to molecules arrested in an ordered phase. Thus, the change in entropy cannot be neglected. This is why the Gibbs free energy, G, has to be considered as the relevant quantity. The general free energy diagram is shown in Fig. 9.3.

Obviously, the molecules must not desorb from the surface. Thus, the binding energy of a single molecule to the surface, referred to as G_{MS} has to be large enough to ensure that the molecules remain on the surface for a sufficiently long time. In analogy to the above made estimate for the diffusion barrier, we can provide an estimate for the binding energy by regarding a molecule to be stable on the surface

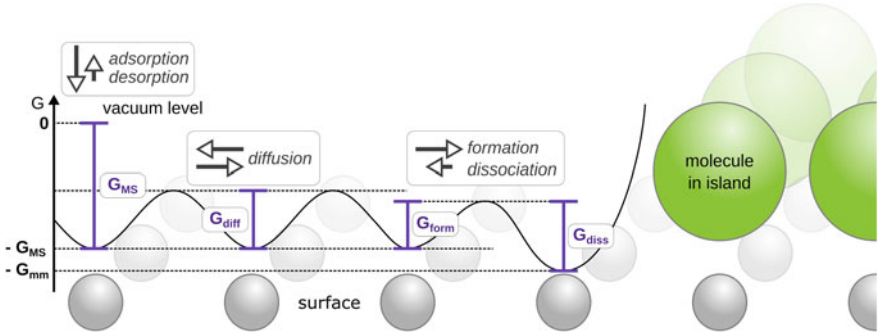

Fig. 9.3 Gibbs free energy for a molecule adsorbing from the gas phase. Note that favorite adsorption sites are arbitrarily chosen to be on *top* of the surface atoms. After adsorption, the molecule can diffuse on the surface until it reaches a spot next to another molecule on the surface (other possible nucleation sites are neglected in this simplified picture). The change in free energy when two molecules (from the gas phase) bind towards each other on the surface, G_{mm}, also includes the effect of the surface. Only in the (very unrealistic) case of a molecular geometry that is unperturbed by the presence of the surface, G_{mm} can be obtained from the superposition of the interaction of the molecules in the gas phase, G_{MM}, and the contribution of the surface G_{MS}

if less than one out of 100 molecules desorbs within a time span of 1 year. This corresponds to a lower bound for the binding energy of 1.3 eV at 300 K.[4]

The individual molecules diffuse on the surface and form islands, which are held together due to intermolecular interactions. In a very simple picture, we neglect the influence of the surface on the intermolecular interaction, i.e., we consider the interaction of two molecules on the surface, G_{mm}, to be the same as in the gas phase, referred to as G_{MM}.

In equilibrium at a given temperature, only a certain fraction of molecules is in the thermodynamic minimum, i.e., forming the desired (thermodynamically most favorable) structure. The other molecules are diffusing on the surface or form unwanted (thermodynamically less favorable) structures. The life time (inverse of the dissociation rate) for a single molecule to remain incorporated into the desired structure needs to be compatible with the desired time scale for the structure to remain unchanged (e.g., the time required for experimental observation or the time of usage in an application). For applications such as self-assembled molecular electronic devices, the inevitable high life time requires a relatively high dissociation barrier, G_{diss} (similar to G_{MS}).

The dissociation barrier of unwanted or kinetically trapped non-equilibrium structures, however, must be overcome within reasonable times, i.e., it cannot be much larger than G_{diff}. For example, a maximum dissociation barrier of 0.9 eV for unwanted structures corresponds to the dissociation of 50 % of the bonds within 15 min.

[4] Alternatively, a cooperative effect can be envisioned. If impinging molecules stay sufficiently long on the surface to meet and form clusters with other molecules before desorption, the assembled molecules can stabilize themselves. This can allow for self-assembly even in a situation where individual molecules would desorb from the surface.

To ensure a structural variety from a subtle balance between intermolecular and molecule-surface interactions, the dissociation barrier needs to be composed of both, G_{MM} and G_{diff} with considerable influence of both components. Assuming a typical pairwise intermolecular attraction adds a value of 0.3 eV to the binding energy of each molecule (and thereby to the dissociation barrier) and further assuming a molecule to be bound to two other molecules, we arrive at a lower bound for the diffusion barrier of 0.7 eV in order to reach a dissociation barrier of 1.3 eV as required for applications like molecular electronics.

From this very simple estimate, we can readily understand why diffusion barriers favoring applicable molecular self-assembly at room temperature are typically in a very narrow energy range (in our estimation 0.7–0.8 eV).

The above estimation contains many simplifications. In the presence of a surface, the intermolecular interaction will be altered due to geometric constraints as well as changes in the electronic structure due to adsorption. Thus, we have to exchange the intermolecular interaction in gas phase by the interaction of two molecules adsorbed onto the surface, G_{mm}. There might be a barrier for the formation of an island, G_{form}, with a corresponding rate, ν_{form}. The latter should be high (corresponding to a small barrier) for self-assembly. Additionally, the dissociation barrier, G_{diss}, might not be obtained by a simple addition of the intermolecular interaction energy, G_{mm}, and the diffusion barrier, G_{diff}.

From the above discussion, a condition for the involved rates can be obtained.

$$\nu_{des} \approx \nu_{diss} \ll \nu_{diff} < \nu_{form} \tag{9.2}$$

According to (9.1), the following relation can be deduced for the energies:

$$G_{MS} \approx G_{diss} > G_{diff} > G_{form} \tag{9.3}$$

It is important to note that, although the rates span a wide range, the relevant barriers are in a very narrow energy range. Thus, molecule-surface and molecule-molecule interactions need to be tuned very precisely with an accuracy typically better than 0.1 eV.

With this discussion, it can be readily understood that metastable structures can form that are favorable kinetically, but unfavorable thermodynamically (see Fig. 9.4). In such a situation, a small (or no) barrier, G_1, exist for the formation of a thermodynamically unstable structure (phase 1), while the formation of the thermodynamically favored structure (phase 2) is hindered by a large activation barrier, G_2. Depending on the barrier height G_2, annealing or simply waiting will drive the system into the thermodynamically favored phase 2. Such a transformation has been observed, e.g., for the deprotonation of 2,5-dihydroxybenzoic acid on calcite(104) [49].

Besides the situation sketched in Fig. 9.4, different structures at different temperatures can also occur because the thermodynamic minimum can change upon temperature due to entropic effects. This situation can be differentiated from the upper mentioned case of a kinetically hindered structure by cycling the temperature [50]. If the thermodynamic minimum changes with temperature, different phases form

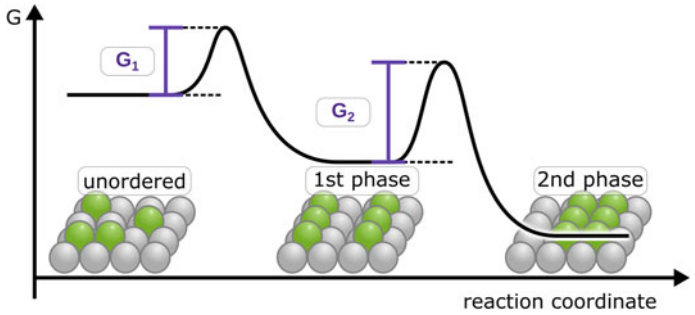

Fig. 9.4 Situation resulting in a metastable structure that transforms with time (or upon annealing) into the thermodynamically favored structure

repeatedly. This is different for a kinetically hindered structure, where the system will remain in the energetically favorable structure independent of the temperature once this structure is reached.

Another aspect that needs to be considered is the coverage dependence of molecular self-assembly. It is known that low-density phases can be favored at low coverages, while increasing coverage can result in high-density phases prior to the formation of a second layer [51]. Often higher densities are accompanied by different adsorption positions and, thereby, a change in the molecule-substrate interaction. On the other hand, the molecule-molecule interaction may increase, since entropy effects such as the preference of mobility over island formation do no longer prevail. Therefore, phase diagrams depending on both temperature and coverage are found in literature [6].

In addition, a general trend exists for the island size depending on temperature, i.e., at low temperatures the rate for diffusion and island dissociation is smaller according to (9.1) and, therefore, the molecules cluster into smaller islands. This also implies that the existence of many small molecule islands indicates a high diffusion and dissociation barrier, while large islands indicate the opposite. In fact, the diffusion barrier can be determined by measuring the size [52] or the density [53] of the islands at different temperatures.

Furthermore, the energy barrier for island formation is usually not independent of the island size. It needs to be considered that nucleation requires higher energies and is less likely than the subsequent island growth. This is why step edges, surface defects or even intentionally added adsorbates [54] can reduce the nucleation barrier and, thus, are often observed as starting point for island growth.

Finally, it should be noted that this very simple discussion does not include specific aspects, such as anisotropic diffusion, details of intermolecular interaction or temperature-dependent attempt frequencies. However, the above discussion readily shows that molecular self-assembly surely requires matching an appropriate balance between the involved energies. Adjusting the involved interactions can be challenging as changing, e.g., the intermolecular interaction by adding specific groups will almost

always simultaneously influence the molecule-surface interaction and vice versa. An interesting strategy to facilitate tuning of the involved energies is, therefore, designing molecules that allow for largely separating intermolecular and molecule-surface interactions as will be discussed in Sect. 9.3.2.

9.2.2 Special Situation on Insulator Surfaces

In contrast to many single-crystal metal surfaces, a favorable balance between the involved interactions is more difficult to achieve for most insulating surfaces investigated so far. Prominent insulating support materials for molecular assemblies are stable cleavage planes of alkali halides [48, 54–81], such as KBr(001), NaCl(001), KCl(001) or RbCl(001), the (111) cleavage plane of the fluoride CaF_2 [53, 82–85], oxide surfaces such as MgO(001) or Al_2O_3(001) [55] as well as diamond and mica [86] surfaces. Recently, the calcite(104) surface [49, 87–98] has gained increasing attention for reasons discussed later.

In particular, the diffusion barrier of many organic molecules on these prototypical insulating surfaces has been found to be very low compared to metallic surfaces. This is illustrated by comparing the diffusion barrier of C_{60} on a metallic and an insulating surface. On a Pd(110) surface, the diffusion barrier is a factor of 7 larger ($\approx$1.4 eV [43]) than on CaF_2(111) ($\approx$0.2 eV [53]). As a consequence, the self-assembled growth is subjected to significantly different energy barriers, commonly leading to significant higher desorption and diffusion rates on CaF_2(111) as compared to metals surfaces. Early work investigating the structure formation of "classical" molecular building blocks, namely prophyrin and perylenetetracarboxylic dianhydride (PTCDA), on KBr(001) and Al_2O_3(0001) surfaces reflects this discussion. High molecular mobility at room temperature and clustering at step edges is a common observation in this study [55]. In another pivotal work, the molecular structure of PTDCA clusters at KBr(001) step edges has been resolved, disclosing the molecular bulk crystal [48]. This finding readily illustrates the absence of substrate templating in this system (see Fig. 9.5a, b). Even molecules with larger dipoles can exhibit low diffusion barriers as highlighted by syn-5,10,15-tris(4-cyanophenylmethyl)truxene on KBr(001) [70] diffusing rapidly at [10] step edges and only anchoring at kink sites (Fig. 9.5c).

Consequently, the weak molecule-substrate interaction found for many prototypical insulating surfaces has severely hampered the formation of self-assembled molecular structures on insulating surfaces at room temperature. However, the weak molecule-surface interaction can at the same time give rise to qualitatively new structures as it allows access to different energetic relations. We illustrate this point by the formation of complex island morphologies upon C_{60} deposition on an insulating substrate, shown in Fig. 9.6. Qualitatively similar islands are obtained regardless whether KBr(001) [57] or CaF_2(111) [83] are used, illustrating the generic character of the formation process on weakly interacting insulator surfaces. The unusual

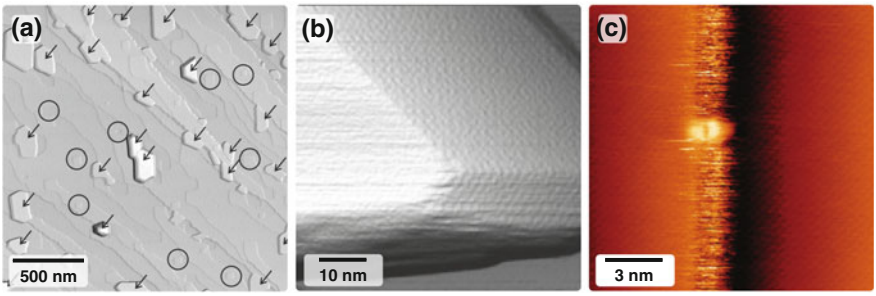

Fig. 9.5 Molecular structures on insulating surfaces, illustrating the high molecular mobility. PTCDA on KBr(001) forms clusters shown in **a** and **b** (reprinted with permission from [48], copyright 2005 by the American Physical Society), while syn-5,10,15-tris(4-cyanophenylmethyl)truxene anchors only at kink sites (bright protrusion at the center of the image) and diffuses rapidly at [010] step edges (reprinted with permission from [70], copyright 2007 American Chemical Society)

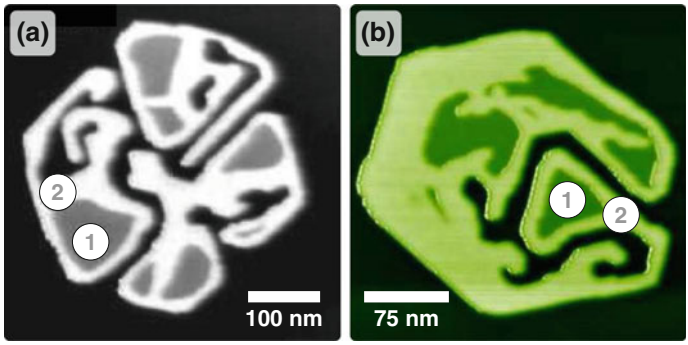

Fig. 9.6 Complex island morphologies with unusual shape obtained upon C_{60} deposition on two different insulating surfaces, namely **a** KBr(001) (reprinted with permission from [57], copyright 2005 by the American Physical Society) and **b** $CaF_2(111)$ (adapted from [83]). The regions marked with 1 are one C_{60} layer high, the regions marked with 2 are twice as high

island shapes have been explained by a process referred to as "facilitated dewetting", which originates from the weak molecule-surface interaction [83]. A specific order of intermolecular interaction strength as well as diffusion and dewetting barrier is required to obtain these islands with the characteristic branched shape, which are absent on metallic surfaces. First when annealing the system to temperatures above room temperature, compact, triangular shaped islands are formed that resemble the *fcc* crystal structure of C_{60}. The unusual islands can, thus, be identified as a transient non-equilibrium structure, which sets them apart from thermodynamically stable, self-assembled structures. Interestingly, the energetic requirements are not met on metallic surfaces, explaining the absence of these morphologies on these supports.

9.3 Studied Systems—State of the Art

In the following, an overview is given over strategies that have been followed for obtaining self-assembled structures on insulating surfaces that are stable at room temperature. While the interaction of individual molecules with the substrate is discussed in the context of increasing the molecule-surface binding, the focus of this chapter is on the concerted structure formation of many molecules on the surface rather than on single-molecule studies (the latter are discussed in other chapters of this book). Likewise, low-temperature studies are omitted in this chapter in favor of investigations that have been carried out at room temperature.

9.3.1 Strategies for Anchoring

To benefit from the general design principles, it does not only appear necessary to tune the molecule-insulator interaction in a well-controlled manner, but also to consider the fundamentally different chemistry between organic molecules and insulators compared to the conclusions drawn for molecule-metal systems.

As a consequence, several strategies have been explored for increasing the molecule-surface interaction for molecular self-assembly on insulating surfaces [95]. Insulators, however, span a wide range from ionic crystals such as KBr or NaCl to covalently bonded crystals such as diamond or TiO_2 to van-der-Waals bonded molecular solids. Insulating materials can even be formed by several different binding motifs, such as a combination of covalent and ionic interactions in calcite, the most stable modification of calcium carbonate. Thus, general anchoring principles are difficult to obtain for such a heterogeneous class of materials, especially when compared to metallic systems, making this task rather challenging for insulating surfaces.

The surface energy can be considered as a macroscopic parameter for obtaining an estimate for the molecule-surface interaction [95]. Surface energies for prototypical metal substrates (ranging from 1000 to 2000 mJ/m^2) are significantly larger than for insulating surfaces (in the order of 100–600 mJ/m^2), readily revealing the inertness of most insulating surfaces studied so far. Especially, this parameter is closely linked to the abovementioned dewetting process. Using the C_{60} molecule as an example, films adsorbed on low surface-energy surfaces have been observed to perform a transition to multilayered and eventually bulk-like structures, while metallic surfaces with large surface energies have been found to confine the molecular film to the first layer [99]. Naturally, this consideration does not include the detailed binding geometry at the molecular level, but it reflects the repeatedly reported weak molecule-surface interaction. Thus, although being a macroscopic parameter, considering the surface energy might serve as a first estimate when searching for an appropriate system for molecular self-assembly.

Conceptually, three aspects emerge when aiming for increasing the molecule-surface interaction as summarized in Fig. 9.7.

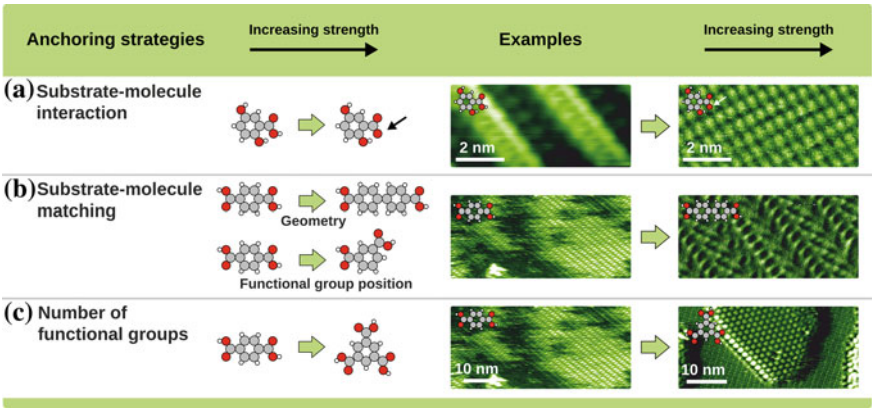

Fig. 9.7 Three different strategies for enhancing the anchoring of organic molecules towards a given surface, namely the calcite(104) surface. Adapted from [95]

The interaction of an individual molecule with the surface might be increased by adding appropriate functional groups such as polar endgroups for electrostatic anchoring or functional moieties that offer special binding options such as carboxylic acid groups for hydrogen bonding (see Fig. 9.7a). Moreover, for substrate templating the structure of the molecule needs to be optimized with respect to the binding sites on the surface, thus, also the molecule-substrate matching needs to be considered (see Fig. 9.7b). Finally, also the number of the available binding sites is of importance (Fig. 9.7c). Although separated conceptually, the three aspects are interlinked and have mutual interdependencies. To give one example, an additive effect is only achieved when the substrate matching is maintained. The mere addition of functional groups can even result in an adverse effect, requiring an additional adjustment of the substrate matching.

9.3.1.1 Increasing the Molecule-Surface Interaction

A straightforward and repeatedly approached concept for increasing the interaction of molecules with ionic crystal surfaces is using molecules bearing a high dipole moment, employing polar electrostatic interactions.

This strategy has successfully been applied for identifying a molecule suitable for molecular self-assembly on $CaF_2(111)$ [82], namely cytosine. This molecule provides a high dipole moment with the local charges being separated by a distance that corresponds to the distance of a pair of oppositely charged ions in the surface. Consequently, a comparatively high diffusion barrier of approximately 0.5 eV has been estimated for cytosine on $CaF_2(111)$ from density functional theory. This value is, however, still too small to provide significant influence of the surface. Interestingly, in combination with the ability of the molecules to form intermolecular hydrogen

bonds, trimers that are stable at room temperature have been identified. As apparent from the experiments, these trimers experience a significantly increased diffusion barrier, which is in this case approximately three times as high as the diffusion barrier of the individual molecules, as the three-fold symmetry of the substrate allows for maintaining the optimum adsorption position even when assembled in the rather rigid trimer structure. This example readily illustrates a cooperative effect in anchoring organic molecules onto surfaces, which involves the molecule-surface and intermolecular interactions as well as the mutual impact of two interactions on each other. The latter aspect is difficult to estimate a priori, but can have significant influence on the resulting force balance.

Another interesting study involving four different helicene derivatives with one or two bromo or cyano groups on the Suzuki(001) surface [81] readily displays the complexity of anchoring molecules to an ionic surface. While the dibromo derivative is expected to bind stronger to the surface than the monobromo derivative, the opposite is observed experimentally. The dibromo molecule desorbs from the surface within few hours after deposition, while the monobromo derivative remains on the surface. This is explained by charge mismatch, since the Br–Br distance in the molecule does not fit to the Na–Na distance on the surface. Additionally, the dibromo molecules bind vertically to the surface. Although a decrease of the desorption barrier has been calculated for this vertical geometry, the molecule-molecule interaction is in turn increased as this geometry allows the dibromo molecules to self-assemble via intermolecular π–π stacking. Also the cyano derivatives adsorb in a vertical position. In this case, the dicyano molecule binds stronger than the monocyano, since the charge distances match to the corresponding distances on the surface. However, the vertical adsorption geometry of the molecules still lowers the desorption barrier compared to a horizontal adsorption geometry. Consequently, desorption is observed after a few weeks. In conclusion, the molecule with the weakest dipole (monobromo) is paradoxically the one with the largest desorption barrier.

This example readily demonstrates that a simple model estimating desorption barrier by counting the anchor groups and taking into account their dipole moments can be wrong as even minute effects can severely alter the expected binding.

The interaction is expected to significantly increase in strength if not only polar molecules are present, but if molecular ions are employed [73, 96]. An example that is ascribed to this anchoring mechanism is 4-iodobenzoic acid on the (104) cleavage plane of calcite [96], as shown in Fig. 9.8. Upon deposition, the molecules are expected to be protonated and, thus, overall charge neutral with only little interaction with the surface. NC-AFM data have revealed a rapid molecular diffusion on the surface, i.e., no islands are found except for situations in which molecules are trapped in a confined geometry. This situation is changed drastically when the sample is annealed. After this annealing step, an extended wetting layer has been observed. The internal structure of this wetting layer can be understood when considering the molecules to be deprotonated. In the deprotonated state, the molecules are expected to stand upright as this allows for increasing the molecule-surface interaction significantly by electrostatic anchoring of the negatively charged carboxylate groups with

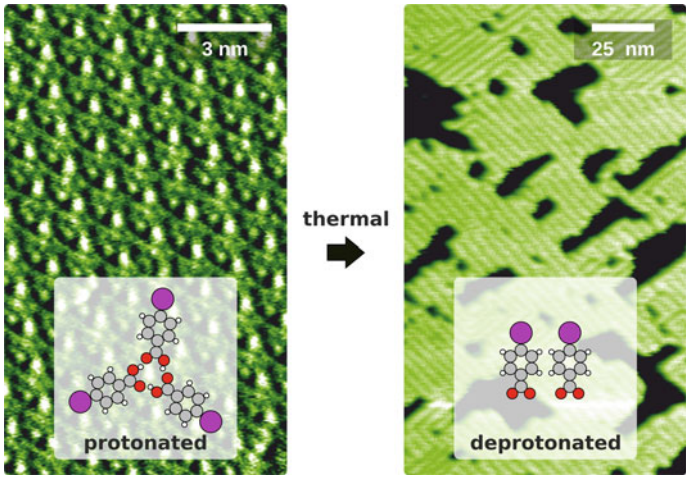

Fig. 9.8 Activation of substrate templating ascribed to deprotonation. 4-iodobenzoic acid on calcite(104) transforms to an upright-standing geometry with an additional increased anchoring that is ascribed to deprotonation. Adapted from [96]

the surface calcium cations. The upright position also allows for the formation of intermolecular π–π bonds, further stabilizing this arrangement.

Apart from anchoring based on electrostatics, more specific binding motifs can be used. A prominent example is hydrogen bonding between the molecular layer and the substrate, e.g., when depositing carboxylic acid or hydroxyl groups onto a surface that provides sites for hydrogen bond formation. This situation has been reported for carboxylic acids on calcite. In this molecule-surface system, hydrogen bonds can be formed between the hydrogen atom of the molecular carboxylic acid group and the oxygen atom of the surface carbonate group. Interestingly, the adsorption of biphenyl-4,4'-dicarboxylic acid (BPDCA) on calcite(104) results in the coexistence of two different structures [90]. One of which closely resembles the molecular bulk structure with a head-to-tail arrangement of the molecules, forming hydrogen-bonded molecular chains on the surface (see Fig. 9.9a(1)). The fact that a bulk-like structure is formed indicates the marginal influence of the underlying substrate on this pattern. Besides the bulk-like structure, however, a clearly substrate-templated assembly is revealed with the molecules arranged in a side-to-side fashion (Fig. 9.9a(2)). This latter structure can be understood by anchoring of the molecules towards the surface with the carboxylic acid groups possibly forming hydrogen bonds with the surface carbonate groups. The coexistence of both structures at room temperature clearly indicates that the two structures are energetically very close, i.e., the system constitutes an example showing the transition from molecular bulk crystal formation towards increasing substrate templating.

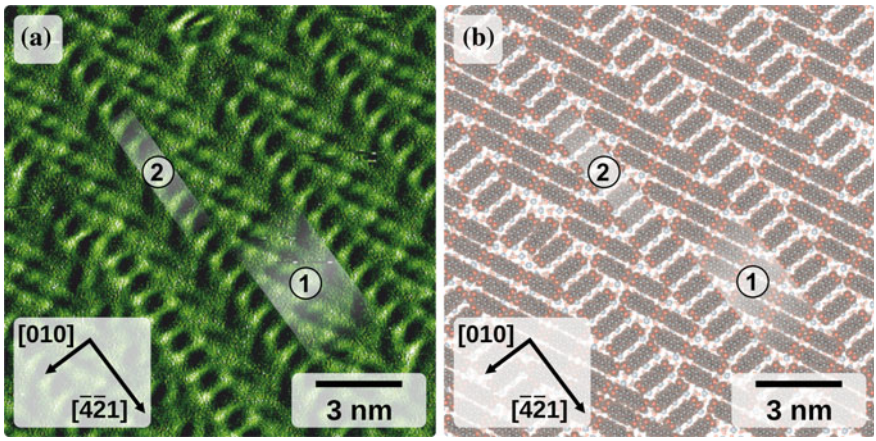

Fig. 9.9 Coexistence of a bulk-like structure (1) and a substrate-templated structure (2) of BPDCA on calcite(104). AFM image (**a**) with structural model (**b**). Adapted from [90]

The molecule-surface interaction motifs described so far are of rather unspecific electrostatic nature (ionic and polar molecules on ionic substrates) or include an uncertain contribution of hydrogen bonding. For a rational design of complex self-assembled structures on insulators it will be mandatory to explore and utilize the bonds of high directionality and selectivity enlisted in Table 9.1 to a higher degree in future work.

9.3.1.2 Optimizing the Molecule-Surface Matching

Besides the detailed nature of the molecule-surface interaction, obviously the geometric matching of the molecular structure to the substrate needs to be considered. This can be readily seen by comparing the structures formed by terephthalic acid (TPA) and BPDCA [90] on calcite(104). While the latter molecule forms both, a substrate-templated structure and a bulk-like structure as shown in Fig. 9.9, the only motif found for the TPA molecule is basically molecular chain formation following the bulk arrangement. Introducing a further benzene ring as in BPDCA is expected to cause a different binding situation to the substrate while leaving the molecule-molecule interaction in the chain arrangement rather similar. With a different separation between the functional groups, the molecule can now attain an adsorption position in which both carboxylic acid groups can form hydrogen bonds towards the surface carbonate groups. The single-molecule adsorption geometry in the substrate-templated structure (denoted 2 in Fig. 9.9) is understood to allow for a stronger molecule-surface bond compared to the situation in the bulk-like assembly (denoted 1 in Fig. 9.9).

The importance of molecule-surface matching has also been shown by the comparison of anchor groups for the already mentioned helicene derivatives [81]. While the distance between two cyano groups fits to the substrate, the dibromo derivative has a shorter distance between the anchor groups, which reduces the binding energy noticeably.

9.3.1.3 Increasing the Number of Functional Groups

A straightforward strategy to increase the molecule-surface interaction is increasing the number of functional groups available for interaction with the surface. Using the calcite(104) surface as the supporting substrate, this strategy has been followed by changing the number of carboxylic acid groups from two as in TPA to three as in trimesic acid (TMA) [49]. In this example, the addition of a third carboxylic acid group has changed both, the intermolecular as well as the molecule-surface interaction, which is illustrated in the very different structures observed for TMA.

However, as mentioned above, the effects of the functional groups are generally noncumulative, as a cross-dependence with the surface matching needs to be considered. When positioned above a different surface site, the additional functional group might not bind similarly strong towards the surface as the first one. In fact, even a repulsive interaction can be envisioned, resulting in an adverse effect. We note that the flexibility of the functional groups can have a second cross-effect on the effective molecular diffusion barrier; the effective diffusion barrier is not necessarily the sum of its constituents [100].

9.3.2 Decoupling Molecule-Surface and Intermolecular Interactions

For controlling the structure formation upon self-assembly, decoupling the intermolecular from the molecule-surface interaction is desired for tuning the involved interaction energies. This is not an easy task as changing the intermolecular interaction does generally also affect the molecule-surface interaction. Therefore, it is of utmost relevance to identify and design molecular building blocks that allow for decoupling the intermolecular from the molecule-surface interaction to a large extent. In the first place, this is a synthesis task, making use of the impressive flexibility and variability of organic chemistry.

As an example, a molecular class with a rather similar binding towards calcite(104) is considered, namely oligo(*p*-benzamide) molecules [93]. These molecules feature two iodine atoms with a distance of approximately 1.35 nm (see Fig. 9.10a). Being electronegative, these two iodine atoms are expected to be electrostatically attracted to the surface calcium cations. Thus, an effective anchor is provided that results in well-defined adsorption positions of the molecules on the surface. The intermolecular

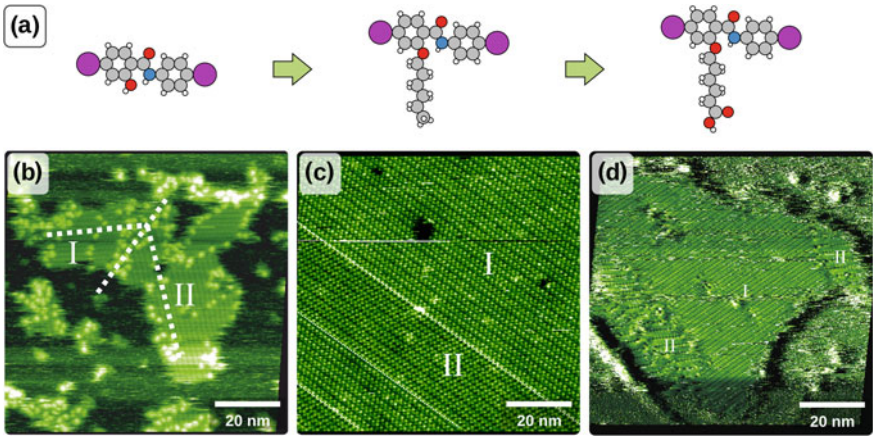

Fig. 9.10 Oligo(*p*-benzamide) molecules on calcite(104) as an example for similar molecule-surface interaction while varying the molecule-molecule interaction [93]

interaction, on the other hand, can be controlled by side groups that are varied in a systematic manner. Interestingly, distinctly different molecular structures can be obtained that are governed by the respective side groups, as shown in Fig. 9.10b–d. Consequently, a variation in molecular structures can be achieved by designing the respective side groups, despite the identical adsorption mechanism. This example, thus, illustrates the successful decoupling of the molecule-surface interaction from the intermolecular interaction.

9.4 Outlook

Despite being a comparatively young research field, molecular self-assembly on insulating surfaces has developed tremendously during the last decade. This is partly due to the impressive improvements of the main experimental tool, namely non-contact atomic force microscopy. On the other hand, the library of functional organic molecules is increasing steadily, providing a plethora of options for novel structural motifs.

Extensive effort has been made to gain precise control over the resulting structure. This control includes the control of structural parameters such as molecular orientation, symmetry and island sizes, to name but a few. Eventually, these efforts aim for converting the structural control into application-oriented functionality. Structures relevant for application will require sufficient stability in a given temperature window as well as dedicated properties that include, e.g., switchability and stimuli-responsive effects. These future demands will push forward the development of steadily increasing structural control, providing the route towards more advanced and complex structures.

Promising strategies to be followed in future will include a concerted action of both synthesis efforts and a clever design of the system and the deposition protocol. A key synthesis task is providing building blocks that offer a high degree of flexibility while at the same time allowing for a well-defined decoupling of intermolecular and molecule-surface interactions. On the surface science experimental side, increasing complexity by codeposition and exploring the potential of various deposition protocols will enhance structural variability. An important aspect of this development includes a precise characterization and quantification of the involved energies and barriers.

Finally, a major challenge of future efforts is transferring the gained knowledge to the liquid/solid interface, which will be of tremendous relevance for applications. A key question to be answered here concerns the role of the solvent in molecular self-assembly at the solid/liquid interface.

References

1. G.M. Whitesides, B. Grzybowski, Self-assembly at all scales. Science **295**(5564), 2418–2421 (2002). doi:10.1126/science.1070821
2. S. Chiang, Scanning tunneling microscopy imaging of small adsorbed molecules on metal surfaces in an ultrahigh vacuum environment. Chem. Rev. **97**(4), 1083–1096 (1997). doi:10.1021/cr940555a
3. S. De Feyter, F.C. De Schryver, Two-dimensional supramolecular self-assembly probed by scanning tunneling microscopy. Chem. Soc. Rev. **32**(3), 139–150 (2003). doi:10.1039/b206566p
4. N.K. Chaki, K. Vijayamohanan, Self-assembled monolayers as a tunable platform for biosensor applications. Biosens. Bioelectron. **17**(1–2), 1–12 (2002). doi:10.1016/S0956-5663(01)00277-9
5. J.C. Love, L.A. Estroff, J.K. Kriebel, R.G. Nuzzo, G.M. Whitesides, Self-assembled monolayers of thiolates on metals as a form of nanotechnology. Chem. Rev. **105**, 1103–1169 (2005). doi:10.1021/cr0300789
6. S.M. Barlow, R. Raval, Complex organic molecules at metal surfaces: bonding, organisation and chirality. Surf. Sci. Rep. **50**(6–8), 201–341 (2003). doi:10.1016/s0167-5729(03)00015-3
7. J.V. Barth, Molecular architectonic on metal surfaces. Annu. Rev. Phys. Chem. **58**, 375–407 (2007). doi:10.1146/annurev.physchem.56.092503.141259
8. F. Cicoira, C. Santato, F. Rosei, Two-dimensional nanotemplates as surface cues for the controlled assembly of organic molecules, in *STM and AFM Studies on (Bio)Molecular Systems: Unravelling the Nanoworld*, vol. 285, Topics in Current Chemistry, ed. by P. Samorì (Springer, Berlin, 2008), pp. 203–267
9. A. Kühnle, Self-assembly of organic molecules at metal surfaces. Curr. Opin. Colloid Interface Sci. **14**, 157–168 (2009). doi:10.1016/j.cocis.2008.01.001
10. L. Bartels, Tailoring molecular layers at metal surfaces. Nat. Chem. **2**(2), 87–95 (2010). doi:10.1038/nchem.517
11. R. Otero, J.M. Gallego, A.L.V. de Parga, N. Martín, R. Miranda, Molecular self-assembly at solid surfaces. Adv. Mater. (Deerfield Beach, Fla.) **23**(44), 5148–5176 (2011). doi:10.1002/adma.201102022
12. G. Binnig, H. Rohrer, Scanning tunneling microscopy. Surf. Sci. **126**(1), 236–244 (1983). doi:10.1016/0039-6028(83)90716-1
13. G. Binnig, C.F. Quate, C. Gerber, Atomic force microscope. Phys. Rev. Lett. **56**(9), 930–933 (1986). doi:10.1103/PhysRevLett.56.930

14. T.R. Albrecht, P. Grütter, D. Horne, D. Rugar, Frequency-modulation detection using high-Q cantilevers for enhanced force microscope sensitivity. J. Appl. Phys. **69**(2), 668–673 (1991). doi:10.1063/1.347347
15. G.M. Whitesides, J.P. Mathias, C.T. Seto, Molecular self-assembly and nanochemistry: a chemical strategy for the synthesis of nanostructures. Science **254**(5036), 1312–1319 (1991). doi:10.1126/science.1962191
16. J.-M. Lehn, Toward self-organization and complex matter. Science **295**(5564), 2400–2403 (2002). doi:10.1126/science.1071063
17. J.M. Lehn, Supramolecular chemistry: from molecular information towards self-organization and complex matter. Rep. Progr. Phys. **67**(3), 249–265 (2004). doi:10.1088/0034-4885/67/3/R02
18. G.R. Desiraju, A bond by any other name. Angew. Chem. **50**(1), 52–59 (2011). doi:10.1002/anie.201002960
19. G.R. Desiraju, P.S. Ho, L. Kloo, A.C. Legon, R. Marquardt, P. Metrangolo, P. Politzer, G. Resnati, K. Rissanen, Definition of the halogen bond (IUPAC Recommendations 2013). Pure Appl. Chem. **85**(8), 1711–1713 (2013). doi:10.1351/PAC-REC-12-05-10
20. S. Scheiner, The pnicogen bond: its relation to hydrogen, halogen, and other noncovalent bonds. Acc. Chem. Res. **46**(2), 280–288 (2013). doi:10.1021/ar3001316
21. D. Mani, E. Arunan, The X–C..Y (X=O/F, Y=O/S/F/Cl/Br/N/P) 'carbon bond' and hydrophobic interactions. Phys. Chem. Chem. Phys. **15**(34), 14377–14383 (2013). doi:10.1039/c3cp51658j
22. C.A. Hunter, J.K.M. Sanders, The nature of π–π interactions. J. Am. Chem. Soc. **112**(14), 5525–5534 (1990). doi:10.1021/ja00170a016
23. H.A. Skinner, J.A. Connor, Metal-ligand bond-energies in organometallic compounds. Pure Appl. Chem. **57**(1), 79–88 (1985). doi:10.1351/pac198557010079
24. R.P. Feynman, Forces in molecules. Phys. Rev. **56**, 340–343 (1939). doi:10.1103/PhysRev.56.340
25. J.N. Israelachvili, *Intermolecular and Surface Forces*, 3rd edn. (Academic Press, San Diego, 2011)
26. J.-M. Lehn, Supramolecular chemistry—scope and perspectives molecules, supermolecules, and molecular devices (Nobel Lecture). Angew. Chem. Int. Ed. Engl. **27**(1), 89–112 (1988). doi:10.1002/anie.198800891
27. L.J. Prins, P. Scrimin, Covalent capture: merging covalent and noncovalent synthesis. Angew. Chem. **48**(13), 2288–2306 (2009). doi:10.1002/anie.200803583
28. V. Oison, M. Koudia, M. Abel, L. Porte, Influence of stress on hydrogen-bond formation in a halogenated phthalocyanine network. Phys. Rev. B **75**(3), 035428 (2007). doi:10.1103/PhysRevB.75.035428
29. M. Forster, M.S. Dyer, M. Persson, R. Raval, Assembly of chiral amino-acids at surfaces from a single molecule perspective: proline on Cu(110). Top. Catal. **54**(1–4), 13–19 (2011). doi:10.1007/s11244-011-9634-9
30. M. Böhringer, K. Morgenstern, W.-D. Schneider, R. Berndt, F. Mauri, A.D. Vita, R. Car, Two-dimensional self-assembly of supramolecular clusters and chains. Phys. Rev. Lett. **83**, 324–327 (1999). doi:10.1103/PhysRevLett.83.324
31. A. Kühnle, L.M. Molina, T.R. Linderoth, B. Hammer, F. Besenbacher, Growth of unidirectional molecular rows of cysteine on Au(110)-(1 × 2) driven by adsorbate-induced surface rearrangements. Phys. Rev. Lett. **93**(8), 086101 (2004). doi:10.1103/PhysRevLett.93.086101
32. A. Schiffrin, A. Riemann, W. Auwärter, Y. Pennec, A. Weber-Bargioni, D. Cvetko, A. Cossaro, A. Morgante, J.V. Barth, Zwitterionic self-assembly of L-methionine nanogratings on the Ag(111) surface. PNAS **104**(13), 5279–5284 (2007). doi:10.1073/pnas.0607867104
33. G. Pawin, K.L. Wong, D. Kim, D.Z. Sun, L. Bartels, S. Hong, T.S. Rahman, R. Carp, M. Marsella, A surface coordination network based on substrate-derived metal adatoms with local charge excess. Angew. Chem. Int. Ed. Engl. **47**(44), 8442–8445 (2008). doi:10.1002/anie.200802543

34. P.A. Staniec, L.M.A. Perdigão, A. Saywell, N.R. Champness, P.H. Beton, Hierarchical organisation on a two-dimensional supramolecular network. Phys. Chem. Chem. Phys. **8**, 2177–2181 (2007). doi:10.1002/cphc.200700513
35. U. Schlickum, R. Decker, F. Klappenberger, G. Zoppellaro, S. Klyatskaya, M. Ruben, I. Silanes, A. Arnau, K. Kern, H. Brune, J.V. Barth, Metal-organic honeycomb nanomeshes with tunable cavity size. Nano Lett. **7**(12), 3813–3817 (2007). doi:10.1021/nl072466m
36. L. Scudiero, K.W. Hipps, D.E. Barlow, A self-organized two-dimensional bimolecular structure. J. Phys. Chem. B **107**(13), 2903–2909 (2003). doi:10.1021/Jp026875c
37. Y.L. Huang, W. Chen, H. Li, J. Ma, J. Pflaum, A.T. Wee, Tunable two-dimensional binary molecular networks. Small **6**(1), 70–75 (2010). doi:10.1002/smll.200901291
38. F. Sedona, M. Di Marino, A. Basagni, L. Colazzo, M. Sambi, Structurally tunable self-assembled 2D cocrystals of C_{60} and porphyrins on the Ag (110) surface. J. Phys. Chem. C **118**(3), 1587–1593 (2014). doi:10.1021/jp409367x
39. D. Bonifazi, S. Mohnani, A. Llanes-Pallas, Supramolecular chemistry at interfaces: molecular recognition on nanopatterned porous surfaces. Chem. Eur. J. **15**(29), 7004–7025 (2009). doi:10.1002/chem.200900900
40. S. Lukas, G. Witte, C. Wöll, Novel mechanism for molecular self-assembly on metal substrates: unidirectional rows of pentacene on Cu(110) produced by a substrate-mediated repulsion. Phys. Rev. Lett. **88**(2), 028301 (2002). doi:10.1103/PhysRevLett.88.028301
41. P. Han, P.S. Weiss, Electronic substrate-mediated interactions. Surf. Sci. Rep. **67**(2), 19–81 (2012). doi:10.1016/j.surfrep.2011.11.001
42. J. Weckesser, J.V. Barth, K. Kern, Direct observation of surface diffusion of large organic molecules at metal surfaces: PVBA on Pd(110). J. Chem. Phys. **110**(11), 5351–5354 (1999). doi:10.1063/1.478430
43. J. Weckesser, J.V. Barth, K. Kern, Mobility and bonding transition of C_{60} on Pd(110). Phys. Rev. B **64**(16), 1403 (2001). doi:10.1103/PhysRevB.64.161403
44. F. Buchner, J. Xiao, E. Zillner, M. Chen, M. Röckert, S. Ditze, M. Stark, H.P. Steinrück, J.M. Gottfried, H. Marbach, Diffusion, rotation, and surface chemical bond of individual 2H-tetraphenylporphyrin molecules on Cu(111). J. Phys. Chem. C **115**(49), 24172–24177 (2011). doi:10.1021/Jp206675u
45. J.V. Barth, Transport of adsorbates at metal surfaces: from thermal migration to hot precursors. Surf. Sci. Rep. **40**(3–5), 75–149 (2000). doi:10.1016/S0167-5729(00)00002-9
46. J. Weckesser, J.V. Barth, C. Cai, B. Muller, K. Kern, Binding and ordering of large organic molecules on an anisotropic metal surface: PVBA on Pd(110). Surf. Sci. **431**(1–3), 168–173 (1999). doi:10.1016/S0039-6028(99)00455-0
47. M. Roos, A. Breitruck, H.E. Hoster, R.J. Behm, Entropic stabilization of large adsorbates on weakly binding substrates-a thermal desorption and scanning tunneling microscopy study. Phys. Chem. Chem. Phys. **12**(4), 818–822 (2010). doi:10.1039/B920481D
48. T. Kunstmann, A. Schlarb, M. Fendrich, T. Wagner, R. Möller, R. Hoffmann, Dynamic force microscopy study of 3,4,9,10-perylenetetracarboxylic dianhydride on KBr(001). Phys. Rev. B **71**(12), 121403 (2005). doi:10.1103/PhysRevB.71.121403
49. M. Kittelmann, P. Rahe, M. Nimmrich, C.M. Hauke, A. Gourdon, A. Kühnle, Direct visualization of molecule deprotonation on an insulating surface. ACS Nano **6**(8), 7406–7411 (2012). doi:10.1021/nn3025942
50. R. Gutzler, L. Cardenas, F. Rosei, Kinetics and thermodynamics in surface-confined molecular self-assembly. Chem. Sci. **2**(12), 2290–2300 (2011). doi:10.1039/C1SC00531F
51. Y.C. Ye, W. Sun, Y.F. Wang, X. Shao, X.G. Xu, F. Cheng, J.L. Li, K. Wu, A unified model: self-assembly of trimesic acid on gold. J. Phys. Chem. C **111**(28), 10138–10141 (2007). doi:10.1021/jp072726o
52. H. Brune, G.S. Bales, J. Jacobsen, C. Boragno, K. Kern, Measuring surface diffusion from nucleation island densities. Phys. Rev. B **60**(8), 5991–6006 (1999). doi:10.1103/PhysRevB.60.5991
53. F. Loske, J. Lübbe, J. Schütte, M. Reichling, A. Kühnle, Quantitative description of C_{60} diffusion on an insulating surface. Phys. Rev. B **82**(15), 155428 (2010). doi:10.1103/PhysRevB.82.155428

54. T. Glatzel, L. Zimmerli, S. Koch, S. Kawai, E. Meyer, Molecular assemblies grown between metallic contacts on insulating surfaces. Appl. Phys. Lett. **94**(6), 063303 (2009). doi:10.1063/1.3080614
55. L. Nony, R. Bennewitz, O. Pfeiffer, E. Gnecco, A. Baratoff, E. Meyer, T. Eguchi, A. Gourdon, C. Joachim, Cu-TBPP and PTCDA molecules on insulating surfaces studied by ultra-high-vacuum non-contact AFM. Nanotechnology **15**(2), S91 (2004). doi:10.1088/0957-4484/15/2/019
56. L. Nony, E. Gnecco, A. Baratoff, A. Alkauskas, R. Bennewitz, O. Pfeiffer, S. Maier, A. Wetzel, E. Meyer, C. Gerber, Observation of individual molecules trapped on a nanostructured insulator. Nano Lett. **4**(11), 2185–2189 (2004). doi:10.1021/nl048693v
57. S.A. Burke, J.M. Mativetsky, R. Hoffmann, P. Grütter, Nucleation and submonolayer growth of C_{60} on KBr. Phys. Rev. Lett. **94**(9), 096102 (2005). doi:10.1103/PhysRevLett.94.096102
58. O. Pfeiffer, E. Gnecco, L. Zimmerli, S. Maier, E. Meyer, L. Nony, R. Bennewitz, F. Diederich, H. Fang, D. Bonifazi, Force microscopy on insulators: imaging of organic molecules. J. Phys. Conf. **19**, 166–174 (2005). doi:10.1088/1742-6596/19/1/027
59. J.M. Mativetsky, S.A. Burke, S. Fostner, P. Grutter, Nanoscale pits as templates for building a molecular device. Small **3**(5), 818–821 (2007). doi:10.1002/smll.200600699
60. L. Zimmerli, S. Maier, G. Th, E. Gnecco, O. Pfeiffer, F. Diederich, L. Fendt, E. Meyer, Formation of molecular wires on nanostructured KBr. J. Phys. Conf. **61**(1), 1357 (2007). doi:10.1088/1742-6596/61/1/268
61. S. Maier, L.-A. Fendt, L. Zimmerli, T. Glatzel, O. Pfeiffer, F. Diederich, E. Meyer, Nanoscale engineering of molecular porphyrin wires on insulating surfaces. Small **4**(8), 1115–1118 (2008). doi:10.1002/smll.200701259
62. S.A. Burke, W. Ji, J.M. Mativetsky, J.M. Topple, S. Fostner, H.J. Gao, H. Guo, P. Grütter, Strain induced dewetting of a molecular system: bimodal growth of PTCDA on NaCl. Phys. Rev. Lett. **100**(18), 186104 (2008). doi:10.1103/PhysRevLett.100.186104
63. T. Dienel, C. Loppacher, S.C.B. Mannsfeld, R. Forker, T. Fritz, Growth-mode-induced narrowing of optical spectra of an organic adlayer. Adv. Mater. **20**(5), 959–963 (2008). doi:10.1002/adma.200701684
64. S.A. Burke, J.M. LeDue, Y. Miyahara, J.M. Topple, S. Fostner, P. Grutter, Determination of the local contact potential difference of PTCDA on NaCl: a comparison of techniques. Nanotechnology **20**(26), 264012 (2009). doi:10.1088/0957-4484/20/26/264012
65. S.A. Burke, J.M. Topple, P. Grütter, Molecular dewetting on insulators. J. Phys. Condens. Matter. **21**(42), 423101 (2009). doi:10.1088/0953-8984/21/42/423101
66. S. Fremy, A. Schwarz, K. Lämmle, M. Prosenc, R. Wiesendanger, The monomer-to-dimer transition and bimodal growth of Co-salen on NaCl(001): a high resolution atomic force microscopy study. Nanotechnology **20**(40), 405608 (2009). doi:10.1088/0957-4484/20/40/405608
67. M. Fendrich, M. Lange, C. Weiss, T. Kunstmann, R. Möller, N, N'-dimethylperylene-3,4,9,10-bis(dicarboximide) on alkali halide (001) surfaces. J. Appl. Phys. **105**(9), 094311 (2009). doi:10.1063/1.3122253
68. S. Kawai, S. Maier, T. Glatzel, S. Koch, B. Such, L. Zimmerli, L.A. Fendt, F. Diederich, E. Meyer, Cutting and self-healing molecular wires studied by dynamic force microscopy. Appl. Phys. Lett. **95**(10), 103109 (2009). doi:10.1063/1.3216057
69. R. Pawlak, L. Nony, F. Bocquet, V. Olson, M. Sassi, J.M. Debierre, C. Loppacher, L. Porte, Supramolecular assemblies of 1,4-Benzene diboronic acid on KCl(001). J. Phys. Chem. C **114**(20), 9290–9295 (2010). doi:10.1021/Jp102044u
70. B. Such, T. Trevethan, T. Glatzel, S. Kawai, L. Zimmerli, E. Meyer, A.L. Shluger, C.H.M. Amijs, P. de Mendoza, A.M. Echavarren, Functionalized truxenes: adsorption and diffusion of single molecules on the KBr(001) surface. ACS Nano **4**(6), 3429–3439 (2010). doi:10.1021/Nn100424g
71. T. Glatzel, L. Zimmerli, S. Kawai, E. Meyer, L.-A. Fendt, F. Diederich, Oriented growth of porphyrin-based molecular wires on ionic crystals analysed by nc-AFM. Beilstein J. Nanotech. **2**, 34–39 (2011). doi:10.3762/bjnano.2.4

72. A. Hinaut, K. Lekhal, G. Aivazian, S. Bataillé, A. Gourdon, D. Martrou, S. Gauthier, NC-AFM study of the adsorption of hexamethoxytriphenylene on KBr(001). J. Phys. Chem. C **115**(27), 13338–13342 (2011). doi:10.1021/Jp202873f
73. L. Nony, F. Bocquet, F. Para, F. Chérioux, E. Duverger, F. Palmino, V. Luzet, C. Loppacher, Dipole-driven self-organization of zwitterionic molecules on alkali halide surfaces. Beilstein J. Nanotech. **3**, 285–293 (2012). doi:10.3762/Bjnano.3.32
74. J.M. Topple, S.A. Burke, W. Ji, S. Fostner, A. Tekiel, P. Gruetter, Tailoring the morphology and dewetting of an organic thin film. J. Phys. Chem. C **115**(1), 217–224 (2011). doi:10.1021/jp107644u
75. T. Trevethan, B. Such, T. Glatzel, S. Kawai, A.L. Shluger, E. Meyer, P. de Mendoza, A.M. Echavarren, Organic molecules reconstruct nanostructures on ionic surfaces. Small **7**(9), 1264–1270 (2011). doi:10.1002/smll.201001910
76. C. Barth, M. Gingras, A.S. Foster, A. Gulans, G. Félix, T. Hynninen, R. Peresutti, C.R. Henry, Two-dimensional nanostructured growth of nanoclusters and molecules on insulating surfaces. Adv. Mater. **24**(24), 3228–3232 (2012). doi:10.1002/adma.201200501
77. F. Bocquet, L. Nony, S.C.B. Mannsfeld, V. Oison, R. Pawlak, L. Porte, C. Loppacher, Inhomogeneous relaxation of a molecular layer on an insulator due to compressive stress. Phys. Rev. Lett. **108**(20), 206103–206103 (2012). doi:10.1103/PhysRevLett.108.206103
78. A. Hinaut, A. Pujol, F. Chaumeton, D. Martrou, A. Gourdon, S. Gauthier, An NC-AFM and KPFM study of the adsorption of a triphenylene derivative on KBr(001). Beilstein J. Nanotech. **3**, 221–229 (2012). doi:10.3762/bjnano.3.25
79. J.L. Neff, J. Götzen, E.H. Li, M. Marz, R. Hoffmann-Vogel, Molecular-resolution imaging of pentacene on KCl(001). Beilstein J. Nanotech. **3**, 186–191 (2012). doi:10.3762/Bjnano.3.20
80. R. Pawlak, S. Kawai, S. Fremy, T. Glatzel, E. Meyer, High-resolution imaging of C_{60} molecules using tuning-fork-based non-contact atomic force microscopy. J. Phys. Condens. Matter **24**(8), 084005 (2012). doi:10.1088/0953-8984/24/8/084005
81. B. Hoff, M. Gingras, R. Peresutti, C.R. Henry, A.S. Foster, C. Barth, Mechanisms of the adsorption and self-assembly of molecules with polarized functional groups on insulating surfaces. J. Phys. Chem. C **118**(26), 14569–14578 (2014). doi:10.1021/Jp501738c
82. J. Schütte, R. Bechstein, M. Rohlfing, M. Reichling, A. Kühnle, Cooperative mechanism for anchoring highly polar molecules at an ionic surface. Phys. Rev. B **80**(20), 205421 (2009). doi:10.1103/PhysRevB.80.205421
83. M. Körner, F. Loske, M. Einax, A. Kühnle, M. Reichling, P. Maass, Second-layer induced island morphologies in thin-film growth of fullerenes. Phys. Rev. Lett. **107**(1), 016101 (2011). doi:10.1103/Physrevlett.107.016101
84. F. Loske, M. Reichling, A. Kühnle, Steering molecular island morphology on an insulator surface by exploiting sequential deposition. Chem. Comm. **47**(37), 10386–10388 (2011). doi:10.1039/C1cc12996a
85. F. Loske, M. Reichling, A. Kühnle, Deposition sequence determines morphology of C_{60} and 3,4,9,10-perylenetetracarboxylic diimide islands on CaF_2(111). Jpn. J. Appl. Phys. **50**(8), 08LB07 (2011). doi:10.1143/Jjap.50.08lb07
86. C. Loppacher, U. Zerweck, D. Koehler, M. Rodenstein, E. Jaehne, R. Luther, H.-J. Adler, L.M. Eng, Physical vapour deposition of alkyl phosphonic acid on mica and HOPG investigated by NC-AFM. Nanotechnology **18**(8), 084003 (2007). doi:10.1088/0957-4484/18/8/084003
87. P. Rahe, M. Nimmrich, A. Greuling, J. Schütte, I.G. Stará, J. Rybáček, G. Huerta-Angeles, I. Starý, M. Rohlfing, A. Kühnle, Toward molecular nanowires self-assembled on an insulating substrate: heptahelicene-2-carboxylic acid on calcite (10–14). J. Phys. Chem. C **114**(3), 1547–1552 (2010). doi:10.1021/jp911287p
88. M. Kittelmann, P. Rahe, M. Nimmrich, C.M. Hauke, A. Gourdon, A. Kühnle, On-surface covalent linking of organic building blocks on a bulk insulator. ACS Nano **5**(10), 8420–8425 (2011). doi:10.1021/nn2033192
89. C.M. Hauke, P. Rahe, M. Nimmrich, J. Schütte, M. Kittelmann, I.G. Stara, I. Stary, J. Rybacek, A. Kühnle, Molecular self-assembly of enantiopure heptahelicene-2-carboxylic acid on calcite (1014). J. Phys. Chem. C **116**(7), 4637–4641 (2012). doi:10.1021/Jp2102258

90. M. Kittelmann, P. Rahe, A. Kühnle, Molecular self-assembly on an insulating surface: interplay between substrate templating and intermolecular interactions. J. Phys. Condens. Matter. **24**(35), 354007–354013 (2012). doi:10.1088/0953-8984/24/35/354007
91. P. Rahe, R. Lindner, M. Kittelmann, M. Nimmrich, A. Kühnle, From dewetting to wetting molecular layers: C_{60} on $CaCO_3$(10 14) as a case study. Phys. Chem. Chem. Phys. **14**(18), 6544–6548 (2012). doi:10.1039/C2cp40172j
92. P. Rahe, M. Nimmrich, A. Kühnle, Substrate templating upon self-assembly of hydrogen-bonded molecular networks on an insulating surface. Small **8**(19), 2968–2968 (2012). doi:10.1002/smll.201290103
93. C.M. Hauke, R. Bechstein, M. Kittelmann, C. Storz, A.F. Kilbinger, P. Rahe, A. Kühnle, Controlling molecular self-assembly on an insulating surface by rationally designing an efficient anchor functionality that maintains structural flexibility. ACS Nano **7**(6), 5491–5498 (2013). doi:10.1021/nn401589u
94. M. Kittelmann, M. Nimmrich, R. Lindner, A. Gourdon, A. Kühnle, Sequential and site-specific on-surface synthesis on a bulk insulator. ACS Nano **7**(6), 5614–5620 (2013). doi:10.1021/nn402018w
95. P. Rahe, M. Kittelmann, J.L. Neff, M. Nimmrich, M. Reichling, P. Maass, A. Kühnle, Tuning molecular self-assembly on bulk insulator surfaces by anchoring of the organic building blocks. Adv. Mater. **25**(29), 3948–3956 (2013). doi:10.1002/adma.201300604
96. M. Kittelmann, M. Nimmrich, J.L. Neff, P. Rahe, W. Gren, X. Bouju, A. Gourdon, A. Kühnle, Controlled activation of substrate templating in molecular self-assembly by deprotonation. J. Phys. Chem. C **117**(45), 23868–23874 (2013). doi:10.1021/jp408664n
97. R. Lindner, P. Rahe, M. Kittelmann, A. Gourdon, R. Bechstein, A. Kühnle, Substrate templating guides the photoinduced reaction of C_{60} on calcite. Angew. Chem. Int. Ed. **53**(30), 7952–7955 (2014). doi:10.1002/anie.201309128
98. J.L. Neff, M. Kittelmann, R. Bechstein, A. Kuhnle, Decisive influence of substitution positions in molecular self-assembly. Phys. Chem. Chem. Phys. **16**(29), 15437–15443 (2014). doi:10.1039/C4CP02077D
99. T. David, J.K. Gimzewski, D. Purdie, B. Reihl, R.R. Schlittler, Epitaxial-growth of C_{60} on Ag(110) studied by scanning tunneling microscopy and tunneling spectroscopy. Phys. Rev. B **50**(8), 5810–5813 (1994). doi:10.1103/PhysRevB.50.5810
100. M. Watkins, T. Trevethan, M.L. Sushko, A.L. Shluger, Designing molecular architecture to control diffusion and adsorption on insulating surfaces. J. Phys. Chem. C **112**(11), 4226–4231 (2008). doi:10.1021/jp077680d

Chapter 10
Atomic-Scale Contrast Formation in AFM Images on Molecular Systems

Fabian Schulz, Sampsa Hämäläinen and Peter Liljeroth

Abstract Imaging individual molecules with atomic resolution is now possible using non-contact atomic force microscopy (AFM). In all cases where atomic resolution imaging of molecules was demonstrated, chemically passivated tips were used. This chapter will discuss the factors influencing the atomic scale imaging of molecular systems. We will first discuss the effect of the tip passivation on the atomic scale contrast. Subsequently, we will consider the factors affecting the quantitative details of the apparent atomic positions (background from the neighbouring atoms, flexibility of the tip apex and non-planar samples). Finally, we will discuss how the tip flexibility affects the appearance of the inter- and intramolecular bonds imaged with AFM.

10.1 Introduction

Imaging individual molecules with atomic resolution is now possible using non-contact atomic force microscopy (AFM) in the frequency modulation mode [1]. As discussed in the chapter by Gross and co-workers, such experiments require passivation of the AFM tip apex. In addition to the direct visualization of the molecular structure, AFM has been used to identify different atomic species [2, 3]. Using molecule-terminated tips, it has been shown that the apparent length of chemical bonds in conjugated organic molecules is correlated to the bond order [4] and the intramolecular charge distribution of planar molecules has been mapped [5]. It has even been suggested that intermolecular hydrogen bonding could be imaged using AFM [6]. These new capabilities will allow AFM to be used in chemistry,

F. Schulz · S. Hämäläinen · P. Liljeroth (✉)
Department of Applied Physics, Aalto University School of Science,
PO Box 15100, 00076 Aalto, Finland
e-mail: peter.liljeroth@aalto.fi

F. Schulz
e-mail: fabian.schulz@aalto.fi

S. Hämäläinen
e-mail: sampsa.hamalainen@aalto.fi

© Springer International Publishing Switzerland 2015

S. Morita et al. (eds.), *Noncontact Atomic Force Microscopy*,
NanoScience and Technology, DOI 10.1007/978-3-319-15588-3_10

molecular electronics, and materials science for structural chemistry at the single-molecule level [7–12].

As mentioned above, in all cases where atomic resolution imaging of molecules was demonstrated, chemically passivated tips were used, typically a carbon monoxide (CO) molecule or a Xe atom adsorbed on the apex [1, 13]. Inert tips are essential to avoid accidental pick-up or lateral manipulation of the molecule of interest by the tip at the small distances and oscillation amplitudes required for atomic resolution imaging. The exact atomic geometry of the tip apex depends on the tip-sample distance, as e.g. the CO is flexible and can bend to reduce the interaction energy between the tip and sample [4, 14–16]. The tip bending can occur both due to attractive and repulsive interactions, i.e. the CO molecule can bend towards or away from the nearest atom. In addition, if the neighboring atoms are not symmetric with respect to the atom directly under the AFM tip, there is a non-symmetric background force on the CO, which will further shift the apparent atomic positions. Finally, the CO bending is sensitive to any saddle points and ridges in the interaction potential energy surface. These will show up as regions of enhanced contrast, irrespective of whether there is an actual bond associated with this region [17, 18].

This chapter will discuss the factors influencing the atomic scale imaging of molecular systems. We will first discuss the effect of the tip passivation on the atomic scale contrast and highlight the complementary nature of the information that can be obtained by AFM and scanning tunneling microscopy (STM). We will then go through the factors affecting the quantitative details of the apparent atomic positions: background forces from the neighboring atoms, flexibility of the tip apex and non-planar samples. Finally, we will discuss the contrast formation mechanism of intra- and intermolecular features in AFM images.

10.2 Tip Reactivity and Atomic Contrast

In non-contact AFM, both the atomic configuration and chemical composition of the tip apex have a profound influence on the imaging contrast at the atomic scale [19–25]. Experiments on model surfaces and with well-defined tip termini are thus crucial in understanding the mechanisms of atomic resolution imaging, which is essential for qualitative and quantitative interpretation of AFM images.

10.2.1 Well-Defined Tips and a Model Surface

The preparation of tips with well-defined apices by picking up single atoms or small organic molecules (commonly referred to as ‘tip functionalization’) is an established technique within the STM community. Demonstrated for the first time more than 20 years ago [26], different functionalizations may allow for improved spatial resolution [26], chemical contrast [27] or spin sensitivity [28]. The advent of low-amplitude

AFM, in particular through the tuning-fork-based qPlus sensors [29], opened up this experimental approach to the AFM community. Since the qPlus sensor can be easily operated at sub-Å oscillation amplitudes, tunneling current and frequency shift can be measured simultaneously with atomic resolution. This has enabled a straightforward adaption of tip functionalization schemes developed previously within the STM community.

Arguably the most prominent example is the functionalization of an AFM tip by picking up a single CO molecule, which yields an atomically well-defined AFM tip with a predefined structure, in contrast to the usual case of e.g. silicon tips. The passivating effect of the CO allows to probe the repulsive force regime of individual molecules, leading to breathtaking images of their chemical structure [1]. Reactive metallic tips, in contrast, typically interact too strongly with single molecules, resulting in lateral or vertical manipulation before the tip-sample distance is sufficiently small for atomic resolution imaging. Thus, to understand how the reactivity of the tip affects the atomic contrast in organic molecular systems, a mechanically stable model surface is required. A convenient choice is an epitaxial graphene monolayer on a metal surface, as the structure of graphene resembles the carbon backbone of organic molecules. Due to the attractive van der Waals (vdW) interaction with a metallic substrate, epitaxial graphene constitutes a mechanically stable surface that can be imaged with reactive and non-reactive tips.

Graphene possesses a very simple structure, made of a single atom thin layer of carbon atoms arranged in a honeycomb lattice, as shown in Fig. 10.1a. This honeycomb structure gives rise to exciting electronic properties in graphene [30, 31], in particular a linear dispersion in the band structure around the Fermi level and a large charge carrier mobility. As a result, graphene holds great promise in electronic applications. At the same time, it continues to be the topic of intense basic physics research as it can host exotic electronic phenomena such as Klein tunnelling, integer and fractional quantum Hall effects, and weak localization [31]. These reasons have resulted in a strong drive to characterize graphene in detail both experimentally and theoretically, making it a well-understood model system.

Among the epitaxial systems, graphene on Ir(111) [G/Ir(111)] has attracted the largest interest, as the graphene can be grown on iridium with high quality [32] by simple chemical vapour deposition (CVD) using small hydrocarbon molecules such as ethylene. In addition, the interaction with the Ir(111) surface is sufficiently weak such that basic electronic properties of the graphene, e.g. the linear dispersion in the band structure, are preserved [33].

G/Ir(111) thus constitutes the desired model surface to study how tip reactivity affects the imaging contrast in AFM. Atomically resolved force-distance spectroscopy and constant-height images of the epitaxial graphene layer reveal that reactive and non-reactive tips exhibit comparable atomic contrast at short tip-sample distances at the onset of Pauli repulsion, while there are striking disparities in the attractive force regime at medium tip-sample distances [24].

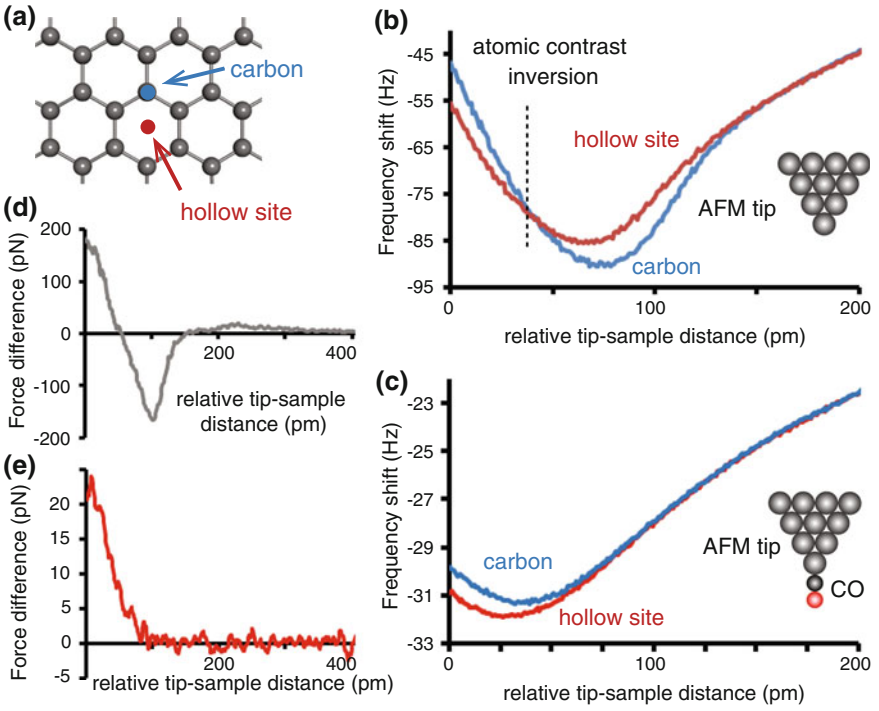

Fig. 10.1 Force spectroscopy on graphene on Ir(111). **a** The carbon honeycomb lattice of graphene. **b** Frequency shift as a function of tip-sample distance for a carbon and a hollow site, measured with a reactive Ir tip. **c** Same as (**b**) but with a non-reactive CO tip. **d** Difference of the measured short-range forces between the carbon atom and the hollow site for the reactive tip. **e** Same as (**d**) but for the non-reactive tip. Adapted with permission from [24]. Copyright (2012) American Chemical Society

10.2.2 Force Spectroscopy with Reactive and Non-Reactive Tips on Epitaxial Graphene

A reactive metallic tip can be prepared by deliberate, microscopic contact formation of the tip with a clean metal substrate, resulting in the pick-up of surface atoms. In the case of AFM measurements on G/Ir(111), this leads to an Ir-terminated tip apex. As iridium is a transition metal with a partially filled $5d$ shell, the Ir tip constitutes a reactive apex that will readily interact with the sample.

The tip-sample interaction can be quantified by measuring the frequency shift (Δf) of the tuning fork as a function of the tip-sample distance (d_{ts}). This is demonstrated in Fig. 10.1 on two characteristic sites of the graphene honeycomb lattice: on top of a carbon atom and in between them on a hollow site (marked in Fig. 10.1a). Both $\Delta f(d_{ts})$ curves are displayed in Fig. 10.1b. At large tip-sample distances, the two curves overlap, since long-range vdW forces between the macroscopic body

of the tip and the sample—with negligible site-specific contributions—dominate. However, as the tip approaches the graphene, short-range forces between the tip apex and the carbon lattice come into play and the two $\Delta f(d_{ts})$ spectra start to deviate: first, at medium distances, the Δf measured over the carbon atom reaches significantly larger negative values compared to the hollow site. Approaching the tip further beyond the minimum Δf sees this trend reversing until the two curves cross. Now, at short tip-sample distances, the carbon atom shows a less negative Δf than the hollow site.

The reactive iridium tip can be passivated by picking up a single CO molecule, yielding a non-reactive tip apex due to the closed-shell character of the CO. The procedure has been demonstrated on weakly reactive metal surfaces such as Cu(111) and Au(111), but it is very difficult to controllably pick up CO from more reactive substrates such as the Ir(111) surface. There are two alternative procedures that can be followed. In the first one, the tip can be prepared on a Cu(111) surface, where the CO pick-up is well-documented. Subsequently, the Cu(111) is exchanged with the desired substrate, in this case the graphene-covered Ir(111) sample and the experiments are carried out. The presence of the CO on the tip can be confirmed afterwards by going back to a Cu(111) substrate and checking the image contrast over a CO adsorbed on the surface in STM feedback. If the images are taken with a CO-terminated tip, CO on Cu(111) has a characteristic sombrero-like appearance [27]. Imaged with a metal tip, it appears as a depression.

The tip termination can also be checked on the G/Ir(111) surface by taking advantage of the moiré superstructure formed by graphene on Ir(111). The lattice mismatch between the graphene and the iridium surface causes a periodic modulation of the atomic registry and adsorption height of the carbon atoms w.r.t. the iridium substrate. Thus, the graphene buckles and forms a periodic pattern of hills and valleys (the moiré pattern) [34]. Typically, with a metal tip the contrast of the graphene moiré is inverted in low-bias STM images. This changes with a CO on the tip apex and the moiré contrast corresponds to the true topography in low-bias STM images. This enables a second procedure to prepare a CO tip, directly on the G/Ir(111) sample without exchanging for a Cu(111) surface. A small amount of CO can be dosed directly into the cryostat and scanner at low temperature, which will lead to the adsorption of a CO molecule on the tip apex in a stochastic process [35].

Having prepared a CO-terminated tip, an equivalent set of measurements is performed (shown in Fig. 10.1c) as was done using the iridium tip. Similarly to the Ir tip, the $\Delta f(d_{ts})$ spectra of the non-reactive CO tip measured over the carbon atom and over the hollow site overlap at large tip-sample distances. At these distances, the tip-reactivity does not play a role as long-range forces dominate and short-range forces between the tip apex and the sample can be neglected. In contrast to the Ir tip, the two curves measured with the CO tip continue to overlap at medium distances as the tip approaches the sample. Only as the tip reaches the Δf minimum and approaches the graphene layer further, the spectra for the carbon atom and the hollow site start to deviate from each other, with the carbon atom exhibiting a less negative Δf, similar to the case of the reactive Ir tip at short distances.

Figure 10.1d, e highlight the differences in the measured tip-sample forces between the two tips: for each tip, the $\Delta f(d_{ts})$ spectrum on the hollow site was subtracted from the spectrum measured over the carbon atom to remove the uniform background due to the long-range van der Waals forces. Subsequently, the difference spectra were converted into force-distance [$\Delta F(d_{ts})$] curves using the Sader-Jarvis formula [36]. Thus, the $\Delta F(d_{ts})$ curves reveal the force between the carbon atom in the graphene lattice and the very apex of the tip (Ir or CO), responsible for the atomic contrast. The reactive Ir tip (Fig. 10.1d) yields considerable differences in the tip-sample forces, both in the attractive and repulsive regime, over a total distance range of 150 pm. Thereby, the maximum attractive force over the carbon atom is 150 pN larger than over the hollow site, in agreement with density functional theory (DFT) predicting the preferred adsorption of Ir atoms on top of the carbon atoms [37]. The passivated CO tip (Fig. 10.1e), on the other hand, does not show any appreciable difference in the attractive force regime between the carbon atom and the hollow site. Only within a narrow region of short tip-sample distances, at the onset of Pauli repulsion, the forces over the two inequivalent lattice sites differ, with the carbon atom being approximately 25 pN more repulsive than the hollow site.

The observed behaviour is in good agreement with DFT calculations of the force between different tips and either graphene or a carbon nanotube [21]. A reactive tip was predicted to cause a re-hybridization of the carbon atoms, resulting in strong short-range attractive forces which are maximal at the carbon lattice site. At closer distances, the larger electron density at the carbon atoms lead to stronger Pauli repulsion and thus, the hollow sites appear with larger attractive force, effectively reversing the atomic contrast. For non-reactive tips, the attractive short-range forces are very small, and atomic contrast between carbon and hollow sites is reached only in the regime of Pauli repulsion, where the differences in electron density yield the same contrast as for reactive tips.

10.2.3 (Non-)Reactivity Determines the Imaging Contrast

The force-distance characteristics between tip and sample will ultimately determine the atomic contrast that is achievable in AFM images. Thus, constant-height images of the Δf signal recorded over the graphene layer, as shown in Fig. 10.2, can be easily interpreted when considering the $\Delta f(d_{ts})$ spectra.

For the reactive Ir tip (Fig. 10.2a, b), two different atomic contrasts can be observed: at larger tip-sample distances ($z = 60$ pm), a hexagonal pattern of local Δf maxima (i.e. less negative Δf) appears, indicating the positions of the less attractive hollow sites. This contrast reverses at short distances ($z = 0$ pm), where the increased Pauli repulsion at the carbon atoms due to the larger electron density results in a honeycomb lattice of less negative Δf.

The additional long-range superstructure visible in the images marks the hills and valleys of the G/Ir(111) moiré pattern. The buckling of the graphene layer allows the observation of both kinds of atomic contrast simultaneously at intermediate

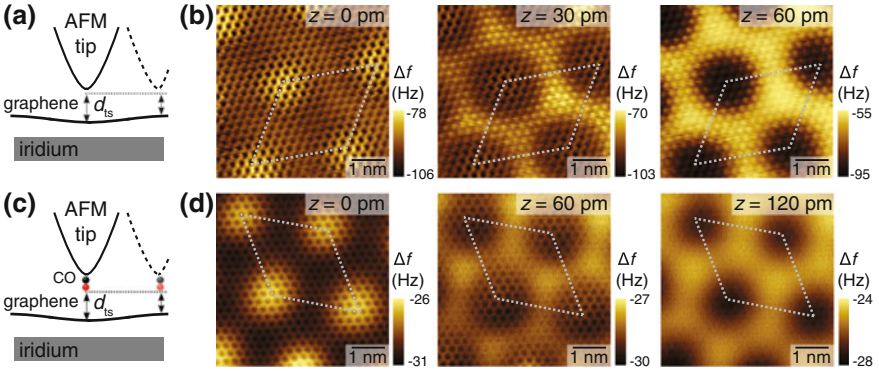

Fig. 10.2 Constant-height images of epitaxial graphene. **a** Schematic of the Ir tip scanning over the G/Ir(111) moiré pattern, which modulates the tip-sample distance. **b** Series of Δf images for increasing tip-sample distance from *left* to *right* (relative tip height indicated on the panels). **c**, **d** Same as (**a**) and (**b**) but for the CO tip. Adapted with permission from [24]. Copyright (2012) American Chemical Society

tip-sample distances ($z = 30$ pm). In this intermediate regime, the tip apex already feels Pauli repulsion on the moiré hills, imaging the carbon lattice with less negative Δf, while on the valleys the atomic contrast is still governed by short-ranged attractive forces and the hollow sites appear with less negative Δf. (Notice that the overall forces are still attractive, as the hills are imaged with larger negative frequency shift than the valleys, while the Pauli forces between the carbon atoms and the tip only cause an additional repulsive modulation on top of the attractive background on the hills.) This proves that both contrasts are characteristic for reactive tips, and the tip-sample distance determines which one is observed.

In accordance with the spectra in Fig. 10.1, the images recorded with a CO tip (Fig. 10.2c, d) do not show atomic contrast in the attractive regime ($z = 120$ pm). Only the long-range periodicity of the moiré pattern is visible, with the hills being imaged with larger negative Δf. At intermediate distances ($z = 60$ pm), the repulsive contrast displaying the honeycomb lattice starts to appear as a modulation of the overall attractive contrast. Finally, the repulsive contrast is observed on the entire graphene surface at short tip-sample distances ($z = 0$ pm), similarly to the reactive tip.

10.3 Relating Electronic Properties with Atomic Structure

As the size of electronic devices continues to shrink, the exact atomic scale structure of the active device area, including the position of individual defects or dopant atoms becomes relevant for the device function. This requires the development of techniques that can simultaneously yield atomic scale structural and electronic information.

AFM based on the qPlus tuning fork design achieves this aim as the small oscillation amplitudes make it possible to carry out simultaneous STM experiments with uncompromised quality [9, 10, 12, 38, 39].

There is intensive research trying to replace silicon transistors with devices where the active element is a single atom or a molecule. Therefore, measurements of structural and electronic properties of such nanostructures are becoming increasingly important. Since their electronic properties are correlated to their precise atomic arrangement and composition, already zero-dimensional defects (also referred to as point defects, e.g. a single missing or substituted atom) can significantly change the electronic structure of such molecular systems, eventually hampering their intended functionality. This is in particular true for many transport properties determined by delocalized electrons, for which defects act as strong scattering potentials [40]. Identifying defects at the atomic scale is thus crucial to understand their effect on the electronic properties, and to develop strategies minimizing their occurrence.

10.3.1 AFM Versus STM and Finite-Size Effects in Graphene

Scanning tunneling microscopy appears as a natural choice to examine atomic scale defects. However, STM measures the local density of states (LDOS) of a sample, and it is doing so only in a narrow energy range around the Fermi energy, being most sensitive to the highest occupied and lowest unoccupied states. In conjugated molecular systems, these states usually host delocalized electrons, whose wave functions can be spread out over the entire backbone of the molecule, while exhibiting a complex structure of lobes and nodal planes. The LDOS of such states does not allow a straight-forward reconstruction of the actual chemical structure of the molecule, as demonstrated in Fig. 10.3a. The presence of defects further complicates the issue, as they act as scattering centers for these delocalized electrons [40], resulting in additional deformations of their wave functions. Identification of the atomic structure of defects by STM is possible only by means of extensive ab initio electronic structure calculations for a set of possible defect structures and subsequent comparison with the experimentally measured wave functions [42].

As has been discussed in the other chapters of this book, AFM is sensitive to the total electron density when probing the repulsive force regime [5], as the strength of Pauli repulsion scales with electron density. Since the total electron density is dominated by core electrons localized at the positions of the atomic nuclei, an AFM image taken in the repulsive regime gives direct information on the atomic structure of the sample. Intensity differences in the sub-molecular contrast can be related to variations in the total electron density, caused by the chemical composition of the molecule or deformations of its structure. Thus, AFM should provide a superior tool to identify the atomic structure and defects in molecular systems.

We illustrate this below using graphene nanoribbons (GNR) synthesized through on-surface polymerization as examples [38, 43]. These graphene nanostructures allow the tuning of the electronic properties through finite-size effects. Infinite

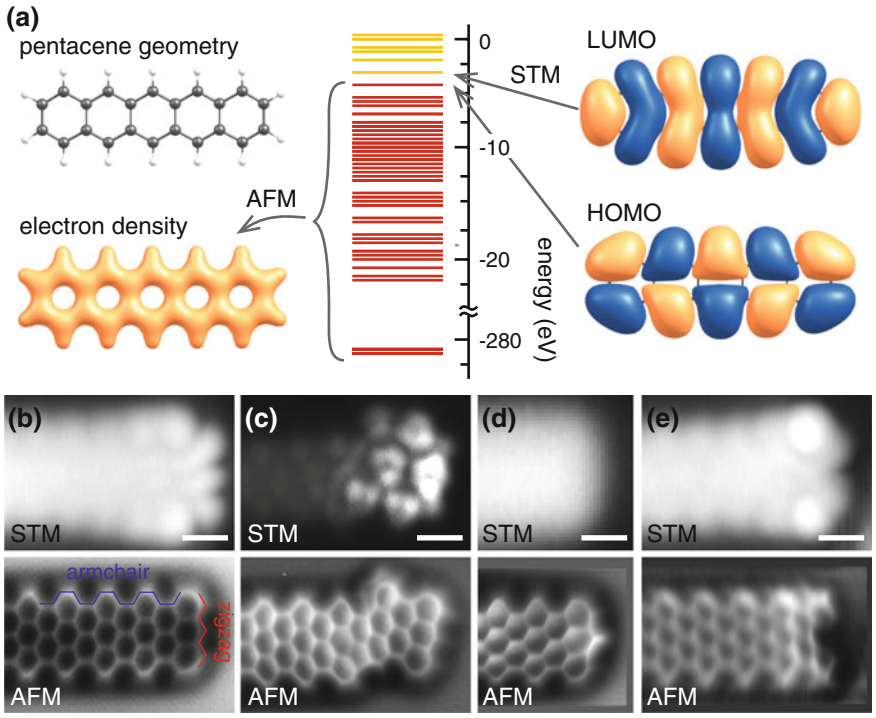

Fig. 10.3 Atomic structure of defects in graphene nanoribbons. **a** Schematic highlighting the different origins of imaging contrast in STM and AFM. STM images molecular orbitals close to the Fermi level (e.g. highest occupied molecular orbital, HOMO and lowest unoccupied molecular orbital, LUMO), while AFM images the total electron density dominated by localized core electrons. **b**–**e** Constant-current STM (*upper panel*) and constant-height AFM (*lower panel*) of (**b**) a defect free GNR exhibiting an edge state at the zigzag (ZZ) edge, but not at the armchair (AC) edge, (**c**) a tilted GNR, (**d**) a GNR with one ZZ edge C atom passivated by two H atoms and (**e**) a GNR with one ZZ edge C atom bonding to the Au(111) substrate. All scale bars are 5 Å. Panels **b**, **d**, and **e** adapted with permission from [38]. Panel **c** adapted with permission from [41]. Copyright (2013) by the American Physical Society

graphene sheets are characterized as semi-metallic or zero-gap semiconductors, due to the crossing of the π bands at the Fermi energy with zero density of states [30]. Quantum confinement effects can open a gap in the band structure in finite graphene flakes of suitable dimensions [44]. In addition, the zigzag (ZZ) edges of graphene (Fig. 10.3b), representing the 'cutting' of graphene along one of its high-symmetry directions, host a non-dispersive electronic edge state at the Fermi energy [31]. This state is neither present in infinite graphene nor on other edge structures [e.g. armchair edges (Fig. 10.3b)]. The interest in graphene zigzag edges stems from the predicted phenomena that would allow the construction of new types of electronic devices (based on e.g. spintronics or valleytronics) [45, 46].

Atomically well-defined GNRs which host edge states can be synthesized on metallic surfaces using molecular precursors [43]. The synthesis is carried out by evaporating the desired precursor onto the substrate [e.g. Au(111)], followed by thermally induced polymerization and cyclodehydrogenation to eventually form the GNR. The beauty of this approach is that the structure of the GNR is uniquely determined by the precursor and this allows for example the width of the GNR to be controlled precisely. The electronic structure of these GNRs is sensitive to chemical modifications of graphene and its edges, and correlating atomic geometry with the electronic structure is an important issue for potential applications [38].

10.3.2 Imaging Defects in Graphene Nanoribbons

Figure 10.3b shows the Δf signal recorded with a CO-passivated tip at constant height over a defect-free GNR. Recorded in the repulsive force regime, the image can be directly interpreted in terms of the atomic structure of the GNR, revealing long edges with armchair (AC, blue) symmetry and a short ZZ edge (red). The corresponding STM image (metallic tip) displays the LDOS of the ZZ edge state, in agreement with simulations (not shown) [38]. The STM image of a different GNR in Fig. 10.3c (CO tip), on the other hand, suggests a deviation at the ribbon termination from the otherwise perfectly straight structure. While a slight tilting at the end of the GNR is already noticeable in the STM image, it does not allow to identify the exact atomic arrangement that causes this tilt. Only the AFM image (Fig. 10.3c), showing the carbon backbone, reveals the origin of the tilt as the displacement of the terminating segment by one graphene lattice vector in combination with the formation of a carbon pentagon [41].

Even more subtle effects such as chemical modifications can be identified in this manner. Figure 10.3d shows the STM image of a GNR ZZ termination displaying no end state. Such contrast was previously assigned to a missing carbon atom [47], destroying the symmetry of the ZZ edge and thereby causing the disappearance of the edge state. However, the corresponding AFM image presented in the same panel unambiguously proves that the carbon backbone is still intact. On the contrary, an increased intensity (i.e. increased repulsion) on the central outermost carbon indicates additional electron density, interpreted as the passivation of the C atom by two hydrogens instead of just one. The corresponding change from sp^2 to sp^3 hybridization would destroy the edge state. It can be recovered by applying a bias voltage pulse with the SPM tip to remove the extra hydrogen atom. Applying a second bias pulse results in a further modification of the GNR edge, as testified by the STM image in Fig. 10.3e. This image, recorded after applying a voltage pulse to an unmodified, defect-free GNR ZZ edge, still resembles that of the ZZ edge state, but the intensity distribution has changed remarkably. The corresponding AFM image shows strongly reduced repulsion at the central outer C atom. An image taken at a smaller tip-sample distance (not shown) reveals an intact carbon backbone, indicating that the GNR edge bends down towards the substrate [38]. This suggests

that the bias pulse removed the single H atom at the central outer C atom, which subsequently formed a bond with the underlying Au(111). This would preserve the sp^2 hybridization of the edge atoms and thus the edge state, while explaining the observed change in the intensity distribution of its wave function.

These experiments highlight the type of complimentary information that can be obtained through combined STM and AFM experiments. These are clearly extremely important for the detailed understanding of the correspondence between the atomic scale structure and the resulting electronic properties of atomically well-defined nanostructures.

10.4 Understanding Measurements with a Flexible Tip Apex

In the preceding sections, we have treated the effects of the tip termination on the observed AFM response and shown how STM and AFM can yield complimentary information on molecules and nanostructures. We will now move on and focus on the quantitative details of AFM imaging with molecule-terminated tips.

10.4.1 Measuring Interaction Energies with a Molecule-Terminated Tip

What is actually measured in an AFM experiment with a molecule-modified tip? It turns out that the tip relaxation has to, in general, be considered for a detailed understanding of the measured forces [4, 9, 14–16]. This process is illustrated in Fig. 10.4, where the relevant interaction terms have been indicated for the measurements of the background signal (Fig. 10.4a) and on the molecule (Fig. 10.4b). The figure and the following discussion consider a CO-terminated tip as an example, but the general principle is naturally applicable to understanding any experiment with a flexible tip apex.

When the tip interacts with the bare substrate, the interaction potential can be formally divided into three terms: the interaction between the body of the tip and

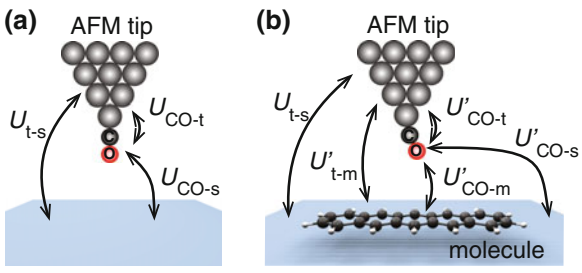

Fig. 10.4 Division of the total interaction energy between a CO-terminated AFM tip and a clean substrate (**a**) and a substrate with an adsorbed molecule (**b**)

the substrate U_{t-s} and the interaction energies between the CO molecule and the substrate $U_{\mathrm{CO}-s}$ and the tip $U_{\mathrm{CO}-t}$, respectively. The situation changes when the tip is brought above a molecule adsorbed on the surface. We have new interaction terms between the body of the tip and the molecule U'_{t-m} and between the CO and the adsorbed molecule $U'_{\mathrm{CO}-m}$. In addition, if the interaction between the CO on the tip with the molecule is sufficiently strong, this will cause the CO molecule to bend. This bending causes interaction energies $U'_{\mathrm{CO}-s}$ and $U'_{\mathrm{CO}-t}$ to change compared to the experiments on the clean surface. The total interaction energy can now be written (for a given tip height)

$$\Delta U = U'_{t-m} + \left(U'_{\mathrm{CO}-t} - U_{\mathrm{CO}-t}\right) + \left(U'_{\mathrm{CO}-s} - U_{\mathrm{CO}-s}\right) + U'_{\mathrm{CO}-m} \qquad (10.1)$$

where the terms U_{t-s} cancel. In terms of measuring interactions between molecules, or for the sake of simple modelling of the AFM response, it would be desirable to be able to measure only the interaction energy $U'_{\mathrm{CO}-m}$. If the CO molecule on the tip does not relax, then the terms in the parenthesis in (10.1) cancel. The term U'_{t-m} can in principle be obtained from a measurement on a molecule before tip functionalization. In that case, it is possible to derive the interaction potential between the CO on the tip and the molecule adsorbed on the substrate purely based on experiments. However, if the CO on the tip relaxes, the terms in the parenthesis are non-zero and there is no direct experimental access to the term $U'_{\mathrm{CO}-m}$. Finally, the above treatment does not take into account the possible relaxation of the molecule on the surface which would further complicate the analysis [14].

10.4.2 Can Atomic Positions Be Measured Quantitatively by AFM with Molecule-Terminated Tips?

In order to understand the atomic-scale imaging mechanism with molecule-terminated tips, it is very helpful to construct a simple model of the tip-sample junction. We have used an approach based on molecular mechanics and pairwise Lennard-Jones (L-J) potentials, where the main tunable parameter is the lateral spring constant k_{CO} of the CO molecule on the tip. While this model is much more simplistic than DFT-based calculations, the major advantage of the present model is that we can freely vary k_{CO} and therefore systematically study the effect of the tip flexibility. In DFT calculations, this number is fixed by the choice of the metal cluster used as a tip model. Details of the model can be found in [15, 18].

We will first consider a well-studied model system to understand in detail the various background contributions to the measured AFM response. For this, we use a pentacene molecule adsorbed directly on a metal (Fig. 10.5) [1, 15]. Simulated constant-height Δf maps with two different lateral spring constants k_{CO} are shown in Fig. 10.5a. It is immediately obvious that both strongly resemble experimental AFM images of pentacene (see chapter by Gross et al.). The simulations are able to

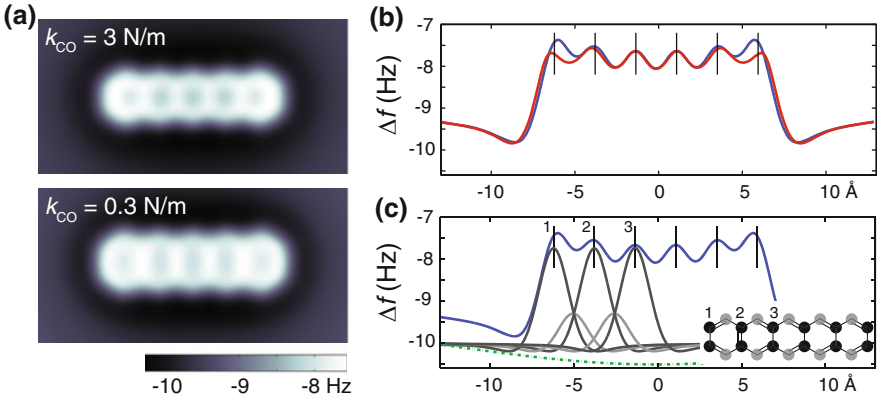

Fig. 10.5 **a** Simulated constant-height AFM images of pentacene with a relatively stiff ($k_{CO} = 3$ N/m) and soft ($k_{CO} = 0.3$ N/m) CO lateral force constant. **b** Extracted line profiles along the center of the pentacene molecule for the two tips (*blue line* corresponds to $k_{CO} = 3$ N/m and *red line* to $k_{CO} = 0.3$ N/m). **c** Line profile over the center of the pentacene molecule for a rigid tip, which also shows the contributions from the individual dimers (*black* and *gray lines*, the corresponding atoms are indicated in the *inset*) and the overall van der Waals background between the CO molecule and the pentacene (*green dotted line*). Adapted with permission from [15]. Copyright (2014) American Chemical Society

reproduce the three main effects where the experimental Δf map differs from the actual structure of the pentacene molecule: (i) all the phenyl rings are elongated in the y-direction; (ii) the edgemost phenyl rings are also elongated in the x-direction; (iii) as the tip-sample distance is reduced, the bonds appear sharper (as discussed in more detail in Sect. 10.4.4) [4, 15–17].

To identify the origin of these effects, we start by extracting the positions of the CO at the end of the tip during each step of the simulation. It shows that the CO bends in response to the tip-sample interaction. The overall bending at the outer edge of the molecule is always towards the center of the molecule and is caused by the attractive van der Waals interaction between the CO molecule and the pentacene. When the tip is over the molecule, it can bend away from the nearest atom at sufficiently small tip-sample distances, irrespective of the vdW background. The maximum CO displacement is of the order of a couple of pm for the stiffer tip, but can reach several tens of pm for the softer tip. This naturally depends on the tip-sample distance.

In addition to the tip bending, the background forces from the neighboring atoms also affect the apparent atomic positions. Figure 10.5b shows Δf line profiles along the center of the pentacene molecule for a flexible ($k_{CO} = 0.3$ N/m, red line) and a stiff ($k_{CO} = 3$ N/m, blue line) tip. The peaks in the Δf line profiles correspond to the apparent positions of the carbon dimers along the middle of the pentacene molecule. Their real, geometric, positions are marked by vertical lines. Finally, Fig. 10.5c gives the contributions from the individual dimers (black solid lines), and the outer most carbon atoms (gray lines, see inset for a schematic) for a rigid tip ($k_{CO} \to \infty$). The

green dotted line gives the overall vdW attraction between the bulk Ir tip and the pentacene molecule.

From Fig. 10.5c it is immediately obvious that the peaks corresponding to the left- and rightmost carbon atoms are shifted significantly towards the center of the molecule (lateral shift of ca. 25 pm). This is due to the asymmetric background signal from the neighboring atoms. All the neighboring atoms contribute to the measured Δf signal, and since the last dimer of the pentacene has neighboring atoms only on one side, this causes an apparent shift in the position of the C–C bond. Contrary to outer dimer 1 being shifted towards the right, the peak corresponding to dimer 2 is shifted towards the left, i.e. the outermost benzene ring appears contracted on both sides. This small shift (around 5 pm depending on the tip height) is due to the slope of the vdW background between the tip and the whole pentacene molecule. While this effect is also also present on the last dimer, the asymmetry in the neighboring atoms has the dominant contribution there. In planar molecules, these effects will always cause an apparent contraction towards the center of the molecule of the outermost rings.

Comparison between the simulations with a rigid ($k_{CO} = 3$ N/m, blue line) and a soft ($k_{CO} = 0.3$ N/m, red line) CO tip shown in Fig. 10.5b allow the assessment of the tip flexibility on the apparent atomic positions. The results obtained with the stiffer tip are quantitatively very close to the rigid tip discussed in Fig. 10.5c. As k_{CO} becomes smaller, the bending of the CO increases. In general, the van der Waals attraction causes the molecule at the tip to bend towards the center of the pentacene. As a result, the outermost bonds appear stretched, both in x- and y-directions. Hence, the effect of tip flexibility is opposite to that of the asymmetric background forces. The dominant contribution depends on k_{CO} and the tip-sample distance.

10.4.3 Can AFM Images Be Background Corrected on the Atomic Scale?

The previous section described how neighbouring atoms affect the measured AFM response and the positions of the Δf maxima corresponding to the atoms. In the general case, it is also possible that the atoms are on different heights, if the molecule or the surface has a three-dimensional shape. We will investigate this on the previously introduced model system of an epitaxial graphene monolayer grown on the Ir(111) surface. According to both experimental and theoretical work [15, 16, 48], AFM in either the constant-height or constant-frequency shift mode will detect apparent lateral changes in the atomic positions on corrugated surfaces. Typically, most of the apparent shift in the atomic position is caused by the asymmetric background from the neighboring atoms that are at different adsorption heights. This suggests that an appropriate background correction or subtraction could be used to correct the experimental data and allow us to extract the actual atomic structure and positions from the experiments. This idea can be tested using the simulated images of graphene on

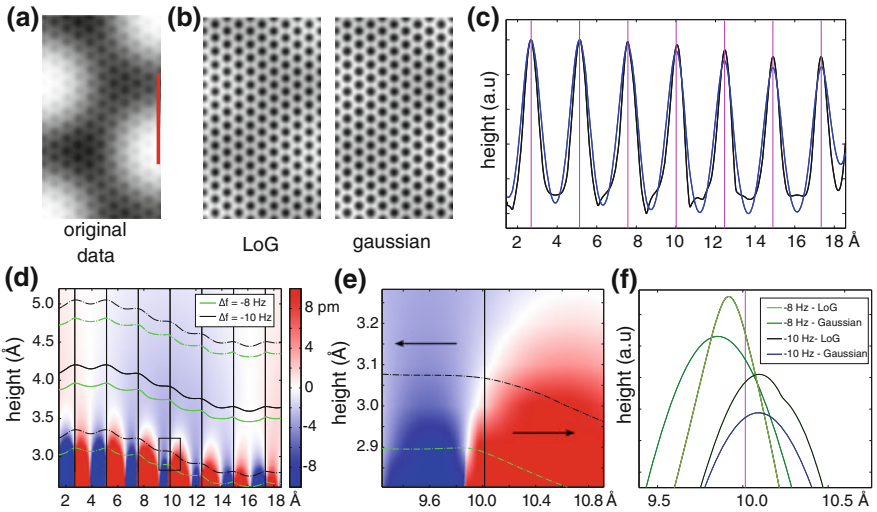

Fig. 10.6 **a** Simulated constant-Δf AFM image of the graphene moiré on Ir(111) with a stiff tip ($k_{CO} = 3$ N/m). **b** Background subtracted images using either a Laplacian of Gaussians filter ($\sigma = 0.6$ Å) or a heavily Gaussian blurred background ($\sigma = 1$ Å). **c** Normalized cross sections of the image in panel a along the *red line* (*blue line* with Gaussian background, *black line* with LoG). The *vertical lines* mark the positions of the bonds. **d** Cross section along the *same line* for a more flexible tip ($k_{CO} = 0.6$ N/m) calculated with two different Δf set points. The *solid lines* correspond to the tip height, while the *dotted lines* show the limits of the oscillation amplitude. The *background color* corresponds to the bending of the CO along the same section. **e** Close-up of the bending in the area marked in panel (**d**). **f** The background corrected cross sections of the same bond. Adapted with permission from [15]. Copyright (2014) American Chemical Society

Ir(111), of which the results are summarized in Fig. 10.6. The simulated constant-Δf image in Fig. 10.6a shows strong long-range corrugation due to the G/Ir(111) moiré pattern, and examples for different background corrections are shown in Fig. 10.6b. In principle, the moiré corrugation can be removed from the simulated images using different filtering schemes. Here, the background was removed either with a Laplacian of Gaussians (LoG) filter, which reduces the contributions from slowly varying long-range corrugations or through estimating the background by heavily blurring the original images by a Gaussian filter and subtracting this from the original image. Line profiles along the segment indicated by a red line in Fig. 10.6a with the two filtering schemes are shown in Fig. 10.6c.

As can be seen in the line scans, background subtraction of the AFM image results in an apparent expansion of the graphene hexagons on the hills of the moiré pattern, which is the reverse trend compared to that in the non-corrected data (not shown in Fig. 10.6) [15]. Background correction improves the match between the apparent and real bond positions in both the constant-frequency shift and constant-height images. The apparent positions in background corrected data can be as close as 1 pm from the real bond positions; however, typically the difference is of the order of 3–5 pm.

While these differences depend on the exact form of the background, the tip-sample distance, the lateral force constant of the tip etc., it appears that using the Gaussian blurred image as the background in constant-frequency shift images results in very accurate estimation of the bond positions to within <2 pm.

As discussed above, the effects of the unequal background from the neighboring atoms can be significantly reduced by the background correction in the case of a stiff tip. What is the situation with a more flexible tip apex? We show simulated line scans with a softer tip ($k_{CO} = 0.6$ N/m) in Fig. 10.6d with two different Δf setpoints (-8 and -10 Hz on the repulsive branch). The main difference between these setpoints is that at $\Delta f = -8$ Hz, the CO reaches the region where it starts to bend away from the top sites (red background) at the bottom of its oscillation cycle. On the other hand in the $\Delta f = -10$ Hz image, the CO remains bent towards the hill of the graphene moiré over the full oscillation cycle. This is shown in the zoomed-in image in Fig. 10.6e. Figure 10.6f shows the same zoom-in after background correction with the two methods described above. In the case of the $\Delta f = -8$ Hz image, the apparent bonds are closer to the hill of the graphene moiré, while for the case $\Delta f = -10$ Hz, they are farther from it. This is in line with the tip bending away and towards the hill of the graphene moiré, respectively. In addition, the flexibility of the CO causes the bonds to appear sharper at the shorter tip-sample distance. This bond sharpening also has a slight effect on the apparent bond positions after background subtraction. Hence, the shift in Fig. 10.6f cannot fully be attributed to the tip bending. However, the shift in Fig. 10.6f is ca. 20 pm, which is larger than the typical shifts due to changes in the peak shape.

10.4.4 AFM Contrast on Intra- and Intermolecular Bonds

The discussion on how bonds and atoms in AFM images get distorted due to the flexibility of the tip apex begs the question of what we are exactly imaging on top of the bonds, i.e. do we really see the bond? As is discussed in the chapter by Gross et al., the repulsive force in AFM is related to the overlap of the electron clouds of the tip apex and the sample [1, 49]. Curiously, images of molecules taken with functionalized tips often exhibit much sharper contrast between atoms than would be expected by just considering the total electron density of the sample [4, 17, 18].

This sharp contrast arises from the flexibility of the tip apex. The basic mechanism can be understood by considering the same simple molecular mechanics tip model presented in the previous section and applying it to two carbon atoms sitting on a surface as shown in Fig. 10.7. The simulated AFM response with a rigid CO on the tip apex, shown in Fig. 10.7a, displays two overlapping spheres, as one would expect for the spherically symmetric L-J interactions used in the model.

Letting the CO relax due to the tip-sample interaction changes the response considerably and a sharp line appears between the atoms (Fig. 10.7b). This sharpening can be related to how the CO bends in the repulsive potential on top of the atoms. The contours in Fig. 10.7c represent the potential felt by the oxygen atom of the CO

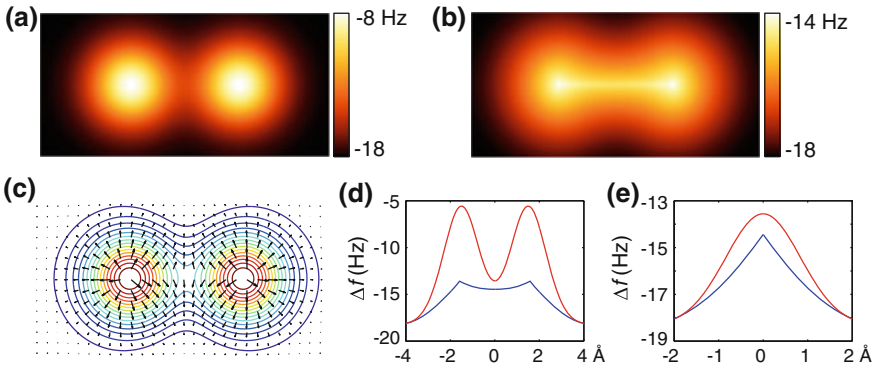

Fig. 10.7 Comparison of contrast in constant-height AFM images on top of two carbon atoms simulated using a tip with a rigid (**a**) and a flexible (**b**) CO apex ($k_{CO} = 0.6$ N/m). **c** Contour of the potential of the oxygen atom on the CO above the two atoms with the quiver plot showing the direction of the CO displacement in the potential. **d** and **e** Cross-sections along and across the apparent bond, respectively. Adapted with permission from [18]. Copyright (2014) by the American Physical Society

on top of the two atoms. As the CO on the tip apex is flexible, it bends away from the atoms at sufficiently small tip-sample distances (quiver plot on top of potential in Fig. 10.7c). The steeper the lateral gradient of the potential, the more the tip bends. In addition to relieving the lateral forces on the tip apex, the bending of the CO also decreases the vertical force, hence affecting the frequency shift.

The curvature of the potential energy defines how the vertical force map is affected. On a convex part of the potential ($\partial^2 U/\partial x^2 < 0$ or $\partial^2 U/\partial y^2 < 0$), the lateral force increases the more the tip bends. This leads to the sharpening of the potential maxima in the force map. On the other hand, a concave potential ($\partial^2 U/\partial x^2 > 0$ or $\partial^2 U/\partial y^2 > 0$) will cause the tip to bend less the farther the tip is moved from the maxima, leading to a flattening of the repulsive region in the force map. This rule of thumb can be applied independently along different coordinate directions. When the tip is scanned well above the plane of the atoms, it feels locally convex potentials centered at the positions of the atoms (assuming the tip is still close enough to reach the repulsive regime). However, the sum of the potentials produces a saddle surface on the line between the atoms. Following the above arguments, F_z is leveled along the saddle surface (concave), but sharpened perpendicular to it (convex). This is evident by comparing the cross sections of the Δf signal along (Fig. 10.7d) and across (Fig. 10.7e) the saddle surface between the atoms.

An interesting feature in the simulated images is that the intensity of the Δf signal decreases the most due to the tip flexibility directly on top of the atoms. In order to understand this, it is useful to directly look at the gradient of the vertical component of the force $\partial F_z/\partial z$. The simulated images in Fig. 10.7a, b take into account the finite oscillation amplitude of the tip (peak-to-peak 1.7 Å in this case), by integrating $\partial F_z/\partial z$ over the oscillation [50].

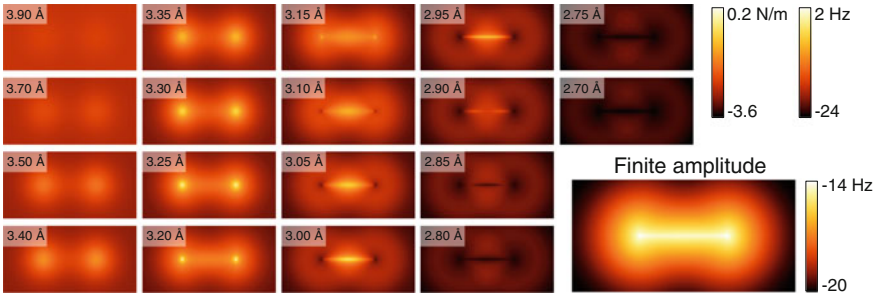

Fig. 10.8 Vertical force gradient ($\partial F_z/\partial z$) at different heights above the two atoms showing the evolution of the contrast at the low amplitude limit; all images with the *same color* scale ($k_{CO} = 0.6$ N/m). The finite amplitude image is calculated from the set assuming an oscillation amplitude ranging over the whole set, i.e. peak-to-peak amplitude $A_{p\text{-}p} = 1.2$ Å

Figure 10.8 shows the evolution of the force gradient as a function of tip height taking into account the tip relaxation. The series starts at a height of 3.9 Å, which is close to the equilibrium distance of the oxygen on the CO and the two carbon atoms on the surface. At this height, the CO does not bend considerably as the forces acting on it are rather weak. Once the tip is brought closer, the force gradient on top of the atoms begins to sharpen due to the CO bending away from the potential on top of the atoms. At around 3.1 Å, the contrast directly on top of the atoms abruptly changes. At this point the CO becomes unstable on top of the atoms. Even thought the lateral forces cancel out on top of the potential maxima, the gradient of the lateral forces eventually exceeds the lateral force constant of the tip and causes the inversion in contrast. Taking the tip even closer to the sample causes the saddle surface of the potential between the atoms to go through a similar evolution; first a sharpening and then eventually a contrast inversion. Finally at very close distances, the tip flexibility starts to dominate and $\partial F_z/\partial z$ starts to level off through-out the image.

However, neither the atoms nor the bonds appear dark when taking into account the full oscillation amplitude by integrating over the panels shown in Fig. 10.8. What happens though is that the relative intensity of the Δf signal on top of the atoms reduces. This causes the atoms and the saddle surface between them to appear almost equally bright and further strengthens the impression of visualizing bonds between the atoms as lines drawn in chemical diagrams.

The above model does not take into account the actual chemical bonds between the atoms in any way. In a covalent bond, the electron density is increased between the bound atoms leading to stronger Pauli repulsion of the CO apex on the bond. With regard to the tip model used here, this would not change the sharpening mechanism as it would just slightly increase the potential on the saddle surface between the bound atoms. The model however allows bond-like contrast to appear in AFM images with no actual bonds, provided that two atoms are close enough to one another to form a saddle surface in the potential between them.

This type of contrast has been observed in AFM images of various systems [6, 9, 18, 51]. In particular, intermolecular contrast has been interpreted as originating from hydrogen bonds, even though it is not clear why a mainly electrostatic interaction should give rise to repulsive contrast in AFM images. It is even possible to observe intermolecular contrast in a system where there is no underlying intermolecular bond [9, 18]. One example of a system where the flexibility of the CO causes bonds to be imaged where no bonds exist is formed by bis(para-pyridyl)acetylene (BPPA) molecules [18]. On an Au(111) substrate, the BPPA molecules form tetramers stabilized by hydrogen bonds between the pyridinic nitrogens and the hydrogens of the adjacent molecules. As a consequence of the hydrogen bonding (red dashed lines in Fig. 10.9b), two nitrogens are pushed close to one another. It is clear that the two nitrogens with their lone electron pairs do not form a bond with one another. The total electron density calculated by DFT in Fig. 10.9c also shows negligible electron density between the nitrogens. Yet, with small tip sample distances, bond-like contrast is observed both on the actual hydrogen bonds and and between the nitrogens.

The formation mechanism of the intermolecular contrast here is the same as in the case of the two atoms presented above and can be reproduced well using the same simple model. The evolution of the intermolecular contrast formation as a

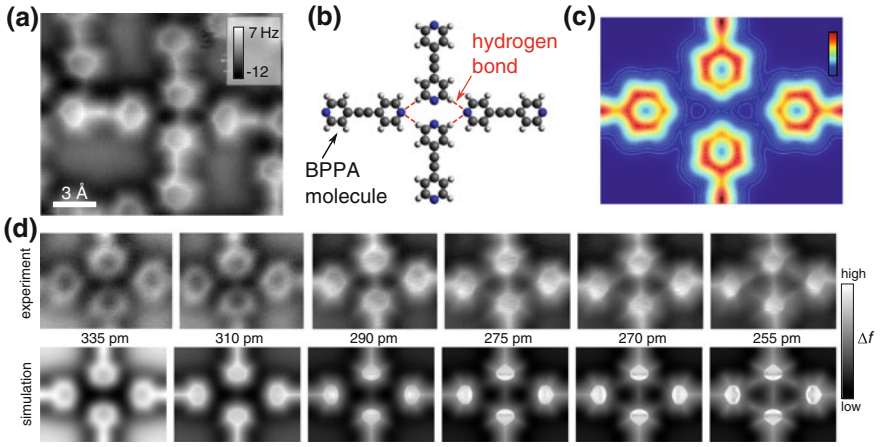

Fig. 10.9 Formation of intermolecular contrast between BPPA molecules. **a** Constant-height AFM image of a BPPA tetramer formed on gold. **b** Schematic representation of the tetramer with the *dashed red lines* marking the hydrogen bonds that stabilize the tetramer. **c** Total electron density given by DFT 3.1 Å above the molecular plane. **d** (*top row*) Experimental constant-height AFM images with a CO tip taken at different heights on top of the tetramer junction showing the appearance of both C–H$\cdots$N and N–N intermolecular contrast at close tip-sample distances. (*bottom row*) Simulated constant-height AFM images with a flexible CO tip ($k_{CO} = 0.6$ N/m) at the given heights showing the appearance of the same intermolecular contrast. The relative height scale is the same in the experimental and simulated images (simulated image at 385 pm matches the experimental image corresponding to the tunneling set-point of 0.1 V/10 pA). The heights correspond to the lowest point of the tip oscillation. Adapted with permission from [18]. Copyright (2014) by the American Physical Society

function of the tip height is shown in Fig. 10.9d. With large tip-sample distances, no intermolecular contrast appears either in simulation or in experiment. At these tip heights, the repulsion from the opposing nitrogens does not reach the middle point between them and no saddle surface is formed. Taking the tip closer, lines start to appear both between the two opposing nitrogens and on the actual hydrogen bonds holding the tetramer together. The contrast first appears between the two opposing nitrogens as they are closer to one another and hence the saddle surface is formed there first. On the hydrogen bonds the saddle surface only starts to appear when the tip reaches the repulsion from the hydrogen in the hydrogen bond.

The contrast saturation at small tip-sample distances demonstrated earlier with the two atoms also appears here. At the closest tip-sample distances, the contrast on the hydrogen bonds and between the nitrogens becomes indistinguishable from the contrast on the acetylene moieties, even though the electron density, and hence the repulsion, is much larger on the acetylene moieties. The reason is the same as in the case of the two atoms (Fig. 10.8). At the point when the CO becomes unstable on the saddle surface, the intensity of the Δf signal no longer increases there. This point is obviously first reached on the acetylene moiety, but eventually also on parts with the intermolecular contrast, rendering the magnitude of the Δf signal the same on both areas. Then, the contrast in the AFM images is dictated by the lateral stiffness of the CO and is no longer related to the magnitude of the tip-sample interaction.

10.5 Conclusions

We have discussed the effects of tip reactivity and flexibility and the role of background forces on the AFM response in molecular systems. Depending on the tip reactivity, it is possible to observe either only repulsive or attractive and repulsive atomic contrast. The apparent atomic positions are affected by the background signal from the neighbouring atoms as well as the possible flexibility of the tip apex.

Tip flexibility has other important consequences for AFM imaging in addition to causing shifts in the apparent atomic positions. The tip bends away from the ridges in the saddle surface of the tip-sample interaction potential, which produces sharp lines between nearby atoms. At the same time, the tip flexibility decreases the Δf signal directly on top of the atoms. These effects enhance the contrast on the bonds which makes it easier to recognize the molecular backbone in the AFM images. On the other hand, at sufficiently small tip-sample separations, the saddle surfaces in the tip-sample interaction potential surface and the atoms become equally bright, irrespective of the electron density of the sample. At this point the contrast formation in AFM is dictated by the lateral stiffness of the CO and is no longer related to the magnitude of the tip-sample interaction. This implies that intermolecular contrast does not directly correspond to the presence of an intermolecular bond. Consequently, quantitative understanding of intra- and intermolecular contrast in AFM images requires taking into account the effects from tip flexibility.

Acknowledgments We are indebted to all our co-authors who have contributed to the work described in this chapter. In particular, we thank Ingmar Swart, Mark Boneschanscher, Joost van der Lit, Zhixiang Sun and Daniël Vanmaekelbergh from Utrecht University, where all the experiments shown in this chapter were conducted, for a fruitful collaboration. This research was supported he European Research Council (ERC-2011-StG No. 278698 "PRECISE-NANO") and the Academy of Finland through its Centre of Excellence "Low-temperature quantum phenomena and devices" (project no. 250280).

References

1. L. Gross, F. Mohn, N. Moll, P. Liljeroth, G. Meyer, Science **325**, 1110 (2009)
2. Y. Sugimoto, P. Pou, O. Custance, P. Jelínek, M. Abe, R. Perez et al., Science **322**, 413 (2008)
3. J. Welker, A.J. Weymouth, F.J. Giessibl, ACS Nano. **7**, 7377 (2013)
4. L. Gross, F. Mohn, N. Moll, B. Schuler, A. Criado, E. Guitián et al., Science **337**, 1326 (2012)
5. F. Mohn, L. Gross, N. Moll, G. Meyer, Nat. Nanotech. **7**, 227 (2012)
6. J. Zhang, P. Chen, B. Yuan, W. Ji, Z. Cheng, X. Qiu, Science **342**, 611 (2013)
7. L. Gross, F. Mohn, N. Moll, G. Meyer, R. Ebel, W.M. Abdel-Mageed et al., Nat. Chem. **2**, 821 (2010)
8. F. Mohn, J. Repp, L. Gross, G. Meyer, M. Dyer, M. Persson, Phys. Rev. Lett. **105**, 266102 (2010)
9. N. Pavliček, B. Fleury, M. Neu, J. Niedenführ, C. Herranz-Lancho, M. Ruben et al., Phys. Rev. Lett. **108**, 086101 (2012)
10. F. Albrecht, M. Neu, C. Quest, I. Swart, J. Repp, J. Am. Chem. Soc. **135**, 9200 (2013)
11. D.G. de Oteyza, P. Gorman, Y.C. Chen, S. Wickenburg, A. Riss, D.J. Mowbray et al., Science **340**, 1434 (2013)
12. A. Riss, S. Wickenburg, P. Gorman, L.Z. Tan, H.Z. Tsai, D.G. de Oteyza et al., Nano. Lett. **14**, 2251 (2014)
13. F. Mohn, B. Schuler, L. Gross, G. Meyer, Appl. Phys. Lett. **102**, 073109 (2013)
14. Z. Sun, M.P. Boneschanscher, I. Swart, D. Vanmaekelbergh, P. Liljeroth, Phys. Rev. Lett. **106**, 046104 (2011)
15. M.P. Boneschanscher, S.K. Hämäläinen, P. Liljeroth, I. Swart, ACS Nano. **8**, 3006 (2014)
16. M. Neu, N. Moll, L. Gross, G. Meyer, F.J. Giessibl, J. Repp, Phys. Rev. B **89**, 205407 (2014)
17. P. Hapala, G. Kichin, C. Wagner, F.S. Tautz, R. Temirov, P. Jelínek, Phys. Rev. B **90**, 085421 (2014)
18. S.K. Hämäläinen, N. van der Heijden, J. van der Lit, S. den Hartog, P. Liljeroth, I. Swart, Phys. Rev. Lett. **113**, 186102 (2014)
19. G.H. Enevoldsen, H.P. Pinto, A.S. Foster, M.C.R. Jensen, A. Kühnle, M. Reichling et al., Phys. Rev. B **78**, 045416 (2008)
20. P. Pou, S.A. Ghasemi, P. Jelínek, T. Lenosky, S. Goedecker, R. Perez, Nanotechnology **20**, 264015 (2009)
21. M. Ondráček, P. Pou, V. Rozsíval, C. González, P. Jelínek, R. Pérez, Phys. Rev. Lett. **106**, 176101 (2011)
22. J. Welker, F.J. Giessibl, Science **336**, 444 (2012)
23. A. Yurtsever, D. Fernández-Torre, C. González, P. Jelínek, P. Pou, Y. Sugimoto et al., Phys. Rev. B **85**, 125416 (2012)
24. M.P. Boneschanscher, J. van der Lit, Z. Sun, I. Swart, P. Liljeroth, D. Vanmaekelbergh, ACS Nano. **6**, 10216 (2012)
25. M. Schneiderbauer, M. Emmrich, A.J. Weymouth, F.J. Giessibl, Phys. Rev. Lett. **112**, 166102 (2014)
26. D.M. Eigler, C.P. Lutz, W.E. Rudge, Nature **352**, 600 (1991)
27. L. Bartels, G. Meyer, K.H. Rieder, Appl. Phys. Lett. **71**, 213 (1997)

28. S. Loth, K. von Bergmann, M. Ternes, A.F. Otte, C.P. Lutz, A.J. Heinrich, Nat. Phys. **6**, 340 (2010)
29. F.J. Giessibl, Appl. Phys. Lett. **73**, 3956 (1998)
30. P.R. Wallace, Phys. Rev. **71**, 622 (1947)
31. A.H. Castro Neto, F. Guinea, N.M.R. Peres, K.S. Novoselov, A.K. Geim, Rev. Mod. Phys. **81**, 109 (2009)
32. J. Coraux, A.T. N'Diaye, C. Busse, T. Michely. Nano. Lett. **8**, 565 (2008)
33. I. Pletikosić, M. Kralj, P. Pervan, R. Brako, J. Coraux, A.T. N'Diaye et al., Phys. Rev. Lett. **102**, 056808 (2009)
34. J. Coraux, T.N. Plasa, C. Busse, T. Michely, New J. Phys. **10**, 043033 (2008)
35. S.K. Hämäläinen, M.P. Boneschanscher, P.H. Jacobse, I. Swart, K. Pussi, W. Moritz et al., Phys. Rev. B **88**, 201406 (2013)
36. J.E. Sader, S.P. Jarvis, Appl. Phys. Lett. **84**, 1801 (2004)
37. P.J. Feibelman, Phys. Rev. B **77**, 165419 (2008)
38. J. van der Lit, M.P. Boneschanscher, D. Vanmaekelbergh, M. Ijäs, A. Uppstu, M. Ervasti et al., Nat. Commun. **4**, 2023 (2013)
39. Z. Yang, M. Corso, R. Robles, C. Lotze, R. Fitzner, E. Mena-Osteritz et al., ACS Nano. **8**, 10715 (2014)
40. G.M. Rutter, J.N. Crain, N.P. Guisinger, T. Li, P.N. First, J.A. Stroscio, Science **317**, 219 (2007)
41. M. Ijäs, M. Ervasti, A. Uppstu, P. Liljeroth, J. van der Lit, I. Swart et al., Phys. Rev. B **88**, 075429 (2013)
42. E. Cockayne, G.M. Rutter, N.P. Guisinger, J.N. Crain, P.N. First, J.A. Stroscio, Phys. Rev. B **83**, 195425 (2011)
43. J. Cai, P. Ruffieux, R. Jaafar, M. Bieri, T. Braun, S. Blankenburg et al., Nature **466**, 470 (2010)
44. L. Yang, C.H. Park, Y.W. Son, M.L. Cohen, S.G. Louie, Phys. Rev. Lett. **99**, 186801 (2007)
45. Y.W. Son, M.L. Cohen, S.G. Louie, Nature **444**, 347 (2006)
46. A. Rycerz, J. Tworzydlo, C.W.J. Beenakker, Nat. Phys. **3**, 172 (2007)
47. M. Koch, F. Ample, C. Joachim, L. Grill, Nat. Nanotech. **7**, 713 (2012)
48. B. Schuler, W. Liu, A. Tkatchenko, N. Moll, G. Meyer, A. Mistry et al., Phys. Rev. Lett. **111**, 106103 (2013)
49. N. Moll, L. Gross, F. Mohn, A. Curioni, G. Meyer, New J. Phys. **12**, 125020 (2010)
50. F.J. Giessibl, Appl. Phys. Lett. **78**, 123 (2001)
51. A.M. Sweetman, S.P. Jarvis, H. Sang, I. Lekkas, P. Rahe, Y. Wang et al., Nat. Commun. **5**, 3931 (2014)

Chapter 11
Single Molecule Force Spectroscopy

Rémy Pawlak, Shigeki Kawai, Thilo Glatzel and Ernst Meyer

Abstract Molecular-scale forces has a pivotal role in biological, chemical and physical processes. *Single molecule force spectroscopy* refers to the study of these forces as well as the mechanical properties of single molecules under applied forces. The term has appeared more than two decades ago in the field of biochemistry, however the recent advances of atomic force microscopy (AFM) operated at low temperature have brought such studies down to the atomic level hence opening new exciting perspectives. At this ultimate level, the intrinsic properties of individual organic species are now quantified by measuring force and conductance informations at the sub-molecular level. Not only restricted to the mechanics of the adsorbates, these techniques are nowadays employed to reveal their chemical structures, their electronic characteristics as well as their optical properties. This chapter reviews proto-typical experiments revealing the fundamental properties of single molecules using advanced spectroscopic techniques at low temperature. First, we will discuss the requirements of such spectroscopic experiments as well as the "essence" of the physical quantities extracted from them. Section 11.3 will respectively show the capability of this approach in the elucidation of the structure of single molecules, the mechanical properties, their internal mechanical behavior under various manipulation processes. Section 11.4 will be dedicated to the study of their electronic and optical properties down to the sub-molecular scale. Finally, Sect. 11.5 will discuss the future prospects.

R. Pawlak (✉) · S. Kawai · T. Glatzel · E. Meyer
Department of Physics, University of Basel, Klingelbergst. 82, 4056 Basel, Switzerland
e-mail: remy.pawlak@unibas.ch

S. Kawai
e-mail: shigeki.kawai@unibas.ch

T. Glatzel
e-mail: thilo.glatzel@unibas.ch

E. Meyer
e-mail: ernst.meyer@unibas.ch

© Springer International Publishing Switzerland 2015

S. Morita et al. (eds.), *Noncontact Atomic Force Microscopy*,
NanoScience and Technology, DOI 10.1007/978-3-319-15588-3_11

11.1 Introduction: Towards Single Molecule Investigations with nc-AFM

Since the development of scanning tunneling microscopy (STM) by Bining et al. [1] and shortly after atomic force microscopy (AFM) [2], exploring and interacting with surfaces with atomic precision is a dream became true [3, 4]. Looking at atoms as well as molecules with such techniques has rapidly opened a widespread interest in various scientific field such as material science, engineering, fundamental physics, chemistry and biology.

Following the first atomic resolution by non-contact atomic force microscopy (ncAFM) [6–8], the technique has proven its ability for observing with atomic resolution metallic [9, 10], semiconducting [6, 8, 11, 12] and insulating surfaces [13–15]. In addition to "see" atoms, many efforts have been focused by the community to quantify forces arising between the interaction of the AFM tip and various surfaces by conducting spectroscopic measurements [16–22]. The remarkable advances in understanding and acquiring these data have then shown the capability of the technique to chemically identify atomic species at surfaces [24–26], manipulate atoms in a controlled way [27–29] or build-up 2D- and 3D-force vector fields with atomic-scale precision [31–35]. An additional benefit of such spectroscopic approaches compared to imaging is the recovery of the normal and lateral forces as well as the potential energy landscape of the tip-sample interactions via post-processing [32, 36–39] which reveal the AFM technique as a unique tool for characterizing forces at the atomic scale.

If real-space observations of single molecules by STM appeared in the early 90's [40], such achievements with ncAFM were slightly delayed [41–44] principally due to the need of technological improvements. For instance, studies of single molecules via force spectroscopy using a silicon cantilever appeared in 2003 with the mechanical switching of a single porphyrin molecule [45] or the observation of single nanotubes with atomic precision [46]. The implementation of quartz tuning forks as force sensor (qPlus sensor [47–49]) brought the ncAFM mode even further by allowing unique experiments combining force and current detection at low temperature. In 2009, the resolution of the chemical structure of a single molecule was demonstrated by L. Gross and coworkers by means of direct imaging and 3D-force spectroscopy [50]. The charge state of single adatoms, point defects in MgO and single molecules on NaCl thin films were also determined by mapping the local potential difference (LCPD) between tip and sample [51–54], a technique which was also employed to reveal the charge distribution within single molecules [55–58]. Further experiments based on force and current spectroscopies were then widely used to understand molecular properties and physical phenomena at the nanoscale [59–69].

Single molecule force spectroscopy reveals the mechanical response of individual molecules under localized forces applied and measured with an AFM. With the latest advances in spectroscopic techniques combining force and current, it is now also possible to reveal their chemical structure, their electronic properties (electronic gap, charge state, internal dipole moment) down to the sub-molecular scale.

In this chapter, we will introduce our recent works on force spectroscopy performed on individual molecules at low temperature. We will briefly discuss experimental requirements such as the isolation of molecules, the precise data acquisition of force and current spectroscopic information simultaneously and their post-processing. Then, we will show the investigation of the structural and mechanical properties of single organic species at the sub-molecular scale as well as their mechanical behaviour during vertical or lateral manipulation with the AFM tip. A second section will focus on combined spectroscopic measurements of force and current giving important insights into the electronic properties of single molecules. Finally, we will discuss future experimental considerations and experiments to observe new physical phenomena at this ultimate level.

11.2 Experimental Requirements

11.2.1 Single Molecules at Surfaces

Performing single molecule force spectroscopy experiments requires the isolation of the organic species on top of atomically cleaned surfaces. Substrates, typically crystal facets of Cu, Ag, and Au, are prepared by several cycles of sputtering/annealing in ultrahigh vacuum. Evaporated from a Knudsen cell heated up to the sublimation temperature of the molecule, the organic species usually possess sufficient amount of kinetic energy to diffuse on the surface at room temperature leading to step adsorption or self-assembly. The molecule-surface interaction has a fundamental role in controlling the diffusion length of the organic species. When adsorbed on reactive metals or semi-conductors having dangling bonds isolated molecules can be found at room temperature, however it is usually not the case when deposited on bulk insulators at room temperature.

A "trick" to overcome this issue introduced by Repp et al. [70, 71] is to conduct such evaporations within the microscope at low temperature (4.8 K) to avoid diffusion. In this way and as depicted in Fig. 11.1, molecules are usually isolated and randomly distributed on the surface while its adsorption geometry is determined by the molecule-substrate interaction. In addition, ultrathin films of an insulating materials such as NaCl can be grown on these metal surfaces to be used as decoupling layers. Molecules deposited on top of them are electronically decoupled from the metals

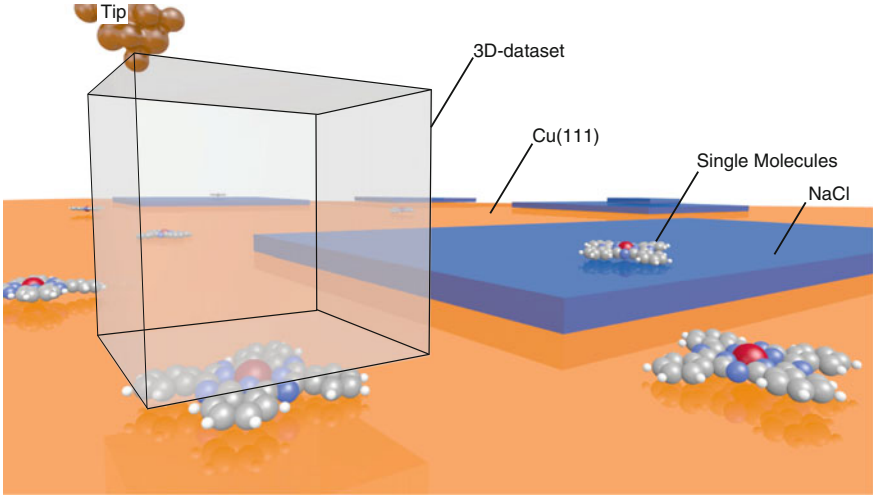

Fig. 11.1 Concept of single molecule force spectroscopy. During molecule evaporation, the substrate is kept at low temperature (below 10 K, within the microscope) to avoid any self-assembly. Insulating thin layers such as NaCl can also be grown on *top* of which molecules are deposited. 3D-spectroscopic dataset of force and current can be then conducted on such "individualized" molecules having different adsorption characteristics and thus variable intrinsic properties

keeping their electronic integrities, which are then probed by STM/nc-AFM experiments [51, 70, 71]. Such reference samples, i.e. NaCl thin films/Cu(111), is also well known for functionalizing tip apexes with various molecules adsorbed on NaCl layers to perform high-resolution imaging [55]. The cuboid of Fig. 11.1 schematizes a 3D-databox where the spectroscopic measurements are usually acquired.

11.2.2 Three-Dimensional Spectroscopic Measurements

11.2.2.1 Acquisition Method and Experimental Setup

3D-dynamic force spectroscopy measurements (3D-DFS) are able to investigate surfaces with sub-angström resolution in real space. In frequency modulation atomic force microscopy (FM-AFM or nc-AFM), the observable is the frequency shift (Δf) with respect to the resonance frequency (f_0) of an oscillator resulting from the interaction forces F between a nano tip and the surface. Using numerical conversion algorithms, 3D-fields of the site-dependent interaction forces as well as the surface potential energy landscape can be extracted above a material in the three dimensions (x, y, z) from the $\Delta f(z)$ spectra (Fig. 11.2b) [72]. Electrostatic forces can be also locally probed by measuring the tip-sample interaction with respect to the sample voltage, V, between tip and sample ($\Delta f(V)$, Fig. 11.2d). Through the measured

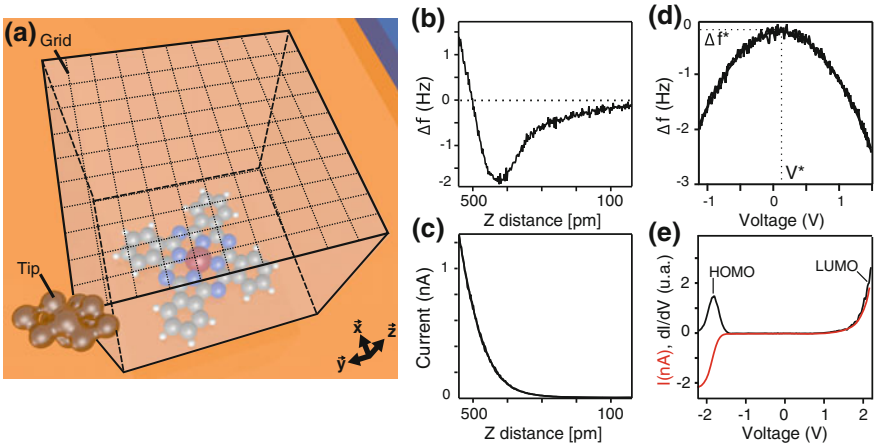

Fig. 11.2 Illustration of a 3D-spectroscopic measurements above a single molecule. The grid on *top* of the molecule set up by the experimentalist predefines the resolution of the final spectroscopic map. At every point of the grid, the variations of Δf and tunneling current I_t versus the tip-sample distance Z or the bias voltage V are recorded. Typical single spectra of $\Delta f(z)$, $I_t(z)$, $\Delta f(V)$ and $I_t(V)$ obtained at one point of the grid are plotted in (**b**), (**c**), (**d**) and (**e**) respectively. In (**e**), HOMO and LUMO refer to Highest Occupied Molecular Orbitals and Lowest Unoccupied Molecular Orbitals respectively

tunneling current I_t versus the tip-sample distance z or V (Fig. 11.2c, e), additional information of the sample conductivity can be obtained such as the electronic band gap of a material and the electronic states of single molecules.

We use a commercial low-temperature STM/AFM system from Omicron GmbH operated with Nanonis electronic from SPECS. Both STM and AFM data are acquired with a tuning fork sensor in the qPlus configuration having an external wire for the tunneling current. The W tip is usually poked into an atomically cleaned metal (Cu(111)) to sharpen and chemically define its apex. The parameters usually used for force spectroscopy are $A = 50$ pm, $k = 1800$ N/m with $Q = 15{,}000$–$60{,}000$ at 5 k and $f_0 \approx 25$ kHz. As depicted in Fig. 11.2a, we usually acquire data with the grid mode [63] meaning that single-point spectroscopies of Δf and tunneling current I_t are recorded simultaneously at each point of the predefined matrix of $x \times y \times z$ nm^3 length containing $x' \times y' \times z'$ data points. Since such force and current mapping usually takes more than 10 h, small thermal drift even existing at helium temperature measurement can induce significant measurement errors. Furthermore, this thermal drift is non-linear in the measurement time-scale. The so-called feed-forward method [37, 73] cannot be used in such cases. Thus, we developed a "drift-corrected three dimensional force and current spectroscopy", in which the tip-sample relative position is corrected between each spectroscopic curve by using atom tracked tip positioning [74]. Figure 11.2b–e shows typical single point spectra of $\Delta f(z)$, $I_t(z)$, $\Delta f(V)$ and $I_t(V)$, *dI/dV* that are used to investigate the fundamental properties of molecules at the atomic scale.

11.2.2.2 Determination of Interaction Forces and Potential

The correlation between normal tip-sample forces F_{ts} and measured Δf has been described in detail by [37–39, 47, 48, 75, 76]. The following part focuses on the essential formulas. During the approach of the oscillating qPlus sensor to the surface, the resonance frequency shifts under the action of the tip-sample interaction forces. The motion of the AFM tip can be described as a weakly perturbed harmonic oscillator [47]. In the case of qPlus sensors operating with small oscillation amplitudes (A<100 pm), the relation between frequency shift $\Delta f = f - f_0$ and the tip-sample force F_{ts} or the tip-sample stiffness k_{ts} can be approximated by:

$$\frac{\Delta f(z)}{f_0} = -\frac{1}{2k}\langle\frac{\partial F_{ts}(z)}{\partial z}\rangle \approx \frac{k_{ts}}{2k} \tag{11.1}$$

where z is the tip-sample distance, f_0 the resonance frequency, k the sensor stiffness, $\langle\partial F_{ts}(z)/\partial z\rangle$ is the averaged force gradient over the tip oscillation cycle which is considered constant for small oscillation amplitudes and thus approximated by $k_{ts} = -\partial F_{ts}(z)/\partial z$, the tip-sample stiffness.

However, k_{ts} can vary by several order of magnitudes when using larger oscillation amplitudes. A more general expression to calculate F_z from the Δf and not restricted to only small oscillation amplitudes was obtained using first-order derivation in the Hamilton-Jacobi approach and given by [47, 76]:

$$\Delta f(z) = -\frac{f_0}{\pi k A}\int_{-1}^{1} F_{ts}(z + A(1+u))\left(\frac{u}{\sqrt{1-u^2}}\right)du \tag{11.2}$$

with f_0 resonance frequency, A oscillation amplitude and k stiffness of the oscillator and F_{ts} tip-sample force interaction. In the integral, the term $u/\sqrt{1-u^2}$ acts as a weight function which help to describe the contribution of Δf with respect to the oscillation amplitude [38]. From this formula, the experimental $\Delta f(z)$ is correlated to the tip-sample interaction force by a mathematical transformation inversion. Several approximation methods have thus been proposed to simplify this inversion [17, 77, 78]. The method we employed is the analytic approximation developed by Sader and Jarvis [75] giving $F_{ts}(d)$ from the measured $\Delta f(z)$ as follows:

$$F_{ts}(d) = \frac{2k}{f_0}\int_d^{\infty}\left(1 + \frac{A^{1/2}}{8\sqrt{\pi(z-d)}} - \frac{A^{3/2}}{\sqrt{2(z-d)}}\frac{\partial}{\partial z}\right)\Delta f(z)dz, \tag{11.3}$$

A further integration gives the tip-sample surface potential $U_{ts}(d)$ as :

$$U_{ts}(d) = \frac{2k}{f_0}\int_d^{\infty}\left(z - d + \frac{A^{1/2}}{4}\sqrt{\frac{z-d}{\pi}} + \frac{A^{2/3}}{\sqrt{2(z-d)}}\right)\Delta f(z)dz \tag{11.4}$$

with d is the closest tip-sample distance, z the tip-sample distance, f_0 the resonance frequency of the oscillator, A its oscillation amplitude and k the stiffness. Even though these analytic expressions can be easily implemented to post-process the $\Delta f(z)$ curves, a particular attention must be taken when acquiring the data to obtain an high accuracy of the extracted F_{ts}. The Sader and Jarvis algorism indeed requires to know the whole $\Delta f(z)$ pathway, from the closest tip-sample distance ($z = d$) up to a distance where the oscillator is unaffected by the tip-surface interactions ($z = \infty$). Since the long-range force contributions are in principle not site-dependent, we always record one "long" $\Delta f(z)$ curve (typical sweep distance 5–10 nm) after acquiring a 3D-dataset in order to extract the long-range vdW background of each single curve [23]. Using Sader and Jarvis algorism, the $\Delta f(z)$ curves must also be free of instabilities or jumps to avoid errors in the force and potential extraction due to the integration process [38]. Finally, the intrinsic parameters of the qPlus (k, A and f_0) have to precisely estimated to avoid further offsets. From the $\Delta f(z)$ spectra taken at each point of a 2D-grid, $F_{ts}(x, y)(z)$ can be determined at every point. In this way, a force field in three dimensions, $F_{ts}(x, y, z)$, can be built up above the choosen surface [60, 61, 63, 74, 79]. A further integration of $F_{ts}(x, y, z)$ will give the tip-surface potential $U_{ts}(x, y, z)$ [32]. The derivation of this potential $U_{ts}(x, y)$ along x and y will also provide maps of the lateral forces $F_l(x, y)$ [36].

11.2.2.3 Local Contact Potential Difference (LCPD) Mapping

Kelvin Probe Force Microscopy (KPFM) is an advanced AFM technique which combines the high spatial resolution of the AFM technique and the measurement of work function introduced by Lord Kelvin [80]. When two parallel plate capacitors face each other and have different work functions ϕ_1 and ϕ_2 are electrically connected via a back electrode, electrons are transferred to align their Fermi levels. A difference of potential appears in the vacuum barrier separating the plates appears, so-called contact potential difference (CPD) and defined as: $V = (\phi_1 - \phi_2)/|e|$ with e the charge of the electron. The original method is thus based on the measurement of displacement current generated between the two plates, induced by the CPD and continuously measured.

Based on the ncAFM mode, KPFM detects the variation of electrostatic forces between tip and surface. A dc-voltage is applied to minimize the electrostatic forces between tip and sample, then defined as $V_{LCPD} = (\phi_{\text{tip}} - \phi_{\text{sample}})/|e|)$, when an ac-voltage modulation is applied to the tip to track the electrostatic force contribution. The curve has a parabola shape because it probes the electrostatic force contribution of tip-sample interactions described by in the simplest approach:

$$F_{el} = \frac{1}{2}\frac{dC}{dz}\Delta V^2 \tag{11.5}$$

where C is the capacitance of the tip-sample capacitor, $\Delta V = V_{\text{tip}} - V_{LCPD}$ is the potential difference between tip and the sample V_{LCPD}. Note that C depends on the tip-sample distance and the geometry of the probe.

An alternative of the conventional dynamic KPFM mode [80] is to determine the LCPD with spectroscopic curves by measuring the tip-sample interaction, $\Delta f(V)$, as a function of the bias voltage V. A typical $\Delta f(V)$ spectra is shown in Fig.11.2d. The LCPD is given by the position of the maximum of the parabola corresponding to the LCPD compensation, noted $V^* = V_{LCPD}$, and estimated by numerical fitting. Based on several $\Delta f(V)$ spectroscopic curves acquired over a 2D- or 3D-matrix, $LCPD(x, y)$ maps can be built-up after extraction of V^* at each position. This approach is slower than KPFM since the curve needs to be acquired over a large bias voltage variation at every point. However, the interpretation of LCPD is more straightforward since it avoids additional feedback loops which can produce crosstalk effects. In the following, we will refer to this spectroscopic technique as LCPD mapping rather than a "true" analogue of the KPFM despite of the fact they measure the same physical quantity.

LCPD mapping at low temperature has already shown the detection of different charge states [50, 52, 53] and the charge distributions within single molecules at the atomic scale [55–57]. The physical origin of these contrasts at the atomic level can be correlated to "work function changes" but further to local dipole moments, inhomogeneties of electron distributions at step edges or point defects as well as local polarization effects. It is important to differentiate the short- and long-range contributions of the electrostatic forces, one being related to bulk properties of a material (long range) and the other one from for example to adatoms or single charged point defects (short-range). Several models have been developed taking into account the short-range, long-range contributions and polarization effects when interpreting the experimental data [81–83]. Combining low temperature spectroscopic experiments with theories is most likely the key to further develop our understanding of atomic-scale measurements of electrostatic forces.

11.2.2.4 Scanning Tunneling Spectroscopy-STS

The tunneling current I_t measured by STM depends on the local density of electronic states (LDOS) close to the Fermi level of the sample. When the STM tip is brought close to the sample, the wavefunctions of tip and sample overlap. In the low bias voltage application, the variation of I_t with respect to the tip-sample distance z is monotonic and expressed as follow [84, 85]:

$$I_t(z) \propto \frac{\text{const.}V}{z}\exp^{-2\kappa z} \tag{11.6}$$

with κ is the inverse decay length. κ is written:

$$\kappa = \sqrt{\frac{2m}{\hbar^2}\frac{(\phi_{\text{tip}} + \phi_{\text{samp}})}{2} - E + \frac{eV}{2}} \tag{11.7}$$

where ϕ_{tip} and ϕ_{samp} are the work function of the tip and sample respectively. A typical experimental curve of $I_t(z)$ is shown in Fig. 11.2b. In constant-current mode, the I_t contribution is approximately the integrated LDOS of the surface. The tunneling current at a fixed (x, y) position and at constant tip-sample distance z and bias voltage V is given by:

$$I_t(V, x, y) \propto \int_0^{eV} \rho_t(E - eV)\rho_s(E, x, y)T(E, V, z)dE \tag{11.8}$$

with ρ_t and ρ_s are the DOS of tip and sample respectively, E the energy and T is a transmission function describing the probability of electrons to tunnel between tip and sample. It is well-established that the derivative of the tunneling current is proportional to the surface LDOS. Its expression is:

$$dI_t/dV \propto T(E, V, z)\rho_s(E, x, y)\rho_t(0) + \int_0^{eV} \rho_s(E, x, y)\frac{d[T(E, V, z)\rho_t(E - eV)}{deV}dE \tag{11.9}$$

At constant height and for low bias voltages, the transmission coefficient T is assumed to be energy independent. Therefore (11.7) thus links directly the derivative *dI/dV* to the LDOS of the sample at a fixed tip-sample position z. Nowadays, the study of molecular systems is widely conducted using *dI/dV* providing a accurate positioning of their filled (Highest Occupied Molecular Orbitals-HOMO) and empty electronic states (Lowest Unoccupied Molecular Orbitals-LUMO) [70]. Combining force and current spectroscopy is a powerful asset to better understand electronic properties of single molecules.

11.3 Probing Mechanical Properties at the Sub-molecular Level

11.3.1 3D-Force Field of Fullerene C_{60}

To reveal the capabilities of force spectroscopic measurements to study single molecules, we first investigated fullerenes C_{60} adsorbed on Cu(111) [60]. The chemical structure of the molecule is shown in Fig. 11.3a and consists of 12 pentagonal and 20 hexagonal carbon rings. C_{60} deposited at room temperature on the surface nucleate at step edges and form 2–3 monolayers islands, but we focused on single molecules adsorbed on top of those islands. The 3D-force field presented in Fig. 11.3 was built up from several $\Delta f(z)$ spectroscopic curves taken above the molecule in a box of $1.1 \times 1.1 \times 0.5$ nm^3 containing $60 \times 60 \times 128$ data points. The total recording time

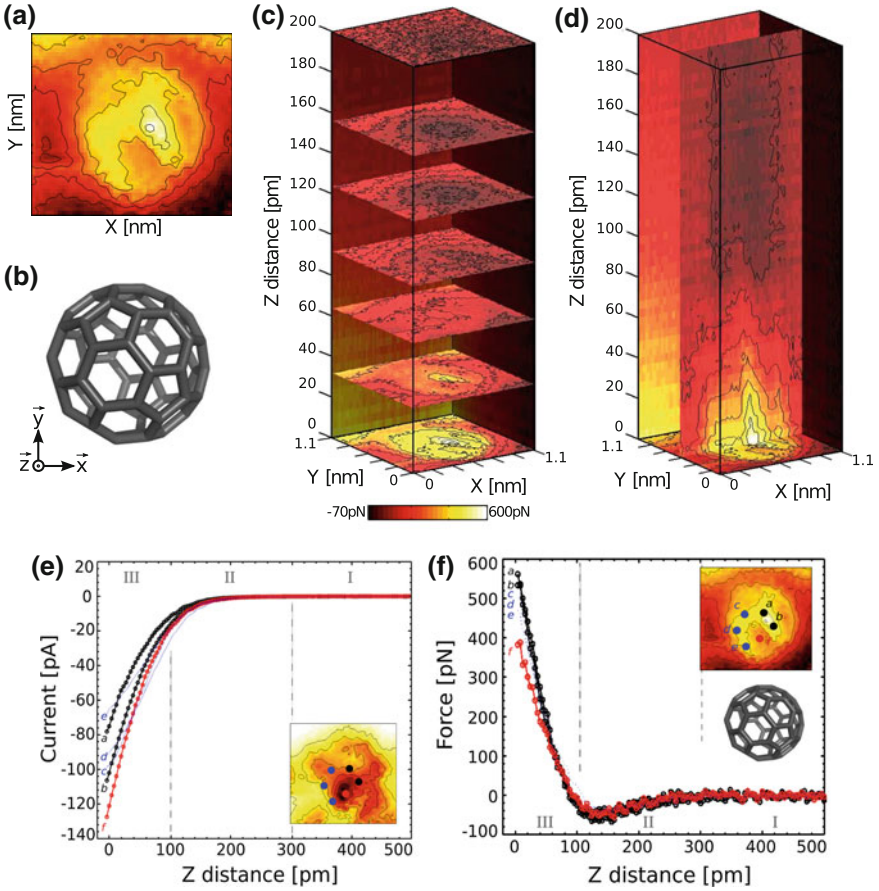

Fig. 11.3 **a** Closest constant-height $F_{ts}(x, y)$ map extracted from a 3D-force field showing intramolecular resolution. **b** Molecular orientation according to the $F_{ts}(x, y)$ map. **c** Successive $F_{ts}(x, y)$ maps at different tip-sample separations, and **d** $F_{ts}(x, z)$ cross-section taken at the center of the molecule, revealing the contrast evolution with respect to the tip-molecule distance z. The z axis is distorted for a better readability. Total 3D-DFS parameters, $1.1 \times 1.1 \times 0.5\,\text{nm}^3$ with $60 \times 60 \times 128$ data points, V $\approx 300\,\mu$V, A $= 60$ pm

was approximately 13 h and, as previously described in Sect. 11.2, we also recorded $\Delta f(z)$ of 10 nm sweep distance to estimate long-range force contributions and extract the total normal force.

Figure 11.3b shows such a $F_{ts}(x, y)$ map obtained at the closest tip-sample z whereas Fig. 11.3c, d show various plots of the 3D-force field $F_{ts}(x, y, z)$. Figure 11.3b clearly shows the chemical structure of the C_{60} with an edge between polygons on top of the molecule and thus allows an unambiguous interpretation of the molecule orientation as depicted in Fig. 11.3a. The data also confirms that intramolecular resolutions of molecules can be obtained via force spectroscopy as first

shown by Gross et al. [50]. In addition to sub-molecular resolution imaging, such results reveal that the dominant force regime in sub-molecular imaging is the Pauli repulsive force regime [50]. With qPlus sensors operated at small amplitudes, intramolecular resolutions are usually obtained by probing the Pauli repulsive regime of forces [50]. The largest repulsive forces is ≈600 pN at the top of the molecule whereas at the periphery of the structure the forces are lowered to ≈400–500 pN due to the curvature of the molecule. In contrast to CO functionalized tip experiments (see Chap. 12), the values of these repulsive forces is sensibly higher, that we assume to result from the more reactive Cu-terminated tips. Figure 11.3c, d describes successive $F_{ts}(x, y)$ constant-height maps at different tip heights and a vertical cross section $F_{ts}(x, z)$ taken at the center of the molecule, respectively. It shows that a variation of the z distance of ≈80 pm is sufficient to induce the disappearance of the structure resolution during constant-height imaging. For tip-sample separations larger than 80 pm, the contrast essentially results from short-range attractive force interactions. The molecules appear as a homogeneous protrusion similar to previous nc-AFM contrasts on insulators or semiconductors [86].

Figure 11.3e, f shows individual tunneling current and force spectroscopic curves obtained at specific (x, y) positions above the molecule (see insets Fig. 11.3f). We particularly focused our interest on the carbon sites of the buckyball structure (marked by blue and back dots) and the center of the carbon ring (red dots). In the I_t curves (Fig. 11.3e), the center of the carbon ring (red curve) has the highest value of tunnelling current (≈130 pA) whereas the different C sites appear with less intensity. In contrast, the force spectroscopic curves (Fig. 11.3f) have a different behaviour. For z distances where the tip probes short- and long-range attractive forces (region I and II), the curves coincide thus indicating site-independent information. When the z distance is smaller than 100 pm, strong differences arise induced by the contribution of site-dependent repulsive forces. We observe that the maximum extracted interaction forces above carbon atoms varies from 450–580 pN depending on the site. This variation is again the consequence of difference of the tip-sample distance z at the closest point due to molecule curvature. The red curve was obtained at the center of the carbon ring (site f in Fig. 11.3f) and exhibits the smallest interaction force at the closest point (390 pN).

Importantly, the slopes of the $F(z)$ curves in the repulsive regime (Fig. 11.3f) correspond to the local force gradient variations and can be interpreted as local elastic properties appearing between the structure of the C_{60} molecule and a Cu-terminated tip. Above carbon atoms, vertical force gradient k_{ts} vary from ≈9 to 7 N/m. At the center of the carbon ring, k_{ts} is lowered to ≈4 N/m. Since the dissipation signal was extremely small (≤10 meV/cycle), we conclude that the local deformations are purely elastic and not plastic. Therefore, these results demonstrate that mechanical properties of single molecules can be probed at the sub-molecular scale via force spectroscopic measurements. However, the interpretation of such data is a challenging task. Concluding whether the tip, the molecule structure, the substrate or the whole system is deformed is not straightforward and often require additional numerical calculations. For example, the deformation of the substrate under the probed C_{60} [66] or the distortion of CO molecules under similar experiments [87, 88] has

been already demonstrated. In the following subsections, we will thus focus on experiments showing that only mechanical properties of adsorbed molecules can be probed at the sub-molecular scale.

11.3.2 Directed Rotation of Porphyrins

In comparison to the fullerene structure which has a high mechanical stability, porphyrin molecules are expected to be more deformable since they contain many "bendable" C–C bonds between their core and the peripheral end-groups. Figure 11.4a depicts the chemical structure of the H_2TBCPP porphyrin molecule that we employed. The molecule consists of a free-base porphyrin core functionalized with two meso-(3,5-dicyanophenyl) and two meso-(3,5-di-tert-butylphenyl) peripheral rings. Carbonitrile groups (CN) are well-known to enhance organometallic complexation, which in our case ensures a strong anchoring to the Cu(111) surface. STM images (Fig. 11.4b) show individual molecules oriented along the [110] and equivalent symmetry directions of the Cu(111) surface.

The single molecules appears by STM (Figs. 11.4b, 11.5a) as two bright spots and two darker one, corresponding to the di-tert-butylphenyl and dicyanophenyl moieties, respectively. Upon adsorption particularly due to the strong CN-Cu interaction between molecule and surface, a conformational change occurs meaning that the molecular structure is strongly deformed. Instead of the C_4 symmetry of the gas phase, molecules are flat-lying and have a C_{2v} symmetry so called saddle-conformation. In this conformation, the dicyanophenyl-groups are slightly rotated out of the surface plane in such way that one CN group always remains closer towards the substrate compared to the other one. Steric hindrance between the adjacent legs further leads to a bending of the pyrrole units of the central macro-cycle up- and downwards by about 20°–30° [89].

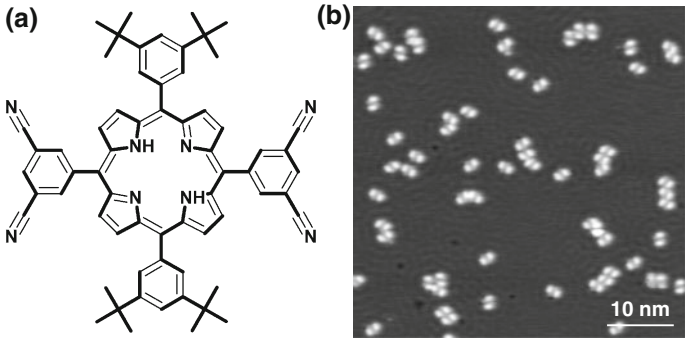

Fig. 11.4 **a** Chemical structure of the free-base porphyrin equipped with two meso-(3,5-dicyanophenyl) and two meso-(3,5-di-tert-butylphenyl) rings. **b** Constant-current STM image of single porphyrins adsorbed on Cu(111) adopting a saddle-shape geometry (I_t = 25 pA, V = 500 mV)

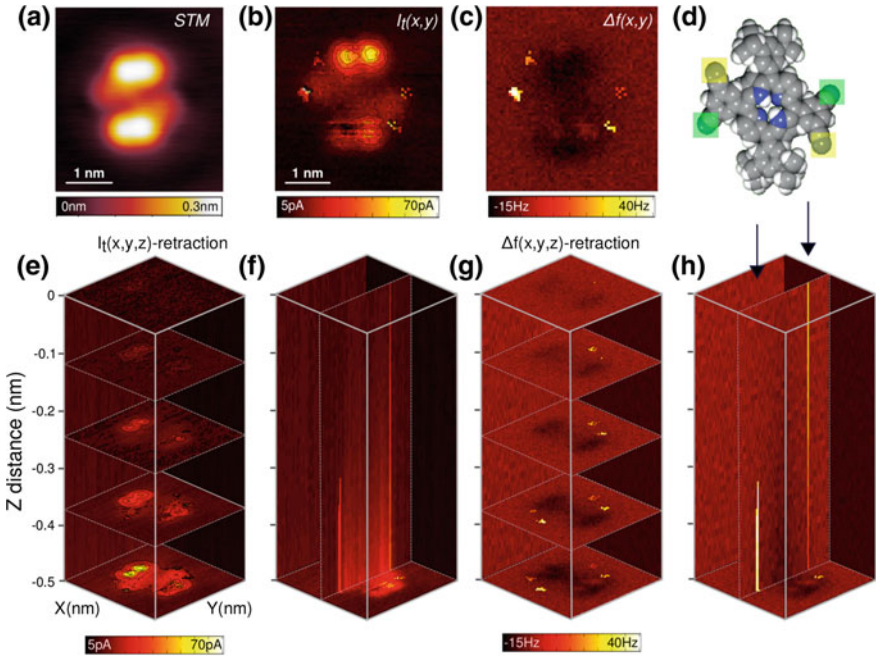

Fig. 11.5 **a–c** show a constant-current STM image, the closest $I_t(x, y)$ and $\Delta f(x, y)$ maps obtained a single porphyrin, respectively. **d** depicts the molecular adsorption symmetry. **e, f** Are $I_t(x, y)$ maps at different tip heights and a $I_t(x, z)$ crosssection, whereas (**g, h**) are the corresponding $\Delta f(x, y)$ maps and $\Delta f(x, z)$ crosssection. Four spots of positive frequency shift are identified with sub-molecular precision in the $\Delta f(x, y)$ maps (**c**) and help the chemical recognition of the N atom locations of the dicyanophenyl side groups in the molecule structure. Tip-molecule chemical bindings can be done through them allowing to apply local deformations to the molecule

11.3.2.1 Carbonitrile Group Recognition and Force-Induced Rotations

Systematic 3D spectroscopic measurements were conducted above single porphyrins in cuboids of $3.2 \times 3.2 \times 0.5$ nm^3 consisting of $68 \times 68 \times 128$ data points. The closest recorded $I_t(x, y)$ map (Fig. 11.5b) reveals the local electronic density of the molecule at the Fermi level and recalls the shape observed by STM (Fig. 11.5a). In contrast, the closest $\Delta f(x, y)$ map and the $\Delta f(x, z)$ cross-sections (Fig. 11.5g, h) show the molecule mainly as a dark protrusion all along the tip-sample z distance. Since only long-range attractive interaction forces are inducing the molecular contrast, the achievement of resolution of the chemical structure cannot be expected. A the periphery of the molecule, four localized peaks with more positive Δf ($\approx$30 Hz) corresponds to the exact location of the N atoms of the CN side groups. The same phenomena is also visible in the current channel, manifested by abrupt jumps to higher currents (Fig. 11.5e, f). The Δf remains positive several hundreds of picometers during the tip retraction (see arrows in Fig. 11.5h).

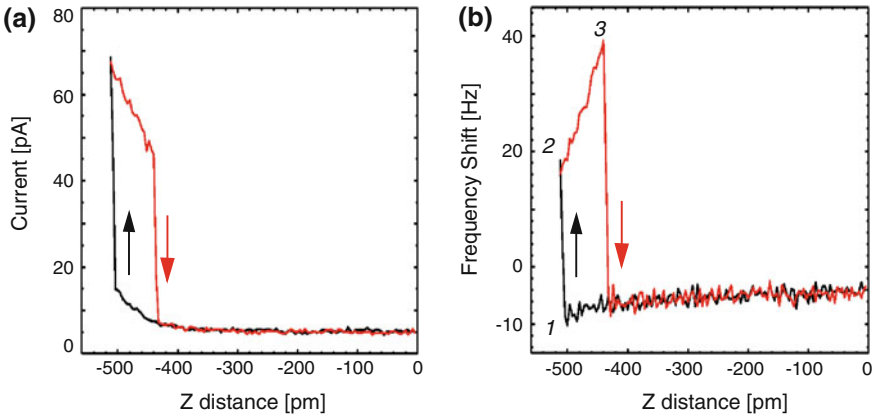

Fig. 11.6 **a** Individual approach-retract $I_t(z)$ and $\Delta f(z)$ curves taken at the N atom position. A tip-molecule junction is formed during approach (transition 1–2 in **b**) which allows the manipulation of the dicyanophenyl leg during retraction (region 2–3)

To better understand these local instabilities, we plot single approach/retract $I_t(z)$ and $\Delta f(z)$ curves recorded at a single N site. Both curves (Fig. 11.6a, b) feature a hysteresis loop close to $z = 0$ between the forward and backward sweeps with abrupt jumps in I_t and Δf, that we attribute to a junction formed between the N atom of the molecule and the Cu-terminated tip. The integration of the $\Delta f(z)$ curve along the z direction up to 1 (Fig. 11.6b) represents the tip-sample interaction force $F_{ts} \approx 180$ pN required to create the bond. The tip-sample stiffness k_{ts} extracted from the Δf is ≈ 1.5 N/m at 1 and corresponds to the stiffness of the tip-molecule junction. This chemical interaction results from the coordination between Cu adatoms of the tip apex and a single N atom of the CN group. While the tip is being retracted (region 2–3), this bond is sufficiently strong to lift the CN group vertically. At larger tip-sample distance ($z \geq 400$ pm), $I_t(z)$ and $\Delta f(z)$ perfectly coincide indicating that the hysteresis process do not induce strong tip changes. Importantly, the manipulated side group recovers its initial position which was systematically confirmed with STM images afterwards. The hysteretical switching is reversible and observed regardless of the considered molecule and the targeted N atom. Therefore, we demonstrate that force spectroscopy can be employed for recognizing specific chemical groups of a single molecules. In the following we used this ability recognize and control this bound in order to apply localized forces to the molecular structure leading to its controlled deformation.

Using this method, we found that a planar rotation of the molecule is reliably induced on the surface with a single z spectroscopic curve when the tip is slightly further approached ($\approx$20 pm) compared to Fig. 11.6. Details of the spectroscopic curves can be found in [62]. The manipulation process, depicted in Fig. 11.7a–c, consists of a 60° rotation. The rotation direction with respect to the initial orientation is mediated by the N atom chosen to generate the tip-molecule junction (Fig. 11.7a). Thereafter,

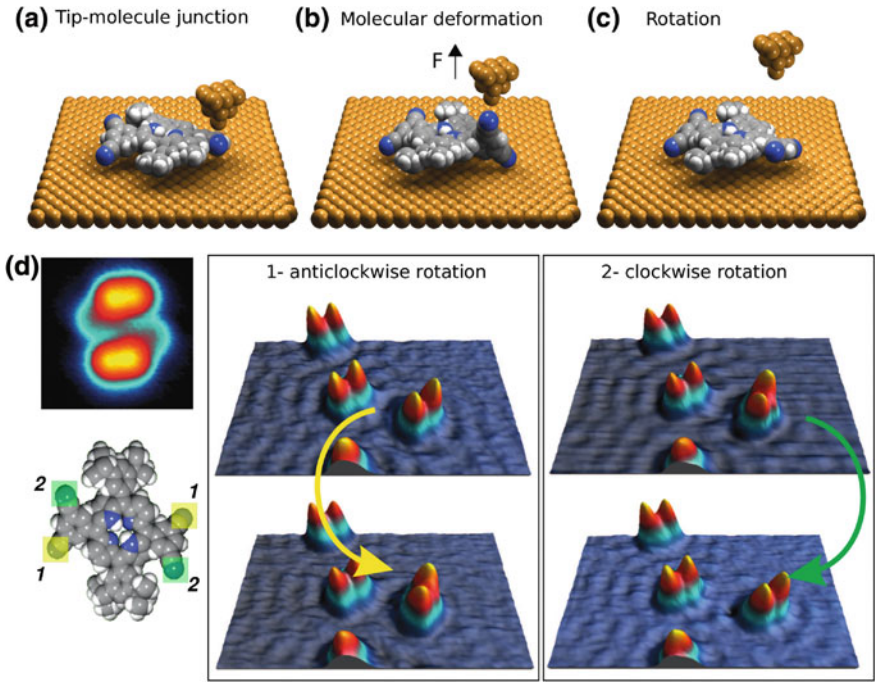

Fig. 11.7 a–c Cartoon of the manipulation experiment consisting of the rotation of the dicyanophenyl end group by the tip. **d** The molecule has four CN function which can be used for the manipulation process. Anti-clockwise and clockwise rotations are induced by taking a single spectroscopic curve at *2* and *1*, respectively

a single spectroscopic curve is acquired inducing the rotation of the dicyanophenyl side groups (Fig. 11.7b) and the distortion of the molecular structure. The manipulation of the porphyrin leg induces the displacement of the CN group in contact with the surface. By further retracting the tip, the tip-molecule junction ruptures and the molecule readopts the saddle conformation and rotates by 60° (Fig. 11.7c). We found that clockwise rotations are induced by attaching the tip to the N sites noted 2, whereas counterclockwise rotations arise from the sites 1 regardless of the chosen enantiomer (Fig. 11.7d). Furthermore, to avoid lateral shifts due to drift or piezo creep and to reach successfully to the N site, atom-tracked tip positioning was activated above one tert-butyl group before the spectroscopic curve. These results thus demonstrate the controlled vertical, lateral and rotational manipulations of isolated porphyrins by means of single force spectroscopy. It particularly opens the study of more complex molecular systems using this technique.

11.3.3 Vertical Manipulation of Long Molecular Chains

To further investigate the mechanical degree of freedom of single molecule structure, we mimicked pulling experiments of long molecular chains as performed in biology with for example proteins and DNA. For that purpose, we used a well-defined polymeric chain synthesized in-situ and measured its mechanical properties with force spectroscopy while lifting it [90].

Based on on-surface chemistry approach [91, 92], polyfluorene molecular chains were synthesized on Au(111) from evaporated dibromoterfluorene molecules (DBTF, Fig. 11.8a). The molecule consist of three fluorene units terminated by Br atoms at both ends. At elevated temperature (490 K), a debromation process occurs allowing the radicals to diffuse and covalently link as molecular chains. Previous experiments

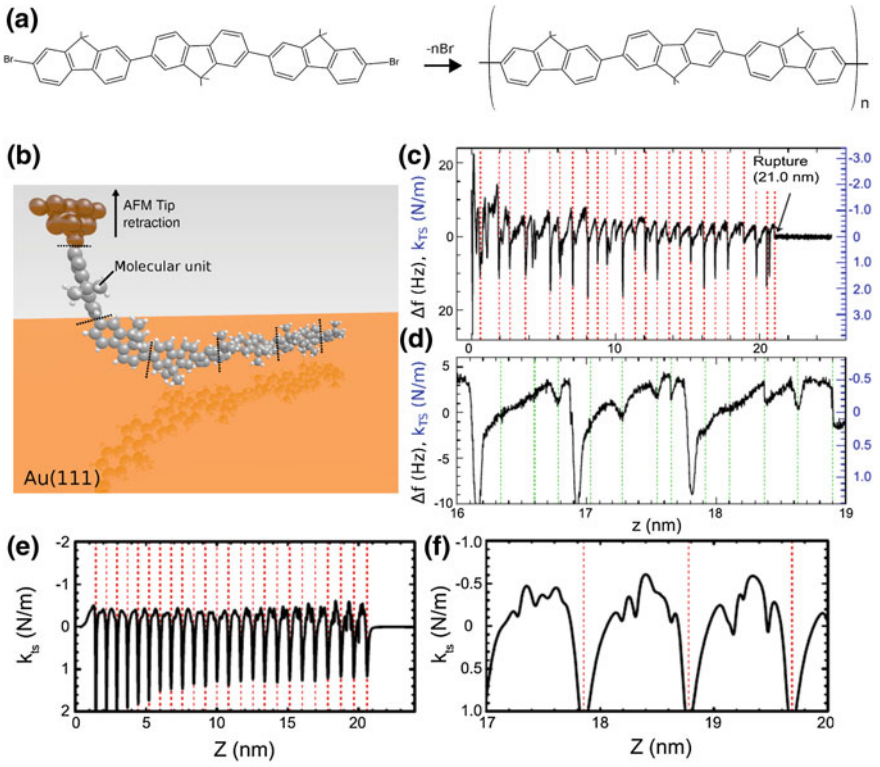

Fig. 11.8 **a** Polymerization reaction induced on Au(111) to produced long molecular chains from dibromoterfluorene (DBTF) molecules. **b** Concept of the experiment: the AFM tip connected to the end of the molecular chain is employed to performed pulling experiments. **c** $\Delta f\,(z)$ curve obtained during the lifting of the macromolecule. The detachment is marked by the *arrow*. **d** Magnification around $z = 17.5$ nm. **e** Calculated dependence of the normal force gradient versus tip-surface distance z. **f** Magnified view showing superimposed modulation between three detachment events

by Lafferentz et al. demonstrated that vertical manipulations of single chains can be further performed to measure their conductance [93]. To do that, the Au-terminated tip apex is positioned precisely at the end of the molecular chain close enough to connect to the chain.

With the same approach, pulling experiments were performed to measure the mechanical behavior of polymers during their lifting as depicted in Fig. 11.8b [90]. Figure 11.8c shows the measured $\Delta f(z)$ curve up to a distance of 25 nm during the vertical manipulation of a 20-nm long chain. The effective stiffness, calculated from the Δf, is indicated on the right scale. A periodic variation is observed, with each period terminated by an abrupt jump (indicated by the red broken lines). The number of periods (24) exactly corresponds to the number of the fluorene units previously observed by STM imaging. At the end of the $\Delta f(z)$ curve, the Δf is $\approx$0 Hz as a result of the detachment of the molecular wire from the surface. Interestingly, the periodicity of the curve is $\approx 0.91 \pm 0.07$ nm which coincides with the length of a single fluorene unit of the chain (0.845 nm). We conclude that the chain has a stepwise detachment from the surface, unit after unit, which is readily detected by force spectroscopy. A closer observation of few periodic events (Fig. 11.8c) also reveals that a second minor modulation marked by green broken lines. Its periodicity is close to the substrate lattice direction along which the molecular chain is sliding while being pulled (0.5 nm).

To quantify further the experimental results and explain these periodic modulations, we developed an extended version of the Frenkel-Kantorova (FK) model. In analogy to the FK model, the molecular chain is approximated by a series of coupled particles connected by equivalent springs of stiffness k and equilibrium length b. Each unit interacts with the substrate through a sinusoidal potential simulating the Au(111) surface. In addition to the FK model, a more realistic interaction potential to estimate the surface-molecule interactions was used, introduced to describe gas-atom solid interactions by Steele [94]. More details about the model can be found in [90]. As shown in Fig. 11.8e, f, the model perfectly reproduces the experimental $\Delta f(z)$ curves revealing that both periodicities resulting from the stepwise detachment as well as the sliding of each unit on the surface. It is however essential that the effective stiffness of the pulled-off segment is large compared to tip-sample stiffness ($\approx$tip-molecule bond).

A remarkable advantage of these simulations is to analytically estimate the normal force required to detach one unit (attractive force of $\approx$0.25 nN) and shows that this force is nearly independent of the length of the chain and the unit position in the chain. In addition, the model provides new insights into normal and lateral forces acting on the pulling tip which are difficult to determine from the measured Δf and energy dissipation without questionable assumptions. This simulation is remarkably simple and its flexibility further allows to adapt it to more complex molecular systems by varying interaction and deformation potentials for different units and/or adjusting parameters to account for specific interactions with atomic lattices. These results confirmed the capability of force spectroscopic experiments to probe mechanical behavior of molecular structure at the sub-molecular level. It further gives new insights into the friction phenomena during manipulation processes.

11.3.4 Lateral Manipulation of Single Porphyrin: Atomic-Scale Friction Pattern

In the following experiment, we particularly studied this sliding characteristic. Instead of pulling a molecule with the tip apex, we manipulated a single molecule laterally attached to the tip apex over an atomically clean surface [95]. To perform these lateral manipulations with single porphyrins, we intentionally terminated the tip apex with a single molecule. The molecule we used is described in Sect. 11.2 Fig. 11.4. The tip apex is decorated by picking up the molecule from the Cu(111) surface via indenting the tip onto the center of the molecule.

The friction experiments are then conducted by approaching the porphyrin-terminated tip to the Cu surface while oscillating the tuning fork sensor with small oscillation amplitudes (≈50 pm). Figure 11.9b shows a typical $\Delta f(x, y)$ map obtained by scanning the Cu(111) surface at constant height. An atomic-scale contrast is clearly observed which resembles the frictional patterns obtained by conventional Friction Force Microscopy on Cu(111). The hexagonal structure has a periodicity of ≈0.26 nm which closed to the expected one for the Cu(111) lattice of ≈0.29 nm. A dark depression is also observed in the bottom right part of the image which corresponds to a Cu vacancy of the surface. Figure 11.9c shows line profile taken within the image of the tip-sample stiffness $k_{ts}(x)$ extracted from the Δf data. The maximum k_{ts} is about 3 N/m and the average stiffness variation Δk_{ts} is ≈5 N/m which corresponds to the tip-surface stiffness mediated by the porphyrin molecule.

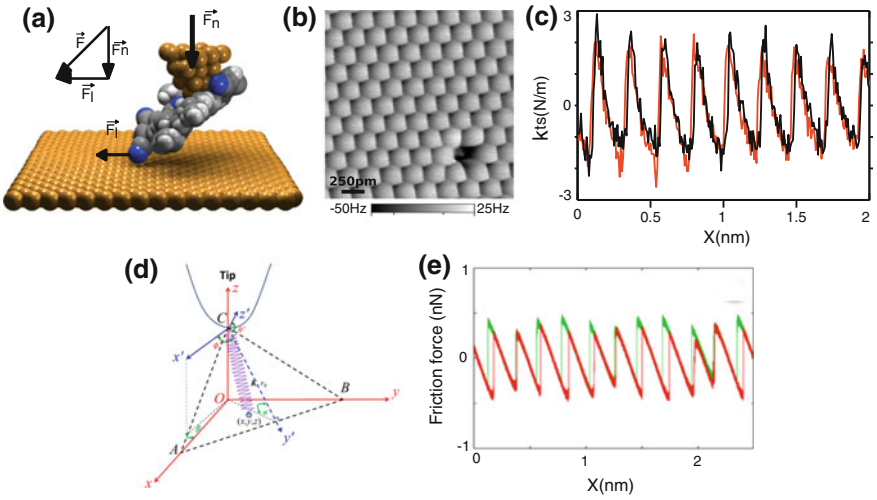

Fig. 11.9 **a** Cartoon of the experiment: a single porphyrin is attached to the tip by vertical manipulation and dragged over a Cu(111) surface. **b** Constant-height $\Delta f(x, y)$ map above the Cu(111) surface revealing a typical friction-like pattern. **c** Profile showing the sawtooth modulation. **d** Model of the simulation based on the generalized Tomlinson model and **e** the simulated profile

We attribute this to the CN end-groups and their ability to coordinate with copper atoms of both the tip and the surface (Cu-coordinated bonds) which ensure the stability of the junction and particularly its atomic nature. Moreover, we assume that the degree of freedom of the dicyanophenyl leg and particularly its σ bond attaching the leg to the porphyrin core ensures the frictional process.

In order to demonstrate this effect on friction and adhesion, we employed a generalization of the Tomlinson model using the Steele potential, that includes the reorientation of the dicyanophenyl ring with respect to the porphyrin core and stretching of the bond. As shown in Fig. 11.9d, the CN-Cu interaction is approximated by a masse m attached to the tip by a spring k. The reorientation of the porphyrin leg with respect to the porphyrin core is described by the polar angles, ϕ' and θ', of this spring as shown in Fig. 11.9d. The stretching of the bond is given by the deviation of the bond length, r' compared to the equilibrium value r_0. All these parameters can change during the simulation which are describe in details in [95].

Figure 11.9e shows the simulation of friction response for a specific scan angle which reproduces the experimental data. Different orientations of the molecule with respect to the tip were also analyzed as well scan angle [95]. As main conclusions, we emphasis that: (1) the friction loop between the forward and backward scans is small showing that, despite of the complex molecular structure attached to the tip, an atomic-scale patterns can be obtained; (2) the friction forces depend on the attachment of the molecule to the tip that is characterized by the angles; (3) forward and backward force traces can exhibit anisotropy that arises from changes of molecule conformation during sliding. Both experiments and simulations thus show that including the dynamics of degrees of freedom of molecules is crucial for understanding mechanism during their lateral and normal manipulations. Understanding such mechanical behavior might help to foresee the appropriate chemical groups with respect to surfaces as well as the preferential displacement of molecular nanomachines in motion.

11.4 Prospects in Probing the Electronic Properties of Single Molecules

With the advent of force spectroscopy at low temperature, it is now possible to investigate local contact potential difference (LCPD) between tip and sample (see Sect. 11.2) which is related to work function changes, local dipole moments, inhomogeneties of charge distributions as well as local polarization effects down to the nanometer scale. Based on the detection of electrostatic forces via $\Delta f(V)$ spectra, LCPD mapping provides insights into charges states at the atomic scale [51–54] or the sub-molecular charge distribution of single molecules [55–58]. The following examples report LCPD maps of the charge distribution of single molecules as well as an experimental approach to investigate their optical properties in the future.

11.4.1 LCPD Mapping of a Donor-Acceptor Molecule

To confirm the ability of LCPD mapping to spatially resolve charge distribution at the sub-molecular scale, we employed donor-acceptor molecules, the 4-(4-(2,3,4,5,6-pentafluorophenylethynyl)-2,3,5,6-tetrafluorophenylethynyl)-phenylethynylbenzene (FFPB), deposited at room temperature on reconstructed (2×1)-Au(110) [57]. As revealed by the STM investigation (Fig. 11.10), chains are spontaneously formed and oriented with respect to the surface orientation. The FFPB consists of four benzene rings interlinked by ethynylene units. Two aromatic benzene rings are substituted with fluorine where the two other are free-based (H-terminated). According to DFT calculation, the electronegativity of the F atoms compared to the H atoms induces a net dipolar moment of 4.27 D along the chain. The electronegativity of the F-substituted benzene rings in FFPB acts as an acceptor compared to the benzene ring of the molecule end, the being donor part. The self-assembly depicted in Fig. 11.10b is mediated by the formation of (C–F...H–C) hydrogen bonds between the fluorine units and H-terminated carbon rings, leading to the structural deformation of the molecular structure which has been confirmed by AFM imaging and DFT calculations [57].

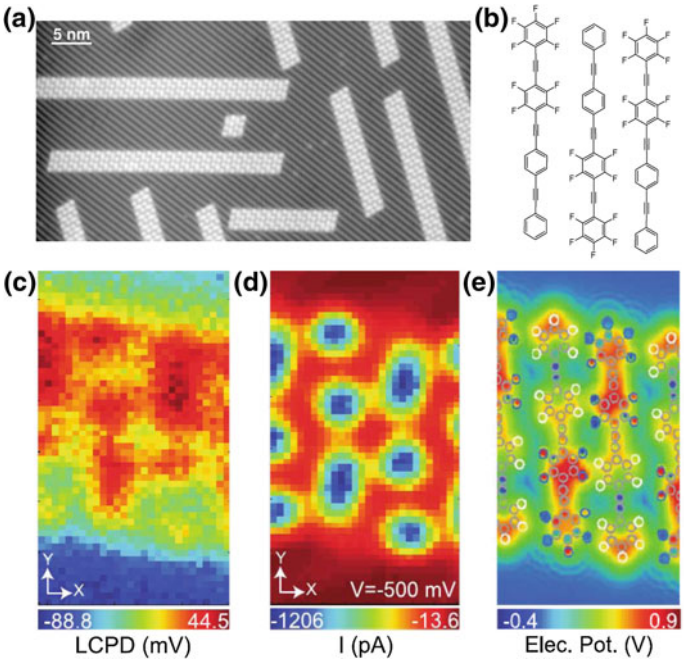

Fig. 11.10 **a** STM image of the FFPB molecules deposited on (2 × 2-Au(110)) at room temperature. **b** The chemical structure of the FFPB molecules and the self-assembly developed on Au(110). **c, d** Constant-height $LCPD(x, y, V^*)$ and $I_t(x, y, V^*)$ maps of a chain revealing intra-molecular resolutions. **e** Electrostatic potential simulated by DFT on a plane above the molecular plane

Figure 11.10c, d shows constant-height $LCPD(x, y, V^*)$ and $I_t(x, y, V^*)$ maps, respectively. The current map shows a similar contrast to the STM data with adjacent molecules in the chain having identical contrast with an opposite direction. In addition, the LCPD map reveals the internal charge distribution of the molecule. The variation of LCPD between the surface and the molecule is about $\Delta LCPD \approx 120$ mV whereas the internal charge distribution shows a $\Delta LCPD \approx 10$ mV. Since the bias voltage is applied to the tip, the negatively charged part has a more positive LCPD value. Therefore, the LCPD map allows a clear identification of the donor-acceptor parts within the molecule as further confirmed by numerical of the electrostatic potential of the system (Fig. 11.10e). With the prospects of studying photo-induced electronic effects in such molecules, LCPD mapping has thus the great advantage to precisely resolve the charge distribution of molecules down to the sub-molecular scale.

11.4.2 LCPD Mapping of Metal-Phtalocyanin on Thin Insulating Films

To preserve the electronic integrity of single molecules and thus their optical properties, it is essential to perform such experiments on insulating layers to avoid "quenching" by the metal. Therefore, we performed similar experiments on Cu-based phtalocyanin (CuPc) (Fig. 11.11a) adsorbed on two NaCl monolayers on Cu(111) [96]. STM images of the single CuPc molecule is shown in the top of Fig. 11.11b. Two molecular resonances derived from respective orbitals are clearly visible and can be attributed to the HOMO (≈2.3 V) and the LUMO (≈1.4 V). STS spectrum (blue curve) recorded at the center of the molecule confirms the positions of the HOMO and LUMO respectively (Fig. 11.11b). Importantly, this suggests that the electronic structure of the molecule is preserved upon adsorption [70]. Furthermore, a STM image acquire within the molecular band gap shows a contrast dominated by the charge distribution close to the Fermi-level, which also features a charge depletion area at the center of the molecule.

Constant-height $I_t(x, y, V^*)/LCPD(x, y, V^*)$ mapping are shown in Fig. 11.11b, c, respectively. Figure 11.11b clearly recalls the constant-current STM obtained in the band gap (Fig. 11.11b). The contrast above the molecule in the LCPD map is shifted to larger LCPD values compared to the substrate with an overall value of ≈80 mV. In addition, a modulation of the LCPD within the molecule is observed of ≈60 mV with a pronounced dip above the central Cu atom. The peripheral rings of the molecule appear with more positive LCPD (≈80 mV). In analogy with the $I_t(x, y)$ maps, the LCPD variation at the center of the molecule most likely reflects the charge depletion at the central Cu atoms of the molecule.

The recent LCPD resolutions of single molecules thus demonstrate that precise determination of the charge distributions of molecules is possible at the sub-molecular scale [55–57]. These results show that force spectroscopy might be able

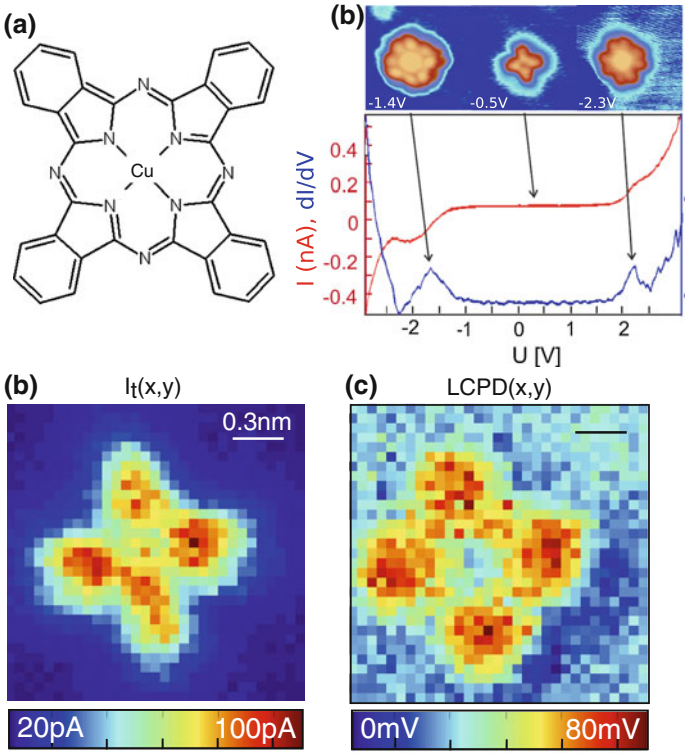

Fig. 11.11 **a** The Cu-phtalocyanin structure. **b** STS spectra and corresponding STM images of the molecule adsorbed on NaCl thin films/Cu(111). **c** Constant-height $I_t(x, y, V^*)$ maps and $LCPD(x, y, V^*)$ maps of the molecule

to detect charge transfer through single molecules via external excitation, for instance molecules contacted between nanoelectrodes or photo-excited. The following experiment describes the experimental approach we employed to detect photo-excited color centers in nanoparticles.

11.4.3 Towards Probing Optical Properties of Single Molecules

Nanodiamonds (NDs) are carbon particles with sizes from two to few tens of nanometers having a diamond structure, that we deposited on graphite in order to probe their structural and optical properties via force spectroscopy. The NDs, characterized by STM in Fig. 11.12b, also contain sub-surface nitrogen-vacancy centers (NV) which are lattice point defects of a crystal inducing new optical absorption bands. These nitrogen centers in diamond consists of a substitutional nitrogen atom associated with a vacancy in the carbon lattice (see inset Fig. 11.12a). They induce additional

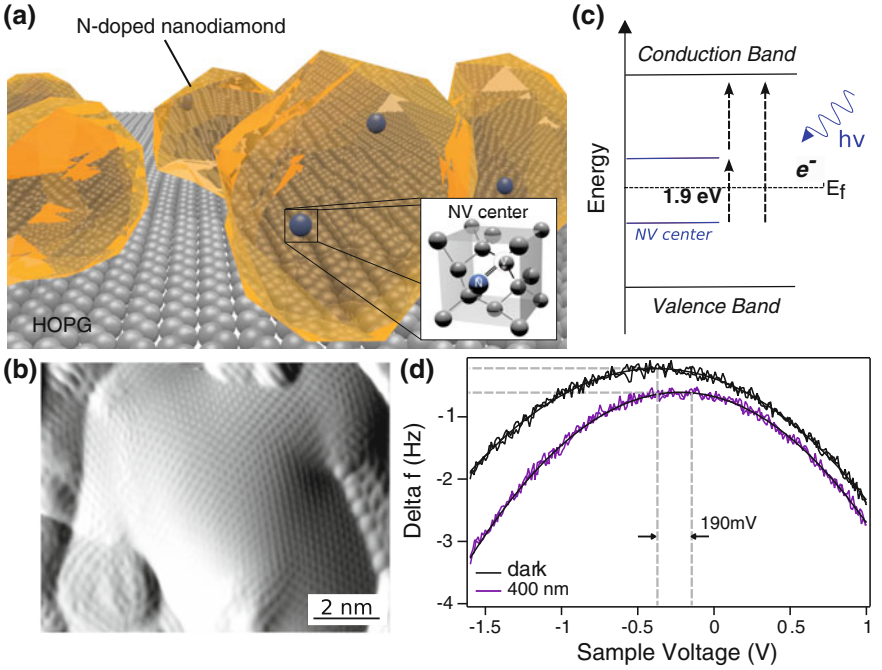

Fig. 11.12 **a** Cartoon of the experiment: nanodiamonds (ND) which contain Nitrogen-Vacancy centers (NV) are deposited on a graphite surface. **b** These *color* centers induce electronic states within the diamond band gap. **c** STM image of a single ND particle. **d** Comparison of single $\Delta f(V)$ spectra obtained above a ND under dark and 400 nm illuminations revealing a clear shift ($\approx$190 mV) of the LCPD

electronic states in the large band gap of diamond (Fig. 11.12c) and have a maximum adsorption at $\lambda = 638$ nm, so-called the zero-phonon line (ZPL). Because these particles are small, probing their optical properties is extremely challenging with conventional optical techniques. We thus conducted force and current spectroscopic measurements at low temperature to address this issue [64].

Figure 11.12d shows a comparison of $\Delta f(z, V)$ curves above the same ND under dark and 400 nm illumination. The extracted LCPD shows a variation of $V_{LCPD} = V^*$ of $\approx$190 mV. Such lateral shift of the parabola maximum is known to result from localized charges in the vicinity of the surface [51]. The vertical shift is related to the stronger electrostatic force contribution most likely arising from these charges. These observations are consistent with the photoexcitation of the defect centers of NDs and thus confirm that optical properties of materials can be measured locally. However, the variation of the force field under illumination might also induce a change of the tip-sample distance reflected then in the LCPD measurements. To ensure the interpretation, the z dependency of the LCPD must thus be know from the long-range to the short-range regime of electrostatic forces.

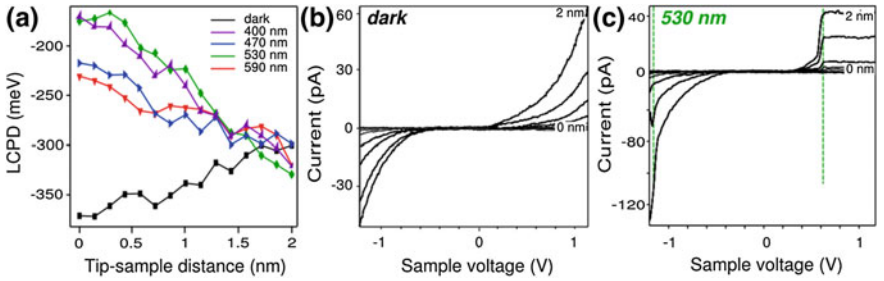

Fig. 11.13 **a** LCPD values as a function of the tipsample distance z above a single diamond under different illumination conditions. In the graph, *colors* correspond to the wavelengths (*purple* 400 nm, *blue* 470 nm, *green* 530 nm, and *red* 590 nm. **b**, **c** $I(V, z)$ spectra at different heights in dark and $\lambda = 530$ nm illumination, the z variation between curves is 15 pm

To do that, we conducted systematic $I_t(z, V)/\Delta f(z, V)$ spectroscopic measurements under five illumination conditions (dark, 400, 470, 530, and 590 nm) above the same diamond (Fig. 11.13a). In dark (dark curve) and at large tip-sample separation (z = 2 nm), the extracted LCPD value is ≈300 mV. When entering the short-range regime of electrostatic forces by decreasing the tipsample distance, the LCPD then decreases to 350 mV as a consequence of the appearance of charge images at the tip apex. At close distance (z = 0 nm), the difference of the LCPD values, $\Delta(V_{LCPD})$, observed between $\lambda = 400$ and 470 nm is ≈50 ± 5 mV and arises from different photoionization processes, i.e. electrons excited from various electronic states are transferred to the conduction band.

When illuminating at $\lambda = 590$ and 530 nm (red and green curves), a positive variation of the LCPD values is also observed which contrasts with the variation in dark. Here, the LCPD variation is induced by the continuous photoexcitation of electrons through the NV electronic states. The photocharges are only localized at the NV centers and not transferred to the conduction band due to lack of photon energy. They are however detected as LCPD variation toward more positive values. The $\Delta LCPD$ between these wavelengths at z = 0 nm is ≈70 ± 5 mV. The maximum of electronic transition for NVs is obtained for $\lambda = 530$ nm which is also the maximum LCPD shift compare to the reference value obtained in dark (190 ± 5 mV). Therefore, we conclude that the comparison of LCPD spectroscopic measurements under continuous illumination conditions is sensitive to photo-created charges in defect centers. To further confirm this claim, we also analysed the simultaneously recorded tunneling current. Figure 11.13c, d shows the evolution of the conductance curves versus the tipsample separation z under dark and $\lambda = 530$ nm illumination, respectively. A comparison of these curves clearly reveals the appearance of steps for the irradiated ND (Fig. 11.13c, green dashed lines) whereas, in dark, they are not present. These kinks in the $I(V)$ curve are the signature of the electronic states of the photo-excited NV centers. The HOMO of the NV centers lies at ≈1.2 eV below the Fermi level whereas the LUMO is found at ≈0.6 eV. The HOMO-LUMO gap is 1.8

eV and coincides with the zero phonon line of the centers obtained experimentally (1.945 eV) or theoretically predicted (1.75–1.85 eV).

Our results demonstrate that combined current and force spectroscopic measurements under continuous illumination can detect at the nanometer scale subsurface color centers of NDs through their optical excitation. We show that the z variation of the short-range electrostatic forces obtained from LCPD spectroscopy also depends on the utilized wavelenghts to photo-excite the system. Similar light-assisted spectroscopic experiments on molecular systems adsorbed on thin insulating layers might thus resolve the effect of radiation on single molecules at the sub-molecular scale.

11.5 Conclusion and Perspectives

With the advent of qPlus sensors operated at low temperature, tunneling current and force spectroscopic measurements are widely employed to reveal atomic-scale physical phenomena at surfaces. In this chapter, we reviewed our recent works applying such spectroscopic techniques to single molecules in order to reveal their intrinsic properties at the atomic scale. Particularly, the extraction of forces from the measured frequency shift helps to probe the structure of single molecules as well as their local mechanical behavior. Although the interpretation of the Δf data must be done with careful experimental considerations, appropriate numerical models provide insights into the degree of freedom of single molecules. We showed that the degree of freedom and the frictional properties of single molecular species during vertical or lateral manipulations can be understood from force spectroscopic data obtained at the sub-molecular level. We foresee that further "mechanical" based phenomena might be elucidated at this level with these techniques such as mechano-chemistry reaction or the mechanical and frictional behavior of molecular nanomachines.

In addition to their mechanical properties, we show that current/force based spectroscopic measurements help studying the electronic character of single molecules. When current information versus the tip-sample voltage V provides molecular band gaps and orbitals, our results also prove that short-range electrostatic force variations obtained from the variation of Δf as a function of V can also image the charge distribution of molecules at the sub-molecular scale. We further demonstrated that spectroscopic measurements under illumination reveal the photo-activity of defect centers in nanoparticles from the creation of localized charges. Although some experimental and theoretical issues must be still addressed, these experiments clearly open the way to study charge transfers through single molecules via external electrodes or their photo-activity under variable illumination conditions at the atomic scale.

Acknowledgments The authors are very grateful to their colleagues: Dr. Sweetlana Fremy for her help on performing the porphyrin experiments and her work on LCPD mapping of CuPc and Dr. Ali Sadeghi and Dr. Alexis Baratoff for fruitful discussions and their precious theoretical contributions. The authors also wish to acknowledge their collaborators: Pr. E. Gnecco for the extended Frenkel-Kantorova model, the group of Pr. F. Diederich for providing the porphyrin molecules, the group of Pr. L. Grill and Pr. S. Hecht for their contribution in the DBTF molecule experiments, the group of

Pr. A. Orita for providing the FFPB molecules, the group of Pr. Urback for the numerical calculations of the friction experiment with porphyrins and the group of Pr. D. Spitzer and Dr. V. Pichot for the preparation of the nanodiamond samples.
These works is supported by the from the Swiss National Science Foundation (NSF), the Swiss nanoscience Institute (SNI), the Swiss National Center of Competence in Research on Nanoscale Science (NCCR-NANO), the PRESTO project of the Japan Science and Technology agency (JST), the Polish-Swiss Project PSPB-085/2010 and the EU Cost action MP13V3.

References

1. G. Binnig, H. Roher, Ch. Gerber, E. Weibel, Phys. Rev. Lett. **49**, 57 (1982)
2. G. Binnig, C.F. Quate, Ch. Gerber, Phys. Rev. Lett. **56**, 930 (1986)
3. S. Morita, R. Wiesendanger, E. Meyer, *Noncontact Atomic Force Microscopy* (Springer, Berlin, 2002)
4. E. Meyer, H.J. Hug, R. Bennewitz, *Scanning Probe Microscopy: The Lab on a Tip* (Springer, Berlin, 2003)
5. K.C. Neuman, A. Nagy, Nature Methods **5**, 491–505 (2008)
6. F.J. Giessibl, Science **267**, 68 (1995)
7. S. Kitamura, M. Iwatsuki, JJAP **34**, L145–L148 (1995)
8. H. Ueyama, M. Ohta, Y. Sugawara, S. Morita, Jpn. J. Appl. Phys. **34**, L1086 (1995)
9. S. Orisaka, T. Minobe, T. Uchihashi, Y. Sugawara, S. Morita, Appl. Surf. Sci. **140**, 243 (1999)
10. Ch. Loppacher, M. Bammerlin, M. Guggisberg, S. Schär, R. Bennewitz, A. Baratoff et al., Phys. Rev. B **62**, 16944 (1999)
11. S.I. Kitamura, M. Iwatsuki, Jpn. J. Appl. Phys. **34**, L145 (1995)
12. A. Schwarz, W. Allers, U.D. Schwarz, R. Wiesendanger, Phys. Rev. B **61**, 2837 (2000)
13. M. Bammelin et al., Probe Microsc. **1**, 3 (1997)
14. W. Allers, A. Schwarz, U.D. Schwarz, R. Wiesendanger, Europhys. Lett. **48**, 276 (1999)
15. C. Barth, M. Reichling, Nature **414**, 54 (2001)
16. B. Gotsmann, D. Krüger, H. Fuchs, Europhys. Lett. **239**, 153 (1997)
17. B. Gotsmann, B. Anczykowski, C. Seidel, H. Fuchs, Appl. Surf. Sci. **140**, 314 (1999)
18. B. Gotsmann, C. Seidel, B. Anczykowski, H. Fuchs, Phys. Rev. B **60**, 11051 (1999)
19. H. Hölscher, W. Allers, A. Schwarz, U.D. Schwarz, R. Wiesendanger, Phys. Rev. Lett. **83**(23), 4780 (2003)
20. H. Hölscher, A. Schwarz, W. Allers, U.D. Schwarz, R. Wiesendanger, Phys. Rev. B **61**, 12678 (2000)
21. H. Hölscher, B. Gotsmann, W. Allers, U.D. Schwarz, H. Fuchs, R. Wiesendanger, Phys. Rev. B **64**, 075402 (2001)
22. H. H ölscher, S.M. Langkat, A. Schwarz, R. Wiesendanger, Appl. Phys. Lett. **81**, 4428 (2002)
23. M.A. Lantz, H.J. Hug, R. Hoffmann, P.J.A. van Schendel, P. Kappenberger, S. Martin et al., Science **291**, 2580 (2001)
24. M. Heyde, G.H. Simon, H.P. Rust, H.-J. Freund, Appl. Phys. Lett. **89**, 263107 (2006)
25. Y. Sugimoto, P. Pou, M. Abe, P. Jelinek, R. Perez, S. Morita, Nature **446**, 64 (2007)
26. J. Welker, A.J. Weymouth, F. Giessibl, ACS Nano **7**, 7377 (2013)
27. Y. Sugimoto, M. Abe, S. Hirayama, N. Oyabu, O. Custance, S. Morita, Nat. Mat. **4**, 156 (2005)
28. Y. Sugimoto, P. Pou, O. Custance, P. Jelinek, M. Abe, R. Perez et al., Science **322**, 413 (2008)
29. S. Kawai, A.S. Foster, F.F. Canova, H. Onodera, S.-I. Kitamura, E. Meyer, Nat. Commun. **5**, 4403 (2014)
30. K. Ruschmeier, A. Schirmeisen, R. Hoffmann, Phys. Rev. Lett. **101**, 156102 (2008)
31. A. Schrimeisen, D. Weiner, H. Fuchs, Phys. Rev. Lett. **97**, 136101 (2006)
32. B.J. Albers, T.C. Schwendemann, M.Z. Baykara, N. Pilet, M. Liebmann, E.I. Altman et al., Nat. Nanotechnol. **4**, 307 (2009)

33. M. Ashino, D. Obergfell, M. Haluska, S. Yang, A.N. Khlobystov, S. Roth et al., Nat. Nanotechnol. **3**, 337 (2008)
34. S. Kawai, Th Glatzel, S. Koch, A. Baratoff, E. Meyer, Phys. Rev. B **83**, 035421 (2011)
35. B. Such, T. Glatzel, S. Kawai, S. Koch, E. Meyer, J. Vac. Sci. Technol. **B 28**, C4B1 (2010)
36. M. Ternes, C.P. Lutz, C.F. Hirjibehedin, F.J. Giessibl, A.J. Heinrich, Science **319**, 1066–1069 (2008)
37. M. Abe, K. Morita, *Noncontact Atomic Force Microscopy, vol. 2* (Springer, Berlin, 2009), Chap. 2, pp. 15–30
38. O. Custance, N. Oyabu, Y. Sugimoto, *Noncontact Atomic Force Microscopy, vol. 2* (Springer, Berlin, 2009), Chap. 3, pp. 31–68
39. A. Schirmeisen, H. Hölscher, U. Schwarz, *Noncontact Atomic Force Microscopy, vol. 2* (Springer, Berlin, 2009), Chap. 5, pp. 95–119
40. R.J. Wilson, G. Meijer, D.S. Bethune, R.D. Johnson, D.D. Chambliss, M.S. de Vries et al., Nature **348**, 621–622 (1990)
41. B. Gotsmann, C. Schmidt, C. Seidel, H. Fuchs, Eur. Phys. J. B. **4**, 267 (1998)
42. A. Sasahara, H. Onishi, *Noncontact Atomic Force Microscopy* (Springer, Berlin, 2002), Chap. 13, pp. 215–232
43. Y. Sugawara, *Noncontact Atomic Force Microscopy* (Springer, Berlin, 2002), Chap. 11, pp. 183–192
44. L. Nony, E. Gnecco, A. Baratoff, A. Alkauskas, R. Bennewitz, O. Pfeiffer et al., Nano Lett. **4**, 2185 (2004)
45. Ch. Loppacher, M. Guggisberg, O. Pfeiffer, E. Meyer, M. Bammerlin, R. Lüthi et al., Phys. Rev. Lett. **90**, 066107 (2003)
46. M. Ashino, A. Schwarz, T. Behnke, R. Wiesendanger, Phys. Rev. Lett. **93**, 136101 (2004)
47. F.J. Giessibl, *Noncontact Atomic Force Microscopy* (Springer, Berlin, 2002), Chap. 6, pp. 121–142
48. F.J. Giessibl, Rev. Mod. Phys. **75**, 949 (2003)
49. M. Heyde, M. Kulawik, H.P. Rust, H.J. Freund, Rev. Sci. Instrum. **75**, 2446 (2004)
50. L. Gross, F. Mohn, P. Liljeroth, J. Repp, F.J. Giessibl, G. Meyer, Science **324**, 1428 (2009)
51. L. Gross, F. Mohn, N. Moll, P. Liljeroth, G. Meyer, Science **325**, 1110 (2009)
52. T. König, G.H. Simon, H.-P. Rust, G. Pacchioni, M. Heyde, H.-J. Freund, JACS **131**, 17544 (2009)
53. T. Leoni, O. Guillermet, H. Walch, V. Langlais, A. Scheuermann, J. Bonvoisin et al., Phys. Rev. Lett. **106**, 216103 (2011)
54. H. Walch, T. Leoni, O. Guillermet, V. Langlais, A. Scheueurmann J. Bonvoisin, S. Gauthier, Phys. Rev. B **86**, 075423 (2012)
55. F. Mohn, L. Gross, N. Moll, G. Meyer, Nat. Nanotechnol. **7**, 227 (2012)
56. B. Schuller, S.-X. Liu, Y. Geng, S. Descurtins, G. Meyer, L. Gross, Nanolett. **14**, 3342–3342 (2014)
57. S. Kawai, A. Sadeghi, X. Feng, P. Lifen, R. Pawlak, T. Glatzel, E. Meyer et al., ACS Nano **7**, 9098 (2013)
58. F. Mohn, B. Schuller, L. Gross, G. Meyer, Appl. Phys. Lett. **102**, 073109 (2013)
59. F. Mohn, L. Gross, G. Meyer, Appl. Phys. Lett. **99**, 053106 (2011)
60. R. Pawlak, S. Kawai, S. Fremy, T. Glatzel, E. Meyer, ACS Nano **5**, 6349 (2011)
61. R. Pawlak, S. Kawai, S. Fremy, T. Glatzel, E. Meyer, J. Phys. Cond. Matter **24**, 084005 (2012)
62. R. Pawlak, S. Fremy, S. Kawai, T. Glatzel, H. Fang, L.-A. Fendt et al., ACS Nano **6**, 6318–6324 (2012)
63. S. Fremy, S. Kawai, R. Pawlak, Th. Glatzel, A. Baratoff, E. Meyer, Nanotechnology **23**, 055401 (2012)
64. R. Pawlak, Th Glatzel, V. Pichot, L. Schmidlin, S. Kawai, S. Fremy et al., Nano Lett. **13**, 5803–5807 (2013)
65. N. Fournier, C. Wagner, C. Weiss, R. Temirov, F.S. Tautz, Phys. Rev. B **84**, 035435 (2011)
66. N. Hauptmann, F. Mohn, L. Gross, G. Meyer, T. Frederiksen, R. Berndt, New. J. Phys. **14**, 073032 (2012)

67. C. Chiutu, A.M. Sweetman, A.J. Lakin, A. Stannard, S. Jarvis, L. Kantorovich et al., Phys. Rev. Lett. **108**, 268302 (2012)
68. A. Sweetman, S.P. Jarvis, H. Sang, I. Lekkas, P. Rahe, Y. Wang et al., Nat. Commun. **5**, 3931 (2014)
69. C. Lotze, M. Corso, K.J. Franke, F. von Oppen, J.I. Pascual, Science **338**, 779 (2012)
70. J. Repp, G. Meyer, S.M. Stojkovic, A. Gourdon, C. Joachim, Phys. Rev. Lett. **94**, 026803 (2005)
71. J. Repp, G. Meyer, S. Paavilainen, F.E. Olsson, M. Persson, Science **312**, 1196 (2006)
72. M.Z. Baykara, T.C. Schwendemann, E.I. Altman, U.D. Schwarz, Adv. Mater. **22**, 2838 (2010)
73. M. Abe, Y. Sugimoto, T. Namikawa, K. Morita, N. Oyabu, S. Morita, Appl. Phys. Lett. **90**, 203103 (2007)
74. S. Kawai, T. Glatzel, S. Koch, A. Baratoff, E. Meyer, Phys. Rev. B **83**, 035421 (2011)
75. J.E. Sader, S.P. Jarvis, Appl. Phys. Lett. **84**, 1801 (2004)
76. F.J. Giessibl, Phys. Rev. B **56**, 16010 (1997)
77. U. Dürig, Appl. Phys. Lett. **76**, 1203 (2000)
78. F.J. Giessibl, Appl. Phys. Lett. **78**, 123 (2001)
79. B. Such, T. Glatzel, S. kawai, S. Koch, E. Meyer, J. Vac. Sci. Technol. **B 29**, C4B1 (2010)
80. S. Sadewasser, T. Glatzel, *Kelvin Probe Force Microscopy: Measuring and Compensating Electrostatic Forces* (Springer, Berlin, 2012)
81. L. Nony, A.S. Foster, F. Bocquet, C. Loppacher, Phys. Rev. Lett. **103**, 036802 (2009)
82. F. Bocquet, L. Nony, C. Loppacher, Phys. Rev. B **83**, 035411 (2011)
83. A. Sadeghi, A. Baratoff, S.A. Ghasemi, S. Goedecker, T. Glatzel, S. Kawai et al., Phys. Rev. B **86**, 075407 (2012)
84. J. Tersoff, D.R. Hamann, Phys. Rev. Lett. **50**, 1998–2001 (1983)
85. J. Tersoff, D.R. Hamann, Phys. Rev. B **31**, 805–13 (1985)
86. S.A. Burke, J.M. Mativetsky, R. Hoffmann, P. Grütter, Phys. Rev. Lett. **94**, 096102 (2005)
87. L. Gross, F. Mohn, N. Moll, B. Schuler, A. Criado, E. Guitian, A. Diego Pena, A. Gourdon, G. Meyer. Science **337**, 1326–1329 (2013)
88. A.J. Weymouth, T. Hofmann, F.J. Giessibl, Science **343**, 1120–1122 (2014)
89. K. Boukari, P. Sonnet, E. Duverger, Chem. Phys. Chem. **13**, 3945–3951 (2012)
90. S. Kawaia, M. Koch, E. Gnecco, A. Sadeghi, R. Pawlak, T. Glatzel et al., Proc. Natl. Acad. Sci. USA **111**, 3968–3972 (2014)
91. L. Grill, M. Dyer, L. Lafferentz, M. Persson, M.V. Peters, S. Hecht, Nat. Nanotechnol. **2**, 687–691 (2007)
92. N.A.A. Zwaneveld, R. Pawlak, M. Abel, D. Catalin, D. Gigmes, D. Bertin et al., JACS **130**, 6678–6679 (2008)
93. L. Lafferentz, F. Ample, H. Yu, S. Hecht, C. Joachim, L. Grill, Science **323**, 1193 (2009)
94. W.A. Steele, Surf. Sci. **36**, 317–357 (1973)
95. R. Pawlak et al., submitted
96. S. Fremy et al., submitted

Chapter 12
Atomic Resolution on Molecules with Functionalized Tips

Leo Gross, Bruno Schuler, Fabian Mohn, Nikolaj Moll, Jascha Repp and Gerhard Meyer

Abstract Atomic resolution on molecules was obtained by employing functionalized tips, that is, deterministic chemical modifications of the last tip atoms, for NC-AFM. The most widely used tip fuctionalization for this purpose to date is a single CO molecule. Here we review the contrast mechanism and compare different tip functionalizations. Furthermore, we describe the use of NC-AFM with functionalized tips for the identification of molecular structures, the determination of molecular adsorption geometries, bond-order discrimination, and for Kelvin probe force microscopy with sub-molecular resolution.

12.1 Experimental Set-up and Tip Functionalization

A prerequisite for increasing the lateral resolution on molecules with NC-AFM was the atomic functionalization of the tip apex with a suitable atom or molecule [1]. The most prominent functionalization for NC-AFM is CO [1–24], but also other functionalizations have led to atomic resolution on molecules [1, 20, 25, 26]. Several

L. Gross (✉) · B. Schuler · F. Mohn · N. Moll · G. Meyer
IBM Research—Zurich, 8803 Rüschlikon, Switzerland
e-mail: lgr@zurich.ibm.com

B. Schuler
e-mail: bsc@zurich.ibm.com

N. Moll
e-mail: nim@zurich.ibm.com

G. Meyer
e-mail: gme@zurich.ibm.com

F. Mohn
ABB Corporate Research, 5405 Baden-Dättwil, Switzerland
e-mail: fabian.mohn@ch.abb.com

J. Repp
Institute of Experimental and Applied Physics, University of Regenburg,
93040 Regensburg, Germany
e-mail: jascha.repp@physik.uni-regensburg.de

© Springer International Publishing Switzerland 2015

S. Morita et al. (eds.), *Noncontact Atomic Force Microscopy*,
NanoScience and Technology, DOI 10.1007/978-3-319-15588-3_12

tip properties are related to its atomic/molecular termination and will significantly affect the AFM contrast and resolution that can be achieved:

- **Tip reactivity**: To obtain atomic resolution on molecules one needs to probe repulsive force contributions. Typically the tip needs to be approached until the maximum attractive interaction between the foremost tip atom and the atoms to be imaged is reached. Therefore one needs a rather inert tip to prevent the molecule to be imaged from being picked up or displaced by the tip.
- **Tip size**: It can be expected that small-sized tip functionalizations are beneficial in terms of lateral resolution. In particular diatomic molecules that are attached vertically to the tip lead to a high aspect ratio, which will be beneficial for resolution on the atomic scale.
- **Tip relaxation**: Atomic relaxations of the tip can occur owing to the forces acting between tip and sample. These relaxations give rise to imaging artifacts, which can lead to an apparent sharpening and may be beneficial or disadvantageous depending on the information that one wants to extract.
- **Tip dipole**: The charge distribution at the tip apex, in particular the tip dipole, plays an important role for the contrast obtained with AFM when electrostatic forces contribute significantly to the image contrast.

All these tip properties do not solely depend on the atomic/molecular functionalizations of the tip alone, but also on the mesoscopic part of the tip, e.g., the tip material [27], the crystallographic orientation of the tip [14], its work function and asperity. However, usually the functionalization itself yields the predominant force contributions for the interaction on the atomic scale [1, 28].

It is advantageous to use atomic manipulation [29] to functionalize the tip rather than using randomly functionalized tips that have to be assigned by their contrast. When the terminating atom or molecule of the tip has been picked up deliberately using atomic manipulation, the tip functionalization is known and can be reproduced on demand. In most cases, the procedure of tip fabrication of a certain atomic/molecular tip termination by means of atomic manipulation consists of the following steps:

1. The atoms or molecules or precursors thereof that are to be used as functionalizations are deposited onto the sample.
2. On the sample surface, they are located using either scanning tunneling microscopy (STM) or AFM. The pickup usually follows an empirical recipe, typically by approaching the tip vertically towards the atom or molecule to be picked up with a certain voltage or voltage ramp applied.
3. Finally, the success of the tip functionalization is confirmed using STM or AFM, to verify that the atom or molecule that should have been picked up is no longer on the sample surface and that the image contrast has changed in a characteristic way.

The list of atomic/molecular functionalizations that have been used for AFM so far include the following:

- Metal atoms: Ag, Au. These tips are formed by picking up individual metal adatoms from NaCl films [1, 30, 31].
- Semiconductor atoms: Si, Ge and Sn, could be extracted from semiconductor surfaces at room temperature [32–35].
- Halogen atoms: Cl and Br, which have been either extracted from thin films as in the case of Cl [1, 30] or have been dissociated from deposited precursor molecules prior to pick-up as in the case of Br [25].
- Noble gas atoms: Xe [20, 25, 29] and Kr [25].
- Diatomic molecules: CO [1, 36] as well as NO [25].
- Larger (aromatic) molecules: pentacene [1], C_{60} [37], naphthalene tetracarboxylic diimide (NTCDI) [26].

The noble gases and the molecules mentioned were all deposited as adsorbates on the surface and then picked up with the tip for functionalization. Closely related to AFM with functionalized tips is a technique called scanning tunneling hydrogen microscopy (STHM) [38], which was demonstrated with H_2, D_2, Xe, CO or CH_4 to yield atomic contrast on molecules with STM feedback [2, 39–41], see Chap. 14 by Temirov and Tautz in this book. Moreover, for orbital imaging with STM [42] the CO functionalization was also used to increase the resolution, owing to the p-wave character of the CO tip [43, 44]. Atomic resolution was recently also demonstrated by inelastic electron tunneling spectroscopy (IETS), achieved by measuring the spatial variations of the frustrated translation of the CO at the tip [45].

STM operation can facilitate tip functionalization because often the recipes to perform a certain manipulation, e.g. the pick-up of a specific atom, are known from earlier STM studies [29, 36, 47]; also, STM usually permits faster scanning speeds and faster z-feedback than AFM. However, all of the terminations mentioned before can also be obtained using AFM only. Figure 12.1a shows an example of a surface prepared for studying individual molecules with different functionalized tips. The molecules to be investigated have been evaporated onto the cold (10 K) sample, here Cu(111) partly covered with bilayer NaCl. Au atoms and CO molecules have been deposited for tip functionalization. The NaCl layer facilitates the pick-up of adsorbates due to their low binding energy and offers functionalization with Cl. Moreover, adsorbates are electronically decoupled from the underlying metallic surface. Typical STM contrast, which serves as an indication for successful functionalization of tips terminated by CO, Cu, and Cl, is shown in Fig. 12.1b–d, respectively.

The experiments are usually performed at cryogenic temperatures using liquid helium cooling, although this is not a stringent requirement, as atomic resolution on molecules has recently also been obtained with liquid nitrogen cooling [26]. In most set-ups, the qPlus sensor [48, 49] is employed, which facilitates working in the small amplitude regime. Typical parameters of the sensors used are spring constants k_0 of about 2 kN/m, quality factors Q of 10^4 up to several 10^5, and cantilever eigenfrequencies f_0 of about 30 kHz. The oscillation amplitude A is usually chosen on the order of 0.5 Å, that is, 1 Å peak-to-peak, as proposed to be ideal for atomic

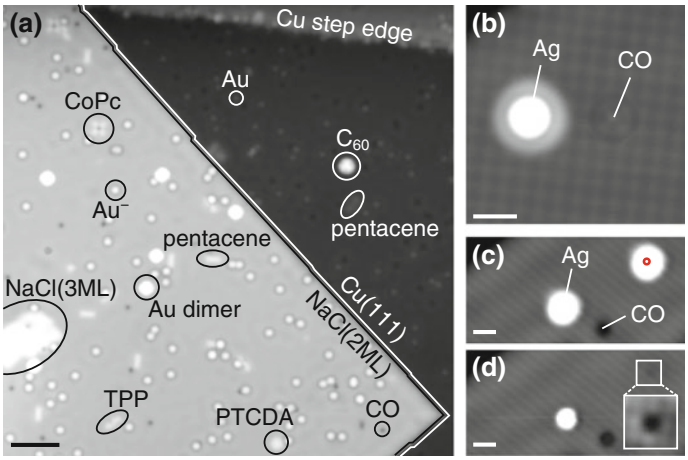

Fig. 12.1 Sample preparation and tip functionalization. **a** STM constant-current overview image (tunnel current $I = 2.5$ pA, sample voltage $V = 0.2$ V) of a typical sample preparation. The Cu(111) substrate and a two-monolayer NaCl island (with a small patch of the third layer on *top*) can be identified. Different adsorbates have been deposited on the surface and can be distinguished from their appearance in the STM topography: Au monomers and dimers, CO, C_{60} fullerenes, terphenyl-pyridine (TPP), 3,4,9,10-perylenetetra-carboxylic-dianhydride (PTCDA), cobalt phthalocyanine (CoPc), and pentacene). **b** Typical STM image ($I = 4$ pA, $V = 0.2$ V) recorded with a CO tip. Enhanced resolution of the NaCl surface is observed, as well as a characteristic appearance of the adsorbates. **c**, **d** STM images ($I = 2.3$ pA, $V = 0.2$ V) before (**c**) and after (**d**) creation of a Cl tip by picking up a AgCl complex from the NaCl surface. The inset ($I = 4$ pA, $V = 0.2$ V) shows that a single Cl vacancy was created. *Scale bars* 50 Å in (**a**) and 10 Å elsewhere. Reproduced with permission from [46]

resolution [50]. Atomically resolved images of molecules are usually obtained using NC-AFM in the frequency-modulation mode [51]. Typically, images are obtained in the constant-height mode: The z-feedback is disabled, the tip is scanned on a predefined plane, usually parallel to the substrate surface, and the frequency shift Δf is recorded. The tip height z is the distance between tip and sample surface. It is practical to lower z successively until atomic resolution is obtained. On molecules this is often the case at the tip height at which the minimum of the frequency shift $\Delta f(z)$ is reached and $\Delta f(z)$ increases with further decreasing z. Reducing z further leads to an apparent increase of resolution, which typically reaches an optimum near the z at which Δf reaches 0 Hz and where the force has its minimum above the molecule. The constant-height AFM image of pentacene with a CO functionalized tip (CO tip) shown in Fig. 12.2 is acquired in this regime. This tip height roughly corresponds to the region of the force minimum, i.e., the height above the molecule at which the most attractive force is reached but not yet to the bonding distance, which is at the minimum of the interaction energy. However, already at this tip height of maximum attractive force are the repulsive contributions significant, which is an important ingredient for achieving atomic resolution. Upon further reducing z,

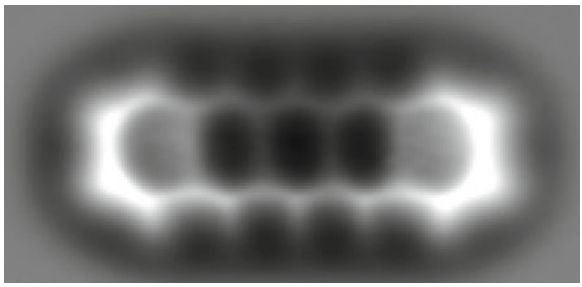

Fig. 12.2 Constant-height AFM measurement of pentacene on Cu(111) acquired with a CO functionalized tip; Δf-scale: –7 Hz (*black*) to –2 Hz (*white*). Reprinted from [1], Copyright © 2009 American Association for the Advancement of Science

imaging eventually becomes unstable. The minimum tip height that can be achieved for imaging without moving or manipulating the molecule under investigation will depend on the tip functionalization and the adsorption energy/diffusion barrier of the molecule on the surface.

12.2 The Origin of Atomic Contrast

For any interpretation of AFM data, understanding of the contrast mechanism is crucial. At first glance, the atomically resolved AFM images as the one shown in Fig. 12.2 being similar to the molecular structure, suggest that the contrast simply reflects the geometry of the molecule. However, the imaging mechanism is far from being simple. First, the AFM signal is composed of several different types of interactions, such as electrostatic forces, van der Waals attraction, chemical bond formation, and Pauli repulsion. Additionally, as these forces act on very different length scales, different parts of the tip and sample structure may contribute to the imaging process. In the following we will discuss how the different aforementioned contributions can be disentangled in order to understand the origin of the atomic contrast. Tip relaxations, which may complicate things even further, will be discussed in the next section.

One great advantage of AFM is that interaction forces and energies can be measured and directly compared with density functional theory (DFT) calculated interaction energies and forces. As will be discussed further below, DFT can be used to discriminate between different force contributions. However, an AFM image as the one shown in Fig. 12.2 is not sufficient to determine the force between the CO molecule at the tip and the pentacene molecule on the surface. To extract the force, the frequency shift has to be recorded as a function of z during the tip approach [52]. Ideally three-dimensional datasets of the frequency shift, so called 3D force maps [7, 53, 54], are recorded (see Chap. 2 by Baykara and Schwarz in this book). The vertical force F_z can then be extracted from the $\Delta f(z)$ data by using the Sader–Jarvis method [55]. Constant-height slices of a 3D force map recorded above a pentacene molecule with a CO tip are shown in Fig. 12.3a, b corresponding to the frequency shift Δf and the extracted vertical force F_z, respectively.

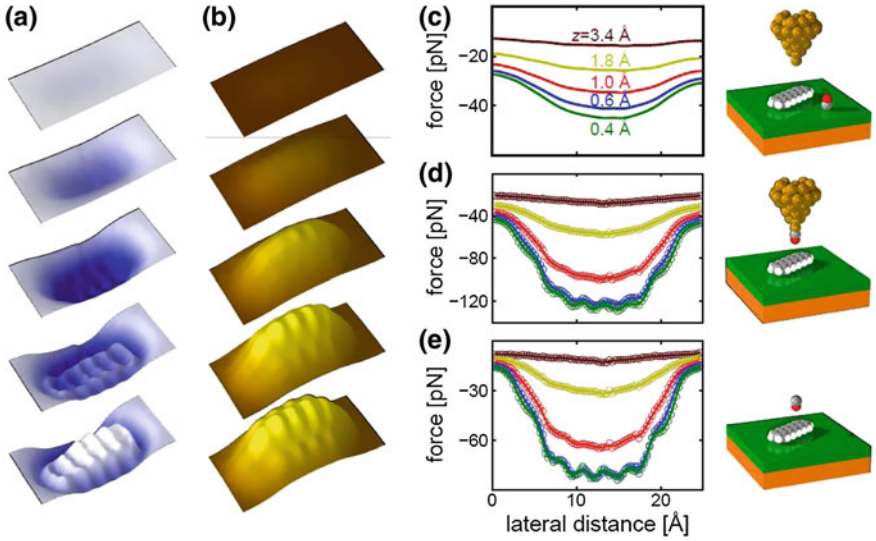

Fig. 12.3 Force map measurements of pentacene on bilayer NaCl on Cu(111). **a**, **b** Maps of measured frequency shift Δf (**a**) and extracted vertical force (**b**) at different tip heights (z = 4.2, 2.6, 1.8, 1.4, and 1.2 Å, decreasing from *top* to *bottom*). The data shown are part of a 3D force field captured with a CO tip in a box of 25 Å × 12.5 Å × 13 Å above the pentacene molecule. The color scales range from –3 Hz (*blue*) to 0 Hz (*white*) and from –120 pN (*yellow*) to 0 pN (*brown*), respectively. **c**–**e** Line scans of the vertical force extracted at different heights from 3D force maps measured with a metal tip (**c**) and with a CO tip (**d**). The difference between the two tips (**e**) yields the CO contribution, as indicated in the schematic representations of the tip and sample system to the right of the graphs. All tip heights are given with respect to the height determined by the STM set point (I = 2 pA, V = 0.2 V) with the CO-terminated tip above the substrate. Reprinted from [1], Copyright © 2009 American Association for the Advancement of Science

The next step is to take into account background forces that stem from the mesoscopic parts of the tip and the sample in order to extract the interaction force between the CO at the tip and the molecule on the surface [56]. The background of the sample can be subtracted by using an on/off method. That is, one records, in addition to the data above the molecule, also the data above the uncovered bare surface at the same absolute tip height, e.g., above the surface in the vicinity of the sample molecule. These forces can be subtracted from the forces measured above the molecule, thus eliminating the force contribution of the surface below the adsorbed molecule.

To eliminate the contribution of the tip bulk behind the CO molecule, a similar method can be employed: Here one records, in addition to the data recorded with a CO tip, the data at the same absolute tip heights, with the same tip, but without the CO molecule at the tip apex. For this, the CO molecule is deposited again on the sample and the change of the STM set-point due to that tip change is recorded [1]. Then by subtraction of the forces recorded with and without CO, one can eliminate the contribution of the bulk tip behind the CO molecule. (Note that the CO and the

molecule on the surface will be polarized upon adsorption and that this will effect electrostatic interaction forces, which cannot be compensated in this way).

Such an experiment in which the background of the tip is investigated is shown in Fig. 12.3c–e. Figure 12.3c shows the force between the metal tip without the CO molecule and Fig. 12.3d the interaction force of the same tip with the CO molecule attached. Note that only one third of the overall measured short-range force (Fig. 12.3d) stems from the metallic bulk part of the tip (Fig. 12.3c) and that the latter contribution shows no atomic resolution. The contribution of the CO molecule only (Fig. 12.3e) is obtained by subtracting the metal tip forces from the CO tip forces. Thus, the CO contribution to the overall force is about two thirds and the CO interaction is solely responsible for the atomic contrast. The disentanglement of the signal by the experimentally performed background correction makes it possible to treat the remaining system (two relatively small molecules) by ab initio calculations using DFT.

DFT calculations [57–59] were performed with the Perdew–Burke–Ernzerhof exchange-correlation functional [60]. To account for van der Waals forces, a contribution proportional to R^{-6} was added to the dispersion energy (where R is the distance to the center of the atom), following a semi-empirical approach [59, 61]. In the calculations, only the pentacene and the CO are included, neglecting both the substrate and the metal part of the tip. The pentacene molecule was assumed to be planar and the CO was restricted to be oriented perpendicularly to the plane of the pentacene molecule, with the O atom pointing towards the pentacene. Therefore possible relaxations of the CO, in particular its tilting at the tip apex, were neglected in these calculations. As we shall see later, these relaxations are important and cause the apparent distortions and apparent sharpening of bonds observed with CO tips [12]. Nevertheless, the calculations without CO relaxations are useful for understanding the origin the of the AFM contrast. The fixed CO was positioned at different lateral (x, y) and vertical (d) positions above the pentacene, where d is the distance from the CO oxygen atom to the pentacene molecular plane, and for each position, the interaction energy E_{int} was calculated [3].

The distance dependence of $E_{int}(d)$ was fitted by a Lennard–Jones-type potential of the form $E_{int}(d) = (a/d)^b - (u/d)^v$, with fitting parameters $a = 6.0\,\text{Å}$, $b = 12.6$, $u = 9.5\,\text{Å}$, $v = 6.1$ for the center of the pentacene, see Fig. 12.4a. The vertical force $F_z(d)$, shown in Fig. 12.4b, and frequency shift $\Delta f(d)$, shown in Fig. 12.4c, were then obtained from the fitted curve by differentiation with respect to d [3, 62]:

$$\Delta f = -\frac{f_0}{2k_0}\frac{\partial F_z}{\partial d} = \frac{f_0}{2k_0}\frac{\partial^2 E_{int}}{\partial d^2}. \tag{12.1}$$

Note that the differentiation of $E_{int}(d)$ with respect to d shifts the minimum in the $F_z(d)$ and $\Delta f(d)$ curves to greater distances, by about –0.45 Å for each differentiation, see Fig. 12.4. Hence, in Δf maps, atomic contrast is observed already at greater distances d than in F_z and $E_{int}(d)$ maps.

The calculated constant-height Δf map of the CO molecule above the pentacene molecule, shown in Fig. 12.5a, corresponds qualitatively and also quantitatively well

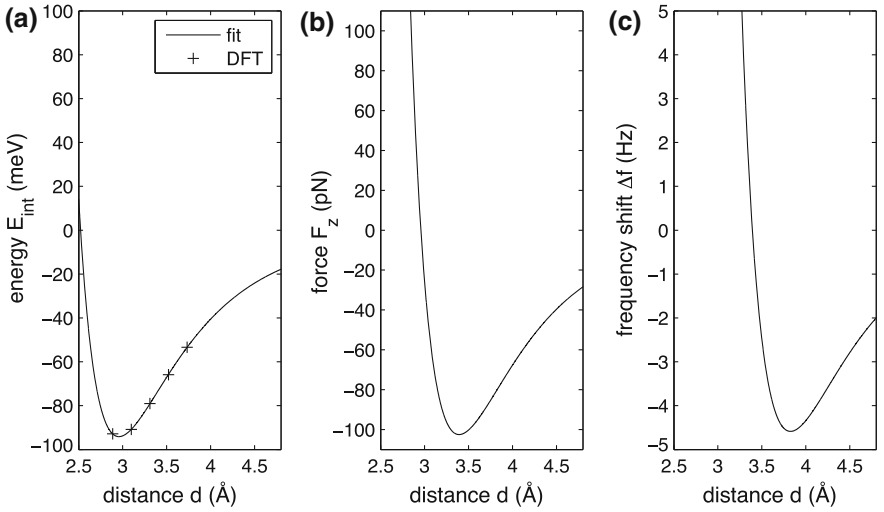

Fig. 12.4 **a** Computed interaction energies (*crosses*) and the corresponding Lennard–Jones fit for the CO molecule above the center of the pentacene molecule, as a function of the intermolecular distance d with respect to the oxygen atom of CO. **b** The force $F_z(d)$ and **c** the frequency shift $\Delta f(d)$, computed from the Lennard–Jones fit. Reprinted from [3]

with the experiment (see Fig. 12.2). A contrast of about 5 Hz is observed in experiment and theory, with the greatest Δf values at the apparent positions of C atoms and C–C bonds. The maximal attractive forces on the order of 100 pN are observed above the hollow sites of the carbon rings in the calculations (Fig. 12.4b), in agreement with the measured and background-corrected forces of the experiment (Fig. 12.3e).

From theory, we can assign the AFM contrast to the different contributing energies which are shown in Fig. 12.5. The interaction energy E_{int} is the sum of the kinetic energy E_{kin}, the van der Waals (vdW) energy E_{vdW} and the (electrostatic + exchange correlation) energy $E_{el} + E_{xc}$. Out of these contributions, only E_{kin} is repulsive and shows atomic contrast. The repulsive atomic contrast that is observed above the molecules, i.e., the bright features at the positions of atoms and bonds, is correlated to the kinetic energy and originates from Pauli repulsion: As the electron wavefunctions of tip and sample overlap, they change because two electrons (Fermions) cannot occupy the same quantum state simultaneously, as formulated in the Pauli exclusion principle [63]. This implies that the overall wavefunction has to be antisymmetric with respect to particle exchange. When two electrons of the same spin state intersect in space, their orthogonalized wavefunctions take on larger slopes to keep their overlap zero. The increase in slope causes an increase in the kinetic energy E_{kin}, which is a large portion of the Pauli repulsion. The Pauli energy can be defined as the energy difference between orthogonalized and non-orthogonalized wavefunctions:

$$E_{Pauli} = E_{int}(\uparrow\downarrow) - E_{int}(\uparrow\uparrow). \tag{12.2}$$

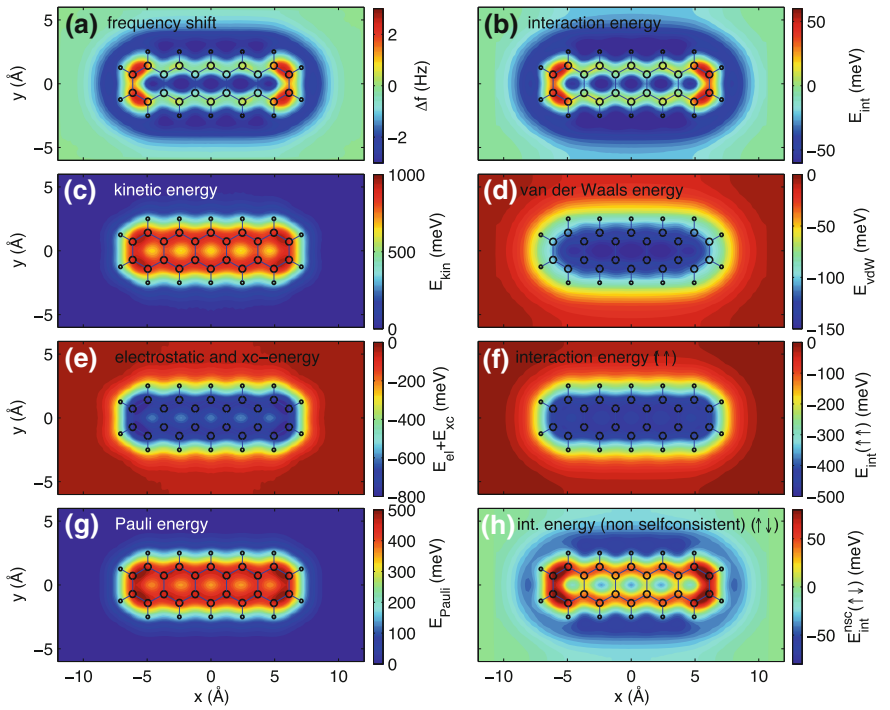

Fig. 12.5 Computed constant-height plots for CO above pentacene of **a** the frequency shift Δf for an intermolecular distance of $d = 3.61$ Å and of (**b**)–(**h**) specific energies for $d = 2.72$ Å. **b** The interaction energy E_{int}. The contributions to E_{int} of **c** the kinetic energy E_{kin}, **d** the van der Waals energy E_{vdW} and **e** the sum of the electrostatic and exchange correlation energies $E_{el} + E_{xc}$. **f** The interaction energy $E_{int}(\uparrow\uparrow)$ calculated using the wavefunctions of the isolated CO and pentacene molecules without orthogonalizing them. **g** The Pauli energy $E_{Pauli} = E_{int} - E_{int}(\uparrow\uparrow)$. **h** The (non-selfconsistent) interaction energy $E_{int}^{nsc}(\uparrow\downarrow)$ using the wavefunctions of the isolated CO and pentacene molecules and orthogonalizing them. Reprinted from [3]

The orthogonalized interaction energy $E_{int}(\uparrow\downarrow)$ is equal to the fully self-consistent interaction energy E_{int} (Fig. 12.5b). The second term, $E_{int}(\uparrow\uparrow)$ (Fig. 12.5f), i.e. the interaction energy of a non-orthogonalized system, is calculated by first determining the wavefunctions of the isolated CO molecule and the isolated pentacene. Using these wavefunctions, the interaction energy is calculated in the standard DFT way, but without orthogonalizing them. The Pauli energy (Fig. 12.5g) is then calculated as the difference of two interaction energies.

Furthermore, the non-selfconsistent interaction energy $E_{int}^{nsc}(\uparrow\downarrow)$ is calculated using the wavefunctions of the isolated CO and pentacene molecules and orthogonalizing but not optimizing them any further, see Fig. 12.5h. This result is very similar to the fully self-consistent interaction energy E_{int} (Fig. 12.5b), indicating that the molecules form no chemical bond. The fact that the CO molecule is chemically inert facilitates the observed high atomic resolution, as the two molecules can be moved closer to each other than the distance of maximum attraction without bond formation.

In atomically resolved AFM images of molecules, the overall interaction forces typically are still attractive, owing to electrostatic and vdW forces, but the atomic contrast stems from repulsive contributions of the shorter-ranged Pauli repulsion. In Fig. 12.3, we can observe how the contrast evolves with decreasing tip height z. For large distances only the attractive "bathtub shape" stemming from vdW and electrostatic forces is visible. At shorter tip heights, this attraction gives rise to the dark halo surrounding the molecules. Atomic resolution, which is due to Pauli repulsion above the atoms and bonds, becomes only apparent for the smallest accessible tip heights. The absolute tip height with respect to the sample is challenging to extract from the experiment. Relative tip heights can be measured with high precision, but the distance d between the last tip atom and the surface plane of atoms cannot be determined very accurately in the experiment. By theory we found that for planar aromatic hydrocarbons imaged with CO tips the minimum of $\Delta f(z)$ is typically reached at $d = 3.9$ Å (see e.g. Fig. 12.4c) above the center of carbon rings, which we will henceforth use in this chapter for tip-height calibration [12].

There are also differences of the image calculated by theory (Fig. 12.5a) with respect to the experimental one (Fig. 12.2). Most of them can be attributed to the tilting of the CO molecule at the tip apex. It turned out that in the case of CO functionalized tips the contrast of AFM images is strongly influenced by tip relaxations. In particular, the CO molecule at the tip apex will tilt under the influence of the interaction forces. This tilting gives rise to an apparent sharpening of the bonds in AFM images and to distortions of the imaged molecular structures as will be explained in Sect. 12.3. Moreover, differences between experiment and theory, i.e., the increased brightness at the molecular ends and the different brightness of the upper and the lower edge of the pentacene molecule seen in the experiment (Fig. 12.2) in part stem from the non-planar adsorption geometry of pentacene, as explained in detail in Sect. 12.4.

12.3 Bond-Order Discrimination and CO-Tip Relaxation

Bond order is an important concept for the prediction of the geometry, stability, aromaticity, reactivity, and electronic structure of covalently bonded molecules. The bond order is related to the bond length and electron density. In general, the bond length decreases and the electron density increases with increasing Pauling bond order [64, 65]. For molecules, not only the chemical species of their constituent atoms can differ, but also the coordination number of atoms, the bond angles, bond order, and bond length. In polycyclic aromatic hydrocarbons (PAHs), the differences in bond order and length are subtle because of the delocalized π-electrons that render the number of electrons participating in a bond non-quantized. However, detecting these small differences is useful for rationalizing the aromaticity and reactivity of such molecules [66]. If single crystals are available, the bond length can be determined experimentally with high accuracy using diffraction methods [67, 68], whereas with AFM also systems can be studied in which single crystals cannot be grown. Moreover,

in contrast to diffraction based techniques, which yield values averaged over large ensembles of molecules, scanning probe microscopy offers the possibility of studying single bonds in individual molecules.

AFM can be used to differentiate bond orders and lengths of individual bonds for C_{60} and large PAHs [12]. In a C_{60} molecule, the bonds fusing two hexagons (h) are electron-rich compared with the bonds fusing a pentagon and a hexagon (p) (see Fig. 12.6e). The Pauling bond order P_b of a bond b in a conjugated molecule is found by counting the number of Kekulé structures (classical resonance formulas) that show b as a double bond and dividing it by the total number of different Kekulé structures of the molecule [64, 65]. Thus, P_b can take values between 0 (single bond) and 1 (double bond); in the case of C_{60}, the Pauling bond orders are $P_h = 0.44$ and $P_p = 0.28$, respectively [69]. Correspondingly, theoretical [70] and experimental investigations using neutron diffraction [71], electron diffraction [72], and x-ray diffraction [73, 74] have shown that the bond h is by ~5 % shorter than the bond p.

AFM images of C_{60} with a hexagon tile exposed towards the tip are shown in Fig. 12.6. Here the tip height z was calibrated using the theoretical finding that the

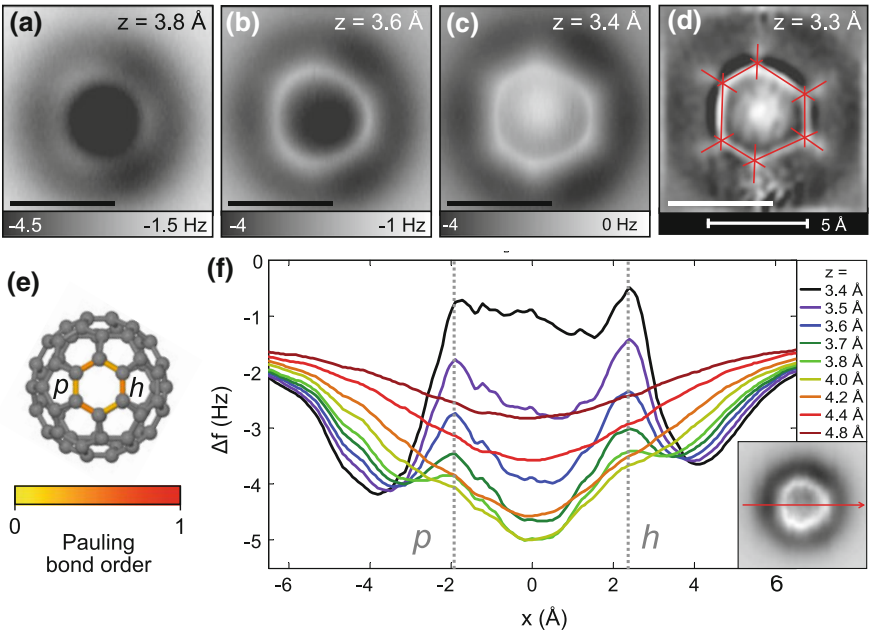

Fig. 12.6 **a–c** Constant-height AFM maps of C_{60} on Cu(111) at different heights z obtained with a CO tip. **d** Laplace- and low-pass-filtered image to measure the apparent bond length L'. **e** Molecule model of C_{60} with the Pauling bond order of the p and the h bond indicated at the *top most ring*. **f** Line profiles $\Delta f(x)$ across a p and h bond extracted from a 3D force map. The position of the line profiles is indicated in the *inset* showing a map of Δf at $z = 3.6$ Å extracted from the same 3D force map. The apparent positions of the p and h bond with respect to the center of the molecule ($x = 0$) are indicated by the *dotted lines*. Scale bars 5 Å. Reprinted from [12], Copyright © 2012 American Association for the Advancement of Science

minimum of the $\Delta f(z)$ curve above a carbon ring center is usually found at a distance of 3.9 Å between the O atom of the CO tip and the carbon ring as described in Sect. 12.2. Two important observations can be made: On the one hand, Δf is larger above the *h* bonds than above the *p* bonds. This effect is best observed for moderate tip heights (Fig. 12.6a). The largest Δf difference of 0.4 Hz was obtained for $z = 3.7$ Å. On the other hand, in images with atomic resolution, the *h* bonds appear shorter than the *p* bonds; this was best observed for the smallest accessible tip heights (see Fig. 12.6c). Figure 12.6d shows a Laplace filtered image that was used to determine the apparent position of the bonds and measure the apparent bond lengths, $L'_h = 2.0(2)$ Å and $L'_p = 2.7(2)$ Å, respectively. Notably, the apparent bond lengths L' measured by AFM qualitatively correctly reflect that the *h* bond is shorter than the *p* bond. However, both bonds appear to be substantially longer than they really are, and the difference in the apparent bond lengths of ∼30 % is much greater than the real difference of ∼5 %.

Both contrast mechanisms, i.e., bond-order discrimination by Δf contrast and by apparent length, were demonstrated on PAHs. Note that different contrast values can be expected due to non-planar molecular topographies [9, 13, 20] and different chemical species, which are both avoided in the case of planar PAHs. However, only bonds with a very similar (vdW and electrostatic) background can be compared, therefore only bonds in the central region of PAHs were compared. Figure 12.7 shows the results for hexabenzocoronene (HBC) on Cu(111) (Fig. 12.7b) and dibenzonaphthoperylene (DBNP) [75] on bilayer NaCl on Cu(111) (Fig. 12.7c). Figure 12.7d, e shows the measured Δf values and apparent bond lengths L', respectively, as a function of the Pauling bond order. For the bonds investigated, it was observed that generally Δf increased and L' decreased with increasing bond order. In Fig. 12.7f, the apparent length is plotted as a function of the realistic bond length extracted from DFT calculations (for DBNP) [12] and x-ray diffraction measurements (for HBC) [76]. The slope of the linear regression is 11; that is, the differences in the apparent bond lengths are about one order of magnitude greater than the differences in real bond lengths.

To understand the contrast mechanisms, DFT calculations were performed. Figure 12.8c shows an image of the calculated interaction energy for a non-flexible CO molecule above the C_{60} that qualitatively reflects the experimental Δf image at moderate tip heights (see Fig. 12.6a) [12]. The brighter appearance of the *h* bonds with respect to the *p* bonds is well reproduced. The contrast is related to the electron density, shown in Fig. 12.8e, which increases with increasing bond order. Increased electron density leads to stronger Pauli repulsion; consequently, Δf is increased above bonds with greater bond order.

To account for tip relaxations, especially CO tilting at the tip apex [6, 9, 12, 14, 77–81], the tip was modeled as a Cu_2 cluster with a CO molecule attached, as shown schematically in Fig. 12.8a. To obtain the Δf in this case, the interaction energies were numerically differentiated twice with respect to the tip height. Calculated $\Delta f(x)$ line profiles (Fig. 12.8d) without relaxations of the tip structure (dashed lines) exhibit the $\Delta f(x)$ maxima exactly above the bond positions (vertical gray lines), reflecting

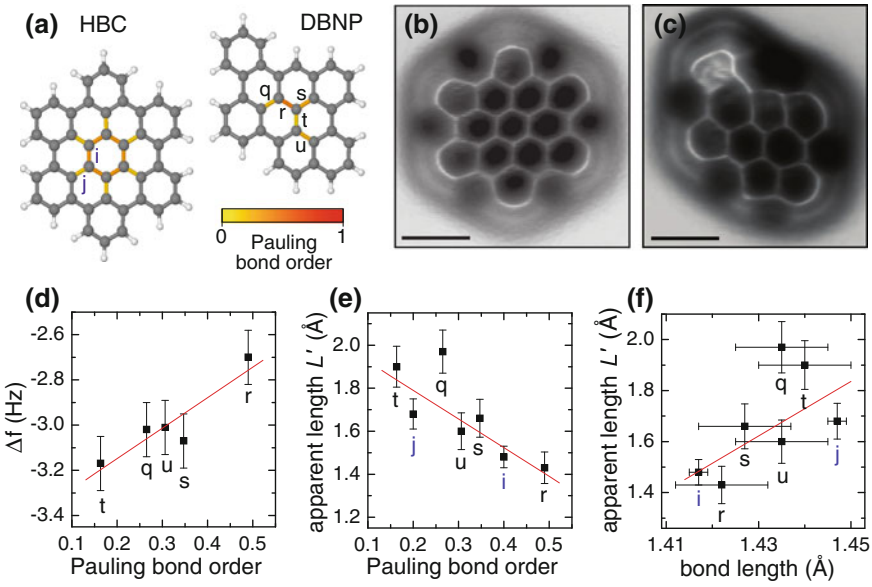

Fig. 12.7 **a** Model of HBC and DBNP with the Pauling bond order of their inner bonds indicated. **b**, **c** Pseudo-3D image of a constant-height AFM map of (**b**) HBC on Cu(111) and (**c**) DBNP on bilayer NaCl on Cu(111). **d** Measured Δf values as a function of the Pauling bond order. **e**, **f** The apparent bond length L' as a function of the Pauling bond order (**e**) and as a function of the realistic bond length (**f**) with linear regressions. *Scale bars* 5 Å. Reprinted from [12], Copyright © 2012 American Association for the Advancement of Science

the differences in the C_{60} electron density. Calculations including tip relaxations (solid lines) show a lateral shift of the $\Delta f(x)$ maxima positions (arrows in Fig. 12.8d) toward greater absolute values of x, leading to an expansion of the molecule in the image. Moreover, this lateral shift is greater for the h bond than for the p bond, in agreement with the experiment, leading to the shorter apparent length of h bonds compared with p bonds. The important tip relaxation for the imaging process is the lateral displacement $\Delta x(x)$ of the oxygen atom at the tip apex (see Fig. 12.8f) caused by a tilting of the CO molecule. As this oxygen atom defines the position of our probe, a locally decreasing $\Delta x(x)$ (falling slope) results in a local expansion, whereas a locally increasing $\Delta x(x)$ (rising slope) results in a local compression along the x direction in that particular region of the image. Molecular bonds often appear elongated because of the increasing long-range attraction towards the molecule due to vdW and electrostatic forces. The lateral forces that act on the tip can be extracted from 3D force maps and can be used to correct the apparent distortions of AFM images caused by CO tilting [78].

The tilting of the CO is responsible for the apparent distortion of the molecular structures in AFM images, and in particular for the amplification of the differences in the apparent bond lengths. Note that only because of this amplification, can differences in apparent bond length be measured within the accuracy of the AFM

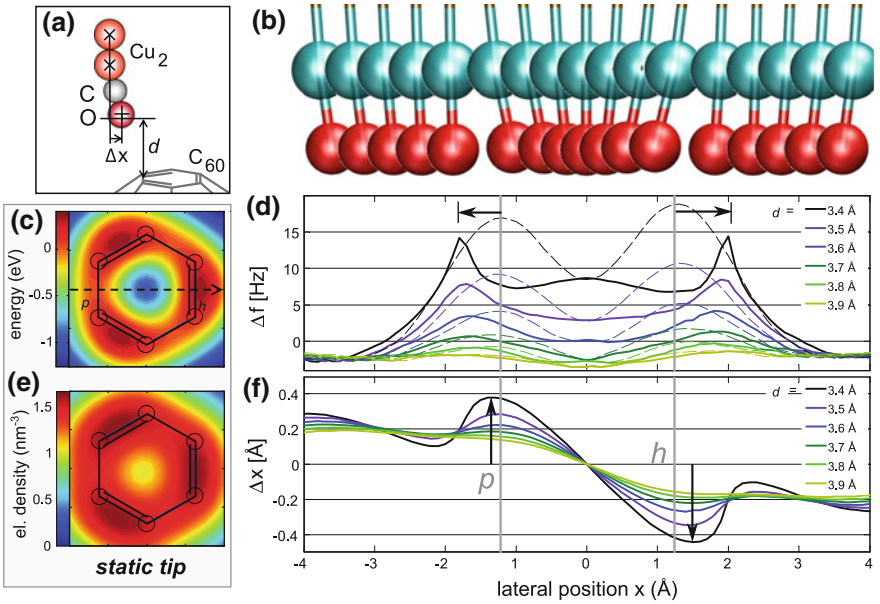

Fig. 12.8 **a** Tip model of a CO tip on a Cu_2 cluster. **b** Tip relaxation when the tip is scanned over the p and h bonds (same x scale as in (**d**), (**f**)). Calculated (**c**) interaction energy and (**e**) electron density at $d = 2.9$ Å above the molecule (image size: 4×4 Å). **d**, **f** Line profiles of Δf and tip displacement $\Delta x(x)$ calculated with a static tip (*dashed lines*) and a relaxed tip (*solid lines*). The *vertical gray lines* in (**d**) and (**f**) indicate the positions of the p and h bonds as expected from the atomic model. The *horizontal black arrows* in (**d**) mark the shift of the bond positions in response to the tip relaxations, which increase in magnitude with decreasing tip height (*vertical arrows* in (**f**)). Reprinted from [12], Copyright © 2012 American Association for the Advancement of Science

instrument. Furthermore, right above the apparent positions of the bonds (that is, when the regions of maximal electron density are probed), $\Delta x(x)$ shows a rising slope, leading to a local lateral compression that gives rise to the very sharp appearance of the bonds at small tip heights. Notably, the calculations with a relaxed CO tip for $d = 3.4$ Å , besides the distortions and the apparent sharpening of the bonds, also reflect several other details of the experiment, such as the appearance of a local maximum in the molecular center and the vanishing Δf contrast between p and h bonds observed for very small tip heights because of the tip relaxations.

The two contrast mechanisms for bond-order discrimination—one based on the frequency shift and the other based on the apparent length measured by AFM—are both corroborated by DFT calculations, and both can be used to differentiate bond orders in individual molecules. Importantly, the tilting of the CO at the tip apex gives rise to an apparent sharpening of the bonds and amplification of the apparent bond-length differences, and thus makes it possible to detect length differences between individual bonds down to 0.03 Å [12].

12.4 Adsorption Geometry Determination

For organic molecules, the adsorption geometry, i.e., the adsorption site, adsorption orientation, adsorption height and molecular tilt, is intimately linked to the electronic properties of the adsorbate and the interaction between adsorbate and substrate [82]. Therefore, the adsorption geometry is a direct indicator of the adsorbate–substrate interaction. The x-ray standing wave method (XSW) [83, 84] is often used for measuring the adsorption height of molecules. However, adsorption sites and tilt angles are challenging to obtain by this method, and because of averaging over large ensembles, individual molecules are not distinguished. In contrast, scanning probe microscopy offers the possibility of studying individual molecules. With AFM, in addition to the adsorption site and in-plane orientation, even quantitative information on the adsorption height and the tilt of individual molecules can be obtained, as will be shown next.

The adsorption site of individual molecules on the substrate lattice can be determined by STM [85] or AFM [20, 86]. To determine however the adsorption height and to identify non-planar adsorption geometries, STM is unsuited owing to the convolution of geometric and electronic information [87]. Pauli repulsive forces probed by AFM, on the other hand, are closely related and very sensitive to the tip–molecule distance, as described in the previous sections.

Qualitative discrimination of adsorption geometries by AFM is shown in Fig. 12.9 for dibenzo[a,h]thianthrene (DBTH) molecules [9]. These belong to the family of thianthrenes, that are folded along the S-S axis, because of the presence of the lone pairs of the thioether groups (see model in Fig. 12.9a). On the surface, the two central S atoms can either stand up or point down towards the surface, giving rise to up "U" or a down "D" conformation, respectively. With STM measurements (inset in Fig. 12.9b), the adsorption geometry could not be assigned, whereas with AFM the unambiguous assignment of the "U" and "D" confirmation was obtained. In the CO-tip constant-height AFM measurement (Fig. 12.9b) the regime of Pauli repulsion is reached only on parts of the molecules that are elevated higher above the surface. Therefore these parts appear bright owing to the onset of repulsive interactions with

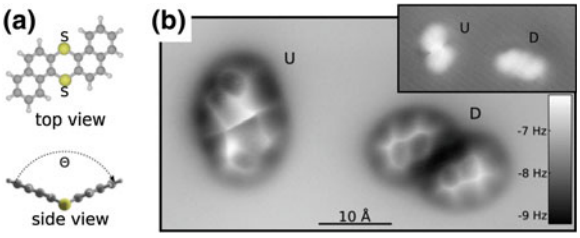

Fig. 12.9 **a** Model of DBTH. **b** Constant-height CO tip AFM measurement of DBTH on bilayer NaCl on Cu(111). *Inset* constant-current STM of the same area. The labels U and D indicate "up" and "down" conformations, respectively Reprinted from [9]

the tip. Hence, the S atoms appear bright in the up conformation, but dark in the down conformation. Note also that a sharp bright feature along the S-S direction appears in the up conformation, reminiscent of apparent bonds imaged by AFM. However, this is not related to a bond, but rather an artifact that stems from the relaxation of the CO tip and again illustrates that these relaxation effects must be carefully considered in the interpretation of AFM measurements obtained with CO tips [9, 12, 78–81, 88].

To quantitatively determine and map the adsorption height, a methodology was developed based on force-distance spectroscopy. The molecular height was correlated to the tip height $z^*(x, y)$ where the background-corrected frequency shift $\Delta f(x, y, z)$ has its minimum:

$$z^*(x, y) = \arg\min_z \{\Delta f(x, y, z)\}. \tag{12.3}$$

The background correction is performed by the on/off method, i.e., the spectrum $\Delta f(z)$ above the bare surface (off the molecule) is subtracted from all $\Delta f(z)$ curves above (on) the molecule. It was demonstrated that maps of z^* reflect the adsorption geometry of molecules [20]. A z^* map of pentacene on Cu(111) is shown in Fig. 12.10a, revealing that the molecule is adsorbed in a bent geometry with its ends farther away from the surface, similar to recent findings for pentacene on Cu(110) [89]. Moreover, the molecule is slightly tilted around the long molecular axis. This non-planar adsorption geometry is the reason for the difference in

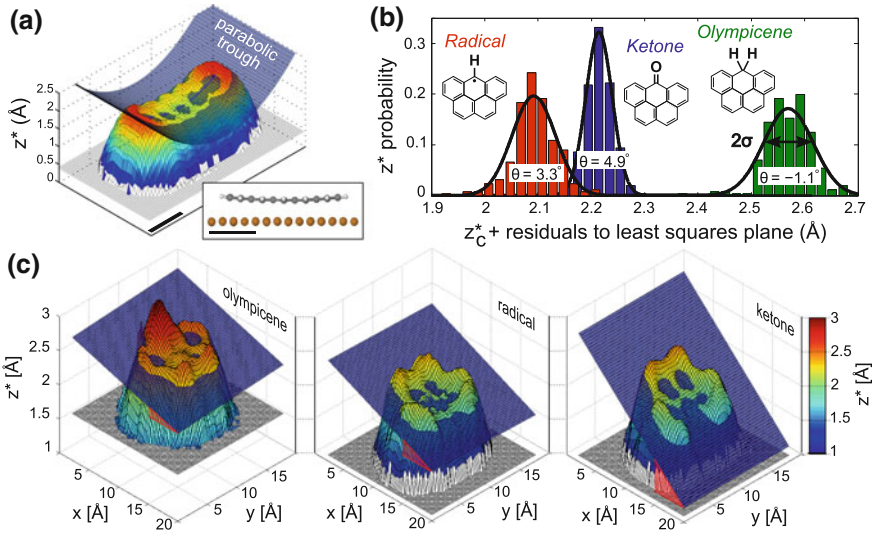

Fig. 12.10 **a** 3D representation of a z^* map recorded with a CO tip on pentacene on Cu(111); a parabolic trough is indicated in *blue*. **b** Probability distribution of z^* recorded with a Xe tip around the least-squares-fitted plane with the molecular tilt angle θ and height for the olympicenes. The *black curves* correspond to fitted Gaussian line shapes. The *insets* illustrate the molecule structures of the olympicenes. **c** 3D representation of z^* maps of the olympicenes. Least-squares-fitted planes are superimposed in *blue*. Reprinted from [20]

brightness of the long molecular edges and the ends of the molecule, which appear very bright (for the latter also bond-order-related contrast contributes) in the constant-height AFM image shown in Fig. 12.2.

To determine absolute adsorption heights by AFM, the method has to be calibrated, that is, z^* has to be correlated to the minimum of $\Delta f(z)$ above the bare surface. This calibration was performed for CO- and Xe-functionalized tips on Cu(111) substrates using systems with known adsorption heights. An accuracy of about 0.2 Å was estimated for this method with these tip functionalizations [20]. It turned out that for adsorption-height determination the Xe functionalization is preferred over the CO functionalization because for this task the tilting of the CO at the tip apex is disadvantageous as it leads to distortions that do not reflect the real geometry of the molecule. With Xe-functionalized tips atomic contrast on molecules can also be achieved, but without the strong distortions and apparent bond sharpening of CO tips [20, 25].

Differences in the adsorption heights of molecules can be measured with higher resolution because here no calibration with respect to the substrate is needed. Furthermore, the accuracy is improved if the same tip is used for comparing the adsorption heights of molecules. This was shown for three molecules of the olympicene family on Cu(111) using a Xe-functionalized tip. These molecules exhibit five fused carbon rings and differ only in the side group at the central ring, being either H_2 (olympicene), H (radical) or O (ketone), see models in Fig. 12.10b. As shown in Fig. 12.10b, c, the three molecules exhibit very distinct adsorption height differences. Comparison with theory showed that olympicene is physisorbed (greatest adsorption height), the ketone is in an intermediate regime between physisorption and chemisorption, whereas the radical is chemisorbed. In the z^* maps shown in Fig. 12.10c, the tilt of the molecules can be observed. For the olympicenes, adsorption height differences were determined by AFM with an accuracy of 0.03 Å and the tilt of the molecular planes with an accuracy of 0.2° [20].

12.5 Molecular Structure Identification

The identification of molecular structure is an important emerging application of high-resolution molecular imaging by AFM with functionalized tips (usually CO tips). In combination with nuclear magnetic resonance (NMR), AFM has been used for the structure elucidation of natural products [2, 10] and for the verification of synthesized compounds [20, 90]. Moreover, AFM has been used to identify reaction products formed by atomic manipulation [4] and by on-surface chemistry [21]. Here again, a strength of AFM is that individual, single molecules are studied. This renders it possible to investigate also samples that are mixtures of molecules and to identify their structures individually. Therefore in reactions that yield several products, these can be addressed individually and even very rare side products of chemical synthesis that cannot be assigned in the NMR spectra can be detected by

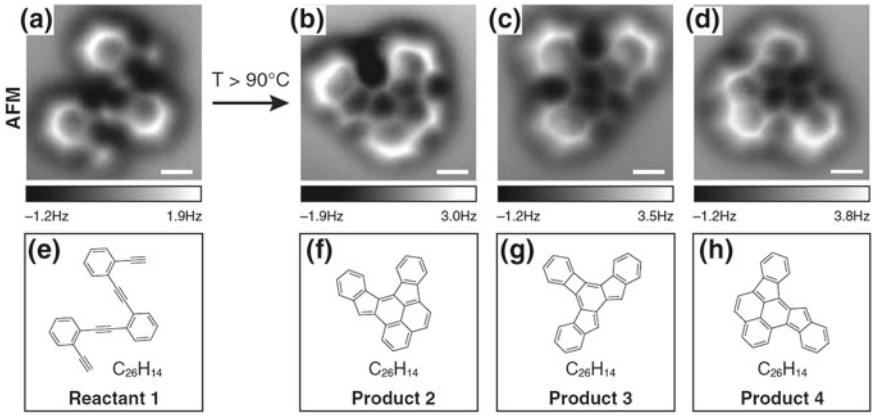

Fig. 12.11 **a–d** Constant-height CO-tip AFM images and respective structure models **e–h** of 1,2-bis((2-ethynylphenyl)ethynyl)benzene, see model in (**e**), and its reaction products (**f–h**) after heating above 90 °C on a Ag(100) surface. *Scale bars* 3 Å. Reprinted with permission from [21], Copyright © 2013 American Association for the Advancement of Science

AFM [91]. Figure 12.11 shows different products, identified by AFM, of a thermally induced enediyne cyclization of 1,2-bis((2-ethynylphenyl)ethynyl)benzene (Fig. 12.11e) [21].

For ab-initio structural characterization of natural compounds, AFM can be used to complement NMR and mass spectrometry (MS). Structure identification by NMR methods becomes challenging on systems with a limited number of hydrogens, in which the carbon skeleton is interrupted by heteroatoms or where there are quaternary carbons that have no long-range correlations to protons [2, 92]. Moreover, often x-ray crystallography is not possible for natural compounds owing to a lack of suitable crystals. In this case, AFM becomes a powerful additional tool, as it needs only very small amounts of the substance to be identified (less then 100 μg) and it often can reveal the connection position and angles between the (NMR-identified) molecular moieties. AFM structure identification of a natural compound was first demonstrated for cephalandole A. In that case, also the measured adsorption site and contrast due to the non-planar adsorption geometry combined with DFT calculations were used to obtain unambiguous structure determination [2]. In another example, the previously unknown structure of breitfussin A was identified by combining NMR, MS, computer-aided structure elucidation (CASE), DFT, and AFM [10]. The molecule contained six different atomic species, and some of them could be differentiated by AFM. In particular, the increased repulsive contrast (increased Pauli repulsion) of iodine with respect to the chemically similar bromine can be rationalized by its larger vdW radius than that of Br, see Fig. 12.12. On crystalline semiconductor surfaces, such chemical resolution by AFM has been demonstrated by Sugimoto et al. [93].

However, chemical fingerprinting of elements within molecules by AFM is still in its infancy and is extremely challenging because of (i) the relatively small bond distances, (ii) different hybridizations of atoms and different bonds between atoms,

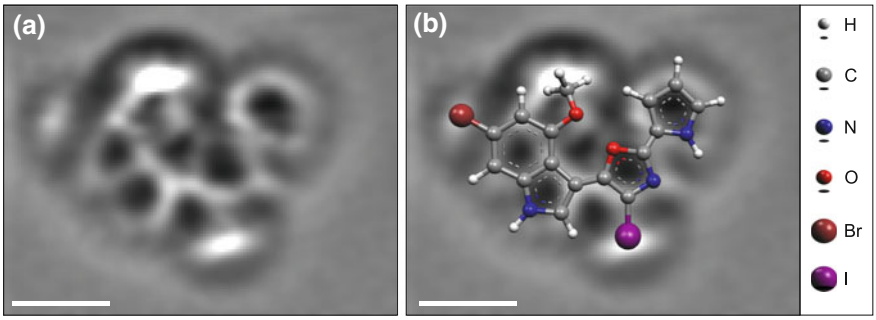

Fig. 12.12 **a** Laplace- and low-pass-filtered constant-height CO-tip AFM image of breitfussin A on Cu(111). **b** Same image as in (**a**) with a model of the identified molecular structure overlaid. *Scale bars* 5 Å. Reprinted from [10]. Copyright © 2012 WILEY-VCH Verlag GmbH & Co. KGaA, Weinheim

(iii) non-planar adsorption geometries and distortions introduced upon adsorption, and (iv) the relatively small diffusion barriers/adsorption energies, limiting the tip height and the reactivity of the functionalizations that can be used. A possible route towards increasing the chemical sensitivity of AFM could involve the additional use of KPFM and the comparison of different tip functionalizations [31].

12.6 Kelvin Probe Force Microscopy with Sub-molecular Resolution

With Kelvin probe force microscopy (KPFM), local variations in the contact potential difference (CPD) can be measured [94, 95] by applying a voltage between the sample and the oscillating AFM tip so that the electric field caused by the CPD and the resulting force on the tip are compensated as much as possible. The compensating voltage V^* for a certain tip position represents the local contact potential difference (LCPD) and can be determined either with a feedback loop or by measuring the $\Delta f(V)$ spectrum and finding its maximum [96–98]. Using KPFM, the LCPD was measured for a wide range of surfaces, in some cases even with atomic resolution [31, 96, 98–103]. Moreover, charge states of single atoms [62], defects [104], and molecules [105] were determined, and sub-molecular resolution was obtained [11, 22, 23].

The schematic of the measurement principle using $\Delta f(V)$ spectroscopy for KPFM at constant height is shown in Fig. 12.13b. LCPD maps as shown in Fig. 12.13c, d display the extracted vertex point V^* of the $\Delta f(V)$ spectra at the different lateral positions. The system studied, naphthalocyanine on bilayer NaCl on Cu(111), represents a hydrogen tautomerization switch that can be operated by inelastic tunneling [106], see schematic in Fig. 12.13a. Figure 12.13c, d shows Cu-tip LCPD maps of the same molecule, before and after the positions of the two central

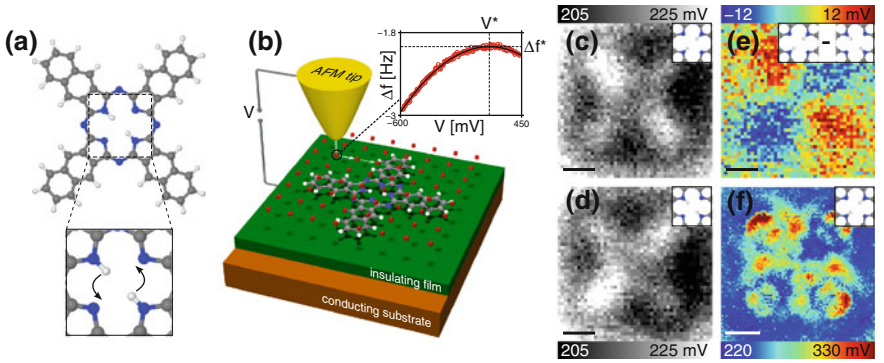

Fig. 12.13 **a** Naphthalocyanine model. The *inset* schematically shows the hydrogen tautomerization reaction [106]. **b** Schematic of the measurement principle for KPFM maps. At constant height, $\Delta f(V)$ spectra are recorded, on a grid of lateral tip positions. The maximum of the fitted parabola (see *inset*) yields V^* (the LCPD) and Δf^* for that position. **c**, **d** LCPD images of naphthalocyanine on bilayer NaCl on Cu(111) before (**c**) and after (**d**) switching the tautomerization state, measured with a Cu tip. **e** Difference image obtained by subtracting (**d**) from (**c**). **f** LCPD image measured with a CO tip. The *insets* in (**c**)–(**f**) indicate the respective positions of the inner hydrogen atoms. *Scale bars* 5 Å. Reprinted from [11]

hydrogen atoms had been switched and Fig. 12.13e shows the difference of these two LCPD maps. With this difference measurement, background effects are effectively compensated, and one qualitatively obtains the electric quadrupole moment of the molecule [11]. Using CO tips and decreasing the tip height, it is also possible to increase the resolution of KPFM, as shown in Fig. 12.13f. The KPFM contrast was found to correspond qualitatively to the calculated z-component of the electrostatic field E_z at a constant-height plane above the molecule [11]. The Cu-tip images, (Fig. 12.13c, d), recorded at comparably large tip heights, reflect E_z at a plane farther away from the molecule than that in the CO-tip image (Fig. 12.13f). Note that E_z is a property of the sample only and not related to any specific tip. Indeed recent experiments using functionalized tips for KPFM corroborated that the qualitative LCPD contrast is independent of the tip functionalization [31].

The simple interpretation that a more positive LCPD corresponds to more negative charge below the tip is not always correct. This was demonstrated for the bipolar charge-transfer complex TTF-PYZ_2, which consists of two pyrazine (PYZ) acceptor units and one central tetrathiafulvalene (TTF) donor unit [23]. The molecular model and a CO-tip AFM measurement are shown in Fig. 12.14a, b, respectively. Although negative charge is transferred from the donor to the acceptor already in the molecular ground state, an increased LCPD is measured by KPFM above the positively charged central donor part and a decreased LCPD above the negatively charged acceptor parts (see Fig. 12.14c). This apparent controversy with respect to the simple interpretation is caused by the higher-order electrostatic multipole moments of the molecule. These arise from the complex three-dimensional charge distribution within the molecule, and increasingly contribute to the LCPD contrast as the tip height decreases. However,

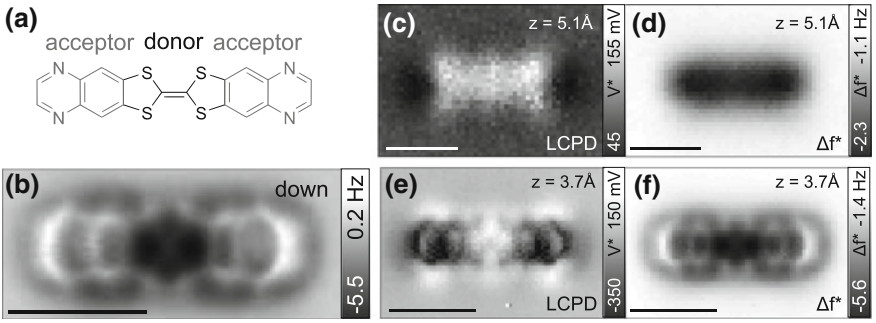

Fig. 12.14 **a** Structural model of the bipolar charge-transfer complex TTF-PYZ_2. AFM measurement **b** and KPFM measurements (**c**)–(**f**) acquired with a CO tip at constant height above TTF-PYZ_2 on bilayer NaCl on Cu(111). **c**, **e** LCPD maps acquired at medium (**c**) and small (**e**) tip heights. **d**, **f** Maps of Δf^*, i.e., Δf at compensated LCPD, simultaneously acquired with (**c**), (**e**), respectively, indicating that the regime of Pauli repulsive forces is entered in (**e**), (**f**), but not in (**c**), (**d**). Reprinted with permission from [23]. Copyright © 2014 American Chemical Society

the contrast of LCPD maps at small tip heights as shown in Figs. 12.13f and 12.14c still agrees well with the calculated E_z. Only for even smaller tip heights, when the regime of Pauli repulsive forces is entered, as shown in Fig. 12.14e, will the LCPD contrast deviate qualitatively from E_z [23].

12.7 Summary

Investigations of individual molecules by AFM with functionalized tips demonstrated atomic resolution, bond-order discrimination, adsorption-geometry determination, structure elucidation, imaging of charge distributions and—to a limited extend—also elemental identification. To demonstrate that these different properties can be resolved, suitable model systems were used in each case. However, differentiating all these properties for less specific systems, e.g., low-symmetry, non-planar molecules containing many different heteroatoms, still is a challenge. Especially the chemical sensitivity should be improved for applications in structure elucidation. A possible path towards this goal might be the comparison of different tip functionalizations combined with the complementation of AFM by KPFM [31].

Acknowledgments The authors thank R. Allenspach, R. Berndt, S. Collazos, G. Costantini, A. Criado, A. Curioni, S. Decurtins, S. Fatayer, D.J. Fox, F.J. Giessibl, A. Gourdon, E. Guitián, K. O. Hanssen, N. Hauptmann J. Isaksson, M. Jaspars, P. Jelinek, S. Kawai, P. Liljeroth, S.-X. Liu, W. Liu, A. Mistry, G. Münnich, M. Neu, N. Pavliček, D. Peña, D. Pérez, M. Persson, A. Pöllmann, M. Ruben, W. Steurer, I. Swart, A. Tkatchenko, and J. Weymouth for collaboration and discussions, and the EU projects ARTIST (contract no. 243421), PAMS (contract no. 610446) and the ERC advanced grant CEMAS for financial support.

References

1. L. Gross, F. Mohn, N. Moll, P. Liljeroth, G. Meyer, Science **325**, 1110 (2009)
2. L. Gross, F. Mohn, N. Moll, G. Meyer, R. Ebel, W.M. Abdel-Mageed, M. Jaspars, Nat. Chem. **2**, 821 (2010)
3. N. Moll, L. Gross, F. Mohn, A. Curioni, G. Meyer, New J. Phys. **12**, 125020 (2010)
4. F. Mohn, J. Repp, L. Gross, G. Meyer, M.S. Dyer, M. Persson, Phys. Rev. Lett. **105**, 266102 (2010)
5. R. Pawlak, S. Kawai, S. Fremy, T. Glatzel, E. Meyer, ACS Nano **5**, 6349 (2011)
6. Z. Sun, M.P. Boneschanscher, I. Swart, D. Vanmaekelbergh, P. Liljeroth, Phys. Rev. Lett. **106**, 046104 (2011)
7. F. Mohn, L. Gross, G. Meyer, Appl. Phys. Lett. **99**, 053106 (2011)
8. O. Guillermet, S. Gauthier, C. Joachim, P. de Mendoza, T. Lauterbach, A. Echavarren, Chem. Phys. Lett. **511**, 482 (2011)
9. N. Pavliček, B. Fleury, M. Neu, J. Niedenführ, C. Herranz-Lancho, M. Ruben, J. Repp, Phys. Rev. Lett. **108**, 086101 (2012)
10. K.Ø. Hanssen, B. Schuler, A. Williams, T.B. Demissie, E. Hansen, J.H. Andersen, J. Svenson, K. Blinov, M. Repisky, F. Mohn, G. Meyer, J.S. Svendsen, R. Ruud, M. Elyashberg, L. Gross, M. Jaspars, J. Isaksson, Angew. Chem. Int. Ed. **51**, 12238 (2012)
11. F. Mohn, L. Gross, N. Moll, G. Meyer, Nat. Nanotechnol. **7**, 227 (2012)
12. L. Gross, F. Mohn, N. Moll, B. Schuler, A. Criado, E. Guitián, D. Peña, A. Gourdon, G. Meyer, Science **337**, 1326 (2012)
13. M.P. Boneschanscher, J. van der Lit, Z. Sun, I. Swart, P. Liljeroth, D. Vanmaekelbergh, ACS Nano **6**, 1021610221 (2012)
14. J. Welker, F.J. Giessibl, Science **336**, 444 (2012)
15. N. Moll, L. Gross, F. Mohn, A. Curioni, G. Meyer, New J. Phys. **14**, 083023 (2012)
16. J. Zhang, P. Chen, B. Yuan, W. Ji, Z. Cheng, X. Qiu, Science **342**, 611 (2013)
17. J. van der Lit, M.P. Boneschanscher, D. Vanmaekelbergh, M. Ijs, A. Uppstu, M. Ervasti, A. Harju, P. Liljeroth, I. Swart, Nat. Commun. **4**, 2023 (2013)
18. F. Albrecht, M. Neu, C. Quest, I. Swart, J. Repp, J. Am. Chem. Soc. **135**, 9200 (2013)
19. N. Pavliček, C. Herranz-Lancho, B. Fleury, M. Neu, J. Niedenführ, M. Ruben, J. Repp, Phys. Status Solidi B **250**, 2424 (2013)
20. B. Schuler, W. Liu, A. Tkatchenko, N. Moll, G. Meyer, A. Mistry, D. Fox, L. Gross, Phys. Rev. Lett. **111**, 106103 (2013)
21. D.G. de Oteyza, P. Gorman, Y.C. Chen, S. Wickenburg, A. Riss, D.J. Mowbray, G. Etkin, Z. Pedramrazi, H.Z. Tsai, A. Rubio, M.F. Crommie, F.R. Fischer, Science **340**, 1434 (2013)
22. S. Kawai, A. Sadeghi, X. Feng, P. Lifen, R. Pawlak, T. Glatzel, A. Willand, A. Orita, J. Otera, S. Goedecker, E. Meyer, ACS Nano **7**, 9098 (2013)
23. B. Schuler, S.X. Liu, Y. Geng, S. Decurtins, G. Meyer, L. Gross, Nano Lett. **14**, 3342 (2014)
24. M. Schneiderbauer, M. Emmrich, A.J. Weymouth, F.J. Giessibl, Phys. Rev. Lett. **112**, 166102 (2014)
25. F. Mohn, B. Schuler, L. Gross, G. Meyer, Appl. Phys. Lett. **102**, 073109 (2013)
26. A.M. Sweetman, S.P. Jarvis, H. Sang, I. Lekkas, P. Rahe, Y. Wang, J. Wang, N.R. Champness, L. Kantorovich, P. Moriarty, Nat. Commun. **5**, 3931 (2014)
27. T. Hofmann, F. Pielmeier, F.J. Giessibl, Phys. Rev. Lett. **112**, 066101 (2014)
28. L. Gross, Nat. Chem. **3**, 273 (2011)
29. D.M. Eigler, C.P. Lutz, W.E. Rudge, Nature **352**, 600 (1991)
30. J. Repp, G. Meyer, S. Paavilainen, F.E. Olsson, M. Persson, Phys. Rev. Lett. **95**, 225503 (2005)
31. L. Gross, B. Schuler, F. Mohn, N. Moll, N. Pavlicek, W. Steurer, I. Scivetti, K. Kotsis, M. Persson, G. Meyer, Phys. Rev. B 90, 155455 (2014)
32. N. Oyabu, O. Custance, I. Yi, Y. Sugawara, S. Morita, Phys. Rev. Lett. 90, 176102 (2003)
33. N. Oyabu, Y. Sugimoto, M. Abe, O. Custance, S. Morita, Nanotechnology 16, S112 (2005)
34. Y. Sugimoto, P. Pou, O. Custance, P. Jelinek, M. Abe, R. Perez, S. Morita, Science, 322, 413 (2008)

35. O. Custance, R. Perez, S. Morita, Nat. Nanotechnol. 4, 803 (2009)
36. L. Bartels, G. Meyer, K.H. Rieder, Appl. Phys. Lett. **71**, 213 (1997)
37. N. Hauptmann, F. Mohn, L. Gross, G. Meyer, T. Frederiksen, R. Berndt, New J. Phys. **14**, 073032 (2012)
38. R. Temirov, S. Soubatch, O. Neucheva, A.C. Lassise, F.S. Tautz, New J. Phys. **10**, 053012 (2008)
39. C. Weiss, C. Wagner, C. Kleinmann, M. Rohlfing, F.S. Tautz, R. Temirov, Phys. Rev. Lett. **105**, 086103 (2010)
40. G. Kichin, C. Weiss, C. Wagner, F.S. Tautz, R. Temirov, J. Am. Chem. Soc. **133**, 16847 (2011)
41. G. Kichin, C. Wagner, F.S. Tautz, R. Temirov, Phys. Rev. B **87**, 081408 (2013)
42. G. Repp, G. Meyer, S.M. Stojkovic, A. Gourdon, C. Joachim, Phys. Rev. Lett. **94**, 026803 (2005)
43. L. Gross, N. Moll, F. Mohn, A. Curioni, G. Meyer, F. Hanke, M. Persson, Phys. Rev. Lett. **107**, 086101 (2011)
44. N. Pavliček, I. Swart, J. Niedenführ, G. Meyer, J. Repp, Phys. Rev. Lett. **110**, 136101 (2013)
45. C.l. Chiang, C. Xu, Z. Han, W. Ho, Science **344**, 885 (2014)
46. F. Mohn, Dissertation, University of Regensburg, 2012
47. G. Meyer, L. Gross, J. Repp, in *Nanoelectronics and Information Technology, Chap. 12*, 3rd edn., ed. by R. Waser (Wiley VCH, Weinheim, 2012), pp. 282–302
48. F.J. Giessibl, Appl. Phys. Lett. **73**, 3956 (1999)
49. F.J. Giessibl, Appl. Phys. Lett. **76**, 1470 (2000)
50. F.J. Giessibl, Rev. Mod. Phys. **75**, 949 (2003)
51. T.R. Albrecht, P. Grütter, D. Horne, D. Rugar, J. Appl. Phys. **69**, 668 (1991)
52. H. Hölscher, S.M. Langkat, A. Schwarz, R. Wiesendanger, Appl. Phys. Lett. **81**, 4428 (2002)
53. B.J. Albers, T.C. Schwendemann, M.Z. Baykara, N. Pilet, M. Liebmann, E.I. Altman, U.D. Schwarz, Nat. Nanotechnol. **4**, 307 (2009)
54. M.Z. Baykara, T.C. Schwendemann, E.I. Altman, U.D. Schwarz, Adv. Mater. **22**, 2838 (2010)
55. J.E. Sader, S.P. Jarvis, Appl. Phys. Lett. **84**, 1801 (2004)
56. S. Kuhn, P. Rahe, Phys. Rev. B **89**, 235417 (2014)
57. CPMD, v. 3.15 (copyright IBM Corp. 1990–2011, copyright MPI für Festkörperforschung Stuttgart 1997–2001)
58. V. Blum, R. Gehrke, F. Hanke, P. Havu, V. Havu, X. Ren, K. Reuter, M. Scheffler, Comput. Phys. Commun. **180**, 2175 (2009)
59. A. Tkatchenko, M. Scheffler, Phys. Rev. Lett. **102**, 073005 (2009)
60. J.P. Perdew, K. Burke, M. Ernzerhof, Phys. Rev. Lett. **77**, 3865 (1996)
61. S. Grimme, J. Comput. Chem. **27**, 1787 (2006)
62. L. Gross, F. Mohn, P. Liljeroth, J. Repp, F.J. Giessibl, G. Meyer, Science **324**, 1428 (2009)
63. W. Pauli, Z. Phys. A: Hadron. Nucl. **31**, 76583 (1925)
64. L. Pauling, L.O. Brockway, J.Y. Beach, J. Am. Chem. Soc. **57**, 2705 (1935)
65. J. Sedlar, I. Andelić, I. Gutman, D. Vukičević, A. Graovac, Chem. Phys. Lett. **427**, 418 (2006)
66. P. von Ragué Schleyer, Chem. Rev. **101**, 1115 (2001)
67. Cambridge Structural Database (CSD 2012, update 5.33) of the Cambridge Crystallographic Data Centre (CCDC)
68. F. H. Allen, O. Kennard, D. G. Watson, L. Brammer, A. G. Orpen, R. Taylor, J. Chem. Soc. Perkin Trans. 2, 12 (1987)
69. S. Narita, T. Morikawa, T. Shibuya, J. Mol. Struct. (Theochem) **532**, 37 (2000)
70. M. Bühl, A. Hirsch, Chem. Rev. **101**, 1153 (2001)
71. W.I.F. David, R.M. Ibberson, J.C. Matthewman, T.J.S. Prassides, K. Dennis, J.P. Hare, H.W. Kroto, R. Taylor, D.R.M. Walton, Nature **353**, 147 (1991)
72. K. Hedberg, L. Hedberg, D.S. Bethune, C.A. Brown, H.C. Dorn, R.D. Johnson, M. de Vries, Science **254**, 410 (1991)
73. P.J. Fagan, J.C. Calabrese, B. Malone, Science **252**, 1160 (1991)
74. S. Liu, Y.J. Lu, M.M. Kappes, J.A. Ibers, Science **254**, 408 (1991)
75. A. Criado, D. Peña, A. Cobas, E. Guitián, Chem. Eur. J. **16**, 9736 (2010)

76. R. Goddard, M.W. Haenel, W.C. Herndon, C. Krueger, M. Zander, J. Am. Chem. Soc. **117**, 30 (1995)
77. A.J. Weymouth, T. Hofmann, F.J. Giessibl, Science **343**, 1120 (2014)
78. M. Neu, N. Moll, L. Gross, G. Meyer, F.J. Giessibl, J. Repp, Phys. Rev. B **89**, 205407 (2014)
79. P. Hapala, G. Kichin, C. Wagner, F.S. Tautz, R. Temirov, P. Jelinek, Phys. Rev. B 90, 085421 (2014)
80. M.P. Boneschanscher, S.K. Hämäläinen, P. Liljeroth, I. Swart, ACS Nano **8**, 3006 (2014)
81. N. Moll, B. Schuler, S. Kawai, F. Xu, L. Peng, A. Orita, J. Otera, A. Curioni, M. Neu, J. Repp, G. Meyer, L. Gross, Nano Lett. **14**, 6127 (2014)
82. S. Henze, O. Bauer, T.L. Lee, M. Sokolowski, F. Tautz, Surf. Sci. **601**, 1566 (2007)
83. J. Zegenhagen, Surf. Sci. Rep. **18**, 202 (1993)
84. D. Woodruff, Prog. Surf. Sci. **57**, 1 (1998)
85. J. Lagoute, K. Kanisawa, S. Fölsch, Phys. Rev. B **70**, 245415 (2004)
86. K. Lämmle, T. Trevethan, A. Schwarz, M. Watkins, A. Shluger, R. Wiesendanger, Nano Lett. **10**, 2965 (2010)
87. T.A. Jung, R.R. Schlittler, J.K. Gimzewski, Nature **386**, 696 (1997)
88. S. K. Hämäläinen, N. van der Heijden, J. van der Lit, S. den Hartog, P. Liljeroth, I. Swart, Phys. Rev. Lett. 113, 186102 (2014)
89. K. Müller, A.P. Seitsonen, T. Brugger, J. Westover, T. Greber, T. Jung, A. Kara, J. Phys. Chem. C **116**, 23465 (2012)
90. B. Schuler, S. Collazos, L. Gross, G. Meyer, D. Pérez, E. Guitián, D. Peña, Angew. Chem. Int. Ed. **126**, 91509152 (2014)
91. A. Mistry, B. Moreton, B. Schuler, F. Mohn, G. Meyer, L. Gross, A. Williams, P. Scott, G. Costantini, D.J. Fox, Chem. Eur. J. 21, 2011 (2015)
92. P. Crews, J. Rodriguez, M. Jaspars, *Organic Structure Analysis* (Oxford University Press, Oxford, 2010)
93. Y. Sugimoto, P. Pou, M. Abe, P. Jelinek, R. Pérez, S. Morita, O. Custance, Nature **446**, 64 (2007)
94. M. Nonnenmacher, M.P. O'Boyle, H.K. Wickramasinghe, Appl. Phys. Lett. **58**, 2921 (1991)
95. S. Sadewasser, T. Glatzel (eds.), *Kelvin Probe Force Microscopy* (Springer, Berlin, 2011)
96. S. Kitamura, K. Yonei, M. Iwatsuki, C.B. Mooney, Y. Fukuda, Jap. J. Appl. Phys. **44**, 8113 (2005)
97. S.A. Burke, J.M. LeDue, Y. Miyahara, J.M. Topple, S. Fostner, P. Grütter, Nanotechnology **20**, 264012 (2009)
98. S. Sadewasser, P. Jelinek, C.K. Fang, O. Custance, Y. Yamada, Y. Sugimoto, M. Abe, S. Morita, Phys. Rev. Lett. **103**, 266103 (2009)
99. R. Stomp, Y. Miyahara, S. Schaer, Q. Sun, H. Guo, P. Grutter, S. Studenikin, P. Poole, A. Sachrajda, Phys. Rev. Lett. **94**, 056802 (2005)
100. F. Bocquet, L. Nony, C. Loppacher, T. Glatzel, Phys. Rev. B **78**, 035410 (2008)
101. G.H. Enevoldsen, T. Glatzel, M.C. Christensen, J.V. Lauritsen, F. Besenbacher, Phys. Rev. Lett. **100**, 236104 (2008)
102. A. Yurtsever, Y. Sugimoto, M. Fukumoto, M. Abe, S. Morita, Appl. Phys. Lett. **101**, 083119 (2012)
103. Z.M. Ma, L. Kou, Y. Naitoh, Y.J. Li, Y. Sugawara, Nanotechnology **24**, 225701 (2013)
104. T. König, G.H. Simon, H.P. Rust, G. Pacchioni, M. Heyde, H.J. Freund, J. Am. Chem. Soc. **131**, 17544 (2009)
105. T. Leoni, O. Guillermet, H. Walch, V. Langlais, A. Scheuermann, J. Bonvoisin, S. Gauthier, Phys. Rev. Lett. **106**, 216103 (2011)
106. P. Liljeroth, J. Repp, G. Meyer, Science **317**, 1203 (2007)

Chapter 13
Mechanochemistry at Silicon Surfaces

Adam Sweetman, Samuel Paul Jarvis and Philip Moriarty

Abstract Non-contact atomic force microscopy has driven the development of a variety of exciting chemomechanical protocols for manipulating metal, semiconductor, and insulating surfaces at the single chemical bond limit. In this chapter we discuss atomic manipulation on silicon surfaces via mechanical force alone (mechanochemistry), with a particular focus on a prototype of a mechanically-actuated atomic switch: the flipping of bi-stable dimers on the Si(100)–c(4 × 2) surface. The importance of the mutual orientation of electronic orbitals in the dimer manipulation process is explored in the broader context of the mechanochemical modification of covalently bonded semiconductors. In addition, variations in surface reactivity play a key role in the ability to generate (and image) atomic-scale modifications and we discuss experimental and theoretical work on H:Si(100) as an exemplar of a passivated and chemically inert substrate, as compared to the relatively high reactivity of the unpassivated Si(100) surface.

13.1 Introduction

A fascinating and sometimes fractious debate between K. Eric Drexler, who pioneered the controversial concept of atomically precise manufacturing via molecular assemblers, and Richard E Smalley, Nobel Laureate and co-discoverer of fullerenes, was published in Chemical and Engineering News (C&EN) in 2003 [1] (shortly before Smalley sadly passed away after losing a battle with lymphocytic leukemia.) In their exchange of views in C&EN, Drexler and Smalley focused on the

A. Sweetman (✉) · S.P. Jarvis · P. Moriarty
School of Physics and Astronomy, University of Nottingham,
Nottingham NG7 2RD, UK
e-mail: adam.sweetman@nottingham.ac.uk

S.P. Jarvis
e-mail: samuel.jarvis@nottingham.ac.uk

P. Moriarty
e-mail: philip.moriarty@nottingham.ac.uk

© Springer International Publishing Switzerland 2015

S. Morita et al. (eds.), *Noncontact Atomic Force Microscopy*,
NanoScience and Technology, DOI 10.1007/978-3-319-15588-3_13

feasibility (or not) of mechanochemical (and mechanosynthetic) reactions driven by computer-actuated molecular 'tools'.[1]

Mechanochemistry, in the context of Drexler's framework, involves the movement of a molecular tool along a deterministic trajectory towards a specific atomic site where an interaction (or reaction) is subsequently driven by mechanical force. As is clear from the various chapters in this book (including our own),[2] there are rather close parallels between the type of mechanochemistry strategy Drexler proposed and the atomic/molecular manipulation protocols now used in a wide variety of NC-AFM experiments.

Smalley argued, however, that there were two key "show-stoppers" associated with Drexler's molecular assembler concept: the so-called "fat" and "sticky" fingers issues. The former relates to steric hindrance—as Smalley saw it, molecular assemblers which were based on computer control of atomically/molecularly sharp tools (very similar to the tips used in NC-AFM) were *verboten* due to the inability of atomically sharp fingers to control reactions in a confined volume. Drexler countered that he had not proposed the type of atomic fingers that Smalley had in mind. The "sticky fingers" issue, on the other hand, relates to the very important matter of the reactivity of the tip tool. This was rather prescient of Smalley, given the current focus on CO-passivated tips in dynamic force microscopy (as described at length elsewhere in this volume). It's also a topic to which we shall return later in this chapter in the context of imaging and manipulating silicon surfaces.

Atomic-precision mechanical manipulation of the type debated by Drexler and Smalley—or, at least, the core protocol of controlling atoms, molecules, and reactions via computer-directed chemomechanical force—is demonstrably possible. There are now a significant number of examples of NC-AFM-driven control of single atoms and molecules including the measurement of the force required to move an atom [3], single molecule translation [4], controlled defect positioning [5], and, of particular relevance to the mechanosynthesis concept, Sugimoto et al. [6]'s pioneering demonstration of force-driven exchange reactions at Si(111) surfaces. In this chapter we focus on the imaging, force-distance "spectroscopy", and mechanochemical manipulation of atoms at silicon surfaces, but with a particular focus on Si(100) and H:Si(100).

The Si(100) surface has a long and rather chequered history of study spanning a number of decades. There was particularly intense debate for a number of years regarding the issue of whether the ground state of the Si(100) surface comprised planar or buckled dimers. A decade ago, Uda et al. [7] wrote a helpful review of the state of knowledge of the ground state of the Si(100) surface at the time, where it was widely accepted—following a period of some controversy in the literature—that the c(4 × 2) reconstruction comprising buckled dimers (see following sections) was indeed the lowest energy configuration. In the same year as that review was published,

[1] One of the authors of this chapter (PM) subsequently debated the physics and chemistry of mechanosynthetic reactions at length with Chris Phoenix, a researcher who had co-authored papers with Drexler on the implications of molecular assembler-based technology [2].

[2] ...and, indeed, previous volumes in the Non-contact Atomic Force Microscopy series.

a careful study of the influence of both tip-sample interactions and surface defects on the c(4 × 2) reconstruction [8] provided clear evidence of the strong sensitivity of the dimer configuration to local and non-local perturbations. Two years later Pennec et al. [9] carried out a very elegant scanning tunnelling microscopy (STM) study of the dynamics of the Si(100)–c(4 × 2) surface, which they "mapped" onto an Ising chain model of the system, probing the dynamics of phason defects (a topic we shall return to below). In the same year, an NC-AFM study carried out at 5 K, with support from density functional theory (DFT) calculations, provided very strong evidence that chemomechanical tip-sample interactions tipped the energy balance between the buckled and planar dimer configurations [10].

This very brief overview of some of the milestones in STM and NC-AFM investigations of the Si(100) surface hopefully provides a hint as to the rich chemical physics (and physical chemistry) associated with the "native" c(4 × 2) reconstruction. Despite its apparent simplicity (as compared to, for example, the Si(111)-(7 × 7) reconstruction), the Si(100) surface has proven to be a source of subtle and counter-intutive physics and chemistry, not least in terms of its response to an NC-AFM probe. In this chapter we discuss a series of experiments, and associated DFT calculations, we have carried out which have focussed on elucidating and exploiting NC-AFM-induced mechanochemistry on Si(100) and H:Si(100) surfaces.

13.2 Experimental Methods

The experimental results presented in this chapter were obtained using two commercial scanning probe instruments. Results describing the imaging and manipulation of the bare Si(100) surface were obtained using an Omicron Nanotechnology GmbH combined low temperature STM/NC-AFM, whilst results on the hydrogen passivated H:Si(100) surface were obtained using a similar instrument manufactured by Createc GmbH. All results were obtained at cryogenic temperatures, either at 77 K using liquid nitrogen for cooling, or at 5 K with liquid helium cooling. Due to the energy barriers associated with dimer manipulation on the Si(100) surface, all controlled manipulation experiments were performed at 5 K.

In both systems clean Si(100) surfaces were produced by flashing the sample at ∼1150 °C before rapid cooling to 900 °C followed by slow cooling to room temperature, maintaining a pressure of below 2×10^{-10} mbar. For preparation of H:Si(100) surfaces, hydrogen was introduced into the chamber via a thermal gas cracker at a pressure of $1-5 \times 10^{-7}$ mbars. The sample was exposed for 3 min whilst held at a temperature of 400 ± 30 °C.

Both systems were equipped with qPlus sensors [11] with electrochemically etched tungsten wire attached to one tine of the tuning fork for use as a scanning probe tip. Sensors were introduced into the system and prepared on the surface using conventional STM and NC-AFM tip preparation techniques such as voltage pulsing and controlled crashes. No other in situ tip preparation was performed (for example heating or argon sputtering), and we attribute successful imaging as being partly

due to the stability afforded by operation at low temperatures, and in particular, the "freezing out" of diffusion of contamination to the tip apex from the shank of the tip. Consequently, we note that imaging at elevated temperatures using this protocol is likely to be problematic, and further tip cleaning and preparation steps are likely to be necessary. Due to the nature of our tip preparation techniques we expect that the apex of the tip is likely terminated by clusters of the surface material (i.e. silicon), rather than tungsten terminated.

The sensors used typically exhibited resonant frequencies (f_0) of approximately 25 kHz, and Q factors of between 1000 and 50,000. We note that while, as expected, the Q factor varies strongly with operating temperature, we also observe a strong dependence on the Q due to the seating of the tuning fork in the scan head and the position of the scan tube on the coarse movement motors. In the experiments described below, oscillation amplitudes (A_0) of between 50 and 400 pm were used.

In order to avoid complicating factors such as electronic crosstalk [12, 13], local induced electrostatic contributions to the force (the so-called "Phantom force" [14]), or perturbation of the surface by tunnelling electrons [8, 9, 15, 16], all controlled manipulation experiments were performed at 0 V applied bias and consequently no tunnelling current signal was detected. In some imaging experiments a small bias was applied, and in these cases average tunnel current signals on the order of a few picoamps were sometimes detected. In all the data presented in this chapter it was ensured that the NC-AFM data was not qualitatively affected by the presence of the tunnel current (where present) by switching the applied bias on and off, and ensuring the imaging was not affected by the presence of the tunnel current signal.

In this chapter images are presented taken in both feedback (constant Δf), and constant height mode. For clarity topographic (Z) images are presented in a yellow colour scale, whilst constant height (Δf) images are presented in a black and white colour scale. All images are presented raw, with the exception of plane correction for the constant Δf topography images. All imaging and spectroscopy experiments were performed in the constant amplitude mode.

Controlled manipulation was performed using a $\Delta f(z)$ (Force spectroscopy) protocol as described in detail elsewhere [17–19]. Briefly, during a scan the tip is positioned in feedback over the site of interest, the feedback is disengaged and the tip retracted a small distance (~1 nm). The tip then slowly approaches a set distance towards the surface whilst recording both the Δf and dissipation signals whilst maintaining constant A_0. The tip is then retracted at the same rate whilst continuing to monitor the aforementioned signals. When the tip reaches its initial starting position the feedback is re-engaged and the scan continued.

13.2.1 Force Extraction

In principle it is now relatively straightforward to convert Δf spectroscopy data into a quantitative force measurement over a range of tip-sample distances via a range of mathematical techniques [20, 21]. In practice, however, a variety of complicating

factors exist which require consideration. These have been described in detail elsewhere [18, 19, 22], but the most pertinent for the data presented here is that the quantity of interest in NC-AFM experiments is not generally the total force between the tip and surface, but rather the short-range (or, more specifically, the "site-specific") forces between the very apex of the tip and the few atoms on the surface directly underneath the terminating atom. These must be separated from any long range ("non-site-specific") interactions, such as electrostatic or van der Waals (vdW) before any rigorous analysis of the force data can be performed.

For the measurement of forces on absorbed adatoms and molecules on metal surfaces [23, 24], large molecules on reactive semiconductor surfaces [25], or surfaces with particular surface features [26], this is most easily accomplished by the so-called "on-minus-off" method, where a measurement is taken in a location without significant site-specific forces (the "off" measurement) and subtracted from the measurement containing both site-specific and non-site-specific forces (the "on" measurement), resulting in a measurement containing only the short-range forces.

In general, however, and including the case of the Si(100) surface, this procedure is not possible as there are no locations completely free from site-specific interaction. In these cases two different approaches are used, subtraction of the long-range forces via a fitting and extrapolation technique [6, 22], or "difference" measurements where only the *relative* forces between different sites, rather than absolute forces, are recovered [27, 28]. In the following section the first method is used where we require a measurement of the absolute force, and the second method is used were relative forces between different sites are discussed. We note explicitly though that any forces recovered by the extrapolation method must necessarily include an additional uncertainty introduced by the fitting and extrapolation, details of which are discussed elsewhere [19, 22]. Once short range Δf curves have been extracted, inversion to force was performed using the Sader-Jarvis [29] algorithm.

13.3 Computational Methods

To gain greater insight into the physical processes underpinning the experimental observations in this chapter we modelled the complete tip-surface system with the ab initio density functional theory (DFT) method as implemented in the SIESTA code [30]. In our calculations we used the GGA Perdew-Burke-Ernzerhof (PBE) density functional and norm-conserving pseudopotentials with a double-zeta polarised basis set providing a total of 13 orbitals to describe the valence electrons on each silicon atom. As a convergence criteria, atomic relaxation was considered complete when forces on atoms were below 0.01 eV/Å.

The Si(100) surface was modelled as a 6-layer slab with 16 surface dimers arranged as 2 rows, each 8 dimers in length. The missing bulk was then simulated by restraining the bottom two layers of silicon and terminating with a hydrogen layer. The large slab size was chosen to limit the effect of the finite cell size on calculations, such that when periodically repeated in each direction there are always

several unaffected dimers between manipulated atoms. For example, when modelling a phason pair (four dimers in length), after periodically repeating the system, four other dimers, in a standard c(4 × 2)/p(2 × 2) buckling configuration, will be present before any repeat of the phason unit. Because of the cell sizes used, only the Γ point was employed in sampling the Brillouin zone in all of our simulations.

Two types of tip cluster were modelled in our simulations, a standard ten atom pyramidal Si tip [31, 32] and a more complicated thirty atom tip cluster terminating in a dimerised tip apex [31, 33, 34]. Whilst only four atoms at the apex of the pyramidal tip are free to move in response to the interaction with the surface, the dimerised tip comprises fifteen atoms free to move, providing a somewhat more realistic tip apex with respect to tip deformation and introduces an asymmetry into the system.

To simulate force-distance curves the tip cluster was positioned at an initial tip-sample separation of 8 Å above the surface, positioned above the lower or upper atom of a surface dimer as required. The vertical distance z is defined as the distance between the surface plane measured by the vertical position of the upper dimer atom and the lowest tip apex atom prior to relaxation. The tip-sample distance was then decreased in quasi-static steps until just beyond the force turning point, at which point the tip was retracted. At each step the geometry of the system was optimised and the vertical forces acting on the fixed tip atoms summed in order to calculate the total force acting on the tip.

13.4 Si(100) Results

13.4.1 The Si(100) Surface Structure Viewed by NC-AFM

The Si(100) surface consists of rows of paired atoms running in perpendicular directions on alternate atomic terraces. The topmost layer of atoms on the Si(100) surface pair up to produce rows of dimers, in order to reduce the number of dangling bonds per atom from two to one. As a result of this dimerisation, there is a strong σ like bond between the two atoms of the dimer, but also a weak π like interaction between the two remaining dangling bonds. This reconstruction produces rows of dimers with a p(2 × 1) periodicity. As the orientation of the dimers switches across atomic steps, two types of step exist. In the first the dimer rows on the upper terrace are perpendicular to the step (called an S_B step), and in the second the dimer rows on the upper terrace are parallel to the step (called an S_A step), as shown in Fig. 13.1a, b.

The surface reconstruction is further complicated by the fact that these symmetric dimers subsequently buckle to further lower the free energy of the surface as part of a Jahn-Teller distortion, resulting in charge transfer from the lower atom of the buckled dimer to the upper atom. This results in a number of different possible surface reconstructions, depending on the arrangement and orientation of the buckled dimers. Primarily these are the c(4 × 2) phase, where dimers in the next row are buckled in anti-phase, and the p(2 × 2) phase, where dimers in the next row are buckled in-phase.

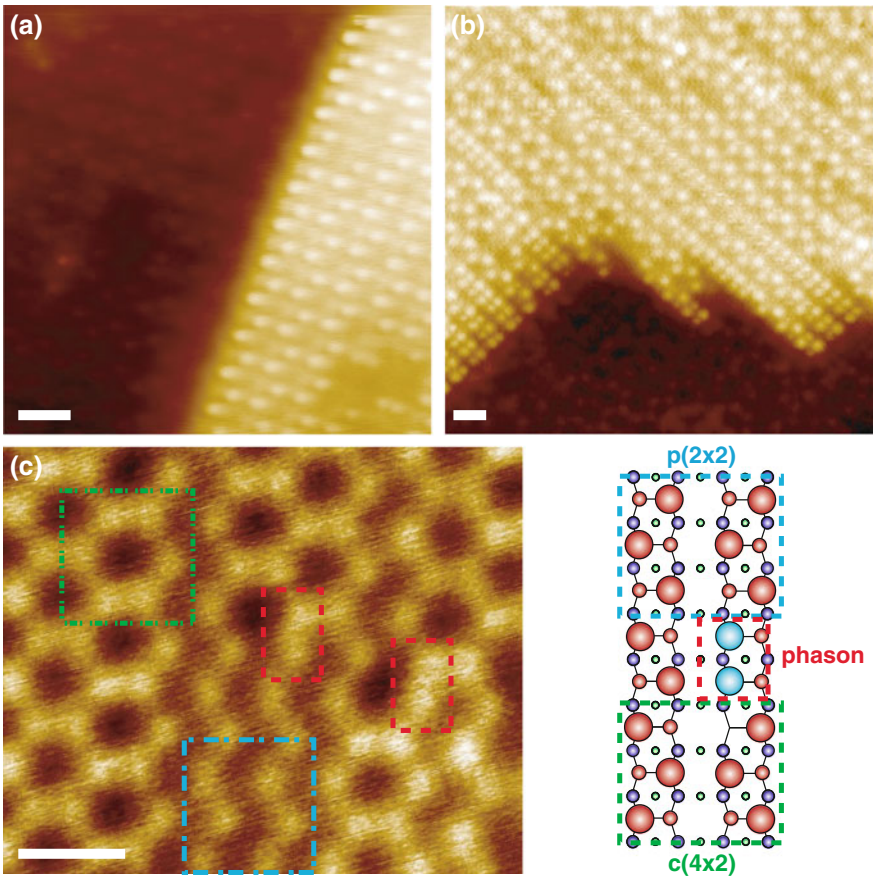

Fig. 13.1 NC-AFM images of the Si(100) surface at low temperatures showing the two types of single atomic steps found on the surface. **a** S_A step imaged at 5 K: $\Delta f = -17.6$ Hz; $A_0 = 250$ pm; $V_{gap} = 0$ V. **b** S_B step imaged at 77 K $\Delta f = -40$ Hz; $A_0 = 100$ pm; $V_{gap} \sim 10$ mV. **c** High-resolution image of the surface and ball and stick model showing the c(4 × 2), p(2 × 2), and phason defect dimer buckling structures. Scale bars = 1 nm. Figure adapted from [17]

Previous studies have concluded that the c(4 × 2) is the true ground state of the system, although the difference between the c(4 × 2) and p(2 × 2) is extremely small [35]. Also observed are 'phase defects' or 'phasons' which consist of two contiguous dimers in the same row with the same buckling structure, and which allow the transition between the two different phase regions. An overview of how the surface appears during NC-AFM imaging at low temperature, and examples of the different buckling structures, is shown in Fig. 13.1c.

Interpretation of scanning probe images of the Si(100) surface at low temperatures can be challenging due to the relatively small energy barriers required for changes in the buckling of the dimers, which can easily be overcome by the influence of the

probe. This can result in an apparent symmetric p(2 × 1) phase resulting from the manipulation of the dimers as the tip passes over them either due to electronic [8, 9, 15, 36, 37] or mechanical [10, 38, 39] effects. Consequently for controlled manipulation experiments it is vital to image at a tip-sample distance that does not disturb the configuration of the surface. At these setpoints only the upper atoms of the dimers are imaged, and the lower atom remains invisible.

13.4.2 Dimer Manipulation by Mechanical Force

In this section we explore the behaviour of the Si(100) surface under atomically precise mechanical perturbation by a scanning probe tip. As noted previously, it is well known that the Si(100) surface is sensitive to perturbation during scanning in STM and AFM experiments, and controlled precise manipulation within a single row has also been demonstrated via tunnel current injection [40, 41]. Crucially, however, there remains an open question: "Can we modify the Si(100) surface by manipulating silicon dimers on an individual basis in order to form complex structures?" [39, 42]. This manipulation of single bond angle stands as a vital precursor to mechanochemistry.

13.4.2.1 Controlled Dimer Manipulation

In order to perform atomically precise manipulation, we first image the surface at parameters such that the interaction during scanning does not itself perturb the surface. Manipulation is performed by extending the tip towards the surface in Z at a specific surface site whilst recording the frequency shift (Δf) of the tuning fork—see Fig. 13.2.

The full protocol for manipulation is as follows—the tip is first positioned over the lower atom of the dimer and a measurement of $\Delta f(z)$ performed. As the tip approaches the surface within a distance of a few Å 's a chemical bond forms between the terminating atom of the tip apex and the lower atom of the dimer, causing the atom to jump up into contact with the tip. This results in the dimer changing configuration, and this jump to contact can be observed as a sharp increase in the frequency shift of the tuning fork. On retraction of the tip the frequency shift follows a different path indicating the tip is now retracting over the up atom of the dimer.

At this stage we highlight that in the experimental data shown in Fig. 13.2 it is not only the dimer underneath the tip which has changed configuration, but also that of one of the neighbouring dimers. The manipulation therefore results in a buckling configuration consisting of what we term a "phason pair". This is in contrast to the expected outcome for a single dimer flip which would result in three dimers buckled with the same angle, which we term "three-in-a-row". We find that by performing the same manipulation procedure on the new down atom of the dimer, as shown in Fig. 13.2b), it is possible to reverse the previous manipulation and restore the native

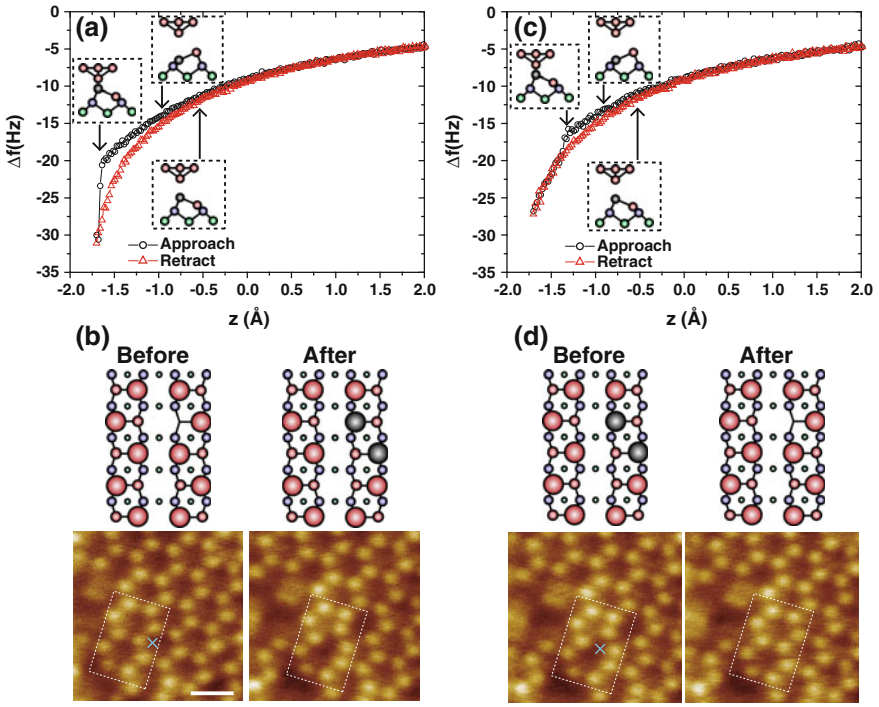

Fig. 13.2 Controlled manipulation of the dimer buckling structure on the Si(100) surface via $\Delta f(z)$ spectroscopy. **a** $\Delta f(z)$ curves showing Δf behaviour during approach (*black circles*) and retraction (*red triangles*) of the tip. Cartoon illustrations show the position of the atoms in the tip-sample junction at each stage of the manipulation. **b** Constant Δf image of surface structure before (*left*) and after (*right*) manipulation. Cross indicates the spectroscopy position. Cartoon shows boxed area with the manipulated dimers highlighted in *black*. **c**, **d** As for (**a**, **b**) but showing the reverse manipulation restoring the original surface structure. (Image parameters: $A_0 = 250$ pm; $\Delta f = -9.1$ Hz). Scale bars = 1 nm. Figure adapted from [18]

buckling structure of the surface. In both cases the manipulation causes a double flip event. We also note that in the reverse manipulation the magnitude of the Δf signal at the location of the jump is reduced compared to the original manipulation. We will return to this, and the origin of the double manipulation, later in the chapter.

13.4.2.2 Quantitative Analysis of Force Required to Flip a Silicon Dimer

In Fig. 13.3 we compare experimental F(z) curves with DFT calculated spectra for a flip from a standard buckled configuration and the reverse manipulation. In each case, during the approach of the tip, there is a sharp increase in the magnitude of the force when a certain threshold is reached, indicating that the dimer has flipped. The lack of any change in the dissipation signal indicates both that the tip is structurally rigid and

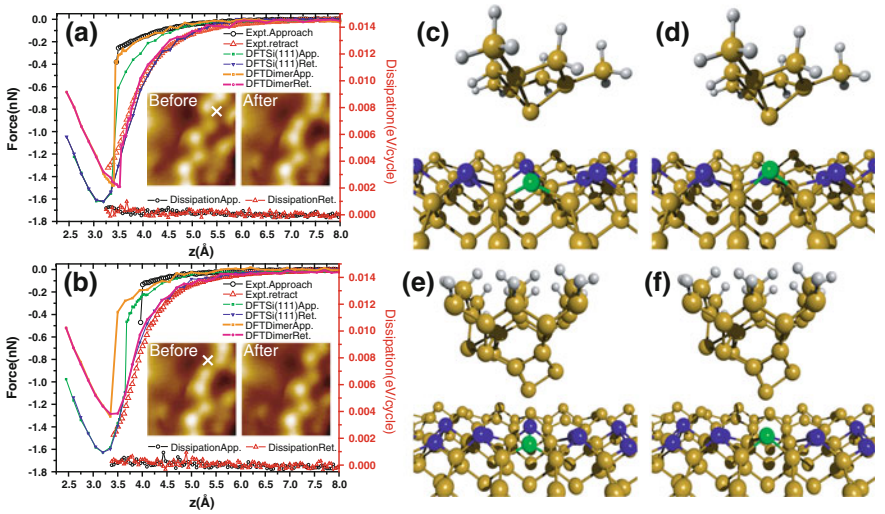

Fig. 13.3 Analysis of the vertical tip-sample forces during dimer manipulation. **a** Experimental and calculated short-range (chemical) force measured during dimer flipping experiment. Also plotted is the experimental dissipation signal which remains flat throughout the manipulation process. *Inset* Constant Δf images of surface structure before (*left*) and after (*right*) manipulation. Imaging parameters $\Delta f = -17\,\text{Hz}$, $A_0 = 50\,\text{pm}$. **b** As for (**a**) but showing the reverse manipulation process from phason pair to buckled structure. **c**, **d** calculated geometries just before, and just after manipulation of the surface dimer by a H3 type tip cluster. **e**, **f** As for (**c**, **d**) but for a dimer type tip cluster. The surface atom directly under the tip is highlighted in *green*. Figure adapted from [18]

that the dimer flip event, occurring as it does during a single tip oscillation period, is associated with a negligible *average* energy loss per cycle. In other experimental datasets we have observed significant dissipation, but assign this either to relaxations within the tip [31, 43], or to apparent dissipation associated with the transfer function between the coupling of the excitation piezo and the tuning fork [44]. Also note that since the force values extracted via the Sader-Jarvis algorithm after a discontinuity in Δf are not strictly valid [6], the force values on the approach curves after toggling of the dimer have not been plotted.

First, we consider the retract F(z) curves, which arise from the interaction of the AFM tip with the surface "up" dimer atom (after being switched from an initial "down" state during the approach curve). Independent of the choice of tip type in the DFT calculations, there is good agreement between experiment and theory for the F(z) spectra acquired above "up" atoms. This provides strong supporting evidence that the force-distance data we have acquired indeed arises from the formation of a single covalent bond between tip and sample.

Comparison of the experimental and calculated curves for the approach spectra is more complicated. DFT simulations predict that both the tip type and the configuration of neighbouring dimers can affect the threshold force required for a dimer flip [17]. Although raw $\Delta f(z)$ spectra also clearly illustrate the influence of the

configuration of neighbouring dimers on the threshold force (note the variation in Δf threshold in Fig. 13.2 for example), we find the error bars associated with the extraction of the short range force from the $\Delta f(z)$ data are of same order as the differences predicted by DFT for different tips. Nonetheless, on the basis of multiple manipulation events, we find that the force required to flip a dimer is significantly less than 1 nN, falling in the range 100–600 pN. We note that in particular, as suggested by the raw $\Delta f(z)$ data, on a given dimer the threshold force required to restore the native buckling structure is smaller that that required to initially create the phason pair structure.

13.4.2.3 Atomically Precise Dimer Manipulation and Force Threshold Variation

Given the results discussed above, a pertinent question is whether truly atomically precise manipulation (i.e. non-correlated single dimer flipping) of the Si(100) surface is possible, or if the intrinsic coupling of the dimers necessarily results in long range relaxations during manipulation. In Fig. 13.4 we show that such manipulation is indeed possible, *providing* the result of a manipulation attempt is not to form a structure with three (or more) contiguous dimers with the same buckling orientation. Via force spectroscopy manipulation, it is possible to change the location of a single phason within a dimer row with single atom precision. Each manipulation results in the target atom jumping up into contact with the tip and changing the buckling configuration of the target dimer without influencing the neighbouring dimers. Conversely, all manipulations (performed using the exact same parameters) that would result in "three-in-a-row" or longer structure, always resulted in long-range relaxation.

In Fig. 13.5 we also show that by performing force spectroscopy operations close to an existing defect it is also possible to produce single phasons, effectively pulling them "out" of the defect. These results strongly suggest that it is not a lack of precision in the experimental technique that prevents the formation of the "three-in-a-row" structure, but rather an intrinsic property of the surface.

In Fig. 13.6 we show force difference measurements (extracted from measurements performed over the dimers, and in between the dimer rows) extracted during single dimer flips at different positions within the same row. Here, the quantity of interest is the *variation* in the force threshold needed to flip the dimer, rather than the absolute magnitude of the force. We observe variation on the order of approximately 100 pN between dimer flips performed at different locations along the row, for what is nominally the same manipulation event in each case. We note that in this instance we do not observe any systematic variation in the threshold force along the row, although this is perhaps not unexpected given the complex effect strain can have on the surface (see Sect. 13.4.4).

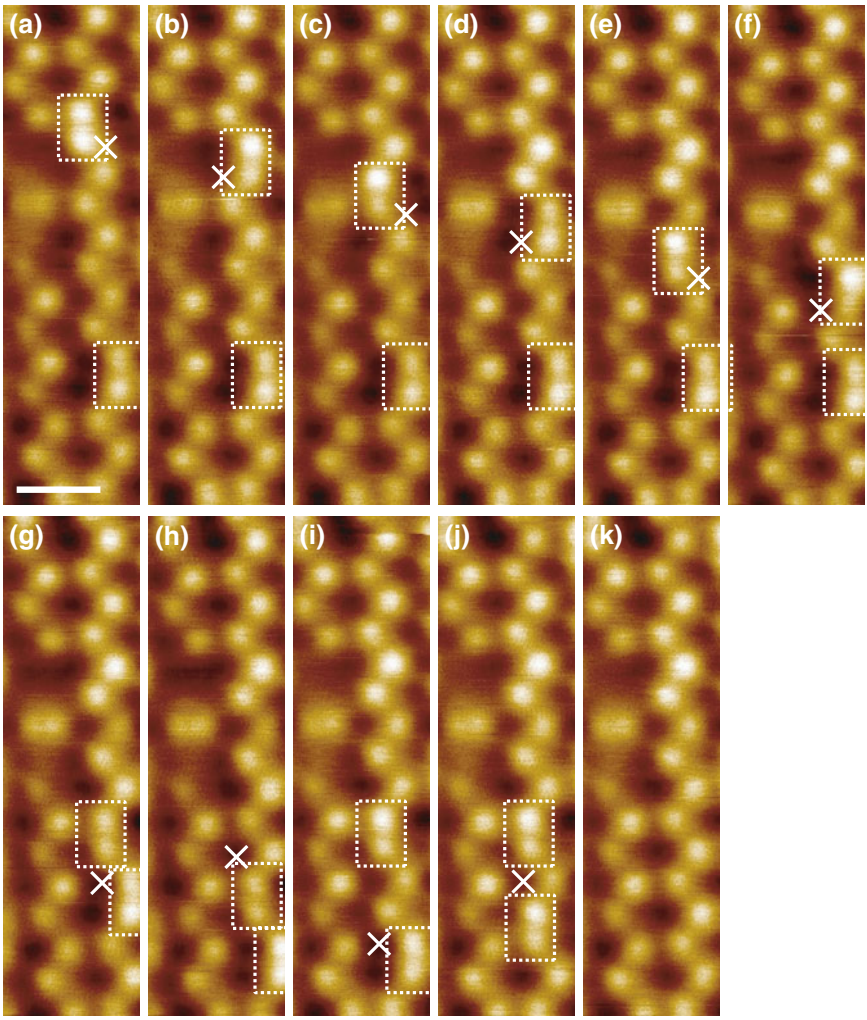

Fig. 13.4 Sequence of images showing atomically precise manipulation of the buckling structure within a single dimer row. In each image the phasons are highlighted and a cross shows the position of the $\Delta f(z)$ spectroscopy point. In **a**–**f** each spectroscopy point causes a change in the buckling of a single dimer, resulting in a manipulation of the upper phason towards the lower phason, one dimer at a time. **g** An attempt is made to create a "three-in-a-row" structure from the phason pair, a long-range relaxation results. In **h** an attempt is made to create a "four-in-a-row" structure, again a long-range relaxation results. In **i** one of the phasons is moved towards the top of the image via a single dimer flip. In **j** an attempt is made to create a "five-in-a-row" structure, again a long-range relaxation results, in this case restoring the native c(4 × 2) buckling structure. Scale bar = 1 nm. Figure adapted from [18]

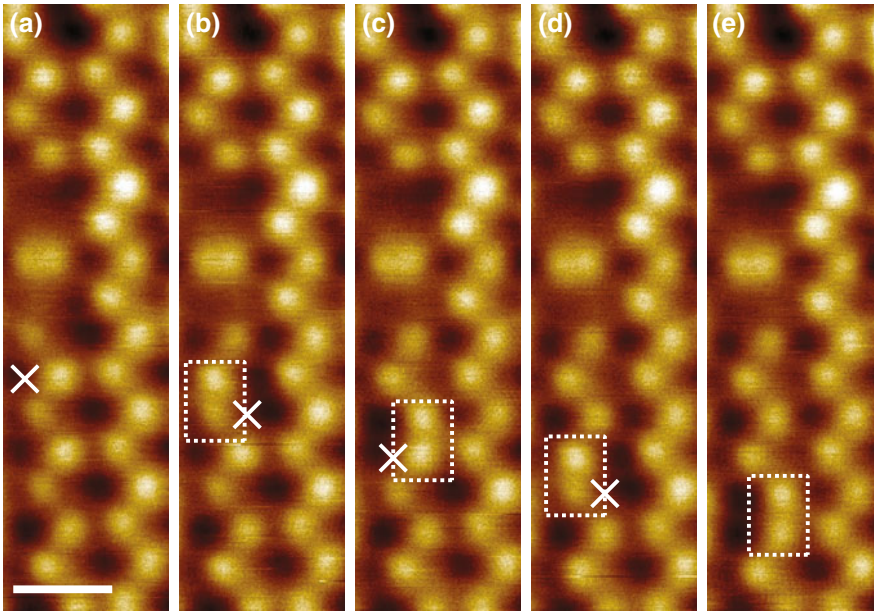

Fig. 13.5 Creation and manipulation of a single phason close to a DV defect. **a** Pristine c(4 × 2) surface, cross shows position of spectroscopy point. **b** A single phason is created as the result of the manipulation (*dotted box*). **c**–**e** The phason is manipulated one dimer at a time along the row by single manipulation events. *Scale bar* = 1 nm

13.4.2.4 Effect of Tip Positioning

At this juncture we must also consider that a significant variation in the threshold force to flip a dimer may also arise from the precise positioning of the tip apex above the down atom, and also critically the relative bond angles of the surface dimer and terminating tip atom. Figure 13.7 shows how the variation in force threshold varies for both a H3 and a dimer type tip in DFT simulated spectroscopy as the tips are moved laterally across the dimer rows. Due to the symmetric nature of the dangling bond on the H3 tip with respect to the surface, the force threshold with position is symmetric around the mirror symmetry of the dimer rows. For the dimer tip in contrast, the tilted angle of the dangling bond at the tip apex results in a strong asymmetry. Therefore it is clear that both the positioning of the tip, *and* the relative orientation of the dangling bonds, play a strong role in determining the outcome of manipulation experiments.

With respect to the experimental data shown in Fig. 13.6, it is worth noting that in each case the tip was positioned centrally above the position of the down atom with a precision better than 0.1 nm. We therefore expect that while variation in the positioning of the tip may account for some of the observed variation the variation in stability of the dimers across the surface remains the dominant factor.

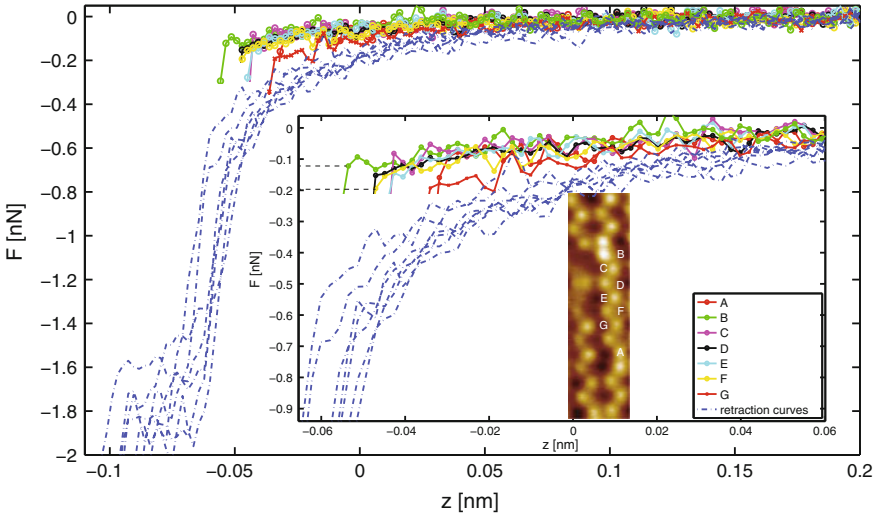

Fig. 13.6 Variation in the force required to flip a single dimer over a range of different positions within a dimer row. Plots of force difference measurements extracted by subtraction of data taken in-between the rows from data taken during phason manipulation. (*Inset*) Zoom of region around the force threshold for dimer manipulation. *Scan* shows region with the locations of each spectra indicated by letters corresponding to the relevant curves. *Dotted lines* on *inset graph* show approximate range of variation in the force threshold

13.4.3 Energetic Pathway to Manipulation

Obtaining a more complete understanding of how and why correlated flipping takes place is particularly challenging. As seen above, although good qualitative agreement is found between the experimental and simulated force spectroscopy, a key aspect of the experimental results which is not reproduced in the simulations is the non-local relaxation of the surface. Specifically, in all simulations of dimer manipulation only the dimer directly under the tip is flipped, resulting in a "three-in-a-row" structure. As discussed above, in all experimental attempts to create contiguously buckled dimers, such as the "three-in-a-row", we *always* observe at least on additional dimer flip leading to a phason structure. We also note that, despite extensive STM and NC-AFM imaging with multiple tips we also never observe a native "three-in-a-row" structure.

In order to investigate this apparent disparity between simulation and experiment we performed extensive nudged elastic band (NEB) calculations to explore the local energy landscape of the complete system during manipulation. Specifically, we simulated the energy barriers required to transit between an initial c(4 × 2) surface arrangement and the final phason pair structure. Critically, the barriers were recalculated in the presence of a silicon tip cluster positioned at different tip-sample separations in order to model the influence of the NC-AFM tip, as shown in Fig. 13.8.

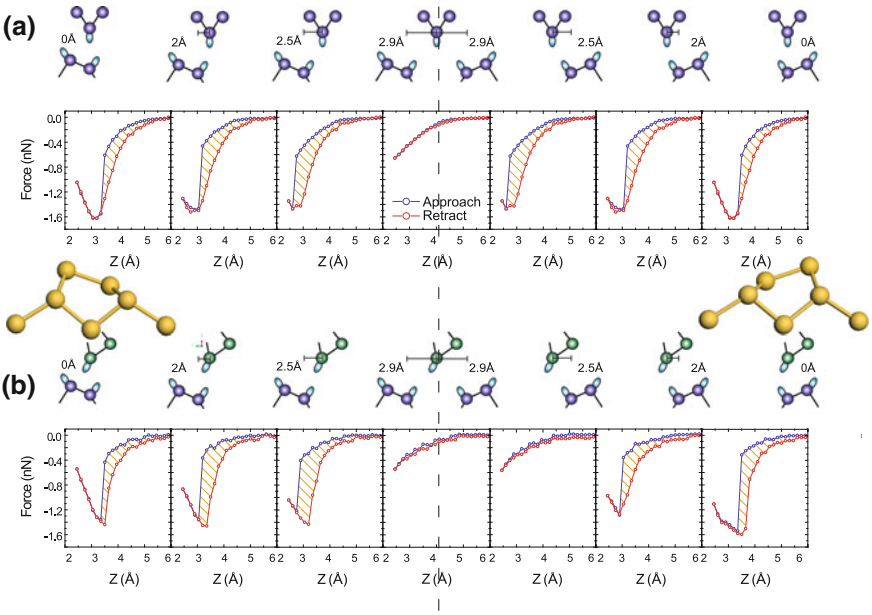

Fig. 13.7 Effect of varying lateral position of tips on simulated force spectroscopy. The **a** H3, and **b** dimer type tip, are positioned directly above a lower dimer atom, then displaced laterally in steps of 50 pm towards the neighbouring dimer row. Clear variations in hysteresis, threshold position and threshold force for dimer manipulation are observed for the dimer tip due to the degree of alignment of the dangling bonds of tip and surface. Figure adapted from [45]

We find that at large tip-sample separations, where the influence of the tip is weakest, two pathways exist to transition from the c(4×2) to the phason pair structure, either directly, via simultaneous flipping of both dimers, or stepwise, via subsequent flipping of one dimer after the other, each with a substantial barrier. As the tip-sample separation is reduced, however, we find that the barriers significantly reduce and that flipping of the dimers in sequence becomes favoured over simultaneous dimer flipping. Moreover, we find that the barrier to transit to the "three-in-a-row" structure collapses as the tip is bought closer to the surface, as suggested by the DFT simulations. Nonetheless, a substantial barrier of 80 meV remains between the "three-in-a-row" and phason pair structure even at close approach of the tip.

It is also important to note that when the tip is far from the surface the barrier between the "three-in-a-row" structure and the original buckled structure becomes extremely small (black curve). This provides a plausible explanation for why it is not possible to observe a "three-in-a-row" structure either by manipulation of natively to the surface. The NEB calculations suggest this structure will be extremely unstable without the stabilising presence of the tip, and even at 5 K the barrier is small enough that the structure simply relaxes back to the ground state. Conversely our calculations

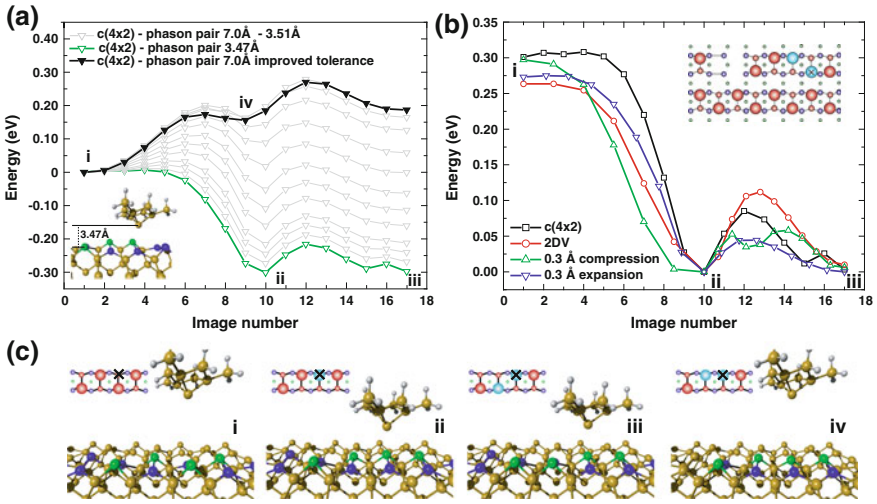

Fig. 13.8 NEB calculated energy landscapes for the transition from c(4 × 2) to phason pair structure. **a** Plot of the energy difference for the system to transit from the c(4 × 2) to phason pair with the tip positioned at different heights above the down atom of the target dimer. Several key configurations on the energy curves are labelled **i**–**iv**, see below for details. **b** Same energy landscape for manipulation with the tip positioned close to the surface for four different surface slabs; the pristine surface slab (c(4 × 2)), a surface slab with a 2 dimer vacancy (2DV) defect introduced (see *inset* model), and a surface slab in the c(4 × 2) configuration with either sub-surface expansion or compression introduced. Note that the introduction of the 2DV defect increases the barrier between the "three-in-a-row" and phason pair structure, whereas both the expansion and compression cause a reduction in barrier height. **c** Calculated geometries and cartoon representation of four key points in the energy landscape: **i** c(4 × 2), tip far from surface, **ii** "three-in-a-row", tip close to surface, **iii** phason pair, tip close to surface, **iv** "three-in-a-row" tip far from surface. Figure adapted from [17, 18]

also suggest that if a phason pair *is* formed it should be kinetically trapped and therefore remain stable at 5 K, supporting the experimental observations.

13.4.3.1 Defect and Symmetry Induced Modification of Energy Barriers

Although our simulations for the pristine surface offer an explanation for the absence of the "three-in-a-row" structure in our experiments, they do not provide an explanation for how the phason pair is created, and why successful manipulations are regularly observed, as a substantial barrier must be crossed to transit from the "three-in-a-row" structure. In order to answer this question we performed an additional series of NEB simulations. These explored the energy landscape with the tip at close approach for a series of surface slabs with a two dimer vacancy (2DV) type defect, or a small sub-surface expansion or compression introduced in order to simulate the effects of long range strain in the surface. In these simulations (Fig. 13.8b) we observe that the introduction of defects significantly changes the barrier to transit to the phason pair

structure, with an increase in the barrier for the 2DV type defect (110 meV), and a reduction in the barrier for the compressive and expansion induced strain (60 and 45 meV respectively). Although none of the simulations presented here resulted in a complete barrier collapse, we suggest that on the real surface the strain field is such that in some locations the barrier for transition is reduced due to the complex strain fields generated by defects, step edges, and sub-surface defects, creating regions where phason pair creation is possible, while in others the defects strongly pin the dimers and prevent manipulation [8, 9, 17]. This correlates well with observations that in some regions of the surface we observe a large number of "failed flips" where the dimer returns to its original configuration as the tip retracts [17].

One subtle effect that has not been discussed, and is not captured in our simplified surface slabs, is that of symmetry breaking. A casual inspection of the model for phason pair creation on the pristine surface (e.g. Fig. 13.2) reveals an interesting paradox—why does the dimer above the target dimer relax, rather than the dimer below (or vice versa)? On a defect free surface with a symmetrically positioned tip there should be no preference for either one to respond over the other. Therefore, some factor, either the strain field at the surface, or the position of the tip, must break this symmetry in order for the system to reproducibly relax one way or the other. Indeed, in some experiments [17, 46] we have observed a weak variation in the outcome of phason pair creation experiments. However, the long range nature of the surface effects that can influence the response of the dimer presents a significant challenge for future simulations, as accurate modelling will require extremely large numbers of atoms in the simulation cell.

13.4.4 Visualising the Effect of Surface Strain on Dimer Stability

The effect of surface strain on the propensity for a successful manipulation attempt described above may be visualised by imaging experiments performed at varying tip-sample separations. Imaging far from the surface and then decreasing the tip-sample separation allows us to observe the onset of uncontrolled manipulation during scanning and in particular to visualise the striking difference in stability of the different surface dimers.

Figure 13.9 shows a series of images taken in constant height mode at various tip-sample separations. Far from the surface most of the rows image as the native $c(4 \times 2)$ buckling structure, while at close approach a number of rows begin to exhibit "slicing" ((b) and (c)) indicating random manipulation. At very close approach a number of rows take on an appearance closer to the $p(2 \times 1)$ phase ((d)), whereas others exhibit a contrast somewhere between $c(4 \times 2)$ and $p(2 \times 1)$. Interestingly, contrast showing a mixture of $p(2 \times 1)/c(4 \times 2)$ predominantly occurs during imaging at intermediate temperatures (77 K)—an observation predicted computationally by Hobbs et al. [39] and ascribed to the interplay between the rate of oscillation of the cantilever and the energy barriers for a flipped dimer to return to its ground state.

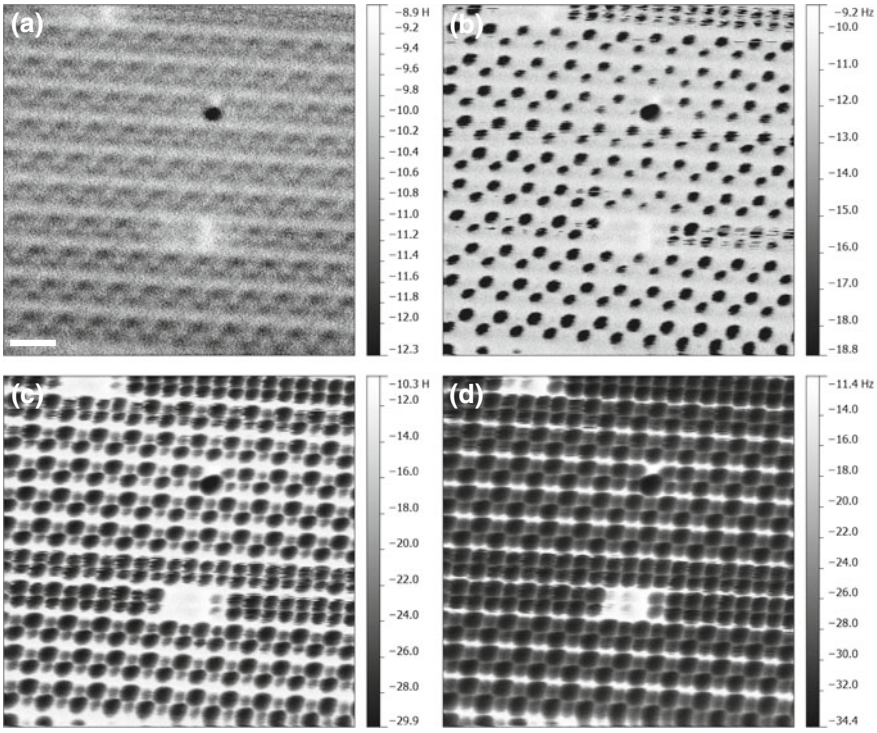

Fig. 13.9 Constant height images of Si(100) at 77 K taken at decreasing tip-sample separation showing variation in dimer stability close to a pair of DV type defects. **a** Far from the surface most rows show buckling structure. **b** Dimers in rows containing defects begin to show 'flickering' indicating uncontrolled manipulation during scanning. **c, d** Strong tip-sample interaction, several rows now exhibit an almost p(2 × 1) appearance. Tip heights relative to initial scan (**a**) 0 pm, (**b**) –10 pm, (**c**) –20 pm, (**d**) –30 pm. *Scale bars* = 1 nm. $A_0 = 0.28$ nm. $V_{gap} = +0.4$V

The observation that some dimers are stable even at very close approach (at least with some tips) correlates well with our observation that in some regions phason pair creation by controlled force spectroscopy is not possible at 5 K. This further highlights that while the dimer structure of the surface may be manipulated with atomic precision, it may not be manipulated *arbitrarily*, and that non-local strain effects place strong constraints on which manipulations may be successfully performed.

13.5 Imaging and Manipulation with Reactive and Passivated Tip Structures

Thus far only the case of reactive silicon tips interacting with the reactive Si(100) surface has been considered. In these instances a relatively strong attractive chemical interaction dominates the force between tip and sample. Recently, however, there has

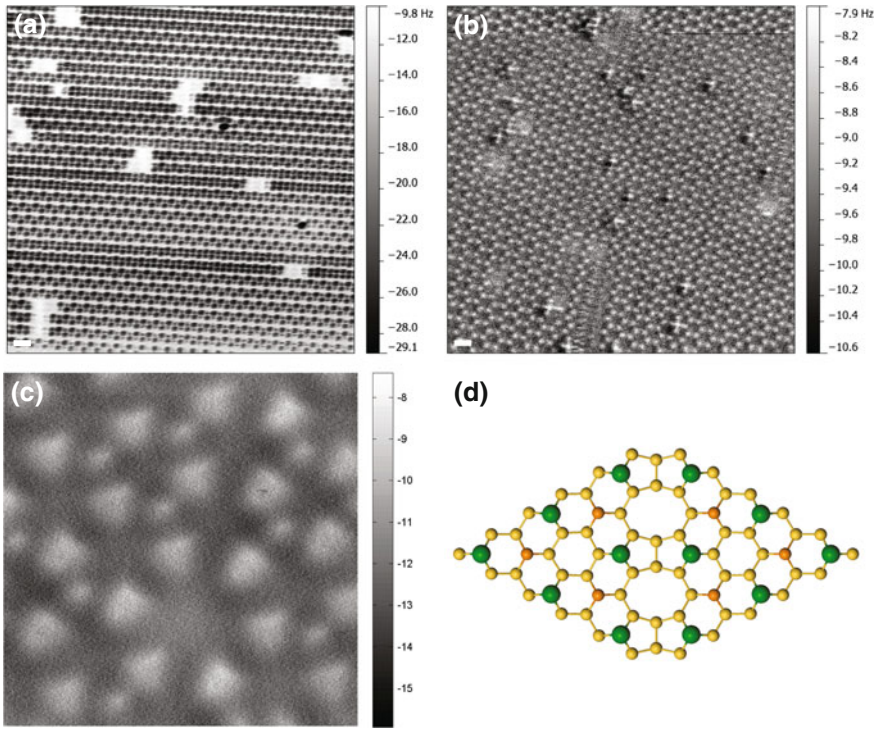

Fig. 13.10 Constant height imaging of Si(100) with different tip types. **a** Image taken with a 'conventional' tip apex showing attractive interaction over the atoms of the surface. $A_0 = 0.28\,\text{nm}$ $V_{gap} = -0.4\,\text{V}$. **b** Image taken with a 'passivated' tip showing repulsive interaction over the atoms of the surface. $A_0 = 0.28\,\text{nm}$ $V_{gap} = +0.3\text{V}$. **c** Image of Si(111)-7 × 7 surface showing similar repulsive interaction over the silicon adatoms as demonstrated in (**b**). $A_0 = 0.28\,\text{nm}$ $V_{gap} = 0\text{V}$. **d** Ball and stick model of Si(111)-7 × 7 unit cell. Scale bars = 1 nm. Data acquired at 77 K

been substantial interest in what are generally termed "passivated tips", primarily due to their ability to approach close to and image planar organic molecules with intra-molecular resolution [24, 47]. It is therefore pertinent to consider how similar tips may interact with reactive semiconductor surfaces, and how their behaviour may differ in regard to the atomic manipulation experiments described above. In Fig. 13.10 we show images of the Si(100) surface, taken in constant height mode at 77 K. Figure 13.10a shows "conventional" imaging, with a strong attractive interaction (negative frequency shifts) dominating the contrast over the surface, similar to that seen in Fig. 13.9. In Fig. 13.10b, however, the atomic structure of the surface images as what appears to be a repulsive interaction (positive frequency shifts) over the up atoms of the dimers. We also recently observed similar contrast on the Si(111)-7 × 7 surface, as shown in Fig. 13.10c [48]. In this case it was shown that only a very weak attractive interaction is present over the surface adatoms, suggesting a passivated tip

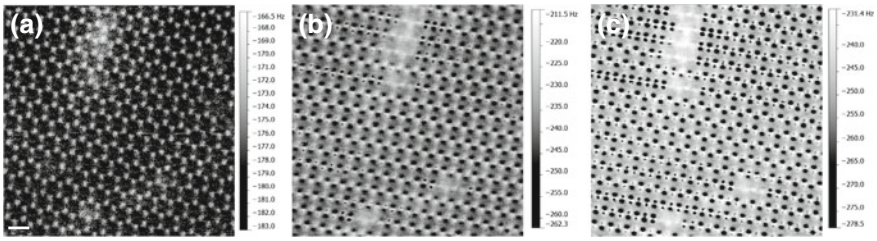

Fig. 13.11 Constant height images of Si(100) at 77 K taken at decreasing tip-sample separation showing variation in dimer stability during imaging with a 'passivated' type tip. **a** Far from the surface all rows show a buckled c(4 × 2) structure. Unusually the DV defect complexes do not clearly image at this tip-sample separation. **b** At intermediate distances a number of rows show evidence of manipulation, some atoms now appear to exhibit attractive interaction (*dark spots*) or attractive lobes in the centre of a repulsive interaction. **c** At very close approach a number of rows show a p(2 × 1) appearance. In the buckled rows there is evidence of an attractive interaction in the centre of repulsive interaction over the up atoms, as well as over the down atoms of the dimer. *Scale bars* = 1 nm. Estimated tip heights relative to initial image (**a**) 0 pm, (**b**) –20 pm, (**c**) –30 pm. $A_0 = 0.11$ nm $V_{gap} = 0$V

was responsible for the contrast (similar results were also obtained on a partially hydrogen terminated Si(111)-7 × 7 surface, at room temperature [49]).

Curiously, however, it is clear passivated tips are also capable of perturbing the surface structure, in a similar fashion to conventional tips. Figure 13.11 shows a sequence of images taken over a range of tip-sample separations with a tip of this type. Far from the surface the native c(4 × 2) buckling structure is apparent, but upon closer approach it is clear a number of the dimer rows begin to exhibit an apparent p(2 × 1) periodicity.

Figure 13.12 shows the results of simulated force spectroscopy for two simple hydrogen passivated tips interacting with the up atom of a silicon dimer. The simulations highlight how tip structure is absolutely critical to determining the outcome of atomic manipulation experiments. For a relatively unreactive dimer-like tip the hydrogen atom is transferred from the tip to the up atom of the surface, resulting in a partly passivated surface and reactive tip. For the much more reactive H3 type tip the hydrogen remains fixed to the tip apex, and instead the dimer is induced to flip via a "pushing" action as opposed to the "pulling" action described in the previous sections for reactive tips.

It is therefore feasible that one possible mechanism for the manipulation observed in Fig. 13.11 is the perturbation the surface via a series of "pushing" manipulations by a passivated tip on the up atoms of the dimer. However, we must highlight that this explanation for the observed manipulation is highly speculative. In particular we must consider that experimental results on the Si(111)-7 × 7 surface show that at sufficiently close approach a strong attractive attraction can occur, possibly due to the movement of the passivating moiety on the tip [50] and crucially that this strong jump to attractive interaction is not well reproduced in simulations of passivated tips

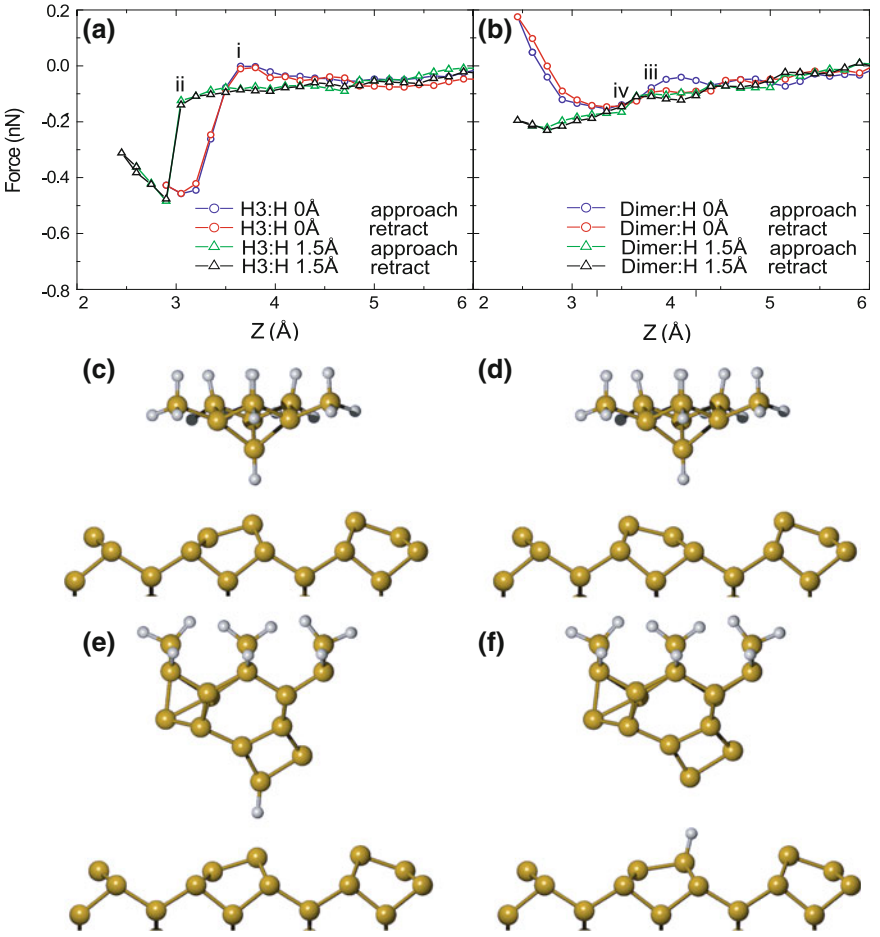

Fig. 13.12 Atomic deposition, and dimer manipulation, dependence on tip type. The H3 and dimer tip structures have their apex dangling bond terminated with hydrogen to simulate the simplest possible passivated tip types and subsequent atom deposition or extraction protocol. Calculated force curves are shown for an **a** H3 tip and **b** dimer tip at two different lateral positions corresponding to 0 and 150 pm offset. Geometries taken from the simulations at 0 pm offset show **c**, **d** H3 tip and **e**, **f** dimer tip at point (i) and (iii) on the force curve during approach and retraction, illustrating that the tip has retained (in the case of the H3 tip) the hydrogen or deposited the hydrogen (in the case of the dimer tip). Note that in the case of the H3 tip the tip buckling has been manipulated via a 'push' type manipulation. Figure adapted from [45]

interacting with silicon adatoms [48]. This suggests that the simplified tip models used do not fully capture some aspect the experimental system.

We note that close inspection of the scans at closer approach in Fig. 13.11b, c appears to reveal similar contrast, with dark spots appearing within the repulsive contrast of the up atoms. It is also clear that significant localised attractive interactions

are present over the locations of the down atoms, which is hard to reconcile with the simplified model of a passivated tip interaction presented above. In particular it is not trivial to predict how dimer manipulation will proceed for the case where the tip-sample interaction undergoes a complex evolution in both the magnitude and direction of the force as the tip approaches the surface.

Irrespective of the actual manipulation mechanism, it is clear that a full understanding of the complex evolution of forces in the atomic junction will become increasingly important in order to understand the behaviours of both types of tip, and note that any prototypical mechano-chemical scheme must necessarily involve the passivation and depassivation of both tip and surface during manipulation.

13.6 The Hydrogen Passivated Silicon Surface: H:Si(100)

Molecular adsorption on semiconductors can be particularly interesting due to the potential to modify the intrinsic chemical and electronic properties of surfaces. An interesting case study arises from one of the simplest molecules, diatomic hydrogen, which can be used to completely passivate Si(100) making it chemically unreactive. Due to its inherent simplicity, hydrogen also serves as a prototypical study of the fundamental limits of mechanochemistry on silicon surfaces. Having considered the role of passivated tips in the imaging of the reactive Si(100) surface, we now turn our attention to NC-AFM imaging of the prototypical (2×1) passivated H:Si(100) surface. Typical images acquired of the H:Si(100) hydrogen passivated surface are shown in Fig. 13.13. In general we find that preparation of tips capable of good NC-AFM imaging is significantly more challenging on H:Si(100) compared to Si(100). We also find that, overwhelmingly, constant Δf images obtained on the surface show inverted contrast, with the hydrogen atoms terminating the silicon dimers showing up as depressions, suggesting a repulsive tip sample interaction.

The nature of the contrast can often make unambiguous assignment of the the atomic positions challenging, and it is important to identify the positions of the atomic rows either by reference to defect structures (as shown Fig. 13.13), or by reference to simultaneously acquired tunnel current data (in the instances where it is possible to collect tunnel current data without distortion of the Δf signal), in order to prevent misassignment of the surface structure [51]. Only very rarely were we able to obtain "conventional" images where the atomic positions appear as protrusions (Fig. 13.13e). In this instance, the NC-AFM tip originally produced similar inverted contrast to that shown in Fig. 13.13c, d prior to a spontaneous tip change leading to imaging the hydrogen atoms as maxima, rather than minima.

An obvious question is whether this increased incidence of inverted contrast arises solely as a result of the surface properties, or in combination with certain tip types that are more commonly formed on the hydrogen passivated surface. In Fig. 13.14 we attempt to address this question by comparison of experimental force difference spectroscopy data with simulated force difference spectroscopy performed with both passivated and reactive tips.

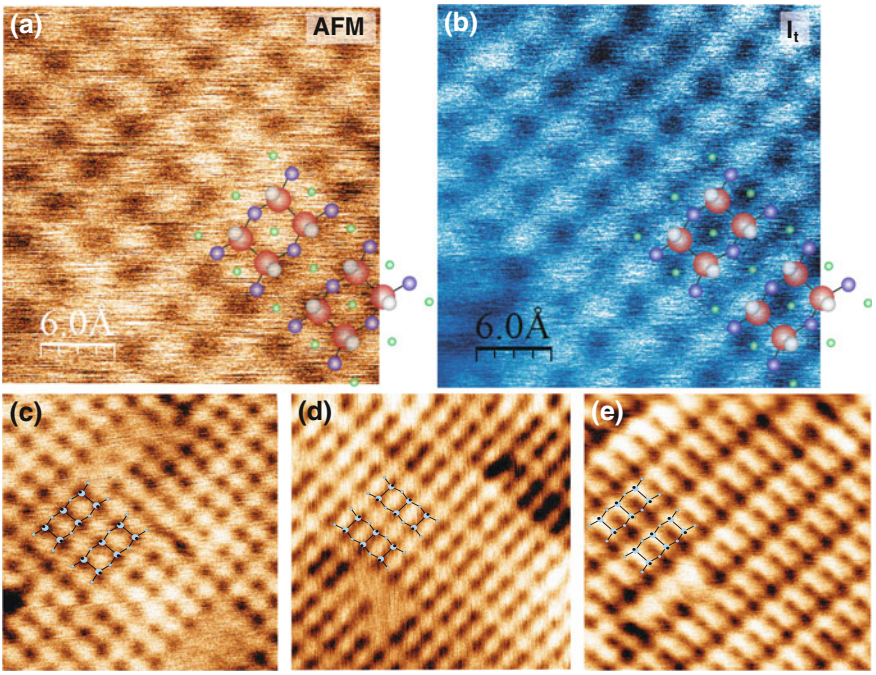

Fig. 13.13 Simultaneous Δf and tunnel current data acquired during constant Δf imaging **a** Constant Δf topography image, $A_0 = 400\,\text{pm}$, $\Delta f = -36.5\,\text{Hz}$ $V_{gap} = +1.2\text{V}$. **b** Simultaneously acquired tunnel current data showing bright protrusions corresponding to positions of H atoms. **c**, **d** Constant Δf images of the H:Si(100) surface acquired at zero applied bias with other tip apexes showing inverted contrast with defect structures for reference. $A_0 = 300$ pm. $\Delta f = -26\,\text{Hz}$ and $\Delta f = -21.5\,\text{Hz}$ respectively. **e** Image of H:Si(100) taken with 'conventional' contrast (i.e. atoms appearing as protrusions), $A_0 = 300\,\text{pm}$, $\Delta f = -26\,\text{Hz}$. Data acquired at 77 K. Figure adapted from [28]

From our experimental measurements (black line) we clearly observe a significantly suppressed interaction as compared to the reactive bare Si(100) surface. Indeed, due to the adopted method of taking difference spectra (over an atom and between two rows), surprisingly, almost no attractive interaction whatsoever is measured. Crucially, by comparing this data to DFT calculations, we find that simulated F(z) measurements using a reactive tip cluster (Fig. 13.14a), although significantly suppressing the interaction, still shows a measurable attractive force. Crucially, we find that for a highly reactive tip, although the surface hydrogen passivation suppresses the chemical interaction between tip and surface, we still see a measurable attractive interaction between tip and hydrogen atom compared to the position located in between the rows.

Therefore for a reactive tip we would also expect to see a measurable attractive interaction experimentally. Our experimental data shows much better agreement with the simulated spectroscopy performed with a passivated tip, where we detect virtually no attractive interaction before the onset of repulsive forces. On the basis

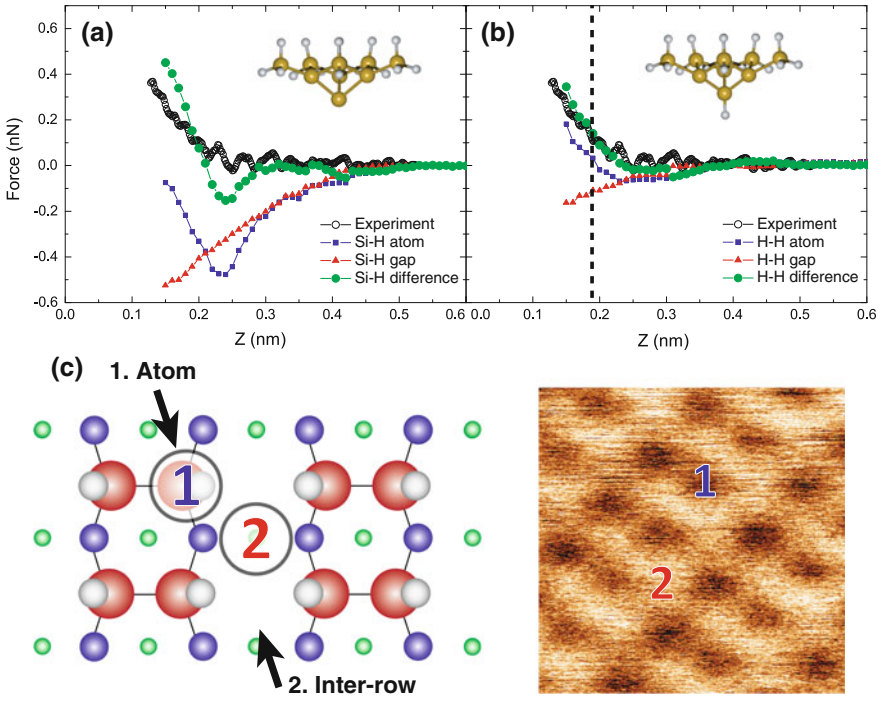

Fig. 13.14 Comparison of DFT simulated and experimental force-difference data on the H:Si(100) surface with **a** a reactive silicon terminated cluster and **b** an unreactive hydrogen terminated silicon cluster. **c** Illustration of the on/off position of the tip both in experiment experimental and DFT simulations. *Blue squares* correspond to location 1 (above a hydrogen atom), *red triangles* correspond to location 2 (between rows). *Green circles* represent simulated force-difference data and *black open circles* show experimental force-difference data. *Dashed* line in (**b**) shows the tip height during experimental image acquisition. Data acquired at 77 K. Figure adapted from [28]

of this comparison we assign the majority of the inverted contrast imaging that we observe on the H:Si(100) surface as resulting from a combination of passivated tip *and* passivated surface. A plausible explanation for this is that during STM/NC-AFM tip preparation on the surface the tip easily becomes terminated with hydrogen from the surface, and that this passivation of the tip is relatively stable over an already passivated surface as the tip rarely encounters a reactive site that would allow for removal of the tip absorbed hydrogen.

13.6.1 Feasibility of Mechanical Extraction of Hydrogen

In light of the experimental results obtained on both the reactive and passivated surface, and extensive simulations, it is perhaps possible to comment on the feasibility the most prototypical mechanochemical step—the transfer of a single proton via mechanical means.

A strong argument put forward against mechano-chemistry was famously outlined by Smalley as the "sticky fingers" argument [1]. We consider this argument in what might be considered a more limited "sticky finger" perspective in the context of mechano-chemical manipulation on semiconductor surfaces.

As shown in Fig. 13.12, and suggested by the experimental data in Fig. 13.11, transfer of absorbed adatoms between tip and surface on Si(100) seems feasible, but we vitally have not addressed how multiple *reversible* transfers can occur at cryogenic temperatures. Any tip reactive enough to remove the moiety from the surface will, *unless a structural change occurs*, necessarily remain too reactive to subsequently deposit the same moiety to a similar surface location. Conversely, any tip able to transfer the adsorbate from the apex to the surface, will remain insufficiently reactive to subsequently remove the same moiety. It seems that only a scheme which could, for example, reversibly change the structure of the tip between more and less reactive forms (e.g. from the H3 to dimer-like in the examples above) would be able to perform multiple extraction and deposition events. We note that thus far the only example of reversible mechanical atom transfer shown at low temperature [52] appears to show a tip evolution of exactly this type, although in this instance the initial tip state was not restored and further manipulation was not possible. Critically, as Fig. 13.7 shows, even if this scheme is experimentally realised, it may not be sufficient to simply consider the general chemical nature of the tip, but also the precise alignment of the bonds in the manipulation junction, suggesting that an extraordinarily high degree of control over the tip state is required.

It is also pertinent to consider that while atomically precise manipulation of the surface is possible with reactive tips, it also seems that the range of possible manipulations may be more limited than had previously been considered due to the effects of long-range strain at the surface.

A comparison can be made with other experimental schemes, both on semiconductors [6], and insulating surfaces [53], where multiple reversible atomic transfers from tip to surface have been demonstrated. A key difference in both these cases is that the experiments were performed at room temperature, where sufficient thermal energy exists to allow atomic exchange reactions to occur even in the absence of the complete collapse of the energy barrier. We also note that at least one of the schemes explicitly required 'regeneration' of the tip between manipulations as suggested above. We speculate that it may therefore be possible that, despite the inherent additional complications of working at elevated temperatures, that ultimately most mechano-chemical schemes may have to rely on thermal energy available from the environment in order to be feasible.

13.7 Summary

In this chapter we have highlighted recent developments in the control of atomic bond angle and atomic transfer by mechano-chemical means at cryogenic temperatures. We have shown that atomically precise control of the Si(100) buckling structure

is possible, but that due to complex long-range interactions, likely dominated by both surface and subsurface defects, arbitrary patterning of the surface remains elusive. The effect of different tip structures has been examined experimentally and theoretically, and we show that the different classes of tip structure may present a range of manipulation possibilities depending on the relative reactivities of both surface and tip. Investigations of the passivated surface suggests that overwhelmingly passivated atoms are transferred to the tip resulting in a high percentage of passivated tip structures. The results of our experiments and simulations highlight that while an exciting degree of control is now possible on semiconductors surfaces using NC-AFM at cryogenic temperatures, sufficient consideration must be paid to the limitations imposed by the mechanical and chemical properties of the system when performing mechanical atomic manipulation experiments.

Acknowledgments The authors would like to thank all of their co-workers who contributed to the work described in this chapter, including, in particular, Lev Kantorovich (King's College London), for numerous fruitful discussions. We acknowledge financial support from the Engineering and Physical Sciences Research Council (EPSRC), the European Framework 6 training networks PATTERNS and NANOCAGE, and the Framework 7 Future and Emerging Technologies (FET) project AtMol. P.M., S.P.J., and A.S. thank the Engineering and Physical Sciences Research Council (EPSRC) and the Leverhulme Trust, respectively, for Grants No. EP/G007837/1, No. EP/J500483/1, and No. F00/114 BI. A.S. thanks the Leverhulme Trust for funding via Grant No. ECF-2013-525.

References

1. K.E. Drexler, R.E. Smalley, December 1, 2003 Vol. 81, No. 48, CENEAR 81 48, pp. 37–42 (2003). ISSN 0009–2347
2. This lengthy debate was uploaded and archived at Richard Jones' Soft Machines blog. http://www.softmachines.org/wordpress/?p=70
3. M. Ternes, C.P. Lutz, C.F. Hirjibehedin, F.J. Giessibl, A.J. Heinrich, Science **319**, 1066 (2008)
4. G. Langewisch, J. Falter, H. Fuchs, A. Schirmeisen, Phys. Rev. Lett. **110**, 036101 (2013)
5. Y. Sugimoto, M. Abe, S. Hirayama, N. Oyabu, Ó. Custance, S. Morita et al., Atom inlays performed at room temperature using atomic force microscopy. Nat. Mater. **4**(2), 156–159 (2005)
6. Y. Sugimoto, P. Pou, O. Custance, P. Jelinek, M. Abe, R. Perez et al., Complex patterning by vertical interchange atom manipulation using atomic force microscopy. Science **322**(5900), 413–417 (2008)
7. T. Uda, H. Shigekawa, Y. Sugawara, S. Mizuno, H. Tochihara, Y. Yamashita et al., Prog. Surf. Sci. **76**, 147 (2004)
8. D. Riedel, M. Lastapis, M.G. Martin, G. Dujardin, Influence of tip-surface interactions and surface defects on Si(100) surface structures by low-temperature (5 K) scanning tunneling microscopy. Phys. Rev. B **69**(12), 121301 (2004)
9. Y. Pennec, M.H. von Hoegen, X. Zhu, D.C. Fortin, M.R. Freeman, Dynamics of an ising chain under local excitation: a scanning tunneling microscopy study of si(100) dimer rows at 5 k. Phys. Rev. Lett. **96**(2), 026102–4 (2006)
10. Y. Li, H. Nomura, N. Ozaki, Y. Naitoh, M. Kageshima, Y. Sugawara et al., Origin of p(21) phase on Si(001) by noncontact atomic force microscopy at 5 K. Phys. Rev. Lett. **96**(10), 106104 (2006)
11. F.J. Giessibl, Atomic resolution on Si(111)-(77) by noncontact atomic force microscopy with a force sensor based on a quartz tuning fork. Appl. Phys. Lett. **76**(11), 1470 (2000)

12. J. Berger, M. Svec, M. Müller, M. Ledinský, A. Fejfar, P. Jelínek et al., Characterization of the mechanical properties of qPlus sensors. Beilstein J. Nanotechnol. **4**, 1–9 (2013)
13. Z. Majzik, M. Setvín, A. Bettac, A. Feltz, V. Cháb, P. Jelínek, Simultaneous current, force and dissipation measurements on the Si(111) 77 surface with an optimized qPlus AFM/STM technique. Beilstein J. Nanotechnol. **3**(1), 249–259 (2012)
14. A. Weymouth, T. Wutscher, J. Welker, T. Hofmann, F. Giessibl, Phantom force induced by tunneling current a char. Phys. Rev. Lett. **106**(22), 1–4 (2011)
15. K. Hata, S. Yasuda, H. Shigekawa, Reinterpretation of the scanning tunneling microscopy images of Si (100)-(21) dimers. Phys. Rev. B **60**(11), 8164–8170 (1999)
16. K. Sagisaka, D. Fujita, Emergence of p(22) on highly doped n-type Si(100) surfaces: a scanning tunneling microscopy and spectroscopy study. Phys. Rev. B **71**(24), 245319 (2005)
17. A. Sweetman, S. Jarvis, R. Danza, J. Bamidele et al., Manipulating Si(100) at 5 K using qPlus frequency modulated atomic force microscopy: the role of defects and dynamics in the mechanical switching of atoms. Phys. Rev. B **84**, 085426 (2011)
18. A. Sweetman, S. Jarvis, R. Danza, J. Bamidele, E. Al, S. Gangopadhyay et al., Toggling bistable atoms via mechanical switching of bond angle. Phys. Rev. Lett. **106**(13), 136101 (2011)
19. A. Sweetman, A. Stannard, Uncertainties in forces extracted from non-contact atomic force microscopy measurements by fitting of long-range background forces. Beilstein J. Nanotechnol. **5**(1), 386–393 (2014)
20. J. Welker, E. Illek, F.J. Giessibl, Analysis of force-deconvolution methods in frequency-modulation atomic force microscopy. Beilstein J. Nanotechnol. **3**, 238–48 (2012)
21. J.E. Sader, S.P. Jarvis, Accurate formulas for interaction force and energy in frequency modulation force spectroscopy. Appl. Phys. Lett. **84**(10), 1801 (2004)
22. S. Kuhn, P. Rahe, Discriminating short-range from van der Waals forces using total force data in noncontact atomic force microscopy. Phys. Rev. B **89**(23), 235417 (2014)
23. M. Ternes, C. González, C.P. Lutz, P. Hapala, F.J. Giessibl, P. Jelínek et al., Interplay of conductance, force, and structural change in metallic point contacts. Phys. Rev. Lett. **106**(1), 16802 (2011)
24. L. Gross, F. Mohn, N. Moll, P. Liljeroth, G. Meyer, The chemical structure of a molecule resolved by atomic force microscopy. Science **325**(5944), 1110–1114 (2009)
25. C. Chiutu, A.M. Sweetman, A.J. Lakin, A. Stannard, E. Al, S. Jarvis, L. Kantorovich, J.L. Dunn, P. Moriarty, Precise orientation of a single C_ 60 molecule on the tip of a scanning probe microscope. Phys. Rev. Lett. **108**(26), 268302 (2012)
26. M.A. Lantz, H.J. Hug, R. Hoffmann, P.J.A. van Schendel, P. Kappenberger, S. Martin et al., Quantitative measurement of short-range chemical bonding forces. Science **291**(5513), 2580–2583 (2001)
27. B. Such, T. Glatzel, S. Kawai, E. Meyer, R. Turanský, J. Brndiar et al., Interplay of the tip sample junction stability and image contrast reversal on a Cu(111) surface revealed by the 3D force field. Nanotechnology **23**(4), 45705 (2012)
28. P. Sharp, S. Jarvis, R. Woolley, A. Sweetman, L. Kantorovich, C. Pakes et al., Identifying passivated dynamic force microscopy tips on H:Si(100). Appl. Phys. Lett. **100**(23), 233120 (2012)
29. J.E. Sader, S.P. Jarvis, Accurate formulas for interaction force and energy in frequency modulation force spectroscopy. Appl. Phys. Lett. **84**(10), 1801 (2004)
30. J.M. Soler, E. Artacho, J.D. Gale, A. Garcia, J. Junquera, P. Ordejon et al., The SIESTA method for ab initio order-N materials simulation. J. Phys.-Condens. Matter **14**(11), 2745–2779 (2002)
31. N. Oyabu, P. Pou, Y. Sugimoto, P. Jelinek, M. Abe, S. Morita et al., Single atomic contact adhesion and dissipation in dynamic force microscopy. Phys. Rev. Lett. **96**(10), 1–4 (2006)
32. R. Perez, I. Stich, M.C. Payne, K. Terakura, Surface-tip interactions in noncontact atomic-force microscopy on reactive surfaces: Si(111). Phys. Rev. B **58**(16), 10835 (1998)
33. R. Bechstein, C. Gonzlez, J. Schtte, P. Jelnek, R. Prez, A. Khnle, All-inclusive imaging of the rutile TiO_2 (110) surface using NC-AFM. Nanotechnology **20**(50), 505703 (2009)
34. P. Pou, S.A. Ghasemi, P. Jelinek, T. Lenosky, S. Goedecker, R. Perez, Structure and stability of semiconductor tip apexes for atomic force microscopy. Nanotechnology **20**(26), 264015 (2009)

35. P. Bokes, I. Stich, L. Mitas, Ground-state reconstruction of the Si (0 0 1) surface: symmetric versus buckled dimers tich. Chem. Phys. Lett. **362**(August), 559–566 (2002)
36. K. Hata, Y. Sainoo, H. Shigekawa, Atomically resolved local variation of the barrier height of the flip-flop motion of single buckled dimers of Si(100). Phys. Rev. Lett. **86**(14), 3084–3087 (2001)
37. K. Sagisaka, D. Fujita, G. Kido, N. Koguchi, Temperature dependence of the phase manipulation feasibility between c(42) and p(22) on the Si(100) surface. Surf. Sci. **566–568**, 767–771 (2004)
38. A. Sweetman, S. Gangopadhyay, R. Danza, N. Berdunov, P. Moriarty, qPlus atomic force microscopy of the Si(100) surface: buckled, split-off, and added dimers. Appl. Phys. Lett. **95**(6), 063112 (2009)
39. L. Kantorovich, C. Hobbs, Probing the Si (001) surface with a Si tip: an ab initio study. Phys. Rev. B **73**(24), 12–245420 (2006)
40. K. Sagisaka, D. Fujita, G. Kido, Phase manipulation between c (42) and p (22) on the Si (100) surface at 4.2 K. Phys. Rev. Lett. **91**(14), 146103 (2003)
41. Y. Takagi, K. Nakatsuji, Y. Yoshimoto, F. Komori, Superstructure manipulation on a clean Ge(001) surface by carrier injection using an STM. Phys. Rev. B **75**(11), 115304 (2007)
42. K. Cho, J. Joannopoulos, Flipping silicon dimers on Si(100) using scanning tip microscopy: a theoretical investigation. Phys. Rev. B **53**(8), 4553–4556 (1996)
43. A. Sweetman, S. Jarvis, R. Danza, E. Al, P. Moriarty, Effect of the tip state during qPlus noncontact atomic force microscopy of Si (100) at 5 K: probing the probe. Beilstein J. Nanotechnol. **3**, 25–32 (2012)
44. A. Labuda, Y. Miyahara, L. Cockins, P.H. Grütter, Decoupling conservative and dissipative forces in frequency modulation atomic force microscopy. Phys. Rev. B **84**(12), 125433 (2011)
45. S. Jarvis, A. Sweetman, J. Bamidele, L. Kantorovich, P. Moriarty, Role of orbital overlap in atomic manipulation. Phys. Rev. B **85**(23), (2012)
46. A. Sweetman, R. Danza, S. Gangopadhyay, P. Moriarty, Imaging and manipulation of the Si(100) surface by small-amplitude NC-AFM at zero and very low applied bias. J. Phys. Condens. Matter: Inst. Phys. J. **24**(8), 084009 (2012)
47. F. Mohn, B. Schuler, L. Gross, G. Meyer, Different tips for high-resolution atomic force microscopy and scanning tunneling microscopy of single molecules. Appl. Phys. Lett. **102**(7), 73104–73109 (2013)
48. A. Sweetman, S.P. Jarvis, P. Rahe, N.R. Champness, L. Kantorovich, P. Moriarty, Intramolecular bonds resolved on a semiconductor surface. Phys. Rev. B **1**–**8**, 165425 (2014)
49. A. Yurtsever, Y. Sugimoto, H. Tanaka, M. Abe, S. Morita, M. Ondráček et al., Force mapping on a partially H-covered Si(111)–(77) surface: influence of tip and surface reactivity. Phys. Rev. B **87**(15), 155403 (2013)
50. A. Sweetman, P. Rahe, P. Moriarty, Unique determination of "subatomic" contrast by imaging covalent backbonding. Nano Lett. **14**(5), 70–2265 (2014)
51. S. Araragi, A. Yoshimoto, N. Nakata, Y. Sugawara, S. Morita, Atomic resolution imaging of Si(1 0 0)11:2H dihydride surface with noncontact atomic force microscopy (NC-AFM). Surf. Sci. Rep. **188**(3–4), 272–278 (2002)
52. N. Oyabu, S. Custance, I. Yi, Y. Sugawara, S. Morita, Ó. Custance, Mechanical vertical manipulation of selected single atoms by soft nanoindentation using near contact atomic force microscopy. Phys. Rev. Lett. **90**(17), 176102 (2003)
53. S. Kawai, A.S. Foster, F.F. Canova, H. Onodera, S.-I. Kitamura, E. Meyer, Atom manipulation on an insulating surface at room temperature. Nat. Commun. **5**, 4403 (2014)

Chapter 14
Scanning Tunnelling Microscopy with Single Molecule Force Sensors

R. Temirov and F.S. Tautz

Abstract If the tunnelling junction of a scanning tunnelling microscope (STM) is functionalized with a nanoscale particle, such as a hydrogen or carbon monoxide molecule or a xenon atom, this particle effectively acts as a nanoscale force sensor. It senses forces stemming from the sample and transduces them into a measurable conductance signal. With this hybrid STM/AFM method images can be obtained that reveal the geometric structure of the substrate, very similar to state-of-the-art non-contact dynamic AFM. This chapter provides a survey of experimental results, explains the mechanism, and discusses the prospects of this novel scanning probe method.

14.1 Introduction

As this is a book about non-contact atomic force microscopy (AFM), it might surprise the reader that the current chapter deals with scanning tunnelling microscopy (STM). However, this is not a mistake. In fact, we discuss here a new operation mode of tunnelling microscopy which effectively turns a scanning tunnelling microscope into an atomic force microscope. As scanning probe techniques, STM and AFM are of course closely related: in both methods a sharp probe (the 'tip') is scanned over a surface and a signal from this probe (tunnelling current for the STM, force for the AFM) is recorded with very high lateral resolution. It is thus not surprising that shortly after the invention of the scanning tunnelling microscope [1] the first atomic force microscope was constructed [2]. But at first glance is does seem astonishing that an STM can be transformed into an AFM, just by attaching a suitable sensor particle, i.e. a single atom or molecule, to the tip of the STM while keeping everything else,

R. Temirov · F.S. Tautz
Peter Grünberg Institut (PGI-3), Forschungszentrum Jülich, 52425 Jülich, Germany
e-mail: r.temirov@fz-juelich.de

F.S. Tautz (✉) · R. Temirov
Jülich Aachen Research Alliance (JARA)—Fundamentals of Future Information Technology, 52425 Jülich, Germany
e-mail: s.tautz@fz-juelich.de

© Springer International Publishing Switzerland 2015

S. Morita et al. (eds.), *Noncontact Atomic Force Microscopy*,
NanoScience and Technology, DOI 10.1007/978-3-319-15588-3_14

including the fact that the tunnelling current is detected, unchanged. This remarkable *ansatz* is subject of the present chapter.

From the very beginning, an important driving force for the development of the AFM technique was increasing the lateral resolution. Rapid advances in AFM have been made in this direction, but until very recently the crown for the best lateral resolution still belonged to STM. Why is atomic resolution more easily achieved in STM than in AFM? In the STM, the excellent lateral resolution stems from the exponential (and therefore extremely sensitive) dependence of the tunnelling current on the distance. This yields a strong STM contrast even for tiny lateral variations of the local electronic structure. Now it is true that short range atomic forces between the outermost tip atom(s) and the substrate depend equally sensitive on the lateral position, but unfortunately in any conventional AFM, in which the force is measured by the static deflection of an elastic beam (cantilever), long range electrostatic and van der Waals forces between the macroscopic cantilever and the sample add to the atomic forces. Since these forces can be orders of magnitude larger than the atomic forces, and since they do not exhibit a marked lateral dependence, this creates a huge background problem in static AFM.

It is important to realize that this is a purely experimental difficulty. From a conceptual point of view, the AFM, if properly restricted to atomic forces of the immediate tip, offers the potential of even *better* resolution than the STM. The reason is indicated schematically in Fig. 14.1, using aromatic organic molecules as an example (the physics underlying the argument is, however, independent of the type of sample). Generally speaking, the achievable lateral resolution is determined by the internal structure of the object(s) that generate(s) the image. For STM, these are the frontier orbitals in the vicinity of the Fermi level. Since these are delocalized over the carbon backbone of the molecule, we cannot expect the STM image to

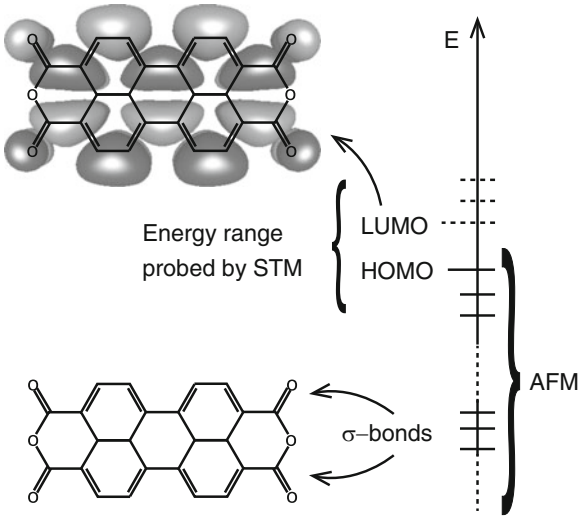

Fig. 14.1 Energy level scheme of a molecule. States which determine the image contrast in STM and AFM images, respectively, are indicated

exhibit features related to the atomic structure of the molecule. On the other hand, the AFM registers forces exerted by the sample onto the tip. These forces are caused by the total electron density of the molecule, including electrons localized in the ionic cores and in the σ-bonds. Therefore, we may expect those structural elements to show up in a well-resolved AFM image.

Several solutions of the background problem in AFM have been suggested and implemented. The one in most widespread use today is dynamic non-contact AFM, and in particular the qPlus tuning fork sensor [3]. When oscillating the cantilever at high frequency (kilohertz range or higher) and recording its frequency shift as a result of the interaction with the sample, AFM becomes sensitive to the force gradient in the direction of the oscillatory movement. Thereby, the contribution of slowly varying forces from macroscopic parts of the cantilever to the signal is suppressed. Dynamic force microscopy is the standard today in high resolution AFM, and it has generated many new opportunities for AFM. For example, it has allowed for the imaging of the internal structure of molecules [4].

It is clear that another, even more radical solution of the background problem in AFM would be the employment of a nanoscale cantilever, since this would eliminate macrosopic forces altogether. This, in fact, is the solution that is the subject of the present chapter: The cantilever is replaced by a single atom or molecule in the junction of the STM. The technique can therefore be understood as an STM/AFM hybrid. It is interesting that the original AFM design of Binnig, Quate and Gerber actually prefigures the hybrid method that we will discuss in this chapter, only at a macroscopic level. Figure 14.2 shows a schematic drawing of the first AFM. The deflection measurement of the force-sensing cantilever was based on a secondary tunnelling contact at the top of the cantilever. This design was quickly replaced and no longer plays a role in today's atomic force microscopes, but if the force sensing cantilever is shrunk down to a single atom or molecule and integrated directly into

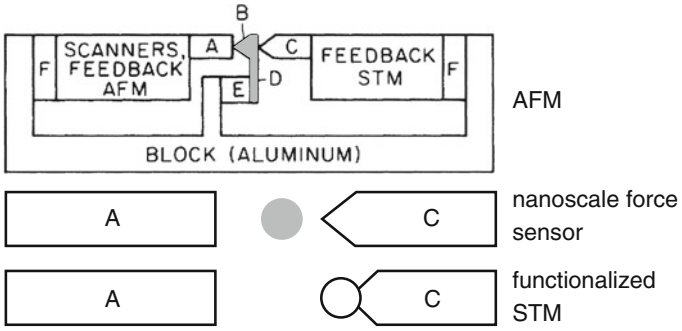

Fig. 14.2 The *top panel* shows a schematic sketch of the first AFM design by Binnig et al. reproduced with permission from [2]. In the *middle panel* the macroscopic cantilever, labelled *B* and *shaded grey* in the *top panel*, is replaced by a single atom or molecule (*grey*) that acts a nanoscale force sensor. The result is a hybrid between AFM on the one hand and STM with a functionalized tip (*bottom panel*) on the other

the tunnelling contact of the STM, then the original AFM design is transformed into the hybrid method which is the subject of the present chapter. The method presented here is thus the ultimate realization of *atomic force* microscopy: not only are the detected forces of atomic origin (as in any AFM), but also (and this is unique) the detecting unit itself is of atomic dimensions.

While the method discussed here belongs to the class of atomic force microscopies (since force is the physical quantity which determines the image), it can also be viewed as a specific variant of STM, because the measured quantity is the tunnelling current. This hybrid character is indicated schematically in Fig. 14.2. The crucial point is that, viewing the method as an STM variant, *functionalized tips* are employed, i.e. some atomic or molecular sensor particle is attached to the outermost metal atom of the tip, thus becoming the 'real' tip. The critical influence of the tip on STM images has been known for a long time, and every practising scanning tunnelling microscopist has observed and discarded many so-called tip-artefacts in their experiments. However, over time it has turned out that some 'artefacts' are very stable and in fact recurrent. A well-known application of functionalized tips is imaging the nodes of wave functions [5].

The method of the present chapter merges AFM and functionalized STM, or, more precisely, develops STM with functionalized tips into a well-controlled AFM technique. This is no freak. As will become clear in the course of this chapter, there is in fact a potential for a whole new range of STM-based microscopies, if the tunnelling junction is imbued with new degrees of freedom. A recent example is the inelastic tunnelling probe technique *itProbe* [6]. And it is interesting that the basic idea that STM can be used to detect forces was already formulated in the first SFM paper by Binnig et al. [2].

Let us conclude this introduction with a brief historical perspective of high resolution molecular imaging, which is so far the prime application of scanning tunnelling microscopy with single molecule force sensors. In 2008, the first ever scanning probe images were reported which revealed the atomic-geometric structure of adsorbed molecules [7, 8]. This was achieved by dosing molecular hydrogen into a low-temperature STM. For this reason, the new technique was named scanning tunnelling hydrogen microscopy (STHM). While it was clear that hydrogen functionalization of the tip played a decisive role, the detailed mechanism was not yet clear, although some crucial elements were already identified. Shortly afterwards, in 2009 the first AFM images showing the geometric structure of a molecule were reported [4]. They were obtained with a CO-functionalized tip. The role of CO is to extend and sharpen the tip and allow for imaging in the repulsive regime without the attractive forces of the remaining tip to become so large that the molecule is displaced during the imaging [9]. In 2010 it was shown that repulsive forces are also responsible for the atomic-geometric STHM contrast, and the sensor-transducer model of STHM that will be discussed in the present chapter was introduced [10, 11]. Today, it is well-established that in both AFM and STM the highest resolution images are obtained with carefully chosen functionalized tips. This has opened entirely new applications

for scanning probe methods, e.g. the experimental determination of covalent bond orders [12] and adsorption heights [13] with AFM or the imaging of structures that are reminiscent of hydrogen bonds in STM and AFM [6, 14–17].

14.2 A Survey of Experimental Results

14.2.1 Geometric Contrast in STM

We start with a survey of STM images that have been recorded in the presence of a single molecule force sensor in the tunnelling junction. Figure 14.3 shows the very first image that was recorded with hydrogen in the junction. In this particular case, the hydrogen was picked up accidentally during standard STM experiments, and only a careful investigation afterwards revealed that hydrogen in the junction was responsible for this type of contrast. Looking at the image, it is immediately obvious that the image shows the *geometric* structure of the molecules. At first sight, this is very surprising, since according to accepted wisdom the signal in STM is proportional to the local density of states (LDOS) of the sample, in an energy region around the Fermi level and at the position of the tip. But, as Fig. 14.1 shows, the spatial distribution of the LDOS at E_F will in general not reflect the atomic-geometric structure, because electronic levels in the vicinity of the Fermi level correspond to strongly delocalized states.

Figure 14.4 shows a few more examples of geometric images recorded with force sensor tips, in comparison with the standard LDOS images that are obtained with bare metal tips. In all cases the differential conductance images that were recorded

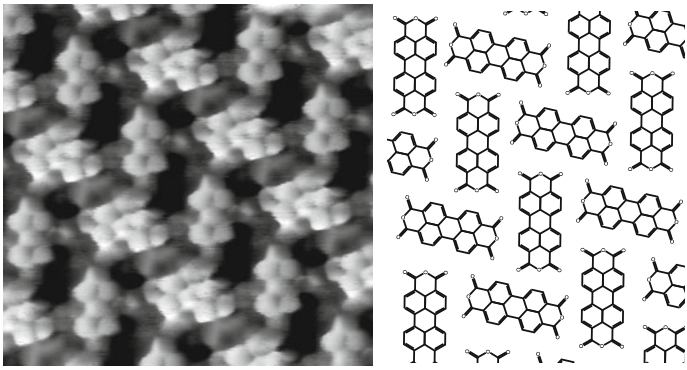

Fig. 14.3 The very first STHM image, recorded in 2006 at Jacobs University Bremen. The image was taken in constant current mode with the following tunnelling parameters: $V_b = -15\,\mathrm{mV}$, $I_t = 2\,\mathrm{nA}$ [7]. The panel on the *right* shows the structure of the imaged monolayer of 3,4,9,10-perylene tetracarboxylic dianhydride (PTCDA) on Ag(111)

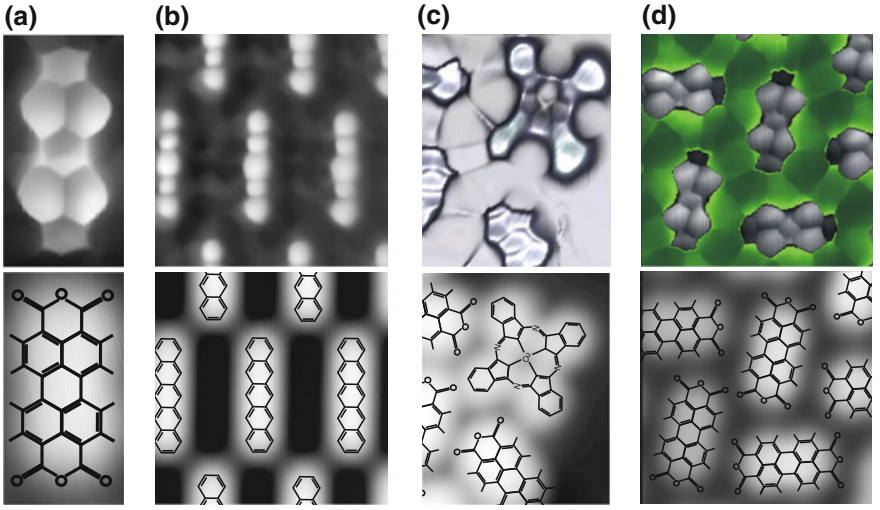

Fig. 14.4 Survey of STM images with geometric contrast, recorded with a nanoscale force sensor (*top row*). For comparison, the *bottom row* shows the corresponding conventional STM LDOS contrast. Switching between the two image modes occurs as a function of bias voltage V_b. All images have been recorded in constant height mode. **a** PTCDA/Au(111), D_2-tip, $V_b = -5$ mV (*top*) and $V_b = 316$ mV (*bottom*) [10]. **b** Pentacene/Ag(111), D_2-tip, $V_b = -2$, mV (*top*), $V_b = -340$ mV (*bottom*) [20]. **c** CuPc/Au(111), Xe-tip, $V_b = 10$ mV (*top*), $V_b = 100$ mV (*bottom*) [15]. **d** PTCDA/Au(111), D_2-tip, $V_b = -2$ mV (*top*), $V_b = 200$ mV (*bottom*) [14]

with a functionalized tip in constant height mode, relatively close to the sample and at low bias voltages, show signatures of the geometric structure. In some cases the quality of the structural image is so good that one could identify an unknown species by its structure, similar to what has been achieved with nc-AFM [18], or an unknown molecular phase. Moreover, panels c and d reveal that even in the region between the molecules the images provide a wealth of information that has been related to intermolecular hydrogen bonds (see Sect. 14.2.6 below).

14.2.2 Tip Functionalization

It has been pointed out already that tip functionalization is crucial for force-sensitive STM. Figure 14.5, in which an STM image recorded with a well-formed bare metal STM is compared to two images with functionalized tips, reveals the wide scope of tip functionalization. In particular, two types of functionalizations must be distinguished. The image in panel b was recorded with a tip that was decorated with PTCDA molecule. This functionalization leads to a remarkable sharpening in the image contrast compared to the bare tip. However, the nature of the contrast does not change. The two bright lobes above the hydrogen-terminated edges of the molecule split in two, and the diffuse area above the backbone breaks up into six separate

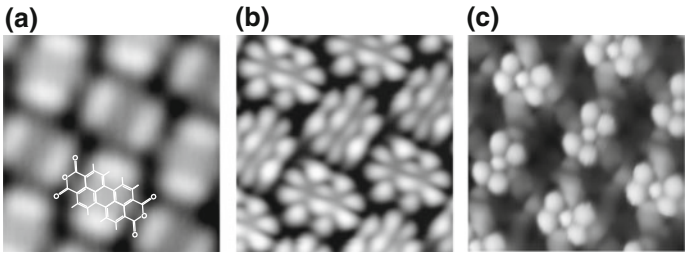

Fig. 14.5 A PTCDA herringbone layer recorded with different tips, illustrating the different types of information that is available depending on the tip functionalization. **a** The bare metal tip shows a blurred version of the LDOS [19]. **b** A tip functionalized with a PTCDA molecule shows a clearly resolved LDOS related to the LUMO of PTCDA [19]. **c** A tip functionalized with D_2 shows the geometric structure of the molecule [7]

lobes, but the overall pattern remains that of the LDOS. In fact, the bare metal image in panel a is a blurred version of the image in panel b, which shows the LUMO of PTCDA. The situation is completely different in panel c. Here a genuinely new contrast arises that is not related to the *electronic* but to the *geometric* structure of the molecule.

After the initial experiments with molecular hydrogen and deuterium [7, 10, 14], geometric contrast was obtained with xenon, carbon monoxide, and methane force sensor tips [15]. Although these are very different tip functionalizations (CO chemisorbs at the end of the tip, while Xe, H_2 and CH_4 are physisorbed), the obtained contrasts are qualitatively similar. This points to a general mechanism that does not depend on the specific details of the tip functionalization. However, on the other hand it must be noted that not every tip functionalization leads to geometric contrast, as mentioned above and illustrated in Fig. 14.5. In Sect. 14.4 we will discuss a model that explains why under special experimental circumstances (essentially short tip-surface distances such that near-contact is established) very different tip functionalizations may lead to similar (geometric) contrasts.

Individual CO molecules or Xe atoms on the substrate can be imaged with STM at low temperatures. If such a particle is picked up by the tip, images with geometric resolution can be recorded straightforwardly. This proves that this kind of imaging can be instigated by a single particle in the junction. For the case of hydrogen, the situation is more difficult. Even at low temperatures, isolated H_2 molecules are mobile on metal surfaces. Hence they cannot be imaged and picked up at will, and it is therefore not clear how many hydrogen molecules are needed in the junction in order to obtain geometric resolution. However, the image in Fig. 14.6a, which was recorded with a very low concentration of hydrogen and in which the contrast in the centre of the image suddenly switches form the LDOS to the geometric type and back again after a few scan lines, shows that also in the case of H_2 it is likely that a single molecule that is accidentally caught in the junction does the trick. If the H_2 coverage is too large then the method does not work any more, as H_2 molecules condense into an ordered phase on the substrate (Fig. 14.6b) and the intermolecular

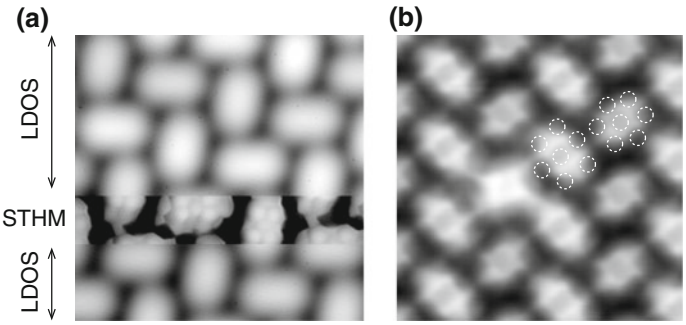

Fig. 14.6 STHM imaging at different H_2 (D_2) coverages. The image in **a** shows spontaneous switching between the conventional LDOS (*top* and *bottom*) and the geometric STHM (*middle*) contrasts at low D_2 coverage (PTCDA/Au(111), constant height image, $V_b = -5\,mV$ [20]). The image in **b** was recorded after longer exposure to H_2 at 5 K and shows an ordered H_2 layer on *top* of the PTCDA (PTCDA/Ag(111), constant height image, $V_b = -154\,mV$ [20]). *Dotted circles* indicate the approximate positions of hydrogen molecules

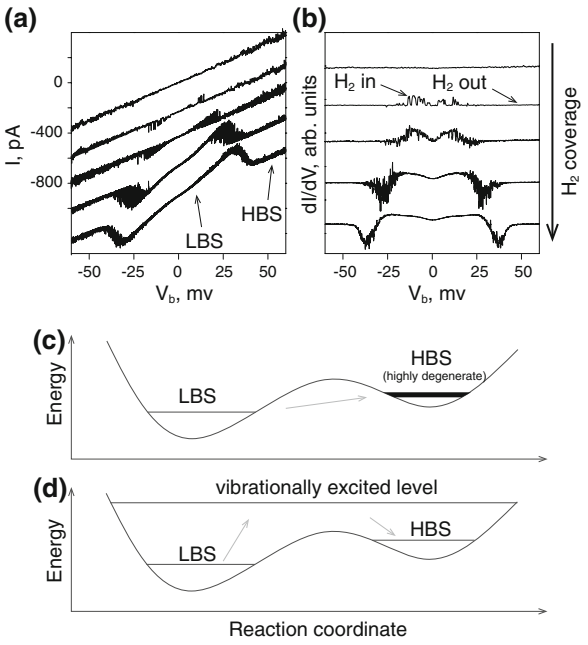

Fig. 14.7 Spectroscopic characterization of the STM junction during and after H_2 exposure. Panel **a** shows $I(V)$, panel **b** the corresponding $dI/dV(V)$ curves, measured at increasing levels of H_2 exposure. After [7]. The curves are shifted vertically for clarity. **c**, **d** Models for two level systems in nanoscale tunnelling junctions. Panel **c** shows the model by Halbritter et al. [21], while panel **d** shows the model by Thijssen et al. [22]

interaction between hydrogen molecules prevents any one of the H_2 molecules from following the tip as it scans across the surface.

In fact, by recording tunnelling spectra during hydrogen exposure, one can directly follow the evolution of the junction [7, 23]. At very low coverage one observes switching noise between the two states 'H_2 molecule in the junction' and 'no H_2 molecule in the junction' (top three curves in Fig. 14.7a, b). At higher

coverage one observes stable spectra which show a low-bias state and a high-bias state, both separated by conductance spikes (Fig. 14.7b). Such spectra are well-known from break junction experiments with hydrogen molecules [22], which proves the presence of hydrogen in the present STM junctions.

The conductance spikes in Fig. 14.7b originate from inelastic transitions. As soon as the bias voltage reaches the threshold value $\pm V_{\text{inel}}$, the tunnelling electrons can transfer the energy eV_{inel} to an excitation in the junction. The difference from conventional inelastic tunnelling spectroscopy (IETS), where steps in the conductance are observed because of the opening of a new transport channel at $\pm V_{\text{inel}}$, lies in the fact that in the present case not just a molecular vibration is excited, but that the excitation leads to a change of the structural state of the junction, which also changes the differential conductance of the junction. The spikes arise since the I–V curves of both the low- and high-bias states must cross at $I = 0$, $V = 0$: if the high-bias state (HBS) has a lower conductance than the low-bias state (LBS), the spikes will therefore point down (negative differential conductance), while in the opposite case the spikes point up. Both situations are observed in experiments. Because geometric images are exclusively observed in the LBS, we can associate the HBS with a situation in which the hydrogen molecule has left the active part of the junction. Although the precise nature of the two states is not yet clear, the fact that these two states are accessible to the hydrogen molecule shows that there is a relatively soft internal degree of freedom in the junction. This turns out to be the crucial ingredient to achieve force-sensitive STM (see Sect. 14.3).

Since the conductance spectra can be measured without hysteresis with increasing as well as with decreasing bias, it is clear that the HBS can only exist because it is stabilized by the continued tunnelling current, i.e. there is either a spontaneous or a current-induced transition back from the HBS to the LBS. Several models of two-level systems (TLS) have been suggested that predict the stabilization of the junction in the HBS through a continued current of electrons with an above-threshold energy, e.g. the vibrationally assisted two-level model (VTLS) of Thijssen et al. [22] and the model of Halbritter et al. [21]. Both are indicated schematically in Fig. 14.7c, d.

14.2.3 Image Distortions

In Fig. 14.8 several images of PTCDA molecules, all recorded with force sensor tips, are presented. The figure shows that there is a considerable variability in the precise form of the geometric contrast. In panel a only the outline of the molecule is perceivable, while in panel b each of the seven rings is discernible, albeit in a very distorted way, which also changes the topology of the structure. Since this image was recorded at extremely short tip-surface distance, direct hybridization between the tip and the molecule may play a role here. The image in panel d is closest to the chemical structural formula of the molecule. The hexagonal shape of all rings is clearly evident, although only the central ring appears as a regular hexagon. In spite of its suggestive clarity, this image also presents surprising features: Firstly,

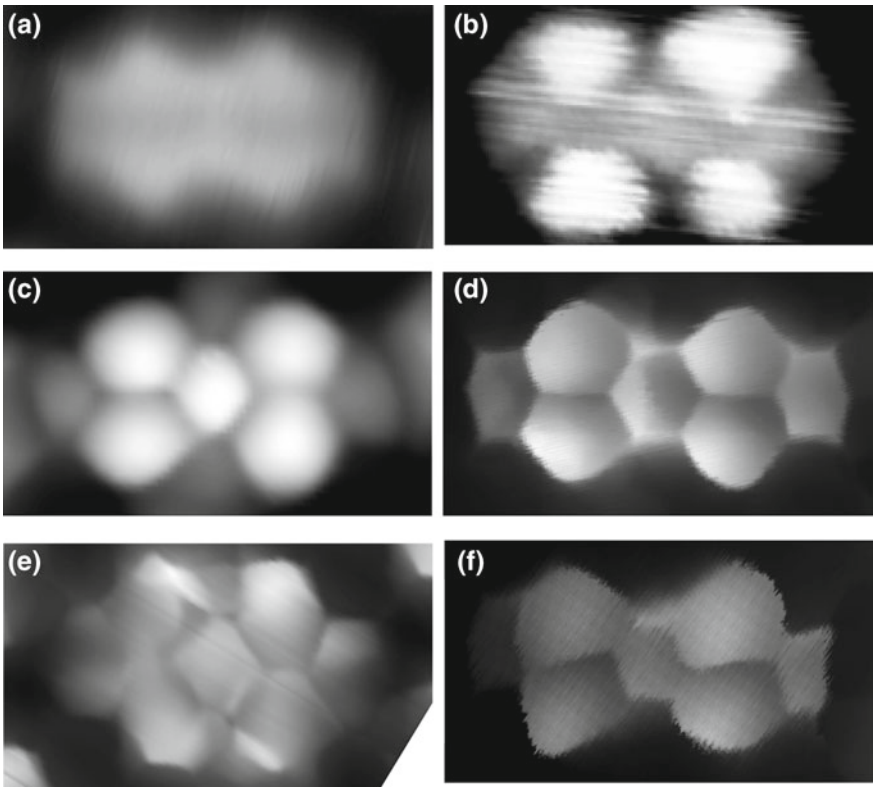

Fig. 14.8 Typical image distortions in STM with nanoscale force sensors (STHM, H_2 or D_2 sensors), illustrated with images of the PTCDA molecule. **a** At large tip-surface separation, conventional LDOS imaging still dominates the blurred intramolecular contrast, while the outline of the molecule begins to show geometric contrast (PTCDA/Au(111), H_2, constant height mode, $V_b = -1$ mV, [20]). **b** At extremely short tip-surface distance, direct hybridization between the tip and the molecule leads to strong image distortions. The image exhibits characteristics of the LUMO LDOS and the geometric structure (PTCDA/Au(111), H_2, constant height mode, $V_b = 5$ mV, [20]). **c** Clear geometric constrast without the shading effect observed in panel (**d**) (PTCDA/Ag(111), D_2, constant height mode, $V_b = -1$ mV [7]). **d** Near-ideal structure with the characteristic 3D shading effect that can be ascribed to an asymmetry of the metal tip (PTCDA/Au(111), D_2, constant height mode, $V_b = -5$ mV [10]). **e** and **f** show additional examples of contrast distortions: **e** PTCDA/Ag(111), H_2, constant height mode, $V_b = -5$ mV [20], **f** PTCDA/Au(111), H_2, constant height mode, $V_b = -1$ mV [20]

the lines between the positions where the atoms must be located (interatomic bonds) appear extremely and unnaturally sharp, and secondly the shading of the rings lends a peculiar three-dimensional impression to the image. Regarding the first point, panel c shows that the sharpness is not always as pronounced, and panels e and f reveal that the image features may be substantially distorted, even appear 'faceted' at times. Although there is a tendency for, e.g., Xe to show less well resolved images than either H_2 or CO (simply a matter of the size of the sensor particle), the kind of variability

shown in Fig. 14.8 is not primarily a consequence of different functionalizations. This suggests that the metal tip also significantly influences the actual appearance of the image.

14.2.4 Structural Sensitivity

The structural variability notwithstanding, there is a clear correlation to the atomic-scale structure of the molecule. This is demonstrated by Fig. 14.9, in which the effect of the abstraction of two hydrogen atoms from one edge of the PTCDA molecule is illustrated. While the influence of this chemical modification on the LDOS image in panel a is minute, the impact on the STHM image in panel b is very large. Essentially, the contrast of the adjacent hexagon and the adjacent area between the molecules is changed completely. Both effects are to be expected, because after abstraction of the hydrogen atoms the carbons may form bonds to the metal substrate, leading to a downward bending of the corresponding carbon ring [24], and because the peripheral hydrogen atoms of PTCDA play an important role in forming the image pattern observed between adjacent PTCDA molecules (see Sect. 14.2.6 below).

14.2.5 Mixed Contrasts

So far we have seen that in STM images two general types of contrast may be observed, the electronic LDOS contrast on the one hand and the geometric contrast on the other. Figure 14.10a shows that under certain circumstances both types of contrast can be superimposed in one image. It turns out that the bias voltage is relevant for geometric imaging only to the extent that a bias voltage too large may

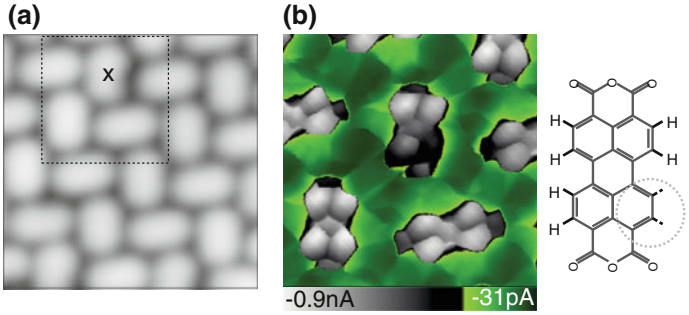

Fig. 14.9 Structural sensitivity of STM imaging with nanoscale force sensors. **a** Conventional STM LDOS image of PTCDA/Au(111). The *black cross marks* the position where a voltage pulse of $V = 4$ V was applied in order to abstract two hydrogen atoms from PTCDA (*grey circle*). **b** The STHM image of the area marked by the *square* in panel (**a**) shows the modified structure (constant height mode, $V_b = 1$ mV [20])

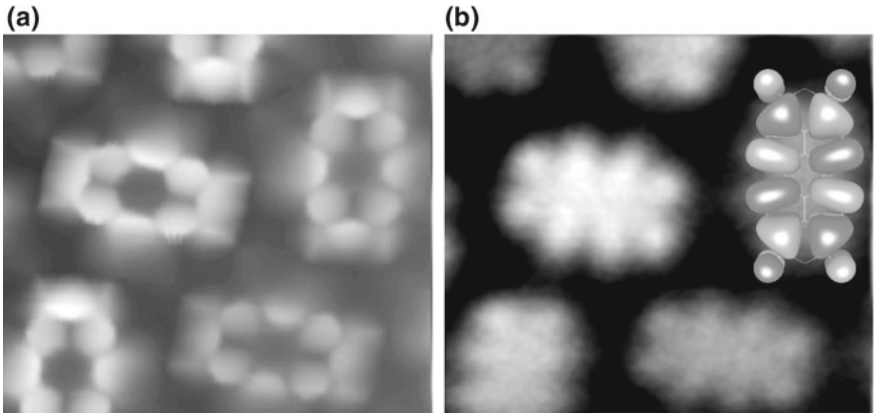

Fig. 14.10 An example in which geometric and conventional electronic LDOS image contrast are superimposed [15]. **a** dI/dV_b image recorded with a CO-tip in constant height mode over PTCDA/Au(111) using the lock-in technique at $V_b = -1.6$ V, **b** dI/dV_b image recorded with a clean Au tip at approximately the same V_b. The calculated image of the PTCDA HOMO is overlaid in the *upper right corner* for comparison with the experimental dI/dV_b contrast

switch the junction into a state where the sensor becomes inactive (see Sect. 14.2.2); other than that there is little influence. In particular, CO sensors cannot be deactivated with an elevated bias voltage, because their binding to the metal tip is too strong. This is of course different for spectroscopic LDOS imaging. Here the bias voltage determines at which energy with respect to the Fermi level the local density of states will be imaged. This is demonstrated in Fig. 14.10b, where an LDOS image has been taken at the binding energy of the HOMO of PTCDA, and indeed the image strongly resembles this orbital, as the inset shows. The image in Fig. 14.10a was recorded with a CO tip relatively close to the surface as a spectroscopic constant height image at the binding energy of the HOMO, and in fact one recognizes features of both types of contrast, LDOS and geometric. In particular, the nodal plane of the HOMO which cuts the molecular plane along the long axis of the molecule leads to a strongly reduced brightness along this line. Remarkably, the 'thickness' of this nodal line depends on the geometric contrast: In the centre of the molecule this line extends over the complete C_6 ring, which therefore appears dark, while in places where an interatomic bond coincides with the nodal line it is much narrower. Next to the darkened central ring one observes remnants of the central lobes of the HOMO orbital. The superposition of both image contrasts shows that, whatever the mechanism of geometric imaging, it operates on top of the LDOS image, i.e. it modulates the LDOS signal.

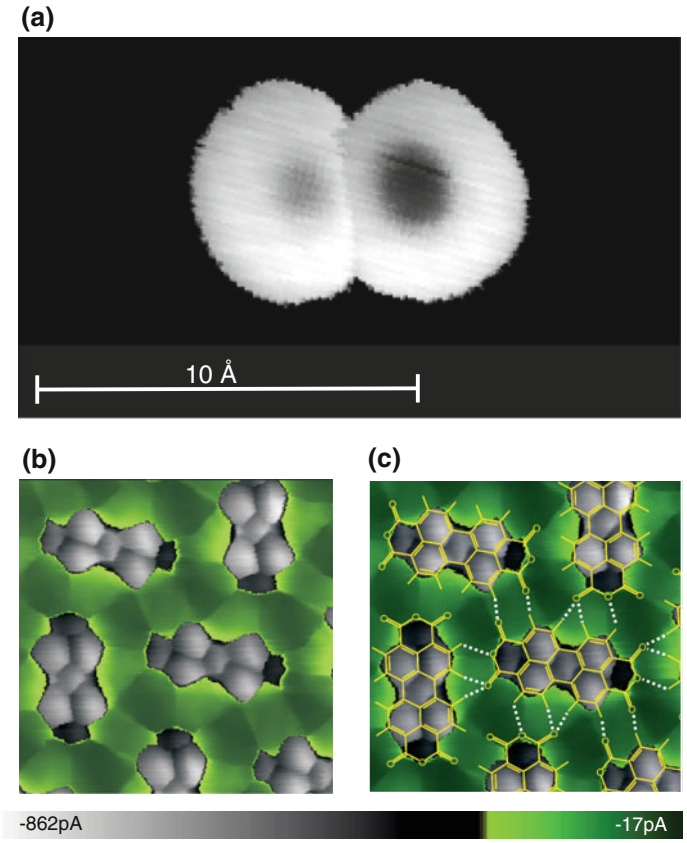

Fig. 14.11 Features in STM with nanoscale force sensors that at first sight do not have a simple structural counterpart. **a** STHM image of an Au dimer on Au(111) with *dark areas* on *top* of the atoms (constant height mode, D_2, $V_b = 2\,mV$) [10]. **b** STHM image of PTCDA/Au(111) with a characteristic tile pattern between the molecules (constant height mode, D_2, $V_b = -2\,mV$, [14]). A *two-color* palette has been used to emphasize the contrast in the interstitial region. **c** Superposition of the image from panel (**b**) with the structure of the molecular layer. Expected hydrogen bonds are shown as *dotted lines*

14.2.6 Further Image Features

Although it is true that the resemblance of images recorded with force sensor tips to the geometric structure of the molecules is their most notable feature, there are other features in the images which do not correspond to geometry, at least not at first sight. Examples of those are displayed in Fig. 14.11. On the one hand, there is the image of an atomic dimer (panel a), in which dark shades appear above the centres of the atoms where the tip comes closest to the atom, and on the other hand there is the rich structure in the area between the molecules in panel b, which is

suggestive of hydrogen bonds (panel c). This remarkable coincidence between the tile pattern in panel b and the hydrogen bonding network was first noted in 2010 [14], but at that stage it was not clear if hydrogen bonds really cause these image features, because at that point the mechanism was not clear. Later, similar features were observed in AFM, and these features were identified with hydrogen bonds [16, 17]. However, this assignment is controversial, and we will discuss in Sect. 14.4 a much more plausible origin for these features. In fact, by their appearance the 'non-structural' image features help to disentangle the geometric imaging mechanism of force sensor STM.

14.3 The Sensor-Transducer Model of Geometric STM Contrast

Looking at the image features discussed in the previous section from a comprehensive point of view, we notice a lot of common ground with ultimate resolution dynamic non-contact AFM images of molecules: in both techniques geometric structure is observed, both are sensitive to structural modifications of the molecules, both suffer from characteristic image distortions, and both also exhibit remarkable image features between the molecules that have been identified with hydrogen bonds. Hence, the early conjecture that in some way forces make their way into the STM images [10] seems justified. We now turn to a more detailed analysis of the experimental data which proves this surmise. We start by briefly considering the two most important experimental findings.

The first important experimental finding is documented in Fig. 14.12, which shows that images with geometric resolution can be obtained from statically recorded spectra. $dI/dV_b(V_b)$ differential conductance spectra were recorded on a grid of 64×64 points in a 13×13 Å^2 area above a PTCDA monolayer. For each spectrum, the tip

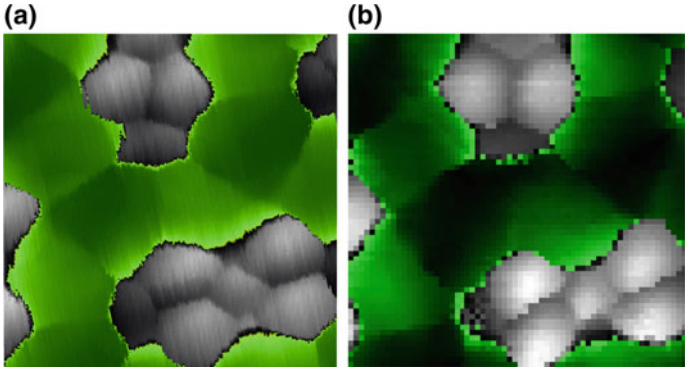

Fig. 14.12 Reconstruction of geometric images from statically recorded spectra of the differential conductance versus bias voltage. **a** Scanned STHM image of PTCDA/Au(111) (constant height mode). **b** Zero bias conductance map extracted from dI/dV_b versus V_b spectra measured at each of the 64×64 pixels of the area shown in panel (**a**).

was at rest (laterally and vertically). All spectra were recorded at the same height. The image in Fig. 14.12b gives the conductance at each grid point, as extracted from the spectra at a bias voltage close to 0 V. The result is virtually identical to the image in Fig. 14.12a, which was recorded as a conventional constant height image in scanning mode. The fact that both images are the same shows that any sliding and/or friction phenomena (such as, e.g., stick-slip) do not play any role in the geometric imaging mode; on the contrary, the comparison of the two images in Fig. 14.12 shows that when geometric images are scanned, *the sensor particle is always in a unique equilibrium position in the junction*. This is different from, e.g., point contact microscopy [10, 25]. Importantly, this finding implies two things: firstly, the mechanism of geometric imaging can be studied on the basis of individual experimental $dI/dV_b(V_b)$ spectra, and secondly, computational image simulations can be performed statically. This is a great simplification. We will make use of it in the present section as far as experimental spectra and in the next section as far as simulated images are concerned.

The second crucial experimental observation is: in the geometric imaging regime the usual exponential increase of the tunnelling conductance with decreasing tip-sample distance is suppressed. This can be seen in Fig. 14.13. The suppression shows that the junction moves into contact, i.e. the tip presses the sensor particle into contact with the sample, and this limits the further exponential increase of the conductance. Only in this distance range, which is characteristic for each sensor particle (partly reflecting its size), geometric resolution is observed [10, 15]. The fact that the suppression of the exponential increase is closely linked to the image formation is furthermore evidenced by the finding that the degree of suppression varies from point to point in the geometric image, with dark areas showing the stronger suppression. Hence, *the suppression 'is' the geometric contrast*. A range of possible mechanisms

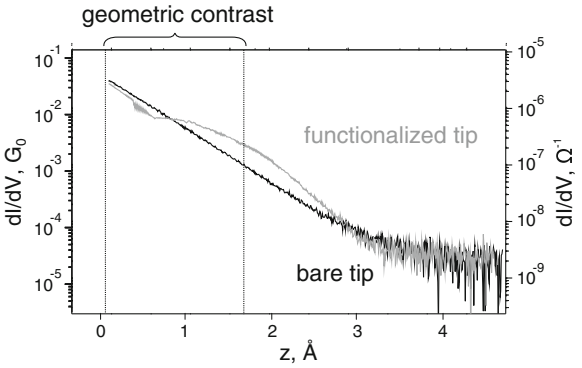

Fig. 14.13 Deviation from exponential tunnelling behaviour in STM with nanoscale force sensors. The *black curve* was measured with a bare metal tip on PTCDA/Au(111), the *grey curve* with D_2 as the nanoscale force sensor. After [10]. The horizontal axis corresponds to the relative tip-surface height z. Compared to the vacuum tunnelling junction, the initial exponential increase in the presence of the sensor particle is stronger. This can be understood as a result of reduced barrier height. The regime in which geometric contrast is observed is indicated

have been suggested for this suppression [27], one of them a depletion of the density of states in the tip due to Pauli repulsion [10]. However, a full understanding can only be obtained once structural sensor particle relaxation, which evidently may contribute to the suppression, is taken into account (see below).

The fact that geometric resolution is observed only once the junction is in contact suggests that *repulsive forces* determine the image contrast. This would also naturally explain why geometric STM images are so similar to high-resolution AFM images, which are well-known to rely on repulsive forces [9]. A proof of this hypothesis is provided by a simultaneous measurement of forces during a geometric STM scan, using a dynamic non-contact AFM in which the force gradient is measured by the frequency shift of an oscillating tuning fork [3]. Figure 14.14a shows force-distance spectra that have been obtained by integrating experimental frequency shift curves. For the functionalized CO tip the onset of repulsive interactions is observed in the dynamic non-contact AFM force distance-spectra, indicated by the reduction of (still attractive) force as tip comes closer to the surface (With a bare metal tip this repulsive range cannot be reached). Precisely in this range both a force contrast and a conductance contrast, evolve between different positions above the molecule, and, as Fig. 14.14b shows, *the conductance contrast is approximately proportional to the force contrast*. This not only shows that the repulsive force contrast determines the conductance contrast, but also allows for the calibration of the latter.

On the basis of the above we can now draw up a sensor-transducer model of geometric STM contrast. This model is sketched schematically in Fig. 14.15 (left). The particle that functionalizes the tip acts as a *nanoscale force sensor*, which, in the given range of tip-sample distances, is subject to repulsive forces from the substrate (also from the tip, but these forces do not carry any information about the

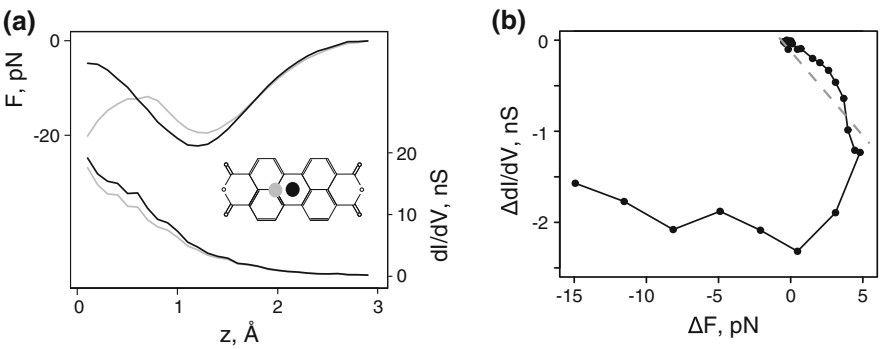

Fig. 14.14 **a** Simultaneously recorded force versus distance (*upper pair*) and differential conductance versus distance (*lower pair*) spectra for two points above PTCDA/Au(111) as indicated in the inset, measured with a CO molecule as nanoscale force sensor. The force versus distance spectra were obtained from frequency shift spectra of a qPlus sensor. z is the relative tip-surface distance. **b** Plot of the force difference ΔF between the *grey* and *black curves* in panel (**a**) against the corresponding conductance difference $\Delta dI/dV_b$. In the initial regime ΔF and $\Delta dI/dV_b$ are nearly proportional to each other (*dotted grey line*). After [28]

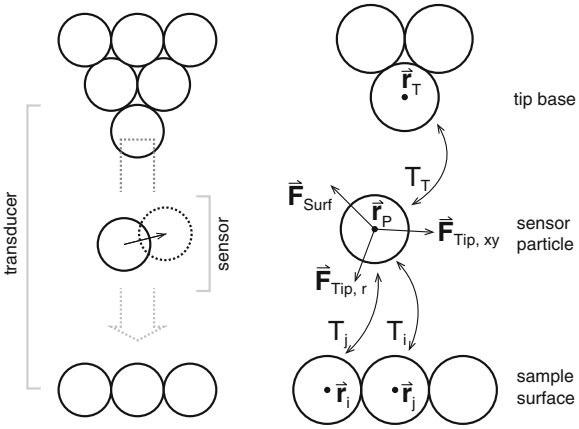

Fig. 14.15 Conceptual sketch of the sensor-transducer model discussed in the text (*left*) and generic model for simulating the tunnelling current (*right*) based on the conceptual model on the *left*

substrate). The response of the sensor to these forces *transduces the force signal into the conductance*, which is the measured quantity in the STM. Although we have not specified the precise mechanism of this transduction yet, we can at this point already say that this mechanism leads to the progressive suppression of the conductance whenever repulsive forces in the junction increase. Incidentally, we note that the presence of a nanoscale force sensor is also essential in dynamic non-contact AFM if the geometric resolution of the molecules is to be measured, since a bare metal tip does not resolve the repulsive interaction (Fig. 14.14). But in the AFM case the transduction mechanism is clear: the forces picked up by the nanoscale sensor modify the resonance frequency of the macroscopic sensor unit (tuning fork), leading to a measurable frequency shift.

A detailed analysis of the transducer action in the STM calls for simulations of the junction. Such simulations have been performed, and they indeed clarify how the nanoscale force sensor responds and how its response modulates the tunnelling current. They are discussed in the next section. It turns out that the transduction mechanism revealed by the simulations also provides natural explanations for the peculiarities of the imaging mechanism that were discussed in Sect. 14.2, namely the extreme sharpness of the images at the molecular σ-bonds, the variability of the images, the apparent 3D shadowing, and the remarkable contrast between the molecules.

14.4 A Unified Model of STM and AFM with Nanoscale Force Sensors

We have seen in previous chapters that the tip-functionalizing particle acts as a nanoscale force sensor, both in dynamic non-contact AFM and in the geometric STM mode. The open question is how the transduction into conductance takes place. To approach this question, let us first ask how the sensor particle may in principle

respond to repulsive forces from the sample. Clearly, the obvious possibility is that it changes its position in the junction (and in case of the polyatomic sensor particles CO and CH_4 also its orientation) to reach a new equilibrium position at which all forces (and torques) acting upon it from surface and tip cancel out. This response will include both vertical and lateral movements. As a consequence, the functionalized tip will relax to a new structure each time the tip moves form one lateral position above the sample to the next. It is clear that the relaxation of such a *soft tip* will potentially influence the tunnelling conductance through the junction, and thus provide a possible mechanism of signal transduction form the force to the conductance. The question thus arises whether considering just this relaxation is enough to explain the observed signal transduction and therefore the geometric contrast, or whether other factors need to be invoked in addition.

In order to test this, a mechanical model that describes the relaxation of the sensor particle was devised, on top of which a generic two-step tunnel process was implemented [29]. The model is schematically shown on the right hand side of Fig. 14.15. The radial tip-induced force $\boldsymbol{F}_{\mathrm{Tip},r}$ is modelled by a Lennard-Jones (LJ) potential, while the lateral tip-induced force $\boldsymbol{F}_{\mathrm{Tip},xy}$ is modeled by a harmonic potential. With these two forces, any sample-induced (repulsive) force $\boldsymbol{F}_{\mathrm{Surf}}$ can be compensated, provided the sensor moves into the correct position. The sample force $\boldsymbol{F}_{\mathrm{Surf}}$ is a sum over pair interactions of the sensor particle with all atoms of the sample, each of these interactions is again modeled by a LJ potential. The tunnelling model assumes a two-step tunnelling process from the tip base atom (i.e. the last metal atom of the tip, to which the sensor particle is bound) to the sensor particle, and from there to the sample, whereby tunnelling to all atoms of the sample is treated as independent. Note that in spite of its simplicity, this tunnelling model can be derived from the Landauer formula for ballistic transport, by invoking certain well-justified approximations, namely the restriction to bias voltages close to zero (corresponding to typical experiments in the geometric imaging mode), the assumption that the electronic level structure of the sensor particle will neither be influenced by the tip nor the sample and vice versa (the sensor particle interacts only weakly), the premise that the sample LDOS is homogeneously spread (confirmed by conventional STM images at relevant tunnelling voltages that show little submolecular contrast), the supposition that all tunnelling channels between sensor particle and sample are independent of each other, and finally the assumption that the densities of states (at the Fermi level) of all constituents of the junction (tip, sensor particle and sample) are unaffected during scanning. The conductance can then be written as [29]

$$\begin{aligned}\frac{dI}{dV}(\boldsymbol{r}_{\mathrm{SP}}, \boldsymbol{r}_{\mathrm{T}}, \boldsymbol{R}_S) &\propto T_{\mathrm{T}}(\boldsymbol{r}_{\mathrm{SP}}, \boldsymbol{r}_{\mathrm{T}}) T_{\mathrm{S}}(\boldsymbol{r}_{\mathrm{SP}}, \boldsymbol{R}_{\mathrm{S}}) \\ &= T_{\mathrm{T}}(\boldsymbol{r}_{\mathrm{SP}}, \boldsymbol{r}_{\mathrm{T}}) \sum_i T_i(\boldsymbol{r}_{\mathrm{SP}}, \boldsymbol{r}_i)\end{aligned}$$

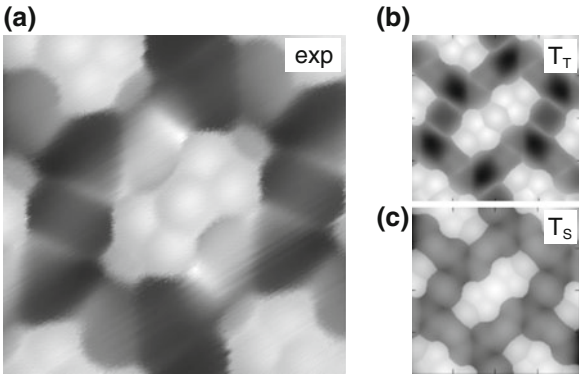

Fig. 14.16 Results of the generic model for geometric mode STM. **a** Experimental constant height image of PTCDA/Ag(111) recorded with a Xe atom as a nanoscale force sensor ($V_b = -4$ mV). **b**, **c** Simulated images in the T_S and T_T channels, respectively. Reproduced from [29] with permission

where $\boldsymbol{r}_{SP}$, $\boldsymbol{r}_T$, and $\boldsymbol{r}_i$ are the positions of sensor particle, tip base atom and sample atom i, respectively ($\boldsymbol{R}_S$ denotes the set af all $\boldsymbol{r}_i$), and the T are the tunnelling transmissions,

$$T_T \approx t_T^\dagger t_T \quad \text{and} \quad T_S \approx \sum_i T_i = \sum_i t_i^\dagger t_i .$$

The t are hopping matrix elements. Note that this model differs from the usual Tersoff-Hamann picture according to which the tunnelling conductance is determined by the compound local density of states of the sample at the position of the tip. The point is that in the present case the tunnelling path does not lead directly from the tip to the sample, hence we consider tunnelling between atomic centres in order to capture this non-trivial transport path. The underlying assumption is that the relevant LDOS of the sample is devoid of any specific orbital structure and can be reconstructed reasonably well by the superposition of atomic densities of states. In order to simulate actual images with the above model, an assumption about the functions $T_T(\boldsymbol{r}_{SP}, \boldsymbol{r}_T)$ and $T_i(\boldsymbol{r}_{SP}, \boldsymbol{r}_i)$ must be made. For simplicity, one can assume the usual exponential distance dependencies of tunnelling, namely $T_T \propto \exp(-\beta_T|\boldsymbol{r}_{SP} - \boldsymbol{r}_T|)$ and $T_i \propto \exp(-\beta_S|\boldsymbol{r}_{SP} - \boldsymbol{r}_i|)$.

As it turns out, this model can explain geometric STM images well (Fig. 14.16). Note that as far as signal transduction is concerned, the model has no other ingredient than sensor particle relaxation, because each of the three components-tip, sample, and sensor particle is assumed to be 'electronically rigid' and only the position of the sensor particle relative to tip and sample changes thus redirecting the tunnelling path as the tip moves laterally. Specifically, the model does not allow for a depletion of the tip DOS.

Because it is essentially a mechanical model of transduction, the model, if valid, must explain dynamic non-contact AFM *and* geometric STM images at the same time and on the same footing. This it does indeed. It has been known for some time that in dynamic non-contact AFM the relaxation of the CO tip quantitatively affects measured bond lengths [12, 30]. The above model shows that, beyond this, also

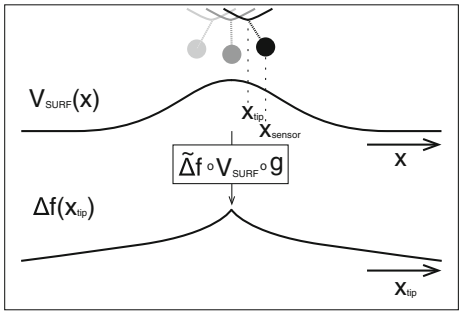

Fig. 14.17 Schematic illustration of the sensor particle relaxation that produces a sharpening of the frequency shift contrast in non-contact dynamic AFM. The *upper curve* shows the surface potential $V_{\mathrm{surf}}(x)$ which is felt by the sensor particle, with stronger repulsion in the centre. The *lower curve* shows the observed frequency shift $\Delta f(x_{\mathrm{tip}})$. The functional form of Δf as a function of x_{tip} is determined by the intrinsic frequency shift function $\tilde{\Delta} f\,[V_{\mathrm{Surf}}(x_{\mathrm{sensor}})]$ and the relaxation function $x_{\mathrm{sensor}} = g(x_{\mathrm{tip}})$, i.e. $\Delta f(x_{\mathrm{tip}}) = (\tilde{\Delta} f \circ V_{\mathrm{surf}} \circ g)(x_{\mathrm{tip}}) = \tilde{\Delta} f\left[V_{\mathrm{Surf}}(g(x_{\mathrm{tip}}))\right]$. The mathematical composition of the two functions V_{surf} and g leads to the sharpening in the observed Δf image. After [29]

salient changes in the qualitative appearance of the images can be explained by sensor particle relaxations. For example, the model naturally explains both the sharpening and inversion of dynamic non-contact AFM contrast as the tip height is reduced: The schematic drawing in Fig. 14.17 shows that tip relaxation must lead to a sharpening of image features, because as the sensor particle comes closer to the sample, the range of lateral tip positions at which it will stay close to the ridge of the sample potential V_{surf} and probe forces there will become narrower. This is indeed what is observed in dynamic non-contact AFM, as Fig. 14.18 demonstrates. Moreover, it is clear that eventually this sharpening must lead to contrast inversion in dynamic non-contact AFM, because for the closest tip-sample distances the sensor particle is essentially confined to positions in the minima of the potential landscape V_{surf} irrespective of the tip position (see top row in Fig. 14.18), and the measured frequency shift for tip positions in the minima is larger because there the sensor particle has nowhere to relax, whereas for tip positions closer to ridges in the potential landscape the sensor particle still sits slightly off-centre in the nearby well and therefore can relax further as the tip oscillates, thus reducing the repulsive force and measured frequency shift. This inversion can also be observed in simulated force curves at two tip positions in Fig. 14.19, as the two curves cross each other. Initially, for large tip heights and small relaxations the repulsive force is larger above the atom, because of the larger total electron density there, but for smaller tip heights an inversion takes place. This crossing of the force curves is also observed in the corresponding experiments (Fig. 14.14).

Evidently, the same mechanism that causes sharpening in dynamic non-contact AFM images is also responsible for the sharp features in geometric STM: this closer the sensor particle comes to the sample, the narrower the range of lateral tip positions

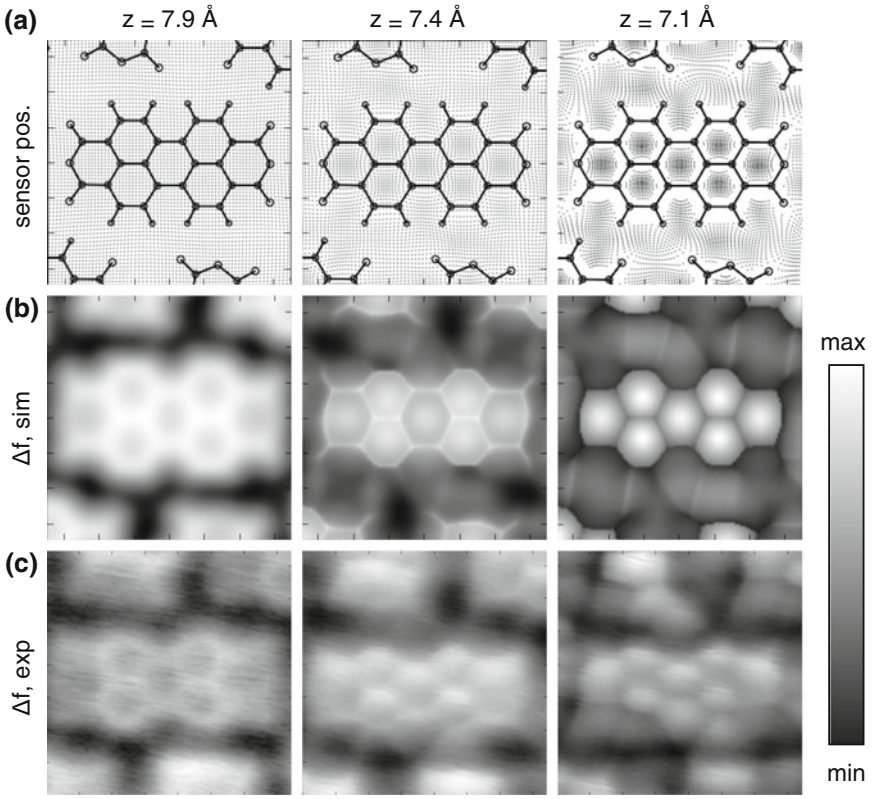

Fig. 14.18 AFM simulation results and comparison to experiments, as a function of tip-surface distance z. **a** Map of simulated sensor particle positions after relaxation. One clearly sees the bunching of sensor particle positions, e.g. in the centres of the carbon rings, governed by the relaxation function $x_{\text{sensor}} = g(x_{\text{tip}})$ as defined in Fig. 14.17. According to the mechanism sketched in Fig. 14.17, this bunching leads to sharpening and contrast inversion of the images in panels (**b**) and (**c**). **b** Simulated AFM image (the frequency shift $\Delta f(x_{\text{tip}})$ is displayed). **c** Experimental AFM images $\Delta f(x_{\text{tip}})$. Reproduced with permission from [29]

for which the sensor particle stays close to ridges in the potential landscape V_{surf} and channels the tunnelling current into this area. However, since tunnelling through the sensitized junctions is a two-step process and the measured overall conductance depends on the position of the sensor particle relative to sample *and* tip (in contrast to the frequency shift, which depends only on the position of the sensor particle relative to the sample), it is impossible to predict by inspection what the conductance pattern should look like for a given sensor particle relaxation pattern. Here the generic transport simulations mentioned above prove invaluable.

Overall, the agreement between the transport simulations and the transport experiment is excellent, as Fig. 14.16 illustrates for the case of a Xe sensor, indicating that the model captures the essential physics. On the basis of this model many features

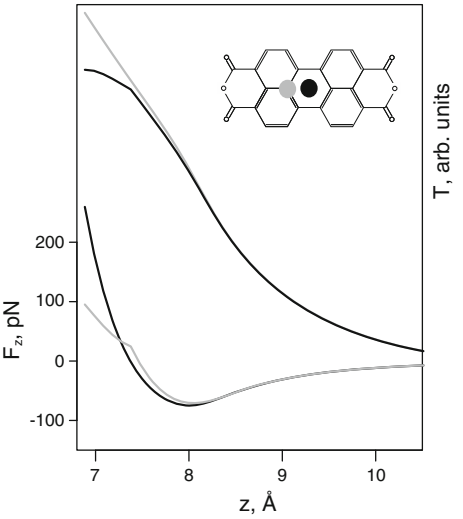

Fig. 14.19 Results of the generic model for geometric mode STM. *Lower pair of curves:* simulated force $F_z(z)$. *Upper pair of curves:* simulated tunnelling probability T_S. Both quantities are plotted as a function of the absolute tip-sample distance z and have been computed over the areas indicated by the *grey* and *black dots* in the PTCDA structure formula. This figure should be compared to the corresponding experimental results in Fig. 14.14a

of the geometric images recorded with force-sensitive STM in general and STHM in particular can finally be understood.

(1) The model explains the damping of the exponential increase of the conductance that is illustrated in Fig. 14.13. Since the junction is 'filled' by the sensor particle, the overall tunnelling distance will not generally become shorter even if the tip comes closer to the sample. What happens instead is that the position of the sensor particle in the junction changes and the tunnel current is guided along a modified two-step path of approximately the same length as before.

(2) According to the model, any geometric STM image is a superposition of two images, one deriving from T_T, the other from T_S (cf. Fig. 14.16). For the T_S image it is true that the measured tunnelling conductance above atoms or bonds in molecules will always be lower than above the centres of (carbon) rings, because in the former position the coordination of the sensor particle to atoms of the sample is lower, leading to a lower conductance. This argument is valid irrespective of the tip height, only the range of lateral tip positions at which the coordination is lower becomes narrower with decreasing tip height (sharpening), cf. top row in Fig. 14.18. For close tip-surface distances, the tunnelling conductance in the T_T image will also be larger in ring positions than above atoms and bonds, because in the ring there is no possibility of a sideways relaxation, which leads to a larger reduction of the distance between the tip-base atom and the sensor particle as the tip approaches the surface. In fact, Fig. 14.16 shows that above the PTCDA molecule the contrast in the T_T image is rather similar to the one in T_S. For larger tip-surface distances the T_T image will tend to show weak contrast, because as a result of weak relaxation the sensor particle rolls around the tip base atom, with little effect on the distance between tip base atom and sensor. Considering the two images together, it is therefore clear that in geometric STM images contrast inversion is usually not observed above molecules.

(3) In the simulation, both T_S and T_T images can of course be analysed separately. Comparison to the measured image therefore permits image features to be traced back to either of the two tunnel processes T_T or T_S. For example, one finds that for a CO sensor the intramolecular contrast is largely determined by T_S [29]. This is a consequence of the relatively strong covalent bond of the CO molecule to the tip: firstly, this means that the distance $|\boldsymbol{r}_{SP} - \boldsymbol{r}_T|$ will not change strongly, whatever the force exerted on the sensor particle by the sample, and secondly the good electronic coupling across the covalent bond implies a small tunnelling decay constant β_T, which further reduces the sensitivity of the T_T channel. This illustrates that as a general tendency the mechanically and electronically more weakly coupled part of the junction tends to determine the high-resolution geometric STM image. For example, Fig. 14.16 reveals that for a Xe sensor the contrast between the molecules is essentially determined by T_T, while on the molecules both T_T and T_S show very similar images.

(4) In special circumstances images can be recorded that are not only a superposition of T_T and T_S tunnelling, but also contain conventional LDOS contrast. In Sect. 14.2.5 an example of this was discussed in connection with Fig. 14.10. Such images can be understood qualitatively if the supposition that the sample LDOS is continuously spread over the molecule is given up. Then, in a Tersoff-Haman picture, the T_S tunnelling will depend on the sample LDOS, which for special tunnelling voltages resembles the probability distribution of the corresponding orbital , or the orbital LDOS structure is distorted by the geometric structure of the molecule, via sensor particle relaxation. However, due to sensor particle relaxation the LDOS will essentially be recorded in the vicinity of the minima of the interaction potential between sensor particle and sample, cf. the top row of Fig. 14.18. As a result, an image is observed in which - depending on the viewpoint - the geometric structure of the molecule is modulated discontinuously with the LDOS of the corresponding orbital, or the orbital LDOS structure is distorted by the geometric structure of the molecule, via sensor particle relaxation. This explains why the whole central ring in Fig. 14.10 appears dark (for all corresponding tip positions the sensor particle is locked close to the nodal line of the HOMO), while the other four perylene rings are bright (sensor particle locked on the lobes of the HOMO). The influence of the nodal line is also obvious between the perylene rings, but, remarkably, not close to the short edges of the molecule. It is clear that because of the complex interplay between LDOS and geometric imaging a full understanding of mixed contrast requires a more elaborate quantitative modelling.

(5) The same mechanism that leads to the sharpening of intramolecular bonds (as illustrated in Fig. 14.17) also leads to the appearance of the rather sharp features in the interstitial region between the molecules in the sample surface, which have been discussed as possible signatures of hydrogen bonds [10], see Figs. 14.11 and 14.16. This can be understood as follows: the mechanism illustrated in Fig. 14.17 is operational and leads to sharp lines in the images whenever a repulsive saddle occurs in the potential felt by the sensor particle. The origin of this saddle can either be the presence of real electron density, as in the case of intramolecular bonds, or the close proximity of atoms in the sample surface. In the latter case, the saddle arises from

the convolution of the electron densities of the sensor particle and the neighbouring sample atoms. Hence, the sharp lines in the images in the interstitial region connect adjacent atoms in neighbouring molecules irrespective of any bond there may be between them [29]. Evidently, if there is a bond, the bonding atoms will be so close to each other that the convolution will likely yield a sharp line. For this reason, in many cases such features appear precisely in locations where hydrogen bonds are expected. However, not every observed line must necessarily correspond to an actual bond. Note that these sharp lines also appear in dynamic non-contact AFM [16, 17], for exactly the same reason as in STM. In AFM, however, it is relatively easy to check whether true electron density or just the convolution effect cause a given feature, since in the former case the electron density also shows up as a broad and smooth structure in AFM images that are recorded at larger tip distances when the sensor particle does not show appreciable relaxation (Fig. 14.18 left column). In this distance range, the geometric STM contrast is usually hardly discernible.

(6) In the simplest implementation of the model the lateral tip force $\boldsymbol{F}_{\mathrm{Tip},xy}$ is isotropic in the xy-plane. For cylindrically symmetric tips this is a realistic assumption. However, most real tips will not be symmetric, leading to an ansiotropic lateral tip force. Evidently, this has the potential to cause image distortions as have been discussed in Sect. 14.2.3. In fact, the apparent 3D shadowing has been simulated with an anisotropic lateral tip force [29].

The above discussion shows that in the framework of a simple mechanical transduction mechanism the sensor-transducer model introduced in Sect. 14.3 can explain virtually all generic features of the geometric STM contrast, in simultaneous consistency with corresponding dynamic non-contact AFM results. On the one hand, this confirms the sensor-transducer model as introduced in the previous section as such, on the other hand it relegates other possible transduction mechanisms [10, 27] to secondary roles, at least in the cases studied so far.

14.5 Conclusion and Outlook

This chapter has been devoted to a force-sensitive operation mode of STM in which the geometric structure of surfaces can be visualized. After summarizing the phenomenology of geometric resolution for the example of molecular monolayers, we have discussed crucial experimental findings. This has allowed for the formulation of a sensor-transducer model according to which a nanoscale force sensor at the tip of the STM transduces repulsive forces from the sample into a tunnelling conductance signal. To confirm the sensor-transducer concept, which can be understood as a miniaturized version of the original AFM design [2], we have considered a simulation approach that allows the extraction of a purely mechanical transduction mechanism based on lateral and vertical sensor particle relaxation. We note that although molecular layers have been used almost exclusively in this chapter to illustrate the force-sensitive STM mode, there is nothing in the mechanism which restricts it to these kinds of samples. It should also be clear from the discussion in this chapter

that any extension of the present tunnelling model that includes more realistic charge transport simulations will not change its essential feature: namely, that the observed STM contrast is directly related to the relaxation of the sensor particle.

The mechanical model of the functionalized STM/AFM junction clarifies all essential features of force-sensitive STM and dynamic non-contact AFM images measured with functionalized tips at close tip-sample distances and establishes the relationship between these two methods. Most importantly, it explains the appearance of the characteristic sharp features. Also, it reveals the nature of the contrast in the intermolecular regions and allows a critical discussion of the appearance of so-called hydrogen bonds in the images. Finally, the method allows for the simulation of dynamic non-contact AFM and geometric mode STM images of complete molecular layers at different tip-sample distances at small computational cost.

There are at least two aspects of the discussion in the present chapter that can be generalized. Firstly, the relaxation of the outermost tip which is utilized here is not specific to *functionalized* tips in STM or AFM, nor is it specific to *non-contact* AFM. In fact, tip relaxation was discussed in the context of contact force microscopy with bare metal tips long ago [31]. Of course, bare metal tips are less bendable, and in contact force microscopy one additionally has a lateral force component due to in-contact sliding, introducing stick-slip and other friction phenomena, but tip relaxation may still lead to a similar phenomenology there as discussed here. For example, for contact force microscopy on graphite it has been pointed out that the structural resolution observed there represents a 'hollow-site resolution' rather than an 'atomic resolution' [32]. Tip relaxation is also important in the imaging of lateral forces [33] and 3D force fields [34] and in point contact microscopy [25, 26].

Secondly, the concept of the STM junctions with sensor-transducer functionality can be generalized beyond the present example of force-sensitive STM, by considering both other measurands to which the sensor may respond and other transduction mechanisms. In the present example, the force from the sample determines the equilibrium position of the sensor particle and thus the tunnelling path. As we have seen, the transduction of the *force signal* is effected via changing equilibrium positions and changing tunnelling paths. But instead of the force at a given position one may, for example, be interested in the *curvature* of the potential there. Evidently, this curvature of the potential landscape of the sample must influence the vibrational frequency of the frustrated translation of the sensor particle at the end of the tip (since the curvature of the sample potential is much smaller than that of the tip, the influence of the former on the vibrational frequency is small, but still measurable), and the latter could be easily measured in inelastic tunnelling spectroscopy (IETS) [35]. In such an experiment the sensor particle would therefore transduce the signal *'curvature of the potential'* into a secondary signal *'inelastic tunnelling current'*. Indeed, inelastic tunnelling images of cobalt phthalocyanine molecules have been recorded recently in precisely this way [6], showing similar submolecular structural detail as force-sensitized STM and dynamic non-contact AFM. Clearly, this the single molecule inelastic probe method (*itProbe*) is yet another example of the sensor-transducer concept in STM and thus beautifully illustrates its universality. In general terms, the concept relies on the presence of at least one internal degree of

freedom in the tunnelling junction (e.g. position of sensor, or frustrated translation mode of sensor) which can sense a certain physical measurand (e.g. force, or curvature of potential) and transduce this signal into another physical quantity (elastic conductance, or vibrational frequency/inelastic conductance). It should be noted that many more sensor-transducer systems are conceivable, all furnishing their specific information about the studied surface. A very recent example is the method of scanning quantum dot microscopy [35], which allows extremely sensitive measurements of the electrostatic potential.

Note that the single molecule inelastic probe method is the dynamic version of STM-based force microscopy: Whereas the nanoscale sensor particle in STHM and related methods plays the role of a *static cantilever*, the single molecule inelastic probe is used as a *'nanoscale tuning fork'* (Accordingly, the second derivative of the potential is measured, as in the case of the macroscopic cantilever). Interestingly, the inelastic tunnelling probe would in principle work even without sensor particle relaxation, because the transduction mechanism is based on exciting vibrations around its equilibrium position, whereas in static STM-based force microscopies the transduction mechanism intrinsically employs relaxation. But, of course, since the bonding of the sensor particle to tip is the same in both cases (it is in fact the same sensor particle), there will always be relaxation, also in the single molecule inelastic probe method. Indeed, the application of an extended version of the simulation model introduced in the previous section has shown that it is again this relaxation which yields the sharp submolecular contrast in *itProbe* experiments [36]. Without relaxation, i.e. for large tip-sample distances, the inelastic probe method provides blurred images, similar to those of conventional STM. Finally, we note that it has been shown that the single molecule inelastic probe method possesses a remarkable sensitivity to intramolecular charge distributions, making it a useful complement to local contact potential difference microscopy [36].

References

1. G. Binnig, H. Rohrer, Ch. Gerber, E. Weibel, Phys. Rev. Lett. **49**, 57 (1982)
2. G. Binnig, C.F. Quate, Ch. Gerber, Phys. Rev. Lett. **56**, 930 (1986)
3. F.J. Giessibl, Rev. Mod. Phys. **75**, 949 (2003)
4. L. Gross, F. Mohn, N. Moll, P. Liljeroth, G. Meyer, Science **325**, 1110 (2009)
5. L. Gross, N. Moll, F. Mohn, A. Curioni, G. Meyer, F. Hanke, M. Persson, Phys. Rev. Lett. **107**, 086101 (2011)
6. C.I. Chiang, C. Xu, Z. Han, W. Ho, Science **344**, 885 (2014)
7. R. Temirov, S. Soubatch, O. Neucheva, A.C. Lassise, F.S. Tautz, New J. Phys. **10**, 053012 (2008)
8. R. Temirov, S. Soubatch, F.S. Tautz, U.S. Patent 8,347,410 (1 Jan 2013)
9. N. Moll, L. Gross, F. Mohn, A. Curioni, G. Meyer, New J. Phys. **12**, 125020 (2010)
10. C. Weiss, C. Wagner, C. Kleimann, M. Rohlfing, F.S. Tautz, R. Temirov, Phys. Rev. Lett. **105**, 086103 (2010)
11. C. Weiss, R. Temirov, F.S. Tautz, U.S. Patent 8,832,860 (9 Sept 2014)
12. L. Gross, F. Mohn, N. Moll, B. Schuler, A. Criado, E. Guitian, D. Pena, A. Gourdon, G. Meyer, Science **337**, 1326 (2012)

13. N. Moll, L. Gross, B. Schuler, F. Mohn, A. Curioni, G. Meyer, Phys. Rev. Lett. **111**, 106103 (2013)
14. C. Weiss, C. Wagner, R. Temirov, F.S. Tautz, J. Am. Chem. Soc. **132**, 11864 (2010)
15. G. Kichin, C. Weiss, C. Wagner, F.S. Tautz, R. Temirov, J. Am. Chem. Soc. **133**, 16847 (2011)
16. J. Zhang, P. Chen, B. Yuan, W. Ji, Z. Cheng, X. Qiu, Science **342**, 611 (2013)
17. A.M. Sweetman, S.P. Jarvis, H. Sang, I. Lekkas, P. Rahe, Y. Wang, J. Wang, N.R. Champness, L. Kantorovich, P. Moriarty, Nat. Comm. 5, 3931 (2014)
18. L. Gross, F. Mohn, N. Moll, G. Meyer, R. Ebel, W.M. Abdel-Mageed, M. Jaspars, Nat. Chem. **10**, 821–825 (2010)
19. R. Temirov, Dissertation, Jacobs University Bremen, 2008
20. C. Weiss, Dissertation, RWTH Aachen, 2012
21. A. Halbritter, P. Makk, S. Csonka, G. Mihaly, Phys. Rev. B **77**, 075402 (2008)
22. W.H.A. Thijssen, D. Djukic, A.F. Otte, R.H. Bremmer, J.M. van Ruitenbeek, Phys. Rev. Lett. **97**, 226806(4) (2006)
23. J.A. Gupta, C.P. Lutz, A.J. Heinrich, D.M. Eigler, Phys. Rev. B **71**, 115416 (2005)
24. Y. Wang, J. Kroger, R. Berndt, H. Vazquez, M. Brandbyge, M. Paulsson, Phys. Rev. Lett. **104**, 176802 (2010)
25. J.A. Stroscio, J.R. Celotta, Science **306**, 242 (2004)
26. Y. Zhang, P. Wahl, K. Kern, Nanoletters **11**, 3838 (2011)
27. M. van der Maas, S. Vasnyov, B.L.M. Hendriksen, O.I. Shklyarevskii, S. Speller, Low Temp. Phys. **38**, 517 (2012)
28. G. Kichin, C. Wagner, F.S. Tautz, R. Temirov, Phys. Rev. B **87**, 081408 (2013)
29. P. Hapala, G. Kichin, C. Wagner, F.S. Tautz, R. Temirov, P. Jelinek, Phys. Rev. B **90**, 085421 (2014)
30. M. Neu, N. Moll, L. Gross, G. Meyer, F.J. Giessibl, J. Repp, Phys. Rev. B **89**, 205407 (2014)
31. H. Holscher, U.D. Schwarz, R. Wiesendanger, Europhys. Lett. **36**, 19 (1996)
32. H. Holscher, U.D. Schwarz, O. Zworner, R. Wiesendanger, Phys. Rev. B **57**, 2477 (1998)
33. M.Z. Baykara, T.C. Schwendemann, B.J. Albers, N. Pilet, H. Monig, E.I. Altman, U.D. Schwarz, Nanotechnology **23**, 405703 (2012)
34. M.Z. Baykara, O.E. Dagdeviren, T.C. Schwendemann, H. Monig, E.I. Altman, U.D. Schwarz, Beilstein J. Nanotechnol. **3**, 637650 (2012)
35. C. Wagner, M.F.B. Green, P. Leinen, T. Deilmann, P. Krüger, M. Rohlfing, R. Temirov, F.S. Tautz, arXiv:1503.07738 [cond-mat.mes-hall]
36. P. Hapala, R. Temirov, F.S. Tautz, P. Jelinek, Phys. Rev. Lett. **113**, 226101 (2014)

Chapter 15
Nanostructured Surfaces of Doped Alkali Halides

Clemens Barth

Abstract In this Chapter, we explore the fascinating world of the nanostructured (001) Suzuki surface of Mg^{2+} and Cd^{2+} doped NaCl single crystals—surfaces that have been recently rediscovered by noncontact AFM and Kelvin probe force microscopy in ultra-high vacuum. The surface morphology, the atomic surface structure and the identification of surface ions will be discussed. At the end of this Chapter two applications exemplify a nanostructured growth of functionalized molecules with polar substituents and metal nanoparticles on the Suzuki surface.

15.1 Introduction

Alkali halides have been extensively studied in condensed matter physics [1], and the crystal and electronic structure, optical properties, defects, doping, the ionic conductivity and surface reactivity related phenomena have been addressed already several decades ago [2, 3]. Before atomic force microscopy (AFM) was introduced in 1986 [4], the morphology of the (001) surface has been mainly studied by the combination of the gold decoration method and transmission electron microscopy (TEM), starting from the end of the 1950s [5, 6]. Such studies gave great insights into diffusion and evaporation related surface phenomena [7–9] as well as into impurity controlled surface modifications [10–12] . After the introduction of frequency modulated noncontact AFM (nc-AFM) [13–16], the surfaces of alkali halides have become yet again *standard model surfaces*. The atomic structure [17–25], defect identification [26–28], indentation [29] as well as adsorbed molecules [30, 31], self-assembled molecules [32–41] but also metal NPs [40, 42–48] have been addressed. In recent revolutionary work, alkali halide thin films have been used to support single molecules for imaging their atomic structure with an unmatched resolution [49–54].

The reason for the extensive use of alkali halide surfaces in nc-AFM is that they can be easily prepared in ultra-high vacuum (UHV): for instance, cleaving a single

C. Barth (✉)
Aix-Marseille Université, CNRS, CINaM UMR 7325,
Campus de Luminy, Case 913, 13288 Marseille Cedex 09, France
e-mail: barth@cinam.univ-mrs.fr

© Springer International Publishing Switzerland 2015

S. Morita et al. (eds.), *Noncontact Atomic Force Microscopy*,
NanoScience and Technology, DOI 10.1007/978-3-319-15588-3_15

crystal along the (001) cleavage plane, which is mostly followed by in-situ annealing at moderate temperatures (∼100 °C) [26, 55, 56], is completely sufficient to obtain clean surfaces with large atomically and stoichiometric flat terraces—ideal conditions for nc-AFM and KPFM. The imaging with atomic resolution and of supported molecules or metal nanoparticles can be easily accomplished. A very important property is that alkali halide surfaces are quite inert in UHV such that measurements can be done within a week during which the surface remains almost clean. Another advantage is that the number of possible defects, which are stable during the acquisition time of AFM experiments, is quite limited: apart from impurities, F^0 centers (anion vacancy with a localized electron inside), cation and anion vacancies are the only candidates. This helps the interpretation of surface phenomena observed by nc-AFM where defects play a fundamental role. Note that high-quality alkali halide surfaces can also be obtained by evaporating a small amount of the alkali halide material onto almost any clean and atomically flat substrate surface (thin alkali halide films) like on silver [57, 58], copper [59, 60], HOPG [61] and even silicon surfaces [62].

Apart from all the latter advantages there is another one of general importance: alkali halides can be easily doped with divalent metal impurity ions such as Mg^{2+} or Cd^{2+}, via adding the respective salt into the melt during the growth of an alkali halide crystal (e.g., $CdCl_2$ or $MgCl_2$ in NaCl, see [63]). Such impurities replace the standard cations and create a cation vacancy in their vicinity to guarantee charge neutrality within the crystal. At specific doping concentrations, new phases with new atomic structures inside the alkali halide can be created. One of such phases is the Suzuki phase discovered by Kazuo Suzuki in 1961.

In this Chapter, we will see that NaCl crystals, which are doped with 1–5 % MgCl or $CdCl_2$, exhibit nanostructured surfaces with two distinct surface regions: one from pure NaCl and one from the Suzuki structure. The surface morphology, which was studied as a function of surface preparation (annealing, impurity concentration, etc.), atomic resolution imaging including identification of surface ions and applications of the surface in the domain of molecular self-assembly and heterogeneous model catalysis will be discussed.

To complete the picture of *doped alkali halides in nc-AFM*, we first describe the surfaces of those alkali halide crystals, which are often referred as to *crystals of highest purity*, and crystals that contain only a few impurity ions (< 1 %). We will see that impurities at low doping level sensitively determine the charge state of the surface by creating a Debye-Frenkel dipole layer at the surface.

15.2 Low Defect Concentration—the Debye-Frenkel Layer

For many nc-AFM experiments, alkali halide crystals of highest purity are purchased from crystal growing companies. When such single crystals are cleaved in UHV, some surface charge is generally detected even at large distances of several tens and hundreds of nanometer, depending on the cleavage [56]. In literature it is quite often mentioned that prior to AFM experiments a crystal is annealed at temperatures

around 100 °C to 'remove the surface charge', which was produced by the cleavage. A fundamental question has been always if all surface charge is removed after the annealing and if the surface is defect-free. To give answers to this question, KPFM can be used because it is sensitive on surface charges and their lateral distribution [26, 64, 65].

Surprisingly, after a preparation by UHV cleavage and annealing KPFM images always show a contrast, which is stable and does not change by time. Apart from a very faint, over large distances smoothly varying Kelvin contrast [56] a very localized, sharp contrast at the steps is regularly observed [26–28] (Fig. 15.1a, b). The latter type of contrast is composed of single round patches, which have a lateral dimension typically of 10–20 nm [26]. Because of the high purity no material other than alkali halide is present on the surface so that the contrast is due to localized charged defects, which change the local electrostatic surface potential at the steps. It is clear that such defects cannot 'aggregate' into nanometer large structures. And indeed, atomic resolution imaging regularly reveals atomic sized defects at the kink and corner sites of steps, exactly at the position of the patches in the Kelvin image [26]. For instance, the defects 1 and 2 at the two kinks in Fig. 15.1c are exactly located at the bright patch (yellow circle) in image Fig. 15.1a, b. Such 'charged defects' are a point source in the KPFM contrast formation: because of its long-range character the electrostatic force is detected by the whole tip apex such that the shape of the apex is imaged

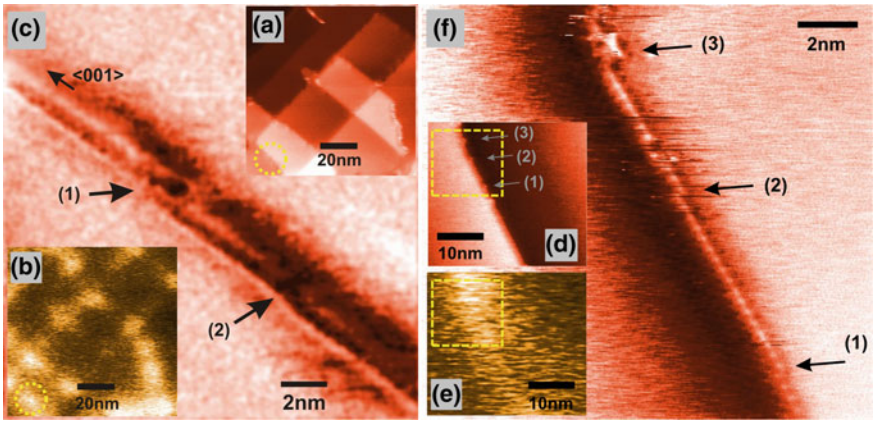

Fig. 15.1 The Debye-Frenkel-Layer on alkali halide crystal surfaces. **a–c** Topography (**a**) and Kelvin image (**b**) simultaneously recorded on the (001) surface of a KCl crystal of highest purity (Kelvin contrast: $U_{step-terrace} = +0.4$ V). **c** Constant height image recorded in the surface region marked by the *dotted circle* in **a**. **d–f** Topography (**d**) and Kelvin image (**e**) simultaneously recorded on a (001) surface of a NaCl crystal, which was doped with 0.1 % $MgCl_2$ (Kelvin contrast: $U_{step-terrace} = +0.3$ V). **f** Constant height image recorded in the surface region marked by the *dotted square* in **d**. The bright patches in the Kelvin images (**b**) and (**e**) correspond to more negative surface sites with respect to the neutral alkali halide terraces. The negative surface sites are created by cation vacancies at kink and corner sites of steps as verified by atomic resolution (**c**) and (**f**) at the respective places. Both crystals were cleaved in UHV and annealed at 150–200 °C (From [26])

when the tip scans a charged defect. This explains the size of the patches but also the observation that in a Kelvin image all patches have the same size.

The most important observation is that the patches always exhibit the same contrast at the steps (e.g., always a bright contrast), which corresponds to a net negative surface charge [26–28]. In fact, it documents a fundamental property of the surfaces of ionic material in condensed matter physics, and is refereed to as the *Double layer* or *Debye-Frenkel layer* introduced by Frenkel in 1946 [66, 67]: if for an ideal pure crystal (no impurities) the free formation energies for the creation of anion and cation vacancies are different in the near surface region, an excess of one type of vacancy is generated by time. Because, e.g., a cation vacancy has 6 or 5 neighboring anions in the bulk or on the terrace, respectively, (anion vacancy: 6 or 5 neighboring cations) it is a very negative site carrying a 'negative charge' (anion vacancy: 'positive charge'). Therefore, an excess of one type of vacancy would charge up the crystal, which is an impossible scenario. A mechanism is therefore needed that balances this excess charge. In fact, a double layer is created such that one type of vacancy is located on the surface whereas the other one is stabilized in a layer below the surface, in a so-called *space charge layer* [68–71]. Both layers form a dipole that modifies the free formation energy for the creation of cation and anion vacancies, which finally balances the electrostatics of the crystal [72]. Note that the free formation energies for anion and cation vacancy creation are indeed different on the surface and strongly depend on the temperature [72]: when monotonously changing the temperature (e.g., from low to high temperatures) the surface charge may become zero and switch its sign, which means that the vacancies change the respective layer. This was verified by a couple of experiments for different alkali halide crystals, explicitly showing a surface charging in dependence on temperature [72].

With respect to the surface site of the vacancies, calculations have shown that the vacancies find their energetic equilibrium position at especially low-coordinated surface sites, which are the kink and corner sites of steps [43, 73, 74]. Because alkali halide crystals are generally annealed prior to nc-AFM experiments the probability to find vacancies at steps is therefore high due to the high mobility of vacancies at room and in particular at elevated temperatures [43, 75].

The latter description of the Debye-Frenkel layer is in fact the *intrinsic case* [68], which is valid for high temperatures only when considering crystals of even highest purity. However, at relatively low temperatures like at room temperature, the so-called *extrinsic case* predominates due to the presence of impurities, which have valences other than +1 or −1 [69]. In fact, any real alkali halide crystal of even highest available purity does contain impurities. In most cases, the crystals contain divalent metal impurity ions like Ca^{2+} or Mg^{2+}. Because of the different valence with respect to the host cations, negative cation vacancies are created in order to conserve charge neutrality. At thermal equilibrium, a Debye-Frenkel layer is created such that the net negative surface charge of the cation vacancies on the surface is compensated by the positive impurities below the surface. Note that already a very small impurity amount of only a few ppm is sufficiently large to create a Debye-Frenkel layer. Furthermore, note that it is difficult to introduce divalent negative impurities, which would lead to

positive anion vacancies. Therefore, a net negative surface charge is created at room temperature by negative cation vacancies only [69].

The ultimate experiment to investigate the Debye-Frenkel layer is to examine the charge state of alkali halide crystals, which are *explicitly* doped with divalent metal impurity ions. In the case of such doped alkali halides, same type of observations must be made and even more, the density of the negative sites at the steps should increase upon an increase of the impurity content, as indeed observed on the (001) surfaces of Mg^{2+} and Cd^{2+} doped NaCl crystal surfaces (Fig. 15.1d–f).

The Debye-Frenkel layer is a fundamental property for surfaces of any ionic material. For instance, a Debye-Frenkel layer could also be observed on the (111) surface of CaF_2 by nc-AFM and KPFM [76]. Not only can the surface acts as a source or sink for charged defects but also dislocations and grain boundaries [67, 77]. In the case of dislocations, the dislocation line carries one type of charge and is surrounded by a symmetric space charge cloud of opposite charge. Charged dislocations could be indeed observed by nc-AFM and KPFM experiments on the (001) surface of bulk KBr, where dislocations were explicitly created by nanoindentation experiments [27].

15.3 High Defect Concentration—The Suzuki Phase

When the amount of divalent impurity cations in alkali halides is increased in the ppm range the (001) surface increases the number of negative vacancies at steps, building up a stronger Debye-Frenkel layer. However, at an impurity content of roughly 1 % a new important mechanism in condensed matter physics takes place inside the crystal:precipitation of impurities into new structures, which are localized in small regions inside the otherwise unchanged pure alkali halide. One important phase amongst others (see [63, 78] for a brief overview) is the so-called *Suzuki phase*, which appears in alkali halides in a doping range between roughly 1 and 10 %. The Suzuki phase was first found in Cd^{2+} doped NaCl (NaCl:Cd^{2+}) by the Japanese Kazuo Suzuki in 1961 thanks to his X-ray diffraction experiments [78]. Apart from the Suzuki phase in NaCl:Cd^{2+} crystals [12, 63, 78–92] the same phase was discussed for Mn^{2+} [10, 11, 63, 82, 83, 86, 88, 90, 93–100], Mg^{2+} [22, 63, 82, 89, 90], Fe^{2+} [11, 63, 82, 86, 90, 101, 102], Ni^{2+} [63, 103], Co^{2+} [104], Sr^{2+} [63, 105] and Pb^{2+} [63, 106] doped NaCl crystals. The host lattice must not necessarily be NaCl, the Suzuki phase may exist also in NaBr (Mn^{2+} [100]), KCl (Sm^{2+} [107], Pb^{2+} [108], Eu^{2+} [109, 110]), KBr (Mn^{2+} [111], Eu^{2+} [110, 112, 113]), LiF (Mg^{2+} [114, 115]), AgCl (Pb^{2+} [116]) and even in oxides (MgO:Mn^{2+} [117–120], NiO:Mn^{2+} [120], CuO:Pb^{2+} [121, 122]). Suzuki phases including two types of metal impurity cations were also found (NaCl:Pb, Eu^{2+} [123] and NaCl:Cd, Pb^{2+} [124]).

In the following, we discuss the Suzuki structure for NaCl crystals. The morphology of the respective (001) surface and atomic resolution imaging in conjunction with the identification of surface ions and vacancies are involved. The Section shall demonstrate that by using nc-AFM and KPFM very important surface properties of doped alkali halide crystals can be characterized.

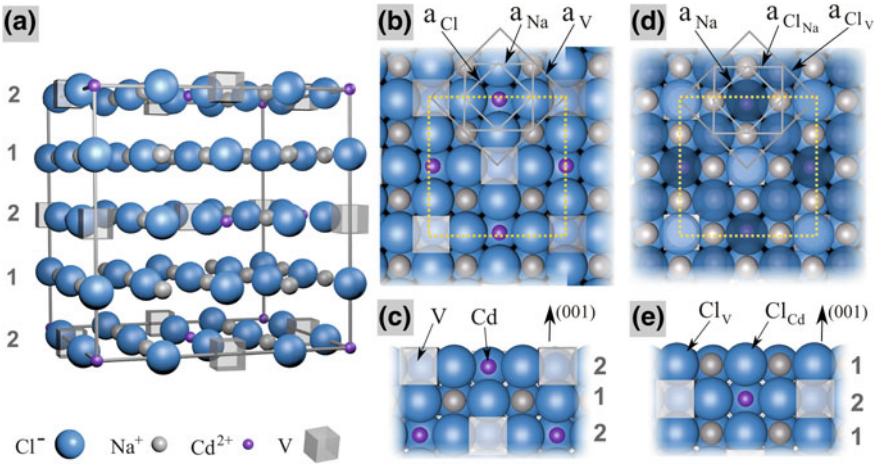

Fig. 15.2 The atomic structure of the Suzuki phase, exemplified for Cd^{2+} doped NaCl. **a** The Suzuki unit cell is almost two times larger ($a_S = 11.24$ Å) than the one of NaCl ($a_{NaCl} = 5.64$ Å) [78]. **b** *Top view* with a projection of the Suzuki unit cell (*yellow dotted square*) on the Suzuki terminated (001) surface. The Cd^{2+} ions and the vacancies form each a sub-lattice with a size of $a_V = a_{Cd^{2+}} = a_S/\sqrt{2}$, which is larger than the sub-lattices of the Na^+ ($a_{Na^+} = a_S/2$) and Cl^- ions ($a_{Cl^-} = a_S/2\sqrt{2}$). **c** *Side view* of the Suzuki terminated (001) surface. **d** *Top view* on the NaCl terminated (001) surface with chlorines above the vacancies (*bright blue*, Cl_V^-), Na^+ ions (*blue*, Cl_{Na}^-) and Cd^{2+} ions (*dark blue*, Cl_{Cd}^-). The Cl_V^- and Cl_{Cd}^- ions form each a sub-lattice with dimension $a_V = a_{Cl_V} = a_{Cl_{Cd}} = a_S/\sqrt{2}$ whereas the Cl_{Na}^- form a smaller sub-lattice with the size $a_{Cl_{Na}} = a_S/2$. The Na^+ ions form the smallest sublattice ($a_{Na^+} = a_S/2\sqrt{2}$). **e** *Side view* of the NaCl terminated (001) surface

15.3.1 Structure and Surface of the Suzuki Phase

The unit cell of the Suzuki phase is cubic and almost twice as large as the one of the corresponding alkali halide (Fig. 15.2a) [78, 91]. The structure is composed of alternating layers of pure NaCl (layer 1) and layers, which include the regular Cl^- ions, a part of the regular Na^+ ions, the positive divalent Cd^{2+} impurities and Na^+ vacancies for compensating the additional positive valence of the impurities (layer 2). Due to the specific structure, the composition is given either by $CdCl_2{\cdot}6NaCl$ or simply Na_6CdCl_8 for Cd in NaCl. Although the size of the unit cell of the Suzuki phase can be precisely measured by X-ray diffraction, slightly deviating values for its size were reported. For NaCl:Cd^{2+} crystals a size between 11.248(3) Å [82] and 11.278 Å [85] was found, which is slightly smaller than the value of 11.39(1) Å calculated at 0 Kelvin [91, 92]. The experimental values show that the Suzuki unit cell is slightly smaller than the double size of the NaCl unit cell, with a mismatch around 0.15 % ($a_{NaCl} = 5.64$ Å, $a_{Suzuki}/2 = 5.624$ Å [82], $a_{Suzuki}/2 = 5.639$ Å [85]). However, thanks to this very small lattice mismatch the Suzuki structure exists in up to 1 μm^3 large cubic precipitates inside real crystals, almost perfectly incorporated in the pure NaCl matrix [89].

With respect to the (001) surface, two possible surface terminations exist: either the surface is terminated by a layer containing regular Na^+ and Cl^- ions, the impurities and vacancies (*Suzuki-termination* , Fig. 15.2b, c) or by a pure NaCl layer (*NaCl-termination*, Fig. 15.2d, e). On the NaCl-terminated surface, the Na^+ ions are located above Cl^- ions of the second layer whereas the Cl^- ions sit either above second layer vacancies, impurities or Na^+ ions. In particular the Cl^- ions above the vacancies experience a strong outward relaxation of 40 pm while those over Cd^{2+} ions remain close to the ideal surface plane [25]. Such surface relaxations lead to a break of the NaCl surface symmetry such that several sub-latices are formed, as now explained for the Suzuki-termination (Fig. 15.2): on the Suzuki-terminated surface the Na^+, Cl^- and Cd^{2+} ions but also the vacancies form each highly symmetric sub-lattices, each of which has a precise dimension and orientation in the (001) plane. Already Kazuo Suzuki concluded from his X-ray diffraction experiments that the Cl^- ions relax towards the Cd^{2+} ions in the (001) surface plane [78], whereas the Na^+ and Cd^{2+} ions stay on the regular sites of the NaCl structure. In literature different values for the surface relaxation δ (fraction of a_{Suzuki}) of the Cl^- ions can be found (δ: 0.028 [78], 0.014 [79], 0.020 [125], 0.0154 [91]). The average of the latter values ($\delta = 0.19$) exemplifies that the Cl^- ions relax 20 pm towards the Cd^{2+} ions in the (001) surface plane.

In Sect. 15.3.3 we will see that thanks to the specific Suzuki structure an identification of all surface ions and the vacancies is possible by imaging the surface with atomic resolution in the nc-AFM mode.

15.3.2 Surface Morphology

15.3.2.1 Surfaces Prepared by Cleavage in UHV

If a doped alkali halide crystal with Suzuki precipitates inside the bulk—a so-called *Suzuki crystal*—is cleaved in UHV a flat (001) surface is obtained, which is called the *Suzuki surface*. Because the cleavage crack passes through the regular pure NaCl but also through some precipitates during the cleavage, two types of surface regions co-exist [126]: one from pure NaCl (*NaCl regions*) and one from a regular Suzuki structure (*Suzuki regions*). Figure 15.3 shows typical characteristics of the (001) surface after the UHV cleavage of a NaCl:Cd^{2+} crystal (4 Mol % of $CdCl_2$): in the middle of the topography image (Fig. 15.3a) two $400 \times 400\,\mathrm{nm}^2$ large square shaped Suzuki regions can be found, which are surrounded by regions of pure NaCl(001). The regions appear in form of depressions whereas their edges are oriented along equivalent ⟨100⟩ surface directions as observed before by TEM on surfaces of as-cleaved crystals [10, 86]. The square shape of the regions is in fact the projection of the almost cubic shape of the Suzuki precipitates onto the (001) surface [86, 94].

An important characteristic are cleavage steps inside the Suzuki regions [126]: the topography image (Fig. 15.3a) shows cleavage steps with a height of 5.6 Å implying that all terraces are either NaCl or Suzuki-terminated. The specific step structure is a

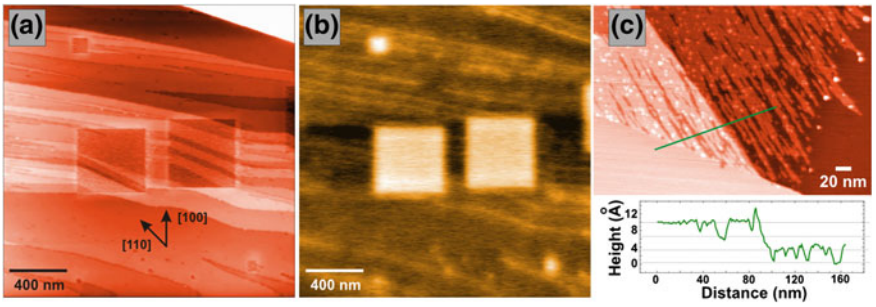

Fig. 15.3 Suzuki precipitates on the (001) surface of an as-cleaved NaCl:Cd^{2+} crystal (4 Mol % of $CdCl_2$). Topography (**a**) and Kelvin image (**b**) simultaneously recorded at a large Suzuki precipitate (Kelvin contrast of the precipitate and NaCl steps: $U_{Suzuki-NaCl_{terrace}} = +1.3$ V and $U_{NaCl_{terrace}-NaCl_{step}} \sim +0.3$ V, respectively). The $a_{Suzuki}/2 \approx 5.6$ Å high steps inside the Suzuki precipitates were created by the cleavage crack, which cut ⟨110⟩ screw dislocations at the Suzuki-NaCl. **c** Another Suzuki precipitate found on the same crystal surface. Steps with a height of only $1/4a_{Suzuki} \approx 2.8$ Å can be seen, exhibiting both, NaCl and Suzuki-terminated streaks (From [126])

result of the cleavage crack, which cuts ⟨110⟩ screw dislocations at the Suzuki-NaCl interface, which leads to ⟨100⟩ slip steps in adjacent NaCl regions. Because the unit cell of the Suzuki phase is not exactly twice that of the NaCl unit cell ($a_{NaCl} = 5.64$ Å and $a_{Suzuki}/2 = 5.624$ Å [82]), the dislocations are a result of the small misfit and release the related strain at the interface [94]. The ⟨110⟩ screw dislocations lie in the {110} planes, which intersect the (001) surface and which are the slip or gliding planes in pure NaCl [127–129]. In other Suzuki regions (Fig. 15.3c) steps with a height of only 2.8 Å $\approx 1/2a_{NaCl} \approx 1/4a_{Suzuki}$ could be found exhibiting both, NaCl and Suzuki-terminated surfaces. Such steps are probably a result of the alternating expansions and contradictions of the Cl^- ions, which appear around the Cd^{2+} ions along ⟨110⟩ directions. These alternating strains are then relieved by partial ⟨110⟩ screw dislocations, which have a magnitude of the burgers vector of $\sqrt{2}\cdot\delta\cdot a_{Suzuki}$ [86].

When KPFM is done on a Suzuki surface a strong contrast in the Suzuki regions is regularly observed, corresponding to voltage differences of one volt and more with respect to the neutral NaCl regions [22, 126] (Fig. 15.3b). The Kelvin contrast is homogeneous inside the Suzuki precipitates and no further details can be obtained even by choosing smaller scanning frames. The bright contrast is due to the high density of negative surface sites in the Suzuki regions: for instance, on the Suzuki-terminated surface a vacancy is surrounded by four Cl^- ions in the first layer and one underneath the vacancy in the second layer, which all form a negative surface site [22]. With respect to the NaCl-terminated Suzuki surface, the Cl^- ions located above the Na^+ vacancies relax by 40 pm from the surface (see Sect. 15.3.1). Such Cl^- ions can be considered as low-coordinated ions with respect to Cl^- ions above the impurities. Comparable to the negative vacancies at kinks of steps (see Sect. 15.2), both sites (vacancies and Cl^- ions above vacancies) create a more negative surface potential [26].

With respect to the uniform Kelvin contrast inside the Suzuki regions, the tip collects the electrostatic tip-surface interaction over a surface region which is comparable to the nanometer size of the tip apex, covering many negative surface sites. This explains not only the homogeneous contrast but also the high voltage difference in the volt range. On the contrary, single Na^+ vacancies at steps in pure NaCl(001) regions, which are well separated from each other, produce a considerably lower bright contrast of ∼300 mV, which is in agreement to earlier findings on pure alkali halide surfaces [26, 27] (see Sect. 15.2).

Interestingly, all Suzuki regions exhibit the same net negative surface charge in Kelvin images as the negative vacancies at the steps inside the NaCl regions. This does not change when the surface is reconstructed by annealing (see next Section). It therefore seems that the Suzuki surface also has a Debye-Frenkel layer (see Sect. 15.2), which formation, structure and function remains unknown so far.

15.3.2.2 Surfaces Modified by Diffusion and Evaporation

If *pure alkali halides* like NaCl are annealed in vacuum at temperatures between 200 and 260 °C the mobility of surface ions is already large enough to significantly change the surface morphology (surface diffusion) [9]. At temperatures higher than ∼260 °C the surface starts to evaporate [8, 130] (surface evaporation) creating well-documented surface evaporation patterns [8, 131].

Quite similar diffusion and evaporation phenomena appear also on the surfaces of *doped alkali halides*. With respect to divalent metal impurity cations, the impurities even decrease the evaporation rate and increase the activation energy of evaporation [132]. Furthermore, a segregation of impurities from the bulk to the surface can have a significant impact onto the surface morphology [133]. For instance, if a NaCl crystal with a relatively large amount of Cd^{2+} (e.g., 4 Mol % $CdCl_2$) is annealed at temperatures around 250 °C the surface diffusion dramatically changes the almost quadratic shape found on as-cleaved surfaces to a more round one [126] (Fig. 15.4a, b). For relatively low impurity concentrations the shape of the Suzuki regions is again almost square-like after annealing (see below), however, the size of the regions is much smaller in comparison to the one of the large, square shaped regions on as-cleaved surfaces (Fig. 15.4c, d)—a signature for a strong diffusion that takes place also on those surfaces.

The size and number of Suzuki precipitates depend on the annealing time [10], the speed of the cooling [11] and the nominal impurity content inside the crystal [12], whereas the location of the regions depends on the step density [22, 126]: Suzuki regions can always be found on the top side of steps where they form a fringe and follow a characteristic zig-zag shape of the steps (Fig. 15.4c, d). The lower terrace is mostly a pure NaCl one (for low impurity concentrations). Interestingly, the steps do not have anymore the preferred ⟨001⟩ surface direction of non-polar steps, which can be observed on pure NaCl(001) surfaces. They run along equivalent ⟨011⟩ directions implying that they are possibly polar steps (Fig. 15.5a). If the step density is relatively low and the terrace width wider than 150–200 nm rectangular Suzuki regions can

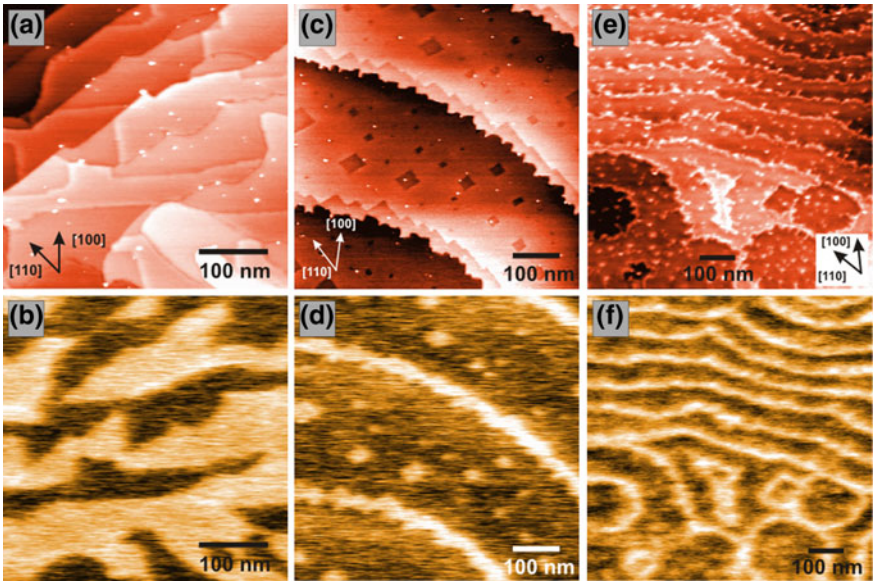

Fig. 15.4 NaCl:Cd^{2+}(001) Suzuki surfaces prepared by UHV cleavage and additional annealing. Shown are surfaces, which were influenced by surface diffusion (**a**) to (**d**) and surface evaporation (**e**) and (**f**). Crystals with a high concentration of impurities exhibit large Suzuki regions **a** and **b** whereas low impurity concentrations lead to smaller regions **c** and **d**. On evaporated surfaces, Suzuki regions can only be found at steps **e** and **f**. Shown are topography images **a**, **c**, **e** and simultaneously recorded Kelvin images **b**, **d** and **f**. Sample preparations: 4 Mol % $CdCl_2$, annealing: T = 230 °C for 5 h **a** and **b**, 1 Mol % $CdCl_2$, annealing: T = 205 °C for 5 h **c** and **d** and 2 Mol % $CdCl_2$, annealing: 340 °C for 35 min (**e**, **f**) (From [126])

also be found on the flat terraces (Fig. 15.4c, d). Obviously, the formation of Suzuki regions at steps is energetically more favorable in comparison to Suzuki regions on the flat terraces.

Very important characteristics of annealed Suzuki surfaces in general are the flatness of the Suzuki regions, the relative height between Suzuki and pure NaCl regions and the interface Suzuki-NaCl [22, 126]: all Suzuki regions are free of steps, which is a signature that, in equilibrium, a Suzuki region prefers an atomically flat surface (see all topography images in Fig. 15.4). Furthermore, both regions are almost on the same height, as it can be observed by atomic resolution imaging at the interface Suzuki-NaCl on the terraces (Fig. 15.5b). In other words, the Suzuki regions are perfectly embedded into the NaCl regions. Last, the interface between the two regions, which always runs along equivalent ⟨001⟩ surface directions, is well-defined at the atomic scale and only measures a few Ångströms (Fig. 15.5b).

When doped crystals are annealed at much higher temperatures (>300 °C), the surface starts to evaporate (surface evaporation) as on the surfaces of pure NaCl [8], in particular at steps and dislocations (Fig. 15.4e, f). In the case of NaCl:Cd^{2+}, the surface is basically comparable to an evaporated surface of pure NaCl, despite a mod-

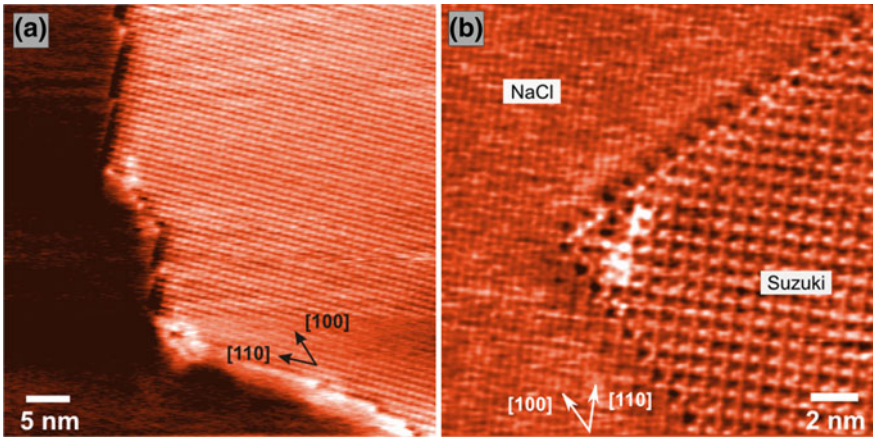

Fig. 15.5 Steps on the Suzuki surface and the interface NaCl-Suzuki on the flat terraces. **a** Constant height image representing a mono-atomic high step ($h = a_{\mathrm{NaCl}}/2$) in atomic resolution. The upper terrace is a Suzuki region, on which the lattice of either the vacancies or the Cd^{2+} ions is visible. Such steps always have a $\langle 011 \rangle$ orientation. **b** Constant height image which shows that the interface formed by the two regions, pure NaCl and Suzuki, is well-defined at the atomic scale. Either the sub-lattice of the vacancies or the Cd^{2+} ions were imaged in Suzuki regions whereas in regions of NaCl either the sub-lattice of the Na^{+}or Cl^{-} ions can be seen **b**. Both images: a dark contrast belongs to more positive detuning values and vice-versa (From [126] **a** and [40] **b**)

ification of the steps by Suzuki regions [126]: for instance, the topography image in Fig. 15.4 e shows curved (top) and circular (bottom) mono-atomic high steps ($h = a_{\mathrm{NaCl}}/2$) forming disc-shaped terraces (bottom). Such evaporation features are comparable to those ones observed on the surfaces of pure NaCl at similar temperatures [8]. However, the steps are not as smooth as on the latter surfaces [8, 131], the steps exhibit rather a zig-zag shape, which is curved on a larger scale forming the disc-shaped holes. Also here, the steps are oriented along equivalent $\langle 110 \rangle$ surface directions whereas the borders of embedded Suzuki regions point along equivalent $\langle 100 \rangle$ surface directions. A striking observation is that on wide terraces no Suzuki regions can be found despite some small pits. The pits are probably a signature that Suzuki regions on terraces are additional surface sites from where evaporation takes place. If so, such regions on the terraces disappear during the evaporation process.

15.3.3 Atomic Resolution and Identification

Atomic resolution imaging on alkali halide surfaces has become nowadays a standard, and all mechanisms of the atomic contrast formation are almost fully understood [134]. Although all atoms in the tip and surface but also tip- and surface-atom relaxations have to be taken into account, one can roughly simplify the contrast formation by considering a single atom at the apex interacting with a single atom in the surface.

For ionic surfaces like NaCl(001) and for ionic tips, the electrostatic potential of the tips' last atom determines the atomic contrast: a cation at the tip apex (e.g., Na^+ ion at the tip) images the Cl^- ions as bright ions due to an attractive force between both, and the Na^+ ions as dark ions (repulsive interaction). Vice-versa, an anion at the tip (e.g., Cl^- ion) images the Na^+ and Cl^- ions as bright and dark ions, respectively—the contrast gets basically reversed when the cation at the tip is replaced with an anion. This contrast formation has been further benchmarked on the Suzuki surface because of its interesting properties (see Sect. 15.3.1): the atomic structure is composed by three different types of ions and additional cation vacancies. Furthermore, it has four sub-lattices, which differ in their dimension and orientation, and last but not least relaxations of some ions of the surface upon tip approach may sensitively influence the contrast formation.

In the following, we qualitatively describe the contrast formation inside the Suzuki regions: when imaging with atomic resolution a regular structure composed of different bright and dark ions is regularly observed (Fig. 15.6), which can vary from surface to surface but also from tip to tip. Figure 15.6a shows an image, which was obtained on a Suzuki terminated NaCl:Mg^{2+}(001) surface (dark contrast: stronger interaction and vice-versa): dark spots (e.g., at position 1) can be seen but also additional bright spots (e.g., at position 2) forming a sub-lattice, which is parallel to the

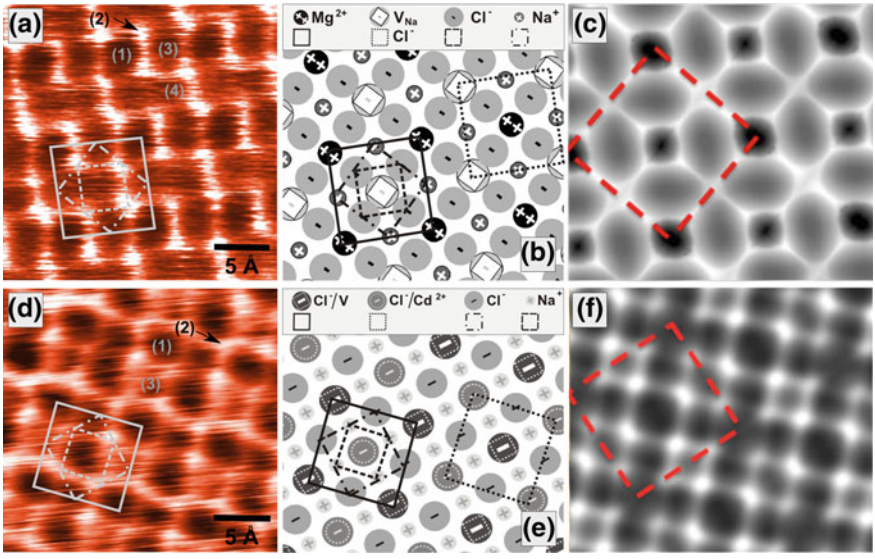

Fig. 15.6 Atomic resolution imaging on the Suzuki surface and identification of ions. Images **a** and **d** are experimental detuning images obtained in the constant height mode on a Suzuki terminated NaCl:Mg^{2+}(001) and NaCl terminated NaCl:Cd^{2+}(001) surface, respectively. Both images represent the ions and vacancies drawn in panel (**b**) and (**d**). Images **c** and **f** are simulated images, which best represent the contrast in image **a** and **c**, respectively. They were calculated with an anion (**c**) and cation terminated tip (**f**). The *red squares* mark the projected unit cell of the Suzuki structure on the (001) surface (**c**) and (**f**) (From [22] (**a**), (**b**) and [25] (**c**) to (**f**))

one of the dark spots but half as large. The dimension of the latter lattice coincides with the smallest possible sub-lattice of the Suzuki phase formed by the Cl^- ions so that the bright ions (2) can be assigned to the Cl^- ions (compare with drawing in Fig. 15.6b). This has the important consequence, that the tip's last atom obviously had a negative potential producing a repulsive interaction with the Cl^- ions. With this the divalent positive Mg^{2+} and Na^+ ions should be imaged in a darker contrast. And indeed, the darkest spots (1) belong to the Mg^{2+} ions because they exhibit a stronger interaction with the tip than the Na^+ ions. The latter Na^+ ions are always in between two dark Mg^{2+} ions (3) with a less darker contrast but also less brighter contrast than the Cl^- ions. As expected, the quadratic sub-lattice of the Na^+ ions is smaller than the Mg^{2+} lattice but larger than the Cl^- one and rotated by 45° with respect to the Cl^- and Mg^{2+} lattices. Last, the vacancies are located in the middle of a Mg^{2+} square, where also a gray contrast can be found (4) in the experimental image.

The latter qualitative description of the contrast formation has been fully supported by a comparison between experiment and Density Functional Theory (DFT) calculations [25] (Fig. 15.6c). Same calculations also simulated the atomic contrast for a cation terminated tip, which is clearly different in comparison to the contrast explained above. A very important result from theory is, that relaxations of surface ions upon an approach of the tip play a fundamental role (Fig. 15.7): when the tip is relatively far away (Fig. 15.7a), the Na^+ ions displace towards the tip's last atom, which has a negative potential as described above. This increases the contrast at the Na^+ being almost comparable to the one of the Mg^{2+} ions despite having only half the charge of the Mg^{2+} ions. The result is that the Na^+ ions produce a similar contrast as the Mg^{2+} ions. However, when the tip comes relatively close to the surface (Fig. 15.7b, c) the interaction with the Mg^{2+} ions becomes dominant so that the Mg^{2+} ions create the strongest contrast in the images.

So far, we have considered the Suzuki termination only. With respect to the NaCl termination similar mechanisms could be observed [25]: Fig. 15.6d shows the contrast of an experimental image of a NaCl:Cd^{2+}(001) Suzuki surface: the contrast is formed by large dark spots (1), which form a sub-lattice equal to the one formed by either the Cd^{2+} ions or the Na^+ vacancies (compare with drawing in Fig. 15.6e). Four bright spots can be found (2) around each dark spot forming a sub-lattice of either Cl^- or Na^+ ions, and some additional less dark spots are in between the large dark spots. Calculations on the *Suzuki terminated* surface were unable to reproduce the observed contrast with any type of tip (anion or cation terminated tip, Fig. 15.7d). Only the *NaCl terminated surface* was able to best reproduce the experimental image with a cation terminated tip (Fig. 15.6f), demonstrating that, in this case, the NaCl:Cd^{2+} Suzuki region most likely had an NaCl termination.

With respect to the development of contrast upon tip approach, atomic displacements play again a fundamental role (Fig. 15.7e, f): in the absence of the tip, the Cl^- ions over vacancies displace strongly outwards from the surface (0.04 nm, Fig. 15.7e), while those over Cd^{2+} remain close to the ideal surface plane. This results in a strong contrast of the Cl^- ions above the second-layer vacancies at long tip-surface distances, strongly enhanced due to large tip-induced displacements of such Cl^- ions.

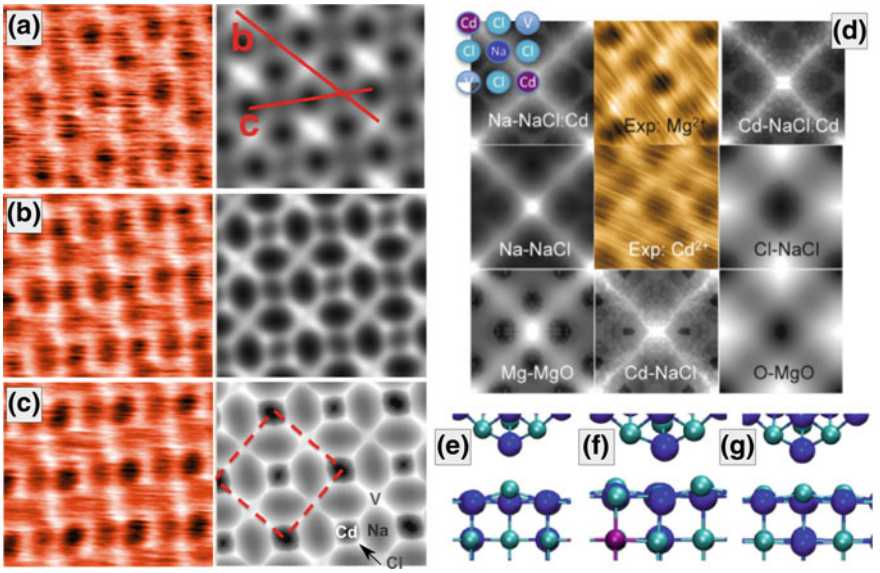

Fig. 15.7 The contrast formation in atomic resolution imaging. **a–c** Comparison of experimental (*left*) and simulated data (*right*) for NaCl:Mg^{2+}. The simulations used a Cl-terminated NaCl tip. The experimental images corresponds to average detuning values of −16, −22 and −24 Hz (*top-bottom*, with a more negative detuning corresponding to imaging closer to the surface). The simulated data corresponds to tip-surface *heights* of 0.45, 0.325 and 0.275 nm, resulting in average detunings of −16.4, −21.8 and −23.0 Hz, respectively. **d** Comparison of experimental images of NaCl:Mg^{2+} and NaCl:Cd^{2+} with simulated images of NaCl:Cd^{2+} (Suzuki termination) using seven different tips X:Y (*gray scale*), where Y is the tip material and X is the terminating atom. None of the 7 images reproduces the contrast of the experimental image in the middle (NaCl:Cd^{2+}). **e–g** Simulation snapshots showing key atomic displacements for a Na-terminated NaCl tip imaging NaCl:Cd^{2+} (NaCl termination) at a tip height of **e** 0.46 nm over a Cl^- site above a vacancy, **f** 0.31 nm over an Na^+ site, and **g** 0.4 nm over a Cl^- site above a Na^+ (From [25])

At close distance, a reduction in repulsion over Na^+ ions due to displacements of neighboring Cl^- ions towards the tip can be observed. Furthermore, the attractive interaction to the rigidly held Cl^- ions above the second-layer Cd^{2+} ions and of the Cl^- ions above the second-layer Na^+ ions increases, also partially due to displacements of the Cl^- ions towards the tip. All this results into an image as shown in Fig. 15.6d where the Cl^- ions above the vacancies still exhibit the strongest contrast, which is, however, comparable to the contrast of Cl^- ions above the Cd^{2+} and Na^+ ions.

The extensive comparison between experiment and theory in [25] shows that the identification of all ions and the vacancies can be done independently of the tip-surface distance, of the chemical nature of the divalent impurity ions inside the Suzuki structure, and despite differences in surface termination. Therefore, with an image library at hand (see Supporting Information of [25]), which shows the atomic contrast for both surface terminations and both types of tips (anion and cation terminated),

all ions in the Suzuki structure can be identified by just atomic resolution imaging, thereby providing characterization of the tip's potential. This identification is possible due to the doping of NaCl with divalent impurity ions and thanks to the geometry of the atomic Suzuki structure, which contrasts the situation on the pure NaCl(001) surface where such chemical identification is not possible. Important to note is that the development of contrast patterns as a function of tip-surface separation is strongly linked to tip-induced atomic displacements, which is significantly different to the contrast formation on the surfaces of pure alkali halides.

Several other Suzuki systems in NaCl exist, including the magnetic impurities Mn^{2+} and Fe^{2+} [10], which probably form an antiferromagnetic ordering [25]. This might be particularly interesting for exchange force microscopy, which could resolve different spin orientations [135]. Other types of host system for the Suzuki phases are oxides like MgO:Mn^{4+} [117] and NiO:Mn^{4+} [120], which could be used as substrates in heterogeneous model catalysis. In general, doping of insulators, in combination with high resolution nc-AFM, provides a general tool for characterizing surfaces at the atomic scale. For instance, the wide use of doping with impurities of different valences in many insulators such as ZrO_2 and CeO_2 [136, 137] suggests that the method could also be used in high resolution studies of their surfaces.

15.4 Supported Nano-objects on the Suzuki Surface

The rediscovery of the nanostructured Suzuki surface by nc-AFM and KPFM is quite promising for applications in nanosciences because of the specific Suzuki structure but also because of the two distinct surface regions that co-exist at the same time. In particular for investigations of deposited molecules and metal NPs the Suzuki surface is an attractive choice. And indeed, as summarized and discussed in the following two sections recent work has shown that metal nanoparticles or molecules exhibit interesting growth modes, which are different in both surface regions and which can only appear on the Suzuki surface at the same time [40, 41].

15.4.1 Metal Nanoparticles

The growth and characterization of metal nanoparticles (NPs) on oxide and similar surfaces is of large interest in heterogeneous model catalysis because the morphology (size and shape), distribution and electronic properties of NPs determine if the rate of a catalytic reaction is increased by the catalysts or not [138, 139]. A very important objective for reactivity measurements, which measure over large surface areas (like molecular beam or temperature programmed desorption experiments), is that the NPs have all the same size and shape: this allows assigning specific properties of a reaction to one type of NP, and by varying the size, shape and composition of the NPs the reaction can be characterized [140]. A narrow size distribution of equally shaped NPs

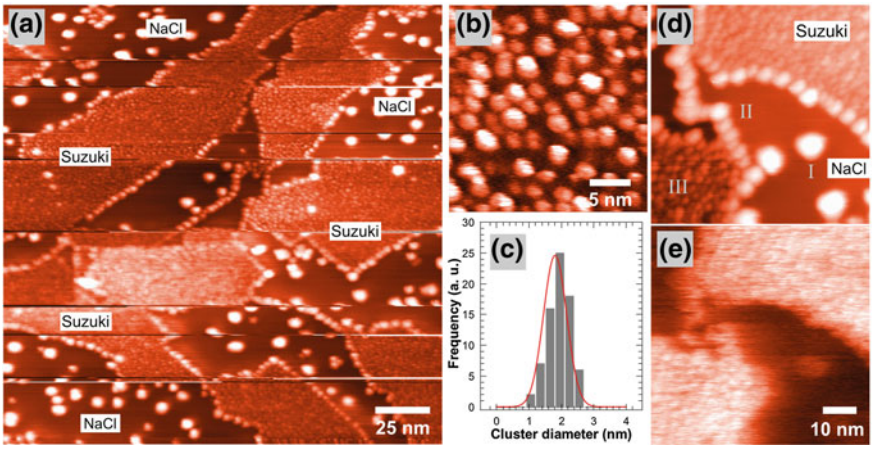

Fig. 15.8 The confined growth of PdNPs in Suzuki regions (quantity: 0.35 mono-layers of Pd, growth at room temperature). **a** Large-scale topography image after the deposition (each *bright dot* is a single NP). Palladium forms NPs preferentially in the Suzuki regions. **b** Constant height image obtained inside a Suzuki region and histogram (**c**) of the NP sizes found from image (**b**). Topography (**d**) and Kelvin image (**e**) obtained in one KPFM measurement. The Kelvin image exhibits large voltage differences between the stoichiometric NaCl terraces and the NPs inside the Suzuki regions (Kelvin contrast: $U_{PdNPs-Suzuki} = +3$ to $+4$ V) (From [40])

can be obtained on nanostructured surfaces, which exhibit an ordered arrangement of defects like on the nanostructured alumina film on $Ni_3Al(111)$ [141]. Therefore, after the rediscovery of the nanostructured Suzuki surface it was promising to test if also on this surface metal NPs can be grown into an ordered NP assembly, with a small NP size distribution inside the Suzuki regions. A recent work considered palladium nanoparticles on the NaCl:Cd^{2+} Suzuki surface, on which we will focus in the following [40].

If Pd atoms are deposited on the (001) surfaces of *pure NaCl* (sample at room temperature) they diffuse on the terraces. Because of the specific kinetics at room temperature the nucleation at steps is faster than on terraces [138] so that Pd preferentially forms nanometer sized NPs decorating the steps [142, 143]. Almost no stable NPs can be found on the terraces. On the contrary, depositing Pd on a *Suzuki surface* results into a completely different surface, which is characterized by three different types of NPs (Fig. 15.8a, d). The first type of NP (I) can be found occasionally on the flat terraces of pure NaCl. Due to the low defect density in these regions, the NPs, once formed, collect a large part of Pd atoms diffusing on the pure NaCl terraces, so that the NPs become quite large (height $h_I = 2.4$ nm, diameter $D_I = 3$–4 nm) [138]. The second type of NP (II) is located at the NaCl-Suzuki boundary where the NP collects obviously less Pd—this can be seen by the smaller size of the nanoparticles ($h_{II} = 1.5$ nm, $D_{II} = 2.5$ nm).

A different situation can be found inside the Suzuki regions, where the PdNPs (III) are much smaller and the NP density much higher (Fig. 15.8b). The density

($\rho_{\text{Suzuki}} \approx 1.3 \times 10^{13}$ NPs/cm^2) is more than forty times higher with respect to the density in the pure NaCl regions ($\rho_{\text{NaCl}} \approx 3 \times 10^{11}$ NPs/cm^2). Each NP divides the surface on a circular surface area with a radius of 1.6 nm and has therefore a mean distance of about 3 nm to their neighboring NPs, which is four times larger than the size of the largest sub-lattice formed by either the Cd^{2+} impurity ions or the vacancies ($a_{V,Cd^{2+}} \approx 0.8$ nm, see Fig. 15.2). Due to the high density of nucleation sites, each NP collects much less Pd during the metal deposition than the NPs in the pure NaCl regions, which explains the quite small size of the NPs: the almost round NPs have a very small diameter, but also a very small height that corresponds to only a few atomic layers ($h_{\text{III}} = 0.6 \pm 0.2$ nm, $D_{\text{III}} = 1.8 \pm 0.4$ nm). Due to the different sizes of the three type of NPs, a NP in the Suzuki region has roughly ~50 atoms, whereas a much larger number of atoms can be found in a NP at the NaCl-Suzuki interface (~400 atoms) and especially in a NP that is located somewhere on the flat NaCl terrace (~1500 atoms).

It is obvious that the specific ionic structure of the Suzuki phase plays a key role in the nucleation of the NPs. An interesting conclusion can be drawn when considering the ratio height-to-diameter: The value is almost the same for the NPs in the NaCl regions and at the interface Suzuki-NaCl ($h_{\text{I}}/D_{\text{I}} = 0.68 \approx h_{\text{II}}/D_{\text{II}} = 0.6$), but two times larger than the value of the NPs inside the Suzuki regions ($h_{\text{III}}/D_{\text{III}} = 0.33$). This is directly related to the adhesion energy E_a: the flatter a NP is, the larger is the substrate-NP interaction [138]. Therefore, the nanoparticle-surface interaction must be stronger inside the Suzuki regions than in the NaCl regions. Since metal especially likes electronegative surface sites [43, 144], potential candidates that can exhibit a strong interaction with the NPs are the negative vacancies on Suzuki terminated surfaces or, on NaCl terminated surfaces, the chlorine ions above the vacancies (Cl_V^-). First principles calculations predict indeed that atomic Pd prefers to adsorb in Suzuki regions by up to 0.4 eV over the ideal NaCl surface with the favored sites of Cl_V^- for the NaCl termination and the vacancies and Cl^- ions for Suzuki termination.

Surprisingly, from the experiments it can be found that not all of these sites are occupied by NPs. Only every ~12th surface site is occupied, which again could be due to kinetics [138], but also due to repulsive forces amongst NPs. It has been shown that NPs may repel each other if elastic forces caused by strain fields in the NP-substrate interface [145] or repulsive electrostatic forces amongst charged NPs occur [146]. The latter repulsive electrostatic interaction amongst NPs seems to be reasonable: because a NP can cover several of equivalent surface sites like vacancies on the Suzuki terminated surface, large polarization or charge effects can be expected. Indeed, Kelvin images show a very bright contrast at the NPs inside the Suzuki regions with respect to the neutral and stoichiometric NaCl regions, which appear dark in the Kelvin images (Fig. 15.8e). The change of contrast from bright to dark corresponds to voltage differences of several volts, which can be sometimes as large as 4 V. These values are much larger than the voltage difference between clean Suzuki and NaCl regions that have been ever measured [126] (see Sect. 15.3.2.1 and 15.3.2.2). In comparison to the small NPs in the Suzuki regions, the large NPs in the pure NaCl regions exhibit a less bright contrast (Kelvin contrast: ~1.5 V), which is because such NPs probably cover only a single vacancy. The Kelvin images therefore

confirm a charging/polarization of NPs inside the Suzuki regions, which explains in turn possible repulsive electrostatic forces amongst the NPs as discussed above.

In conclusion, a narrow size distribution of very small, nanometer sized PdNPs can be obtained on the Suzuki surface unlike on the surfaces of pure alkali halides. This is thanks to the selective growth of palladium inside the Suzuki regions and the specific structure of the Suzuki phase. The work motivates studying the detailed growth of any kind of NP as a function of NP material (one and two componant NPs like bi-metallic NPs), NP quantity and growth temperature. The small nanometer size and narrow size distribution is ideal for reactivity measurements, which measure over large surface areas, but also for nc-AFM and KPFM that can contribute to reactivity studies as exemplified by a recent KPFM work on PdNPs on graphite [147]. Although the Suzuki surface is not relevant in heterogeneous catalysis adsorption, desorption and reactivity related phenomena at NPs could yield suitable information at, at least, low temperatures ($<100\,^{\circ}\mathrm{C}$).

15.4.2 Functionalized Molecules

In recent years, it has been discussed how small molecules adsorb on ionic insulating surfaces [31, 37, 40, 148, 149] and which impact the adsorption has on the self-assembly of molecules [150]. A common finding is that the adsorption of, e.g., non-polar molecules is relatively weak due to van der Waals forces, which are not strongly site specific—the molecules can occupy almost any position on the surface [30]. However, as soon as a molecule includes atoms carrying a partial charge or polar groups, the polar groups of the molecule can directly bind to the ionic surface lattice via an electrostatic interaction (*charge matching*) [31, 37, 40, 148, 149].

Because the Suzuki surface exhibits two distinct surface regions (pure NaCl and Suzuki regions) which differ in their atomic structure (e.g., see Sect. 15.3.2 and 15.3.3), it is quite appealing to study phenomena of adsorption and self-assembly as a function of surface site to shed more light onto the detailed mechanisms involved. Recently, the adsorption and self-assembly of four functionalized pentahelicene molecules ([5]helicene, neutral molecule: $C_{22}H_{14}$) (Fig. 15.9a) have been studied as a function of adsorption geometry and dipole strength on the Suzuki surface [40, 41]. The molecules were functionalized either with one or two bromine substituents or cyano substituents (MonoBromo, DiBromo, MonoCyano and DiCyano) substituting regular hydrogens at positions 6 and 7 of the molecules (racemic samples). The molecules differ in their dipole strength (from MonoBromo to DiCyano: -1.92, -2.88, -5.76 and -9.27 Debye) but also in the geometry if two substituents are attached to the molecule (distance d of substituents: 0.34 nm (DiBromo) and 0.41 nm (DiCyano, N–N)).

Experiments with MonoBromo have shown that it only adsorbs at defects of the NaCl surface, which can be best observed on the surfaces of *pure NaCl crystals* [40]: the molecules stick exclusively at the steps and form molecular wires. The whole adsorption changes, if MonoBromo is deposited onto the *Suzuki surface* (Fig. 15.9b): the molecules cover all Suzuki regions by forming flat homogeneous islands, and

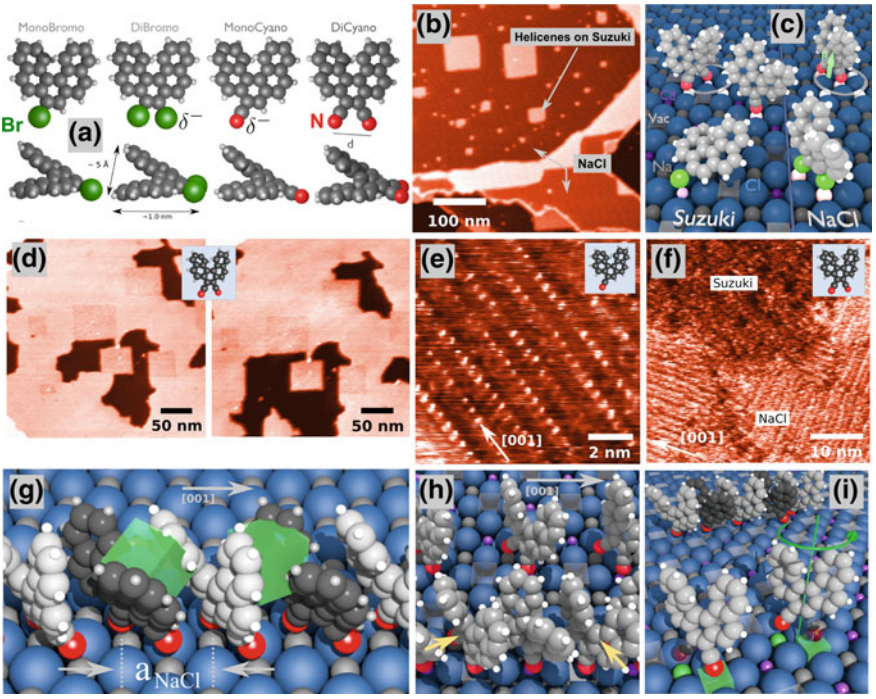

Fig. 15.9 Functionalized [5]helicene molecules on the NaCl:Cd^{2+}(001) surface **a** MonoBromo, DiBromo, MonoCyano and DiCyano. **b** A single molecular layer of MonoBromo perfectly decorates all Suzuki regions. **c** Model of adsorption based on the charge-matching principle. **d** The desorption of DiCyano from regions of pure NaCl (3.4 h distance between images). **e** Self-assembly in one molecular layer of MonoCyano inside a Suzuki region. Each *bright spot* is a single molecule. **f** DiCyano inside a Suzuki (amorphous) and NaCl region (self-assembled). **g** Result from theory showing the π-π stacking of DiCyano along ⟨001⟩ surface directions. Both enantiomers are alternately placed along the row. The *green box* has a dimension of 3.5 Å symbolizing the typical π-π bonding distance. **h** Half of the DiCyano molecules are placed above the negative vacancies of the Suzuki surface (*bottom row*, *yellow arrows*), they need to be removed (*top row*). **i** By turning MonoCyano around its long axis (*bottom*) the single cyano group can always be positioned above a cation such that self-assembly becomes possible in the Suzuki regions as exemplified by the *top row* of molecules (From [40] (**b**) and [41] (**a**, **c**) to (**i**))

no molecule is located in the NaCl regions. Due to the two-dimensional shape of the Suzuki regions and the well-defined NaCl-Suzuki interface the monolayer high islands have exactly the same shape and size as the Suzuki regions. A comparison between experiment and theory has shown that the molecules are lying flat on the surface such that the bromine atom with its partial negative charge is charge-matched at a cation (bottom left molecule in Fig. 15.9c). Two-thirds of the adsorption energy ($\overline{E}_{ad} \approx 0.87$ eV [1]) stems from a van der Waals contribution between the surface and

[1]The adsorption energy $\overline{E}_{ad}$ is an average value of the two adsorption energies obtained on the Suzuki and NaCl terminated surface.

the closest benzene rings, and one third is due to an electrostatic interaction between the bromine atom and the cation, which pins MonoBromo on the surface.

In contrast to MonoBromo, which remains on the surface for all time after its deposition, all other three [5]helicene molecules desorb within hours days and weeks from the surface as a function of their dipole strength (see desorption of DiCyano in (Fig. 15.9d). Furthermore, they are all standing perpendicular on the surface, in contrast to MonoBromo. An analysis of all the experimental data and assisting theory developed a conclusive model of adsorption (Fig. 15.9c): MonoBromo adsorbs in a flat configuration (see above) whereas DiBromo stands perpendicular on the surface (bottom right molecule in (Fig. 15.9c). However, DiBromo desorbs within hours due to its very small dipole and the resulting small coupling to the cations, the mismatch between the two bromines and the surface cations and the missing van der Waals interaction ($\overline{E}_{\mathrm{ad}} \approx 0.23$ eV). Both cyanated molecules are also in a perpendicular position (top molecules in (Fig. 15.9c), with their negative cyano substituents charge-matched at the cations. Due to their strong dipole, the adsorption energy is considerably larger in comparison to the one of DiBromo but smaller than the one of the flat lying MonoBromo (MonoCyano: $\overline{E}_{\mathrm{ad}} \approx 0.50$ eV, DiCyano: $\overline{E}_{\mathrm{ad}} \approx 0.74$ eV). In particular the two cyano groups of DiCyano perfectly match with two cations (distance $d_{\mathrm{Na–Na}} = d_{\mathrm{Na–Cd}} = 0.40$ nm) resulting into a strong interaction. All this explains why both cyanated molecules remain for a relatively long time of ∼2 weeks on the surface.

Both cyanated [5]helicene molecules form self-assembled molecular rows along the $\langle 001 \rangle_{\mathrm{NaCl}}$ surface direction (Fig. 15.9e, f). A major observation is that MonoCyano self-assembles in the Suzuki regions and probably also in the NaCl regions, which could not be verified due to the weak adsorption of the molecules—the molecules desorbed from the surface under the influence of the AFM tip. In contrast, DiCyano only self-assembles in the NaCl regions of the Suzuki surface but not inside the Suzuki regions, in which only an amorphous structure of DiCyano could be observed. Thanks to the combination of experiment and theory it could be shown that the molecules have a distance of the NaCl unit cell (0.564 nm) along the $\langle 001 \rangle_{\mathrm{NaCl}}$ direction, which permits a π-π stacking of adjacent benzenoid rings of the helicene molecules, with a typical bonding distance in the order of ∼3.5 Å (Fig. 15.9g). The stacking of molecules increases the total energy of the system by 0.2 eV/molecule, which is also one of the reason why the molecules are in a perpendicular position on the surface. With respect to DiCyano, a molecular row placed inside the Suzuki regions positions the substituents of half of the molecules above the negative vacancies of the Suzuki surface (bottom row in Fig. 15.9h). In this case, the adsorption is very small ($\triangle E_{\mathrm{ad}} = 0.18$ eV) so that half of the molecules need to be removed destroying the self-assembly (top row in Fig. 15.9h), which explains the amorphous structure observed in experiments. In contrast, MonoCyano can self-assemble in the Suzuki regions (top row in Fig. 15.9i) since the single substituent can always be positioned above a cation by a rotation of the molecule along its long axis, which stands perpendicular on the surface (bottom in Fig. 15.9i).

In summary, the mechanisms of adsorption and self-assembly of functionalized helicene molecules can be studied in great detail on the Suzuki surface, which is

thanks to the two distinct surface regions and the specific atomic structure of the Suzuki surface. The rule of thumbs for the adsorption and self-assembly might help to predict the adsorption and self-assembly of other helicene molecules, e.g., helicene molecules functionalized with three substitutents. By meeting the charge matching criteria, such molecules probably bind more selectively in a flat and stable position such that flat molecular templates can be created, which is interesting for chiral recognition and templating applications. It is clear that in general, the Suzuki surface is attractive also for many other molecules, opening promising perspectives in the domain of self-assembled molecules on insulating surfaces.

Acknowledgments The author expresses his great appreciation to A. S. Foster, T. Hynninen, C. R. Henry, B. Hoff, and in particular to A. L. Shluger and S. Gauthier for stimulating discussions. The author acknowledges the European Science Foundation for financial support through the FANAS project NOMCIS and the French agency for Research (*Agence Nationale pour la Recherche*, ANR) for financial support through the programs CANA and MISS. Support by the European COST through action D41 is highly acknowledged.

References

1. W. Hayes, A.M. Stoneham (eds.), *Defects and Defect Processes in Nonmetallic Solids* (Wiley-Interscience, New York, 1985)
2. F. Seitz, Rev. Mod. Phys. **18**, 384 (1946)
3. F. Seitz, Rev. Mod. Phys. **26**, 7 (1954)
4. G. Binnig, C.F. Quate, Ch. Gerber, Phys. Rev. Lett. **56**, 930 (1986)
5. G.A. Bassett, Philos. Mag. **3**, 1042 (1958)
6. H. Bethge, J. Heydenreich (eds.), *Elektronenmikroskopie in der Festkörperphysik* (Springer, Berlin, 1982)
7. H. Bethge, Surf. Sci. **3**, 33 (1964)
8. H. Bethge, K.W. Keller, J. Cryst. Growth **23**, 105 (1974)
9. H. Höche, H. Bethge, J. Cryst. Growth **33**, 246 (1976)
10. G.A. Bassett, M.J. Yacamán, Thin Solid Films **31**, 375 (1976)
11. M.J. Yacamán, J.P. Hirth, Thin Solid Films **38**, 215 (1976)
12. G. Grange, Surf. Sci. **105**, 265 (1981)
13. T.R. Albrecht, P. Grütter, D. Horne, D. Rugar, J. Appl. Phys. **69**, 668 (1991)
14. S. Morita, R. Wiesendanger, E. Meyer (eds.), *Noncontact Atomic Force Microscopy* (Springer-Verlag, Berlin, 2002)
15. F.J. Giessibl, Rev. Mod. Phys. **75**, 949 (2003)
16. C. Barth, A.S. Foster, C.R. Henry, A.L. Shluger, Adv. Mater. **23**, 477 (2011)
17. M. Bammerlin, R. Lüthi, E. Meyer, A. Baratoff, J. Lü, M. Guggisberg, C. Loppacher, C. Gerber, H.-J. Güntherodt, Appl. Phys. A **66**, S293 (1998)
18. R. Bennewitz, S. Schär, E. Gnecco, O. Pfeiffer, M. Bammerlin, E. Meyer, Appl. Phys. A **78**, 837 (2004)
19. R. Hoffmann, L.N. Kantorovich, A. Baratoff, H.-J. Hug, H.-J. Güntherodt, Phys. Rev. Lett. **92**, 146103 (2004)
20. S.A. Burke, J.M. Mativetsky, R. Hoffmann, P. Grütter, Phys. Rev. Lett. **94**, 96102 (2005)
21. A. Schirmeisen, D. Weiner, H. Fuchs, Phys. Rev. Lett. **97**, 136101 (2006)
22. C. Barth, C.R. Henry, Phys. Rev. Lett. **100**, 096101 (2008)
23. K. Ruschmeier, A. Schirmeisen, R. Hoffmann, Phys. Rev. Lett. **101**, 1 (2008)

24. M.A. Cerda, J. Abad, A. Madgavkar, D. Martrou, S. Gauthier, Nanotechnology **19**, 045503 (2008)
25. A.S. Foster, C. Barth, C.R. Henry, Phys. Rev. Lett. **102**, 256103 (2009)
26. C. Barth, C.R. Henry, Phys. Rev. Lett. **98**, 136804 (2007)
27. P. Egberts, T. Filleter, R. Bennewitz, Nanotechnology **20**, 264005 (2009)
28. A. Hinaut, Dissertation, Université Toulouse III Paul Sabatier, 2012
29. T. Filleter, S. Maier, R. Bennewitz, Phys. Rev. B **73**, 1 (2006)
30. O.H. Pakarinen, J.M. Mativetsky, A. Gulans, M.J. Puska, A.S. Foster, P. Grütter, Phys. Rev. B **80**, 85401 (2009)
31. B. Such, T. Trevethan, T. Glatzel, S. Kawai, L. Zimmerli, E. Meyer, A.L. Shluger, C.H.M. Amijs, P. de Mendoza, A.M. Echavarren, ACS Nano **4**, 3429 (2010)
32. L. Nony, E. Gnecco, A. Baratoff, A. Alkauskas, R. Bennewitz, O. Pfeiffer, S. Maier, A. Wetzel, E. Meyer, Ch. Gerber, Nano Lett. **4**, 2185 (2004)
33. T. Kunstmann, A. Schlarb, M. Fendrich, T. Wagner, R. Möller, R. Hoffmann, Phys. Rev. B **71**, 121403 (2005)
34. T. Dienel, C. Loppacher, S.C.B. Mannsfeld, R. Forker, T. Fritz, Adv. Mater. **20**, 959 (2008)
35. S.A. Burke, W. Ji, J.M. Mativetsky, J.M. Topple, S. Fostner, H.-J. Gao, H. Guo, P. Grütter, Phys. Rev. Lett. **100**, 186104 (2008)
36. S.A. Burke, J.M. LeDue, J.M. Topple, Sh Fostner, P. Grütter, Adv. Mater. **21**, 2029 (2009)
37. A. Hinaut, A. Pujol, F. Chaumeton, D. Martrou, A. Gourdon, S. Gauthier, Beilstein J. Nanotechnol. **3**, 221 (2012)
38. L. Nony, F. Bocquet, F. Para, F. Chérioux, E. Duverger, F. Palmino, V. Luzet, C. Loppacher, Beilstein J. Nanotechnol. **3**, 285 (2012)
39. F. Bocquet, L. Nony, S.C.B. Mannsfeld, V. Oison, R. Pawlak, L. Porte, C. Loppacher, Phys. Rev. Lett. **108**, 206103 (2012)
40. C. Barth, M. Gingras, A.S. Foster, A. Gulans, G. Félix, T. Hynninen, R. Peresutti, C.R. Henry, Adv. Mater. **24**, 3228 (2012)
41. B. Hoff, M. Gingras, A.S. Foster, R. Peresutti, C.R. Henry, C. Barth, J. Phys. Chem. C **118**, 14569 (2014)
42. C. Barth, C.R. Henry, Nanotechnology **15**, 1264 (2004)
43. O.H. Pakarinen, C. Barth, A.S. Foster, C.R. Henry, Phys. Rev. B **73**, 235428 (2006)
44. C. Barth, C.R. Henry, Appl. Phys. Lett. **89**, 252119 (2006)
45. J.M. Mativetsky, S.A. Burke, S. Fostner, P. Grutter, Small **3**, 818 (2007)
46. J.M. Mativetsky, S. Fostner, S.A. Burke, P. Grutter, Phys. Rev. B **80**, 45430 (2009)
47. T. Glatzel, L. Zimmerli, S. Koch, S. Kawai, E. Meyer, Appl. Phys. Lett. **94**, 063303 (2009)
48. A. Tekiel, Y. Miyahara, J.M. Topple, P. Grütter, ACS Nano **7**, 4683 (2013)
49. L. Gross, F. Mohn, N. Moll, P. Liljeroth, G. Meyer, Science **325**, 1110 (2009)
50. L. Gross, F. Mohn, N. Moll, G. Meyer, R. Ebel, W.M. Abdel-Mageed, M. Jaspars, Nat. Chem. **2**, 821 (2010)
51. O. Guillermet, S. Gauthier, C. Joachim, P. de Mendoza, T. Lauterbach, A. Echavarren, Chem. Phys. Lett. **511**, 482 (2011)
52. L. Gross, F. Mohn, N. Moll, B. Schuler, A. Criado, E. Guitián, D. Peña, A. Gourdon, G. Meyer, Science **337**, 1326 (2012)
53. F. Mohn, B. Schuler, L. Gross, G. Meyer, Appl. Phys. Lett. **102**, 073109 (2013)
54. J. Zhang, P. Chen, B. Yuan, W. Ji, Z. Cheng, X. Qiu, Science **342**, 611 (2013)
55. C. Barth, C. Claeys, C.R. Henry, Rev. Sci. Instr. **76**, 083907 (2005)
56. C. Barth, C.R. Henry, Nanotechnology **17**, S155 (2006)
57. M. Pivetta, F. Patthey, M. Stengel, A. Baldereschi, W.D. Schneider, Phys. Rev. B **72**, 115404 (2005)
58. G. Cabailh, C.R. Henry, C. Barth, New J. Phys. **14**, 103037 (2012)
59. S. Fölsch, A. Riemann, J. Repp, G. Meyer, K.-H. Rieder, Phys. Rev. B **66**, 161409 (2002)
60. Ch. Bombis, F. Ample, J. Mielke, M. Mannsberger, C.J. Villagómez, Ch. Roth, C. Joachim, L. Grill, Phys. Rev. Lett. **104**, 185502 (2010)
61. O. Mahapatra, P.J. Kowalczyk, S.A. Brown, Surf. Sci. **620**, 45 (2014)

62. F. Golek, P. Mazur, Z. Ryszka, S. Zuber, Surf. Sci. **600**, 1689 (2006)
63. H.E. Carrillo, H.A. Carrillo, O.J. Rubio, Phys. Status Solidi **101**, 315 (1987)
64. C. Sommerhalter, T.W. Matthes, T. Glatzel, A. Jäger-Waldau, M.C. Lux-Steiner, Appl. Phys. Lett. **75**, 286 (1999)
65. T. Glatzel, S. Sadewasser, R. Shikler, Y. Rosenwaks, M.C. Lux-Steiner, Mater. Sci. Eng. B **102**, 138 (2003)
66. Y. Frenkel (ed.), *Kinetic Theory of Liquids* (The Clarendon Press, Berlin, 1946)
67. R.W. Whitworth, Adv. Phys. **24**, 203 (1975)
68. K.L. Kliewer, J.S. Koehler, Phys. Rev. **140**, A1226 (1965)
69. K.L. Kliewer, Phys. Rev. **140**, A1241 (1965)
70. K. Kliewer, J. Phys. Chem. Solids **27**, 705 (1966)
71. R.B. Poeppel, J.M. Blakely, Surf. Sci. **15**, 507 (1969)
72. M.F. Butman, A.A. Smirnov, L.S. Kudin, Z.A. Munir, Surf. Sci. **458**, 106 (2000)
73. R.C. Baetzold, Phys. Rev. B **52**, 11424 (1995)
74. J.M. Blakely, S. Danyluk, Surf. Sci. **40**, 37 (1973)
75. A.S. Foster, T. Trevethan, A.L. Shluger, Phys. Rev. B **80**, 115421 (2009)
76. H.H. Pieper, C. Barth, M. Reichling, Appl. Phys. Lett. **101**, 051601 (2012)
77. K.P. McKenna, A.L. Shluger, Nat. Mater. **7**, 859 (2008)
78. K. Suzuki, J. Phys. Soc. Jpn. **16**, 67 (1961)
79. K. Toman, Czech. J. Phys. **12**, 542 (1962)
80. D. Figueroa, E. Laredo, Solid State Commun. **11**, 1209 (1972)
81. W. Spengler, R. Kaiser, Phys. Status Solidi B **66**, 107 (1974)
82. C.J.J. Van Loon, D.J.W. Ijdo, Acta Crystallogr. B **31**, 770 (1975)
83. A. Sors, E. Lilley, Phys. Status Solidi A **32**, 533 (1975)
84. D. Figueroa, E. Laredo, M. Puma, Solid State Commun. **25**, 509 (1978)
85. N. Bonanos, E. Lilley, Mater. Res. Bull. **14**, 1609 (1979)
86. M.J. Yacamán, R.A. Gómez, J.P. Hirth, Philos. Mag. A **39**, 709 (1979)
87. N. Bonanos, E. Lilley, Solid State Ionics **1**, 223 (1980)
88. J.M. Calleja, A. Ruiz, F. Flores, V.R. Velasco, E. Lilley, J. Phys. Chem. Solids **41**, 1367 (1980)
89. A.L. Guerrero, E.P. Butler, P.L. Pratt, L.W. Hobbs, Philos. Mag. A **43**, 1359 (1981)
90. P. Aceituno, F. Cussó, A. de Andrés, F. Jaque, Solid State Commun. **49**, 209 (1984)
91. M. Chall, B. Winkler, P. Blaha, K. Schwarz, J. Phys. Chem. B **104**, 1191 (2000)
92. M. Chall, Ph.D. thesis, Kiel, Germany, 2000
93. D.L. Kirk, R.M. Innes, Thin Solid Films **28**, 243 (1975)
94. M. Yacaman, L.W. Hobbs, M.J. Goringe, Phys. Status Solidi A **39**, K85 (1977)
95. M.G. Moreno, J.C. Sal, J. Aramburu, F. Rodríguez, J.L. Tholence, F. Jaque, Phys. Rev. B **29**, 4192 (1984)
96. O.J. Rubio, F.A. Muñoz, M. Patrón, Solid State Commun. **55**, 109 (1985)
97. J.C. Gomez-Sal, M. Moreno, F. Rodríguez, A. Revex, J.L. Tholence, J. Phys. C Solid State Phys. **20**, L421 (1987)
98. J.C. Gómez Sal, F. Rodríguez, M. Moreno, J.L. Tholence, Phys. Rev. B **37**, 454 (1988)
99. F. Rodriguez, J.C. Gomez, Sal, M. Moreno, A. de Geyer, C. Janot. Phys. Rev. B **43**, 7519 (1991)
100. M.C. Marco de Lucas, F. Rodríguez, M. Moreno, Phys. Status Solidi B **184**, 247 (1994)
101. M.J. Yacamán, G.A. Bassett, J. Appl. Phys. **47**, 2313 (1975)
102. D. Barb, S. Constantinescu, S. Nistor, D. Tarinã, Hyperfine Interact. **53**, 279 (1990)
103. G. Benedek, J.M. Calleja, R. Capelletti, A. Breitschwerdt, J. Phys. Chem. Solids **45**, 741 (1984)
104. A. De Andrés, J.M. Calleja, I. Pollini, G. Benedek, J. Chem. Phys. **83**, 4967 (1985)
105. M. Hartmanova, I. Thurzo, Š. Besedičová, J. Phys. Chem. Solids **38**, 587 (1977)
106. J.E. Oliveira, J. Mendes-Filho, J.E. Moreira, J. Phys. C Solid State Phys. **14**, 2527 (1981)
107. A.J. Ramponi, J.C. Wright, Phys. Rev. B **31**, 3965 (1985)
108. B.S. Acharya, J. Mater. Sci. Lett. **4**, 593 (1985)
109. F.J. López, S.H. Murrieta, A.J. Hernández, O.J. Rubio, Phys. Rev. B **22**, 6428 (1980)

110. R. Pérez-Salas, T.M. Piters, R. Aceves, R. Rodríguez-Mijangos, M. Barboza-Flores, Rev. Mex. Fis. **49**, 102 (2003)
111. M.C. Marco de Lucas, F. Rodríguez, M. Moreno, Phys. Status Solidi B **172**, 719 (1992)
112. E.V. Mejía-Uriarte, R. Castañeda-Guzmán, M. Villagrán-Muniz, E. Camarillo, A.J. Hernández, S.H. Murrieta, M. Navarette, J. Phys. Condens. Matter **15**, 6889 (2003)
113. E.V. Mejía-Uriarte, E. Camarillo, A.J. Hernández, M. Navarette, M. Villagrán-Muniz, S.H. Murrieta, Opt. Mater. **27**, 1316 (2005)
114. E. Lilley, J.B. Newkirk, J. Mater. Sci. **2**, 567 (1967)
115. J.L. Gavartin, E.K. Shidlovskaya, A.L. Shluger, A.N. Varaksin, J. Phys. Condens. Matter **3**, 2237 (1991)
116. M.T. Bennebroek, A. Arnold, O.G. Poluektov, P.G. Baranov, J. Schmidt, Phys. Rev. B **54**, 11276 (1996)
117. J.S. Kasper, J.S. Prenner, Acta Crystallogr. **7**, 246 (1953)
118. P. Porta, M. Valigi, J. Solid State Chem. **6**, 344 (1973)
119. N. Valverde-Diez, D. Grande-Fernández, Solid State Ionics **28–30**, 1697 (1988)
120. P. Porta, G. Minelli, I.L. Botto, E.J. Baran, J. Solid State Chem. **92**, 202 (1991)
121. C.L. Christ, J.R. Clark, Am. Mineral. **40**, 907 (1955)
122. B. Winkler, M. Chall, C.J. Pickard, V. Milman, J. White, Acta Crystallogr. B **56**, 22 (2000)
123. J.E. Muñoz-Santiuste, J. García-Solé, M. Manfredi, Phys. Status Solidi B **163**, 191 (1991)
124. G.H. Verdiguel, C. Flores, F. Jaque, A.J. Hernández, S.H. Murrieta, J. Phys. Condens. Matter **6**, 5223 (1994)
125. A. Sors, E. Lilley, Phys. Status Solidi A **27**, 469 (1975)
126. C. Barth, C.R. Henry, New J. Phys. **11**, 043003 (2009)
127. J.J. Gilman, Trans. Am. Inst. Met. **209**, 1449 (1957)
128. J.L. Robins, T.N. Rhodin, R.L. Gerlach, J. Appl. Phys. **37**, 3893 (1966)
129. M.T. Sprackling (ed.), *The Plastic Deformation of Simple Ionic Crystals* (Academic Press, London, 1976)
130. H. Höche, H. Bethge, J. Cryst. Growth **42**, 110 (1977)
131. A.H. Ostadrahimi, H. Dabringhaus, K. Wandelt, Surf. Sci. **521**, 139 (2002)
132. J.E. Lester, G.A. Somorjai, J. Chem. Phys. **49**, 2940 (1968)
133. M.J. Yacamán, Phys. Status Solidi B **56**, 429 (1973)
134. W.A. Hofer, A.S. Foster, A.L. Shluger, Rev. Mod. Phys. **75**, 1287 (2003)
135. U. Kaiser, A. Schwarz, R. Wiesendanger, Nature **446**, 522 (2007)
136. A. Trovarelli (ed.), *Catalysis by Ceria and Related Materials*, vol. 2 (Imperial College Press, London, 2006)
137. J.V. Lauritsen, M. Reichling, J. Phys. Condens. Matter **22**, 263001 (2010)
138. C.R. Henry, Surf. Sci. Rep. **31**, 231 (1998)
139. C.R. Henry, in *The Chemical Physics of Solid Surfaces*, ed. by D.P. Woodruff, B. Elsevier, V. Warwick (UK, 2003)
140. G. Sitja, S. Le Moal, M. Marsault, G. Hamm, F. Leroy, C.R. Henry, Nano Lett. **13**, 1977 (2013)
141. M. Marsault, G. Hamm, A. Worz, G. Sitja, C. Barth, C.R. Henry, Faraday Discuss. **138**, 407 (2008)
142. Z. Gai, J.Y. Howe, J. Guo, D.A. Blom, E.W. Plummer, J. Shen, Appl. Phys. Lett. **86**, 023107 (2005)
143. M. Goryl, F. Buatier de Mongeot, F. Krok, A. Vevecka-Priftaj, M. Szymonski, Phys. Rev. B **76**, 75423 (2007)
144. M.H. Hakala, O.H. Pakarinen, A.S. Foster, Phys. Rev. B **78**, 045418 (2008)
145. J.C. Zanghi, J.J. Métois, R. Kern, Surf. Sci. **52**, 556 (1975)
146. R.B. Marcus, W.B. Joyce, Thin Solid Films **7**, R3 (1971)
147. E. Palacios-Lidon, C.R. Henry, C. Barth, ACS Catal. **4**, 1838 (2014)
148. M. Watkins, T. Trevethan, M.L. Sushko, A.L. Shluger, J. Phys. Chem. C **112**, 4226 (2008)
149. T. Trevethan, A.L. Shluger, J. Phys. Chem. C **112**, 19577 (2008)
150. Ph. Rahe, M. Kittelmann, J.L. Neff, M. Nimmrich, M. Reichling, Ph. Maass, A. Kühnle, Adv. Mater. **25**, 3948 (2013)

Chapter 16
The Atomic Structure of Two-Dimensional Silica

Christin Büchner, Leonid Lichtenstein, Markus Heyde and Hans-Joachim Freund

Abstract Determining the structure of amorphous materials used to be challenging due to the complexity of this material class. Despite many attempts to resolve amorphous materials by various diffraction methods as well as scanning probe methods, no-one has yet been able to carry out atomic imaging and to clearly identify the structure of amorphous materials. Only modern preparation methods in combination with advanced scanning tunneling and atomic force microscopy have succeeded in decrypting the everyday material glass. A bilayer silicate film on a ruthenium single crystal has been developed at the Fritz-Haber Institute. On the atomic level, this film is flat and ideal for using scanning probe microscopy. For the first time a clear image of an amorphous material has been obtained which allowed for the derivation of atomic sites and a detailed analysis from real space coordinates. The text book example of the vitreous silica structure proposed by William Zachariasen in 1932 has thereby finally been verified.

16.1 Introduction

The aim of this work is to explore previously unresolved complex surface structures and to address one of the biggest riddles in solid state physics, namely the structure of amorphous materials. Resolving and characterizing the real surface morphology

C. Büchner · L. Lichtenstein · M. Heyde (✉) · H.-J. Freund
Fritz-Haber-Institute of the Max-Planck-Society, Faradayweg 4-6,
14195 Berlin, Germany
e-mail: heyde@fhi-berlin.mpg.de

C. Büchner
e-mail: buechner@fhi-berlin.mpg.de

L. Lichtenstein
e-mail: leonid.lichtenstein@gmail.com

H.-J. Freund
e-mail: freund@fhi-berlin.mpg.de

© Springer International Publishing Switzerland 2015

S. Morita et al. (eds.), *Noncontact Atomic Force Microscopy*,
NanoScience and Technology, DOI 10.1007/978-3-319-15588-3_16

at the atomic scale is key to answering this fundamental question in surface science. Often the focus in surface science studies is on crystalline, ordered, and well defined surfaces. But the atomic arrangement of oxides, and in particular their surface and defect structures, can range from highly ordered and symmetric to more complex and even completely amorphous networks.

The prototype for amorphous network structures is silicon dioxide. This material is the simplest and most common type of glass. Many elements and compounds can form glasses and some of the oldest man-made objects found are glass materials [1–3].

Glasses are remarkably versatile and important as an engineering material. Glass manufacturers envision the future organization of communication and connectivity involving glass in a variety of forms and functions [4]. Their ideas range from hand-held display glass, electrochromic glass, architectural glass, automotive display and design glass, photovoltaic glass, glass optical fibers to all weather surface glass. Towards this end, glasses should have tunable properties depending on their application. For example, being thin, lightweight, damage resistant, touch sensitive, color sensitive, ultraviolet and visible light filtering, thermally insulating, durable and so on. Glass materials and especially silicates are relevant in various branches of modern technologies, e.g., in semiconductor devices, optical fibers and as a support in industrial catalysis. In order to push this material class forward, we must develop greater understanding of their structures and properties at the atomic scale.

Glasses show unique properties that often depend on the precise process by which they are formed. A common way of making glass is by rapidly cooling from a highly viscous liquid to avoid crystallization. The atomic and molecular processes by which liquids transform into amorphous solids are not fully understood. A review on the current theoretical knowledge of the complex process of glass formation was presented by Debenedetti and Stillinger [5]. A detailed understanding of the glass transition would have widespread implications not only for inorganic glasses, but also for organic polymers, protein dynamics, protein folding and population. To gain a clearer understanding of the complex dynamics involved, the identification of a relationship between different minimum states on the energy landscape is necessary. There is clearly a need for resolving the structure of glass forming materials in their various phases.

Figure 16.1a illustrates how similar crystalline and amorphous samples can be. It shows a crystalline silicate, also called quartz, together with an amorphous silicate, i.e. a glass. The two samples exhibit many similar physical properties [7]. For example, due to very similar optical transparency, it is not possible to distinguish the two states with simply the naked eye. But what is the difference between these two phases? Comparative investigations of crystalline and amorphous silicon dioxide samples were undertaken around a hundred years ago, almost as soon as the Laue method for the diffraction of X-ray or neutron beams on solid bodies had been developed. These methods average over large sample volumes on the macroscopic scale and primarily provide information in reciprocal space. Crystalline samples produce discrete diffraction patterns while glasses do not. The diffraction information obtained from glasses can be compared with theoretical models of possible atomic

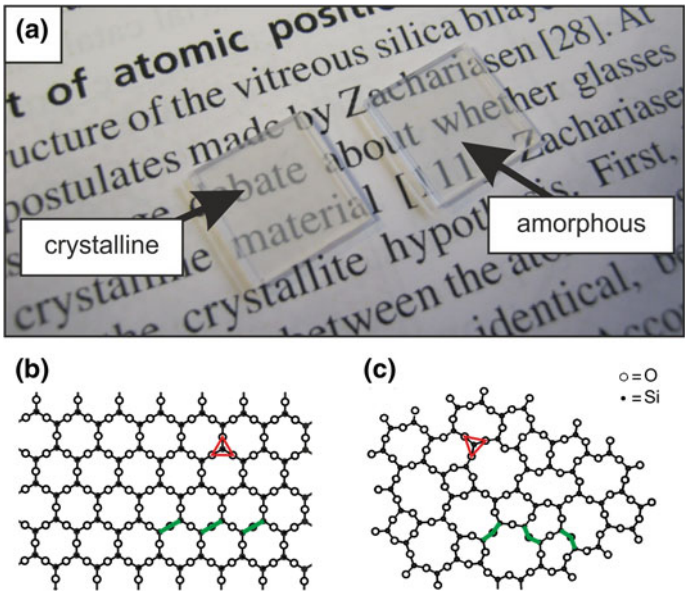

Fig. 16.1 Comparison of the structure of crystalline and amorphous materials. Illustration **a** shows a crystalline silicate sample next to an amorphous one. Both samples are optically transparent. Surprisingly, this similarity also holds for most of the mechanical and physical properties for these two phases. W.H. Zachariasen postulated a model for crystalline (**b**) and amorphous (**c**) structures in a two-dimensional representation, depicted here following the example of [6]

arrangements, but do not allow an unequivocal structural assignment. This is one of the greatest problems at the interface between experiment and theory, to get beyond the "averaged" character of diffraction data. For surfaces, at least, the following sections provide a solution beyond this.

16.2 The 2D Glass Model

W.H. Zachariasen postulated the so-called "Random Network Theory" 80 years ago to explain the structure of amorphous materials [6]. At that time, there was a large debate about whether glasses are built up from crystalline material [8]. Zachariasen attempted to rule out the crystallite hypothesis. Due to the comparable mechanical properties of amorphous and crystalline materials he assumed that the bonding forces between the atoms in the two phases should be essentially identical. The lack of periodicity and symmetry are the main features that distinguish a glass from a crystal. Early on it had been suggested that tetrahedral atomic configurations were required to form glasses. Zachariasen used these predictions to sketch an atomic

picture of a glass. In his paper he reduced the three-dimensional (3D) picture into a two dimensions (2D) analogy (Fig. 16.1b, c).

For silicon dioxide, the simplest structural unit in the 3D case is a SiO_4 tetrahedron. If the complexity of the system is reduced from 3D to 2D, the simplest structural unit for silicon dioxide changes from the SiO_4 tetrahedron to a SiO_3 triangle. The red triangle in Fig. 16.1b, c marks the SiO_3 building unit. In Fig. 16.1b these SiO_3 triangles are linked to each other as individual building blocks at fixed 180° angles, corresponding to a crystalline material. This creates long-range order and periodicity.

If the angle between these structural units varies, the building blocks can develop an extended network with rings of different sizes. As can be seen in Fig. 16.1c, the uniform structural units are linked to each other at apparently random angles. Zachariasen drew a 2D diagram in which trigonal units are linked together to create the amorphous network. Due to the large variety of Si–O–Si angles which bridge two neighboring building units, the glass structure lacks periodicity and long range order.

The illustration of the atomic structure in Fig. 16.1c became the most widespread picture for glass. This model was compatible with the existing data from X-ray and neutron diffraction of amorphous materials. Therefore, these postulates were very useful in explaining diffraction experiments on glasses [9].

Although this model has been widely used to explain structures in amorphous materials, it has never been observed in real space before. Can a similar reduction of the 3D structure to a 2D model system also be realized and characterized experimentally?

16.3 The Realization of an Amorphous Model System

The “Chemical Physics” Department of the Fritz Haber Institute is developing and studying model systems in the context of catalytically important processes. Our model systems make it possible to depict part of the complexity of dispersed real catalysts and investigate them by surface science tools. This involves producing thin, well-ordered oxide films on metal single-crystal substrates, which can also be studied under the experimental conditions of surface physics.

The first steps in surface science studies are to determine where the atoms are situated at the surface and to assign the different chemical species. In this context a reduction of complexity is necessary, and thus model systems which allow for a high degree of control over the preparation conditions are required.

In our department thin silicate films had already been specifically prepared back in 2000 [10] in order to be able to study catalytic surface reactions. The first studies investigated silicate films on molybdenum single crystals [10]. More recent work for other metal substrates, including ruthenium [11, 12], has been presented. By using different metal single-crystal substrates it is possible to exert a crucial influence on the growth of these thin silicate films. While on the molybdenum single crystals predominantly crystalline films of monolayer thickness are formed, with ruthenium

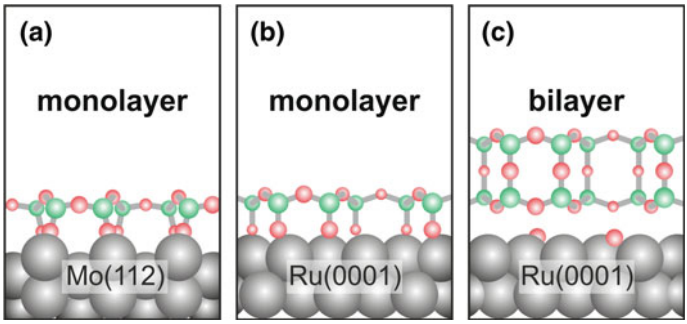

Fig. 16.2 *Side view* of the different silicate films with respect to different single-crystal substrate. **a** Silicate monolayer on a molybdenum single crystal [10], **b** silicate monolayer on a ruthenium single crystal, **c** silicate bilayer on a ruthenium single crystal [11, 12]

single crystals it is possible to specifically produce monolayers as well as bilayer silicate films. A detailed description of the sample preparation procedure can be found in [12].

Figure 16.2 shows a side view of models for these film systems. In (a) and (b) the monolayer silicates have an oxygen back bonding to the underlying metal substrate.

In contrast, the bilayer film sketched in (c) is only weakly coupled to the metal support. Surprisingly, the bilayer silicate film on ruthenium single crystals can be produced in crystalline [11] as well as amorphous structure [12]. The film's registry to the underlying crystalline metal substrate can be lost. Thus, the film is structurally decoupled from the metal support. This is evident from measurements with low-energy electron diffraction (LEED).

But can this model film system be used to observe the atomic structure directly and thus corroborate the postulate of amorphous materials?

16.4 The Limits of Scanning Probe Methods

Today, there are promising new surface science tools available. During the last decades the development of scanning probe microscopy (SPM) has had a tremendous impact as an analytical tool to determine structural, spectroscopic as well as dynamical aspects from all kinds of surfaces. Just a few years after its invention by the group of Binnig and Rohrer, the scanning tunneling microscope (STM) [13, 14] turned into one of the most widely used surface analytical methods. In 1986, Quate together with Binnig presented the principle of the atomic force microscope (AFM) [15]. The AFM is an important addition to the STM, because it does not require conducting sample surfaces. However, it should be mentioned that it took almost ten more years to record atomically resolved images by AFM after its invention [16]. Up to today the number of research groups working with advanced AFM

techniques, especially noncontact atomic force microscopy (nc-AFM), is relatively small compared to STM [17, 18].

SPM has been applied to a large variety of problems throughout the natural sciences, ranging from solid state physics to structural biology. Its cheap and relatively simple design, and the large range of applications by SPM methods, make it a valuable tool to study nature. SPM imaging can be done on a wide range of sample types, from atomically flat metal surfaces to living cells [19], and can be performed in vacuum, air, or liquid. This opens up a wide scope for experiments. Special setups were developed for low [20–23], ultralow [24, 25] and variable-temperature studies [26, 27] in ultrahigh vacuum (UHV). Adaptations to perform measurements under high pressure [28], in liquids [29], at high speed [30, 31], time-resolved [32], or in magnetic fields [33] have been conducted as well.

STM and AFM have been used extensively in the field of surface science to characterize surface morphology, structure, physical and chemical properties of bulk and epitaxial samples [34]. The direct observation of molecular film structures [35, 36] as well as the recent achievements in resolving the chemical structure of single molecules supported on flat crystals [37] are promising results. Besides the pure structural analysis, even individual atoms [38] and molecules [39, 40] were manipulated by SPM.

Nevertheless, the atomic resolution of complex surface structures with large unit cells and individual defect network structures still remains a challenge, and only a few examples have been published [41]. The idea of characterizing amorphous surfaces by STM was proposed by Wiesendanger et al. [42] in 1987. Since then, many attempts have been made to atomically resolve amorphous materials, e.g. by SPM [43–48]. However, this goal has never been achieved so far. An early measurements on glass samples made by the research group of Klaus Wandelt and colleagues showed the potential of these methods. However, it has been heavily debated, whether these results provide real atomic coordinates or not.

What is the reason behind this and what are the principle limitations of SPM methods in general? These techniques often suffer from tip convolution effects [49]. Slightly lower lying surface sites are often not imaged due to shielding effects of the neighboring atoms. In the case of corrugated sample surfaces a complicated convolution between tip and sample species takes place. The situation has been sketched in Fig. 16.3 where the number of involved tip atoms is different for corrugated (a) compared to planar (b) sample surfaces.

Furthermore, it is often very demanding to separate electronic from topographic features in STM [44], as well as to distinguish the chemical sensitivity of changing tip apexes towards different surface sites, both in STM and AFM. In a stable imaging mode typically only one type of species is imaged on the sample surface, either the anionic or the cationic site, depending on the actual tip configuration. However, if the probing tip apex is changing then this situation is hard to disentangle.

Clearly, a solution to these challenges is the reduction of dimensionality by using well defined thin film systems grown on metal single crystals while retaining essential aspects of the complexity of real systems. The growth of two-dimensionally flat

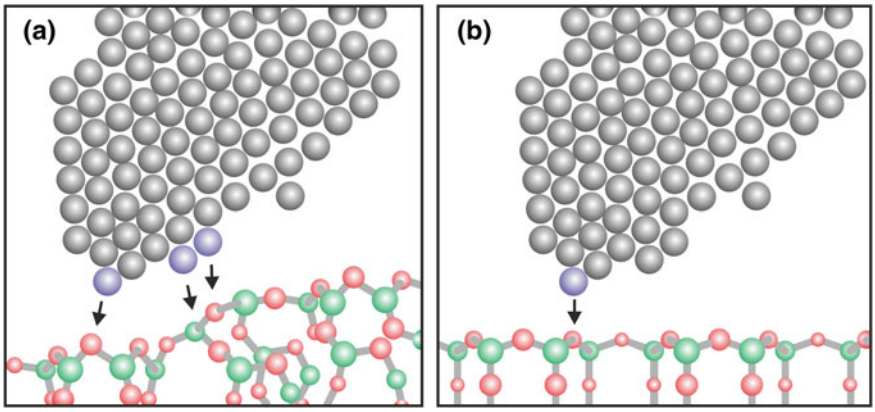

Fig. 16.3 *Side view* of a scanning probe tip with respect to a corrugated sample surface in (**a**) and a 2D flat film system depicted in (**b**). Although the same tip is assumed in both cases, there is a different number of tip atoms with a similar distance to the underlying sample surface atoms. Depending on the probe position, three or more tip atoms contribute directly to the imaging signal for the corrugated sample surface in (**a**), while in the case of flat film terraces one atomic tip site is favored in (**b**)

model systems under carefully controlled preparation conditions allows the use of SPM to gain insight into individual atomic scale surface structures as presented in this book chapter.

16.5 Assignment of Atomic Positions

Here, we present the atomic arrangement of a thin vitreous silica bilayer film grown on Ru(0001) [12]. Details on the experimental setup can by found in the text book series "Noncontact Atomic Force Microscopy Volume 2" in Chap. 7 [18] as well as in the following [50–53]. An atomically resolved constant height nc-AFM image of the vitreous silica film is shown in Fig. 16.4a (scan size = 5.0 nm × 3.8 nm). It is useful to look again at the postulates made by Zachariasen in 1932 [6], sketched for comparison in the lower part of Fig. 16.4a. The complex atomic arrangement of this 2D network film shows a striking similarity.

The observed protrusions at atomic separations are arranged in triangles. By comparing to Zachariasen's model and based on this triangular symmetry the protrusions can be assigned to one face of a tetrahedral SiO_4 building block. Consequently, the protrusions correspond to O atoms (red balls in Fig. 16.4b). Such a triangular unit has been marked by a red triangle in Fig. 16.4.

Here, an O sensitive contrast is observed and the position of the Si atoms has been calculated based on the O coordinates. The Si coordinates are determined using a circumscribed circle around every O triangle. The position determined by this

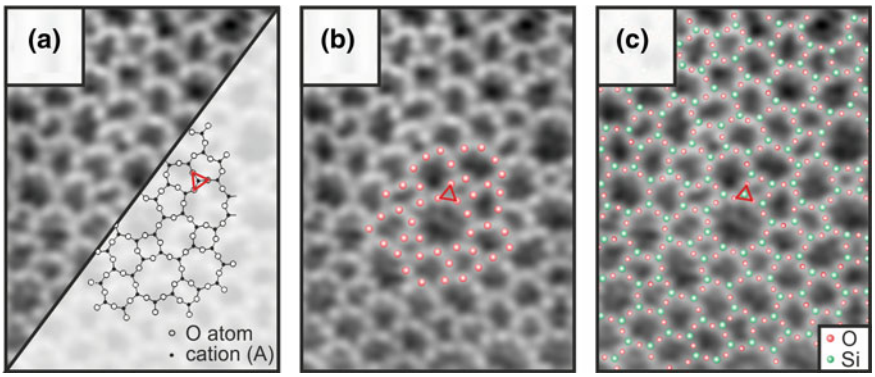

Fig. 16.4 Assignment of atomic positions [54]. **a** Constant height nc-AFM image with atomic resolution ($V_S = 100$ mV, $A_{OSC} = 2.7$ Å, scan range = 5.0 nm × 3.8 nm), Zachariasen's picture of the atomic arrangement in a glass is shown for comparison [6]. **b** Image from (**a**), partly overlayed with O model (*red balls*). **c** Image from (**b**), overlayed with the complete model of the topmost Si (*green balls*) and O atoms

method has the same distance to all the triangle's corners. By placing a green ball in the center of each resulting circle the Si atom is marked. In this way the 2D model of the topmost O and Si atoms has been completed.

Such a structural model completely covers the nc-AFM image presented in Fig. 16.4c. The film consists of rings with different sizes. No crystalline order is observed in this film structure. All of these atoms as viewed from the top plane of the bilayer are arranged in SiO_3 triangles. No under- or over-coordinated species were observed.

This structure corresponds to a network of corner-sharing SiO_4 tetrahedra. The film is highly ordered in the z-direction, while it is vitreous in the xy-plane (image plane). The SiO_4 tetrahedra of the first layer are linked via bridging O atoms to the SiO_4 units of the second layer with a Si–O–Si angle of 180°. The linking O atoms represent a mirror plane. The character of this 2D flat film is a result of these particular structural elements. Looking from the side, the film structure as shown in Fig. 16.2c consists of four-membered rings standing upright and connected randomly, forming the 2D ring network. A height difference between the topmost Si and O atoms from the density functional theory (DFT) model for the crystalline silica bilayer (52 pm) [11] has been used to compensate for the lack of information in the third dimension for the later evaluations of the atomic coordinates. This assumption has been proven valid in [55].

Let us look again at the observable image contrast in nc-AFM and STM images [55]. Both techniques provide a contrast that allows for identification of individual atomic sites. The observed chemical sensitivity of nc-AFM and STM strongly depends on the microscopic tip configuration. A modified tip termination can make the Si instead of the O positions visible [55]. A sensitivity to the Si positions results in a different local arrangement and distance between the resolved atomic sites.

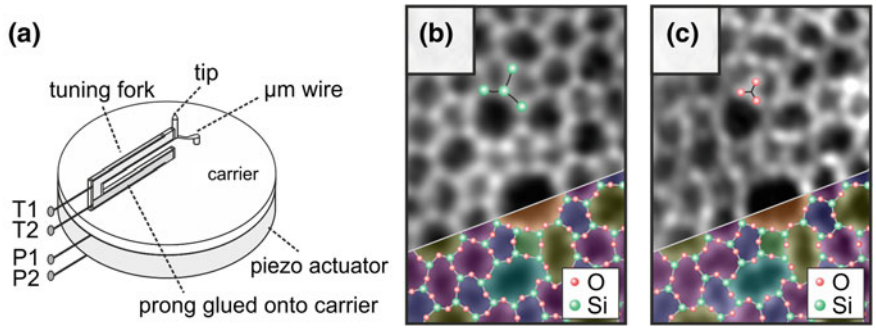

Fig. 16.5 **a** Sketch of the used tuning fork sensor device for nc-AFM/STM [52]. The STM tip is electrically connected by a thin Pt/Rh wire with a diameter of 50 µm. Both the tip and Pt/Rh wire are insulated from the tuning fork and its electrodes. This is necessary to prevent a cross coupling between the nc-AFM and the STM signal. **b**, **c** Both images represent a single atomically resolved constant height measurement, where (**b**) shows the nc-AFM and (**c**) the STM channel. Imaging parameters **b** oscillation amplitude = 0.27 nm, *gray scale* from −1.0 (*dark*) to +0.6 Hz (*bright*); **c** $V_S = 100$ mV, *gray scale* from 50 (*dark*) to 500 pA (*bright*); **b**, **c** scan area = 2.7 nm × 3.9 nm. In (**b**) the structure of the Si atoms is visible, whereas (**c**) reveals the arrangement of the O atoms. Also here an atomic model of the topmost layer of the silica film is superimposed onto the lower right corner of the images in (**b**) and (**c**) (*green balls* Si atoms, *red balls* O atoms)

Our sensor device has the capability to directly combine nc-AFM and STM. This device is sketched in Fig. 16.5a. When the tip is probing the sample surface, we can detect the interaction force and the tunneling current independently. Here, we can simultaneously and at the same atomic site gather data about interaction forces and electronic structure without cross-talk. Essentially we develop a more complete understanding of the surface by employing the full benefits of AFM and the full benefits of STM in parallel. These provide distinct, but complementary information about the surface.

This unique setup is capable of resolving clearly separated features from the surface in these two detection channels. Figure 16.5b, c represent one single atomically resolved constant height nc-AFM and STM measurement above a vitreous region of the silica film. Figure 16.5b is a map of the frequency shift (Δf), while Fig. 16.5c is the simultaneously recorded map of the tunneling current (I_T). Both images show a ring network with pores of various sizes. The power of this approach becomes clear if we take a closer look at the atomic structures that were resolved. While the Δf-map in Fig. 16.5b shows the Si positions (green balls), the I_T-image in Fig. 16.5c reveals the O positions (red balls) of the topmost silica layer.

In the top part of Fig. 16.5b, c this can be verified by looking at the nearest neighbor (NN) configurations of the imaged protrusions. In Fig. 16.5c the contrast in the STM signal is similar to nc-AFM image in Fig. 16.4. Every three protrusions (red balls) form a triangle representing one triangular side of an SiO_4 tetrahedron. Therefore, these positions correspond to O atoms. However, in Fig. 16.5b, four protrusions (green balls) form a three-bladed windmill with one protrusions sitting in

its center. These positions represent the centers of four different tetrahedra and therefore correspond to the Si atoms. Furthermore, the NN distances are characteristic for a certain atom type and are significantly larger for Si than for O. The structural information of both channels can be combined in this case to obtain a complete surface model without any further assumptions as plotted in the bottom part of Fig. 16.5b, c.

Please note, that also combinations of nc-AFM and STM images have been observed in which the same surface species have been detected.

In the following analysis the atomically resolved nc-AFM image and the derived model of the topmost layer from Fig. 16.4 has been used as a starting point for further evaluation of the thin film's structure.

16.6 Atomic Force Microscopy Challenges X-Ray Diffraction

In the following section, the atomic structure of the vitreous silica bilayer is discussed and compared to the structural data available from diffraction methods. Since the invention of X-ray diffraction by von Laue, crystalline and amorphous materials have been analyzed over the last century. Figure 16.6a provides the diffraction pattern

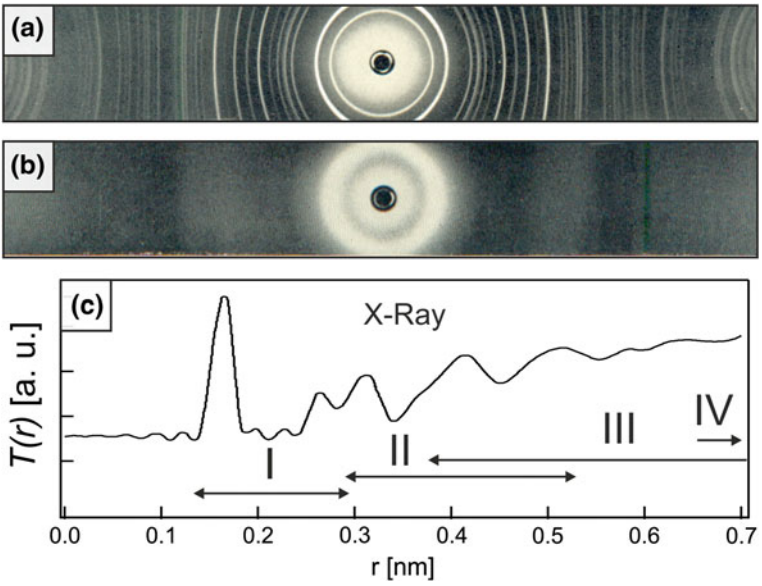

Fig. 16.6 Silica X-ray diffraction data. **a** X-ray diffraction pattern from a powder sample of α-quartz (**a**) and vitreous silica (**b**) [58]. **c** X-ray PCF of bulk vitreous silica taken from [59]. Within this plot the ranges of order as proposed by Wright have been indicated for range I, II, III, and IV [56]

of a powder sample from α-quartz. Herein, the randomly oriented crystalline grains in the powder produce a sharp ring pattern. The diffraction pattern of vitreous silica given in (b) only exhibits diffuse halos. Figure 16.6c shows a typical pair correlation function derived from X-ray diffraction data from vitreous silica. A classification introduced by Wright, who divided the order in network solids in four ranges, is used. The following section is divided accordingly into the ranges: I structural unit, II interconnection of adjacent structural units, III network topology, and IV longer range density fluctuations [56, 57].

In range I, the basic structural unit (SiO_4 tetrahedron) is addressed and parameters from the X-ray PCF can be extracted by using peak fitting techniques. However, in ranges II and III, simple extraction of structural parameters is not possible and models are required for interpretations. In range II the interconnection and relative orientation of two corner-sharing SiO_4 units is involved. Here, the variable parameters of the Si–O–Si bond angle and torsion angles can be defined. In this range the first example of disorder in comparison to crystalline modification can be observed. Range III describes the network topology of amorphous network solids. In this range a description of the first neighbors and shortest path statistics has always been desired, but has never been observed in real space before. In the literature a controversial discussion can be found, where theoretical models have been tested by comparison to PCFs from XRD or ND. In range IV the long range density fluctuations are addressed. However, the density differences between more and less ordered regions are likely to be relative small. While there is quantitative knowledge about ranges I and II, ranges III and IV are still much less understood and hence leave opportunities for new developments.

The different orders are visualized by snapshots of atomic structures in Fig. 16.7. This classification turned out to be extremely useful to discuss and interpret the structural information in diffraction experiments.

16.6.1 Structural Unit—Range I

This range deals with the tetrahedron unit schematically drawn in the inset of Fig. 16.8e. A tetrahedron is primarily defined by the side length and the tetrahedral angle. The distance from the center to one corner is another characteristic parameter. With this respect the Si–O, the O–O distance, and the O–Si–O angle have been analyzed.

Figure 16.8a shows the model from Fig. 16.4a with colored bars connecting all Si–O nearest neighbors (NNs). A color coded scale bar represents the Si–O bond length.

Figure 16.8b displays the corresponding histogram of the Si–O distances. A Gaussian distribution was fit to the data and yielded an Si–O mean distance of 0.16 nm with a standard deviation of 0.01 nm. This is in excellent agreement to XRD [59] and ND [60] data obtained on bulk vitreous silica, which are indicated by black arrows in Fig. 16.8b.

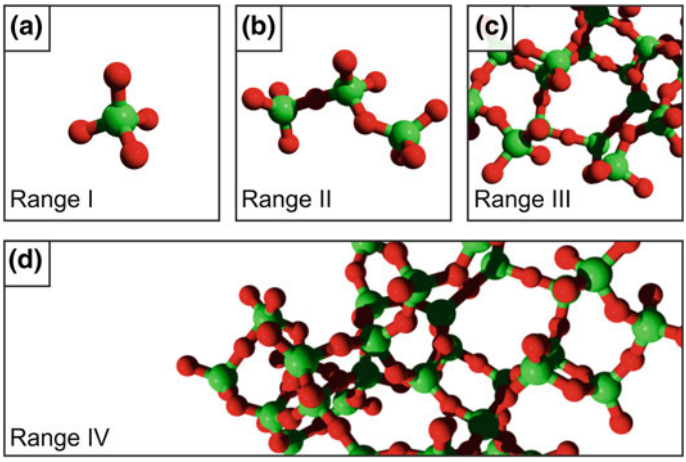

Fig. 16.7 Ranges of order in network solids. A 3D arrangement of silica structures for different length scales has been plotted (Si *green*, O *red*). **a** The structural unit of the SiO_4 tetrahedron is assigned as range I. **b** is range II where adjacent units are interconnected. **c** Range III is the network topology while **d** is range IV in which longer range density fluctuations can be analyzed

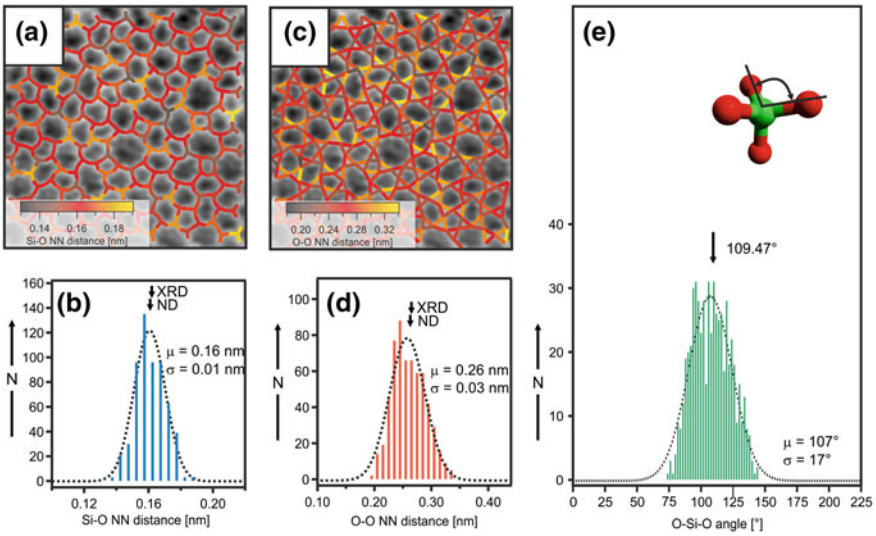

Fig. 16.8 Characterization of the structural unit in range I [54]. **a** Constant height nc-AFM image ($V_S = 100$ mV, $A_{OSC} = 2.7$ Å, scan range = 5.0 nm × 5.0 nm), colored bars representing the Si–O nearest neighbor (NN) distance (see *scale bar*). A cut-out of this image is also given in Fig. 16.4a. **b** Histogram of the Si–O NN distances. Average values from diffraction experiments on bulk vitreous silica are indicated by *black arrows* [59, 60]. **c** Same nc-AFM image from (**a**), superimposed by colored bars representing the O–O NN distance (see *scale bar*). **d** O–O NN distances given in a histogram. Results from diffraction experiments on bulk vitreous silica are indicated by *black arrows* [59, 60]. **e** O–Si–O angles in a histogram plot. The *black arrow* indicates the angle of 109.47°, corresponding to a regular tetrahedron

In Fig. 16.8c the O–O NN distances are visualized. The O–O distances exhibit similar lengths throughout the whole image. The O–O NN distance histogram is shown in Fig. 16.8d. By fitting the data with a Gaussian distribution one can obtain a mean O–O NN distance of 0.26 ± 0.03 nm. As the black arrows indicate, this experimental value agrees well with XRD and ND measurements on bulk vitreous silica [59, 60].

Furthermore, all O–Si–O angles in the atomic model have been computed in the histogram of Fig. 16.8e. A symmetric distribution with an average of 107° and a standard deviation of 17° of the intratetrahedral angle is shown. Once again, this value agrees well with the 109.47° angle in a regular tetrahedron and the 109.8° angle deduced from XRD experiments on bulk vitreous silica [59].

In the order of range I the thin vitreous silica film reproduces the structural parameters derived from diffraction measurements on bulk vitreous silica. Nevertheless, range I order is not determining the characteristic features of the vitreous state. This range consists of well-defined building blocks (SiO_4 tetrahedra) and is defined by the chemical Si–O bond characteristics. Characteristic features of the vitreous structure can be found in the longer ranges.

16.6.2 Interconnection of Silica Units—Range II

This range is characterized by the interconnection of neighboring tetrahedral building blocks. By looking at the distance between the tetrahedral centers and the connection angle, this linkage can be evaluated. In this section, the Si–Si NN distance and the Si–O–Si angle are analyzed. A schematic is plotted in Fig. 16.9c marked by arrows.

The real space distribution of Si–Si NN distances is shown in Fig. 16.9a. The colored bars represent the distance between two neighboring Si atoms. The corresponding length is given in nm in the scale bar. In Fig. 16.9b the corresponding histogram for the Si–Si NN distances is plotted for the image in (a). A mean Si–Si NN distance of 0.30 ± 0.02 nm has been derived from a Gaussian fit to the data. The derived measurements are compared to XRD and ND results on bulk vitreous silica, indicated by black arrows. The small offset can be explained by a larger variety of Si–O–Si angles in 3D bulk silica compared to the 2D film structure.

Therefore, a histogram of the Si–O–Si angles is shown in Fig. 16.9d. In the Si–O–Si angle distribution a characteristic asymmetric shape is visible. A mean Si–O–Si angle of 139° with a standard deviation of 3° is obtained by fitting the data with a Gaussian function.

In the literature this Si–O–Si angle has been largely debated within the glass community [57, 63]. It is a very important angle for vitreous networks, describing the interconnection of two tetrahedral building blocks. A Si–O–Si value of 144° has been determined by XRD measurements on bulk vitreous silica [59]. Later, the data were re-analyzed by another group yielding a Si–O–Si angle of 152° [64].

A similar value has been obtained from a hand-built model of bulk vitreous silica by Bell and Dean [62]. Poor agreement between experiment and model was observed,

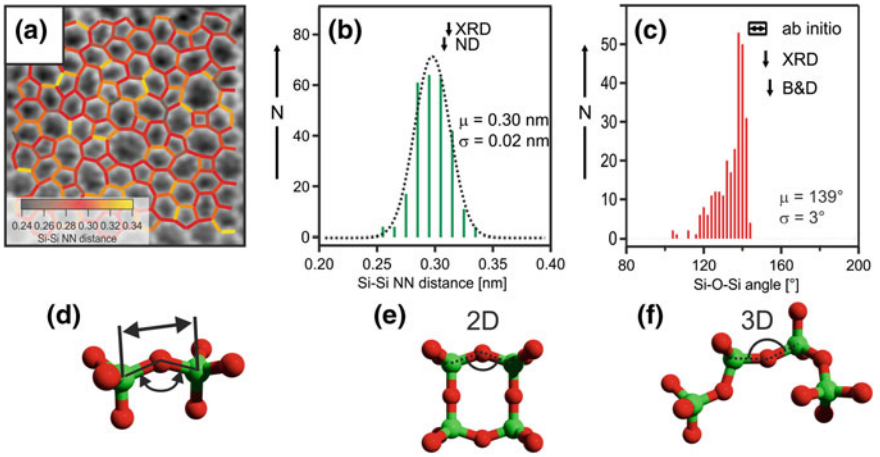

Fig. 16.9 Features of the interconnection in range II for the vitreous silica film [54]. **a** Image from Fig. 16.4a, overlayed with *colored bars* representing the Si–Si NN distance (see *scale bar*). **b** Histogram of the Si–Si NN distances. *Black arrows* indicate the average values from diffraction experiments on bulk vitreous silica [59, 60]. **c** Histogram of the Si–O–Si angles. For a comparison, *black arrows* indicate the values from ab initio calculations [61], XRD [59] and molecular model from Bell and Dean [62]. **d** Two SiO_4 tetrahedral units connected via the bridging O atom. *Black arrows* indicate the Si–Si distance and the Si–O–Si angle. **e**, **f** Comparison of Si–O–Si angles in 2D and 3D vitreous networks (Si *green*, O *red*) [55]. **e** *Side view* on the building block of the 2D vitreous silica bilayer. Here, the Si–O–Si angle is restricted by the flat film structure of the bilayer. **f** Four SiO_4 tetrahedra connected in 3D space. Due to more degrees of freedom in the Si–O–Si-angles a wider spectrum of values can be assumed

when the authors attempted to build a structure with a mean Si–O–Si value of 144°. Later on, ab initio simulations of bulk vitreous silica yielded mean Si–O–Si angles ranging from 143.4° to 152.2°. The angles depended on the potential, basis set and the applied structural optimization scheme [61]. An overview of the literature on measured and simulated Si–O–Si angles can be found in [63]. Here, the most probable Si–O–Si angle of bulk vitreous silica has been estimated to be near 147° with a standard deviation of 10°–13°. A sharp boundary in the distribution is absent [63]. The Si–O–Si-angles terminated from our real space data deviate from the values found in the literature by 4°–13°.

It is clear that the smaller Si–O–Si angle is an intrinsic feature of 2D vitreous networks. The different interconnections of tetrahedral units in 2D and 3D vitreous silica are illustrated in Fig. 16.9e, f. In the side view of the film structure in Fig. 16.9e, building blocks made out of 4 tetrahedra become visible. These building blocks introduce the flatness of the 2D film structure. The Si atoms of the bottom and top layer lie all in one plane, respectively. Therefore, the bonding arrangement in the z-direction is predetermined. The angles in which the three remaining bonds per Si atoms can arrange is limited. A certain Si–O–Si angle can not be exceeded in this structural arrangement. The characteristic sharp edge in the Si–O–Si angle

distribution of a 2D vitreous network visible in Fig. 16.9c can be assigned to this effect. In the 3D case, structures with a larger degree of freedom (f) are allowed (sketched in Fig. 16.9), resulting in a larger range of values for the Si–O–Si angles. In this range II, small but distinct differences due to the increased symmetry of the vitreous silica film structure have been observed in comparison to bulk silica. This increased symmetry causes the film to be atomically flat, which allows us to tackle the even more important range of the network topology, described in the following section.

16.6.3 Network Topology—Range III

This range of order is the most discussed and least understood topic in the glass community. In this range the differences between crystals, with periodicity and order, and glass, with no periodicity and no order is most striking. In both phases the initial buildings block are the same. The difference between a crystalline and a glass phase is in the relative orientation of these building blocks. A detailed comparison of crystalline and vitreous regions of the thin silica film is given in [55]. Characterization of the larger radial distances, ring statistics, and Si–Si–Si angles have been evaluated for the thin silica film.

In direct comparison to diffraction data a PCF helps to characterize the atomic order in a material. The computed long range distances for the silica film structure can be compared to literature values. Radial pair distances for Si–O (blue), O–O (red), and Si–Si (green) measured from the nc-AFM model are indicated in Fig. 16.10a. A histogram of distances between all atoms in the model is plotted versus the radial distance (r) in the so called pair distance histograms (PDHs) in (b). Vertical colored bars mark significant peak positions.

The first peaks in all three distributions correspond to the first respective NN distances. The origin of these positions has been presented in Sects. 16.6.1 and 16.6.2. Second peaks of each curve represent the next NN distances.

The second peaks exhibit a larger background compared to the first peaks. They are broader and more diffuse, which is an intrinsic feature of the vitreous nature of the film. The first peaks represent order of ranges I and II introduced by the chemical bonding of the building blocks. The following peaks are broader and characterize range III.

By summing up the different PDHs using X-ray and neutron scattering factors of Si and O according to the formula in [62, 65], total pair correlation functions of the experimentally derived structural model, ($T_{\text{nc-AFM}}(r)$), have been obtained. Due to the 2D structure of the thin film, $T_{\text{nc-AFM}}(r)$ was normalized by r^{-1}. The PCF obtained in an XRD experiment and ND measurements on bulk vitreous silica in Fig. 16.10c, d have been plotted together with the respective curves $T_{\text{nc-AFM}}(r)$ calculated for the silica film structure. Reasonable agreement with the XRD and ND PCFs with $T_{\text{nc-AFM}}(r)$ was achieved for the major peak positions, their relative magnitudes and peak shapes. But as already indicated in the discussion of range II,

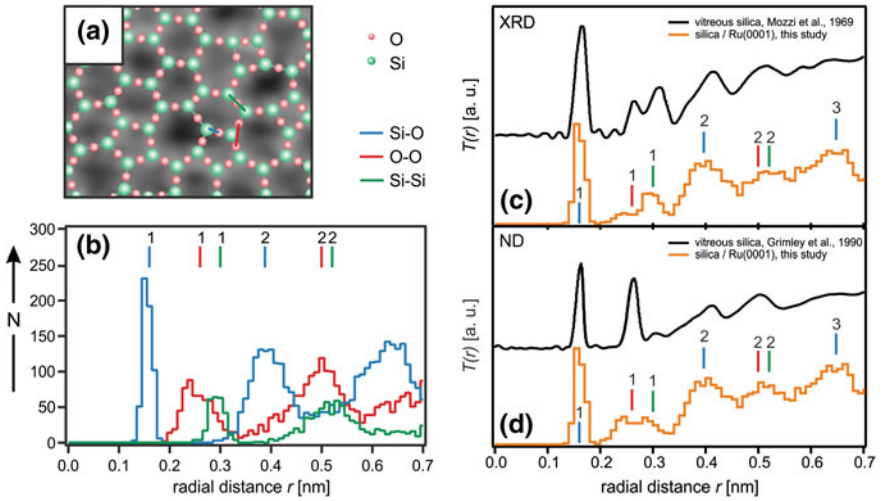

Fig. 16.10 Analysis of pair distance histograms and pair correlation functions of the silica film in comparison to diffraction data [54]. **a** Cutout of a vitreous silica image with a superimposed atomic model. *Colored bars* indicate the types of distances that are evaluated in (**b**). **b** Pair distance histograms (PDHs) derived from the nc-AFM image given in Fig. 16.4. Radial distances for Si–O (*blue curve*), O–O (*red curve*), and Si–Si (*green curve*) are plotted. Peaks are indicated by *vertical colored bars* for first and second NN. **c** Comparison of the total PCF, $T_{\text{nc-AFM}}(r)$ (*orange curve*), with the PCF obtained from X-ray diffraction measurements on bulk vitreous silica (*black curve* has been retraced from [59]). **d** Comparison of $T_{\text{nc-AFM}}(r)$ (*orange curve*) to results from ND on bulk vitreous silica (*black curve* has been retraced from [60]). The PDH peak positions are in line with the respective colored bars from (**b**)

small deviations induced by the different dimensionality of the two systems are visible. While the silica glass studied in diffraction experiments is 3D, the silica bilayer on Ru(0001) is 2D. Nevertheless, a good agreement between the PCFs obtained in diffraction studies of bulk vitreous silica and the vitreous silica film is achieved.

Looking at the ring size distribution of the thin vitreous silica film is another way to characterize the network topology. From diffraction measurements and other averaging techniques such ring size distribution are not directly attainable. This quantity can only be obtained from real space data and represents the biggest advantage this model system has to offer. The ring size s is defined as the number of Si atoms per ring. These rings are quite large objects and therefore a large statistical sample is required. For this analysis the atomically resolved STM image in Fig. 16.11a has been used. This particular STM image shows a sensitivity to the Si atoms in contrast to the nc-AFM image from Fig. 16.4, where O atoms are visualized. The sensitivity of the scanning probe is mainly dominated by the microscopic tip termination. An overview of different tip contrasts for this film system has been presented in [55]. The lower right part of Fig. 16.11a is superimposed with the atomic model of the topmost Si and O atoms. A complex ring network is revealed similar to Fig. 16.4c.

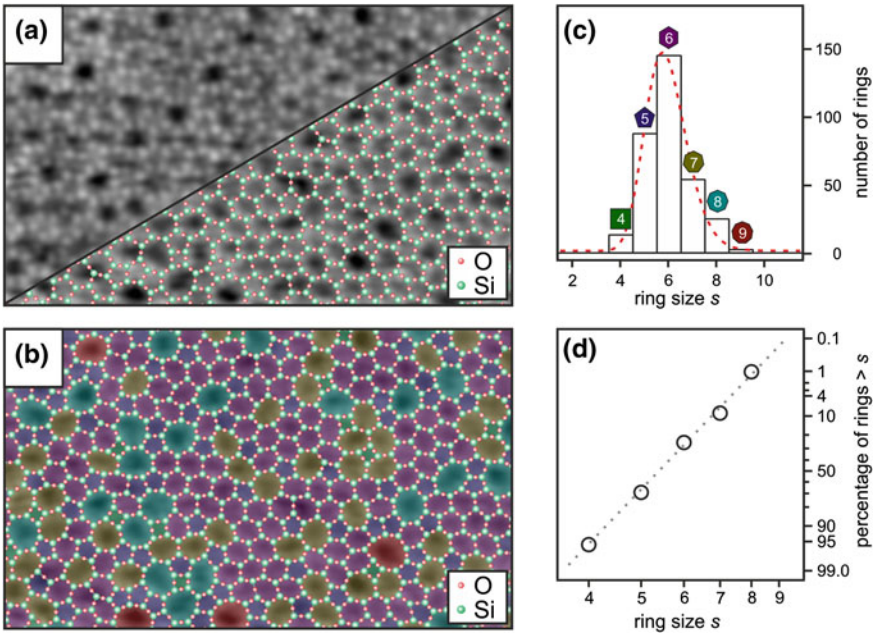

Fig. 16.11 The 2D vitreous silica ring size distribution [55]. **a** Large scale STM image of the vitreous silica film with a sensitivity to Si sites ($V_S = 2$ V, $I_T = 50$ pA, scan range = 11.2 nm × 6.6 nm). Half of this image is superimposed by the atomic model of the topmost Si and O atoms. **b** Visualization of the ring size distribution in real space. The different rings are indicated by *colored polygons*. **c** Histogram of the ring size distribution from the STM image in (**b**). A log-normal fit to the data is given by a *red dashed curve*. **d** A log-normal plot of the ring size distribution guided by a *dashed line*

Figure 16.11b presents the real space visualization of the ring size distribution. The polygonal area spanned by the Si atoms has been color coded for every ring. The environment of a ring apears to depend on its size. Rings with more than six Si atoms tend to be surrounded by smaller rings. The possible angles inside an SiO_4 tetrahedron govern the ring arrangement.

In Fig. 16.11c a histogram of the ring sizes from the STM image is depicted. The distribution of rings ranges from four Si atoms to nine Si atoms. The most common ring has six Si atoms. The distribution is asymmetric regarding the maximum. A log-normal behavior characterizes the ring size distribution of the vitreous film. Such analysis was first presented by James F. Shackelford and Brian D. Brown for an extended Zachariasen network [66]. Therein, they have also used a log-normal ring size distribution to characterize the 2D random network. The connectivity requirements of 2D random network seem to be the origin for the behavior of the ring size distribution [66]. The silica/Ru(0001) ring size distribution can be fitted by a log-normal function or a line in the log-normal plot (dashed lines in Fig. 16.11c, d) with good agreement.

Surprisingly, the ring size distribution over several sample preparations, even within a certain range of preparation conditions, have provided very similar distributions for vitreous silica film regions. The properties of bulk glasses strongly depend on their preparation conditions and it is believed that these are presumably influenced through their ring size statistics. Thereby an important parameter seems to be the fictive temperature from which the glass was quenched from the liquid state. It is expected that the ring statistics would also depend on preparation parameters for the silica film. However, our current preparation procedures seem to always yield an ideal 2D glass configuration. Currently, we are only able to change the ratio between crystalline and vitreous regions in our sample systems by controlling the bilayer coverage.

From Fig. 16.11b Si–Si–Si angles can be computed. The internal structure of the ring is guided by the Si–Si–Si angle. For four- to nine-membered rings histogram plots of the internal Si–Si–Si angles are shown in Fig. 16.12a–f. The corresponding edge angle of the regular polyhedron is marked by a black arrow for every ring size. Since the rings in the vitreous silica film can have a flexible shape, a broadening of the Si–Si–Si angle is observed. The mean value of each distribution, however, is in good agreement with the ideal polyhedral angle. The sum of all ring contributions is plotted in Fig. 16.13. The Si–Si–Si angle shows a broad distribution, having a

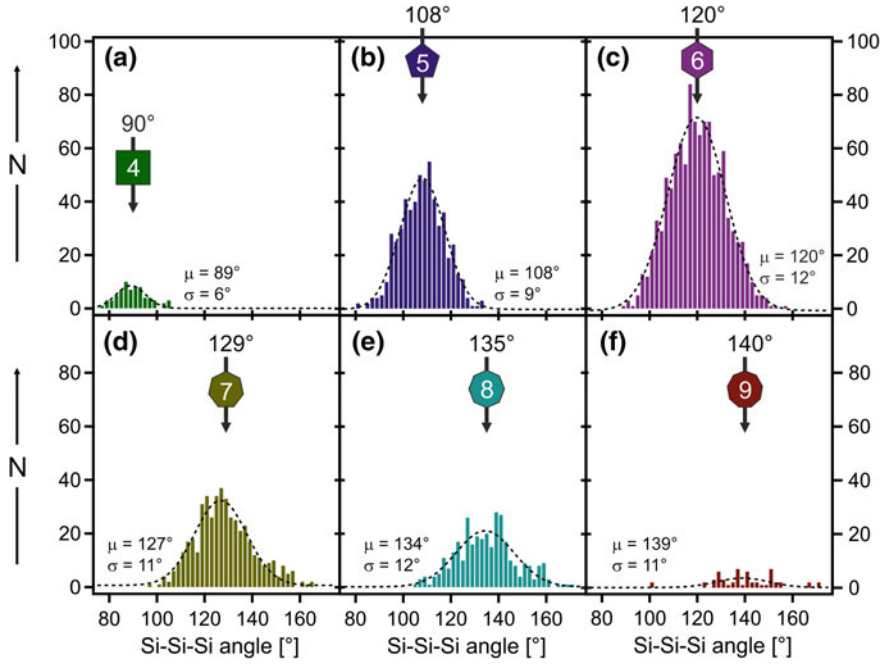

Fig. 16.12 Histograms of Si–Si–Si angles [55]. **a–f** Histograms of Si–Si–Si angles in four- to nine-membered rings are plotted separately. Internal angles of regular polyhedra are indicated by *arrows* and *numbers* at the *top*

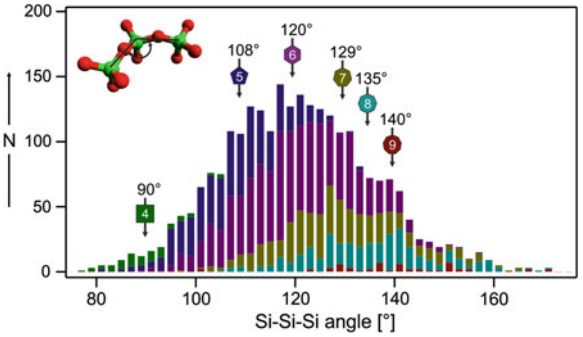

Fig. 16.13 Total Si–Si–Si angle distribution [55]. Comparison of the Si–Si–Si angle distribution for different ring sizes. The ring sizes are *colored* correspondingly

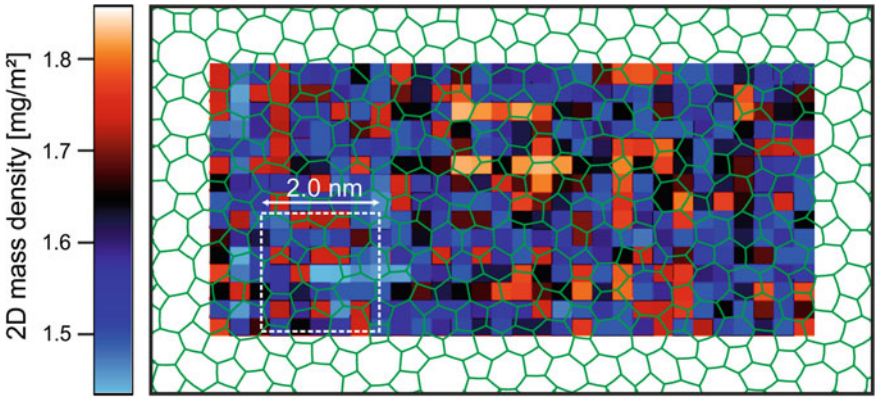

Fig. 16.14 2D mass density analysis of the silica film [54]. The *green* wireframe corresponds to the model from Fig. 16.11b. The *white dashed box* displays a bilayer slab used to calculate the 2D mass density. *Colored boxes* represent the lateral variation of the 2D mass density (see *scale bar*)

maximum at 120° corresponding to the average edge angle inside the most frequent, i.e., sixfold, ring. The broadness of the distribution further shows how flexible this 2D amorphous structure can be.

16.6.4 Density Fluctuations—Range IV

The data in Fig. 16.11b for this silica film allows us to address even range IV, where the long range mass density is evaluated. In Fig. 16.14 the 2D mass density has been visualized. The green wireframe was used as a model for the density determination. Under the wireframe, small colored boxes depict the local mass density in mg/m^2. The boxes have dimensions of 0.34 nm $\times$ 0.30 nm. For each box the local mass

density from a 2 nm × 2 nm slab around it was calculated. One slab has been indicated by a white dashed square. Its dimensions have been chosen to be larger than a typical ring size. The 2D mass density varies from 1.46 to 1.83 mg/m^2 and has been color coded in the small boxes for each slab. In the calculated 2D mass densities the complete bilayer structure has been considered. Both the topmost SiO_4 tetrahedra and the lower ones have been taken into account.

A total 2D mass density of 1.65 mg/m^2 has been calculated for the silica film. A pure crystalline phase of the silica bilayer has a slightly higher 2D mass density of 1.68 mg/m^2. Small local fluctuations of the 2D mass density are observed for the vitreous film. This might be induced by the local ring environment. Larger rings have a lower density than areas consisting of smaller rings. The center of the image is dominated by smaller rings (four to sevenfold) indicated by the higher mass density, while in the lower left corner larger rings with a lower density are observed. This evaluation is just a starting point for the range IV order. Further insights might be gained by a detailed analysis of the ring size environments.

16.7 Crystalline-Vitreous Interface in 2D Silica

Interface structures between crystalline and amorphous phases are of great interest. In the glass community, there has always been a controversy about how crystalline and vitreous phases are connected to one another. From the experimental point of view, a real-time observation at the atomic scale of an active front during a glass transition process is not currently feasible. But a static image of such an interface region can be gained.

In this silica film a transition between crystalline and amorphous regions has been imaged and characterized [67], as shown in Fig. 16.15. The image of this boundary layer makes a direct contribution to understanding the topological glass transition at the atomic level. Figure 16.15a shows an atomically resolved STM image of an interfacial area [67]. This image has been superimposed with Si and O positions in Fig. 16.15b. A smooth interface without under- or overcoordinated atomic sites has been found. No new building blocks were observed. A detailed analysis of atomic distances and angular distributions has been performed [67]. In the crystalline, the vitreous, and the interfacial region the Si–Si distances appeared to remain constant. However, the orientation of the Si–Si directed distances showed a clear change at the interface. Three discrete peaks in the angular distribution representing the crystalline axes are observed in the crystalline area. In the vitreous part these orientations are randomly distributed in all directions.

For a further analysis the image in Fig. 16.15b has then been partitioned into slices, which are indicated below. Thereafter, the number of rings of a certain size within the segment has been counted (Fig. 16.15c).

With this approach it is also possible to plot the occurrence of the various ring sizes in the interface region. This is shown in Fig. 16.15c by the color-coded number of

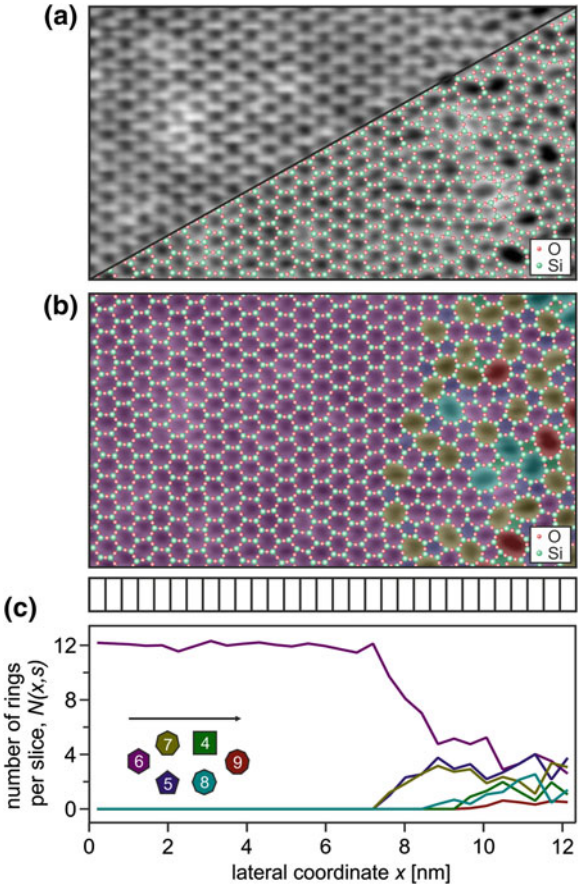

Fig. 16.15 2D structure of a crystalline-amorphous transition in a silica film [67]. **a** STM image with atomic positions marked. **b** Image from (**a**) with *color-coded* rings to emphasize their distribution along the structural transition from crystalline to amorphous. The change in the ring sizes from *left* to *right* is depicted in (**c**). The counts of ring size over the lateral position has been determined. The purely crystalline phase contains only rings of 6; rings of 5 and 7 first appear at the transition, until the typical ring size distribution of the amorphous phase can be seen on the *right*

rings per slice. The various ring sizes do not occur at the same position in the interface region. In fact, certain ring sizes occur simultaneously, and some combinations occur closer to the crystal domain than others, as the interface region is entered from the crystalline domain. Based on calculations of how much energy is necessary to change an arrangement of four six-membered rings into two five- and two seven-membered rings versus two four- and two eight-membered rings, it turns out that the former costs less energy than the latter. This is consistent with the general knowledge, that the Stone-Wales defect (a combination of five- and seven-membered rings) is the lowest energy defect in a hexagonal network [68].

Wooten and Weaire generated an early calculation of a crystalline-amorphous interface for silicon [69]. In crystalline silicon the shortest-path rings of atoms are all six-membered. By repeating random rearrangements of bonds, different ring sizes were generated that lead to an amorphous phase. In the interface region between the crystalline and amorphous phases, incorporation of five and sevenfold rings occurs.

This structural evolution is very similar to the one observed in our silica film.

Huang et al. reported recently on the observation of structural rearrangements in this amorphous silica bilayer film [70]. The authors used a probing electron beam of a transmission electron microscope (TEM) to deliberately cause rearrangements. Remarkable images and videos show the movements of structural building blocks at the atomic scale. The opening and closing of ring structures and the subsequent rearrangements can be directly observed. The results confirm our early models and DFT calculations [12] and open new ground for future modeling of dynamics in glasses. By providing the opportunity to study vitreous materials at the atomic level, this unique model system is likely to have great impact on the general understanding of dynamic processes in amorphous bulk materials. Future work might allow a direct assessment of atomic structures at the transition temperatures, where the liquid solidifies to either the crystalline or the amorphous state.

16.8 Topological Analyzes of Two-Dimensional Network Structures

The presented advances in structural research allow one to search for a means of new classification for amorphous solids. Different concepts of classification and comparisons encompassing a number of non-ordered natural and theoretical systems were described in a milestone publication by Weaire and Rivier [71].

In a recent paper [72], the silica film structures in its crystalline and vitreous state were compared to structural elements and configurations of other network structures, e.g., Si(111) 7×7 reconstruction [73], triangle rafts [66], amorphous graphene [74], copper oxide [75], molecular network structures [76], and bubble rafts [77, 78].

For all these networks, we can analyze real space structure data to determine characteristic properties and define descriptors of amorphous structures. The different network systems range from highly-ordered to completely unordered, include experiments and theoretical models, and span length scales from Ångströms to millimeters in bond length equivalents (Fig. 16.16).

All networks consist of rings that are defined by the number of comprised connection points (structural equivalents to Si atoms in the silica film). For each system, a ring size distribution with six-membered rings as the most abundant species can be determined. By calculating the second and third central moment of each ring size probability distribution, the variance and the skewness of a distribution can be captured in one number and allow for quick comparison.

The ring size probability can also be plotted versus the ring size on a logarithmic axis. This lognormal probability plot was suggested by Shackelford and Brown [66]. They postulated that a lognormal ring size distribution is inherent to all amorphous networks. We find that this is true except for the network formed by the bubble raft.

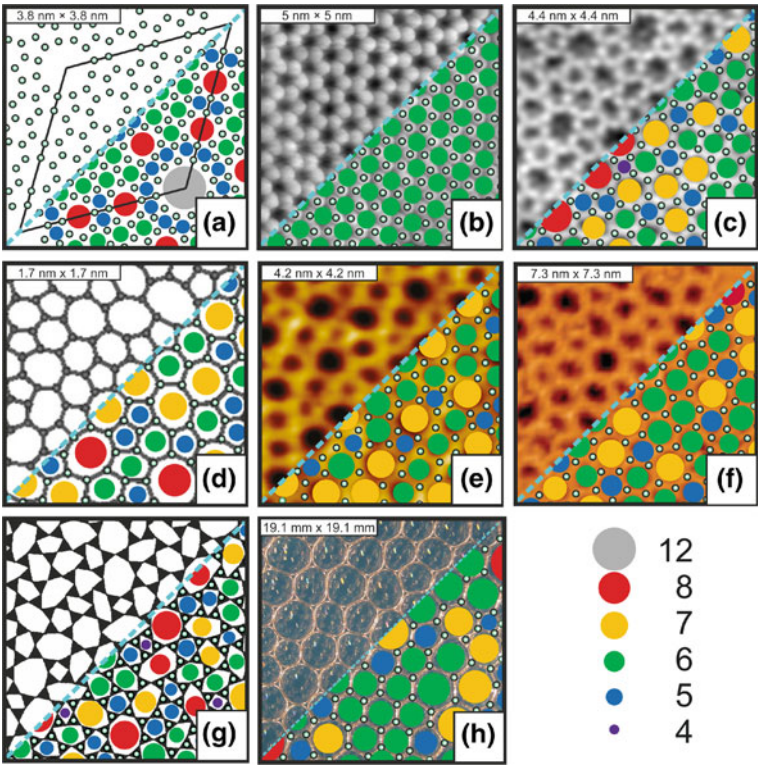

Fig. 16.16 Comparison of different network structures. Connection points in the center of the occurring ring structures are marked with *small green circles*. Different sized rings are indicated with respective *colors* and partially superimposed onto the images. **a** Model of a Si(111) surface in the 7 × 7 reconstruction [73]. A *rhombus shape* indicates the unit cell. Si positions are marked with *small green circles*, different ring sizes are marked in *different colors* on part of the model. Five-, six- and eight-membered rings, occur in this complex crystalline surface. The unit cell also contains one 12-membered ring. **b** STM image of a crystalline SiO_2 sheet (taken from [55]). The contrast reveals the Si positions of the SiO_2 film, which are partly marked with *small green circles*. Six-membered rings (marked with *large green circles* on part of the image) are the only ring size in this highly ordered system. **c** nc-AFM image reveals the atomic structure of an amorphous SiO_2 bilayer [72]. Four- to nine-membered rings occur, six-membered rings exhibit the highest occurrence. **d** A computational model for a sheet of amorphous graphene [74]. On part of the image, C positions are indicated with *small green circles* and different ring sizes are shown with *colored circles*. In addition to the five- to nine-membered rings also two 12-membered rings occur. **e** STM image of a defect-rich $Cu_2O(111)$ surface is shown [75]. It is partly superimposed with *small green spheres* at the O positions and *colored circles* indicating polygon size. In the Cu_2O, only five-, six- and seven-membered rings are observed. **f** STM image of an amorphous film of polymerized TBPB-Molecules on a Au(111) substrate [76]. The molecule centers constitute the connection points of the resulting amorphous network, marked with *small green circles*. Rings from four to eight connection points are observed. **g** The image shows a triangle raft suggested by J. Shackelford as a model for amorphous SiO_2 networks [66]. The algorithm for creating the triangle raft limits possible ring sizes from four to eight. **h** Photo of a macroscopic bubble raft. Soap bubbles form a space-filling arrangement that exhibits different sized polygons (shown with *colored circles*) and lacks long-range order. Ring sizes from four to eight are observed

This deviation is attributed to the larger variation in connection point distances, since the formation is not governed by chemical bond length or angle limitations.

Diffraction techniques yield total pair correlation functions including all atomic positions. An advantage of real space information is the possibility to discern between different species. Atomic position data were used to create partial pair correlation functions of the connection points. They allow conclusions regarding characteristic building unit distances and degree of order in the system. All systems exhibit similar characteristic bond distances far beyond the primary tetrahedral building block.

An additional benefit of real space information is the information regarding network topology over a larger scale. Several preferred arrangements of ring sizes have been identified as characteristic larger building units. They all consist of four rings in a cluster of the sequence A-B-B-A with two rings of size B sharing two Si-atoms and a ring of size A on either side, sharing one of those Si atoms, respectively. The occurrence of the 5-7-7-5, 7-5-5-7, the 5-8-8-5 and the 8-5-5-8 clusters have been analyzed and their occurrence probability is in line with a qualitative model of ring strain.

These different approaches at structure analysis can serve as a starting point for discussing and comparing unordered network structures in the future.

16.9 Summary

This vitreous silica model system, which can be investigated by well-established surface science tools, provides the unique possibility to study an amorphous model system with atomic resolution in real space.

The structure of this atomically flat and extended vitreous silica film on Ru(0001) has been presented. nc-AFM/STM revealed the thin film's atomic arrangement consisting of corner-sharing SiO_4 units. These silica building blocks form a complex network which lacks long-range order and registry to the substrate. This model system corroborates Zachariasen's predictions of a random network theory for glass structures. An atomic model of the topmost Si and O atoms has been directly derived from nc-AFM/STM images. The atomic structure has been discussed in the following ranges: the SiO_4 tetrahedral unit, interconnection of adjacent structural units, network topology, and longer range density fluctuations. Distances, angles, PCFs and histograms of ring sizes were given. A comparison between the PCF derived from our experimental model and the PCF obtained in diffraction experiments on bulk vitreous silica was drawn and showed satisfying agreement.

The behavior of the ring size distribution at a crystalline-vitreous interface was investigated. A gradual and smooth transition at the interface was found, where five and sevenfold rings occur closer to the crystalline region than four-, eight-, and nine-membered rings.

Certainly, such structural studies are a step forward in developing of a comprehensive framework for understanding amorphous networks.

In future experiments, the aim is to directly follow glass-formation phenomena. A possible route to do so is the application of the spectro-microscope SMART (spectro-microscope with aberration correction for many relevant techniques) [79] that was installed at the BESSY II (Berliner Elektronen-Speicherring-Gesellschaft für Synchrotronstrahlung) electron storage ring. This instrument enables for real-time observation of layer growth, structure formation, diffusion and reaction fronts as well as phase transitions. Future work might allow for a direct assessment of atomic structures at transition temperatures, where the liquid solidifies to either the crystalline or the amorphous state. In current experiments, the preparation of this unique silica film is adapted to the SMART setup. But also certain designs of SPMs presented in the literature have been shown to be, in principle, capable of following atomic motions at elevated temperature. Results from such machines may open new room for modeling the dynamics in glasses [80]. Studying vitreous materials at this scale will have a great impact on the general understanding of dynamic processes in amorphous bulk materials [3].

The silica film might also be used in the context of Cr-doped porous silica glass as a model material to describe Phillips catalyst properties [81]. Doping [82], additional growth [83], adsorption, and chemical reactivity [84] studies on this silica based film system are still the focus of ongoing experiments.

It should be mentioned that these silica films can be grown on various substrates [12, 85–87], which leaves room for the possibility of a completely new materials class of its own. Band structure measurements or other materials properties of this silica film might reveal unexpected features similar to those of graphene. This film may even find applications as a new gate material in the semiconductor industry. However, this strongly depends on the final stability and properties of this film system.

To conclude, by this work our understanding of oxide surface structures and complex materials, e.g., amorphous solids, was significantly enhanced owing to the use of high-resolution imaging and spectroscopy by SPM. The presented work can be referenced as a stepping-stone for future studies.

Acknowledgments The authors would like to thank Hans-Peter Rust and Gero Thielsch for major contributions to the development and maintenance of the experimental setup. Furthermore, we would like to acknowledge Kristen Burson, Thomas König, Georg Hermann Simon and Stefanie Stuckenholz for fruitful discussions.

References

1. S. Sastry, P.G. Debenedetti, F.H. Stillinger, Nature **393**, 554 (1998)
2. R. Zallen, *The Physics of Amorphous Solids* (Wiley-VCH Verlag GmbH & Co. KGaA, Weinheim, 2004)
3. L. Berthier, G. Biroli, Rev. Mod. Phys. **83**, 587 (2011)
4. Corning Incorporated, One Riverfront Plaza Corning, NY 14831 USA
5. P.G. Debenedetti, F.H. Stillinger, Nature **410**, 259 (2001)
6. W.H. Zachariasen, J. Am. Chem. Soc. **54**, 3841 (1932)
7. M. Wuttig, Phys. Status Solidi B **249**, 1843 (2012)

8. J.T. Randall, H.P. Rooksby, B.S. Cooper, Z. Krist **75**, 196 (1930)
9. B.E. Warren, J. Am. Ceram. Soc. **17**, 249 (1934)
10. T. Schroeder, M. Adelt, B. Richter, M. Naschitzki, M. Bäumer, H.-J. Freund, Surf. Rev. Lett. **7**, 7 (2000)
11. D. Löffler, J.J. Uhlrich, M. Baron, B. Yang, X. Yu, L. Lichtenstein, L. Heinke, C. Büchner, M. Heyde, S. Shaikhutdinov, H.-J. Freund, R. Włodarczyk, M. Sierka, J. Sauer, Phys. Rev. Lett. **105**, 146104 (2010)
12. L. Lichtenstein, C. Büchner, B. Yang, S. Shaikhutdinov, M. Heyde, M. Sierka, R. Włodarczyk, J. Sauer, H.-J. Freund, Angew. Chem. Int. Ed. **51**, 404 (2012)
13. G. Binnig, H. Rohrer, Helv. Phys. Acta **55**, 726 (1982)
14. G. Binnig, H. Rohrer, C. Gerber, E. Weibel, Phys. Rev. Lett. **49**, 57 (1982)
15. G. Binnig, C.F. Quate, C. Gerber, Phys. Rev. Lett. **56**, 930 (1986)
16. F.J. Giessibl, Science **267**, 68 (1995)
17. S. Morita, R. Wiesendanger, E. Meyer (eds.), *Noncontact Atomic Force Microscopy* (Springer, Berlin, 2002)
18. S. Morita, R. Wiesendanger, F.J. Giessibl (eds.), *Noncontact Atomic Force Microscopy*, vol 2 (Springer, Berlin, 2009)
19. W. Häberle, J. Hörber, F. Ohnesorge, D. Smith, G. Binnig, Ultramicroscopy **42–44**, 1161 (1992)
20. S.A. Elrod, A.L. de Lozanne, C.F. Quate, Appl. Phys. Lett. **45**, 1240 (1984)
21. D.P.E. Smith, G. Binnig, Rev. Sci. Instrum. **57**, 2630 (1986)
22. G. Meyer, Rev. Sci. Instrum. **67**, 2960 (1996)
23. C. Wittneven, R. Dombrowski, S.H. Pan, R. Wiesendanger, Rev. Sci. Instrum. **68**, 3806 (1997)
24. S.H. Pan, E.W. Hudson, J.C. Davis, Rev. Sci. Instrum. **70**, 1459 (1999)
25. M. Kugler, C. Renner, Ø. Fischer, V. Mikheev, G. Batey, Rev. Sci. Instrum. **71**, 1475 (2000)
26. J.W. Lyding, S. Skala, J.S. Hubacek, R. Brockenbough, G. Gammie, Rev. Sci. Instrum. **59**, 1897 (1988)
27. B.C. Stipe, M.A. Rezaei, W. Ho, Rev. Sci. Instrum. **70**, 137 (1999)
28. B.J. McIntyre, M. Salmeron, G.A. Somorjai, Rev. Sci. Instrum. **64**, 687 (1993)
29. F. Ohnesorge, G. Binnig, Science **260**, 1451 (1993)
30. J. Wintterlin, J. Trost, S. Renisch, R. Schuster, T. Zambelli, G. Ertl, Surf. Sci. **394**, 159 (1997)
31. M.J. Rost, L. Crama, P. Schakel, E. van Tol, G.B.E.M. van Velzen-Williams, C.F. Overgauw, H. ter Horst, H. Dekker, B. Okhuijsen, M. Seynen, A. Vijftigschild, P. Han, A.J. Katan, K. Schoots, R. Schumm, W. van Loo, T.H. Oosterkamp, J.W.M. Frenken, Rev. Sci. Instrum. **76**, 0537101 (2005)
32. A. Bryant, D.P.E. Smith, C.F. Quate, Appl. Phys. Lett. **48**, 832 (1986)
33. R. Wiesendanger, Rev. Mod. Phys. **81**, 1495 (2009)
34. C.J. Chen, *Introduction to Scanning Tunneling Microscopy* (Oxford University Press, Oxford, 2009)
35. J.P. Rabe, S. Buchholz, Science **253**, 424 (1991)
36. J.P. Rabe, S. Buchholz, Phys. Rev. Lett. **66**, 2096 (1991)
37. L. Gross, F. Mohn, N. Moll, P. Liljeroth, G. Meyer, Science **325**, 1110 (2009)
38. D.M. Eigler, E.K. Schweizer, Nature **344**, 524 (1990)
39. S.-W. Hla, L. Bartels, G. Meyer, K.-H. Rieder, Phys. Rev. Lett. **85**, 2777 (2000)
40. D.G. de Oteyza, P. Gorman, Y.-C. Chen, S. Wickenburg, A. Riss, D.J. Mowbray, G. Etkin, Z. Pedramrazi, H.-Z. Tsai, A. Rubio, M.F. Crommie, F.R. Fischer, Science **340**, 1434 (2013)
41. J.V. Lauritsen, M. Reichling, J. Phys. Condens. Matter **22**, 263001 (2010)
42. R. Wiesendanger, M. Ringger, L. Rosenthaler, H. Hidber, P. Oelhafen, H. Rudin, H.-J. Güntherodt, Surf. Sci. **181**, 46 (1987)
43. W. Raberg, K. Wandelt, Appl. Phys. A Mater. Sci. Process. **66**, 1143 (1998)
44. D.E. Bürgler, C.M. Schmidt, D.M. Schaller, F. Meisinger, T.M. Schaub, A. Baratoff, H.-J. Güntherodt, Phys. Rev. B **59**, 10895 (1999)
45. H. Schlenz, A. Kirfel, K. Schulmeister, N. Wartner, W. Mader, W. Raberg, K. Wandelt, C. Oligschleger, S. Bender, R. Franke, J. Hormes, W. Hoffbauer, V. Lansmann, M. Jansen, N. Zotov, C. Marian, H. Putz, J. Neuefeind, J. Non-Cryst. Solids **297**, 37 (2002)

46. J.-F. Poggemann, G. Heide, G. Frischat, J. Non-Cryst. Solids **326–327**, 15 (2003)
47. G. Frischat, J.-F. Poggemann, G. Heide, J. Non-Cryst. Solids **345–346**, 197 (2004)
48. W. Raberg, A. Ostadrahimi, T. Kayser, K. Wandelt, J. Non-Cryst. Solids **351**, 1089 (2005)
49. J.S. Villarrubia, J. Res. Nat. Inst. Stand. Technol. **102**, 425 (1997)
50. M. Heyde, M. Kulawik, H.-P. Rust, H.-J. Freund, Rev. Sci. Instrum. **75**, 2446 (2004)
51. H.-P. Rust, M. Heyde, H.-J. Freund, Rev. Sci. Instrum. **77**, 043710 (2006)
52. M. Heyde, G.H. Simon, H.-P. Rust, H.-J. Freund, Appl. Phys. Lett. **89**, 263107 (2006)
53. T. König, G.H. Simon, L. Heinke, L. Lichtenstein, M. Heyde, Beilstein J. Nanotechnol. **2**, 1 (2011)
54. M. Heyde, G.H. Simon, L. Lichtenstein, Phys. Status Solidi B **250**, 895 (2013)
55. L. Lichtenstein, M. Heyde, H.-J. Freund, J. Phys. Chem. C **116**, 20426 (2012)
56. A.C. Wright, J. Non-Cryst. Solids **106**, 1 (1988)
57. A.C. Wright, J. Non-Cryst. Solids **179**, 84 (1994)
58. H.S. Peiser, H.P. Rooksby, A.J.C. Wilson (eds.), X-Ray Diffraction by Polycrystalline Materials (Institute of Physics, London, 1955)
59. R.L. Mozzi, B.E. Warren, J. Appl. Crystallogr. **2**, 164 (1969)
60. D.I. Grimley, A.C. Wright, R.N. Sinclair, J. Non-Cryst. Solids **119**, 49 (1990)
61. R.M. Van Ginhoven, H. Jónsson, L.R. Corrales, Phys. Rev. B **71**, 024208 (2005)
62. R.J. Bell, P. Dean, Philos. Mag. **25**, 1381 (1972)
63. X. Yuan, A. Cormack, J. Non-Cryst. Solids **319**, 31 (2003)
64. J.R.G. Da Silva, D.G. Pinatti, C.E. Anderson, M.L. Rudee, Philos. Mag. **31**, 713 (1975)
65. L. Gladden, J. Non-Cryst. Solids **119**, 318 (1990)
66. J.F. Shackelford, B.D. Brown, J. Non-Cryst Solids **44**, 379 (1981)
67. L. Lichtenstein, M. Heyde, H.-J. Freund, Phys. Rev. Lett. **109**, 106101 (2012)
68. A. Stone, D. Wales, Chem. Phys. Lett. **128**, 501 (1986)
69. F. Wooten, D. Weaire, J. Non-Cryst. Solids **144**(Part 2), 681 (1989)
70. P.Y. Huang, S. Kurasch, J.S. Alden, A. Shekhawat, A.A. Alemi, P.L. McEuen, J.P. Sethna, U. Kaiser, D.A. Muller, Science **342**, 224 (2013)
71. D. Weaire, N. Rivier, Contem. Phys. **50**, 199 (2009)
72. C. Büchner, P. Schlexer, L. Lichtenstein, S. Stuckenholz, M. Heyde, H.-J. Freund, Zeitschrift für Physikalische Chemie **228**, 587 (2014)
73. K. Takayanagi, Y. Tanishiro, M. Takahashi, S. Takahashi, J. Vac. Sci. Technol. A **3**, 1502 (1985)
74. Y. Li, D.A. Drabold, Phys. Status Solidi B **250**, 1012 (2013)
75. F. Yang, Y. Choi, P. Liu, D. Stacchiola, J. Hrbek, J.A. Rodriguez, J. Am. Chem. Soc. **133**, 11474 (2011)
76. M.O. Blunt, J.C. Russell, N.R. Champness, P.H. Beton, Chem. Commun. **46**, 7157 (2010)
77. L. Bragg, J.F. Nye, Naturwissenschaften **34**, 328 (1947)
78. L. Bragg, J.F. Nye, Proc. R. Soc. Lond. Ser. A. Math. Phys. Sci. **190**, 474 (1947)
79. R. Fink, M. Weiss, E. Umbach, D. Preikszas, H. Rose, R. Spehr, P. Hartel, W. Engel, R. Degenhardt, R. Wichtendahl, H. Kuhlenbeck, W. Erlebach, K. Ihmann, R. Schlögl, H.-J. Freund, A. Bradshaw, G. Lilienkamp, T. Schmidt, E. Bauer, G. Benner, J. Electron Spectrosc. Relat. Phenom. **84**, 231 (1997)
80. P.W. Anderson, Proc. Natl. Acad. Sci. **92**, 6653 (1995)
81. A. Budnyk, A. Damin, C. Barzan, E. Groppo, C. Lamberti, S. Bordiga, A. Zecchina, J. Catal. **308**, 319 (2013)
82. J.A. Boscoboinik, X. Yu, B. Yang, F.D. Fischer, R. Włodarczyk, M. Sierka, S. Shaikhutdinov, J. Sauer, H.-J. Freund, Angew. Chem. Int. Ed. **51**, 6005 (2012)
83. B. Yang, W.E. Kaden, X. Yu, J.A. Boscoboinik, Y. Martynova, L. Lichtenstein, M. Heyde, M. Sterrer, R. Włodarczyk, M. Sierka, J. Sauer, S. Shaikhutdinov, H.-J. Freund, Phys. Chem. Chem. Phys. **14**, 11344 (2012)
84. J.A. Boscoboinik, X. Yu, E. Emmez, B. Yang, S. Shaikhutdinov, F.D. Fischer, J. Sauer, H.-J. Freund, J. Phys. Chem. C **117**, 13547 (2013)
85. X. Yu, B. Yang, J.A. Boscoboinik, S. Shaikhutdinov, H.-J. Freund, Appl. Phys. Lett. **100**, 151608 (2012)
86. P.Y. Huang, S. Kurasch, A. Srivastava, V. Skakalova, J. Kotakoski, A.V. Krasheninnikov, R. Hovden, Q. Mao, J.C. Meyer, J. Smet, D.A. Muller, U. Kaiser, Nano Lett. **12**, 1081 (2012)
87. E.I. Altman, U.D. Schwarz, Adv. Mater. Interf. **1**, 1400108 (2014)

Chapter 17
Imaging Molecules on Bulk Insulators Using Metallic Tips

David Z. Gao, Alexander Schwarz and Alexander L. Shluger

Abstract We describe how one can produce, control, and characterize sharp metal coated tips and how these tips can achieve atomic resolution on insulating surfaces at large tip-surface separations. Our experimental results combined with DFT calculations confirm that the Cr tips possess permanent electric dipoles with the positive ends oriented towards the sample surface. By imaging the surface ions with atomic resolution, we determine the effective tip dipole moment using the image corrugation. Chemical resolution of surface ions and images of small adsorbed molecules can then be determined by using a point dipole model for representing the tip. Moreover, we demonstrate that these tips may be able to probe the dipole moment of polar molecules at the surface. Thus using metallic tips greatly reduces the complexity of interpreting experimental data while allowing for an unambiguous identification of ionic species on polar surfaces.

17.1 Introduction

Understanding the atomic surface structure and the mechanisms of adsorption, interaction, and the assembly of atoms and molecules at insulating surfaces is fundamental to many areas of surface science as well as to applications in catalysis [1], lubrication [2, 3], and molecular electronics [4–6]. Studies of individual surface defects, molecules, molecular aggregates, and more complex structures at insulating surfaces inevitably involve Noncontact Atomic Force Microscopy (NC-AFM) [7–17].

D.Z. Gao (✉) · A.L. Shluger
Department of Physics and Astronomy, University College London,
Gower Street, London WC1E 6BT, UK
e-mail: david.gao.10@ucl.ac.uk

A.L. Shluger
e-mail: a.shluger@ucl.ac.uk

A. Schwarz
Institute of Applied Physics and Microstructure Research Center, University of Hamburg,
Jungiusstr. 11, 20355 Hamburg, Germany
e-mail: aschwarz@physnet.uni-hamburg.de

© Springer International Publishing Switzerland 2015

S. Morita et al. (eds.), *Noncontact Atomic Force Microscopy*,
NanoScience and Technology, DOI 10.1007/978-3-319-15588-3_17

However, unambiguous interpretation of experimental NC-AFM images is often difficult due to the unknown structure and polarity of the NC-AFM tip apex [18, 19].

Several ways have recently been proposed to characterize and control the atomic structure of the tip. One approach has been to characterize tips using Field Ion Microscopy (FIM) [20]. Although this approach is very illuminating, it is still not practical to analyze every tip used before and/or after measurements. In Scanning Tunnelling Microscopy (STM) experiments, many sample system are known where single atoms or small molecules [19, 21] can be controllably and reproducibly transferred to the tip apex. This technique also became popular in NC-AFM albeit mainly in qplus set-ups, where NC-AFM and STM can be applied on the same sample system and thus the well-known STM recipes can be applied. In particular, CO functionalized tips have been used successfully to resolve atoms and bonds inside organic molecules [21, 22]. The imaging technique with such tips is based on measuring in the short-range repulsive regime [23], which has both advantages (it provides intramolecular resolution) and disadvantages (it may distort the image or manipulate mobile molecules). Controlled functionalization of the tip is, however, difficult to achieve on many sample surfaces, particularly at room temperature. For this reason micro-fabricated Si cantilevers with integrated pyramidal Si tips are often used in NC-AFM. However, due to the presence of directional covalent bonds, Si or oxidized Si tip apices exhibit many possible stable tip structures. Tip contamination by water and surface material makes finding tip models that provide reasonable agreement between simulated images and experiment particularly difficult (see e.g. [24, 25]).

We have recently observed that Cr coated Si tips provide atomic and chemical resolution when imaging is carried out at rather large (>0.5 nm) tip-surface separations on binary ionic surfaces [26–29]. Such tips can be prepared via thermal evaporation in-situ [26]. Moreover, the conductivity of the coated tip can be checked to ensure that it is indeed metallic [27]. These metallic tips can be used to atomically resolve flat surfaces at relatively large distances with minimal risk of contamination from the surface. Such tips were successfully employed to determine the adsorption site and adsorption geometry of single molecules on insulating surfaces with atomic accuracy [28, 29]. The chemical resolution achieved with metallic tips on the ionic substrates has been attributed to the existence of an electrostatic dipole moment at its apex. However, the magnitude and origin of this dipole is still poorly characterized.

In this chapter we describe how one can produce, control, and characterize sharp metal coated tips and how these tips can achieve atomic resolution on insulating surfaces at large tip-surface separations. By imaging the surface ions with atomic resolution, one can determine the effective tip dipole moment using the image corrugation. Chemical resolution of surface ions and images of small adsorbed molecules can then be obtained by using a point dipole model for representing the tip. This greatly reduces the complexity of interpreting experimental data while allowing for an unambiguous identification of ionic species on polar surfaces.

17.2 Experimental Set-Up and Procedures

All experiments described in this chapter were performed with a home-built low temperature atomic force microscope in ultrahigh vacuum conditions at a base temperature of about 8 K [30]. Imaging was performed in the constant Δf mode using the frequency modulation technique [31] at a constant amplitude A typically of a few nm. 3D force field spectroscopy data were recorded as described in [32].

To prepare clean sample surfaces the side faces of NaCl and NiO crystals were coated with a metal and clamped (not glued) onto metallic holders. After in-situ cleavage along (001) planes the samples were heated to about 600 and 800 K, respectively, to remove residual charges. Note that the metallized side faces facilitate the discharge process.

Co-Salen and CO molecules were deposited onto the cold substrates located on the sample stage inside the microscope. Co-Salen molecules were evaporated from a miniaturized evaporator inserted into the cantilever stage during the deposition process [33]. CO was simply dosed into the cryostat chamber via a leak valve.

17.2.1 Tip Preparation and Control

It is well established that on polar surfaces, the polarity of the tip apex determines whether anions or cations are imaged as protrusions [19]. Hence it is often difficult to assign image features to particular surface atoms without knowing the tip polarity. Moreover, the stability and reproducibility of atomically resolved images are still hampered by difficulties in preparing and characterizing the tip apex and by structural instabilities caused by the strong tip-surface interaction [24].

In the experiments discussed in this chapter we used metal coated Si cantilevers. These tips were prepared using the following procedure. The as-purchased Si cantilevers with integrated tips (typical eigenfrequencies f_0 of about 200 kHz and spring constants c_z of about 150 N/m) possess an oxide layer, either due to the manufacturing process itself or by oxidation in air. We note in passing that this is also true for tips made from metal wires such as the ones used in qplus set-ups. After introduction into a UHV system they are cleaned from air-borne contaminations by heating in in-situ to about 600 K. Thereafter, a few nm of Cr are deposited onto the whole cantilever by thermal evaporation so that a conductive path between the tip apex and cantilever holder was formed. Cr adheres well to the silicon oxide layer and thin Cr films have been used in the past to improve the deposition of other metals [34–36] on oxidized Si. Note that our pre-cleaning does not remove this oxide layer. We also tried depositing other metals, including Fe and Ti. They behave similarly, but, unlike Cr and Ti, Fe do not adhere well to the oxidized Si. After metallization, the cantilevers are transferred into the low temperature microscope and further characterized by $\Delta f\,(U)$-curves; cf. Fig. 17.1. Such curves can be recorded repeatedly, e.g., after tip changes.

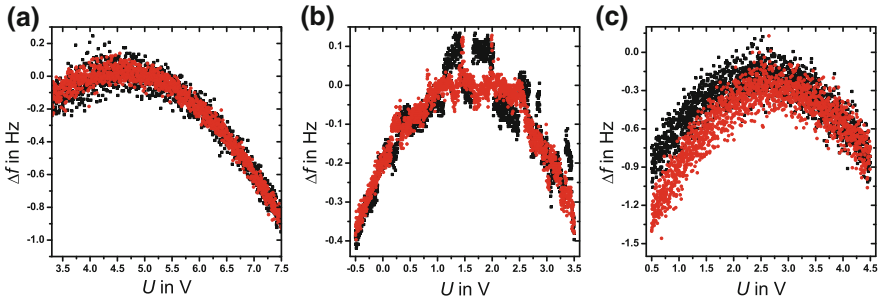

Fig. 17.1 Three types of exemplary $\Delta f(U)$-curves obtained with initially metal coated tips. The actual conductivity of the tip apex can be evaluated as follows: **a** metallic tip apex; **b** insulating tip apex with localized states; **c** badly conducting tip

Figure 17.1 displays three representative $\Delta f(U)$-curves with Cr-coated tips. A sign of formation of a metallic tip are smooth parabolic curves without jumps, which look identical independent of the sweeping direction (i.e. no hysteretic behaviour between bias sweep from positive to negative voltages and vice versa), cf. Fig. 17.1a. Tips that do not possess a metallic apex, exhibit discontinuities in the curves indicative of charge reconfigurations due to tunnelling processes between localized states at the tip apex; cf. Fig. 17.1b. For such tips, either the Cr coating was not sufficient or the tip-sample interaction led to a transfer of Cr to the surface exposing an insulating oxide layer on a Si tip. To exclude tunnelling from a metallic tip into localized states in an insulating sample, we recorded $\Delta f(U)$-curves at rather large tip-sample distances. Figure 17.1c shows another type of $\Delta f(U)$-curves. The apparent hysteresis can be attributed to slow charge relaxation processes implicating a badly conducting tip apex. It should be mentioned that discrete jumps are probably more difficult to observe at room temperature and one has to make sure that the hysteresis does not stem from a drifting tip-sample distance during recording of a $\Delta f(U)$-curve.

Although curves similar to those shown in Fig. 17.1a, are in our experience an unambiguous sign of a metallic tip, we cannot be absolutely sure that the tip has not picked up single surface atoms. However, calculations [28] demonstrate that this is unlikely for Cr tips on flat polar surfaces without forming a hard contact with the surface. Moreover, using the metal coated tips for several years we have noticed that they are much more likely to lose rather than pick up material if hard contact is avoided: after tip changes, we usually observe bumps rather than holes on the surface and contacting the surface leads to tips that are usually shorter (visible by the movement of the z-piezo to keep Δf constant) and blunter (a larger negative Δf is required to obtain the same image quality).

If a tip apex becomes non-metallic, it is often possible to transfer enough atoms from a metallic sample to the apex by dipping the tip into the surface. If insulating surfaces are studied, it is sometimes possible to switch to a metallic sample (Cu is very suitable, because it is a rather soft material) to make the tip apex metallic again and the original sample can be investigated further. However, if the metallic

sample used to make the tip apex metallic again is chemically different from the previously evaporated material, the tip apex material will be most likely different as well. More specifically, about 90 % of Fe, Cr, and Ti coated tips are suitable for atomic resolution; however, frequently only after intended or unintended tip changes. About 70 % remain metallic before atomic resolution is obtained for the first time. Subsequent tip changes sooner or later result either in non-metallic or blunt tips.

17.3 Theoretical Methodology

It is now customary in the NC-AFM community that experimental observations are compared with theoretical images obtained using tip-surface interaction force-fields. The latter are produced with density functional theory (DFT) based calculations or with atomistic modelling using classical inter-atomic potentials and images then simulated using virtual AFM (vAFM) or other less sophisticated methods [19]. Since vAFM codes integrate the equation of motion of the cantilever motion and model feedback circuits found in a real apparatus [37–40], this approach can provide a complete simulation of the real experiment.

The DFT calculations presented in this chapter were performed using the CP2K code [41, 42]. Simulating organic molecules at surfaces requires special care to account for basis set superposition error (BSSE). A semi empirical correction method [43] was employed to account for long-range dispersion interactions. The methods used in our work are described in detail in several publications [28, 29, 44]. Once the electronic structure of the system is properly calculated, it can be used to predict the electrostatic interactions between a metallic AFM tip and the sample.

Cr surfaces and tip asperities were constructed based on prior experimental studies. Scanning electron micrographs of sputtered Cr films on SiO_2 [34] show that deposited Cr films may be rough and decorated with a variety of asperities. On the other hand, FIM experiments [20] on W tips show that metal coated tips appear spherical and possess (110) terraces near the tip apex. Using these results, Cr coated tips were approximated as macroscopic spheres terminated by (110) terraces decorated by a variety of asperities. Representative nano-tips were constructed as pyramidal asperities on the Cr(110) surface terrace, as shown in Fig. 17.3. Asperities on the Cr(001) surface were constructed in the same way. Calculations were carried out using a 2D periodic slab model [44].

Dipole moments of these asperities can be calculated by considering the electrostatic potential averaged across the xy-plane in the 2D periodic cell. The presence of an asperity will shift the vacuum level on either side of the slab and change the work function. This effect can be considered using the parallel plate capacitor model [45]. The work function change is related to the magnitude of the dipole moment and the surface area as follows:

$$\Delta W = \frac{eD}{\epsilon_0 A}, \tag{17.1}$$

where D is the dipole moment due to the presence of an asperity, A is the area of the system, ϵ_0 is the electric permittivity of vacuum, and e is the unit of elementary charge.

If the tip-surface distance is large enough, it is reasonable to assume that the structural deformation of both the metallic tip and the surface can be neglected. However, electronic relaxations may be more significant and need to be considered. Image charges and dipoles in particular may contribute significantly to the forces. Fortunately, when studying bulk insulating surfaces, the only image charge that can be induced within our system is the one in the metallic tip by a surface feature. The distance between the image and the surface will be much larger than the distance between the tip apex and the surface, resulting in a greatly reduced contribution. The forces resulting from image interactions can be calculated using methods described e.g. in [46]. In our case, these contributions are weak and are neglected for the sake of simplicity.

The remaining contribution to mid-range forces can be calculated as an electrostatic interaction between the dipole of the metallic tip and the surface. The AFM tip in this model is approximated by a point dipole far from the surface and the forces experienced by this tip can be calculated as follows:

$$F_z = \frac{d}{dz}[D_x \frac{dV_E}{dx} + D_y \frac{dV_E}{dy} + D_z \frac{dV_E}{dz}], \tag{17.2}$$

where F is the normal force felt by the tip, D_{xyz} represents the orientation and magnitude of the dipole moment of the AFM tip, and V_E is the electrostatic potential of the surface at each point of interaction. In the case of blunt tips, the tip structure is represented using an array of point dipoles. The forces experienced by a blunt tip consisting of n dipoles can be calculated as follows:

$$F_z = \sum_{i=1}^{n} \frac{d}{dz}[D_{ix} \frac{dV_E}{dx} + D_{iy} \frac{dV_E}{dy} + D_{iz} \frac{dV_E}{dz}]. \tag{17.3}$$

These forces are combined with the long range contributions to generate a complete 3-dimensional force-field. Finally, vAFM simulations are performed using a previously developed code [37].

17.4 Chemical Resolution on NaCl(001) and NiO(001)

We first briefly review the recent results on NC-AFM imaging of Co-Salen molecules adsorbed on the (001) surface of bulk NaCl and NiO [28, 29]. Co-Salen ($Co(C_{16}H_{14}N_2O_2)$),[1] is a complex that is known for its ability to reversibly coordinate molecular oxygen [47] and is used in numerous applications in material chemistry

[1] Other names for Co-Salen are Salcomine and N, N′-1,2-Ethylenebis(salicylideniminato)-cobalt(II).

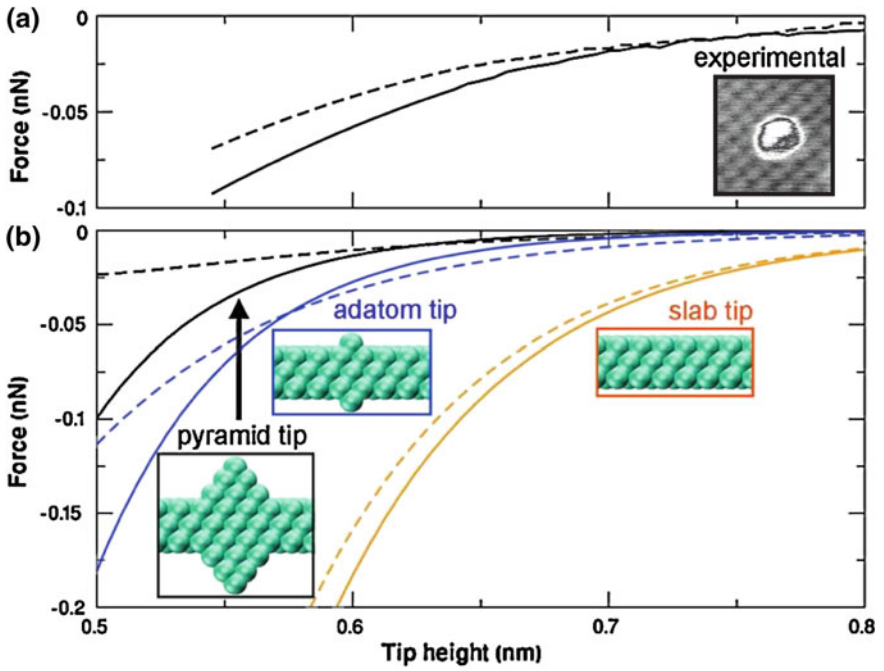

Fig. 17.2 **a** Short range experimental force curves above Cl (*solid line*) and Na (*dashed line*) ions, where the tip height at closest approach has been set to match the difference in forces of the pyramid tip model. The *inset* shows the atomically resolved NaCl(001) substrate with Co-Salen marker molecule in the *center*. **b** Simulated force curves for each of the three tip models (see *insets*) above Cl and Na ions, represented by maxima and minima, respectively, in the *inset* of (**a**)

and transition metal catalysis [48]. Using carefully prepared Cr-coated tips allowed us to unambiguously identify the surface atoms, image the molecule on the atomically resolved surface, and identify the surface adsorption site and geometry.

Atomic resolution imaging and subsequent 3D force field spectroscopy [32] with a metallic Cr-coated tip ($\Delta f(U)$-curve as in Fig. 17.1a) have first been performed on NaCl(001) with adsorbed Co-Salen molecules in [28] (see image in the inset of Fig. 17.2a). Details of the procedure used to extract force curves from the experimental $\Delta f(x, y, z)$ data set can be found in [27].

Although no absolute z-scale can be obtained from experimental spectroscopy curves alone, the presence of a marker molecule provides an estimate of the lower limit of absolute tip-sample separation. In the presented data set, the distance of closest approach was chosen to obtain the best resolution of the surface ions in the vicinity of the molecule, but without altering the original position of the molecule. DFT calculations [28] have demonstrated that the Co-Salen molecule adsorbs on NaCl(001) in a planar configuration at $\approx$0.38 nm above the surface plane with the Co ion directly above the surface Cl ion. Calculations presented in [27] demonstrate that the short-range interaction between the Cr tip apex and the Co-Salen enters

the repulsive regime at a separation about 0.15 nm. Assuming that closer approach would lead to strong deformation or displacement of the molecule, we estimate that the minimum tip-surface separation required to avoid manipulating the molecule is ≈0.53 nm.

Based on the position of the Co-Salen marker molecule, which adsorbs with its central Co-atom on top of Cl surface sites, protrusions in the inset of Fig. 17.2a represent the surface Cl ions [28]. The exemplary force curves recorded above a protrusion (Cl) and depression (Na), respectively, are shown in Fig. 17.2a. These observations led to the suggestion [27] that imaging with clean metallic tips at relatively long tip-surface separations (>0.5 nm) can directly and unambiguously identify anions in atomically resolved NC-AFM images of binary ionic insulators and probably other more complex polar surfaces.

To test whether one can unambiguously identify oxygen ions on a cubic oxide surface using a Cr coated tip, individual Co-Salen molecules have been imaged on a more chemically reactive (001) surface of the antiferromagnetic oxide NiO. The latter has the same crystal structure as NaCl, but a much smaller lattice constant [29]. The (001) surface of NiO is a well-defined charge neutral easy cleavage plane that can be prepared cleanly under ultrahigh vacuum conditions. Using a Cr coated metallic tip we were able to simultaneously image both the molecule and the substrate. Our results demonstrate that Co-Salen binds more strongly to NiO (001) than to NaCl (001) with the center of the molecule approximately above a protrusion in the image. Our theoretical calculations demonstrate that Co-Salen adsorbs with the Co atom directly above a surface O ion. Combined, these results show that the protrusions or bright spots in the NC-AFM image correspond to O ions of the surface. This confirms the conclusion of our study of Co-Salen on NaCl(001) [27] that protrusions in NC-AFM images of binary insulator surfaces obtained with metallic tips should correspond to surface anions. These results also demonstrate that using metallic tips allows one to determine the adsorption sites and the geometry of individual molecules on inert insulating surfaces, such as NaCl(001) and NiO(001).

17.5 Metallic Tip Characterization and Imaging Mechanisms

The fact that metal-coated tips interact with ionic surfaces at long distances strong enough to resolve the surface ions has been explained by the presence of a dipole moment at the tip apex which interacts with the surface electrostatic potential. It is generally accepted that step features at metal surfaces possess dipole moments due to the incomplete screening of positive ion cores by conduction electrons due to the Smoluchowski effect [49]. This is consistent with the work function measurements performed on the Au(111) [50, 51], Cu(111) [51], Pt(111) [52], and W(110) [52] surfaces, which all indicated the presence of a 0.1–0.2 D dipole moment. Calculations using the jellium model predict that this dipole is proportional to step height and

screening length [53]. Therefore, it was suggested that the Smoluchowski effect is also the origin of the dipole moment at metallic tip apices. However, the magnitude of the dipole moment observed at step edges appears to be too small to explain the experimentally observed image contrast at large tip-surface separations. The required larger dipole moment at the tip apex in its turn demands sharper tip features [27] with more lower-coordinated atoms. Such atomically sharp stable metallic tip apices can be expected to have a close-packed pyramid-like pointed structure [54]. The existence of such features can be inferred from NC-AFM and other experiments, but cannot be proven directly by imaging metal coated Si tips. Furthermore, $\Delta f(U)$-curves only indicate that a tip is metallic, but more quantitative information, e.g., the magnitude of the dipole moment at the tip apex, cannot be extracted from them. The recent results [44] presented below address these important issues.

17.5.1 Characterizing Metallic AFM Tips

To gain further insight into the mechanism of the interaction of Cr-coated tips with polar surfaces, we first construct a simple tip model. The deposited Cr exposes the (110) surface and these films are known to be quite rough; their morphology depends on the method of deposition and the film thickness [34–36]. Therefore we approximate our Cr coated tips as macroscopic spheres terminated by Cr(110) terraces (Cr crystallized in the bcc structure). Representative nano-tips were constructed as pyramidal asperities on the Cr(110) surface, as shown in Fig. 17.3. The pyramid structure was chosen according to classic Wulff construction [55] to minimize the total surface energy of the asperity. The total dipole moment of the surface with a pyramidal nano-tip was calculated from a change in the work function of the system (see [44]). We note that using Cr clusters rather than surface slabs with pyramidal asperities shown in Fig. 17.3 may lead to incorrect predictions [56].

The dependence of the magnitude of the tip dipole moment on the number of atomic layers in the pyramid is shown in Fig. 17.4. These results agree with prior calculations [27] that predicted 1.2 D for a single adatom and 6 D for a three atom high nano-asperity and are comparable to the experimental measurements on the Au and Cu surfaces [51]. In these experiments, the dipole moment was determined to be 0.16 D/step atom on Au and 0.5 D/step atom on Cu surfaces [51]. While these results present dipole moments that are significantly smaller, they correspond to edge atoms that are better coordinated than single adatoms. It has indeed been previously predicted that the Smoluchowski effect should increase with increasing step height and decreasing coordination [53]. Larger pyramid features containing lower coordinated atoms are expected to possess much larger dipole moments than step edges.

Our results show, however, that the dipole moment of a pyramidal nano-tip does not scale linearly with pyramid height. This effect can be explained by the difference in work function between the (110) and (100) surfaces of Cr. The work function of Cr (110) was calculated to be 4.8 eV while the work function of Cr(100) was calculated

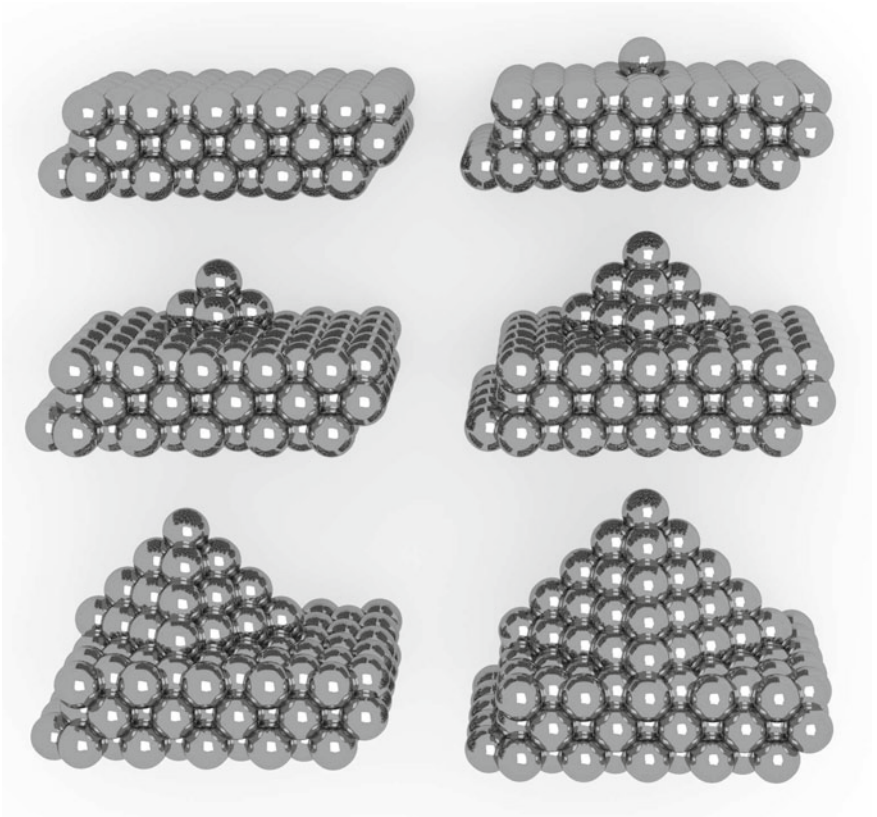

Fig. 17.3 An array of pyramid features ranging from 0 to 5 atomic layers in height constructed on the Cr(110) surface. These pyramid features represent some possible stable atomic structures found on a vapor deposited Cr tip or surface

to be 4.0 eV. As Cr(100) facets are exposed as sides of the pyramid tip on the surface of Cr(110), a charge transfer occurs that contributes to the total dipole moment of the tip. The work function near these asperities decreases until it eventually converges to the value of the Cr(100) surface itself. At this point the total dipole moment of the tip should converge as well. This suggests that the Smoluchowski effect is not the only mechanism involved and that charge transfer due to a difference in work function must be considered. It then follows that the dipole moment may be greatly reduced or even inverted in some materials [44]. The same effect can occur, if the foremost tip apex atom and the tip material are chemically different.

To illustrate this point further, we have also considered pyramidal asperities grown on the less stable Cr(100) surface. In this case, one can expect that the surface may transfer charge to the tip apex instead. The dipole moment of several pyramidal asperities grown on Cr(100) are shown in Fig. 17.5. These results show that asperities

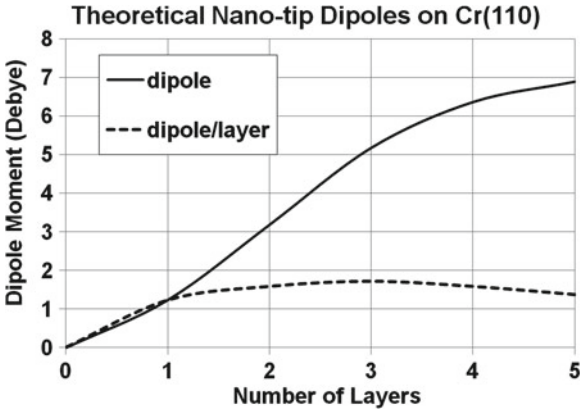

Fig. 17.4 The total dipole moment of various pyramidal nano-tips as a function of pyramid height. These tips were constructed as pyramidal asperities on the Cr(110) surface. The dipole moment found at the tip apex of these asperities increases with pyramid size but should eventually converge to a maximum value

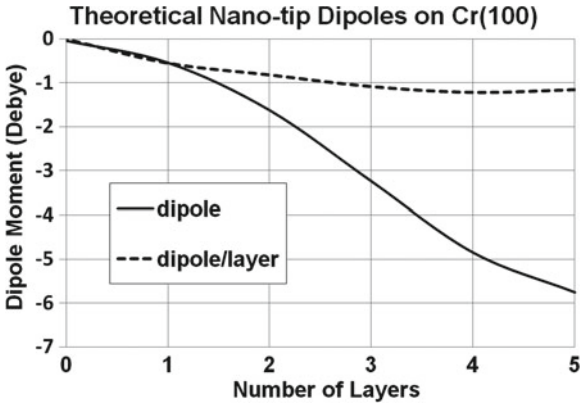

Fig. 17.5 The total dipole moment of a series of pyramidal nano-tips on Cr(100) as a function of pyramid height. The work function of the Cr(100) surface is much lower than that of the Cr(110) surface, resulting in charge transfer from the surface to the asperity apex instead

on less stable surfaces may possess dipole moments of opposite sign due to charge transfer from the surface to the asperity apex.

On Cr(110) the orientation of the dipole moment due to charge transfer matches the contribution from the Smoluchowski effect. On Cr(100), however, the two contributions work against each other and result in a lower absolute value of the dipole moment. The magnitude of these dipole moments is indeed on average 1 D lower than those predicted for the Cr(110) surface. Since it is difficult to define the work function of a small facet, this discussion is only qualitative. At the genuine nanoscale the distinction between these two effects blurs and all that can be considered is the net effect of electron density redistribution round the nano-tip.

In the following discussion we assume that the exposed surfaces in experimentally produced tips are the most stable ones, i.e., pyramidal nano-tips on Cr(110). Such tips would possess dipole moments with the positive pole oriented towards the surface. We then show that at large tip-surface separations the tip dipole can be represented using a point dipole.

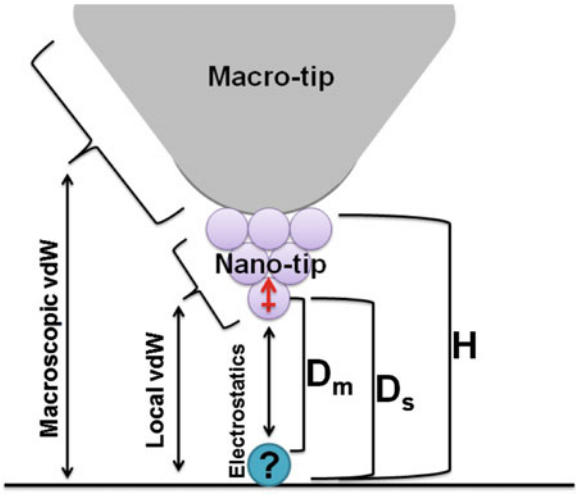

Fig. 17.6 A schematic of the proposed tip model imaging the surface and a small molecule. The main contributions to force are macroscopic vdW interactions, local vdW interactions, and mid-range electrostatic interactions. Distance between the macro-tip and the surface is defined as H, distance between the nano-tip and the surface is defined as D_s, and distance between the nano-tip and the molecule is defined as D_m

17.5.2 Explicit Determination of Tip Dipoles

To further quantify this model, we used the experimental force versus distance curves and surface images obtained on NiO(001) with Cr coated tips. We demonstrate that, assuming the point dipole approximation for a metallic AFM tip, the magnitude and orientation of this dipole can be determined from comparison of the experimental and calculated atomic corrugation on this ionic surface. To make such comparison, one needs to calculate the total tip-surface interaction.

The total tip-surface interaction force can be decomposed into long-range vdW interactions between the macro-tip and the surface, local vdW-interactions between the nano-tip and the surface, and mid-range electrostatic interactions between localized dipoles in the tip and the sample, as illustrated in Fig. 17.6. At large tip-sample distances the contribution from short-range repulsive interactions can be ignored. Note that long-range electrostatic interactions are negligible, as the average contact potential difference is compensated for by applying an appropriate bias voltage between the tip and sample.

At large tip-surface separations, only the forces due to macroscopic vdW interactions are present. This component can be accounted for using an analytical expression and fitting a set of parameters directly to the experimental data. In this simple model a tip is represented by a conical section with a spherical cap [57] and the force can be calculated with respect to the distance between the macro-tip and the surface H. To achieve that, a long-range theoretical force curve was fit to an experimental force

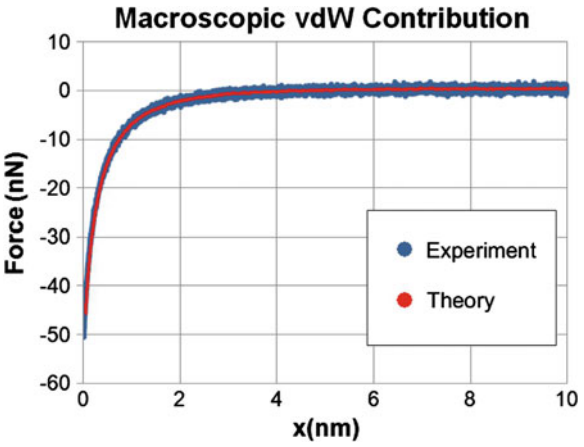

Fig. 17.7 The experimental long-range force curve compared with the theoretical long-range force curve. The mathematical functions used were chosen to physically represent the metal coated AFM tip [57]. Experimental parameters: f_0 = 186.278 kHz, $c = 144 \pm 21$ N/m, $A_0 = 0.6 \pm 0.1$ nm, Q = 20,996. Optimized tip model parameters: $A_H = 39.6 \pm 11.2 \times 10^{-20}$ J, $R = 3.95 \pm 0.87$ nm, $\gamma = 16.42° \pm 1.24°$

curve measured above the NiO(001) surface and compared in Fig. 17.7. In order to obtain a physically meaningful and unique fit, the parameters of the model were constrained in the context of what we know about our tip and the materials used in the system. The Hamaker constant A_H can be calculated using the Lifshitz theory from dielectric constants and refractive indices for a variety of inorganic materials [58]. In our case, we have constrained the value to be within a realistic range of 5×10^{-20}–60×10^{-20} J. Since the uncoated sharp Si tip had a starting radius of 2.0 nm, the Cr coated tip radius R was constrained within the range of 1.0–10.0 nm. Finally since the tip is believed to be quite sharp, the tip cone angle γ was constrained within a range of 0°–90°. The sample surface plane was defined by taking the average position of atomic nuclei on the NiO(001) surface and the macro-tip to sample distance H was defined as the minimum distance between the surface plane and the macroscopic tip sphere.

Within these constraints, the experimental data can be well described by $A_H = 39.6 \pm 11.2 \times 10^{-20}$ J, $R = 3.95 \pm 0.87$ nm and γ of $16.42° \pm 1.24°$. Using these parameters we were then able to extrapolate the absolute height H of the macroscopic tip at a given Δf from the theoretical force curve.

The second major contribution to the total force comes from the electrostatic interaction between the localized charges present in the metallic tip and the sample. Note that this very local electrostatic interaction is not nullified when compensating for the long-range average contact potential difference. This interaction determines the image contrast when the nano-tip to surface distance D_s is between 0.5 and 1.0 nm. In order to estimate the value and position of the dipole moment, we examined the electrostatic potential near a three layer Cr nano-tip on the Cr(110) surface, as shown in Fig. 17.8.

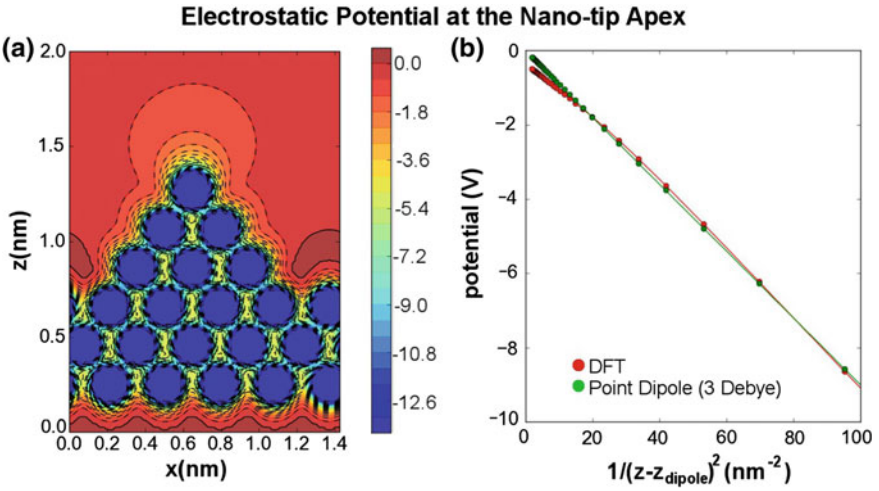

Fig. 17.8 **a** The electrostatic potential of a system containing a three layer nano-asperity on Cr(110) with a total dipole moment of 5 D. When the isosurface of this electrostatic potential is visualized, a large spherical feature appears above the apex atom that can be interpreted as the positive lobe of a dipole moment. **b** A plot of the electrostatic potential with respect to distance away from the nano-tip apex. A 3 D point dipole positioned at the atomic coordinates of the apex atom is able to reproduce the local electrostatic potential obtained from DFT calculations

A contour plot of the electrostatic potential obtained from DFT calculations depicted in Fig. 17.8a shows a spherical feature above the asperity, which may be interpreted as the positive lobe of a dipole moment. According to Fig. 17.4, the total dipole moment of a three layer pyramidal nano-tip is 5 D. However, the local electrostatic potential near the tip apex can be reproduced by positioning a 3 D point dipole at the apex atom, as shown in Fig. 17.8b. The interaction between this point dipole and the electrostatic potential of the sample is then obtained from DFT calculations. Finally, we produce the macroscopic van der Waal interaction plus the electrostatic force field and use the vAFM code [37] to simulate NC-AFM scan-lines at the experimental parameters of AFM operation.

The final contribution to the total force in our model comes from local vdW interactions between the nano-tip and the surface. The local vdW interactions between a pyramidal nano-tip and the surface is computed using a semi-empirical method [43]. Since this contribution is heavily dependent on the precise atomic structure of the nano-tip, which cannot be deduced from experimental data, we do not include these interactions in our initial vAFM simulations. Their importance is analyzed afterwards to gain insight into the differences between theoretical and experimental images.

Experimentally, we have measured NC-AFM images with atomic resolution of the bare NiO(001) surface. 23 scan-lines in the [100] direction from one such image were averaged to obtain the mean atomic corrugation amplitude. The dipole moment at the tip and the height of the nano-asperity were then fit to reproduce this scan-line, as shown in Fig. 17.9. The height of the macro-tip above the surface H required to

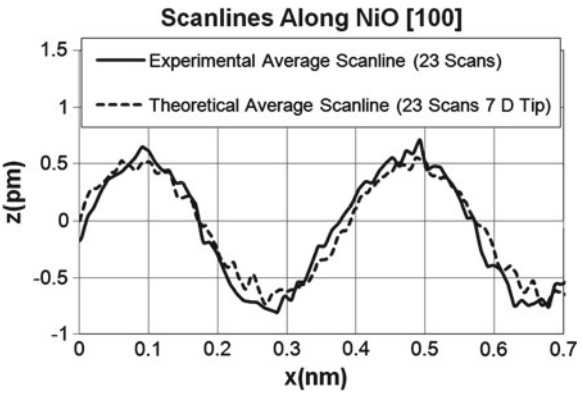

Fig. 17.9 Experimental and theoretical scan-lines above the bare NiO(001) surface in the [100] direction. The theoretical scanline was generated using a 7 D dipole moment and compared to the experimental average scanline. Experimental parameters: $f_0 = 186.278725$ kHz, $c = 144 \pm 21$ N/m, $A_0 = 0.6 \pm 0.1$ nm, $Q = 20{,}996$, $\Delta f = -50$ Hz

produce the experimental Δf of -50 Hz was calculated to be 1.24 nm. Point dipoles from 1 to 20 D were then placed at various positions corresponding to the apex atoms of asperities consisting of 1–5 atomic layers. The best fit was achieved with a tip dipole moment of 7 D positioned at the tip apex of a three atomic layer high nano-asperity (0.6 nm away from the macro-tip). The noise in the calculated scan-line is due to the digital phase lock loop and the integration timestep employed within the vAFM.

Although the agreement between experimental and theoretical scan-lines for this dipole moment value is remarkably good, we note that the magnitude and position of the point dipole are interrelated and cannot be uniquely defined. They provide only plausible information about the actual atomic structure of the tip. The local vdW interactions between the nano-tip and the surface will differ, depending on the exact structure of the nano-tip. In the distance regime proposed here, for a three layer pyramidal nano-tip model, this contribution to the image contrast is negligible and therefore not considered. At smaller nano-tip to surface distances D_s, however, these interactions will become important.

These results demonstrate that at relatively large tip-surface separations, a Cr coated tip can be consistently represented by a spherical macroscopic tip terminated by a pyramidal nano-tip consisting of several atomic layers with a dipole moment of a few Debye. Out of 36 metal coated tips, 26 were observed to possess sufficiently large dipole moments and were capable of atomic resolution. In the other nine cases the tip was either too blunt or not metallic. Additionally, similar results were obtained on NaCl(001) [27].

We now show that this point dipole model can also provide a quantitative interpretation of the image contrast pattern obtained on CO molecule absorbed on NiO(001).

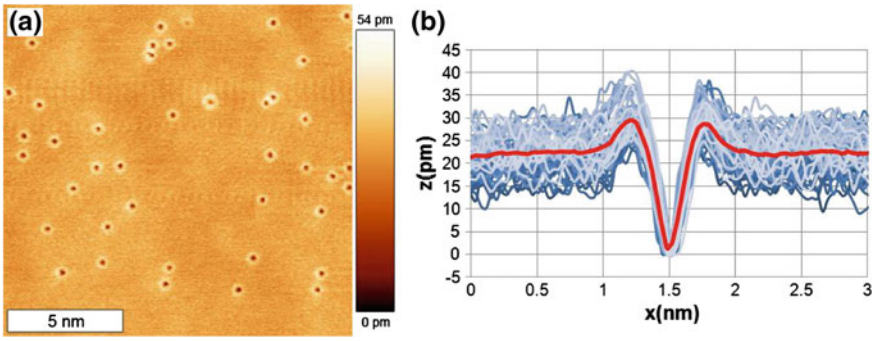

Fig. 17.10 **a** CO molecules on the NiO (100) surface imaged at 8 K as bright rings with a central depression (donuts). **b** 60 scan-lines above CO molecules along the [100] direction and a representative average scanline. Experimental parameters: $f_0 = 186.278$ kHz, $c = 144 \pm 21$ N/m, $A_0 = 0.6 \pm 0.1$ nm, $Q = 20{,}996$, $\Delta f = -48$ Hz

17.5.3 Imaging the CO Molecule

CO molecules were deposited onto the NiO(001) surface and imaged using the same Cr coated tip as the one used to obtain atomic resolution on the surface. We use exactly the same tip parameters as determined by evaluating the atomic corrugation on the bare surface in the previous section and quantitatively compare simulated and experimentally observed contrast patterns with each other.

Figure 17.10a shows a typical NiO(001) surface after deposition of CO using the same tip as in Fig. 17.9. A large number of bright rings with central depressions (donuts), corresponding to individual CO molecules, can be seen in constant Δf images of the surface. We find that CO molecules adsorbed on NiO(001) are still quite mobile at 8 K. Since we observed positional changes even after retracting the tip and imaging the same area after some hours, diffusion is clearly thermally induced and not tip induced. Figure 17.10b shows scan-lines over the centers of 60 CO molecules on NiO(001) in the [100] direction. These were then averaged to generate a mean scan-line to compare with theoretical predictions using the same point dipole model parameters that reproduced the atomically resolved data on NiO(001) in the previous section.

DFT calculations of the CO molecule predict a 0.1 D dipole moment in the gas phase with the positive pole at the O atom. The CO molecule then adsorbs perpendicular to the surface with the C atom above a surface Ni ion and an adsorption energy of 0.3 eV. In the adsorbed state, the CO dipole moment increases to 0.4 D with its positive end pointing away from the surface. The molecule is tilted 6° towards a Ni atom with Ni–C contributing 2° and C–O contributing 4°. This is qualitatively in agreement with prior theoretical predictions [59, 60] and within the error range of experimental estimates [61] of $12° \pm 12°$. This small tilt could be observable with a point dipole tip if vAFM images are generated from static DFT calculations performed at 0 K. However, due to high surface symmetry, there are four energetically

equivalent configurations that must be considered. Transitions between these configurations occur through the purely upright configuration with an energy barrier of only 0.006 eV, which is within the error range of DFT and may be interpreted as negligible. Furthermore, molecular dynamics simulations performed at 8 K estimate that the attempt frequency for switching between these equivalent states is 10^{13} Hz. Therefore, the molecule is rapidly switching between equivalent tilted configurations. Since AFM scan rates are many orders of magnitude slower than the switching frequency of CO on the surface, an average of the upright configuration and four equivalent tilted configurations must be considered when producing vAFM images or scan-lines.

When the AFM tip approaches a CO molecule on the surface from the side, there is an attraction due to lateral interactions between the tip and the molecule, as shown in Fig. 17.11a. This interaction is responsible for the bright rings in the image. However, when the dipole of the tip and the CO molecule on the surface are nearly on top of each other and aligned with the positive ends pointed towards each other, the resulting local repulsive electrostatic interaction is responsible for the dark spot within the bright rings. Note that this local electrostatic interaction cannot be compensated for by applying an averaged U_{CPD}.

The experimental scan-line over an adsorbed CO molecule averaged over 60 scan-lines and a simulated scan-line obtained using vAFM are compared in Fig. 17.11a. The simulated scan-line was calculated using the model of the tip-surface vdW interaction described in the previous section, i.e., a 7 D point dipole was positioned

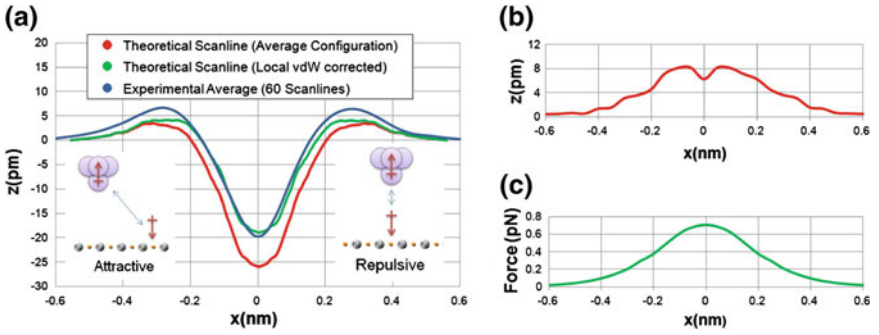

Fig. 17.11 **a** Experimental and simulated scan-lines of CO adsorbed onto the NiO(001) surface in the [100] direction. They were produced using the same experimental parameters of $f_0 = 190.444039$ kHz, $c = 151 \pm 21$ N/m, $A_0 = 1.0 \pm 0.1$ nm, $Q = 175{,}903$, $\Delta f = -48$ Hz. The theoretical long range forces were fit to experimental data and the tip was represented as a 7 D point dipole 0.6 nm below the macro-tip. The experimental scan-line was produced by averaging over the data for 60 CO molecules on the NiO surface and the theoretical scan-line was produced by averaging over four energetically equivalent tilted states on the surface as well as the upright configuration. Including local vdW interactions improves agreement with experiment. **b** The difference between experimental and uncorrected theoretical scan-lines with x = 0 representing the center of the CO molecule. **c** Local vdW interactions between the pyramidal nano-tip scanning 0.46 nm above a CO molecule. This contribution was computed using a semi-empirical scheme [43] assuming an upright configuration for CO

0.6 nm below the macro-tip. This dipole was used to represent the Cr coated tip while the electrostatic potential of the CO molecule on the NiO(001) surface was obtained from DFT calculations. The absolute minimum distance between the CO-molecule and the nano-tip (D_m) in this case was calculated to be 0.46 nm. The corresponding minimum distance between the nano-tip and the NiO(001) surface (D_s) is 0.78 nm. At this tip-surface distance, atomic resolution of the surface should no longer be possible, in agreement with experimental data. It also supports the presumption that Pauli repulsion is negligible [62].

Theory predicts that the CO molecule is observed as a bright ring with a dark spot indicating repulsion at the center. Since surface atoms can no longer be resolved at this tip-sample distance, the surface level can simply be defined as the cantilever height far away from the CO molecule. The bright ring is 3 pm above the surface level while the depression is 26 pm below the surface level. The diameter of the ring is 0.6 nm in this case and defined as the horizontal distance between maxima on opposite sides of the bright ring. Averaged experimental scan lines give a similar bright ring 6 pm above the surface level with a standard deviation of 3 pm and an average depression that lies 20 pm below the surface level with a standard deviation of 2.5 pm. The experimental diameter of the bright ring was observed to be 0.52 nm with a standard deviation of 4 pm. The total size of the CO molecule is about 1.5 nm in both theory and experiment. Furthermore, the average height difference between maxima on opposite sides of the molecule is only 0.7 pm with a standard deviation of 2.2 pm. This indicates that the height of the ring is constant along the entire perimeter and that the dipole moment of the tip is therefore oriented nearly perpendicular with respect to the surface plane. Since the total size of the CO molecule is identical in the experiment and the simulation, tip-convolution effects are negligible, indicating an atomically sharp tip.

The difference between the experimental and theoretical scan-lines is shown in Fig. 17.11b. The largest discrepancy is found near the center of the CO molecule and falls off with increasing distance. This difference may be accounted for by examining the vdW interactions between the CO molecule and the pyramidal nano-tip, as suggested in [62]. Since this contribution is always attractive, it would reduce the depth of the depression and increase the height of the ring. The Local vdW interactions between a pyramidal nano-tip scanning 0.78 nm (D_s) above the surface and an adsorbed CO molecule were computed using a semi-empirical scheme [43], as shown in Fig. 17.11c. At the center of the CO molecule, these attractive local vdW forces are roughly 30 % as large as the repulsive electrostatic contribution, which improves the agreement between theory and experiment, as shown in Fig. 17.11a. While these forces are of the appropriate magnitude and sign to explain the difference between simulated and experimental scan lines and fall off at the appropriate distance away from the center of the CO molecule, they depend heavily on the height and on the precise geometry of the nano-tip. Since many of our tip parameters are already interdependent, simply correcting for these vdW interactions is difficult. If CO molecules spend more time, on average, in the fully upright configuration than in the tilted configurations, the width of the ring and the depth of the depression may differ. These interactions may prove to be of critical importance at shorter tip-sample

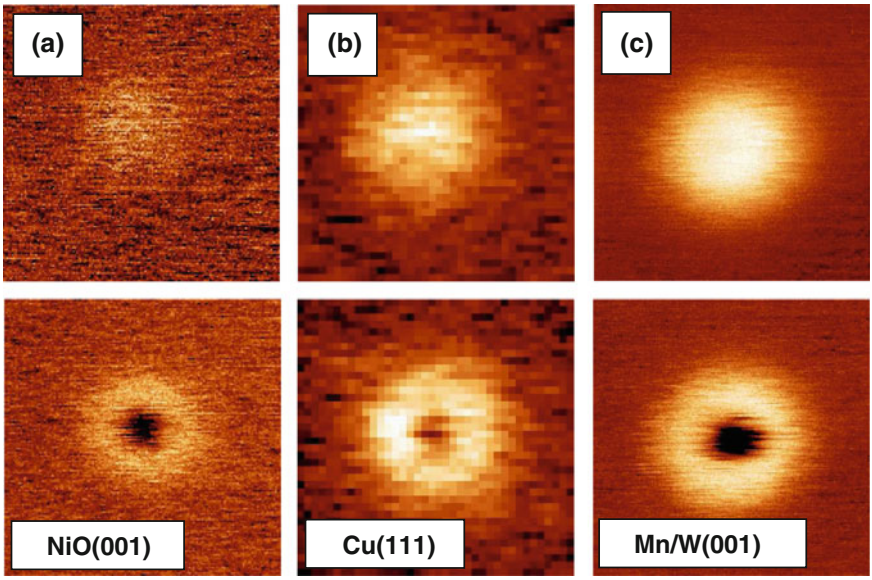

Fig. 17.12 Constant Δf images of single CO molecules on **a** NiO(001), **b** Cu(111) and **c** Mn/W(001). In the *upper row* (relatively large tip-sample separations) the vdW interaction dominates, resulting in bumps, which represent the CO molecule. Images in the *lower row* were recorded with more negative Δf set-points leading to a 0.2 nm smaller tip-sample separations. Here electrostatic interactions between the molecular dipole and the tip dipole dominate, resulting in a donut-shaped contrast pattern

distances, however, our results clearly demonstrate that at intermediate tip-surface separations, i.e., were the local electrostatic interaction dominate, good agreement with experiment can be achieved using a simple point dipole model alone. At larger separations the long-range vdW dominate and the CO molecule is imaged as a bump. This can be seen in Fig. 17.12a.

Figure 17.12 also shows that this behaviour found for CO adsorbed on NiO(001) is quite universal: it can be seen on Cu(111) and Mn/W(001) as well [62]. In all three case the vdW forces dominate at relatively large tip-sample separations (bump), while the local electrostatic interactions dominate when metallic tips are used at smaller tip-sample separations (donut). It should be mentioned that Pauli repulsion could also be responsible for the local repulsion [63, 64]. However, at least on NiO(001) it is probably impossible to reach the Pauli repulsion regime without displacing the molecule sideways, as the diffusion barrier is so low that thermally activated displacements still occurs at 8 K. On Cu(111) it is well known that at small tip-sample separation tip-induced molecular displacements occur, which also would prevent imaging in the Pauli repulsion regime [65]. CO on Mn/W(001) is not displaced so easily, but in any case electrostatic repulsion will be of longer range than Pauli repulsion and thus detectable first.

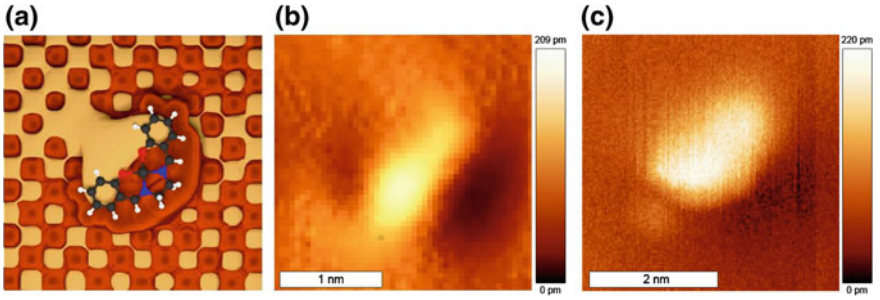

Fig. 17.13 **a** The electrostatic potential of a single Co-Salen molecule adsorbed onto NiO(001). *Bright areas* represent the negative isosurface (−0.54 eV) where the tip would experience an attractive potential while *dark areas* represent the positive isosurface (0.08 eV) or repulsive potential at long distances. **b** A vAFM image taken far from the surface. It shows the Co-Salen molecule as a *bright oval* with a *dark shadow* on one side. At this range the metallic coated Cr tip is unable to distinguish between similar C or H atoms within the molecule. **c** An experimental NC-AFM image of a Co-Salen molecule on NiO(001) taken at long range. Individual Co-Salen molecules do appear as large *bright ovals* with smaller *dark shadows*. Experimental parameters: $f_0 = 186.894$ kHz, $Q = 21{,}392$, $A_0 = 5.0 \pm 0.5$ nm, $c = 145 \pm 22$ N/m, $\Delta f = -0.71$ Hz

17.5.4 Imaging Larger Polar Molecules

Unlike CO functionalized tips, metallic tips appear unable to image larger molecules with intramolecular resolution in the Pauli-repulsion regime on insulators, as the recent studies of Co-Salen molecules on NaCl(001) [28] and NiO(001) [29] suggest. However, since metallic tips possess much larger dipole moments (a few Debye) than CO functionalized tips (a few 0.1 Debye), they may be well suited to probe the dipole moments (or the electrostatic potential) of larger molecules. Co-Salen is a large polar molecule and provides a good example to illustrate this point.

Previous calculations show that the Co-Salen molecule on NiO(001) possesses a 6 D dipole moment aligned along the symmetry axis [29]. The positive end of this dipole moment is oriented towards the N atoms while the negative end is oriented towards the O atoms. This molecular dipole moment can be visualized using the electrostatic potential of the system from DFT calculations, as seen in Fig. 17.13a. The negative iso-surface (Bright) of the electrostatic potential shows areas where the positive end of a dipole moment would feel an attractive interaction. Experimentally, these areas should result in bright spots in the image. The positive iso-surface (Dark) highlights areas where the tip would be repelled and should result in dark spots or shadows. Note that the iso-value of the repulsive region (0.08 eV) is much smaller than the attractive region (−0.54 eV), indicating a weaker interaction. A smaller iso-value was used in order to enlarge the repulsive region for the illustration. When adsorbed to NiO(001), the Co-Salen molecule also acquires a 4.4 D vertical dipole moment due to distortion of the molecule and electronic polarization of the system [29]. When this vertical component is added to the horizontal component, the symmetry of the imaged dipole moment is broken. The bright attractive

region should now be roughly twice as large as the dark repulsive one, as seen in Fig. 17.13b. Although the atoms within the Co-Salen molecule are not resolved, it may be possible to image the positive and negative lobes of the molecular dipole.

In previous studies of Co-Salen this imaging mechanism was used to obtain atomic resolution of the NiO surface while the molecule itself was probed at a distance where both Pauli-repulsion and electrostatic interactions were present. At such ranges, the bright and dark lobes of the molecule itself could not be consistently identified. However, when Co-Salen molecules are imaged at much greater distances, where the surface atoms are no longer visible, it may be possible to resolve the horizontal dipole moment of a Co-Salen molecule, as shown in Fig. 17.13c. This image consists of a large bright oval and a smaller dark shadow. The shadow appears in both the trace and retrace images, indicating that these dark regions are not due to z-feedback artefact. The bright region of the molecule is indeed much larger than the dark repulsive region, which is consistent with theoretical predictions of a tilted total dipole moment on the surface. The angle of this tilt, however, cannot easily be determined from this particular set of data and this interpretation is not unambiguous.

17.6 Discussion and Conclusions

Our experimental results combined with DFT calculations confirm that the Cr tips possess permanent dipoles with the positive ends oriented towards the sample surface. The magnitude of a point dipole positioned at the tip apex was fit to experimental scan-lines exhibiting atomic resolution on NiO(001) using the vAFM. The point dipole tip model was tested on CO molecules adsorbed on NiO(001), which were imaged as donuts using the very same tip. Moreover, we demonstrate that these tips may be able to probe the dipole moments of polar molecules at the surface.

Based on these findings we more generally suggest that apices of atomically sharp metallic tips, produced by either metal coating of Si cantilevers or from metal wire, end in a nano-asperity which can be well described as a pyramid. This greatly reduces the number of possible tip structures that must be considered. In contrast, Si or oxidized Si-tips can possess a large number of stable configurations. Therefore, several likely tip structures must be tested in order to achieve reasonable agreement between theory and experiment [66]. Metallic tip apices also possess a rather large electric dipole moment of a few Debye that usually points with its positive end towards the surface and can be well modelled as a point dipole. This property facilitates unambiguous atom identification on polar surfaces at rather large tip-sample separations and substantially reduces the complexity of interpreting experimental data.

Metallic tips may also be functionalized by picking up small molecules such as CO [21]. Such tips have recently been used to obtain intramolecular resolution in the repulsive regime using constant height imaging [67, 68]. However, due to the small tip-sample distance and the resulting strong tip-sample interaction in the repulsive regime, image distortions and relaxation effects have to be considered. Since CO possesses an intrinsic dipole moment with its positive pole on the O atom and adsorbs

with its C atom onto metal surfaces, it will likely also possess a dipole moment with its positive pole pointing towards the surface. Note that the dipole moment of the metallic nano-tip on which CO adsorbs tends to increase the total dipole moment of the adsorbed molecule due to polarization effects. Therefore, CO functionalized tips can be expected to behave similarly to metal tips, even though their dipole moment is probably smaller. Unfortunately, CO functionalized tips can only be prepared at low temperatures (otherwise CO is too mobile) and not all sample systems are suitable for CO adsorption.

From a practical point of view one has to be aware that all tip apices can become contaminated with sample material during scanning. Therefore, tip changes should be monitored. Whether tip material was lost (the tip becomes shorter) or sample material has been picked up (the tip becomes longer) can be determined by observing the z-signal. In the latter case atom identification on ionic surfaces using metallic tips becomes ambiguous, as the image contrast is determined by the charge state of the foremost tip-apex atom. Note that this is true for silicon, silicon oxide, and functionalized tips as well. However, if a metallic tip picks up non-conductive sample material, the bias spectroscopy curve becomes non-metallic, i.e., the smooth parabola exhibits jumps or hysteresis [27]. In this way, bias spectroscopy provides a convenient in-situ tool to characterize metallic tip apices and monitor contamination by non-conductive sample material. If the tip becomes non-metallic, it can be dipped into a metallic substrate, e.g. Cu, to metallize the tip apex again (voltage pulses are also an option). The use of monitored metallic tips will be advantageous when performing Kelvin probe force microscopy (KPFM) or electrostatic force microscopy (EFM), avoiding the complications of interpretation described by Bieletzki et al. [69].

In summary, metallic tips can be conveniently prepared in-situ and re-metallized if they become contaminated. The most stable and thus most likely atomic configuration of the tip apex is a pyramid that possesses a large electric dipole moment of a few Debye with its positive pole pointing towards the surface. This greatly reduces the complexity of interpreting experimental data while allowing for an unambiguous identification of ionic species on polar surfaces at relatively large tip-sample distances. Metallic tips can also be used to detect the electric dipole moments of adsorbed molecules and in KPFM and EFM experiments (Chap. 12). It is worth mentioning that if magnetic metals are used, even magnetic moments can be resolved with atomic resolution (Chap. 7) [70, 71]. In this context pyramidal nano-tips provided excellent agreement between DFT calculations and experimental data regarding the magnitude and distance dependence of the magnetic exchange interaction [72].

Acknowledgments Financial support from the Deutsche Forschungsgemeinschaft (SFB 668-A5) is gratefully acknowledged. D.Z.G. is grateful to Chevron Oronite Company and to UCL for financial support. The authors are grateful to Matthew Watkins and Filippo Federici Canova for valuable comments and help in calculations. D.Z.G. and A. L. S. acknowledge the use of the HECToR and Archer High Performance Computing Facilities via our membership to the UK's HPC Materials Chemistry Consortium, which is funded by EPSRC (EP/F067496). D.Z.G. acknowledges the use of the Serenity computing cluster and support services provided by Nanolayers.com for the completion of this work.

References

1. F. Besenbacher, J.V. Lauritsen, S. Wendt, Nano Today **2**, 30 (2007)
2. G. Bhalla, M.H. Tsang, D. Gao, Q. Chen, W. Ruhe, N. Ushioda, SAE Int. **5**, 496 (2012)
3. A.M. Barnes, K.D. Bartle, V.R.A. Thibon, Tribol. Int. 34 (2001)
4. C. Joachim, J.K. Gimzewski, A. Aviram, Nature **408**, 541 (2000)
5. J.R. Heath, Rev. Mater. Res. **39**, 1 (2009)
6. H. Song, M.A. Reed, T. Lee, Adv. Mater. **23**, 1583 (2011)
7. H. Onishi, A. Sasahara, H. Uetsuka, T. Ishibashi, Appl. Surf. Sci. **188**, 265 (2002)
8. Y. Namai, K. Fukui, Y. Iwasawa, Nanotechnology **15**, S49 (2004)
9. L. Nony, R. Bennewitz, O. Pfeiffer, E. Gnecco, A. Baratoff, E. Meyer, T. Eguchi, A. Gourdon, C. Joachim, Nanotechnology **15**, S91 (2004)
10. S.A. Burke, J.M. Mativetsky, R. Hoffmann, P. Grutter, Phys. Rev. Lett. **94**, 096102 (2005)
11. T. Kunstmann, A. Schlarb, M. Fendrich, T. Wagner, R. Moller, Phys. Rev. B **71**, 121403 (2005)
12. T. Dienel, C. Loppacher, S.C.B. Mannfeld, R. Forker, T. Fritz, Adv. Mater. **20**, 959 (2008)
13. S.A. Burke, W. Ji, J.M. Mativetsky, J. Topple, S. Fostner, H.J. Gao, H. Guo, P. Grutter, Phys. Rev. Lett. **100**, 7 (2008)
14. J. Schutte, R. Bechstein, P. Rahe, A. Kuhnle, H. Langhals, Phys. Rev. B **79**, 045428 (2009)
15. F. Loske, R. Bechstein, J. Schutte, F. Ostendorf, M. Reichling, A. Kuhnle, Nanotechnology **20**, 065606 (2009)
16. M. Kittelmann, P. Rahe, A. Kuhnle, J. Phys. Condens. Matter **24**, 354007 (2012)
17. A. Hinaut, A. Pujol, F. Chaumeton, D. Martrou, A. Gourdon, S. Gauthier, Beilstein J. Nanotechnol. **3**, 221 (2012)
18. W.A. Hofer, A.S. Foster, A.L. Shluger, Rev. Mod. Phys. **75**, 1287 (2003)
19. C. Barth, A. Foster, C. Henry, A. Shluger, Adv. Mater. **23**, 477 (2011)
20. W. Paul, Y. Miyahara, P. Grütter, Nanotechnology **23**, 335702 (2012)
21. L. Gross, Nat. Chem. **3**, 273 (2011)
22. B. Schuler, W. Liu, A. Tkatchenko, N. Moll, G. Meyer, A. Mistry, D. Fox, L. Gross, Phys. Rev. Lett. **111**, 106103 (2013)
23. L. Gross, F. Mohn, N. Moll, B. Schuler, A. Criado, E. Guitian, D. Pena, A. Gourdon, G. Meyer, Science **337**, 1326 (2012)
24. G. Enevoldsen, H. Pinto, A. Foster, M. Jensen, A. Külne, M. Reichling, W. Hofer, J. Lauritsen, F. Besenbacher, Phys. Rev. B **78**, 045416 (2008)
25. M. Ondracek, P. Pou, V. Rozsival, C. Gonzalez, P. Jelinek, R. Perez, Phys. Rev. Lett. **106**, 176101 (2011)
26. A. Schwarz, U. Kaiser, R. Wiesendanger, Nanotechnology **20**, 264017 (2009)
27. G. Teobaldi, K. Lämmle, T. Trevethan, M. Watkins, A. Schwarz, R. Wiesendanger, A.L. Shluger, Phys. Rev. Lett. **106**, 216102 (2011)
28. K. Lämmle, T. Trevethan, A. Schwarz, M. Watkins, A. Shluger, R. Wiesendanger, Nano Lett. **10**, 2965 (2010)
29. A. Schwarz, D. Gao, K. Lämmle, J. Grenz, M. Watkins, A. Shluger, R. Wiesendanger, J. Phys. Chem. C **117**, 1105 (2013)
30. M. Liebmann, A. Schwarz, S.M. Langkat, R. Wiesendanger, Rev. Sci. Instrum. **73**, 3508 (2002)
31. T.R. Albrecht, P. Grütter, D. Horne, D. Rugar, J. Appl. Phys. **69**, 668 (1991)
32. H. Hölscher, S. Langkat, A. Schwarz, R. Wiesendanger, Appl. Phys. Lett. **82**, 4428 (2002)
33. K. Lämmle, A. Schwarz, R. Wiesendanger, Rev. Sci. Instrum. **81**, 053902 (2010)
34. J. Kim, S. Seo, J. Park, J. Lee, Y. Lee, B. Ju, J. Korean Phys. Soc. **39**, S101 (2001)
35. C. Liu, J. Erdmann, A. Macrander, Thin Solid Films **355–356**, 41 (1999)
36. M. Hu, S. Noda, T. Okubo, K.H. Appl. Phys. A **79**, 625 (2004)
37. F. Federici Canova, A.S. Foster, M.K. Rasmussen, K. Meinander, F. Besenbacher, J.V. Lauristen, Nanotechnology **23**, 1 (2012)
38. G. Couturier, J. Aime, J. Salardenne, R. Boisgard, Eur. Phys. J. Appl. Phys. **15**, 141 (2001)
39. L. Nony, A. Baratoff, Phys. Rev. B **74**, 235439 (2006)

40. J. Polesel-Maris, S. Gauthier, J. Appl. Phys. **97**, 044902 (2005)
41. G. Lippert, J. Hutter, M. Parrinello, M. Mol, Phys. **92**, 477 (1997)
42. J. VandeVondele, M. Krack, F. Mohamed, M. Parrinello, T. Chassaing, J. Hutter, Comput. Phys. Commun. **167**, 103 (2005)
43. S. Grimme, J. Comput. Chem. **27**, 1787 (2006)
44. D. Gao, J. Grenz, M. Watkins, F.F. Canova, A. Schwarz, R. Wiesendanger, A. Shluger, ACS Nano **8**, 5339 (2014)
45. J. Jackson Classical Electrodynamics; Wiley, New York, (1998)
46. L. Kantorovich, A.I. Livshits, M. Stoneham, J. Phys. Condens. Matter **12**, 795 (2000)
47. T. Tsumaki, Bull. Chem. Soc. Jpn. **13**, 252 (1938)
48. N.S. Vankataramanan, G. Kuppuraj, S. Rajagopal, Coord. Chem. Rev. **249**, 1249 (2005)
49. R. Smoluchowski, Phys. Rev. **60**, 661 (1941)
50. K. Besocke, H. Wagner, Phys. Rev. B **8**, 4597 (1973)
51. J.F. Jia, K. Inoue, Y. Hasegawa, W.S. Yang, T. Sakurai, Phys. Rev. B **58**, 1193 (1998)
52. K. Besocke, B. Kral-Urban, H. Wagner, Surf. Sci. **68**, 39 (1977)
53. H. Ishida, A. Liebsch, Phys. Rev. B **46**, 7153 (1992)
54. C. Lazo, V. Caciuc, H. Holscher, S. Heinze, Phys. Rev. B **78**, 214416 (2008)
55. G. Wulff, Zeitschr. Krystallogr. Mineral. **34**, 449 (1901)
56. T. Trevethan, M. Watkins, A. Shluger, Beilstein J. Nanotechnol. **3**, 329 (2012)
57. C. Argento, R.H. French, J. Appl. Phys. **80**, 6081 (1996)
58. L. Bergstrom, Adv. Colloid Interf. Sci. **70**, 125 (1997)
59. W. Wang, J. Li, Y. Zhang, Appl. Surf. Sci. **252**, 2673 (2006)
60. A. Rohrbach, J. Hafner, G. Kreese, Phys. Rev. B **70**, 125426 (2004)
61. M. Kittel, J.T. Hoeft, S. Bao, M. Polcik, R.L. Toomes, J.H. Kang, D.P. Woodruff, M. Pascal, C.L.A. Lamont, Surf. Sci. **499**, 1 (2002)
62. A. Schwarz, A. Köhler, J. Grenz, R. Wiesendanger, Appl. Phys. Lett. **105**, 011606 (2014)
63. Z. Sun, M. Boneschanscher, I. Swart, D. Vanmaekelbergh, P. Liljeroth, Phys. Rev. Lett. **106**, 046104 (2011)
64. J. Welker, F. Giessibl, Science **336**, 444 (2012)
65. M. Ternes, C. Lutz, C. Hirjibehedin, F. Giessibl, A. Heinrich, Science **319**, 1066 (2008)
66. P. Pou, S.A. Ghasemi, P. Jelinek, T. Lenosky, S. Goedecker, R. Perez, Nanotechnology **20**, 264015 (2009)
67. F. Mohn, L. Gross, N. Moll, G. Meyer, Nature Nanotech. **7**, 227 (2012)
68. P. Liljeroth, J. Repp, G. Meyer, Science **317**, 1203 (2007)
69. M. Bieletzki, T. Hynninen, T.M. Soini, M. Pivetta, C.R. Henry, A.S. Foster, F. Esch, C. Barth, U. Heiz, Phys. Chem. Chem. Phys. **12**, 3203 (2010)
70. U. Kaiser, A. Schwarz, R. Wiesendanger, Nature **446**, 522 (2007)
71. M. Granovskij, A. Schron, F. Bechstedt, New J. Phys. **16**, 023020 (2014)
72. R. Schmidt, C. Lazo, U. Kaiser, A. Schwarz, S. Heinze, R. Wiesendanger, Phys. Rev. Lett. **106**, 257202 (2011)

Chapter 18
Simulating Solid-Liquid Interfaces in Atomic Force Microscopy

Bernhard Reischl, Filippo Federici Canova, Peter Spijker, Matt Watkins and Adam Foster

Abstract In this chapter, we will cover the main approaches taken to model AFM in liquids in a variety of different systems, discussing the advantages and problems of different methods, outlining the main issues to take into account in general, while also attempting to build a perspective for the future of the field. We hope this will provide a fundamental platform of understanding for future Atomic Force Microscopy studies of solid-liquid interfaces at the nanoscale.

18.1 Introduction

Atomic Force Microscopy (AFM) lies at the heart of developments in nanotechnology and is increasingly being used for nanoscale characterization for a wide variety of physical, biological and chemical processes [1, 2]. Pioneering experimental studies are now providing atomic scale insight into, for example, friction, catalytic reactions, electron transport and optical response, with the laboratory effectively at the end of an AFM tip. At this scale, the convolution of the measurement and the signal means that theoretical modelling is required to understand experiments, and it has to be much

B. Reischl · P. Spijker · A. Foster (✉)
Department of Applied Physics, COMP Centre of Excellence, Aalto University School of Science, P.O. Box 11100, 00076 Helsinki, Finland
e-mail: adam.foster@aalto.fi

B. Reischl
e-mail: bernhard.reischl@curtin.edu.au

P. Spijker
e-mail: peter.spijker@aalto.fi

F.F. Canova
WPI-AIMR Tohoku University, Sendai 980-8577, Japan
e-mail: felix@wpi-aimr.tohoku.ac.jp

M. Watkins
School of Mathematics and Physics,
University of Lincoln, Brayford Pool, Lincoln LN6 7TS, UK
e-mail: MWatkins@lincoln.ac.uk

© Springer International Publishing Switzerland 2015

S. Morita et al. (eds.), *Noncontact Atomic Force Microscopy*,
NanoScience and Technology, DOI 10.1007/978-3-319-15588-3_18

less abstract than in conventional theoretical studies—really offering a simulation of the fundamentals of the experiment. For many of the most exciting developments in AFM, particularly measurements outside vacuum conditions or those considering dynamic processes, modelling lags far behind experiments.

The fundamental components common to all AFM experimental setups are the tip, cantilever and surface. Beyond this, the setup for a given AFM experiment is determined mainly by the system under investigation, and the desired thermal and chemical environment. Most observations are made by monitoring normal and torsional cantilever deflections induced by the tip-surface interaction using various optical methods [3, 4]. In initial AFM designs the tip was pressed to the surface either by the van der Waals force or by an external elastic force of the cantilever, and imaging was performed in the so-called contact mode. Although providing interesting insights into nanotribology and adhesion physics, this technique proved unreliable for imaging in atomic resolution. In contact the tip and surface were constantly exchanging material during scanning, changing the nature of the interactions [5–7]. Attempts to avoid 'hard' contact were thwarted by the tip's propensity to jump-to-contact even at large tip-surface distances, the generally attractive van der Waals force overcoming the stiffness of the cantilever within a certain distance. However, it has been demonstrated that one can obtain much better sensitivity in measuring force variations on the atomic scale by employing dynamic force microscopy [8]. In this case the cantilever is vibrated at a certain frequency above the surface, greatly reducing (but not eliminating) the problems of jump-to-contact and tip crashes. Since in this case the tip is thought not to be in direct hard contact with the surface, this technique is often also called non-contact AFM (nc-AFM) [9].

In nc-AFM, a cantilever is maintained in oscillations at a constant amplitude via a feedback loop, and can be considered as a self-driven oscillator. Generally, during experiments the tip-surface distance is varied in order to achieve a constant frequency change Δf, and the resulting topography map provides the image of the surface (equivalently the tip can be kept at a constant height over the surface and Δf recorded). When applying nc-AFM for traditional applications in surface science, such as the research of surface reconstructions, surface growth, surface dynamics, and surface chemistry, the instrument is suspended in ultra-high vacuum (UHV) chambers of less than 10^{-9} torr. Although many of the recent success stories of AFM have been achieved in these UHV conditions [10–13], for most applications this is not a particularly relevant environment, e.g., studies in liquid would mimic the physiological conditions relevant to biological systems [1, 2]. Of course, the first AFM studies were in air [14, 15], and some early high-resolution studies were in water [16]. In these studies, AFM is operated in contact mode, and suffers from similar problems to studies of systems in UHV in contact, i.e., the imaging process is invasive, and the large, lateral tip-surface forces damage or deform the sample. This is particularly a problem in organic or biological systems, where molecules are often only physisorbed to the surface by weak van der Waals interactions.

In UHV studies, a natural route to reduce the lateral forces experienced by the sample is to reduce the amount of time the tip spends in contact by introducing vertical cantilever motion [17], and this dynamic mode could also be applied in

liquids. Its ultimate resolution is limited to the nanometre level by the large noise in liquid environments. However, it was recognized fairly early in the development of nc-AFM that stiffer cantilevers and small amplitudes could offer dramatic increases in the signal-to-noise ratio [18], and this has proved to be a breakthrough in high resolution imaging in liquids [19–24]. Using ultra-small amplitudes of tenths of a nanometre, lateral resolution of a few hundred picometres was achieved in water on molecular crystals, mica [24] and a lipid bilayer [22]. Refinements in sensitivity offer the potential for an order of magnitude improvement in resolution [25], and the use of small cantilevers could improve this further [26].

In the future, molecular and atomic resolution in liquids is certain to become almost routine, and greater efforts will be made in interpretation and understanding the influence of the environment on both the measurement and the sample. As such, it is critical that the theoretical tools are already developed to model nc-AFM in liquids. Previous studies in UHV have emphasized the importance of partnering theoretical studies with experimental efforts [27–29], but significant progress must be made in simulation methodology to offer the same for nc-AFM in liquids. At present, a comprehensive, proven methodology for simulating nc-AFM in liquids does not exist and many aspects of breakthrough experiments remain difficult to interpret. In this chapter we will cover the main approaches taken to model AFM in liquids in a variety of different systems, discussing the advantages and problems of different methods, outlining the main issues to take into account in general, while also attempting to build a perspective for the future of the field. We hope this will provide a fundamental platform of understanding for future studies of solid-liquid interfaces at the nanoscale.

18.2 Methodology

Standard modelling approaches for Atomic Force Microscopy (AFM) are fairly well-developed, with most approaches for UHV studies applying first principles methods (also known as ab initio or quantum mechanical methods) [30–38], including van der Waals interactions if necessary [39–41], to calculate accurate force fields. The most difficult questions involve identifying the atomic structure of the tip and surface, although in the former case, breakthroughs in tip functionalization have made the task sometimes much easier [12, 42, 43]. When considering characterization of solid-liquid interfaces with AFM, the modelling task becomes considerably harder.

It has become apparent from the oscillatory force profiles obtained from experimental AFM imaging in liquid, that the molecular structure of the liquid influences the force on the tip apex in the vicinity of the surface. In fact any type of solvent will exhibit a degree of layering at an interface with a solid. But in the particular case of a polar liquid, such as water, in contact with an ionic crystal, molecules are arranged in well-defined hydration layers. The spatial distribution and orientation of these water molecules is the result of the interactions with ions in the substrate, as well as with neighbouring water molecules in a hydrogen-bonded network. First-principles

simulations confirm the results from calculations with atomistic potentials, that these hydration layers extend up to several Ångström above the surface, before the water reaches bulk structure [44]. It is important to note that although water molecules have equilibrium positions in the hydration layers, at room temperature this equilibrium is highly dynamic, with frequent exchange of water molecules between these positions, and the bulk solution, on a timescale of nanoseconds.

This dynamics means that conventional, static modelling approaches are not appropriate, and molecular dynamics (MD) techniques must be used. At its core, MD simulations solve Newton's equations of motion for all particles in the system [45, 46]. The interactions between all individual particles are determined by appropriate potential energy functions, which can be as simple or as complex as required, from which forces acting on each other can be determined, necessary for the integration of the equations of motion. In general, the timescales required for equilibrating the solid-liquid system prohibit the use of quantum mechanical methods, and initial attempts have been made with classical approaches to represent the interactions [47–52]. More details on the force fields and interactions that they involve will be discussed in Sect. 18.2.4.

18.2.1 Simulation Level

When modelling solid-liquid interfaces, in order to provide ample comparison with experimentally obtained AFM data like images and force curves, approximations with different complexity exist. For instance, it is a natural expectation that the tip disturbs the hydration structures on the surface during imaging, making direct visualization of intrinsic hydration structures almost impossible. This is further complicated by the influence of the solvation shell formed on the tip apex itself, and the overlap between hydration and solvation structures on both the tip and the surface. The most elaborate modelling approach thus includes modelling the solid surface, the liquid and the tip, but because entropic contributions from the water molecules cannot be ignored, free energy calculations are mandatory. This free energy modelling approach will be discussed in more depth in Sect. 18.2.2. Even though this is by far the most realistic modelling approach feasible today, it still is computationally expensive, and other, simpler approximations are also possible.

It has been argued that water molecules strongly bound to a hydrophilic tip may effectively work as a probe themselves [53, 54]. This allows approximation of the full system by focusing on individual water molecules instead and ignoring the tip entirely. Force curves can then be directly constructed from the local water density [53]. Comparison of force curves computed both using the free energy approach and this more simple approach by using the water density, showed that in some cases this simplification is indeed possible, especially further away from the surface [53]. An even more simple approach is to look at the local liquid density only and whether the observed structuring corresponds qualitatively to AFM topography images. Both of these more simple approaches assume that the scanning process

should not be invasive at all, and, hence, the equilibrium liquid structure on the solid surface should be the one also observed by the AFM. Some recent observations show that experimental force curves measured by nc-AFM [55, 56] do show features that can be correlated with those measured by X-ray reflection experiments [57, 58], which strengthens the approximation that the tip might not always perturb the local hydration structure. Furthermore, these approximations also do away with the need for individual simulations for every tip location (as is the case with the free energy approach), and can speed up the simulations by three orders of magnitude. Each of these levels of approximation will be considered in the case studies in Sect. 18.3.

18.2.2 Free Energy Calculations

In order to simulate AFM imaging in liquid at atomistic level, we will assume that the force felt by the AFM tip is dominated by the forces acting on the AFM tip apex. In particular, forces arising from interactions between the region of the tip further away from the surface as well as the cantilever will not be specific to the position of the tip with respect to the sample. These interactions only lead to viscous drag of the cantilever through a continuous fluid. Analogous to the simulation methodology developed in UHV, the AFM tip apex can be modelled by a nanocluster of an appropriate material. For instance, silicon (or silicon nitride) tips commonly used for imaging in liquid will be covered in an amorphous silicon dioxide layer several nanometres thick, which in water will further react and form silanol groups on its surface. If the tip is charged, ions in solution will likely aggregate at the apex. Finally, if the tip is crashed into the surface, or the surface material is soluble, the tip apex may even be simulated as being made of the same material as the surface. The role of the tip will be examined more closely in Sect. 18.2.5.

Conventional cantilevers used in FM-AFM imaging in liquid oscillate with an amplitude <1 nm, at frequencies around 150 kHz. Ultra-short cantilevers developed recently to increase force sensitivity in liquids have higher eigenfrequencies in the MHz range. This puts the timescale of the cantilever oscillation in the microsecond range. However, as the cantilever oscillation is typically not a fully reversible process, many oscillation cycles would have to be simulated in a molecular dynamics simulation, in order to get a statistically meaningful signal for each cantilever position. This is beyond what can be achieved in a reasonable amount of time, even when using empirical interaction potentials. Fortunately, the time scale of thermal motion of water molecules is much shorter than that of the cantilever oscillation: hydrogen bond networks in bulk water re-arrange on a picosecond timescale [59], and even the fluctuations of hydration layer structures happen on a nanosecond timescale. In addition, the full oscillation amplitude is typically only of the order of the diameter of a single water molecule. Therefore we may assume that the water is in (or very close to) equilibrium at every instantaneous position of the tip during the oscillation. Finally, the AFM scanning speeds are again much slower than the cantilever oscillation, and the detected signal is an average over many oscillation cycles at almost

the same reference position, another argument in favour of choosing an equilibrium approach. This enables us to apply a wide class of methods developed in the context of computational statistical mechanics to the simulation of AFM in liquids.

However, it should be noted that calculations of the residence time of water near the tip or surface may challenge the approximation of *equilibrium* water [60]. In one specific example on the CaF_2 (111) surface, the dynamics of water molecules between the tip apex and surface slow significantly when a tip is at a height of about 0.6 nm from the surface. At even closer tip approach, about 0.2 nm, molecules do not diffuse during an extended simulation of approximately 25 ns. We have previously assumed and stated that water motion is very rapid compared to that of the AFM cantilever, which may typically spend 10^{-7} s close to the surface; we now have some water molecules with a lower bound on their residence times heading towards 10^{-8} s. This indicates that at very close approach, the sampling of water configurations around the tip will be less efficient than when imaging through a couple of water layers. This is an issue for both simulation and the real experiment. Experimentally, it could give rise to an increase in noise and, perhaps, provide a mechanism for dissipation—this finding is consistent with the data presented in [61], where significant increases in energy dissipated by the AFM cantilever were found at close approach.

Liquids or soft matter systems differ from solids in that the relevant energy scales are often comparable to the thermal energy $k_B T$, where k_B denotes Boltzmann's constant and T is the temperature. The relevant quantity in these systems is not the internal energy U, but the free energy, which takes into account entropic contributions. Depending on whether we consider a system at constant temperature and constant volume (NVT), or constant pressure (NPT), the corresponding thermodynamic potentials are either the Helmholtz free energy,

$$F = U - TS, \tag{18.1}$$

or the Gibbs free energy,

$$G = U - TS + pV, \tag{18.2}$$

where S denotes entropy, V volume, and p pressure, respectively. The textbooks by Chandler [62] or Frenkel and Smit [46] give a good overview of computational statistical mechanics, and free energy calculations. In the context of simulating AFM in liquid, if we can calculate the change in free energy of the model system as a function of the position of the AFM tip apex, the derivative of the free energy with respect to the tip-surface separation distance will be the best approximation for the force acting on the AFM tip, taking into account entropic contributions from the liquid. We emphasize here that such a calculation yields an equilibrium property of the system; there is no distinction between tip approach or retraction.

Several computational methods for free energy calculations exist, and we have benchmarked two of them for the use in simulation of AFM in liquids [51]: umbrella sampling (US) and free energy perturbation (FEP). In both methods, we calculate a free energy profile—the change in free energy as a function of a collective variable—which is taken to be the tip-surface separation distance z, for a fixed lateral position

of the tip. In umbrella sampling [63, 64], the free energy profile is calculated from the probability P of observing a certain value of z in the course of a simulation:

$$F(z) = -k_{\mathrm{B}}T \ln P(z). \tag{18.3}$$

In order to ensure adequate sampling of distances with high free energies, a series of independent simulations are carried out, where the tip-surface distance is biased to a certain range of values by an umbrella potential, $U_i = \frac{k}{2}(z - z_i)^2$. The global, unbiased distribution can be constructed through self-consistent histogram re-weighting from the overlapping biased distributions obtained in each umbrella window.

In free energy perturbation, part of the tip is constrained to a fixed point in space. At this point a molecular dynamics simulation is performed and a set of representative configurations saved. The free energy change ΔF to move from point $\mathbf{r}_0$ to point $\mathbf{r}_1$ is then found by perturbing the tip in each of the saved configurations by a rigid translation from point $\mathbf{r}_0$ to $\mathbf{r}_1$ using Zwanzig's relation [65]

$$\begin{aligned} \Delta F &= F(\mathbf{r}_1) - F(\mathbf{r}_0) \\ &= -k_{\mathrm{B}}T \ln \left\langle \exp\left(-\frac{U(\mathbf{r}_1) - U(\mathbf{r}_0)}{k_{\mathrm{B}}T} \right) \right\rangle_0 , \end{aligned} \tag{18.4}$$

where the subscript 0 indicates that the average is taken over the configurations collected when the tip is at point $\mathbf{r}_0$ and the potential energies are calculated at the unperturbed (subscript 0) and perturbed (subscript 1) locations. The total free energy change of the tip approaching the surface is then built up by adding together the individual contributions.

18.2.3 Simulation Setup

In order to set up starting configurations of the simulation system, consisting of a surface slab, AFM tip model and liquid, we found it most efficient to proceed by steps: First a simulation box containing only the surface slab with correct lattice vectors along x and y directions, and appropriate thickness along z is constructed. The thickness of the surface slab depends on the type of solid under consideration, but it is typically advised to make it large enough such that the innermost crystal layers of the surface slab behave as if they were in the bulk material, i.e., surface effects are negligible. Due to periodic boundary conditions, the surface slab is effectively infinitely large in the lateral directions. In the direction perpendicular to the surface the size of the simulation box is chosen in such a way that the solvent is capable of achieving bulk properties far away from the surface. As a rule of thumb one can say that the z-size of the liquid part of the simulation is roughly at least three to four times the size of the solid part, although this can depend on the system under investigation.

As in the lateral directions, in the z-direction periodic boundaries are also applied, and in that sense it is irrelevant where exactly the surface slab is positioned within the simulation box. Placing the surface slab in the centre of the box though facilitates easy visualization and analysis.

The remaining volume of the simulation box is filled with the solvent, most commonly to date water, which is pre-equilibrated in a box of similar dimensions. This system consisting of surface and water needs to be equilibrated in NPT using a semi-isotropic barostat, keeping the box vectors in x and y fixed. In this way, the z direction of the box will equilibrate to yield the equilibrium hydration layer structures at the solid-liquid interface, and the correct bulk solvent density far away from the interface region. For interfaces between water and ionic crystals, the hydration layer structure typically takes less than 100 ps to form. This system can now be used to, e.g. study properties of the hydration layers, from time averages obtained in NPT or NVT. To avoid drift of the slab, a layer of atoms in the centre of the slab can be constrained (e.g. with a harmonic spring), removing the translational degree of freedom. This 'anchors' the system in the absolute frame of reference of the simulation box and facilitates analysis of atomic positions. In order to obtain accurate and reliable statistics, MD simulations should typically run for at least several nanoseconds, after equilibration.

For an AFM simulation, a nanocluster tip model has to be introduced in the simulation box far from the interface, and all overlapping water molecules need to be removed. A final equilibration in semi-isotropic NPT will equilibrate the hydration structures around the nanocluster as well and adjust the box vector along z, to obtain the correct water density far from the cluster and the surface. It should be ensured that the simulation box is large enough to avoid interactions between the hydration structures of the nanocluster with the hydration layers of the periodic image of the surface slab, when the tip is 'far away' from the surface. Furthermore, the lateral dimensions of the simulation box should be chosen so that the hydration structures around the tip do not interact through the periodic boundaries along x and y with its own copy. A summary of the simulation set-up described above is presented in Fig. 18.1.

In order to generate several different starting configurations for a free energy calculation (at different tip-surface distances and above different surface atoms), a steered MD simulation, where the tip model is slowly moved towards (or away from) the surface along z, can be used. Using such a steered MD simulation directly to model an AFM tip approach is not possible, as the pulling speeds accessible in an atomistic simulation (typically of the order of nm/ns) are orders of magnitudes faster than the oscillation of an AFM cantilever. Thus, trajectories obtained in this way will be far from equilibrium and do not resemble experimental conditions, though in future construction of free energy profiles from multiple non-equilibrium simulations may become practical. Also the force-distance curves will be noisy and exhibit large hysteresis between approach and retraction. After selecting the appropriate frames from the steered MD simulations, the above described equilibration simulations have to be repeated for every point of interest. This is the main reason why the rigorous free energy modelling approach to AFM is computationally expensive, as for one

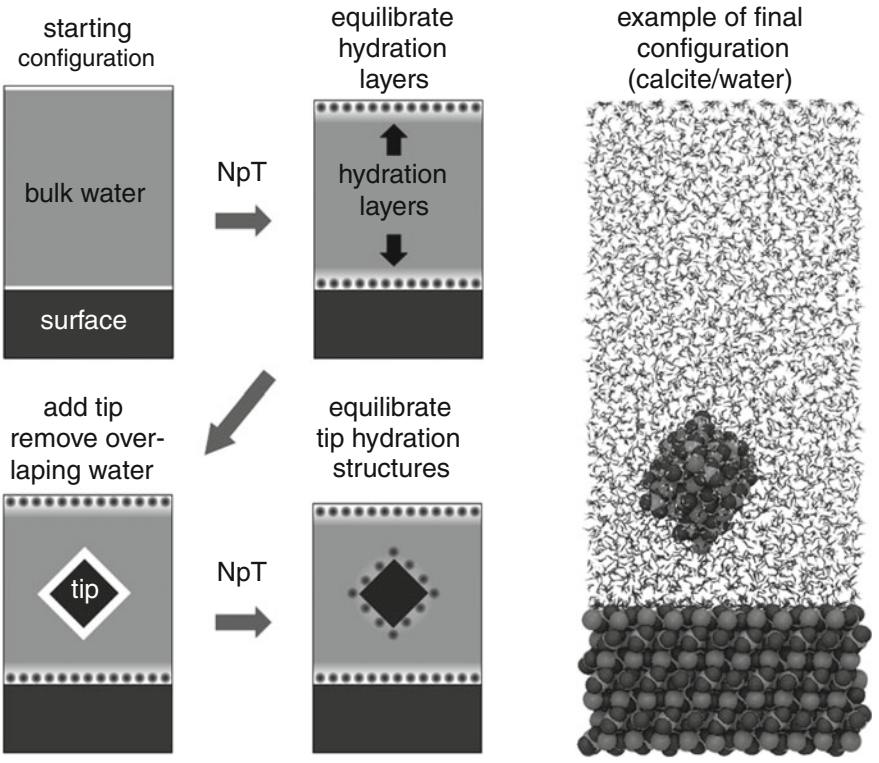

Fig. 18.1 Setting up a system for simulation of AFM in liquid

system several tens to hundreds of individual simulations have to be performed, each of several nanoseconds length.

18.2.4 Interactions

MD simulations differ from first principle simulations in that they rely on empirically developed force fields, although both simulation techniques can be used to investigate dynamical properties. These force fields come in many different forms and depend most of the time on the system under investigation. For instance biomolecular force fields focus less on modelling the properties of solids correctly and are optimized for the large dynamic systems typically encountered in biophysics (e.g., proteins, lipid bilayers). On the other hand, in solids the topology rarely changes and more computational resources can be spent on accurately modelling important solid properties (e.g., lattice constant, bulk modulus, phonon spectra). To date there exists no fully consistent force field to model solid-liquid interactions accurately,

although a few exist that focus on getting some specific properties (thermodynamical or structural) as correct as possible. But all force fields have in common that they have non-bonded interactions (electrostatics and van der Waals) and bonded interactions (bonds, angles, dihedrals, and impropers). To model a solid-liquid system as accurately as possible all of these interactions need to be well balanced, and with sometimes hundreds of different and independent parameters, that is not an easy problem.

Depending on the type of system under investigation, one can use general purpose force fields like CHARMM [66], AMBER [67] or OPLS [68], but this limits the solids to organic and ionic crystals. Most of these general purpose force fields can model the interactions between a solvent (likely to be water) and the atoms within the crystal accurately, but the solid atoms might need some additional simulation constraints, as these force fields do not necessarily model the solid phase accurately. While this affects solid properties, the interaction between solid and liquid is most likely not influenced significantly.

Currently only a few force fields exist that are specifically aimed to model all phases encountered in AFM systems (solid, liquid and the interface) correctly. For example, the CLAYFF force field [69], which is a general force field suitable for the simulation of hydrated and multicomponent mineral systems and their interfaces with aqueous solutions, has recently been shown to be compatible with the TIP3P water-model of the CHARMM force field [70–73]. Another dedicated example is a recently developed calcium carbonate ($CaCO_3$) and water force field [74, 75]. This force field has been extensively validated against experimental thermodynamic data, including the free energy difference between calcite and aragonite, the free energy of solvation of the component ions, and the enthalpy of dissolution for calcite, as well as structural data and properties of the two relevant phases. The hydration layer structure of calcite, predicted by this force field, has recently been compared to specular X-ray reflectivity data [76].

In general, selecting the force field for the simulations is one of the most crucial and important steps in the entire modelling process, as it can have profound influence on the results. Attention should be paid to which properties (like liquid density or diffusivity, crystal structure, bulk modulus, phase diagrams, etc.) are of importance for the system under investigation and whether the desired force field models these properties accurately. Nonetheless, some rules of thumb on which kind of interactions (electrostatic, intramolecular, van der Waals, etc.) are important for solid-liquid interfaces can be given. In the case of ionic and organic crystals the electrostatic interactions typically dominate the interaction between the solvent and the crystal and, hence, the charge distribution on each of the involved molecules must be accurately modelled. For more inert materials, like graphene, the van der Waals interactions are more important, and for metallic surfaces the effects of the electronic structure must also be accounted for.

Not only the cross interactions between the solid and the liquid have to be modelled correctly, also the choice of force field for the liquid is important. For instance, in the case of water, several different models exist [77], ranging from three to five charge point models, flexible and rigid models (see Fig. 18.2a). Again, the choice for the

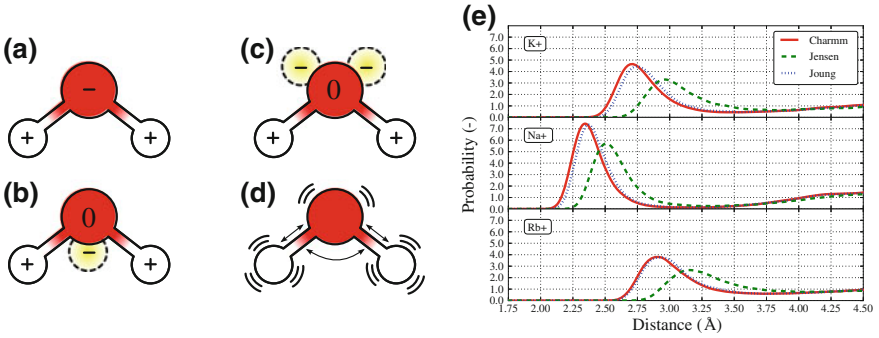

Fig. 18.2 In **a**–**d** schematics of different water models are depicted, where **a** is represents the 3-point model, **b** the 4-point model and **c** the 5-point model. Note, the change and placement of the charges. In **d** the intramolecular motions like bond and angle bending are depicted. In **e** the radial distribution function for three different monovalent ions (sodium, potassium and rubidium) with TIP3P water as represented by three different force fields (see text) are shown

water model depends on the system under investigation, but typically flexible three point models like the previously mentioned TIP3P and the SPC [78, 79] models are sufficiently accurate to model solid-liquid interfaces.

Finally, most AFM experiments are done in solutions where ions are present. Either these ions are deliberately part of the buffer solution or they appear because parts of the surface dissolve over time. The spatial arrangement of ions at solid-liquid interfaces is currently of great interest, because when immersed into a liquid, most solids develop charges at their surface. To maintain electric neutrality, the (counter)ions dissolved in the liquid tend to accumulate close to the solid's surface, forming an electrostatic double layer that counterbalances the surface charge. Similarly, these ions can accumulate close to the tip as well and the effect of these ions is currently one of the most important fundamental questions to better understand the AFM imaging mechanism in liquids. Thus, in MD simulations of solid-liquid interfaces, ions need to be treated accurately as well, and, like with water, there are many different ion models. In Fig. 18.2e the characteristic radial distribution function for the water oxygen atom with three different ions (sodium, potassium and rubidium) for three different ion models (CHARMM, Jensen [80] and Joung [81]) show significant differences.

18.2.5 Tips and Tricks

As explained previously, assuming that a single water molecule can be strongly bound to the tip and act as a probe itself, allows for a more simple modelling approach. The assumption implies a direct correlation between the unperturbed water density above a sample and the force measured by a nc-AFM. It has also been observed that

whilst quantitative differences exist in measurements above well prepared surfaces, qualitatively measurements using different cantilevers and taken at different times are often in good agreement [82], suggesting that there may be common features to many solvated AFM tips that lead to well defined classes of contrast.

Two classes of tip that might exist fairly universally in aqueous solution are:

- sharp hydroxylated tips—for instance an isolated silanol (Si–OH) group on the end of an ultrasharp silicon or silicon nitride tip that has been partly oxidised.
- tightly bound water molecules—if a tip is terminated by an ionic material with significantly charged cations (e.g. $Si–OH_2$ or $Ca–OH_2$ in tips terminated with silica or fluorite clusters), it is expected that water molecules will adsorb quite strongly. On a time average they will be present during the imaging process between the *actual tip* and surface. In this case any closely bound water layer is actually part of the tip.

Molecular dynamics simulations of solvated nanoclusters of fluorite [47, 60] and silica [83] show that these functional groups are common and are present for large parts of the simulation time; by this we mean that even though the residence time of a water molecule above a given cation site is only ∼0.25 ns [60], as soon as it leaves, another water molecule will take its place, reforming the tip model. Particular examples taken from molecular dynamics simulations illustrating both of the classes of tip terminations are shown in Fig. 18.3.

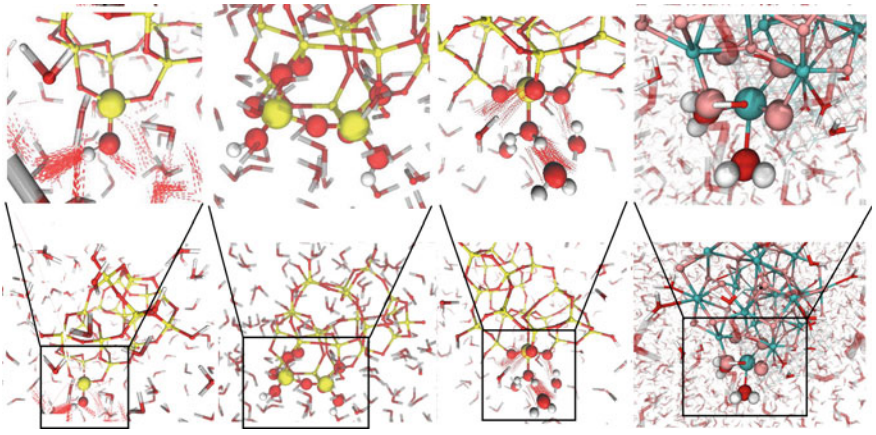

Fig. 18.3 Tip models extracted from molecular dynamics simulations that expose a flexible OH group to the environment. Bulk solvent molecules are shown as transparent "v" shapes with O *red* and H *white*. Atoms shown as *larger balls* are the tip terminus and its local environment. Silicon is *yellow*, oxygen *red*, calcium *turquoise* and fluorine *pink*. *Upper figures* show overall views of the nanoclusters, *lower figures* zoom in out from the area of interest to give an idea how they fit into our tip models from *left* to *right*; silanol group—Si–OH—on a silica cluster; two neighbouring (vicinal) silanol groups on a silica cluster (geminal $Si(OH)_2$ groups are also possible); water molecule adsorbed on a silica cluster; water molecule adsorbed on a CaF_2 cluster

From the arguments developed above based on the observation of molecular dynamics trajectories of tips in water and the likelihood of common types of tip termination, we take a single water molecule as the tip model and calculate the change in free energy as it approaches the surface over different lateral sites.the explicit free energy calculations we use free energy perturbation (FEP) theory [65] in exactly the same way as in our previous simulations of the force on a nc-AFM tip, [60], but using a water molecule as a tip. The calculations are readily performed, converging much more rapidly than when a larger nanocluster is used to represent the AFM tip.

The free energy difference for a water molecule to move from bulk to a certain position $\mathbf{r}$ is

$$\Delta F(\mathbf{r}) = -k_{\mathrm{B}}T \ln(Z(\mathbf{r})/Z_N). \tag{18.5}$$

In a MD simulation, the time-averaged ratio of local and bulk water density, $\rho(\mathbf{r})/\rho_0$ corresponds to the ratio of the constrained and full configurational partition functions $Z(\mathbf{r})/Z_N$ in the equation above. Therefore the force on the AFM tip is given by the derivative of the free energy with respect to the tip-surface distance,

$$f(z) = -\frac{\mathrm{d}F(z)}{\mathrm{d}z} = \frac{k_{\mathrm{B}}T}{\rho(z)}\frac{\mathrm{d}\rho(z)}{\mathrm{d}z}. \tag{18.6}$$

The curves obtained by the FEP calculation of the water model tip, and those obtained directly from the unperturbed water density are in excellent agreement. We note that the method proposed here is close to being a simulation counterpart to the experimental method of Cleveland et al. for the reconstruction of hydration forces in contact mode AFM [84].

The significance of this, is that it should be possible to very closely link force measurements to the equilibrium, undisturbed water structure, providing a significant boost in the understanding of water structuring at interfaces. It also implies that hydroxylated tips and tip apexes with closely bound water molecules are not invasive and come closest to directly measuring the unperturbed water density above a surface. Indeed, it should be possible to convert force spectroscopy data directly into water density. Conversely, it is possible to take the natural logarithm of water density on a grid obtained from simulation to obtain the short range force "spectrum" measured by nc-AFM. On well characterised samples, it should be possible to see how well the actual tip corresponds to this idealised situation by comparing the measured force to theory or other experimental measurements (e.g. X-ray or SFA). In our hypothetical ideal nc-AFM measurement, it is the water density that is directly probed—not the surface.

18.3 Case Studies

18.3.1 Simple Ionic Surfaces

18.3.1.1 CaF_2

To achieve a qualitative understanding of the forces involved in FM-AFM imaging we considered fluorite CaF_2 (111) and carried out simulations of its interaction with different nanoclusters modelling AFM tips in aqueous solution. CaF_2 is probably the best understood system in UHV [27], and is rather insoluble making it an attractive target to transfer our understanding from the vacuum to the solvated system, though this assumption has proved to be somewhat suspect [85]. The systems considered include a cluster model of an AFM tip apex (or nano-tip), a surface, and a solvent (water), see Fig. 18.1. We assumed that the tip apex is likely to be formed from the same material as the surface through accumulation of material during scanning [27] and used a set of representative model nano-tips with different polarities of the tip apex and "sharpness" of the tip directed to the surface.The change in free energy as a tip approaches a surface is calculated using the perturbation method of Zwanzig [65] using classical molecular dynamics.

Figure 18.4 shows approach curves for a blunt tip over topmost fluorine (Fh). To better understand the data we have decomposed the interaction into potential energy and entropic contributions [47] and direct and water mediated components, plotted in Fig. 18.4. The decomposition into direct and water mediated components is carried out as detailed in the appendix of [86]. In all cases we calculate an attractive entropic contribution to the free energy change arising from the increase in translational and rotational degrees of freedom when water initially confined near the tip or surface is forced away into bulk-like positions by tip-surface proximity. By contrast, in vacuum

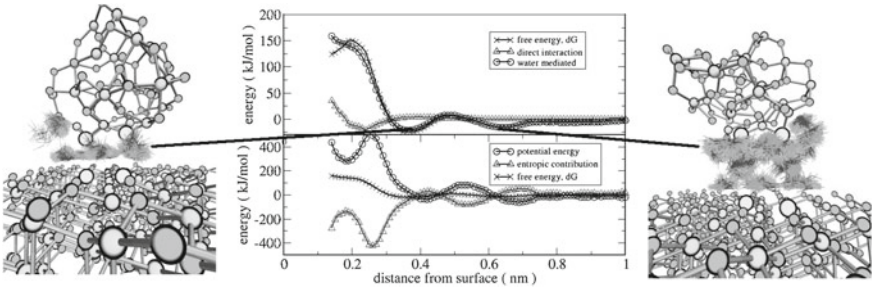

Fig. 18.4 The approach of a blunt CaF_2 tip over a surface Fh ion. The molecular cartoons show the tip, surface and nearby water molecules when the tip is located at the two most stable heights above the surface at this lateral location. Every 2 ps of simulation all water molecules having a hydrogen atom within 0.3 nm of the highlighted surface fluorine atoms were drawn. Waters orientate to screen the tip and surface fluorine ions leading to a net attractive interaction when the entropic contribution is also considered

the evolution of potential energy is almost indistinguishable from the overall free energy change and the entropic contribution is negligible. The observed force is thus a balance between largely repulsive potential energy changes as the tip approaches and the entropic gain when water is sterically prevented from occupying sites near the tip and surface. The entropic terms increase sharply when the tip encounters higher water densities near the surface.

We find that direct tip-surface interactions are similar to those found in UHV. For example, taking a sharp fluorine terminated tip above a Ca ion of the surface, the direct interaction is significant at heights of *ca.* 0.2–0.4 nm. Conversely, the blunt tip has only a weak direct interaction with the surface, which results from the interactions of several tip and surface ions and the overall interaction becomes strongly repulsive before the direct interaction could be measurable: the overall force is totally dominated by the water mediated interaction, Fig. 18.4. The ratio of direct to water mediated force is enhanced for sharper tips as they displace less water at a given tip height.

The water mediated interactions are more complex and represent the main difference from UHV. We can roughly divide these interactions in two types. An energetic cost to displace water that is bound to the hydrophilic surface causes variations in the tip-surface force that approximately follow changes in the water density above different surface sites, as discussed elsewhere. A second type of water mediated interaction occurs from the creation of favourable water locations between tip and surface when they are separated by distances comparable to diameter of a water molecule. In Fig. 18.4 we show the positions of water molecules that have a hydrogen atom within 0.3 nm of the two tip apex ions of the blunt tip when the tip is at a height of 0.37 nm above the surface. The hydrogen ions of the water molecules are generally located to interact favourably with both the tip and surface fluoride ions that stabilizes the system–the water is still mobile enough to act as a highly efficient dielectric. These favourable collective water interactions between tip and surface appear to be a general phenomenon.

The total force curves for the two tips approaching the surface over surface Ca or Fh sites demonstrate variations in free energy and force between surface sites of similar magnitude to those observed in vacuum and shown to provide good atomic contrast [27].

18.3.1.2 Alkali Halides

As one of the most simple ionic crystals, alkali halide crystals are of interest as a benchmark set for both experiment and simulations. They also differ considerably in their water solubility, with for instance NaCl and KBr easily dissolved in water, but NaF and LiF much less soluble. Understanding the nature of this different solubility from a molecular level is interesting and potentially interesting for medical use and radiation detection.

Because of the wide range of solubility for the alkali halides obtaining experimental AFM images on flat surfaces is particularly challenging. Therefore, as a first

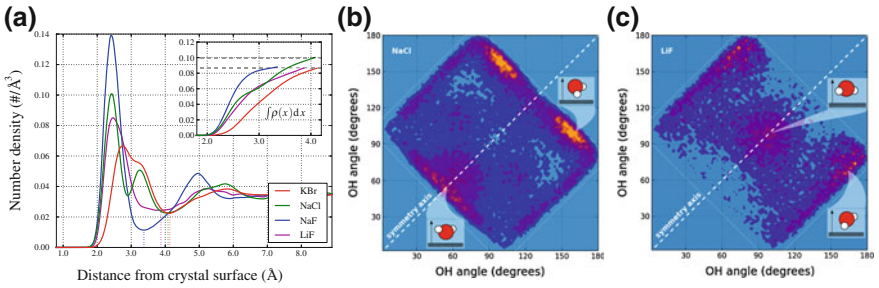

Fig. 18.5 In **a** the water-oxygen densities for the different alkali halides (see legend) perpendicular to the crystal surface is shown. In the *inset* the integral of these water densities is shown up to the end of the first hydration layer (*vertical dotted line* in main figure). The *horizontal dashed lines* in the *inset* show the same water coverage for KBr, NaF and LiF, but a higher coverage for NaCl. In **b** and **c** the correlation between the angles of the OH-bonds in the water molecules (with respect to the surface normal) is shown for NaCl and LiF, respectively. A more *bright color* means a higher correlation

step is to look in detail at the hydration structure at these interfaces without an AFM tip present. As almost all alkali halides crystalize in the face centered cubic form, building systems for simulations is relatively easy. In this case study we will focus on the solid-liquid interface of the four previously mentioned alkali halides (in order of decreasing lattice constant): KBr, NaCl, NaF, and LiF.

On all of the four (001) surfaces we observe structuring of the water, see Fig. 18.5a, and several hydration layers in the first 10 Å are clearly visible. Whereas NaF and LiF show a single density peak for their first hydration layer, the picture is slightly more complicated for KBr and NaCl. For the former a wide first peak with a shoulder around 3.2 Å is visible, and for the latter two distinct peaks (at 2.4 and 3.2 Å) can be identified. Closer analysis identified that for both KBr and NaCl the second peak and shoulder are caused by water molecules being coordinated above the anions of the respective crystal. On the two less soluble alkali halides, NaF and LiF, different coordination on top of anions or cations was also observed, but they happened within the same distance from the surface, and as such, no difference in the perpendicular profiles can be observed, except for the fact that the densities for these two systems is higher than for the more soluble ones.

Clearly, the water molecules are differently oriented on top of anions than on cations for each of the alkali halide systems. To better understand how water molecules are oriented we looked at the correlation between the angles both water OH-bonds make with the surface normal. For instance, if one of the OH-bonds would be pointing down to the surface along its normal and the other OH-bond away from the surface (such that the internal angle of the water molecule remains 104°), we would find for both OH-angles 0° and 76°, respectively. When this process is done for all water molecules in the first hydration layer (which ends at the dotted vertical lines in Fig. 18.5a), correlation plots like those in Fig. 18.5b, c can be constructed. From these two plots (for NaCl and LiF) we can observe that the water is very differently oriented on both surfaces (see the water molecule cartoon insets). In the case of NaCl

the water molecules are either positioned with the hydrogen atoms pointing away from the surface (on top of the cation, lower left) or with one hydrogen pointing toward the surface and the other one away (on top of the anions). For LiF, the water molecules are lying much more flat on the surface and only on top of the anions the water can position itself more or less similar compared to water on top of NaCl.

The major origin for this different water coverage is most likely caused by the difference in lattice constants for each of the alkali halides. When the lattices are slightly larger (as is the case for KBr and NaCl, with lattice constants of 3.3 and 2.8 Å respectively) the water can be accommodated much better and hence strong orientational preferences can occur above the cations and the anions. When the lattice constants are a lot smaller (for NaF and LiF, 2.3 and 2.0 Å respectively), this accommodation can no longer occur, leading to a more frustrated hydration structure. It is probably this better water accommodation that allows for a stronger dissolution process in the presence of defects on the surfaces, although this has to be verified in the future.

In order to verify the coverage of the crystal surface by water molecules, we computed the integral of the densities up to the end of the first hydration layer (see inset in the Fig. 18.5a). Now it can be clearly seen that all systems have the same amount of water molecules on their surfaces, except for NaCl, which has approximately 15 % more water molecules on its surface. Given the difference in solubility (NaCl is by far the most soluble of the four alkali halides under investigation), this is not surprising.

18.3.2 Calcite

Because of their relevance and relative ease of sample preparation, calcite surfaces have been studied extensively by LEED, XPS, as well as AFM in UHV, air, and different liquids [23, 87, 88]. In fact, one of the earliest AFM studies yielding atomic scale contrast was obtained on a calcite surface under a thin film of water, in contact mode [16]. Rode and co-workers published the first true atomically resolved images of the calcite surface in aqueous solution, using FM-AFM [23]. Even though the cantilever oscillation amplitudes in this study were 0.2–0.3 nm, which corresponds roughly to the van der Waals diameter of a single water molecule, the interpretation of the contrast assumed that atoms in the calcite surface were being imaged. The possible role of water molecules in hydration layers (see Fig. 18.6b) in the contrast formation was not addressed.

The first simulations of AFM imaging of calcite in water [51], based on the free energy approach described earlier, and using a calcite nanocluster tip, yield free energy profiles that could account for the atomic resolution in images obtained by Rode et al. [23]. Simulated virtual AFM images [89], using a 3D force map derived from the free energy data, with parameters for the cantilever oscillation matching the ones in [23], show strong resemblance to experiment. However, a full explanation of the imaging mechanism was not attempted. First, the exact tip-surface distance in 2D AFM images is not known, making direct comparison to simulation difficult. Second, the relative instability of the 125 atom calcite nanocluster tip's apex leads

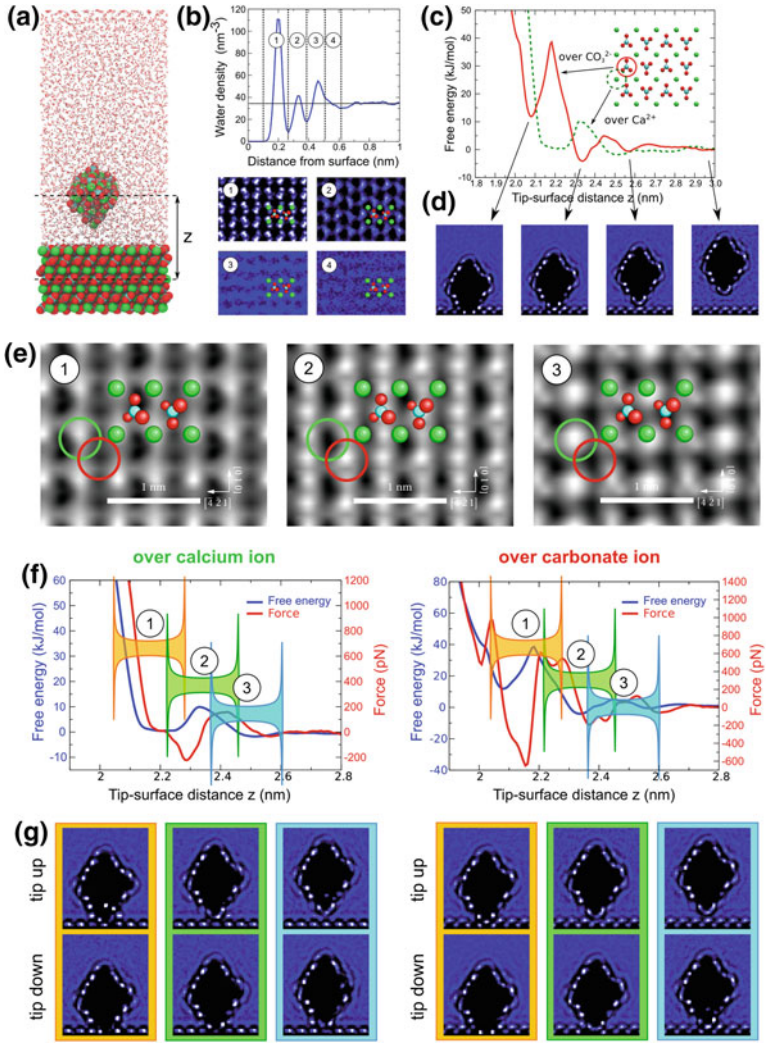

Fig. 18.6 Simulation of AFM imaging of calcite ($10\bar{1}4$) in water. **a** Simulation snapshot, indicating the tip-surface distance z, defined as the z-component of the centre of mass distance between the calcite nanocluster tip (here, terminated by a calcium ion) and the surface slab. **b** Calcite hydration layer structures. **c** Free energy profiles over a calcium and carbonate surface site. **d** Average water density in 0.2 nm thick x, z–slices through the tip apex at the positions of free energy minima approaching a carbonate ion in the surface. **e** Virtual AFM frequency shift images obtained at three different heights, using a 3D force field derived from free energy profiles, and cantilever oscillation parameters matching the experiment. **f** The tip oscillation ranges corresponding to the three imaging heights in panel **e** are indicated by *orange*, *green*, and *turquoise bars* on top of the free energy (and force)—distance profiles obtained from simulation. The width of the oscillation range indicators is proportional to the sampling at that distance. **g** Cross-sections of local water density at the upper and lower turning points of the tip oscillation, which contribute most to the measured signal

to ambiguities in the actual tip termination and hinders a thorough analysis of the simulation data. Finally, the simulations have been carried out in pure water, whereas some of the experimental images have been obtained in dilute ionic solution. Other MD simulations show that different counter ion species occupy specific positions within the hydration layers of calcite, depending on their size and charge [90], pointing out the importance of considering the ion concentration in the liquid. This adds a layer of complexity to the imaging mechanism, currently beyond the scope of our modelling approach.

To resolve the computational issues mentioned above, it is necessary to repeat the free energy calculations using a larger calcite nanocluster, consisting of 160 atoms and exhibiting a more cubic shape (see Fig. 18.6a). 32 $CaCO_3$ units is a stable size for small calcite nanoclusters [91], and this cluster can be rotated so that either a calcium or a carbonate ion is at the corner exposed towards the surface. Due to the improved stability of the tip model, free energy profiles can now be computed all the way down to hard contact between tip and surface. For the experiments, it now becomes possible to record 3D force data in FM-AFM on a calcite surface in pure water, mainly due to the use of ultrashort cantilevers [26], and so, for the first time, a direct comparison between 3D force data from experiment and atomistic simulation is possible [92].

These simulations show that successive free energy minima encountered as the tip approaches the surface correspond to distances where the combined tip and surface hydration structures resemble their intrinsic states, when the tip is far away from the surface, as shown in Fig. 18.6c, d. The free energy peaks correspond to rearrangement of the combined tip and surface hydration structures. Simulated frequency shift images are obtained with a virtual AFM, using the 3D force map derived from the free energy profiles, and parameters for an ultrashort cantilever ($f_0 = 3.5$ MHz, $A_0 = 0.12$ nm, $k = 50$ N/m and $Q = 6$). They show alternating changes in contrast over calcium and carbonate surface sites (see Fig. 18.6e), similar to the peaks in water density distribution in the hydration layers of calcite, shown in Fig. 18.6b. The analysis of the contrast mechanism, based on the collective changes in water density during the tip approach, remains a complicated task: even for small cantilever oscillations, the amplitude is of the same order as the variations of the free energy or force profiles (Fig. 18.6f), and significant changes in the combined hydration structure of tip apex and surface occur during an oscillation cycle (Fig. 18.6g). However, we find good agreement between the 3D force data in experiment and simulation, validating our computational model. The best agreement is found with the simulations using the calcium-terminated tip. Based on the average water density distributions between the tip and surface in the simulation, we find that the repulsive forces on the AFM tip are mainly due to the compression of the tip apex against the hydration structures. Once the build up of force is large enough to induce a re-arrangement of the hydration structure, the tip feels a considerable attractive force towards the surface, until a new free energy minimum is reached. We also confirm that at the maximum repulsive force encountered in stable AFM imaging conditions in water, the first hydration layer is heavily perturbed, but water molecules are still found between tip apex and surface.

18.3.3 Molecular Crystal p-Nitroaniline

The previous examples all belong to the class of ionic crystals. An entirely different set of surfaces is formed by the molecular crystals, with the organic crystals being the vast majority. An example a molecular crystal that has recently been investigated in AFM experiments is *p*-nitroaniline [93, 94]. This organic compound is of interest as it contains two polar groups (amino and nitro) present on opposite ends of a non-polar benzene ring (phenylene), allowing the control of the heterogeneity of the surface. Understanding how the interfacial water structures itself near this organic compound is an important benchmark case, which allows us to better understand dissolution and crystallization processes.

For this particular molecular crystal two different space group settings can be identified, but for both the preferred cleavage plane is supposedly along the (101) plane, which also provides a well-developed facet for recrystallization [95]. For one the two representations the *p*-nitroaniline molecules all align with the cleavage plane, but for the other one, half of the molecules in the unit cell are perpendicular to the cleavage plane, see Fig. 18.7a, respectively named the P21/m and P21/c crystals.

The first indication that structuring of the solvent near the crystal surface occurs, can be seen in the particle density plots perpendicular to the surface, see Fig. 18.7b. Water exhibits a strong structuring in multiple layers, which fades after about 1.2 nm distance from the surface. Comparison of the P21/m and P21/c shows the density profiles being much flatter for the latter, although the differences disappear further away from the surface. The most plausible explanation for these lowered densities is the nature of the exposed surface. For P21/m this is a rather homogeneous structure, whereas the surface for the P21/c exhibits much more heterogeneity, see Fig. 18.7a.

In the AFM experiments two different topographies have been observed, one with two spots of equal brightness in the unit cell (observed only in limited cases, named 'rare' here) and one with bright and a less bright spot in each unit cell (named

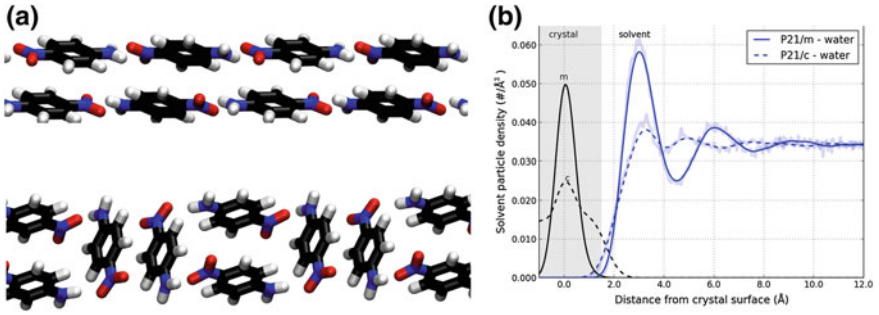

Fig. 18.7 In **a** the side views of the (101) surfaces for the two possible crystal structures for *p*-nitroaniline are depicted (*top* P21/m, *bottom* P21/c). In **b** the time-averaged water particle density (in number of particles per cubic Å) is shown for both crystal structures as a function of the distance to the crystal surface. The distances are measured with respect to the centre of the in-plane molecules in the outermost layer of the crystal, which is set at zero (*black lines* to the *left* indicate the crystal densities, not to scale)

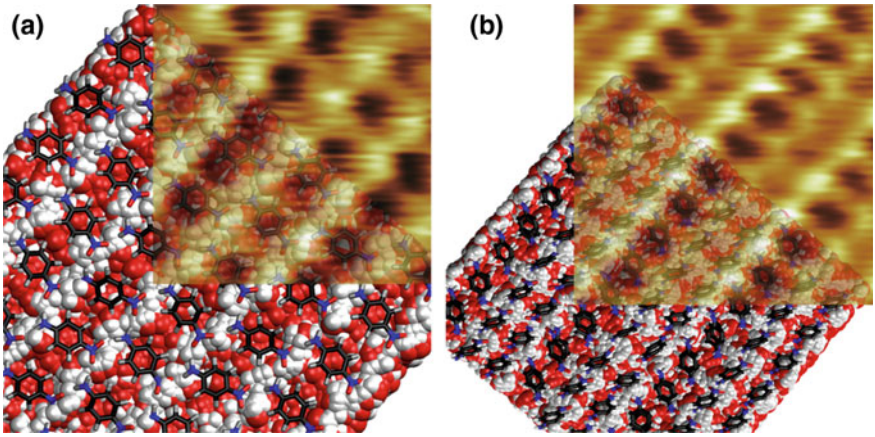

Fig. 18.8 Composite images of AFM experiments and MD simulations. In **a** and **b** topographic images from the rare and common AFM experiments are compared to the MD snapshots for the P21/m and P21/c respectively

'common'). In order to compare our MD results directly with the AFM experiments we computed the two dimensional density profiles parallel to the surface for each of the hydration layers. Since in general, localization of water is strongest in the first hydration layer, we focus our studies of the water density in this regime as a first approximation of what the AFM experiments are likely to see. Furthermore, we assume the local densities to be directly related to the forces the AFM feels, leading to the topography image. This is a simplification and more elaborate methods exist, such as modeling the tip as a nanocluster [51] or converting local densities through Boltzmann inversion into free energy curves [53], but in the end it is the local density (if left largely undisturbed by the tip) that determines the AFM image. So at least a qualitative comparison is possible and to enhance the comparison between experiments and simulations we aligned our obtained density images with the experimental topography ones, see Fig. 18.8.

By extensively using two possible surface arrangements (the P21/m and P21/c) it is possible to match the results from the AFM water experiments with different topography images almost exactly with the results from the MD simulations. Although in some situations the P21/m appears in the AFM experiments, the P21/c surface structure is much more commonly observed [93]. Currently this different surface structure has not been directly observed in crystallography (or any other non-AFM) experiments, as these were mainly focused on the bulk phase instead, but the simulations here point to a possible surface reconstruction, offering different ordering of water on the surface, all in excellent agreement with the majority of experimental results. As such these findings on a possible reconstruction are quite new and open experimental challenges for it to be confirmed.

18.3.4 Ionic Liquids

In this chapter, we have already introduced some of the challenges faced when simulating different solvents and including the role of ions in solution. However, the complexities are significantly increased when the solvent itself is ionic. Ionic liquids (IL), originally discovered in the 1930s, are room-temperature molten salts, often composed of organic molecules, commonly used in synthesis [96, 97] and catalysis [98, 99]. Their popularity among synthetic chemists stems from the need to constantly replace solvents that are labelled too toxic or dangerous and banned by the authorities. ILs are chemically more stable than other organic solvents, non-flammable, non-volatile, and that is why, despite some are still toxic, they are considered the green solvents of the future [100]. Recently their properties have been experimentally studied more extensively, since they are quite suitable for many applied fields [101]. Thanks to their ionic nature, they can store electrostatic energy by forming a stable, charged layered structure at the interface with charged metals [102]. This mechanism was found to greatly extend the potential of super-capacitors [103]. They can also be used as electrolytes in Li-air batteries, where their chemical stability enables the use of a pure Li metal anode with tremendous energy density [104, 105], and prevent atmospheric water from leaking inside the device. Moreover, strong electrostatic intermolecular forces ensure negligible vapour pressure, so that ILs could be used to coat biological material, allowing electron microscopy studies of cells without deforming them in ultra-high vacuum environments [106]. Lastly, they have been found to lubricate surfaces efficiently [107], giving low friction coefficient [108] and excellent protection against wear [109].

Given the freedom in choosing cation/anion molecules, it has been estimated that more than millions of ILs exist, each with slightly different properties [110], implying the possibility to optimise, or even design, ILs for a specific task. At present, this cannot be achieved because there are no clear relationships connecting the atomic scale properties of IL molecules and surface, to the performance of system. For this reason, research efforts are focussed on understanding the atomic scale origin of IL-solid interface properties, and AFM is indeed one of the most promising techniques, capable of providing such detailed information.

It is generally thought that ILs form layers of alternating charge on surfaces, although the example of 1-butyl-3-methylimidazolium bis(trifluoromethylsulfonyl) imide ([BMIM][NTF2]) and 1-butyl-3-methylimidazolium tetrafluoroborate ([BMIM][BF4]) on hydroxylated crystalline silica reveal how the effect can be dependent on the nature of the liquid [111]. Calculations showed that BF4 anions adsorb at the center of the triangular structures delimited by silanol groups. The small size of the molecule allow them to fit in this seemingly void space, and sink in the surface plane forming a negative layer. BMIM cations, being larger, cannot adsorb as close, and are located above. This causes all subsequent layers to have alternating charge as well, and the liquid resembles a binary FCC (111) lattice. NTF2 anions are much larger than BF4, and adsorb at the same height as BMIM cations, forming an overall neutral boundary layer with NTF2 and BMIM molecules in equal amount.

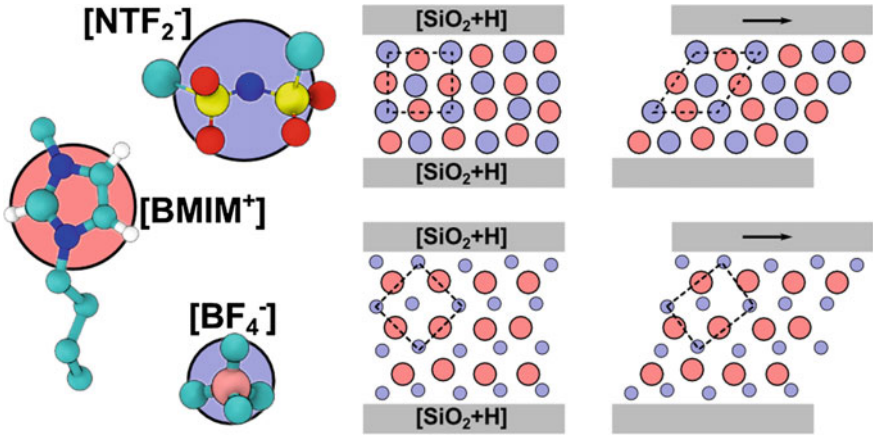

Fig. 18.9 Schematic representation of the ionic liquid structures under nano-confinement. [BMIM][NTF2] (*top*) organises into neutral layers, which become unstable when sheared. [BMIM][BF4] (*bottom*) shows alternating charged layers that flow against each other, with minimal reconstruction

All successive layers are forced to have the same structure, with opposite charges, so that the liquid resembles a binary FCC (100) lattice.

The structures of the two liquids have different symmetry with respect to the surface plane, and this determines their stability to shear stress (Fig. 18.9). The neutral layer structure of [BMIM][NTF2] is more prone to instability under shear stress, causing irregular dynamics of the liquid, and large fluctuations in the lateral force. The charged layers of [BMIM][BF4] can shear on top of each other, better maintaining electrostatic balance [111]. This difference in flow dynamics is also reflected in the friction coefficient, which is higher for nano-confined [BMIM][NTF2].

With these simulations, we are able to explain the behaviour of these fluids observed in previous experiments [112], and trace its origin to the size and shape of the molecules. Although only two liquids are studied, the results hint to the existence of relationships between molecular properties and nano-confined behaviour. However, it is not possible to draw general conclusions for all possible ILs and surfaces.

When simulating the structure of ILs on surfaces, the time-scale issue of MD becomes important. The strong electrostatic interactions between IL molecules ensure a molecular structure that is more tightly bound than what can be seen in apolar and polar liquids. Molecular fluctuations and diffusion are then hampered, so that sampling the configuration space of the system can require up to 100 ns simulations. The situation is even worse in presence of an interface with a solid surface. Molecules at the boundary layer do not diffuse during the whole simulated time, and, as required by the electrostatics, the entire layered structure hardly show any fluctuation. For these reasons, free-energy methods to compute tip-sample interactions in ILs have not been employed so far, and comparison between simulations and experiments is done indirectly.

18.4 Discussion

It is clear that significant progress has been made in simulating AFM in liquids, building upon the vast methods already established in the wider molecular simulation community. At first order, a great deal of insight can be obtained just by looking at the water density on the surface, especially combined with models providing a direct link between this density and measured forces. However, the results also show that one must be careful in making too many assumptions about the relationship between the observed contrast and water distribution on the surface—it is very clear that measurements capture a convolution of the interactions between the surface, tip and their respective hydration layers, and only in certain cases is this well-represented by the water density at the surface itself. Certainly free energy approaches, explicitly including the tip, offer a general approach to the problem, and the efficiency of modern codes combined with massively parallel computing means that it is often entirely feasible to perform such complete simulations routinely. This, of course, depends on the existence of accurate classical force fields for the complete system, and as research moves into ever more complex materials and environments, their existence is increasingly rare. As such, all the levels of modelling AFM in liquids presented in this chapter will still have a key role to play, particularly where the basic simulations have to be done at the quantum mechanical level and free energy approaches are extremely expensive [44, 113].

Beyond basic methodological developments, the increasing realism demanded in simulations, combined with the rapid expansion of systems considered, means that the future of high resolution studies in liquids must address an intimidating list of challenges. Most pressingly, as always in AFM studies, the nature of the tip and its influence on contrast requires much further study. Although simulations indicate that in stable imaging conditions in liquid, the tip probably does not come into hard contact with the surface, it can easily happen prior to imaging. Furthermore, when imaging in saturated solutions, crystallization can occur directly at the tip. In the future, tip models should account for all these varieties, comparing oxidized and hydroxylated variants of the nominal tip material along with models based on the constituents of the surface and solution.

It is very clear that ions or other small molecules near or in the solid-liquid interface very likely influence crystal growth and surface chemistry, and the presence of the AFM tip might change this. The influence of ions and molecules have on the AFM imaging mechanism is as yet unknown, and only limited information is available on the location of solvated ions in the solid-liquid interface and only for specific systems [90, 114]. More importantly, almost nothing is known on how these ions affect the structure of the interface or even prevent other molecules or ions from reaching the surface. It has been established that the presence of ions in the buffer solution makes it significantly easier to achieve high resolution in AFM, but the source of this improvement remains unclear. This can happen because the ions adhere to an AFM tip and act as a local probe or that they create the electrostatic double layer by which the background forces experienced by the tip are reduced, allowing for more

favourable imaging conditions. However, none of these explanations are supported by comprehensive experimental and theoretical evidence. Obtaining knowledge of the underlying physical principles associated with these solvated ions and molecules would be of great importance, not only to better understand the imaging mechanism, but also in the development of many nanosystems relying on surface chemistry.

The greatest challenges will certainly be offered by the wide variety of systems being studied in high resolution. The AFM can also be used to study the growth or dissolution of crystal surfaces, and in principle, could even be used to study the mechanism by which molecules adsorb to defects or steps and act as growth modifiers in *crystal engineering* [115]. However, atomistic simulation will be necessary to understand how the presence of the tip affects these mechanisms. As discussed in the introduction, a significant motivation for studies of AFM in liquids was for the study of biological systems in high-resolution [2]. As yet, this area has not seen significant joint activity between experimental and theoretical groups. However, the simulation experience in the area of molecular biology is vast, and the techniques discussed here could be readily integrated with the tools common used to model biological systems. Other directions will perhaps find it more challenging for systematic combined studies. Applying electric fields across solid-liquid interfaces [116] in Kelvin probe force microscopy touches the realms of electrochemistry [117], an area of intense theoretical development itself, without introducing the complexities of AFM. In self-assembly, research is now demonstrating the extra control offered by assembly in liquids [118], with solvent, impurity concentration and pH, all parameters that can dramatically change the molecular structure that assembles on a surface, and that is subsequently imaged in AFM. Understanding this requires modelling molecular chemistry in solution as a function of all these parameters, a very large step beyond the current approach of using fairly inert, homogeneous solvents. However, each of these systems and processes is critical to maintain the AFM family's position at the forefront of characterization in next generation technology and biomedicine, and we are confident that by building on the tools discussed in this chapter, future simulations will keep pace, or even take the lead.

References

1. G. Kada, F. Kienberger, P. Hinterdorfer, Atomic force microscopy in bionanotechnology. Nano Today **3**, 12–19 (2008)
2. D.J. Müller, Y.F. Dufrêne, Atomic force microscopy as a multifunctional molecular toolbox in nanobiotechnology. Nat. Nanotechnol. **3**(5), 261–269 (2008)
3. H.J. Güntherodt, D. Anselmetti, E. Meyer, *Forces in Scanning Probe Methods* (Kluwer, Dordrecht, 1995)
4. S. Morita, R. Wiesendanger, E. Meyer, *Noncontact Atomic Force Microscopy* (Springer, Berlin, 2002)
5. F.J. Giessibl, Atomic-force microscopy in ultrahigh-vacuum. Jpn. J. Appl. Phys. **33**(6B), 3726–3734 (1994)
6. A.L. Shluger, A.I. Livshits, A.S. Foster, C.R.A. Catlow, Models of image contrast in scanning force microscopy on insulators. J. Phys. Condens. Matter **11**(26), R295–R322 (1999)

7. D.A. Bonnell, *Probe Microscopy and Spectroscopy: Theory and Applications* (Wiley, New York, 2000)
8. F.J. Giessibl, Atomic resolution of the silicon (111)-(7×7) surface by atomic force microscopy. Science **267**(5194), 68–71 (1995)
9. F. Giessibl, Advances in atomic force microscopy. Rev. Mod. Phys. **75**, 949–983 (2003)
10. Y. Sugimoto, P. Pou, M. Abe, P. Jelinek, R. Perez, S. Morita, O. Custance, Chemical identification of individual surface atoms by atomic force microscopy. Nature **446**(7131), 64–67 (2007)
11. Y. Sugimoto, P. Pou, O. Custance, P. Jelinek, M. Abe, R. Perez, S. Morita, Complex patterning by vertical interchange atom manipulation using atomic force microscopy. Science **322**(5900), 413–417 (2008)
12. L. Gross, F. Mohn, N. Moll, P. Liljeroth, G. Meyer, The chemical structure of a molecule resolved by atomic force microscopy. Science **325**(5944), 1110–1114 (2009)
13. L. Gross, F. Mohn, N. Moll, B. Schuler, A. Criado, E. Guitian, D. Pena, A. Gourdon, G. Meyer, Bond-order discrimination by atomic force microscopy. Science **337**(6100), 1326–1329 (2012)
14. G. Binnig, C.F. Quate, C. Gerber, Atomic force microscope. Phys. Rev. Lett. **56**(9), 930–933 (1986)
15. G. Binnig, C. Gerber, E. Stoll, T.R. Albrecht, C.F. Quate, Atomic resolution with atomic force microscope. Europhys. Lett. **3**(12), 1281–1286 (1987)
16. F. Ohnesorge, G. Binnig, True atomic resolution by atomic force microscopy through repulsive and attractive forces. Science **260**(5113), 1451 (1993)
17. Y. Martin, C.C. Williams, H.K. Wickramasinghe, Atomic force microscope-force mapping and profiling on a sub 100-Å scale. J. Appl. Phys. **61**(10), 4723 (1987)
18. F.J. Giessibl, H. Bielefeldt, S. Hembacher, J. Mannhart, Calculation of the optimal imaging parameters for frequency modulation atomic force microscopy. Appl. Surf. Sci. **140**, 352–357 (1999)
19. T. Uchihashi, M.J. Higgins, S. Yasuda, S.P. Jarvis, S. Akita, Y. Nakayama, J.E. Sader, Quantitative force measurements in liquid using frequency modulation atomic force microscopy. Appl. Phys. Lett. **85**(16), 3575 (2004)
20. T. Fukuma, K. Kobayashi, K. Matsushige, H. Yamada, True molecular resolution in liquid by frequency-modulation atomic force microscopy. Appl. Phys. Lett. **86**(19), 193108 (2005)
21. T. Fukuma, K. Kobayashi, K. Matsushige, H. Yamada, True atomic resolution in liquid by frequency-modulation atomic force microscopy. Appl. Phys. Lett. **87**(3), 034101 (2005)
22. T. Fukuma, M. Higgins, S. Jarvis, Direct imaging of lipid-ion network formation under physiological conditions by frequency modulation atomic force microscopy. Phys. Rev. Lett. **98**(10), 106101 (2007)
23. S. Rode, N. Oyabu, K. Kobayashi, H. Yamada, A. Kühnle, True atomic-resolution imaging of $(10\bar{1}4)$ calcite in aqueous solution by frequency modulation atomic force microscopy. Langmuir **25**(5), 2850–2853 (2009)
24. T. Fukuma, Water distribution at solid/liquid interfaces visualized by frequency modulation atomic force microscopy. Sci. Tech. Adv. Mater. **11**(3), 033003 (2010)
25. B.W. Hoogenboom, H.J. Hug, Y. Pellmont, S. Martin, P.L.T.M. Frederix, D. Fotiadis, A. Engel, Quantitative dynamic-mode scanning force microscopy in liquid. Appl. Phys. Lett. **88**(19), 193109 (2006)
26. T. Fukuma, K. Onishi, N. Kobayashi, A. Matsuki, H. Asakawa, Atomic-resolution imaging in liquid by frequency modulation atomic force microscopy using small cantilevers with megahertz-order resonance frequencies. Nanotechnology **23**, 135706 (2012)
27. W.A. Hofer, A.S. Foster, A.L. Shluger, Theories of scanning probe microscopy at the atomic scale. Rev. Mod. Phys. **75**, 1287–1331 (2003)
28. A.S. Foster, W.A. Hofer, *Scanning Probe Microscopes: Atomic Scale Engineering by Forces and Currents* (Springer, New York, 2006)

29. C. Barth, A.S. Foster, C.R. Henry, A.L. Shluger, Recent trends in surface characterization and chemistry with high-resolution scanning force methods. Adv. Mater. **23**(4), 477–501 (2011)
30. R. Perez, M. Payne, I. Stich, K. Terakura, Role of covalent tip-surface interactions in noncontact atomic force microscopy on reactive surfaces. Phys. Rev. Lett. **78**(4), 678–681 (1997)
31. I. Stich, J. Tobik, R. Perez, K. Terakura, S. Ke, Tip-surface interactions in noncontact atomic force microscopy on reactive surfaces. Prog. Surf. Sci. **64**(3–8), 179–191 (2000)
32. N. Sasaki, H. Aizawa, M. Tsukada, Theoretical simulation of noncontact AFM images of Si(111) 33-Ag surface based on Fourier expansion method. Appl. Surf. Sci. **157**(4), 367–372 (2000)
33. A. Foster, A. Gal, J. Gale, Y. Lee, R. Nieminen, A. Shluger, Interaction of silicon dangling bonds with insulating surfaces. Phys. Rev. Lett. **92**(3), 036101 (2004)
34. N. Oyabu, P. Pou, Y. Sugimoto, P. Jelinek, M. Abe, S. Morita, R. Perez, O. Custance, Single atomic contact adhesion and dissipation in dynamic force microscopy. Phys. Rev. Lett. **96**(10), 106101 (2006)
35. O. Custance, R. Perez, S. Morita, Atomic force microscopy as a tool for atom manipulation. Nat. Nanotechnol. **4**(12), 803–810 (2009)
36. M. Rasmussen, A. Foster, B. Hinnemann, F. Canova, S. Helveg, K. Meinander, N. Martin, J. Knudsen, A. Vlad, E. Lundgren, A. Stierle, F. Besenbacher, J. Lauritsen, Stable cation inversion at the $MGAl_2O_4$(100) surface. Phys. Rev. Lett. **107**(3), 036102 (2011)
37. G. Teobaldi, K. Lämmle, T. Trevethan, M. Watkins, A. Schwarz, R. Wiesendanger, A.L. Shluger, Chemical resolution at ionic crystal surfaces using dynamic atomic force microscopy with metallic tips. Phys. Rev. Lett. **106**, 216102 (2011)
38. S. Kawai, A.S. Foster, F.F. Canova, H. Onodera, S.i. Kitamura, E. Meyer, Atom manipulation on an insulating surface at room temperature, Nat. Commun. **5**, 4403 (2014)
39. M. Ondráček, P. Pou, V. Rozsíval, C. Gonzalez, P. Jelinek, R. Perez, Forces and currents in carbon nanostructures: are we imaging atoms? Phys. Rev. Lett. **106**(17), 176101 (2011)
40. J. Bamidele, S.H. Lee, Y. Kinoshita, R. Turanský, Y. Naitoh, Y.J. Li, Y. Sugawara, I. Stich, L. Kantorovich, Vertical atomic manipulation with dynamic atomic-force microscopy without tip change via a multi-step mechanism. Nat. Commun. **5**, 4476 (2014)
41. A.M. Sweetman, S.P. Jarvis, H. Sang, I. Lekkas, P. Rahe, Y. Wang, J. Wang, N.R. Champness, L. Kantorovich, P. Moriarty, Mapping the force field of a hydrogen-bonded assembly. Nat. Commun. **5**, 3931 (2014)
42. N. Moll, L. Gross, F. Mohn, A. Curioni, G. Meyer, A simple model of molecular imaging with noncontact atomic force microscopy. New J. Phys. **14**(8), 083023 (2012)
43. D.Z. Gao, J. Grenz, M.B. Watkins, F. Federici, Canova, A. Schwarz, R. Wiesendanger, A.L. Shluger, Using metallic noncontact atomic force microscope tips for imaging insulators and polar molecules: tip characterization and imaging mechanisms. ACS nano **8**(5), 5339–5351 (2014)
44. J.C. Chen, B. Reischl, P. Spijker, N. Holmberg, K. Laasonen, A.S. Foster, Ab initio kinetic monte carlo simulations of dissolution at the NACl-water interface. Phys. Chem. Chem. Phys. **16**, 22545–22554 (2014)
45. M.P. Allen, D.J. Tildesley, *Computer Simulation of Liquids* (Oxford University Press, Oxford, 1987)
46. D. Frenkel, B. Smit, *Understanding Molecular Simulation: From Algorithms to Applications*, 2nd edn. (Computational Science, Academic Press, San Diego, 2002)
47. M. Watkins, A.L. Shluger, Mechanism of contrast formation in atomic force microscopy in water. Phys. Rev. Lett. **105**(19), 196101 (2010)
48. K. Kimura, S. Ido, N. Oyabu, K. Kobayashi, Y. Hirata, T. Imai, H. Yamada, Visualizing water molecule distribution by atomic force microscopy. J. Chem. Phys. **132**(19), 194705 (2010)
49. M. Harada, M. Tsukada, Tip-sample interaction force mediated by water molecules for AFM in water: three-dimensional reference interaction site model theory. Phys. Rev. B **80**(3), 035414 (2010)
50. M. Tsukada, N. Watanabe, M. Harada, K. Tagami, Theoretical simulation of noncontact atomic force microscopy in liquids. J. Vac. Sci. Tech. B. **28**(3), C4C1–C4C4 (2010)

51. B. Reischl, M. Watkins, A.S. Foster, Free energy approaches for modeling atomic force microscopy in liquids. J. Chem. Theory Comput. **9**(1), 600–608 (2013)
52. D. Argyris, A. Phan, A. Striolo, P.D. Ashby, Hydration structure at the α-Al_2O_3(0001) surface: insights from experimental atomic force spectroscopic data and atomistic molecular dynamics simulations. J. Phys. Chem. C **117**(20), 10433–10444 (2013)
53. M. Watkins, B. Reischl, A simple approximation for forces exerted on an AFM tip in liquid. J. Chem. Phys. **138**(15), 154703 (2013)
54. K.i. Amano, K. Suzuki, T. Fukuma, O. Takahashi, H. Onishi, The relationship between local liquid density and force applied on a tip of atomic force microscope: a theoretical analysis for simple liquids. J. Chem. Phys. **139**(22), 224710 (2013)
55. T. Fukuma, Y. Ueda, S. Yoshioka, H. Asakawa, Atomic-scale distribution of water molecules at the mica-water interface visualized by three-dimensional scanning force microscopy. Phys. Rev. Lett. **104**(1), 016101 (2010)
56. T. Hiasa, K. Kimura, H. Onishi, M. Ohta, K. Watanabe, R. Kokawa, N. Oyabu, K. Kobayashi, H. Yamada, Aqueous solution structure over α-$Al_2O_3(01\bar{1}2)$ probed by frequency-modulation atomic force microscopy. J. Phys. Chem. C **114**(49), 21423–21426 (2010)
57. J.G. Catalano, C. Park, Z. Zhang, P. Fenter, Termination and water adsorption at the α-Al_2O_3 (012)-aqueous solution interface. Langmuir **22**(10), 4668–4673 (2006)
58. L. Cheng, P. Fenter, K.L. Nagy, M.L. Schlegel, N.C. Sturchio, Molecular-scale density oscillations in water adjacent to a mica surface. Phys. Rev. Lett. **87**, 156103 (2001)
59. J.D. Eaves, J.J. Loparo, C.J. Fecko, S.T. Roberts, A. Tokmakoff, P.L. Geissler, Hydrogen bonds in liquid water are broken only fleetingly. Proc. Natl. Acad. Sci. USA **102**(37), 13019–13022 (2005)
60. M. Watkins, M.L. Berkowitz, A.L. Shluger, Role of water in atomic resolution AFM in solutions. Phys. Chem. Chem. Phys. **13**(27), 12584–12594 (2011)
61. K. Voïtchovsky, J.J. Kuna, S.A. Contera, E. Tosatti, F. Stellacci, Direct mapping of the solid-liquid adhesion energy with subnanometre resolution. Nat. Nanotechnol. **5**(6), 401–405 (2010)
62. D. Chandler, *Introduction to Modern Statistical Mechanics* (Oxford University Press, New York, 1987)
63. G.M. Torrie, J.P. Valleau, Monte Carlo free energy estimates using non-Boltzmann sampling: application to the sub-critical Lennard-Jones fluid. Chem. Phys. Lett. **28**, 578–581 (1974)
64. S. Kumar, D. Bouzida, R.H. Swendsen, P.A. Kollman, J.M. Rosenberg, The weighted histogram analysis method for free-energy calculations on biomolecules. I. The method. J. Comput. Chem. **13**, 1011–1021 (1992)
65. R.W. Zwanzig, Statistical mechanical theory of transport processes. VII. The coefficient of thermal conductivity of monatomic liquids. J. Chem. Phys. **22**(8), 1420–1426 (1954)
66. A.D. MacKerell Jr, D. Bashford, M. Bellott, R.L. Dunbrack Jr, J.D. Evanseck, M.J. Field, S. Fischer, J. Gao, H. Guo, S. Ha, D. Joseph-McCarthy, L. Kuchnir, K. Kuczera, F.T.K. Lau, C. Mattos, S. Michnick, T. Ngo, D.T. Nguyen, B. Prodhom, W.E. Reiher III, B. Roux, M. Schlenkrich, J.C. Smith, R. Stote, J. Straub, M. Watanabe, J. Wiorkiewicz-Kuczera, D. Yin, M. Karplus, All-atom empirical potential for molecular modeling and dynamics studies of proteins. J. Phys. Chem. B **102**, 3586–3616 (1998)
67. W.D. Cornell, P. Cieplak, C.I. Bayly, I.R. Gould, K.M. Merz, D.M. Ferguson, D.C. Spellmeyer, T. Fox, J.W. Caldwell, P.A. Kollman, A second generation force field for the simulation of proteins, nucleic acids, and organic molecules. J. Am. Chem. Soc. **117**(19), 5179–5197 (1995)
68. W.L. Jorgensen, D.S. Maxwell, J. Tirado-Rives, Development and testing of the OPLS all-atom force field on conformational energetics and properties of organic liquids. J. Am. Chem. Soc. **118**(45), 11225–11236 (1996)
69. R.T. Cygan, J.J. Liang, A.G. Kalinichev, Molecular models of hydroxide. oxyhydroxide, and clay phases and the development of a general force field. J. Phys. Chem. B **108**, 1255–1266 (2004)
70. D.R. Heine, A.R. Rammohan, J. Balakrishnan, Atomistic simulations of the interaction between lipid bilayers and substrates **33**, 391–397 (2007)

71. C.M. Payne, X. Zhao, L. Vlcek, P.T. Cummings, Molecular dynamics simulation of ss-dna translocation between copper nanoelectrodes incorporating electrode charge. Dynamics **112**, 1712–1717 (2008)
72. A.A. Skelton, P. Fenter, J.D. Kubicki, D.J. Wesolowski, P.T. Cummings, Simulations of the quartz(1011)/water interface: a comparison of classical force fields. Ab initio molecular dynamics, and X-ray reflectivity experiments. J. Phys. Chem. B **115**, 2076–2088 (2011)
73. S. Kang, T. Huynh, Z. Xia, Y. Zhang, H. Fang, G. Wei, R. Zhou, Hydrophobic interactions drives surface-assisted epitaxial assembly of amyloid-like. Peptides **135**, 3150–3157 (2013)
74. P. Raiteri, J.D. Gale, D. Quigley, P.M. Rodger, Derivation of an accurate force-field for simulating the growth of calcium carbonate from aqueous solution: a new model for the calcite-water interface. J. Phys. Chem. C **114**(13), 5997–6010 (2010)
75. P. Raiteri, J.D. Gale, Water is the key to nonclassical nucleation of amorphous calcium carbonate. J. Am. Chem. Soc. **132**(49), 17623–17634 (2010)
76. P. Fenter, S. Kerisit, P. Raiteri, J.D. Gale, Is the calcite-water interface understood? Direct comparisons of molecular dynamics simulations with specular X-ray reflectivity data. J. Phys. Chem. C **117**(10), 5028–5042 (2013)
77. B. Guillot, A reappraisal of what we have learnt during three decades of computer simulations on water. J. Mol. Liq. **101**(1–3), 219–260 (2002)
78. H.J.C. Berendsen, J.R. Grigera, T.P. Straatsma, The missing term in effective pair potentials. J. Phys. Chem. **91**, 6269–6271 (1987)
79. K. Toukan, A. Rahman, Molecular-dynamics study of atomic motions in water. Phys. Rev. B **31**, 2643–2648 (1985)
80. K.P. Jensen, W.L. Jorgensen, Halide, Ammonium, and Alkali metal ion parameters for modeling aqueous solutions. J. Chem. Theory Comput. **2**, 1499–1509 (2006)
81. I.S. Joung, T.E. Cheatham III, Determination of alkali and halide monovalent ion parameters for use in explicitly solvated biomolecular simulations. J. Phys. Chem. B **112**, 9020–9041 (2008)
82. T. Hiasa, K. Kimura, H. Onishi, Hydration of hydrophilic thiolate monolayers visualized by atomic force microscopy. Phys. Chem. Chem. Phys. **14**(23), 8419–8424 (2012)
83. M. Watkins, A.L. Shluger, Properties of SiO_2 clusters in aqueous solution from first principles molecular dynamics (2013) (in preparation)
84. J.P. Cleveland, T.E. Schäffer, P.K. Hansma, Probing oscillatory hydration potentials using thermal-mechanical noise in an atomic-force microscope. Phys. Rev. B **52**(12), 8692–8695 (1995)
85. N. Kobayashi, S. Itakura, H. Asakawa, T. Fukuma, Atomic-scale processes at the fluorite-water interface visualized by frequency modulation atomic force microscopy. J. Phys. Chem. C **117**(46), 24388–24396 (2013)
86. C. Eun, M.L. Berkowitz, Origin of the hydration force: water-mediated interaction between two hydrophilic plates. J. Phys. Chem. B **113**(40), 13222–13228 (2009)
87. J. Schütte, P. Rahe, L. Tröger, S. Rode, R. Bechstein, M. Reichling, A. Kühnle, Clear signature of the (2×1) reconstruction of calcite $(10\bar{1}4)$. Langmuir **26**(11), 8295–8300 (2010)
88. H. Imada, K. Kimura, H. Onishi, Water and 2-propanol structured on calcite (104) probed by frequency-modulation atomic force microscopy. Langmuir **29**(34), 10744–10751 (2013)
89. J. Tracey, F. Federici Canova, O. Keisanen, A.S. Foster, Flexible and efficient virtual scanning probe microscope (2014) (in preparation)
90. M. Ricci, P. Spijker, F. Stellacci, J.F. Molinari, K. Voïtchovsky, Langmuir **29**(7), 2207–2216 (2013)
91. D.J. Cooke, J.A. Elliott, Atomistic simulations of calcite nanoparticles and their interaction with water. J. Chem. Phys. **127**(10), 104706 (2007)
92. T. Fukuma, N. Kobayashi, B. Reischl, P. Spijker, F. Federici Canova, K. Miyazawa, A.S. Foster, Direct imaging of three-dimensional hydration structures at solid-liquid interfaces with subnanometer resolution (2014) (in preparation)
93. R. Nishioka, T. Hiasa, K. Kimura, H. Onishi, J. Phys. Chem. C **117**(6), 2939–2943 (2013)

94. P. Spijker, T. Hiasa, T. Musso, R. Nishioka, H. Onishi, A.S. Foster, Understanding the interface of liquids with an organic crystal surface from atomistic simulations and AFM experiments. J. Phys. Chem. C **118**(4), 2058–2066 (2014)
95. S.C. Abrahams, J.M. Robertson, The crystal structure of p-nitroaniline, $NO_2.C_6H_4.NH_2$, Acta Cryst. **1**, 252–259 (1948)
96. D.C. Forbes, K.J. Weaver, Bronsted acidic ionic liquids: the dependence on water of the fischer esterification of acetic acid and ethanol. Ionic liquids as promising alternative media for organic synthesis and catalysis, J. Mol. Cat. A, **214** (1):129–132 (2004)
97. J.S. Wilkes, P. Wasserscheid, T. Welton, *Ionic Liquids in Synthesis* (Wiley-VCH Verlag GmbH & Co, KGaA, Weinheim, 2008)
98. T. Welton, Room-temperature ionic liquids. Solvents for synthesis and catalysis. Chem. Rev. **99**(8), 2071–2084 (1999)
99. T. Moriguchi, T. Yanagi, M. Kunimori, T. Wada, M. Sekine, Synthesis and properties of aminoacylamido-AMP: chemical optimization for the construction of an N-Acyl phosphoramidate linkage, J. Org. Chem. **65**(24), 8229–8238 (2000) (pMID: 11101378)
100. R.D. Rogers, K.R. Seddon (eds.), *Ionic Liquids as Green Solvents* (American Chemical Society, Washington, D.C., 2003)
101. N.V. Plechkova, K.R. Seddon, Applications of ionic liquids in the chemical industry. Chem. Soc. Rev. **37**, 123–150 (2008)
102. G. Feng, J.S. Zhang, R. Qiao, Microstructure and capacitance of the electrical double layers at the interface of ionic liquids and planar electrodes. J. Phys. Chem. C **113**(11), 4549–4559 (2009)
103. A. Balducci, U. Bardi, S. Caporali, M. Mastragostino, F. Soavi, Ionic liquids for hybrid supercapacitors. Electrochem. Commun. **6**(6), 566–570 (2004)
104. T. Kuboki, T. Okuyama, T. Ohsaki, N. Takami, Lithium-air batteries using hydrophobic room temperature ionic liquid electrolyte. J. Power Sour. **146**, 766–769 (2005)
105. M. Park, H. Sun, H. Lee, J. Lee, J. Cho, Lithium-air batteries: survey on the current status and perspectives towards automotive applications from a battery industry standpoint. Adv. Energy Mater. **2**(7), 780–800 (2012)
106. T. Tsuda, N. Nemoto, K. Kawakami, E. Mochizuki, S. Kishida, T. Tajiri, T. Kushibiki, S. Kuwabata, SEM observation of wet biological specimens pretreated with room-temperature ionic liquid. Chem. Bio. Chem. **12**(17), 2547–2550 (2011)
107. A.E. Somers, P.C. Howlett, D.R. MacFarlane, M. Forsyth, A review of ionic liquid lubricants. Lubricants **1**(1), 3–21 (2013)
108. M. Palacio, B. Bhushan, A review of ionic liquids for green molecular lubrication in nanotechnology. Tribol. Lett. **40**, 247–268 (2010)
109. R. González, A. Hernández, Battez, D. Blanco, J. Viesca, A. Fernández-González, Lubrication of TiN, CrN and DLC PVD coatings with 1-Butyl-1-Methylpyrrolidinium tris(pentafluoroethyl)trifluorophosphate. Tribol. Lett. **40**(2), 269–277 (2010)
110. F. Zhou, Y. Liang, W. Liu, Ionic liquid lubricants: designed chemistry for engineering applications. Chem. Soc. Rev. **38**, 2590–2599 (2009)
111. F. Federici Canova, H. Matsubara, M. Mizukami, K. Kurihara, A.L. Shluger, Shear dynamics of nanoconfined ionic liquids. Phys. Chem. Chem. Phys. **16**, 8247–8256 (2014)
112. K. Ueno, M. Kasuya, M. Watanabe, M. Mizukami, K. Kurihara, Resonance shear measurement of nanoconfined ionic liquids. Phys. Chem. Chem. Phys. **12**, 4066 (2010)
113. N. Holmberg, J.C. Chen, A.S. Foster, K. Laasonen, Dissolution of NaCl nanocrystals: an ab initio molecular dynamics study. Phys. Chem. Chem. Phys. **16**, 17437–17446 (2014)
114. M. Ricci, P. Spijker, K. Voïtchovsky, Water-induced correlation between single ions imaged at the solid-liquid interface. Nat. Commun. **5**, 4400 (2014)
115. E.H.H. Chow, D.K. Bučar, V. Jones, New opportunities in crystal engineering-the role of atomic force microscopy in studies of molecular crystals. Chem. Comm. **48**(74), 9210 (2012)

116. K.i. Umeda, K. Kobayashi, N. Oyabu, Y. Hirata, K. Matsushige, H. Yamada, Practical aspects of Kelvin-probe force microscopy at solid/liquid interfaces in various liquid media. J. Appl. Phys. **116**(13), 134307 (2014)
117. N.M. Markovic, Electrocatalysis: interfacing electrochemistry. Nat. Mat. **12**(2), 101–102 (2013)
118. M. Schreiber, M. Eckardt, S. Klassen, H. Adam, M. Nalbach, L. Greifenstein, F. Kling, M. Kittelmann, R. Bechstein, A. Kühnle, How deprotonation changes molecular self-assembly-an AFM study in liquid environment. Soft Matter **9**(29), 7145–7149 (2013)

Chapter 19
Recent Progress in Frequency Modulation Atomic Force Microscopy in Liquids

Kei Kobayashi and Hirofumi Yamada

Abstract Recent progress in frequency modulation atomic force microscopy (FM-AFM) working in liquids has allowed us to directly investigate a wide variety of physical, chemical and biological processes at molecular scale, including various "in vivo" biological interactions. In particular, two/three-dimensional (2D/3D) force mapping based on quantitative FM-AFM force measurements has been applied to various solid-liquid interface studies on a molecular scale. In this chapter, after a brief overview of FM-AFM working in liquids, crucial conditions required for quantitative force measurement are described. In addition we show the applications of 2D/3D force mapping to the visualization of molecular-scale hydration structures as well as that of local electric double layer forces. Finally high-resolution FM-AFM images of biological molecules such as double-helix structure of DNA and immunoglobulin G (IgG) antibody molecules obtained in quasi-physiological environments are presented.

19.1 Brief Overview

19.1.1 Introduction

Solid-liquid interfaces play a critical role in a large variety of physical, chemical and biological processes, such as crystal growth, catalytic reactions and various biochemical functions. Investigations of molecular-scale structures and interactions at solid-liquid interfaces are, therefore, essentially crucial for understanding theses microscopic processes. Recent, significant progress in frequency modulation atomic

H. Yamada (✉)
Department of Electronic Science and Engineering, Kyoto University,
Katsura, Nishikyo, Kyoto 615-8510, Japan
e-mail: h-yamada@kuee.kyoto-u.ac.jp

K. Kobayashi
The Hakubi Center for Advanced Research, Kyoto University,
Katsura, Nishikyo, Kyoto 615-8520, Japan
e-mail: keicoba@iic.kyoto-u.ac.jp

© Springer International Publishing Switzerland 2015

S. Morita et al. (eds.), *Noncontact Atomic Force Microscopy*,
NanoScience and Technology, DOI 10.1007/978-3-319-15588-3_19

force microscopy (FM-AFM) [1] working in liquids has allowed us to directly study such molecular-scale processes, including various "in vivo" biological interactions. In this article, after the characteristic features in solid-liquid interface measurements by FM-AFM are briefly mentioned, essential conditions required for quantitative force measurement in liquids are explained, which is essentially important for the interaction force analysis based on two/three-dimensional (2D/3D) force mapping [2–4]. In fact the method was successfully applied to the visualization of 2D/3D molecular-scale hydration structures at solid-liquid interfaces [2, 3] as well as those around biomolecules [4]. It was also applied to the visualization of local electric double layer (EDL) forces on molecular assemblies in electrolyte solution [5]. The quantitative force measurement allows us to obtain the molecular-scale surface charge density utilizing a modified DLVO (Derjaguin, Landau, Verwey and Overbeek) theory. Furthermore, some recent results on high-resolution FM-AFM imaging of biomolecules in quasi-physiological environments [5, 6] are also presented.

19.1.2 Characteristic Features in FM-AFM Solid-Liquid Interface Measurements

19.1.2.1 Viscous Damping of Cantilever in Fluid

In liquid environments the oscillation of the AFM cantilever is heavily damped by the fluid resistance so that the quality factor (Q-factor) of the cantilever is extremely reduced. This large reduction in Q-factor causes a large increase in frequency noise and hence deteriorates FM-AFM imaging. Sader and co-workers introduced dimensionless "hydrodynamic function" Γ [8, 9] having both real and imaginary parts ($\Gamma = \Gamma_r + i\Gamma_i$) for expressing the amplitude transfer function, $A(\omega)$, of the cantilever oscillation in liquids. When the cantilever has a rectangular shape with a width b, a thickness h and a density ρ, $A(\omega)$ is expressed by

$$A(\omega) = \frac{{\omega_{0(\mathrm{liq})}}^2}{-\omega^2 + {\omega_{0(\mathrm{liq})}}^2 + i\omega\omega_{0(\mathrm{liq})}/Q_{\mathrm{liq}}} A_{\mathrm{d}}, \tag{19.1}$$

where

$${\omega_{0(\mathrm{liq})}}^2 = \frac{1}{1 + \left(\pi\rho_{\mathrm{liq}} b/4\rho h\right)\Gamma_r}{\omega_0}^2 \text{ and } Q_{\mathrm{liq}} = \frac{\left(4\rho h/\pi\rho_{\mathrm{liq}} b\right) + \Gamma_r}{\Gamma_i}. \tag{19.2}$$

Here A_d and ρ_{liq} are the drive amplitude and the liquid density, respectively. These equations describe the reduction in Q-factor (Q_{liq}) caused by the viscous resistance as well as the decrease of the resonance frequency ($\omega_{0(\mathrm{liq})}$) due to the increase of the effective mass. Using the following modified Reynolds number Re,

$$\mathrm{Re} = \frac{\rho_{\mathrm{liq}}\omega b^2}{4\mu}, \tag{19.3}$$

where μ is the liquid viscosity, Γ can be approximated by using [8, 10]

$$\Gamma_r = a_1 + \frac{a_2}{\sqrt{2\,\mathrm{Re}}} \text{ and } \Gamma_i = \frac{b_1}{\sqrt{2\,\mathrm{Re}}} + \frac{b_2}{2\,\mathrm{Re}}, \tag{19.4}$$

where $a_1 = 1.0553$, $a_2 = 3.7997$, $b_1 = 3.8018$, $b_2 = 2.7364$. For a rectangular Si cantilever with $b = 35\,\mu\mathrm{m}$, $L = 125\,\mu\mathrm{m}$, and $h = 3.8\,\mu\mathrm{m}$ ($k = 42\,\mathrm{N/m}$, $f_0 = 335\,\mathrm{kHz}$), the approximation gives $Q_{\mathrm{liq}} = 10$ and $f_{0(\mathrm{liq})} = 155\,\mathrm{kHz}$. These numbers are close to the measured values, $Q_{\mathrm{liq}} = 7$–8, $f_{0(\mathrm{liq})} = 150\,\mathrm{kHz}$.

19.1.2.2 Frequency Noise in FM-AFM in Liquids

In FM-AFM the cantilever is vibrated at its resonance frequency f_0 with an oscillation amplitude A by the FM-AFM electronics. When the interaction forces act on the cantilever, the resonance frequency is shifted by a frequency shift Δf (frequency shift). In a high-Q environment such as in vacuum, the frequency noise density $n_{\delta f}^{(\text{high-}Q)}$ [Hz/$\sqrt{\text{Hz}}$] is expressed as

$$n_{\delta f}^{(\text{high-}Q)} = \frac{1}{A}\sqrt{\frac{f_0 k_\mathrm{B} T}{\pi k Q} + 2N_{\mathrm{ds}}^2 {f_\mathrm{m}}^2}, \tag{19.5}$$

where k, Q, k_B, and T are the spring constant, the Q-factor, the Boltzmann constant and the temperature, respectively [1]. f_m and N_{ds} denote the modulation frequency [Hz] and the displacement noise density of the deflection sensor [m/$\sqrt{\text{Hz}}$], respectively. The first term is the intrinsic frequency noise of the cantilever, which is caused by the thermal Brownian motion. The second term shows the well-known FM noise. In contrast, the frequency fluctuation of the oscillator has to be considered in a low-Q environment such as in water. In fact we recently found [11] that the frequency noise density in the low-Q environment $n_{\delta f}^{(\text{low-}Q)}$ is expressed as

$$n_{\delta f}^{(\text{low-}Q)} = \frac{1}{A}\sqrt{\frac{f_0 k_\mathrm{B} T}{\pi k Q} + \frac{f_0^2 N_{\mathrm{ds}}}{2Q^2}}. \tag{19.6}$$

Since f_0/Q is much larger than f_m in liquids, the magnitude of the second term of the above equation is much larger than that of (19.5). Thus, the reduction of the deflection sensor noise N_{ds} is essentially important. The noise was actually reduced by decreasing the coherence of the laser light used in the optical beam deflection sensor [12].

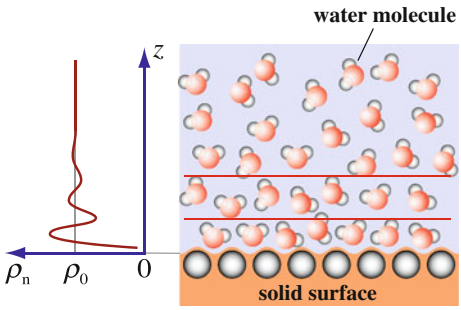

Fig. 19.1 Schematic of hydration structure formed on a flat solid surface. Molecule number density (ρ_n) plotted against z-distance (z) shows an oscillatory curve with an approximate period of the water molecule size (*left*)

19.1.2.3 Solvation (Hydration) Force

While liquid is treated as uniform continuum in fluid dynamics, the size effect of the liquid molecule has to be considered on a molecular scale. For instance, liquid density around an arbitrarily chosen single molecule cannot be uniform because of preferential coordination of neighboring molecules, which is described as density distribution function. This is also the case with the density distribution at a liquid-solid interface, which is known as solvation (hydration) structure (see Fig. 19.1). Typical molecule density distribution shows a diminishing oscillation structure with an approximate periodicity of the molecule size. Since force (frequency shift) versus distance curves were found to directly reflect the hydration structures formed at solid-liquid interfaces, 2D/3D force mapping has been applied to the study of molecular-scale hydration structures. When the tip is sufficiently sharp and hydrated, it can be treated as a water molecule tip, which makes the theoretical relationship between the measured force $F_{ts}(z)$ and the local molecule number density $\rho_n(z)$ extremely simple as follows [13],

$$F_{ts}(z) = k_B T \frac{d \log \rho_n(z)}{dz}. \tag{19.7}$$

However, the quantitative relationship between them is generally not straightforward because the interaction force acting on the tip caused by the hydration structure is strongly affected by the tip geometry and the hydration structure on the tip side, which requires careful theoretical calculation using molecular dynamics (MD) simulation or 3D reference interaction site model (RISM) theory [14].

19.1.2.4 Electric Double Layer Force

Sample surface is often charged in liquid due to the ionization of surface groups and/or ion absorption and the resultant local electrostatic force extremely complicates the interpretation. Surface charge is electrically balanced by the counter ions existing in the proximity of the surface so that an electric double layer is formed on the

surface (diffused double layer). An electric double layer also exists on the tip surface. When the tip is brought into close proximity of the sample surface, an interaction is caused between both electric double layers (electric double layer force). EDL force is the addition of Maxwell stress, electrostatic interaction, and osmotic pressure, statistical effect. Electrostatic potential in an electrolyte solution is $\phi(\mathbf{r})$ described by the following Poisson-Boltzmann equation,

$$\nabla^2\phi(\mathbf{r}) = \frac{Zen_0}{\varepsilon}\kappa^2 \sinh\left[Ze\phi(\mathbf{r})/k_\mathrm{B}T\right] \tag{19.8}$$

with

$$\kappa^{-1} = \sqrt{\frac{\varepsilon k_\mathrm{B}T}{2n_\mathrm{ion}\,(Ze)^2}}, \tag{19.9}$$

where n_ion, Z, e and ε are ion density, ion valence, elementary charge and dielectric constant of the solution, respectively. κ^{-1} is so called the Debye screening length corresponding to the thickness of the electric double layer in a simple system such as planar, parallel plates. When $e\phi \ll k_\mathrm{B}T$ and the system can be approximated as parallel plate, the equation can be solved (Derjaguin approximation) [15]. For instance when the AFM tip and the sample are modeled as a sphere with a radius R and a simple plane located at a distance d from the tip, respectively, EDL force F_EDL is expressed by

$$F_\mathrm{EDL} = \frac{2\pi R}{\varepsilon\kappa}\left[\left(\sigma_\mathrm{t}^2 + \sigma_\mathrm{s}^2\right)e^{-2\kappa d} + 2\sigma_\mathrm{t}\sigma_\mathrm{s}e^{-\kappa d}\right]\frac{1}{1-e^{-2\kappa d}}, \tag{19.10}$$

where σ_t and σ_s are the surface charge density of the tip and sample, respectively. EDL force was first intensively studied by Derjaguin, Landau, Verwey and Overbeek in connection with colloidal dispersions in electrolyte solutions. The addition of EDL force and van der Waals force (F_vdW) is called DLVO force, $F_\mathrm{DLVO}(= F_\mathrm{EDL} + F_\mathrm{vdW})$.

19.2 Quantitative Force/Dissipation Measurement Using FM-AFM in Liquids

19.2.1 Effect of Phase Shifting Elements in FM-AFM

Figure 19.2 shows a block diagram of FM-AFM instrument using an optical beam deflection sensor. In FM-AFM, a cantilever is oscillated by an excitation system, typically an acoustic excitation system using a piezoelectric actuator, driven by an excitation signal. The FM-AFM supplies the excitation signal such that the displacement signal reflecting the tip motion has a constant phase delay to the excitation

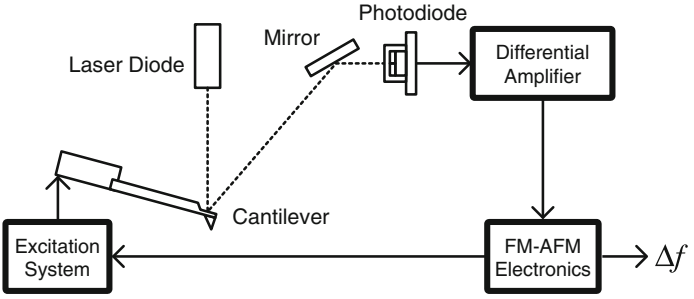

Fig. 19.2 Block diagram of FM-AFM using optical beam deflection sensor

signal. Thereby the frequency of the excitation signal matches the resonance frequency of the cantilever, and the resonance frequency of the cantilever is measured [1].

When the cantilever is excited indirectly by using a piezoelectric actuator in liquids, the actuator excites not only the base of the cantilever but causes unwanted vibration of surrounding components because the Q-factor of the cantilever is low. In such cases, the amplitude and phase transfer functions of the cantilever are distorted with spurious resonance peaks [16]. Moreover, other elements such as the displacement sensor or FM-AFM electronics may have frequency-dependent phase shift in the frequency range of the cantilever resonance frequency. Here we analyze the effect of these phase shifting elements (PSEs), which modify the phase versus frequency curve of the cantilever, on the signal and noise of the frequency shift in FM-AFM [11, 17].

The oscillation frequency of the cantilever is the frequency at which the phase criterion

$$\theta(f) + \theta_{\mathrm{E}}(f) = 2\mathrm{n}\pi \tag{19.11}$$

is met, where $\theta(f)$ is the phase transfer function of the cantilever and $\theta_{\mathrm{E}}(f)$ is the phase shift of the FM-AFM electronics. Since the phase shift of the cantilever at f_0, i.e. $\theta(f_0)$, is $-\pi/2$, $\theta_{\mathrm{E}}(f)$ is kept constant at $\pi/2 + 2\mathrm{n}\pi$ during experiments. However, due to the presence of the PSE, the phase criterion determining the oscillation frequency in actual FM-AFM instrument often becomes

$$\theta_{\mathrm{eff}}(f) + \theta_{\mathrm{E}}(f) = 2\mathrm{n}\pi, \tag{19.12}$$

where $\theta_{\mathrm{eff}}(f)$ is apparent phase transfer function with the presence of the PSE. Schematics of the phase transfer functions of the cantilever without any PSE ($\theta(f)$) and with the PSE ($\theta_{\mathrm{eff}}(f)$) are shown in Fig. 19.3a as thin and thick curves, respectively. Their slopes at f_0 are given by

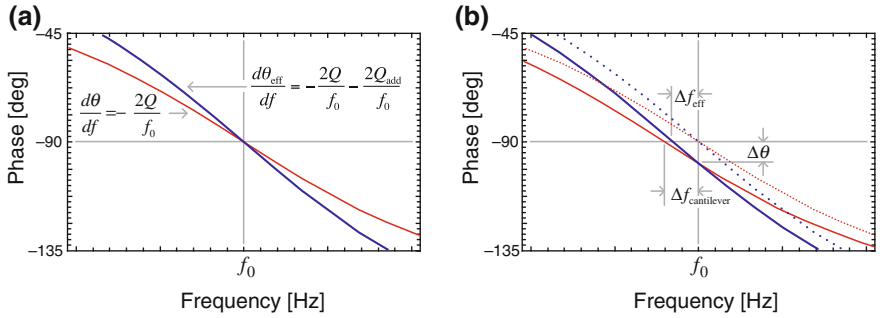

Fig. 19.3 **a** Schematic of apparent phase versus frequency curves of the cantilever without any PSE (*thin curve*) and with the PSE (*thick curve*). **b** Schematic illustration showing that the oscillation frequency deviates from the resonance frequency

$$\left.\frac{d\theta}{df}\right|_{f=f_0} = -\frac{2Q}{f_0} \tag{19.13}$$

and

$$\left.\frac{d\theta_{\rm eff}}{df}\right|_{f=f_0} = -\frac{2Q}{f_0} - \frac{2Q_{\rm add}}{f_0} = -\frac{2Q_{\rm eff}}{f_0}, \tag{19.14}$$

where Q and $Q_{\rm eff}$ are intrinsic and effective Q-factors, respectively. $Q_{\rm add}$ corresponds to the Q-factor of the PSE, which is defined by the slope of $\theta_{\rm add}$ at f_0. If we consider the situation where $\theta(f)$ is slightly shifted by $\Delta f_{\rm cantilever}$ due to the tip-sample interaction force, and the resonance frequency moves to $f_0 + \Delta f_{\rm cantilever}$, the phase response of the cantilever at f_0 shifts to $-\pi/2 + \Delta\theta$, where $\Delta\theta$ is given by

$$\Delta\theta = 2Q\frac{\Delta f_{\rm cantilever}}{f_0} \tag{19.15}$$

as shown in Fig. 19.3b. This phase shift is instantaneously nulled by the FM-AFM electronics, which adjust the oscillation frequency to $f_0 + \Delta f_{\rm cantilever}$. However, with the presence of the PSE, the phase shift $\Delta\theta$ is nulled by adjusting the oscillation frequency to $f_0 + \Delta f_{\rm eff}$, which is given by

$$\Delta f_{\rm eff} = \Delta\theta\left(\left|\frac{d\theta_{\rm eff}}{df}\right|_{f=f_0}\right)^{-1} = \frac{Q}{Q_{\rm eff}}\Delta f, \tag{19.16}$$

where $\Delta f_{\rm eff}$ represents the effective frequency shift tracked by the FM-AFM electronics with the presence of the PSE. This equation shows that the measured frequency shift is smaller than the actual frequency shift of the cantilever by a factor of $Q/Q_{\rm eff}$. Note that the signal to noise ratio of the FM-AFM is not affected by the PSE as the

equations for the frequency noises integrated over the measurement bandwidth with and without the PSE,

$$\delta f^{(\text{low-}Q)} = \frac{1}{A}\sqrt{\frac{f_0 k_\text{B} T B}{\pi k Q} + \frac{{f_0}^2 {N_\text{ds}}^2 B}{2Q^2}} \tag{19.17}$$

and

$$\delta f_\text{eff}^{(\text{low-}Q)} = \frac{1}{A}\sqrt{\frac{Q f_0 k_\text{B} T B}{\pi k Q_\text{eff}^2} + \frac{f_0^2 {N_\text{ds}}^2 B}{2{Q_\text{eff}}^2}} = \frac{Q}{Q_\text{eff}}\delta f^{(\text{low-}Q)}, \tag{19.18}$$

show that the frequency noise is also reduced by a factor of Q/Q_eff with the presence of the PSE.

19.2.2 Photothermal Excitation of Cantilevers in Liquids

Ideal amplitude and phase transfer functions of the cantilever are obtained by direct excitation methods such as magnetic [18] or photothermal excitation methods [19, 20]. While the former method requires attachment of magnetic particle or magnetic coating on the cantilever, the latter method can be readily applicable for any cantilevers without additional requirements.

Figure 19.4 shows a schematic diagram of the photothermal excitation system [17, 21]. We focused a blue-violet laser diode near the base of the cantilever, as shown in Fig. 19.4a. As the cantilever displacement is proportional to the incident laser power, the excitation signal is coupled to the laser drive current while the average drive current is regulated to keep the average incident power constant, as shown in Fig. 19.4b. Figure 19.4c shows the amplitude transfer functions of a Si cantilever (PPP-NCH) in water driven by acoustic excitation and photothermal excitation methods. While the transfer function obtained by the acoustic excitation method showed

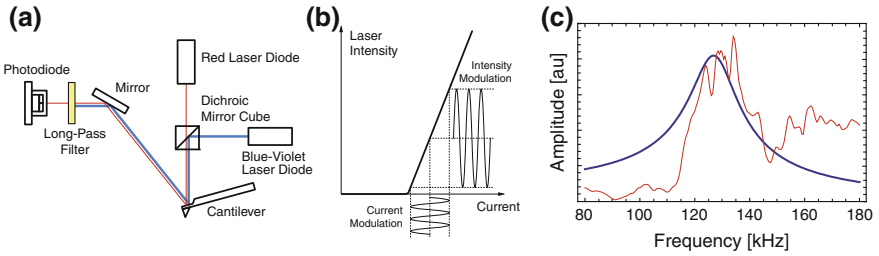

Fig. 19.4 **a** Schematic of photothermal excitation system. **b** Schematic of intensity versus laser current of laser diode for photothermal excitation. **c** Amplitude transfer functions of a cantilever in water by acoustic excitation and photothermal excitation

"forest of peaks" [16], that obtained by the photothermal excitation method showed the ideal damped harmonic oscillator response.

19.2.3 Optimum Oscillation Amplitude for FM-AFM in Liquids

The optimum oscillation amplitude of the cantilever for FM-AFM depends on the characteristic decay length of the interaction forces [22]. For nanometer-scale or atomic-scale topographic imaging in liquids, the characteristic decay length of the short-range repulsive force is on the order of a nanometer, and therefore the optimum oscillation amplitude is on the order of a nanometer. One can tune the oscillation amplitude to obtain the highest resolution images by using the procedures described below. On the other hand, the characteristic decay length of the hydration force is close to the size of the water molecules [2–4], and therefore the oscillation amplitude should be as small as the size of the water molecules or less, otherwise the oscillatory frequency shift as a function of the tip-sample distance is averaged out and not detectable.

Here we describe practical procedures to find the optimum oscillation amplitude for high-resolution topographic imaging by FM-AFM. First, the tip oscillated at a certain amplitude (a); e.g. 1 nm, is engaged to the sample surface in the constant frequency shift mode with a decent frequency setpoint. While acquiring some topographic images, the frequency setpoint is increased as high as possible ($\Delta f_{\max}$) before the cantilever oscillation becomes unstable. As the closest tip position during an oscillation cycle is now in a near-contact region, the tip position at which the frequency shift reaches $\Delta f_{\max}$ with a is defined as $z_{\min}$. Then we record the frequency shift versus distance curve from far above the surface to $z_{\min}$ under the same oscillation amplitude (a). The obtained frequency shift versus distance curve can be converted to the interaction force (F_{ts}) versus distance curve using the following equation [23],

$$F_{\mathrm{ts}}(z) = \frac{2k}{f_0}\int_z^{\infty}\left(\Delta f(\tau) + \frac{1}{8}\sqrt{\frac{a}{\pi(\tau - z)}}\Delta f(\tau) - \frac{a^{3/2}}{\sqrt{2(\tau - z)}}\frac{d\Delta f(\tau)}{d\tau}\right)d\tau. \tag{19.19}$$

The maximum interaction force in the curve corresponds to the interaction force exerted on the tip at $z_{\min}$ is defined as $F_{\max}$. From the force versus distance curve, the frequency shift versus distance curve for arbitrary oscillation amplitudes (A) can be simulated using the following equation [23, 24],

$$\Delta f(A, z) = -\frac{f_0}{\pi A k_z}\int_{-1}^{1} F(z + A(1 + u))\frac{u}{\sqrt{1 - u^2}}du. \tag{19.20}$$

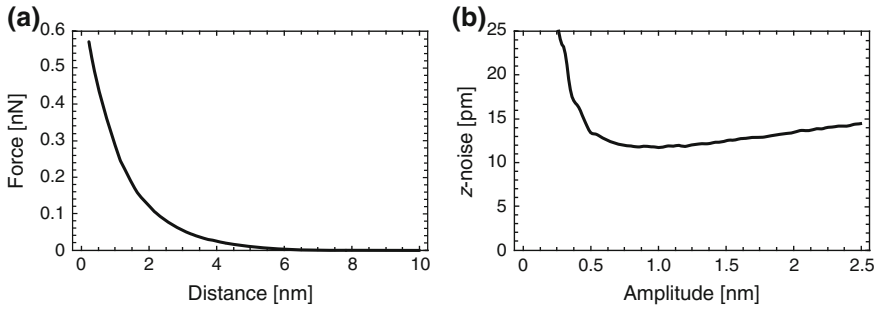

Fig. 19.5 **a** Force versus distance curve measured on bacteriorhodopsin protein molecules. **b** z-noise during high-resolution imaging of bacteriorhodopsin protein molecules calculated using the experimental parameters and force versus distance curve

Then the frequency shift at the closest tip distance ($z_{\min}$) is calculated as the maximum frequency shift in the simulated curve for arbitrary oscillation amplitudes as $\Delta f_{\max}(A)$. As the frequency noise is inversely proportional to the oscillation amplitude (A), as shown in (19.17), one can calculate z-noise at $z_{\min}$, defined as $\delta z = \delta f/(\partial \Delta f_{\max}(A)/\partial z)$ [22].

Figure 19.5a is a force versus distance curve measured on bacteriorhodopsin protein molecules in a purple membrane using a Si cantilever (PPP-NCH) [25]. z-noise was calculated as a function of the oscillation amplitude and plotted in Fig. 19.5b, showing the optimum oscillation amplitude is about 1 nm.

19.2.4 2D and 3D Force Mapping Techniques

The 2D/3D force mapping techniques are similar to those called force curve imaging spectroscopy [26] or force mapping [27]. The 3D mapping of the cantilever frequency shift by FM-AFM has been demonstrated in vacuum at low temperatures, by measuring a frequency shift versus tip-sample distance curve at individual pixels on the sample surface [28], and by obtaining a 2D frequency shift image at various tip-sample distances [29]. On the other hand, since the tip-sample distance feedback control should be disabled in both methods, it has been difficult to perform 3D frequency shift mapping by FM-AFM working in liquids without affected by the thermal drift. To overcome this problem, we implemented drift correction and tip retraction functions in the control software.

Procedures of 3D frequency shift mapping in our AFM system are schematically shown in Fig. 19.6. The tip was engaged to the sample surface, and the tip-sample distance was controlled by keeping the frequency shift constant. A slow ramp signal was added to the scan signals of the sample scanner for linear drift correction throughout the measurements [30]. After the tip-sample distance feedback control was disabled, and 2D frequency shift maps in z–x planes which are slightly separated in y direction

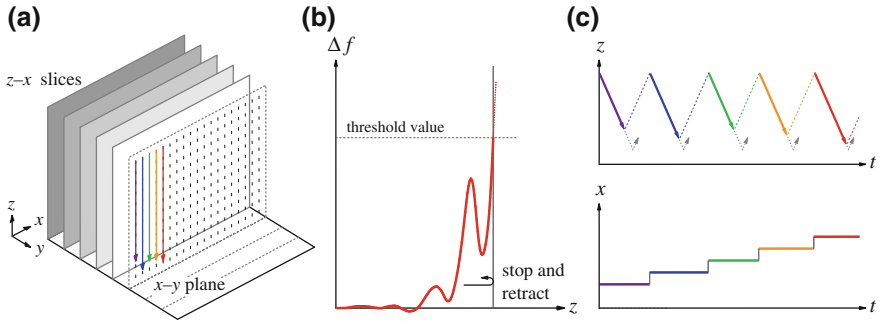

Fig. 19.6 **a** 3D frequency shift data was collected by performing 2D frequency shift mapping in z–x planes which are slightly separated in y direction. **b** In each frequency shift curve measurement, the tip was retracted immediately if the frequency shift reached the threshold value. **c** Timing charts during 2D frequency shift mapping

were collected as shown in Fig. 19.6(a). At each x position, the frequency shift versus distance curve was recorded while the tip was approached to the sample surface by applying a ramp signal to z piezo. The ramp signal was immediately stopped when the frequency shift signal reached a predetermined threshold value, and the tip was retracted to the original position as shown in Fig. 19.6b, c. This threshold frequency shift was determined at the maximum in the range where the frequency shift curves could be reproducibly collected; if the threshold frequency shift was set at a larger value than this, the measurements were not reliable because of unstable cantilever oscillation or tip change.

19.3 Application of FM-AFM 1: 2D/3D Force Mapping

19.3.1 3D Hydration Force Mapping on Muscovite Mica

We first demonstrated visualization of structured water layers by performing 2D frequency shift mapping by FM-AFM on a mica surface and a graphite surface, and on bacteriorhodopsin proteins in a purple membrane [4, 31]. However, precise comparison of the experimental data with theoretically calculated hydration structures or hydration forces [32, 33] requires 3D data, which allows us to identify the relationship between the atomic and molecular species on the surfaces and their specific hydration structures.

We performed 3D frequency shift mapping on a cleaved muscovite mica in 1 mol/l KCl solution. A Si cantilever (PPP-NCHAuD) was used with a constant oscillation amplitude of 0.24 nm peak-to-peak. We collected 67 slices of 2D frequency map (z–x slice). The threshold frequency shift (see Sect. 19.2.4) was set to 2250 Hz, which corresponded to the interaction force of about 0.4 nN. The 3D data set with dimensions of 3 nm (x) × 2.3 nm (y) × 1.6 nm (z) was obtained in 168 s [3].

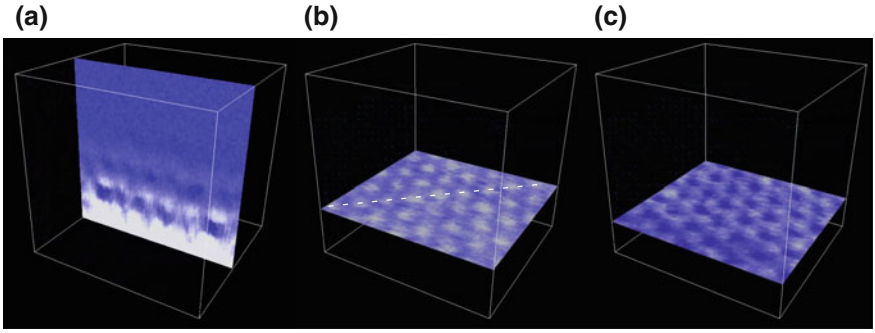

Fig. 19.7 Snapshots from movie files of 3D frequency shift map obtained on muscovite mica in aqueous solution

Figure 19.7 shows snapshots from movie files of the 3D frequency shift map. Figure 19.7a is a z–x slice, as originally obtained in the experiments. The z–x slice shows complicated contrasts reflecting 2D hydration structures. Figure 19.7b, c are x–y slices, reconstructed from the 3D frequency shift data, show variations of the frequency shift in x–y planes, namely a dot-like pattern and a honeycomb-like pattern, respectively. The separation of the two x–y slices in z direction was 0.2 nm.

Figure 19.8a shows a 2D frequency shift map in the z–x plane including the dotted line in Fig. 19.7b, which crosses the bright dots of the dot-like pattern. The locations of the two x–y slices in Fig. 19.7b, c are indicated by the triangles. In this figure, it becomes clear that the dark contrasts are beneath the bright dots, namely the inversion of the contrast.

We compared the 3D frequency shift data and force data to theoretical 3D data of atomic distribution of water molecules by a statistical-mechanical theory of solvation, known as 3D-RISM theory [4, 15]. The surface of the mica model used in the 3D-RISM calculation is shown in Fig. 19.8b. We found the oxygen density also shows similar dot-like and honeycomb-like patterns with a separation of about 0.2 nm with each other. Two x–y slices reconstructed from the 3D oxygen density data are shown in Fig. 19.8c, d. These x–y slices show variation of the oxygen density which is equivalent to the water molecule density. The honeycomb-like pattern follows locations of the surface atoms while the dots in the dot-like pattern are on the hollow sites. Figure 19.8e shows a 2D oxygen density map in the z–x plane including the dotted line in Fig. 19.8c, which crosses the bright dots of the dot-like pattern. The locations of the two x–y slices in Fig. 19.8c, d are indicated by the triangles in the same way as the experimental result. Here the inversion of the contrast between Fig. 19.8c, d were represented, which showed a good agreement with the experimental result.

Figure 19.9a shows an averaged frequency shift versus distance curve in for all pixels in x–y plane. There are three distinct maxima in the averaged frequency shift curve, at $z = 0.5$–0.6 nm, $z = 0.9$–1.0 nm, and $z = 1.4$ nm. An averaged force versus distance curve was also plotted in the figure. The triangles in the plot indicate the locations at which the dot-like and honeycomb-like patterns were obtained.

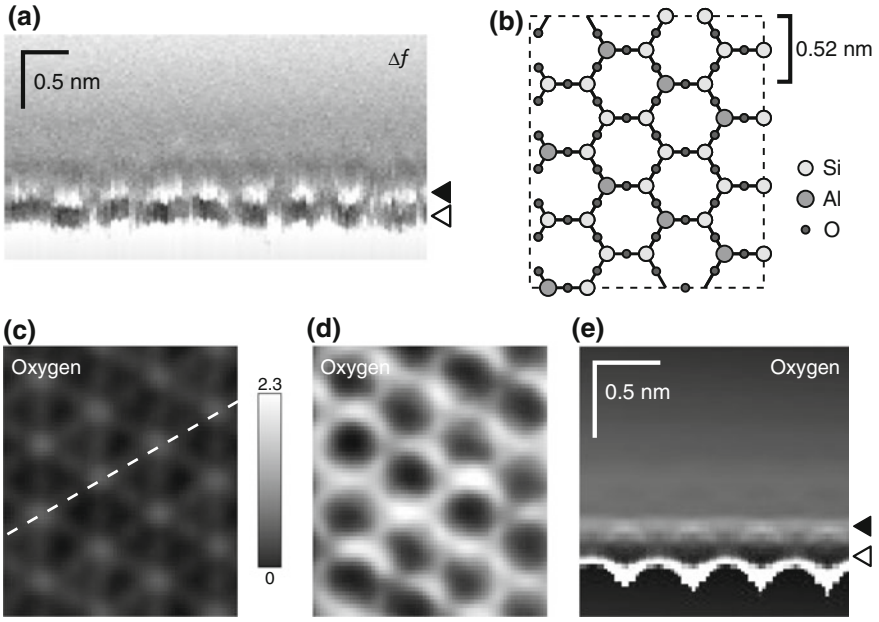

Fig. 19.8 **a** 2D frequency shift map in the *z*–*x* plane including the *dotted line* in Fig. 19.7b. **b** Schematic of surface atoms of the muscovite mica model. **c**, **d** are calculated 2D oxygen density maps showing *dot-like* and *honeycomb-like* features. **e** Calculated 2D oxygen density map in the *z*–*x* plane including the *dotted line* in (**c**)

Figure 19.9b is an averaged normalized oxygen density profile as a function of the distance from the surface atoms obtained by the 3D-RISM calculation. The locations of the maxima and minima in Fig. 19.9b well correspond to those in Fig. 19.9a, namely the maxima in the frequency shift or force correspond to the hydration layers, in which the water densities are greater than the bulk density.

The frequency shift maximum in the averaged frequency shift curve at $z = 0.5$–0.6 nm corresponds to the hydration layer in the 3D-RISM data, which was also reported by the X-ray crystal truncated rod measurement and referred to as the second hydration layer [34]. The dot-like pattern reflects the lateral structures of the second hydration layer, while the honeycomb-like pattern reflects the lateral structures of the first layer. We consider that it would be difficult to visualize the adsorbate layer by FM-AFM because the tip should pick the ditrigonal cavity and displace the water molecule inside, which is not probable with a tip of a radius on the order of nanometers, as simulated by the MD calculation [32].

Figure 19.10a is the *x*–*y* slice reconstructed from the 3D force data, at the tip-sample separation same as that in Fig. 19.7b. The interaction force versus distance curve on the site 1 corresponding to the honeycomb core of the mica surface, that on the site 2 corresponding to the bridge site, and that on the site 3 corresponding to Si or Al site were plotted in Fig. 19.10b. We found all these curves are qualitatively similar to those by the MD simulation.

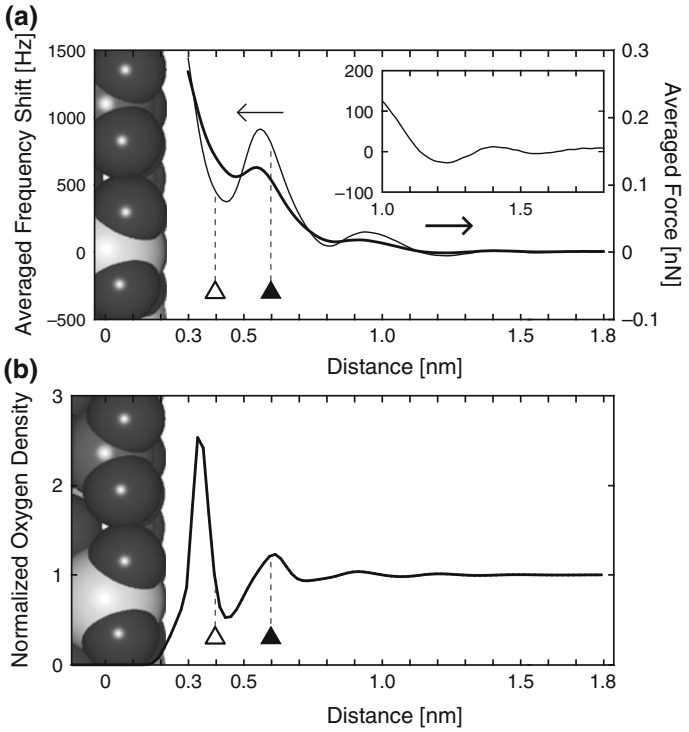

Fig. 19.9 **a** Averaged frequency shift versus distance curve and averaged force versus distance curve on mica surface. *Inset* shows a magnified frequency shift curve to clearly show the oscillatory features. **b** Normalized oxygen density profile derived by averaging 3D oxygen density map obtained by the 3D-RISM calculation

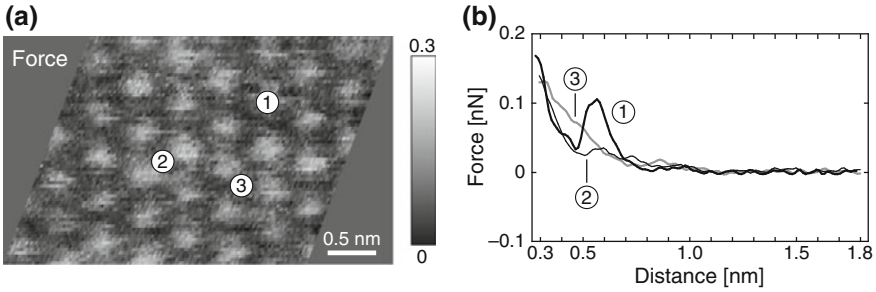

Fig. 19.10 **a** 2D force map (*x*–*y* slice) at the same tip-sample separation of Fig. 19.7b, reconstructed from the 3D force data. **b** Site-specific interaction force versus distance curves on the locations indicated in (**a**)

19.3.2 3D Electrostatic Force Mapping on Surfactant Aggregates

We applied the 3D force mapping method using FM-AFM to the investigation of the surface charge distribution and the structures of self-assembled surfactant aggregates at graphite aqueous solution interfaces [5]. We successfully visualized the 3D EDL force on the surface aggregates with molecular-scale resolution and obtained the local variation in the surface charge density on the aggregate by fitting the experimental 2D force map to the theoretical 2D EDL force map.

We deposited an aqueous solution of sodium dodecyl sulfate (SDS), $CH_3(CH_2)_{11}OSO_3^-Na^+$, on a cleaved graphite surface. A Si cantilever (PPP-NCH) was oscillated with the photothermal excitation method (see Sect. 19.2).

Figure 19.11a, b show FM-AFM images of a graphite substrate covered with SDS self-assemblies. The stripe structures having a spacing of about 4.8 nm were imaged with a domain boundary. According to the previous studies [35, 36], the SDS molecules are expected to form hemicylindrical surface micelles on the graphite surface with their hydrophilic head groups protruding outward and their sodium cations partially dissociated, as shown in Fig. 19.11b.

Figure 19.12 shows a 3D frequency shift map obtained at the interface between a graphite surface and an SDS aqueous solution (34 mM). The bright contrast of the image corresponds to the magnitude of the positive frequency shift. When the tip was brought closer to the micelle surface from a position located far from the surface, the repulsive force exponentially increased with the distance, which is a characteristic of the EDL force, until the tip penetrated the micelle surface. Although the tip penetrated the micelle surface at each frequency shift curve measurement, the obtained curves were highly reproducible, which means that the micelle structure was immediately recovered after each tip retraction. In fact each retract frequency shift curve was almost completely overlapped with the corresponding approach curve. In the 3D map, the hemicylindrical structure of the SDS aggregates was clearly visualized as a boundary between the bright and dark regions. In the reconstructed x–y slice at the distance closer to the graphite surface after the tip penetration, the parallel stripe

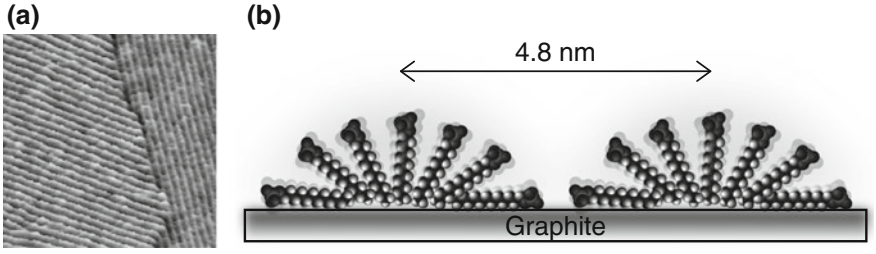

Fig. 19.11 **a** Topographic FM-AFM image of SDS self-assembled aggregates on graphite (Scan range: 133 nm × 133 nm). **b** Schematic of hemicylindrical SDS aggregates formed on graphite surface

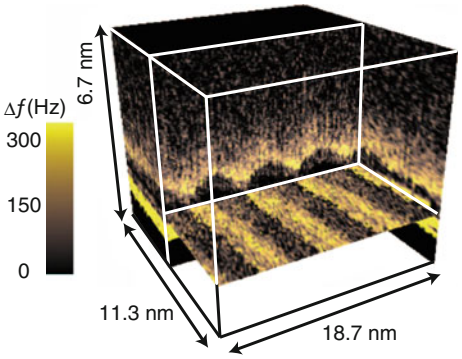

Fig. 19.12 Snapshot from a movie of 3D frequency shift map obtained at the interface between a graphite surface and an SDS aqueous solution

features were observed, suggesting that the SDS molecules were rearranged by the tip to form molecular layers parallel to the graphite surface.

We modeled the tip and the SDS aggregates, and then the EDL force between a spherical tip and an arbitrary shape is calculated at each tip location based on the single-layer potential method for the linearized Poisson-Boltzmann equation, which allows us to obtain a theoretical 3D EDL force map. Finally, the theoretical force map is fitted to the experimental data to find the surface charge density distribution function on the SDS aggregates. As the structure is uniform in the longitudinal axis of the hemicylinder and the charge density distribution was obviously periodic, the single layer potential function can be expanded as a Fourier series. The 2D EDL force map extracted from the theoretical 3D EDL force map was fitted to the experimentally obtained 2D force map. Figure 19.13 shows a surface charge density distribution on the SDS aggregate calculated from the fitting parameters that gave the

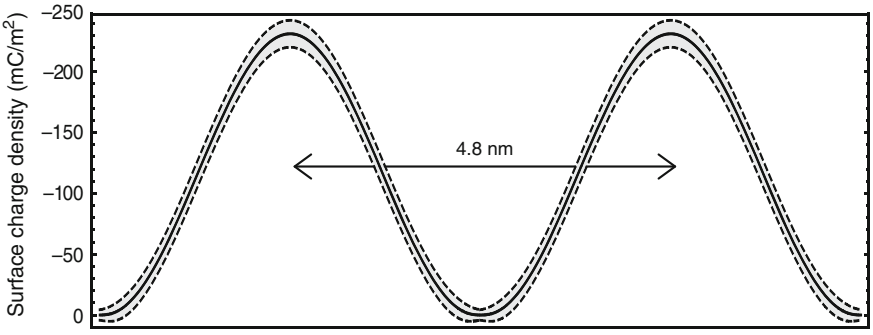

Fig. 19.13 Surface charge density distribution on SDS aggregates obtained from the force curves fitted to the experimental data. *Shaded area* represents the error in the charge density distribution estimated by taking the measurement noise in the force data into account

best fit. The variation in the charge density distribution is (grey region) also shown. This figure shows that the surface charge density on the SDS aggregate varies from 0 to $-250\mathrm{mC/m^2}$ depending on the position on a molecular scale.

19.4 Application of FM-AFM 2: High-Resolution Imaging of Biomolecules

19.4.1 DNA

It has been well known that most double-stranded DNA (dsDNA) molecules adopt the B-form conformation under physiological conditions. B-form DNA (B-DNA) molecules have right-handed helical structures and distinctive major and minor grooves, which are ideally described by the Watson-Crick model of DNA [37].

Bacterial plasmid pUC18 (2686 base pairs), which is a closed circular DNA, was immobilized onto a freshly cleaved muscovite mica substrate and FM-AFM imaging was performed in 50 mM $NiCl_2$ solution. Because both the cleaved surface of muscovite mica and the sugar-phosphate backbone are negatively charged, nickel ions weakly bind DNA onto the mica substrate by electrostatic interactions [38]. The tip-sample distance was regulated by keeping the frequency shift constant at about +80 Hz, which corresponds to the tip-sample interaction force of about +40 pN.

A typical FM-AFM topographic image of the plasmid DNA in 50 mM $NiCl_2$ solution is shown in Fig. 19.14. The plasmid DNA molecules are interwound, as previously reported [39]. Figure 19.15 is a high-resolution FM-AFM image of the plasmid DNA, which was obtained in the area indicated by the rectangle in Fig. 19.14. The measured height of the DNA backbones from the substrate was about 2 nm,

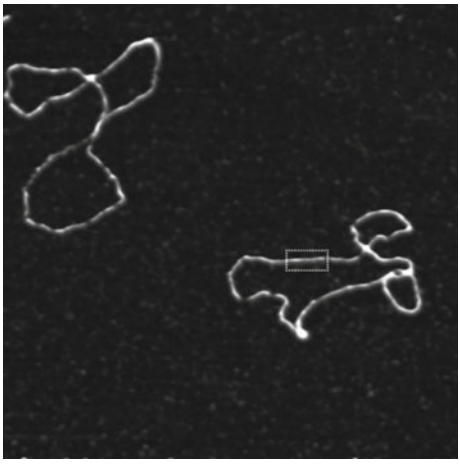

Fig. 19.14 FM-AFM image of plasmid DNA in aqueous solution (50 mM $NiCl_2$) (Scan range: 540 nm × 540 nm)

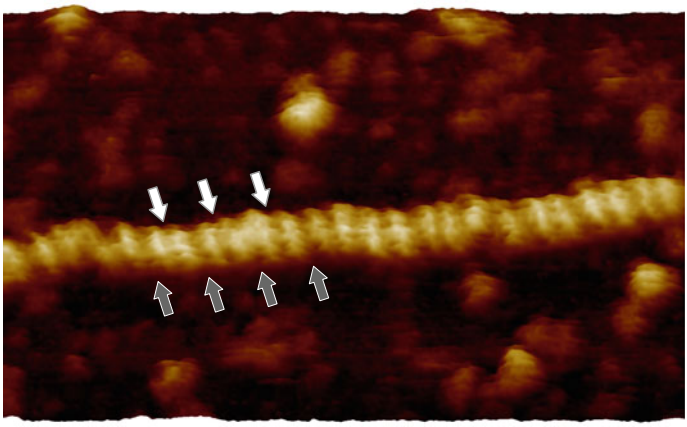

Fig. 19.15 FM-AFM image of plasmid DNA in aqueous solution (50 mM $NiCl_2$) (Scan range: 48 nm × 20 nm)

which agrees well with the diameter of B-DNA (2.0 nm). There are a lot of globular features around the plasmid DNA which are assumed to be the adsorbates, as the mica surface was often partially covered with adsorbates from the $NiCl_2$ solution, such as nickel hydroxides, $Ni(OH)_2$. In this figure, deep grooves between the sugar-phosphate backbones of DNA are clearly resolved. We found that two distinct types of grooves with different widths appeared alternately, as partly indicated by white and grey arrows in Fig. 19.15, respectively. By carefully measuring the groove widths (distances between the adjacent DNA backbones) along the local helix axis of the DNA, two groove widths were quantitatively differentiated. These grooves are attributed to the major and minor grooves of B-DNA. The sum of the major and minor groove widths, which correspond to the B-DNA helix pitch, was 3.7 nm with a standard deviation of 0.15 nm. The helix pitch of B-DNA in water has been reported to be 3.6 nm (axial rise: 10.5 bp/turn on average [40]), and this value was determined to be slightly larger than that of the classic Watson-Crick model (3.4 nm) on the basis of an X-ray fiber diffraction study [37]. In addition, plasmid DNA isolated from cells is regularly underwound (negatively supercoiled) [41]. Therefore, we conclude that the helix pitch of 3.7 nm observed in our study reflects the nature of real plasmid DNA under physiological conditions.

We also performed the 2D frequency shift mapping on the plasmid DNA. Figure 19.16 is an FM-AFM topographic image of the plasmid DNA in 50 mM $NiCl_2$ solution. Along the A-B line indicated in the figure, we obtained a 2D frequency shift map shown in Fig. 19.16b. On the plasmid DNA, a very complicated pattern was observed, which reflects the complex distribution of the water molecules around the DNA. On the other hand, stripe patterns parallel to the surface contour were observed on the surrounding adsorbates, which are presumably from nickel chloride solution.

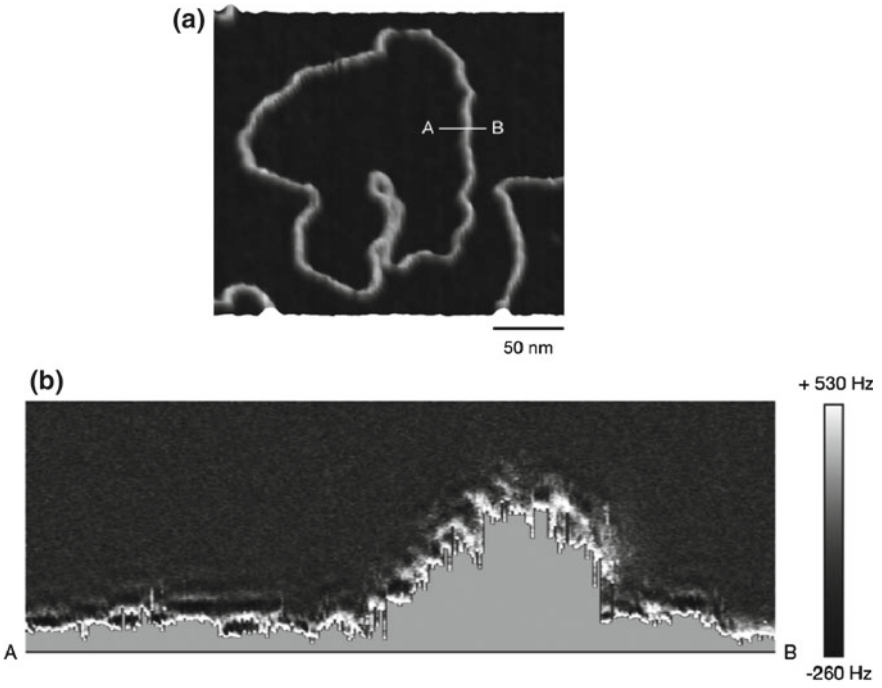

Fig. 19.16 2D frequency shift mapping of plasmid DNA in aqueous solution (50 mM $NiCl_2$). **a** FM-AFM image of plasmid DNA (Scan range: 100 nm × 82 nm). **b** 2D frequency shift map obtained along the *A-B line* in (**a**)

19.4.2 Self-assembled Monoclonal Antibodies

Antibodies are protein molecules that play a critical role in humoral immunity. Immunoglobulin G (IgG, 150 kDa) is one of the five isotypes of antibodies (IgA, IgD, IgE, IgG and IgM) and is most abundant in the serum. IgG molecules have Y-shaped structures with three arms, including two antigen-binding fragments (Fab regions) and one crystallizable fragment (Fc region). The Fab and Fc regions are connected via hinge regions, which contain conformationally flexible polypeptide chains, as shown in Fig. 19.17.

Anti-human serum albumin (HSA) mouse monoclonal antibodies (IgG1 isotype) were immobilized onto a freshly cleaved muscovite mica substrate, and FM-AFM imaging was performed in an electrolyte solution. Because both the cleaved surface of mica and IgG molecules are negatively charged at a neutral pH, cations weakly bind IgG molecules on the mica substrate via electrostatic interactions [38]. Figure 19.17b shows an FM-AFM image of an IgG molecule in 50 mM $ZnCl_2$. In this solution, IgG molecules with various conformations were individually adsorbed onto the mica substrate. Because isolated molecules have conformational flexibilities, they can

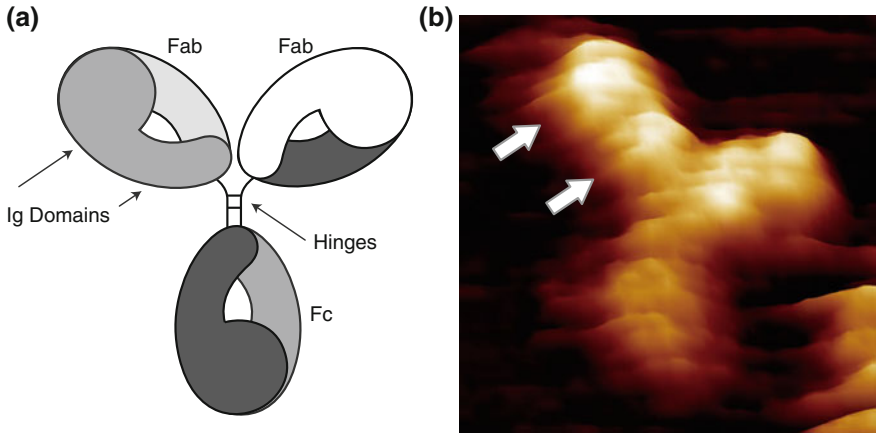

Fig. 19.17 **a** Ideal structural model of IgG molecule. **b** FM-AFM image of mouse monoclonal antibody (IgG1) in aqueous solution (50 mM $ZnCl_2$) (Scan range: 23 nm × 23 nm)

exhibit various binding structures when they are adsorbed on a substrate. The figure shows the three arms of IgG, reflecting its Y-shaped structure. We found that the heights of the two upper arms in Fig. 19.17b measured from the substrate were slightly higher than that of the remaining arm, based on which we assigned these two arms as Fab regions. We also identified two globular structures within each Fab region, as indicated by the arrows in Fig. 19.17b. These structures were assigned as immunoglobulin (Ig) domains, which are protein domain structures, and were composed of beta-sheet secondary structures (β-barrels).

We found that monoclonal IgG molecules self-assembled into well-ordered oligomers in aqueous solution. Figure 19.18a shows an FM-AFM image of IgG molecules in 50 mM $MgCl_2$. Under these conditions, we routinely observed flower-like structures with a diameter of approximately 30 nm. The hexamer formed by the self-association of six Fc regions via lateral Fc–Fc interactions [42, 43]. The Fc regions formed a donut-like inner assembly area at the center of the hexamer, and the outer petal-like structures were composed of six pairs of Fab regions. The two Fab regions in each petal belonged to different IgG molecules, as discussed below (see Fig. 19.19). Interestingly, the self-assembled IgG hexamer resembled IgM antibodies, which form donut-like pentamers, in which Fc regions are located at the centre of the oligomer and Fab regions stretched outward.

We also discovered that IgG hexamers self-assembled into ordered 2D crystals in aqueous solution, as shown in Fig. 19.18b. The mica substrate was fully covered with hexagonally arranged IgG hexamers with a lattice constant of 28 nm. We presumed that the 2D crystallization of IgG hexamers was induced by lateral Fab–Fab interactions among four Fab regions [44, 45]. Based on the height of the hexamers from the substrate, we concluded that only a monolayer (2D) crystal is formed and multi-layer (3D) crystallization does not occur on the mica substrate.

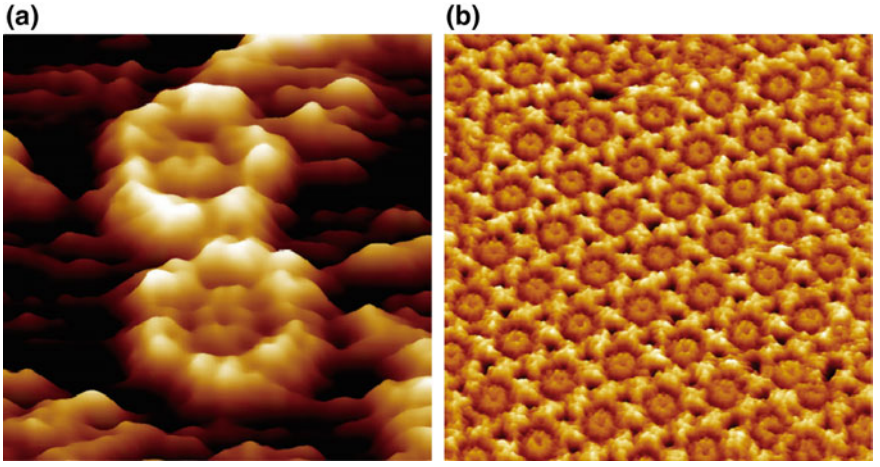

Fig. 19.18 **a** FM-AFM image of hexamers of mouse monoclonal antibody (IgG1) in aqueous solution (50 mM $MgCl_2$) (Scan range: 80 nm × 80 nm). **b** FM-AFM image of hexamers of mouse monoclonal antibody (IgG1) in aqueous solution (50 mM $MgCl_2$) (Scan range: 200 nm × 200 nm)

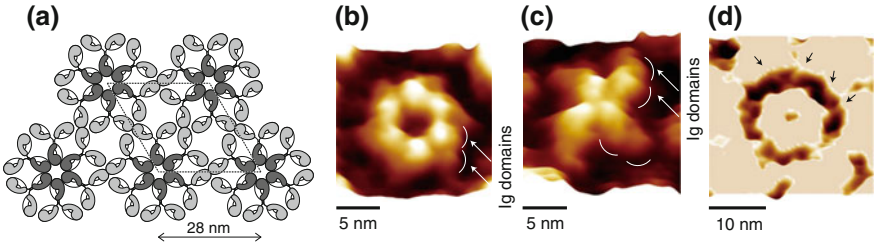

Fig. 19.19 **a** Structural model of self-assembled 2D IgG crystals determined by FM-AFM observation. **b–d** are FM-AFM images of self-assembly of six Fc regions in a 2D IgG crystal in aqueous solution (50 mM $MgCl_2$)

Figure 19.19a is a schematic of a structural model of the self-assembled 2D IgG crystals determined by FM-AFM observation. In this schematic, Fc and Fab regions are depicted as a comma-shaped model and a mirrored-comma shape, respectively, reflecting the different shapes of the regions. Using these models, the six-Fc assembly in the center of the hexamer, shown in Fig. 19.19b, can be represented as six comma shapes. In contrast, the four-Fab regions, shown in Fig. 19.19c, can be depicted as four mirrored-comma shapes. In Fig. 19.19b, c, pairs of globular structures corresponding to Ig domains within the Fc and Fab regions were also resolved, as indicated by the white arrows. In the deep circular groove surrounding the six-Fc assembly, several pairs of single polypeptide chains in the hinge regions were also resolved in the contrast-enhanced FM-AFM image shown in Fig. 19.19d, as indicated by the black arrows.

19.5 Summary and Outlook

This chapter has focused mainly on recent, rapid progress in FM-AFM in liquids. The 2D/3D force mapping based on the quantitative force curve measurement is a powerful, promising technique having a wide variety of applications to molecular-scale solid-liquid interface studies. The required conditions for the quantitative force measurement in liquids were specifically explained. The photothermal excitation of the cantilever oscillation is extremely suitable for obtaining the ideal amplitude and phase transfer functions, satisfying these conditions. In addition we showed the applications of 2D/3D force mapping to the molecular-scale visualization of hydration structures on muscovite mica. The results indicated that the water molecule density over the mica surface is modulated, directly reflecting the surface crystal site. The electric double layer force on surfactant aggregates was also three-dimensionally visualized, which allowed us to obtain nanometer-scale surface charge distribution on the aggregates. Furthermore, high-resolution FM-AFM images of biological molecules such as double-helix structure of DNA and hexamers of IgG antibody molecules obtained in quasi-physiological environments were presented.

Although the force versus distance curve measurement with the aid of the DLVO theory enables us to precisely study local EDL force analysis, which can basically give us the surface charge information, the method is not necessarily applied to general surface charge/potential studies. This is because charging processes at solid-liquid interfaces are quite complicated, including protonation/deprotonation phenomena and cation adsorption/desorption. In addition, the electrical state on the tip surface can significantly affect the surface charge of the sample. Chemical and/or electrochemical control of the tip surface might be necessary for further studies.

Recent, amazing progress in super high-resolution FM-AFM imaging of molecules using a molecule (CO) tip in ultrahigh-vacuum conditions at a low temperature has brought a novel insight into single-molecule science [46, 47]. Although its experimental environment is completely different from the liquid FM-AFM measurement, it must be a good opportunity for us to reconsider the possibility of breaking through the present imaging resolution in liquids.

References

1. T.R. Albrecht, P. Gruütter, P. Horne, D. Rugar, J. Appl. Phys. **69**, 668 (1991)
2. A. Labuda, K. Kobayashi, D. Kiracofe, K. Suzuki, P.H. Grütter, H. Yamada, AIP Adv. **1**, 022136 (2011)
3. K. Kobayashi, N. Oyabu, K. Kimura, S. Ido, K. Suzuki, T. Imai, K. Tagami, M. Tsukada, H. Yamada, J. Chem. Phys. **138**, 184704 (2013)
4. K. Kimura, S. Ido, N. Oyabu, K. Kobayashi, Y. Hirata, T. Imai, H. Yamada, J. Chem. Phys. **132**, 194705 (2010)
5. K. Suzuki, K. Kobayashi, N. Oyabu, K. Matsushige, H. Yamada, J. Chem. Phys. **140**, 054704 (2014)

6. S. Ido, K. Kimura, N. Oyabu, K. Kobayashi, M. Tsukada, K. Matsushige, H. Yamada, ACS Nano **7**, 1817 (2013)
7. S. Ido, H. Kimiya, K. Kobayashi, H. Kominami, K. Matsushige, H. Yamada, Nat. Mater. **13**, 264 (2014)
8. J.E. Sader, J. Appl. Phys. **84**, 64 (1998)
9. C.P. Green, J.E. Sader, J. Appl. Phys. **98**, 114913 (2005)
10. A. Maali, C. Hurth, R. Boisgard, C. Jai, T. Cohen-Bouhacina, J.P. Aime, J. Appl. Phys. **97**, 074907 (2005)
11. K. Kobayashi, H. Yamada, K. Matsushige, Rev. Sci. Instrum. **80**, 043708 (2009)
12. T. Fukuma, M. Kimura, K. Kobayashi, K. Matsushige, H. Yamada, Rev. Sci. Instrum. **76**, 053704 (2005)
13. M. Watkins, B. Reischl, J. Chem. Phys. **138**, 154703 (2013)
14. A. Kovalenko, F. Hirata, J. Chem. Phys. **110**, 10095 (1999)
15. J.N. Israelachivili, *Intermolecular and Surface Forces*, 3rd edn. (Academic Press, London, 2011)
16. T. Schäffer, J.P. Cleveland, F. Ohnesorge, D.A. Walters, P.K. Hansma, J. Appl. Phys. **80**, 3622 (1996)
17. K. Kobayashi, H. Yamada, K. Matsushige, Rev. Sci. Instrum. **82**, 033708 (2011)
18. S.P. Jarvis, A. Oral, T.P. Weihs, J.B. Pethica, Rev. Sci. Instrum. **64**, 3515 (1993)
19. N. Umeda, S. Ishizaki, H. Uwai, J. Vac. Sci. Technol. B **9**, 1318 (1990)
20. G.C. Ratcliff, D.A. Erie, R. Superfine, Appl. Phys. Lett. **72**, 1911 (1998)
21. D. Kiracofe, K. Kobayashi, A. Labuda, A. Raman, H. Yamada, Rev. Sci. Instrum. **82**, 013702 (2011)
22. F. Giessibl, H. Bielefeldt, S. Hembacher, J. Mannhart, Appl. Surf. Sci. **140**, 352 (1999)
23. J.E. Sader, S.P. Jarvis, Appl. Phys. Lett. **84**, 1801 (2004)
24. F. Giessibl, Phys. Rev. B **56**, 16010 (1997)
25. H. Yamada, K. Kobayashi, T. Fukuma, Y. Hirata, T. Kajita, K. Matsushige, Appl. Phys. Express **2**, 095007 (2009)
26. D.R. Baselt, J.D. Baldeschwieler, J. Appl. Phys. **76**, 33 (1994)
27. D.E. Laney, R.A. Garcia, S.M. Parsons, H.G. Hansma, Biophys. J. **72**, 806 (1997)
28. A. Schwarz, H. Hölscher, S.M. Langkat, R. Wiesendanger, AIP Conf. Proc. **696**, 68 (2003)
29. B.J. Albers, T.C. Schwendemann, M.Z. Baykara, N. Pilet, M. Liebmann, E.I. Altman, U.D. Schwarz, Nat. Nanotechnol. **4**, 307 (2009)
30. D. Sawada, Y. Sugimoto, K. Morita, M. Abe, S. Morita, Appl. Phys. Lett. **94**, 173117 (2009)
31. K. Suzuki, N. Oyabu, K. Kobayashi, K. Matsushige, H. Yamada, Appl. Phys. Express **4**, 125102 (2012)
32. M. Tsukada, N. Watanabe, M. Harada, K. Tagami, J. Vac. Sci. Technol. B **28**, C4C1 (2010)
33. M. Watkins, A.L. Shluger, Phys. Rev. Lett. **105**, 196101 (2010)
34. L. Cheng, P. Fenter, K.L. Nagy, M.L. Schlegel, N.C. Sturchio, Phys. Rev. Lett. **87**, 156103 (2001)
35. E.J. Wanless, W.A. Ducker, J. Phys. Chem. **100**, 3207 (1996)
36. V.K. Paruchuri, J. Nalaskowski, D.O. Shah, J.D. Miller, Colloids Surf. A **272**, 157 (2006)
37. J.D. Watson, F.H.C. Crick, Nature **171**, 737 (1953)
38. H.G. Hansma, D.E. Laney, Biophys. J. **70**, 1933 (1996)
39. H.G. Hansma, Science **256**, 1180 (1992)
40. D. Rhodes, A. Klug, Nature **286**, 573 (1980)
41. T.C. Boles, J.H. White, N.R. Cozzarelli, J. Mol. Biol. **213**, 931 (1990)
42. L. Pinteric, R.H. Painter, G.E. Connell, Immunochemistry **8**, 1041 (1971)
43. D.R. Burton, Mol. Immunol. **22**, 161 (1985)
44. H. Yagi, N. Takahashi, Y. Yamaguchi, K. Kato, Mol. Immunol. **41**, 1211 (2004)
45. S. Kanai, J. Liu, T.W. Patapoff, S.J. Shire, J. Pharm. Sci. **97**, 4219 (2008)
46. L. Gross, F. Mohn, N. Moll, P. Liljeroth, G. Meyer, Science **325**, 1110 (2009)
47. L. Gross, F. Mohn, N. Moll, G. Meyer, R. Ebel, W.M. Abdel-Mageed, M. Jaspars, Nat. Chem. **2**, 821 (2010)

Chapter 20
Advanced Instrumentation of Frequency Modulation AFM for Subnanometer-Scale 2D/3D Measurements at Solid-Liquid Interfaces

Takeshi Fukuma

Abstract Since the first demonstration of true atomic-resolution imaging by frequency modulation atomic force microscopy (FM-AFM) in liquid, the method has been used for imaging subnanometer-scale structures of various materials including minerals, biological systems and other organic molecules. Rencetly, there have been further advancements in the FM-AFM instrumentation. Three-dimensional (3D) force measurement techniques are proposed for visualizing 3D hydration structures formed at a solid-liquid interface. These methods further enabled to visualize 3D distributions of flexible surface structures at interfaces between soft materials and water. Furthermore, the fundamental performance such as force sensitivity and operation speed have been significantly improved using a small cantilever and high-speed phase detector. These technical advancements enabled direct visualization of atomic-scale interfacial phenomena at 1 frame/s. In this chapter, these recent advancements in the FM-AFM instrumentation and their applications to the studies on various interfacial phenomena are presented.

20.1 Introduction

In 1991, frequency modulation atomic force microscopy was invented by Albrecht et al. for operating dynamic-mode AFM in vacuum [1]. In vacuum, a Q factor of a cantilever resonance (Q) is much higher than that in air. While the higher Q factor provides a better minimum detectable force (F_{min}), it results in a narrower measurement bandwidth (B) in amplitude modulation AFM (AM-AFM). FM-AFM is free from this problem, as B is independent of Q.

T. Fukuma (✉)
Division of Electrical Engineering and Computer Science, Kanazawa University,
Kakuma-machi, Kanazawa 920-1192, Japan
e-mail: fukuma@staff.kanazawa-u.ac.jp

© Springer International Publishing Switzerland 2015

S. Morita et al. (eds.), *Noncontact Atomic Force Microscopy*,
NanoScience and Technology, DOI 10.1007/978-3-319-15588-3_20

In 1995, Giessibl et al. presented the first true atomic-resolution images obtained by FM-AFM in ultrahigh vacuum (UHV) environment [2]. Since then, FM-AFM has been widely used for atomic- or molecular-scale studies on conducting, semiconducting and insulating materials [3]. Until 2005, the method was used mostly in UHV while only few studies were performed in liquid [4–10] or air [6, 11]. This is partially because many researchers considered that the high Q factor in vacuum is essential for the high performance of FM-AFM and hence found no merits in liquid-environment operation. In addition, early studies of the liquid-environment FM-AFM revealed a number of technical difficulties in operating FM-AFM in liquid wtih sufficient stability and resolution [4–8].

In 2005, Fukuma et al. presented the first true atomic-resolution images obtained by FM-AFM in liquid [12]. This breakthrough was achieved by the following three technical improvements. First, they used a relatively stiff cantilever (spring constant: $k > 20$ N/m) for suppressing instabilities such as cantilever thermal vibration and adhesion events known as jump-to-contact. Secondly, they used a small cantilever oscillation amplitude (peak-to-zero amplitude: $A < 0.5$ nm) for enhancing the sensitivity to short-range interaction force. Finally, they developed a low-noise cantilever deflection sensor to achieve thermal-noise-limited performance with a stiff cantilever and a small oscillation amplitude [13].

Since 2005, FM-AFM has been used for subnanometer-scale imaging of various materials in liquid. Examples of the early applications include minerals [12, 14–16] and biological systems [14, 17–22]. While these results highlighted the high spatial resolution and wide applicability of liquid-environment FM-AFM, they also clarified its fundamental limitation. At solid-liquid interfaces, all the interactions are mediated by solvent molecules (typically water). The solvent molecules have non-uniform three-dimensional (3D) distribution. Thus, the two-dimensional (2D) information obtained by FM-AFM is often insufficient for understanding the mechanisms of solid-liquid interfacial phenomena.

In 2010, Fukuma et al. presented the first subnanometer-resolution imaging of 3D force distribution at a solid-liquid interface [23]. In the method, the tip is scanned vertically as well as laterally to cover the whole 3D interfacial space. During the scan, the frequency shift (Δf) of the cantilever resonance is recorded to produce a 3D Δf image. The obtained 3D Δf image can be converted to a 3D force image using Sader-Jarvis equation [24]. As the force applied to the tip should be strongly influenced by the local distribution of solvent molecules, the subnanometer-scale contrasts observed in a 3D force image are often attributed to the 3D solvation structures. This argument has been further supported by the agreement between the experimentally obtained 3D force images of mica-water interface and water density distributions calculated by simulation [23, 25].

Since 2010, FM-AFM has been used for visualizing vertical-2D or 3D force distributions at various solid-liquid interfaces [23, 25–35]. For interfaces between water and a rigid inorganic crystal, atomistic molecular dynamics (MD) simulation studies have been started towards detailed understanding of the imaging mechanism [36–41]. In the meanwhile, 3D measurements at interfaces between water and soft materials such as lipid bilayers [26] suggested another possibility of this

technique. At a soft interface, not only solvent molecules but also surface structures are thermally fluctuating. Thus, 3D force distribution images should reflect 3D distributions of water and flexible surface structures. While this may add another complexity in the interpretation of the obtained 3D data, the capability of direct 3D imaging of soft interfacial structures can make significant advancements in molecular-scale understanding of various interfacial phenomena.

As described above, the application techniques of liquid-environment FM-AFM have been making rapid progress. However, the fundamental AFM performance such as force sensitivity and operation speed has remained almost unchanged. Recently, this has started to limit the application range of this technique. For example, insufficient B of FM-AFM often prevents imaging dynamic behaviors of interfacial phenomena. Insufficient F_{min} often prevents increasing pixel resolution in 3D force measurements and studying inhomogeneous interfacial structures. To overcome these limitations, we have recently made some improvements in the fundamental performance.

In the first part of this chapter, we describe recent progress in the instrumentation of liquid-environment FM-AFM. We explain the basic principle of our 3D force measurement technique referred to as 3D scanning force microscopy (3D-SFM). We also present the technical development that we made for the improvement of the fundamental performance such as force sensitivity and operation speed. In the second part of this chapter, we present high-resolution 2D and 3D FM-AFM imaging of various materials including minerals, organic molecules and biological systems. We show subnanometer-scale 2D imaging of lipid-cholesterol complexes, $CaF_2(111)$ surfaces and tubulin protofilaments. We also present the results of subnanometer-scale 3D imaging of mica-water and lipid-water interfaces.

20.2 Advanced Instrumentation

High-resolution imaging by FM-AFM in liquid requires the use of a relatively stiff cantilever, small cantilever oscillation amplitude and low noise cantilever deflection sensor. In addition, stable operation of FM-AFM and accurate force measurements by FM-AFM require the use of a direct cantilever excitation method such as the magnetic [42] or photothermal [43] excitation method instead of the standard piezoelectric excitation method [44]. Details of such basic instrumentation of liquid-environment FM-AFM is well summarized in the previous volume of this NC-AFM book series [45]. In this section, we focus on the advanced instrumentation works that we performed since 2007.

20.2.1 3D Scanning Force Microscopy

There have been proposed several different techniques for 3D force measurements by FM-AFM. In 2002, Hölscher et al. presented a full 3D force distribution image of a NiO/vacuum interface obtained in ultrahigh vacuum (UHV) at low temperature [46]. In their method, Δf versus distance curves were measured at 32×32 grid positions with a measurement time of 80 min. In 2009, Albers et al. introduced another method for 3D imaging of a HOPG/vacuum interface obtained in UHV at low temperature [47]. They collected 2D Δf images with a constant height mode at different Z positions. Based on the correlation between the obtained 2D images, they can correct the XY drift of the tip position. Although it took them 40 h to complete a single 3D imaging, the obtained image has a high pixel density (256×119 pixels). In these previous techniques, the imaging time is typically longer than 1 h. This is acceptable for experiments in UHV at low temperature, where thermal drift of the tip position is very small. However, this imaging time is too long for liquid-environment experiments at room temperature, where non-linear drift of the tip position is caused by the swelling of the materials adjacent to the imaging solution.

To overcome this problem, we have developed another 3D force measurement technique referred to as 3D-SFM (Fig. 20.1) [23]. In conventional AFM, a tip is laterally scanned with the tip-sample distance kept almost constant by the constant Δf feedback control (Fig. 20.1a). In 3D-SFM, while a tip is slowly scanned laterally, it is also vertically scanned with a much faster scan speed (Fig. 20.1b). In this way, the tip is scanned in the whole 3D interfacial space. During the tip scan, the fast variation of Δf is recorded in real time to produce a 3D Δf image. In the meantime, the averaged tip-sample distance is controlled such that the averaged Δf is kept constant. In this way, we can avoid a tip crash into the surface even if there is any surface tilt or a tip drift.

A typical experimental setup for 3D-SFM is schematically shown in Fig. 20.1c. The setup is very similar to the one for a standard FM-AFM instrument. Thus, here we explain only the difference from it. For the Z tip scan, we produce a sine wave (z_m) with a modulation frequency much faster than the bandwidth of the tip-sample distance regulation. This signal is added to the output from the feedback controller (z_0). The Δf signal from the phase-locked loop (PLL) circuit is recorded to produce a 3D Δf image. The obtained image is converted to a 3D force image by Sader-Jarvis equation [24]. In the meanwhile, z_0 signal is also recorded to produce a 2D height image.

Owing to the continuous Z scan signal, 3D-SFM is much faster than the previously proposed 3D measurement methods [46, 47]. We typically obtain a full 3D Δf image in 53 s with a scan size of $4 \times 4 \times 2$ nm^2 and a pixel resolution of $64 \times 64 \times 256$ pixels in XYZ. In spite of the fast scan speed, we can visualize a 3D force distribution with subnanometer-scale resolution (the inset in Fig. 20.1).

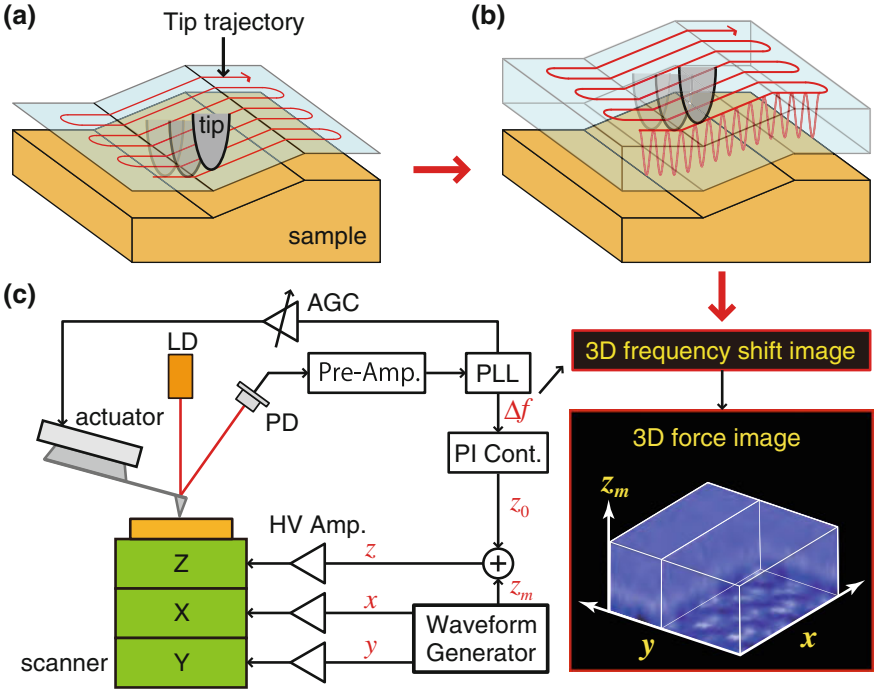

Fig. 20.1 Basic principles of **a** conventional AFM and **b** 3D-SFM. **c** Experimental setup for the developed 3D-SFM. The *inset* shows a 3D force image obtained at a mica-water interface ($2 \times 2 \times 0.78\,\text{nm}^3$) (Reused with permission from Fukuma et al. [23]. Copyright 2010, American Physical Society)

20.2.2 Improvements of Fundamental Performance

Since 2007, we have been working on the improvement of fundamental performance of FM-AFM such as force sensitivity and operation speed. Recently, we finally obtained some outcome from these efforts, which has significantly expanded the applicability of liquid-environment FM-AFM. Here, I summarize key issues in these developments.

20.2.2.1 Force Resolution

True atomic-resolution imaging by FM-AFM in liquid typically requires F_{min} of 10 pN at $B = 100\,\text{Hz}$. Thus, the present FM-AFM barely satisfies this requirement. Such small margin of the performance leads to poor reproducibility or strong dependence on the user skill and often prevents systematic studies by FM-AFM. Furthermore, 3D measurements of hydration structures imposes a more stringent

requirement, $F_{\min}$ of 10 pN at $B = 1$ kHz, because of the faster scanning speed in Z. This requirement is not fully satisfied by the present FM-AFM and hence it may fail to visualize important features related to the interfacial phenomenon that we are interested in. To solve these problems, we have improved $F_{\min}$ of liquid-environment FM-AFM.

$F_{\min}$ of FM-AFM is approximately given by [1]

$$F_{\min} = \sqrt{\frac{4kk_BTB}{\pi f_0 Q}}, \tag{20.1}$$

where k_B, T, Q and f_0 denote Boltzmann's constant, temperature, Q factor of the cantilever resonance and cantilever resonance frequency, respectively. Among the parameters in the right side of this equation, k_B, T and B are determined by the requirements for individual applications. Thus, we cannot arbitrarily change it for improving $F_{\min}$. The rest of the parameters are all relevant to the cantilever characteristics. Therefore, $F_{\min}$ is practically determined by the cantilever characteristics.

Among k, Q and f_0, the only parameter that we can arbitrarily change for improving $F_{\min}$ without deteriorating other performance is f_0. For increasing f_0 without causing significant change in Q or k, we should reduce the cantilever size in length, width and thickness. This idea is not very new but was proposed in the early stage of the AFM development [48–50]. In spite of the previous efforts, the use of a small cantilever has not been common. This is due to the following technical difficulties. First, it was difficult to produce such small cantilevers with an acceptable cost. Secondly, AFM instruments were not designed for using such a small cantilever.

Recently, this situation has started to change. Major AFM probe manufacturers have established a mass production process of small cantilevers with a reasonable yield rate (e.g. USC, Nanoworld and AC55, Olympus). They recently commercialized these cantilevers with an affordable price. In the meanwhile, we have been working with these companies as a test user and have developed an FM-AFM instrument compatible with the small cantilevers [51].

Figure 20.2a, b show scanning electron microscopy (SEM) images of the conventional (NCH) and small cantilevers (USC (prototype)) provided by Nanoworld. The SEM images show that the size of the USC cantilever is much smaller than that of NCH. Owing to this small size, f_0 of USC is as high as 3–4 MHz in water. This is much higher than that of NCH (typically 120–160 kHz in water). In the meanwhile, Q and k of USC are almost the same as those of NCH. From (20.1), USC should provide $\sim$5 times smaller $F_{\min}$ than NCH.

This expectation is true only when we can achieve the optimal performance limited by the thermal cantilever vibration. To achieve this performance, we need to satisfy two technical requirements. First, a cantilever deflection sensor should have sufficiently low noise and wide bandwidth. For detecting the cantilever vibration at 3–4 MHz, the deflection sensor should have a bandwidth higher than 10 MHz. We satisfied this requirement by optimizing the circuit design of the preamplifier and the differential amplifier in the deflection sensor [52]. To achieve the thermal-noise-limited performance, the deflection noise density caused by the deflection

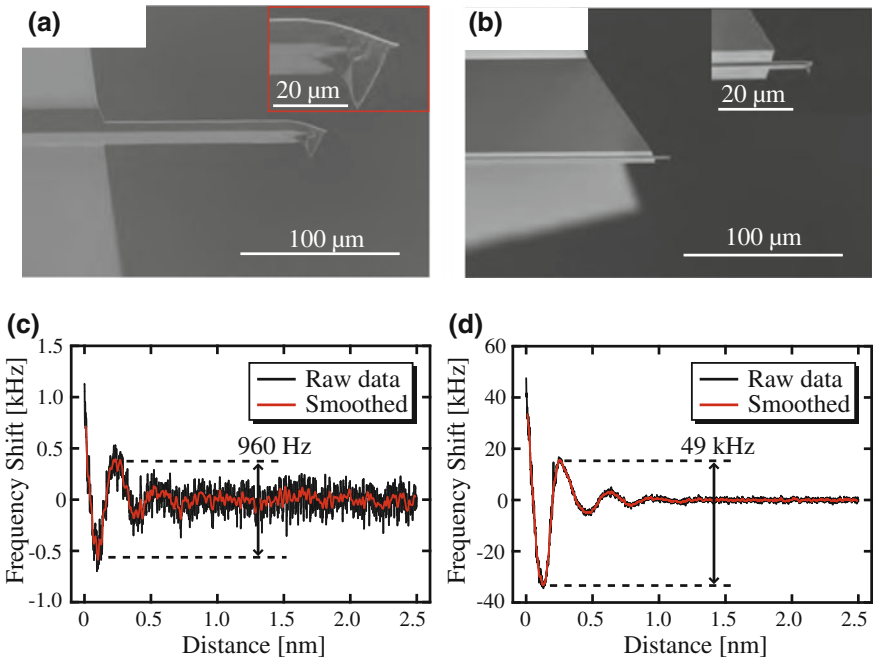

Fig. 20.2 SEM images of **a** the conventional cantilever (NCH, Nanoworld) and **b** the small cantilever (USC (prototype), Nanoworld). Δf versus distance curves measured on mica in PBS solution by **a** NCH and **b** USC cantilevers (Reused with permission from Fukuma et al. [51]. Copyright 2012, Institute of Physics)

sensor (n_{zs}) should be sufficiently smaller than that by the cantilever Brownian motion (n_{zB}).

n_{zB} is given by

$$n_{zB} = \sqrt{\frac{2k_BT}{\pi f_0 kQ} \frac{1}{[1-(f/f_0)^2]^2 + [f/(f_0Q)]^2}}. \tag{20.2}$$

The noise component that influences FM-AFM performance is in the frequence range from $f_0 - B$ to $f_0 + B$. In this frequency range, n_{zB} is almost constant due to the small Q factor. From (20.2), the n_{zB} value at f_0 is given by

$$n_{zB}(f_0) = \sqrt{\frac{2k_BTQ}{\pi f_0 k}}. \tag{20.3}$$

This value is proportional to $1/\sqrt{f_0}$. Thus, the high f_0 of the small cantilever makes it difficult to achieve the thermal-noise-limited performance. If we define the required value as the half of $n_{zB}(f_0)$, it is typically 40 fm/$\sqrt{\text{Hz}}$ for NCH while 10 fm/$\sqrt{\text{Hz}}$ for USC cantilever.

We satisfied this requirement by developing a low noise cantilever deflection sensor using radio frequency (RF) laser power modulation technique [13] and a replaceable objective lens system [53]. Owing to these improvements, the n_{zs} obtained by our deflection sensor is $\sim$5 fm/$\sqrt{\text{Hz}}$, which is much smaller than the required value for achieving the thermal-noise-limited performance with USC.

The second requirement for achieving the thermal-noise-limited performance is a stable cantilever excitation system. We satisfied this requirement by developing a stable photothermal excitation system. A stable operation of dynamic-mode AFM in liquid and accurate measurements by it generally require a direct cantilever excitation method such as the magnetic [42] or photothermal [43] excitation method. For the small cantilever excitation, the photothermal excitation method is more suitable than the magnetic excitation method. This is because the magnetic force applied to the cantilever is reduced by the reduction of the cantilever size and the generation of a sufficiently strong magnetic field becomes difficult with increasing the drive frequency. Thus, we used the photothermal excitation method.

However, we found that stable excitation of a small cantilever requires a higher stability of the excitation laser beam than that of a conventional cantilever [51]. This is because even a small spatial fluctuation of the laser beam position or shape can give a significant influence on the excitation characteristics of a small cantilever. We overcame this problem by improving the stability of the photothermal excitation setup. Before the improvement, a laser diode module and lens system was integrated into the AFM head. In the improved setup, we used a fiber pig-tailed laser beam source that is separeted from the AFM head. The temperature of the laser source was kept constant while the current for driving the laser diode was kept constant by an automatic current constant (ACC) circuit. To transfer the laser light to the AFM head, we used a polarization-maintaining optical fiber, which is known to have a higher immunity to the thermal and mechanical disturbance than a standard single-mode optical fiber. With these improvements, we made it possible to achieve the thermal-noise-limited performance with a USC cantilever.

With the developed cantilever deflection sensor and the photothermal excitation system, we measured Δf versus distance curves on mica in phosphate buffered saline (PBS) solution by NCH and USC cantilevers (Fig. 20.2c, d) [51]. Both the curves show an oscillatory profile corresponding to the hydration structure formed at the mica-water interfaces. This figure shows that USC provides a better signal-to-noise ratio in the force curve measurements. This is due to the significant improvement of the force sensitivity provided by the high f_0. The Δf difference between the minimum and the maximum peak is 960 Hz for NCH and 49 kHz for USC. The result shows that the small cantilever provides $\sim$50 times improvement in the force sensitivity. However, the enhancement of f_0 also increases Δf noise. Consequently, F_{min} is improved from 10.7 to 1.44 pN for $B = 100$ Hz. Therefore, we can achieve approximately seven-fold improvement by the small cantilever. This improvement should give enough margin of the performance in the 2D FM-AFM imaging. In addition, now we have sufficient F_{min} for 3D force measurements. Thus, we may be able to visualize important features of 3D hydration structures that have not been accessible by conventional FM-AFM.

20.2.2.2 Operation Speed

FM-AFM has been traditionally used for atomic- or molecular-resolution imaging of various materials in vacuum [3]. For those applications, it has not been very important to have a high operation speed. However, at solid-liquid interfaces, surface structures are often dynamically changing. In addition, there have been growing interests in dynamic processes such as biomolecular interactions and electrochemical reactions. To visualize these dynamic processes, we should increase the operation speed of FM-AFM. Even for the imaging of static surface structures, biological applications often require a wider feedback bandwidth of the tip-sample distance regulation. This is because the surface corrugations and inhomogeneities of biological samples are much larger than those of atomically or molecularly flat samples that have been investigated by FM-AFM in vacuum. To solve these problems, we have improved the operation speed of FM-AFM.

To increase the measurement bandwidth B of FM-AFM without deteriorating other performance, we need to satisfy the following two requirements. Firstly, we should have sufficient F_{min} for a given B. We satisfied this requirement by using the small cantilever [51]. As discussed above, the small cantilever gives seven-fold improvement in F_{min} for a given B. From (20.1), this implies that B can be increased by 50 times for a given F_{min}. We can operate a conventional FM-AFM with $F_{\mathrm{min}} = 10$ pN at $B = 100$ Hz and obtain an atomic-resolution image at 1 min/frame. Thus, with the small cantilever, we should be able to operate FM-AFM with $F_{\mathrm{min}} = 10$ pN at $B = 5$ kHz and obtain an atomic-resolution image at 1 s/frame.

Secondly, to perform such a fast imaging, we need to increase the bandwidth and to reduce the latency of all the components constituting an FM-AFM. To satisfy this requirement, we improved most of the components in our FM-AFM setup. We improved the circuit design of the cantilever deflection sensor and improved its bandwidth to ∼10 MHz [52]. We replaced the piezoelectric excitation mechanism with the photothermal excitation system and achieved over 10 MHz bandwidth [52]. We developed a separate-type high-speed XY sample and Z tip scanner and enabled their operation at ∼1 and ∼10 kHz, respectively [54]. We also developed a high-speed and low noise high-voltage amplifier that can achieve 200 kHz bandwidth with a 100 nF capacitive load [54], which is a typical capacitance of a piezoelectric actuator used in an AFM scanner. We also improved the bandwidth and the latency of the PLL circuit used for Δf detection and cantilever oscillation control [55, 56].

Among these components, the PLL circuit is the core part of an FM-AFM setup. In the improvement of the PLL circuit, we proposed a unique digital signal processing algorithm for implementing a high-speed phase detector (PD) [56]. Figure 20.3 shows a schematic diagram of the developed PD. In this design, the cantilever deflection signal $A\cos(\omega t + \phi)$ is fed into the IQ demodulator. ω and ϕ denote frequency and phase of the cantilever oscillation, respectively. In the IQ demodulator, the input signal is multiplied by the reference signals [$\cos(\omega t)$ and $\sin(\omega t)$] and converted to dc and 2ω components. While the dc components are eliminated by the high-pass filters (HPFs), the 2ω components [$A\cos(2\omega t + \phi)$ and $A\sin(2\omega t + \phi)$] are passed

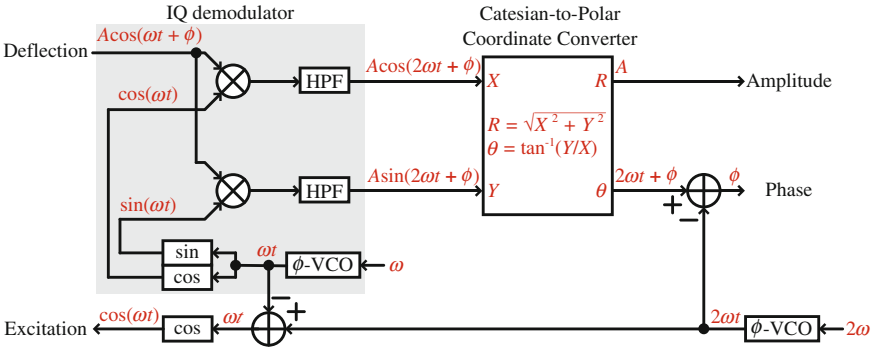

Fig. 20.3 Schematic diagram of the developed PD (Reused with permission from Miyata et al. [56]. Copyright 2013, American Institute of Physics)

to a Cartesian-to-Polar coordinate converter. In the circuit, amplitude (A) and phase ($2\omega t + \phi$) of the complex signal are calculated.

In the developed PD, phase signals, ωt and $2\omega t$, are generated by phase-output voltage controlled oscillators (ϕ-VCOs). The ωt signal is fed into sine and cosine converters to produce the two reference signals. The $2\omega t$ signal is subtracted from the ($2\omega t + \phi$) signal to produce the final output of the PD (ϕ). The difference between the $2\omega t$ and ωt signals is calculated and fed into a cosine converter to produce the cantilever excitation signal [cos (ωt)].

We implemented the proposed circuit in a field programmable gate array (FPGA) chip (Vertex-5, Xilinx). The clock frequency of the FPGA was set at 100 MHz. The sampling rates of the analog-to-digital and digital-to-analog converters were set at 100 MSPS.

In the proposed algorithm, the significant improvement is achieved by the HPFs. If we use a small cantilever with a f_0 of 3 MHz, the deflection signal is converted to the dc and 6 MHz components. While the dc components are eliminated by the HPFs, 6 MHz components are passed through the HPFs. At the pass band frequency, the HPFs have only 0.13 clk group delay. Therefore, this algorithm enables IQ demodulation with almost no delay. This is a remarkable improvement from the conventional PD, which utilizes a multiplier and low-pass filters (LPFs).

The developed PD has a bandwidth of 3 MHz, which is the same frequency as the input signal. Namely, the bandwidth of the PD is determined by the input signal frequency at least for a signal slower than 10 MHz. However, this does not mean that the circuit has an infinite speed. In fact, the circuit causes a finite delay, which is referred to as latency. The latency of the PD for a 3 MHz input signal is 0.97 μs. This latency causes only 1.8° phase delay at 5 kHz. Thus, the PD is fast enough to achieve 5 kHz B in the AFM measurement.

Figure 20.4 shows high-speed phase modulation AFM (PM-AFM) images of a cleaved calcite surface obtained in water using the developed PD. These images are selected from the 44 successive images taken at 1 s/frame. In the images, the lateral motion of the step edge caused by the crystal growth is clearly visualized with atomic

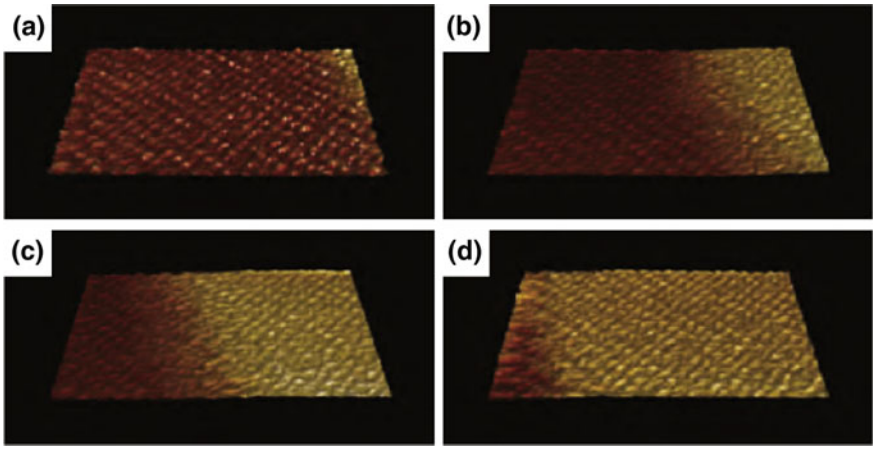

Fig. 20.4 Phase modulation AFM images of the cleaved calcite surface obtained in water. The images were selected from the 44 successive images obtained at 1 s/frame. **a** 0 s. **b** 5 s. **c** 10 s. **d** 15 s. Scan size: $10 \times 5\,\text{nm}^2$. Scan rate: 100 Hz. Pixel size: $200 \times 100\,\text{pix}^2$ (Reused with permission from Miyata et al. [56] Copyright 2013, American Institute of Physics)

resolution. The distance between the adjacent atomic-scale corrugations is ∼0.5 nm while the tip velocity is 2 μm/s. Thus, the frequency of the corrugations to be detected (f_{cr}) is ∼4 kHz. This is close to the maximum B (5 kHz) that we can achieve without deteriorating F_{min}.

In the above application example, we used the developed PD for operating PM-AFM. We also developed a PLL circuit using the high-speed PD and obtained some preliminary results. Therefore, the proposed PD is also applicable to the high-speed operation of FM-AFM. The developed high-speed AFM should enable in-situ imaging of various interfacial phenomena such as crystal growth, dissolution and corrosion processes with atomic-scale resolution.

20.3 Applications of Liquid-Environment FM-AFM

Since 2005, FM-AFM has been used for subnanometer-scale imaging of various surfaces. Some of the early works are summarized in the previous volume of this NC-AFM book series [3, 45]. In this chapter, I focus on the recent applications that we reported after the publication of the previous volume in 2009.

20.3.1 2D Imaging

After the first demonstration of the true atomic-resolution imaging by FM-AFM in liquid, the method has been used for the imaging of various materials including

minerals, biological systems and other organic molecules. Among these applications, here we present the imaging studies of lipid-cholesterol complexes [22], tubulin protofilaments [57] and $CaF_2(111)$ surfaces [25].

20.3.1.1 Lipid-Cholesterol Mixed Bilayers

Cholesterol is one of the major components of biological membranes. It is known to influence various membrane properties such as elasticity, mechanical strength and molecular fluidity [58, 59]. Local variations in the membrane properties caused by the existence or absence of cholesterols are closely related to the formation of nanoscale domains referred to as lipid rafts. The existence of lipid rafts with different affinity to membrane proteins may provide a driving force for protein trafficking or present a local environment that is favorable to specific protein function [60].

To date, biological and physical roles of cholesterols have been intensively studied using a lipid bilayer as a model biological membrane. However, it has been difficult to clarify molecular-scale behavior of the cholesterols and discuss its influence on global membrane properties. For example, studies by nuclear magnetic resonance (NMR) [61] suggested that the cholesterol molecules are inserted between lipid molecules to induce conformational changes in lipid acyl chains. However, the real-space description of local structure formed by the cholesterol-lipid interaction has not been understood due to the lack of a method able to directly visualize the molecular-scale structures in real space.

We investigated mixed dipalmitoylphosphatidylcholine (DPPC) and cholesterol (1:1) bilayers by FM-AFM. Figure 20.5a shows an FM-AFM image of the DPPC-

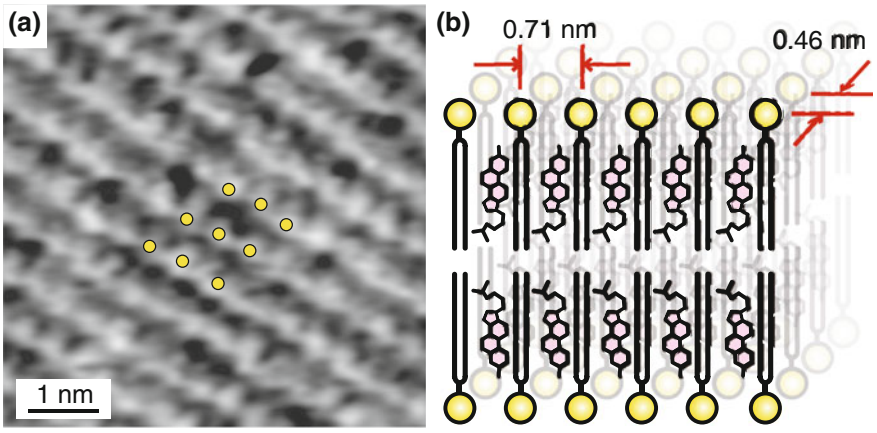

Fig. 20.5 **a** FM-AFM image of a DPPC-cholesterol (1:1) mixed bilayer obtained in PBS solution. Scan size: 5 nm × 5 nm. $A = 0.19$ nm. $\Delta f = +207$ Hz. Tip velocity: 200 nm/s. $k = 33.4$ N/m. Image height: 60 pm. **b** Proposed model for the DPPC-cholesterol (1:1) mixed bilayer (Reused with permission from Asakawa et al. [22]. Copyright 2009, Institute of Physics)

cholesterol bilayer. The image shows the stripe features separated by 0.71 nm. Individual stripes consists of DPPC molecules separated by 0.46 nm. The image reveals that the mixed bilayer has a rhombic molecular arrangement. This is a clear difference from the molecular arrangement in a DPPC bilayer, where molecules are hexagonally packed with a spacing of ∼0.5 nm.

A previous study using MD simulation [62] reported that the lateral spacing of DPPC molecules is expanded by inserting cholesterols between the acyl chains of DPPC molecules. An important finding of our experiment is that a DPPC-cholesterol bilayer exhibits an anisotropic packing, whereas a pure DPPC bilayer presents a hexagonal pseudo-isotropic packing. The result indicated that the inserted cholesterol molecules are linearly aligned between the DPPC molecules in the direction as shown in Fig. 20.5b. So far, such a linear arrangement of the inserted cholesterols has been tentatively suggested by some of the simulation studies as a possible short-range ordering [63]. Although 50 % molar content of cholesterol is much larger than that in the physiological conditions, our result clarified that the DPPC-cholesterol mixture favors such an arrangement when sufficient number of cholesterols exist in the local area of lipid bilayer.

20.3.1.2 Tubulin Protofilaments

Tubulins are globular proteins with a diameter of approximately 4 nm [64]. The $\alpha\beta$-tubulin heterodimers are known as the smallest unit of building blocks of microtubules, which are one of the components of the cytoskeleton with a diameter of 25 nm. Microtubules serve as structural components within cells and are involved in many cellular processes. For example, microtubules act as a molecular rail for motor proteins, such as kinesin and dynein, in intracellular transportation. Previous studies have demonstrated that the carboxyl-terminal (C-terminal) domain of tubulin has strong influence on the interaction with these motor proteins. The interactions between tubulins and motor proteins are regulated by post-translational modifications of the C-terminal tails [65]. In spite of the importance, detailed structure of tubulin C-termini and its relation to their functions have not been clarified even with X-ray or NMR studies [64].

We have investigated the tubulin assemblies by FM-AFM in liquid to visualize local secondary structures, including the C-terminal tails [57]. In Fig. 20.6a, one of the protofilaments constituting a sheet-like structure was imaged. The image shows nanoscale repeating structures corresponding to the tubulin monomers as well as subnanometer-scale features within each molecule. In particular, the fine features indicated by the arrows in Fig. 20.6a exhibit a periodic corrugation with a spacing of 0.53 nm, as revealed by a cross-sectional plot taken along line A–B (Fig. 20.6b). This average spacing is in agreement with the common pitch of an α-helix backbone (0.54 nm), as illustrated in Fig. 20.6c, which strongly suggests that the periodic features correspond to α-helices at the tubulin surface.

The direct imaging of α-helices provides useful information for identifying the orientation of a tubulin protofilament. Although the structural model of a tubulin protofilament is known, to interpret the subnanometer-scale features in an FM-AFM

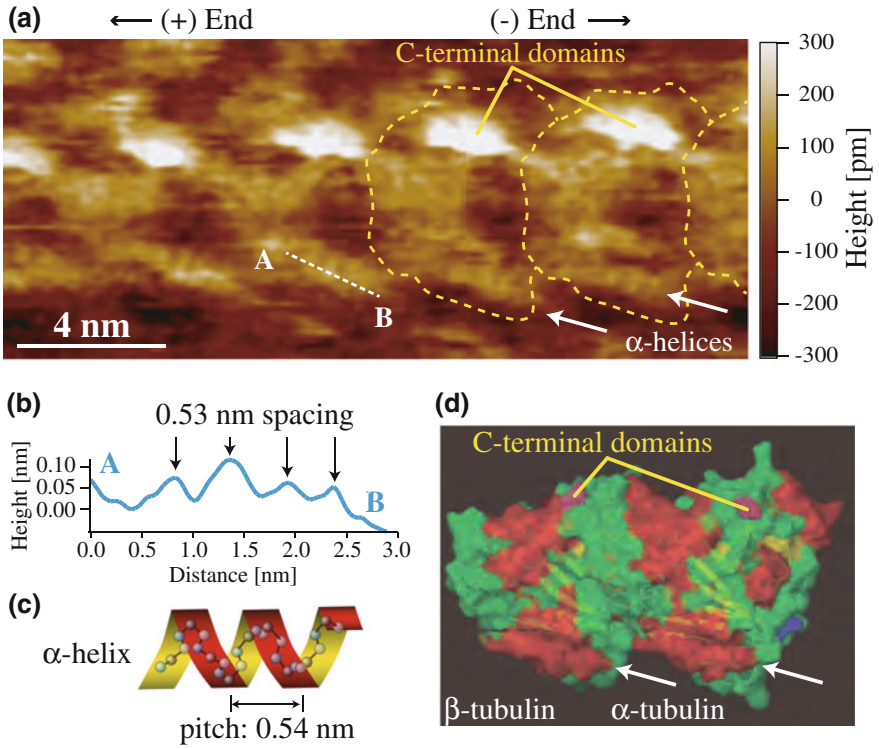

Fig. 20.6 **a** FM-AFM image of a tubulin protofilament in a sheet-like structure ($\Delta f = +3.0$ Hz, $A = 0.30$ nm, tip velocity: 100 nm/s). **b** Height profile measured along line A–B in panel a (average spacing: 0.53 nm, standard deviation: 0.056, $n = 12$). **c** Schematic illustration of a-helix backbone. **d** Structural model of a tubulin heterodimer (PDB ID: 1JFF) (Reused with permission from Asakawa et al. [57]. Copyright 2011, Biophysical Society)

image, one must determine the rotation angle of the protofilament. We compared the subnanometer-resolution FM-AFM image (Fig. 20.6a) with the known structural model of the tubulin heterodimer (PDB ID: 1JFF) with various rotation angles. As a result, we found that the arrangement of the observed α-helices exhibits the best agreement with that of the structural model when the rotation angle is set as shown in Fig. 20.6d. The red regions of the structural model represent α-helices at the surface of tubulins. Although it is difficult to distinguish between α- and β-tubulins in the FM-AFM image, the result allowed us to determine the directions of the (+) and (−) ends of the tubulin protofilament, as shown in Fig. 20.6a. Moreover, the good agreement between the AFM image and the structural model allowed us to interpret local features in the high-resolution FM-AFM image. The positions of the bright protrusions observed in the FM-AFM image (Fig. 20.6a) agree with those of the C-terminal domains in the structural model (Fig. 20.6d). This result demonstrates that the C-terminal domains of tubulins can be directly imaged by FM-AFM in liquid.

The results obtained in this study demonstrate that FM-AFM is capable of identifying arrangements of secondary structures such as α-helices and C-terminal domains at the tubulin surface. This capability should be important in future studies on the molecular-scale mechanisms of tubulin functions.

20.3.1.3 CaF_2(111) Surface

Fluorite (CaF_2) crystals are widely used for various industrial applications. Examples include optical components for semiconductor lithography and other laser technologies [66, 67] and scintillator for radioactivity investigations [68, 69]. Thus, the crystal growth and dissolution processes of fluorite have intensively been studied to improve the crystal quality [70, 71]. In addition, these processes play important roles in the formation of tooth enamel and pathogenesis of dental caries [72, 73], as well as in the desalination for oil and gas recovery [74–76] and water purification [77–79]. Therefore, the physicochemical processes taking place at fluorite-water interface are important in industrial, environmental and medical research fields.

AFM has widely been used for investigating crystal growth and dissolution processes of various minerals. So far, Hillner et al. imaged crystal growth of a fluorite(111) surface in supersaturated solution by contact-mode AFM [80]. They reported the vertical growth of sharp asperities with a height of 10–500 nm on a flat terrace. Subsequently, Bosbach et al. imaged a fluorite(111) surface in an undersaturated solution by contact-mode AFM [81]. They found that the dissolution takes place by the formation of pits on terraces followed by the retreat of step edges. They also found the formation of nanoscale protrusions. Jordan et al. investigated the formation mechanism and the composition of the nanoscale protrusions by imaging fluorite(111) surface in various solutions with different pH [82]. Based on the results, they suggested that the protrusions correspond to multinuclear calcium (aquo) hydroxo complexes $[Ca_x(OH)_y^{2x-y}(aq)]$ connected to surface hydroxyl groups.

The previous research clarified nanoscale behavior of fluorite(111) surface in water such as the crystal growth and dissolution, and the formation of the protrusions. However, to understand the mechanism of these processes, we should also clarify atomic-scale interfacial phenomena such as adsorption or weak interaction of ions or other chemical species in the interfacial space with the crystal surface. Due to the limited resolution and the relatively large loading force of the conventional AFM, it has been difficult to visualize such delicate atomic-scale interfacial phenomena.

We have investigated atomic-scale processes taking place at fluorite-water interface [25]. We performed FM-AFM imaging of the fluorite(111) surface in various solutions including water (pH = 2 and 6.5), saturated solution (pH = 2 and 6) and supersaturated solution (pH = 6, σ = 10 and 100). The observed interfacial phenomena are summarized in Table 20.1. By analyzing the results, we obtained the following three major findings.

First, we found that the atomic-scale surface roughening takes place at low pH probably due to the proton adsorption as shown in Fig. 20.7a. In the previous report, the increase of H-bonds on fluorite(111) surface has been suggested based on the

Table 20.1 Summary of the interfacial phenomena observed in various aqueous solutions

	Crystal Growth	Protrusions	Adsorbates	Protons
Water (pH: 6.5)	Dissolution	Yes	Yes	No
Acidified water (pH: 2)	Dissolution	No	No	Yes
Saturated (pH: 6)	Equilibrium	Yes	Yes	No
Acidified saturated (pH: 2)	Equilibrium	No	No	Yes
Supersaturated (pH: 6, σ: 10)	Growth	No	Yes	No
Supersaturated (pH: 6, σ: 100)	Growth	No	No	No

results obtained by the force curve measurements [82]. The atomic-scale images obtained in this study further strengthened this idea and provided a real-space description of this interfacial phenomenon.

Secondly, we found the existence of the surface adsorbates at high pH as indicated by the arrow A in Fig. 20.7b. Based on their behavior, we consider that they are most likely to be calcium hydroxo complexes. Unlike the nanoscale protrusions indicated by the arrow B in Fig. 20.7b, the lateral distribution of the surface adsorbates is not limited to the vicinity of the F^- vacancies. This is because they are not connected to the surface hydroxyl groups but weakly interact with the fluorite surface.

Finally, we found that the increase of fluorite concentration in solution can prevent the formation of the calcium hydroxo complexes, as shown in Fig. 20.7c, d. The increase of the fluorite concentration results in the increase of Ca^{2+} and F^- and the decrease of OH^- concentrations in the electric double layer. Consequently, the formation of the calcium hydroxo complexes is suppressed. In addition, we suggest that the increased concentration of F^- ions in the electric double layer fills in the surface F^- vacancies, which prevents the formation of the surface hydroxyl groups and hence the nanoscale protrusions.

These findings improve our understanding of the interfacial phenomena taking place at the fluorite-water interface. So far, such an atomic-scale study of the interfacial phenomena has been hindered by the limited performance of the conventional AFM. Owing to the high spatial resolution and the small loading force of FM-AFM, we were able to directly visualize atomic-scale interfacial phenomena. This capability should also be useful in other studies on various interfacial phenomena such as crystal growth and dissolution, catalytic reactions and corrosion processes. Therefore, the results obtained here should stimulate the future applications of FM-AFM to the studies in physical chemistry.

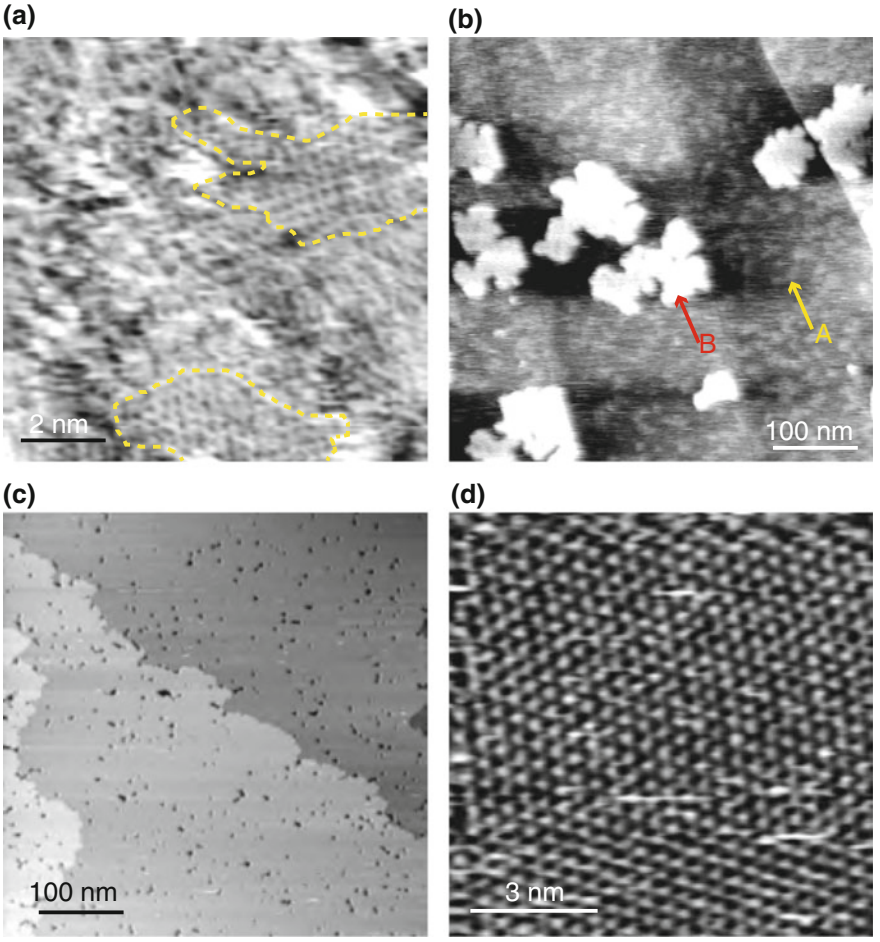

Fig. 20.7 FM-AFM images of fluorite(111) surfaces in various solution. **a** In acidified water (pH: 2). **b** In saturated solution (pH: 6). **c**, **d** In supersaturated solution (pH: 6) (Reused with permission from Kobayashi et al. [25]. Copyright 2013, American Chemical Society)

20.3.2 3D Imaging

In 2010, we demonstrated the first 3D force distribution imaging at mica-water interface [23]. The result shows the possibility of direct imaging of 3D hydration structures with subnanometer-scale resolution. In addition, we applied this technique to investigate a lipid-water interface that has a much softer interfacial structures [26]. The obtained result suggested the possibility of 3D imaging flexible surface structures such as lipid headgroups. Here, I summarize main issues in the two applications.

20.3.2.1 Mica-Water Interface

Muscovite mica is known as a prototype of clay minerals and hence has importance in fundamental research regarding clay swelling in geological science [83–85] and cloud seeding in ecological science [86, 87]. In addition, owing to the ease of cleavage to present an atomically flat surface, mica-water interface has been widely used as a model system to investigate nanofluidics in engineering and physics [88], lubrication in tribology, and molecular adsorption and diffusion in biology and chemistry. To date, water distribution at mica-water interface has been extensively studied by various techniques [89–95]. However, its atomistic model has not been established due to the difficulties in visualizing molecular-scale water distribution directly at a solid-liquid interface.

We have investigated the hydration structures formed at a mica-water interface by 3D-SFM [23]. From the measured 3D force distribution, an *XY* averaged force curve was obtained by plotting force values averaged over an *XY* cross section at each *Z* tip position z_t (Fig. 20.8a). This curve shows an oscillatory profile with a peak (arrow in Fig. 20.8a) having a width of 0.2–0.3 nm, which agrees with the diameter of a water molecule. Owing to this agreement and previous studies on mica-water interface [12, 96], we attributed the repulsive peak to the interaction with a hydration layer.

From *XY* cross sections at different z_t (Fig. 20.8b–e), continuous z_t dependence of *XY* force distribution is obtained. The *XY* cross section in Fig. 20.8b does not show any contrast, which reveals the uniform lateral distribution of water in the hydration layer. As the tip approaches the surface, the *XY* cross section shows an atomic-scale contrast (Fig. 20.8c–e), reflecting the appearance of the short-range interaction force between the tip front atom and the atoms constituting the mica surface. With further decrease of z_t, the hexagonally arranged force peaks found in Fig. 20.8d change to the pairs of smaller peaks (Fig. 20.8e).

The periodic pairs of the force peaks found in Fig. 20.8e appear to be uniform, which gives rise to a question whether the contrast represents the structure of mica surface or the tip apex [97]. However, we confirmed that a similar contrast is reproduced in a 2D FM-AFM image obtained with a different tip as shown in Fig. 20.8f. In the image, the height of individual atoms has irregular variations, which strongly suggests that the contrast is unlikely to be originated from a tip artifact. By comparing the image shown in Fig. 20.8f and the atomic-scale model of mica, we attributed the observed pairs of force peaks to the repulsive forces measured on the two adjacent Si atoms as indicated by the model overlaid on the image in Fig. 20.8f. The height variations of the individual peaks are likely to represent the difference between Si and Al atoms as reported previously [12].

A remarkable feature found in the images is an enhanced contrast at the center of the cavity surrounded by a hexagonal ring. The overlaid model shown in Fig. 20.8f reveals that the *XY* position of the enhanced contrast corresponds to that of a OH group located at the bottom of the cavity. The vertical corrugation of the mica surface makes it difficult to analyze correlation between the atomic-scale structure and the force distribution with a 2D FM-AFM image having no vertical extent. Such an

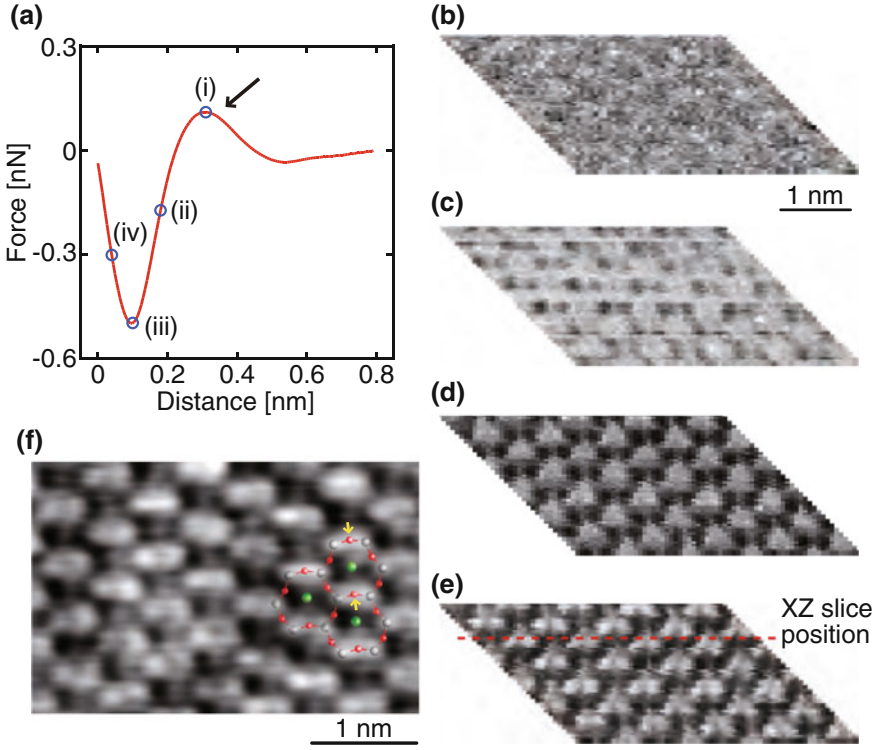

Fig. 20.8 3D and 2D images of mica-water interface obtained in PBS solution. **a** *XY* averaged force curve. The position for the zero *Z* tip position ($z_t = 0$) is arbitrary. **b**–**e** *XY* cross sections of the 3D-SFM image at $z_t = 0.31$, 0.18, 0.10 and 0.04 nm, which respectively correspond to the z_t positions indicated by *Circles* (i)–(iv) in (**b**). A linear drift correction was applied to the *XY* cross sections so that the periodic contrasts match the known lattice constants of a cleaved mica surface. The *dotted line* in (**e**) indicates the *Y* position of the *XZ* cross section shown in Fig. 20.9a. **f** 2D FM-AFM image ($A = 0.26$ nm, $\Delta f = 67.1$ Hz) obtained with a different tip from the one used for the 3D-SFM imaging (Reused with permission from Fukuma et al. [23]. Copyright 2010, American Physical Society)

analysis becomes possible by extracting a vertical cross section from a 3D-SFM image as shown in Fig. 20.9a. The left half of the *XZ* cross section is shown with a low contrast to visualize the localized force distribution above a OH group while the right half of the image is shown with a high contrast to visualize the layer-like force distribution over the entire surface. The layer-like force distribution corresponds to the repulsive peak indicated by the arrow in Fig. 20.8a and has been attributed to the hydration layer.

Extracting individual *Z* profiles constituting the *XZ* cross section, we obtained site specific force profiles as shown in Fig. 20.9b. The *Z* profiles show strong site dependence especially at the *Z* distance range $z_t < 0.2$ nm. Profile 1 shows a large attractive force due to the absence of an underlying atom. Profile 2 shows a relatively

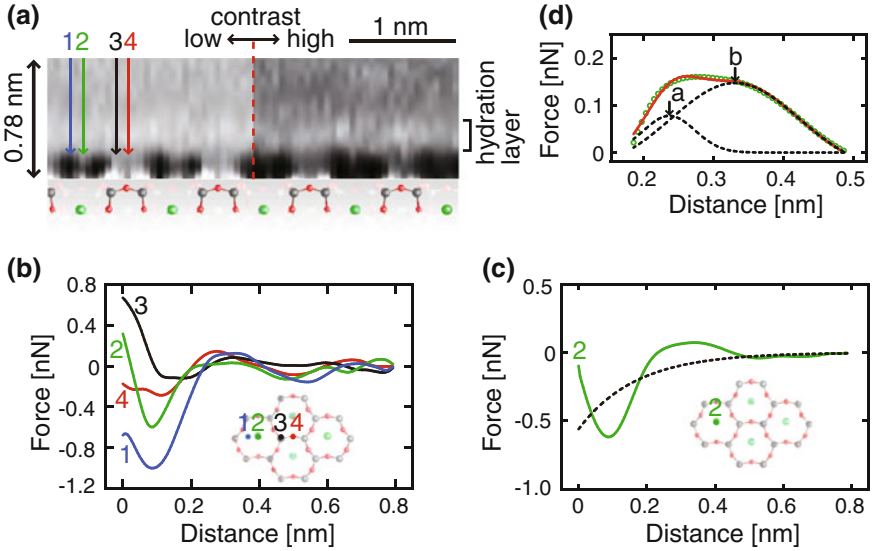

Fig. 20.9 *XZ* cross section and *Z* profiles of 3D-SFM image of mica-water interface obtained in PBS solution. **a** *XZ* cross section obtained at the *Y* position indicated by a *dotted line* in Fig. 20.8e. An atomic-scale model of [1 1 0] projection of muscovite mica is shown below the *XZ* cross section. **b** *Z* profiles measured along Line 1–4 indicated in (**a**). **c** An average of 48 *Z* profiles measured on OH sites. The *dotted line* was obtained by fitting the curve with an exponential function. The *insets* in (**b**) and (**c**) show the measurement positions for the *Z* profiles. **d** The *circles* show the peak profile obtained by subtracting the *dotted line* in (**c**) from the *solid line* in (**c**). The *dotted lines* show the double Gaussian peak profiles obtained by fitting the peak profile. z_t values for Peaks *a* and *b* are 0.237 and 0.331 nm, respectively. The *solid line* shows summation of the *two dotted lines* (Reused with permission from Fukuma et al. [23]. Copyright 2010, American Physical Society)

broad repulsive peak due to the localized force distribution above an OH group. On the contrary, Profile 3 shows a shallow and broad attractive peak due to the competition between the attractive van der Waals or hydration force and a repulsive interaction force between the tip and the Si atom. This means that the repulsive force component measured on the Si site starts to increase at a higher z_t than it does on the OH site owing to their height difference.

Profile 2 shows a relatively broad repulsive peak due to the influence of the localized force distribution above an OH group. To quantitatively analyze the peak profile, 48 *Z* profiles measured on OH sites are taken from the 3D-SFM image and averaged to obtain a smoothed profile (Fig. 20.9c). The averaged curve was fitted to an exponential function to obtain a long-range background component as indicated by the dotted line in Fig. 20.9c. This long-range component is subtracted from the averaged force profile to obtain the peak profile as shown in Fig. 20.9d. The peak shows a broad profile with a plateau on top of it, which does not appear to be a single peak but a summation of double peaks. Thus, we fitted the peak profile to a double Gaussian distribution function as indicated by the dotted lines in Fig. 20.9d.

According to the fitting parameters, the minor peak at $z_t = 0.237$ nm (Peak *a*) has a width of 0.103 nm while the major peak at $z_t = 0.331$ nm (Peak *b*) has a width of 0.258 nm.

So far, some of the previous studies on the mica-water interface supported the existence of "ice-like" water [89–91] while others suggested the existence of more disordered "liquid-like" water [92, 93]. Recently, studies using x-ray reflectometry [94] and Monte Carlo simulation [95] consistently suggested the existence of adsorbed water molecules presenting localized water distribution above OH groups in addition to the laterally distributed hydration layer. The water density profiles obtained in these previous studies revealed the *Z* distance between the peaks corresponding to the hydration layer and adsorbed water molecules is 0.12 nm. This value approximately agrees with the peak distance (0.094 nm) measured in Fig. 20.9d, which indicates that the enhanced contrast measured on OH sites should represent the localized distribution of adsorbed water molecules.

Therefore, the results obtained in this study support the model proposed by Cheng et al. [94], where the adsorbed and laterally-distributed water molecules co-exists at the interface. The co-existence of water molecules having a long relaxation time (adsorbed water) and laterally-distributed disordered water molecules (2D hydration layer) may reconcile the two opposing ideas of "ice-like" and "liquid-like" water molecules at the mica-water interface.

20.3.2.2 Lipid-Water Interface

At the interface between a biological system and its surrounding physiological solution, water molecules interact with biomolecules constituting the surface. Through the interaction, water molecules give significant influence on the structure and function of biomolecules and their assembly [98–100]. Therefore, understanding of the structure and function of a biological system requires investigations on the behavior of interfacial water.

The surface of a biological membrane mainly consists of hydrophilic lipid headgroups. So far, the membrane-water interface has been extensively studied by various techniques [17, 19, 101–106]. These previous works have shown that the water molecules adjacent to a membrane strongly interact with the headgroups and give significant influence on its mechanical strength and fluidity [107–109]. However, molecular-scale origin for such influence has remained elusive.

One of the major difficulties in such a study lies in the measurement of molecular-scale structure of a membrane-water interface. As the lipid headgroups exhibit thermal fluctuations, the surface structure of a membrane is inherently ill-defined. In addition, the fluctuating lipid headgroups interact with mobile water, through which the interfacial water presents non-uniform density distribution known as hydration structure. Thus, the understanding of the whole structure of membrane-water interface should require a method to visualize 3D distribution of mobile water as well as fluctuating lipid headgroups.

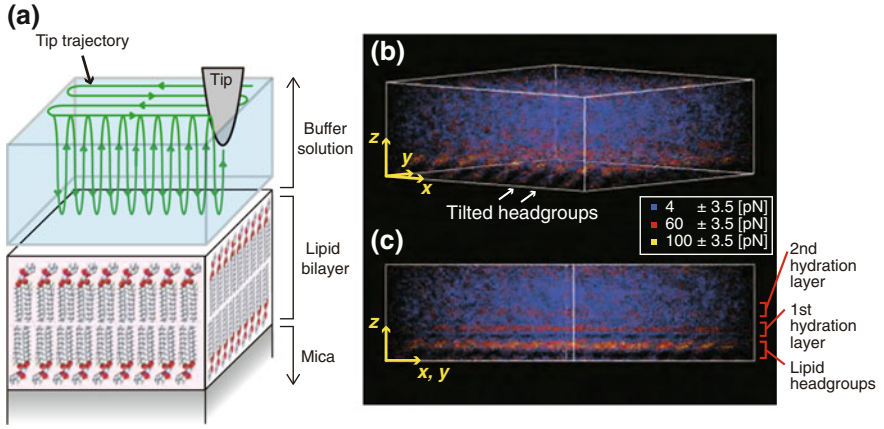

Fig. 20.10 **a** Illustration of 3D-SFM imaging at an interface between a DPPC bilayer and HEPES buffer solution. **b**, **c** Scatter plots of the 3D short-range force image of the lipid-water interface (Reused with permission from Asakawa et al. [26]. Copyright 2012, American Chemical Society)

We have investigated the lipid-water interface by 3D-SFM [26]. We measured a 3D force distribution at the interface between fluctuating lipid headgroups and HEPES buffer solution (Fig. 20.10a). The obtained 3D image showed molecular-scale tilted contrasts reflecting the averaged conformation of the headgroups as well as layer-like contrasts corresponding to the hydration layer (Fig. 20.10b, c). The results show that we can visualize averaged 3D distribution of fluctuating surface structures as well as that of mobile water (i.e. hydration structure).

There are many other examples where local interaction between fluctuating structures and water influences structure and dynamics of biological systems. However, the information obtained by the conventional techniques is not necessarily sufficient to achieve molecular-scale understanding of such interfacial phenomena. The results obtained in this study suggest that 3D-SFM can complement the missing piece of information. This unique capability should contribute to the progress in the molecular-scale understanding of the various phenomena at biological interfaces.

20.4 Summary

In this chapter, we presented the advanced instrumentation and applications of liquid-environment FM-AFM. For instrumentation, we presented the development of 3D-SFM and the improvements of the fundamental performance of FM-AFM such as force sensitivity and operation speed. 3D-SFM allows us to visualize a 3D force distribution at a solid-liquid interface in less than 1 min with subnanometer resolution. The use of small cantilever gives a seven-fold improvement in the force resolution or a 50 times improvement in the operation speed. By developing a high-speed phase

detector, we enabled an atomic-resolution imaging at 1 s/frame. These instrumentation works have significantly broaden the application range of liquid-environment FM-AFM.

For applications, we showed recent examples of 2D and 3D imaging studies. Compared with the 2D imaging studies reported in the early stage of the liquid-environment FM-AFM development, the applications are more focused on the understanding of important issues in the individual research field. In the 3D imaging studies, we presented two unique capabilities of 3D-SFM. In the imaging of mica-water interfaces, we demonstrated the possibility of imaging 3D hydration structures. In the imaging of lipid-water interfaces, we suggested the possibility of direct 3D visualization of flexible surface structures.

In the next five years, I expect that the 2D and 3D imaging techniques will be used for more practical applications in various research fields. For high-speed FM-AFM, first applications in physical chemistry and biology will be demonstrated, which should give strong impacts on the researchers in those areas. In the meanwhile, basic studies on the contrast formation mechanism of the 3D force imaging should be performed to understand the correlation between the contrasts and the hydration structures as well as the flexible surface structures. Another important topic will be the development of surface property measurement techniques based on FM-AFM such as distributions of charges, potential, hydrophilicity, viscoelasticity and chemical sensitivity. Most of these instrumentation and application studies have been already started. Therefore, I expect that the rapid progress of the liquid-environment FM-AFM techniques should continue at least in the next 5 years.

Acknowledgments This work was supported by KAKENHI (25706023), Japan Society for the Promotion of Science and ACT-C, Japan Science and Technology Agency.

References

1. T.R. Albrecht, P. Grütter, D. Horne, D. Ruger, J. Appl. Phys. **69**, 668 (1991)
2. F.J. Giessibl, Science **267**, 68 (1995)
3. S. Morita, R. Wiesendanger, E. Meyer (eds.), *Noncontact Atomic Force Microscopy (Nanoscience and Technology)* (Springer, Berlin, 2002)
4. S.P. Jarvis, T. Uchihashi, T. Ishida, H. Tokumoto, Y. Nakayama, J. Phys. Chem. B **104**, 6091 (2000)
5. S.P. Jarvis, T. Ishida, T. Uchihashi, Y. Nakayama, H. Tokumoto, Appl. Phys. A **72**, S129 (2001)
6. K. Kobayashi, H. Yamada, K. Matsushige, Appl. Surf. Sci. **188**, 430 (2002)
7. T. Okajima, H. Sekiguchi, H. Arakawa, A. Ikai, Appl. Surf. Sci. **68**, 210 (2003)
8. H. Sekiguchi, T. Okajima, H. Arakawa, S. Maeda, A. Takashima, A. Ikai, Appl. Surf. Sci. **61**, 210 (2003)
9. T. Uchihashi, M.J. Higgins, Y. Nakayama, J.E. Sader, S.P. Jarvis, Nanotechnology **16**, S49 (2005)
10. M.J. Higgins, C.K. Riener, T. Uchihashi, J.E. Sader, R. McKendry, S.P. Jarvis, Nanotechnology **16**, S85 (2005)
11. A. Sasahara, S. Kitamura, H. Uetsuka, H. Onishi, J. Phys. Chem. B **108**, 15735 (2004)

12. T. Fukuma, K. Kobayashi, K. Matsushige, H. Yamada, Appl. Phys. Lett. **87**, 034101 (2005)
13. T. Fukuma, M. Kimura, K. Kobayashi, K. Matsushige, H. Yamada, Rev. Sci. Instrum. **76**, 053704 (2005)
14. B.W. Hoogenboom, H.J. Hug, Y. Pellmont, S. Martin, P.L.T.M. Frederix, D. Fotiadis, A. Engel, Appl. Phys. Lett. **88**, 193109 (2006)
15. S. Nishida, D. Kobayashi, T. Sakurada, T. Nakazawa, Y. Hoshi, H. Kawakatsu, Rev. Sci. Instrum. **79**, 123703 (2008)
16. S. Rode, N. Oyabu, K. Kobayashi, H. Yamada, A. Kühnle, Langmuir **25**, 2850 (2009)
17. M. Higgins, M. Polcik, T. Fukuma, J. Sader, Y. Nakayama, S.P. Jarvis, Biophys. J. **91**, 2532 (2006)
18. T. Fukuma, M.J. Higgins, S.P. Jarvis, Biophys. J. **92**, 3603 (2007)
19. T. Fukuma, M.J. Higgins, S.P. Jarvis, Phys. Rev. Lett. **98**, 106101 (2007)
20. T. Fukuma, A.S. Mostaert, S.P. Jarvis, Nanotechnology **19**, 384010 (2008)
21. H. Yamada, K. Kobayashi, T. Fukuma, Y. Hirata, T. Kajita, K. Matsushige, Appl. Phys. Express **2**, 095007 (2009)
22. H. Asakawa, T. Fukuma, Nanotechnology **20**, 264008 (2009)
23. T. Fukuma, Y. Ueda, S. Yoshioka, H. Asakawa, Phys. Rev. Lett. **104**, 016101 (2010)
24. J.E. Sader, S.P. Jarvis, Appl. Phys. Lett. **84**, 1801 (2004)
25. N. Kobayashi, S. Itakura, H. Asakawa, T. Fukuma, J. Phys. Chem. C **117**, 24388 (2013)
26. H. Asakawa, S. Yoshioka, K. Nishimura, T. Fukuma, ACS NANO **6**, 9013 (2012)
27. K. Kimura, S. Ido, N. Oyabu, K. Kobayashi, Y. Hirata, T. Imai, H. Yamada, J. Chem. Phys. **132**, 194705 (2010)
28. T. Hiasa, K. Kimura, H. Onishi, M. Ohta, K. Watanabe, R. Kokawa, N. Oyabu, K. Kobayashi, H. Yamada, J. Phys. Chem. C **114**, 21423 (2010)
29. T. Hiasa, K. Kimura, H. Onishi, Phys. Chem. Chem. Phys. **14**, 8419 (2012)
30. T. Hiasa, K. Kimura, H. Onishi, Coll. Surf. A **396**, 203 (2012)
31. T. Hiasa, K. Kimura, H. Onishi, J. Phys. Chem. C **116**, 26475 (2012)
32. R. Nishioka, T. Hiasa, K. Kimura, H. Onishi, J. Phys. Chem. C **117**, 2939 (2013)
33. T. Sugihara, I. Hayashi, H. Onishi, K. Kimura, A. Tamura, Chem. Phys. **419**, 74 (2013)
34. T. Hiasa, H. Onishi, Langmuir **29**, 5801 (2013)
35. T. Hiasa, K. Kenjiro, H. Onishi, J. Phys. Chem. C **117**, 5730 (2013)
36. M. Watkins, A.L. Shluger, Phys. Rev. Lett. **105**, 196101 (2010)
37. M. Harada, M. Tsukada, Phys. Rev. B **80**, 035414 (2010)
38. M. Tsukada, N. Watanabe, M. Harada, K. Tagami, J. Vac. Sci. Technol. B **28**, C4C1 (2010)
39. M. Watkins, M.L. Berkowitz, A. Shluger, Phys. Chem. Chem. Phys. **13**, 12584 (2011)
40. M. Watkins, B. Reischl, J. Chem. Phys. **138**, 154703 (2013)
41. B. Reischl, M. Watkins, A. S. Foster, J. Chem. Theory Comput. **9**, 600 (2013)
42. S.P. Jarvis, A. Oral, T.P. Weihs, J.B. Pethica, Rev. Sci. Instrum. **64**, 3515 (1993)
43. N. Umeda, S. Ishizaki, H. Uwai, J. Vac. Sci. Technol. B **9**, 1318 (1991)
44. Y. Martin, C.C. Williams, H.K. Wickramasinghe, J. Appl. Phys. **61**, 4723 (1987)
45. S. Morita, R. Wiesendanger, F.J. Giessibl (eds.), *Noncontact Atomic Force Microscopy Volume 2 (Nanoscience and Technology)* (Springer, Berlin, 2009)
46. H. Hölscher, S.M. Langkat, A. Schwarz, R. Wiesendanger, Appl. Phys. Lett. **81**, 4428 (2002)
47. B.J. Albers, T.C. Schwendemann, M.Z. Baykara, N. Pilet, M. Liebmann, E.I. Altman, U.D. Schwarz, Nat. Nanotech. **4**, 307 (2009)
48. M.B. Viani, T.E. Schäffer, A. Chand, M. Rief, H.E. Gaub, P.K. Hansma, J. Appl. Phys. **86**, 2258 (1999)
49. S. Hosaka, K. Etoh, A. Kikukawa, H. Koyanagi, K. Itoh, Microelectron. Eng. **46**, 109 (1999)
50. T.E. Schäffer, P.K. Hansma, J. Appl. Phys. **84**, 4661 (1998)
51. T. Fukuma, K. Onishi, N. Kobayashi, A. Matsuki, H. Asakawa, Nanotechnology **23**, 135706 (2012)
52. T. Fukuma, Rev. Sci. Instrum. **80**, 023707 (2009)
53. T. Fukuma, S.P. Jarvis, Rev. Sci. Instrum. **77**, 043701 (2006)

54. K. Miyata, S. Usho, S. Yamada, S. Furuya, K. Yoshida, H. Asakawa, T. Fukuma, Rev. Sci. Instrum. **84**, 043705 (2013)
55. Y. Mitani, M. Kubo, K. Muramoto, T. Fukuma, Rev. Sci. Instrum. **80**, 083705 (2009)
56. K. Miyata, H. Asakawa, T. Fukuma, Appl. Phys. Lett. **103**, 203104 (2013)
57. H. Asakawa, K. Ikegami, M. Setou, N. Watanabe, M. Tsukada, T. Fukuma, Biophys. J. **101**, 1270 (2011)
58. J. Hendriksen, A.C. Rowat, E. Brief, Y.W. Hsueh, J.L. Thewalt, M.J. Zuckermann, J.H. Ipsen, Biophys. J. **90**, 1639 (2006)
59. T.J. McIntosh, A.D. Magid, S.A. Simon, Biochemistry **28**, 17 (1989)
60. C. Mineo, G.L. James, E.J. Smart, R.G.W. Anderson, **271**, 11930 (1996)
61. M.R. Vist, J.H. Davis, Biochemistry **29**, 451 (1990)
62. A.M. Smondyrev, M.L. Berkowitz, Biophys. J. **771**, 2075 (1999)
63. L. Miao, M. Nielsen, J. Thewalt, J.H. Ipsen, M. Bloom, M.J. Zuckermann, O.G. Mouritsen, Biophys. J. **82**, 1429 (2002)
64. E. Nogales, S.G. Wolf, K.H. Downing, Nature **391**, 199 (1998)
65. Y. Kimura, N. Kurabe, K. Ikegami, K. Tsutsumi, Y. Konishi, O.I. Kaplan, H. Kunitomo, Y. Iino, O.E. Blacque, M. Setou **285**, 22934 (2010)
66. N. Senguttuvan, M. Aoshima, K. Sumiya, H. Ishibashi, J. Cryst. Growth **280**, 462 (2005)
67. I. Nicoara, M. Stef, A. Pruna, J. Cryst. Growth **310**, 1470 (2008)
68. S. Wakahara, Y. Furuya, T. Yanagida, Y. Yokota, J. Pejchal, M. Sugiyama, N. Kawaguchi, D. Totsuka, A. Yoshikawa, Opt. Mater. **34**, 729 (2012)
69. Y. Zhang, X. Xiang, W.J. Weber, Nucl. Instr. Meth. **266**, 2750 (2008)
70. L.A. Perez, G.H. Nancollas, Coll. Surf. **52**, 231 (1991)
71. H. Moller, H.E.L. Madsen, J. Cryst. Growth **71**, 673 (1985)
72. T. Aoba, O. Fejerskov, Crit. Rev. Oral Biol. Med. **13**, 155 (2002)
73. O. Prymak, V. Sokolova, T. Peitsch, M. Epple **6**, 498 (2006)
74. S.M. Hamza, S.K. Hamdona, J. Phys. Chem. **95**, 3149 (1991)
75. Z. Amjad, Langmuir **9**, 597 (1993)
76. C.H. de Vreugd, J.H. ter Horst, P.F.M. Durville, G.J. Witkamp, G.M. van Rosmalen, Coll. Surf. A **154**, 259 (1999)
77. C.Y. Tai, J. Cryst. Growth **206**, 109 (1999)
78. C.Y. Tai, P.C. Chen, T.M. Tsao, J. Cryst. Growth **290**, 576 (2006)
79. J.J. Eksteen, M. Pelser, M.S. Onyango, L. Lorenzen, C. Aldrich, G.A. Georgalli, Hydrometallurgy **91**, 104 (2008)
80. P.E. Hillner, S. Manne, P.K. Hansma, A.J. Gratz, Faraday Discuss. **95**, 191 (1993)
81. D. Bosbach, G. Jordan, W. Rammensee, Eur. J. Mineral. **7**, 267 (1995)
82. G. Jordan, W. Rammensee, Surf. Sci. **371**, 371 (1997)
83. M.H. Jr., A.F. White (eds.), Review in Mineralogy: Mineral Water Interface Geochemicstry (Mineralogical Society of America, 1990)
84. E.S. Boek, P.V. Coveney, N.T. Skipper, J. Am. Chem. Soc. **117**, 12608 (1995)
85. S. Karaborni, B. Smit, W. Heidug, J. Urai, E. van Oort, Science **271**, 1102 (1996)
86. G.R. Edwards, L.F. Evans, A.F. Zipper, Trans. Faraday Soc. **66**, 220 (1970)
87. J.L. Caslavsky, K. Vedam, J. Appl. Phys. **42**, 516 (1971)
88. Y. Leng, P.T. Cummings, J. Chem. Phys. **124**, 074711 (2006)
89. G. Sposito, R. Prost, Chem. Rev. **82**, 553 (1982)
90. M. Odelius, M. Bernasconi, M. Parrinello, Phys. Rev. Lett. **78**, 2855 (1997)
91. P.B. Miranda, L. Xu, Y.R. Shen, M. Salmeron, Phys. Rev. Lett. **81**, 5876 (1998)
92. R. Bergman, J. Swenson, Nature **403**, 283 (2000)
93. J. Swenson, R. Bergman, W. Howells, J. Chem. Phys. **113**, 2873 (2000)
94. L. Cheng, P. Fenter, K.L. Nagy, M.L. Schlegel, N.C. Sturchio, Phys. Rev. Lett. **87**, 156103 (2001)
95. S.H. Park, G. Sposito, Phys. Rev. Lett. **89**, 085501 (2002)
96. J.N. Israelachvili, G.E. Adams, Nature **262**, 774 (1976)
97. F.J. Giessibl, S. Hembacher, H. Bielefeldt, J. Mannhart, Science **289**, 422 (2000)

98. M. Ge, J.H. Freed, Biophys. J. **85**, 4023 (2003)
99. P. Ball, Chem. Rev. **108**, 74 (2008)
100. Y. Levy, J.N. Onuchic, Annu. Rev. Biophys. Biomol. Struct. **35**, 389 (2006)
101. J.F. Nagle, S. Tristram-Nagle, Biochim. Biophys. Acta **1469**, 159 (2000)
102. J. Milhaud, Biochim. Biophys. Acta **1663**, 19 (2004)
103. E. Márazková, P. Hobza, M. Bohl, D.R. Gauger, W. Pohle, J. Phys. Chem. **109**, 15126 (2005)
104. J. Sýkora, P. Kapusta, V. Fidler, M. Hof, Langmuir **18**, 571 (2002)
105. M.L. Berkowitz, D.L. Bostick, S. Pandit, Chem. Rev. **106**, 1527 (2006)
106. J. Cheng, S. Pautot, D.A. Weitz, X.S. Xie, Proc. Natl. Acad. Sci. USA **100**, 9826 (2003)
107. M. Pasenkiewicz-Gierula, Y. Takaoka, H. Miyagawa, K. Kitamura, A. Kusumi, J. Phys. Chem. A **101**, 3677 (1997)
108. J. Fitter, R.E. Lechner, N.A. Dencher, J. Phys. Chem. **103**, 8036 (1999)
109. W. Zhao, D.E. Moilanen, E.E. Fenn, M.D. Fayer, Biophys. J. **130**, 13927 (2008)

Chapter 21
Electrochemical Applications of Frequency Modulation Atomic Force Microscopy

Yasuyuki Yokota and Ken-ichi Fukui

Abstract In this chapter, applications of frequency modulation AFM (FM-AFM) to electrochemical issues, especially potential-dependent interface structures of adsorbates and electrolyte solutions, are described. One of the difference between electrochemical FM-AFM (EC-FM-AFM) and FM-AFM in liquids is that the sample potential with respect to the potential of the bulk electrolyte solution is controlled by a potentiostat used for general electrochemical measurements. Measurement principles and major parts of the EC-FM-AFM apparatus are similar to the FM-AFM in liquids, thus authors refer the reader to Chaps. 19, 20 in this book (Vol. 3) and Chaps. 15, 16 and 18 in Vol. 2 for some details.

21.1 Surface Electrochemistry

21.1.1 Electrochemical Interfaces

Since Volta invented the voltaic pile late in the eighteenth century, electrochemistry has been one of the most important fields of study not only for academia but for industry. For instance, some parts of thermodynamics and kinetics chapters in the textbook of physical chemistry were developed by electrochemistry, and recent energy-related subjects, such as fuel cell, secondary battery, solar cell, and electric double-layer capacitor, are included in electrochemical applications.

In general, a difference in electric potential, so-called electromotive force for the electrochemical cell, can be measured between the electrodes 1 and 2 immersed in electrolyte solutions [1].

$$E = E_1 - E_2 \tag{21.1}$$

Y. Yokota · K. Fukui (✉)
Division of Chemistry, Department of Materials Engineering Science, Graduate School of Engineering Science, Osaka University, Osaka, Japan
e-mail: kfukui@chem.es.osaka-u.ac.jp

Y. Yokota
e-mail: yyokota@chem.es.osaka-u.ac.jp

© Springer International Publishing Switzerland 2015

S. Morita et al. (eds.), *Noncontact Atomic Force Microscopy*,
NanoScience and Technology, DOI 10.1007/978-3-319-15588-3_21

In the case that the n electron transfer equilibrium between the oxidized and reduced species (Ox and Red) at the electrode x can be assumed,

$$\mathrm{Ox} + ne^{-} = \mathrm{Red} \tag{21.2}$$

Nernst equation is written as follows,

$$E_x = E^{\circ} + \frac{RT}{nF} \ln \frac{a_{\mathrm{Ox}}}{a_{\mathrm{Red}}} \tag{21.3}$$

where E° is standard potential with respect to the appropriate reference electrode, R is the gas constant, T is temperature, F is the Faraday constant. a_{X} represents the activity of species X. One rewrites the Nernst equation as follows, due to the difficulty of determining a_{Ox} and a_{Red} by experiments.

$$E_x = E^{\circ\prime} + \frac{RT}{nF} \ln \frac{[\mathrm{Ox}]}{[\mathrm{Red}]} \tag{21.4}$$

$$E^{\circ\prime} = E^{\circ} + \frac{RT}{nF} \ln \frac{\gamma_{\mathrm{Ox}}}{\gamma_{\mathrm{Red}}} \tag{21.5}$$

where [X] and γ_{X} are the concentration and the activity coefficient of species X, respectively. We note that the electrical potential is determined by the concentration of electroactive species. In other words, we can control the concentration by choosing the appropriate electrode potential.

To understand the meaning of E_x, we consider the electric double layer formed at the electrolyte/electrode interface. Figure 21.1 shows the schematic of the distribution of excess electrolyte ions close to the interface as a function of the electrostatic potential. Potential of zero charge (pzc) is a characteristic value of the electrode potential at which the electrode does not acquire an electrical charge when it comes into contact with the electrolyte. We note that the specific adsorption of ions and some adsorbates on the electrode are negligible at the pzc potential (see middle part of Fig. 21.1). When the electrode potential is negative with respect to pzc, positive ions are attracted to the electrode from the solution (see upper part of Fig. 21.1), while when positive, negative ions are attracted. In both cases, the surface charge at the electrode is screened by the counter ions. The screening length is called Debye length and about the size of electrolyte ions ($\sim$1 nm). In general, the Debye length increases with the decrease of the electrolyte concentration. Above pictures of the electric double layer are quantitatively described by models of Gouy-Chapman, Stern, and others [1].

By the virtue of the thermodynamics, there is a general consensus concerning the fundamental aspects of electrolyte/electrode interfaces, as mentioned above. Many kinetic theories of electrode reactions have also been reported [2]. Although classical models can explain the electrochemical measurements to some extent, the macroscopic theory and measurements do not provide molecular scale pictures

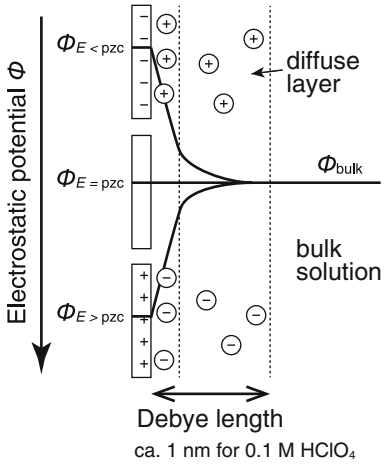

Fig. 21.1 Electric double layer at the electrolyte/electrode interface

of the electrolyte/electrode interfaces. For example, understanding the effects of microscopic structure of electrode surface and intermolecular interactions, important factors for the practical electrochemical measurements, are difficult to obtain from the classical models. Based on these considerations, many research groups have investigated the microscopic properties of electrolyte/electrode interfaces by modern surface science techniques for the last several decades.

21.1.2 Surface Analysis

Microscopic structure of electrolyte/electrode interfaces is the most fundamental information not only for understanding the data of electrochemical measurements but for designing novel electrochemical devices. Since the atomic and molecular scale investigations of solid surfaces have been performed in the field of surface science for a long time, it is a general choice to adapt surface science techniques for electrochemical interfaces. Various types of so-called in situ techniques, without taking the electrode out of electrolyte solutions, have been developed by the special modification of the surface science techniques being applicable to electrochemical environments, and they have become indispensable tools today. Among them, photon-related techniques played a central role in advances in microscopic studies of electrolyte/electrode interfaces due to the relatively less constraint under electrochemical environments.

Surface X-ray scattering (SXS) has been an important technique for structure determination in the surface science research. The penetrating nature of X-rays, unlike electron probes, allows measurements of the surface structures under electrochemical environments. By using in situ SXS, Wang et al. have proved the potential dependent surface reconstruction of an Au(111) electrode immersed in aqueous

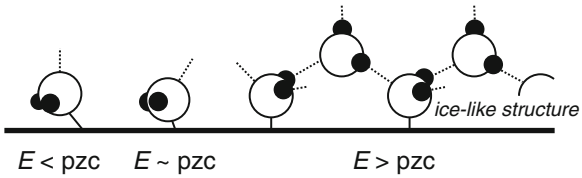

Fig. 21.2 Proposed orientation of water molecules at the electrolyte/electrode interface

solution, which had been suggested by other experimental results [3]. According to the report, surface gold atoms of the Au(111) electrode show a reversible phase transition between the (1 × 1) bulk termination at positive potential and the (23 × $\sqrt{3}$) reconstructed phase at negative potential. SXS techniques have also revealed that the properties of interfacial water are quite different from the bulk water [4]. Recently, Kondo et al. reported potential-dependent structure of ions and water on Au(100) and Au(111) electrodes as well as surface reconstructions of gold atoms [5]. Thus, SXS technique is an important method to investigate the three-dimensional interface structure at an atomistic level.

One of the most fundamental question for electrochemistry is that the orientation of the electrolyte solvent molecules at the electrified interface. Especially, various researchers have discussed the potential-dependent orientation of interfacial water molecules, because each water molecule possesses a large dipole moment. According to the strict surface selection rule of infrared (IR) spectroscopy at flat metal substrates, in situ IR measurements seem to be the most appropriate tools for revealing the orientation issue. Figure 21.2 shows an orientation model of interfacial water on the Au(111) electrode at potential below, around, and above the pzc, proposed by Osawa and co-workers according to their in situ IR measurements [6–8]. Interestingly, they have also reported that the orientation of interfacial water depends not only on the applied potential (i.e. surface charge), but on electrode materials and electrolyte ions.

21.1.3 Electrochemical Scanning Probe Microscopy

It has been well-known that the invention of scanning tunneling microscopy (STM) by Binnig and Rohrer in 1982 drastically accelerated the research field of surface science by the virtue of the atomic resolution capability in real-space. Soon after the invention in ultrahigh vacuum (UHV) environment, Hansma et al. reported the STM images taken in liquids in 1986 [9], and so-called electrochemical STM (EC-STM) were developed in 1988 by several groups [10]. The measurement principle of STM and EC-STM is similar except for using a bipotentiostat for EC-STM to control the both tip and sample potentials (E_{tip} and E_{sample}) independently. To increase the ratio between the tunneling current and undesired electrochemical current, the EC-STM tip is coated with insulating materials except at the very end.

Figure 21.3 shows potential dependent EC-STM images of Au(111) taken in 0.05 M H_2SO_4 aqueous solution with corresponding current versus potential curves,

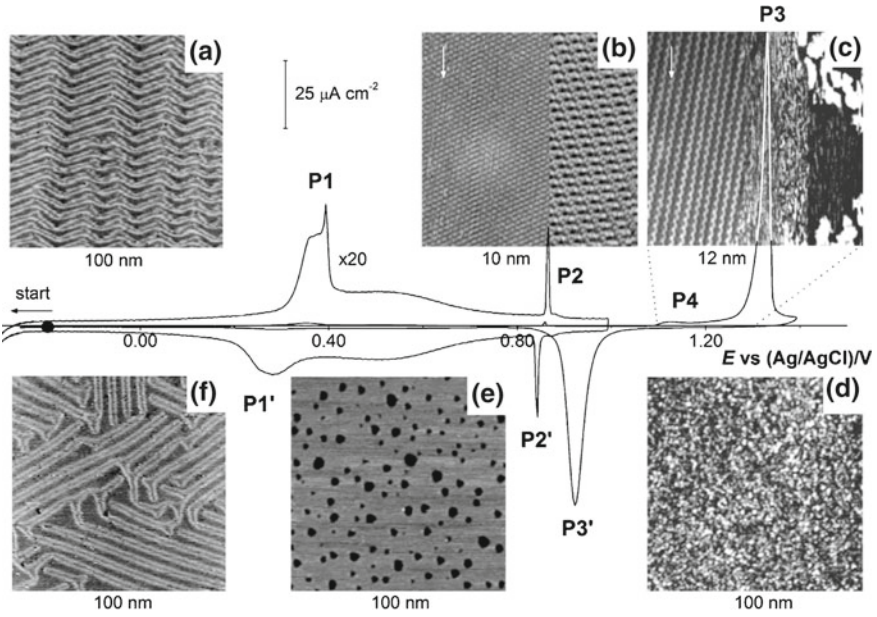

Fig. 21.3 Cyclic voltammograms of an Au(111) single crystal electrode in 0.05 M H_2SO_4. The EC-STM images taken at **a** −0.20, **b** 0.80–0.90 **c** 1.10–1.30 **d** 1.40 **e** 0.60, and **f** 0.00 V versus Ag/AgCl illustrate characteristic surface structures. (Reused with permission from Wandlowski et al. [11] Copyright 2013, Elsevier)

so-called cyclic voltammograms (CVs) [11]. In the case of negative potential (Fig. 21.3a), an EC-STM image reveals the well-defined herringbone structure ($(23 \times \sqrt{3})$ reconstructed phase), as in UHV environment. When the sample potential was shifted to higher and then lower potentials, the electrode structure drastically changed in accordance with the several peaks seen in the CVs. For example, left part of Fig. 21.3b shows the (1 × 1) structure due to the potential induced lifting of the surface reconstruction. Although both EC-STM images of Fig. 21.3a, f shows the reconstructed surface at the same sample potential, the herringbone structure disappeared after the potential cycling. Such a high resolution imaging capability in real-space makes EC-STM a unique tool among many in situ techniques.

Although EC-STM is useful for studying atomic scale structure at the electrified interfaces, one must be careful for interpretation of the height information of EC-STM images when the electronic structure of the imaging object is quite different. Figure 21.4 shows such an example, where the islands of ferrocene (Fc) derivative embedded in *n*-alkanethiol self-assembled monolayer (SAM) on an Au(111) electrode were imaged by EC-STM [12]. Figure 21.4a shows the typical CVs of a Fc-terminated SAM, where a vertical dotted line represents the formal potential $E^{\circ\prime}$. EC-STM images in Fig. 21.4b–d were taken by changing the sample potential to alter the oxidation state of the Fc islands with fixing the tip potential to −0.9 V

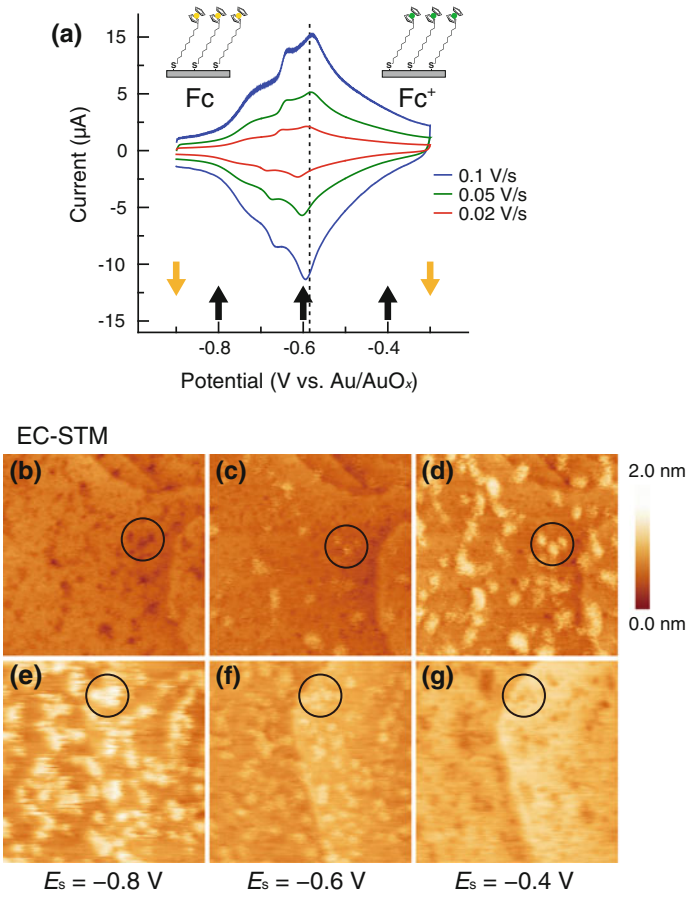

Fig. 21.4 **a** Cyclic voltammograms of a full-coverage $FcC_{11}H_{22}SH$ SAM on an Au(111) electrode in a 0.05 M $HClO_4$ solution. *Vertical dotted line* shows the formal potential. *Upward* and *downward arrows* indicate the sample and the tip potentials, at which EC-STM measurements were performed, respectively. **b–g** EC-STM images ($100 \times 100\,nm^2$) of $FcC_{11}H_{22}SH$ islands embedded in $C_{10}H_{21}SH$ SAM. **b–d** $E_t = -0.9$ V, **e–g** $E_t = -0.3$ V versus Au/AuO_x

($E_{bias} = E_{sample} - E_{tip} > 0$). Protrusions in Fig. 21.4d indicate the Fc islands and other parts are composed of *n*-alkanethiol matrix. It is clear from these images that the apparent height of the Fc islands increases with increase of oxidized Fc^+ species. However, when the tip potential was changed to −0.3 V to reverse the bias polarity ($E_{bias} = E_{sample} - E_{tip} < 0$), the order of the apparent height became opposite, indicating that the height values obtained by EC-STM depended on both the tip and sample potentials. Thus, EC-STM is not appropriate for the structural investigation of the electrified interface in some cases.

Atomic force microscopy (AFM) has also been applied to the electrified interface since its invention. Because instrumental setup of typical AFM and electrochemical measurements are independent, only an external potentiostat is necessary

to provide potential control for EC-AFM. Early imaging studies using contact- or tapping-mode EC-AFM were thoroughly reviewed by Gewirth and Niece in 1997 [13]. The useful aspects of EC-AFM seemed to be force curve measurements between the tip and sample, rather than imaging due to its lower spatial resolution compared to EC-STM. The force curve measurements using contact-mode EC-AFM can be divided into two categories; approach curves reveal the tip and sample interaction via electrolyte solutions as a function of displacement, and retract curves provide the adhesion force to separate the tip and sample in electrolyte solutions [14]. The approach curve is analyzed by the electric double layer model to gain the information of interfacial electrostatics. On the other hand, the adhesion force measurements are used to obtain the interfacial energy with high spatial resolution (∼10 nm).

Figure 21.5 shows an example of approach and retract force curve measurements for a tip and an electrode modified with electroactive molecules [15]. As schematically shown in Fig. 21.5a, both the tip and the sample are covered by Fc-terminated SAMs and are under potential control by using bipotentiostat. The blue curves in Fig. 21.5b show the typical retract curves measured between reduced (Fc/Fc) and oxidized (Fc^+/Fc^+) tip and sample. These data revealed that when Fc-terminated SAMs are oxidized (positively charged), the adhesion force decreases due to the decrease of the interfacial energy; it is easy to separate the tip and the sample of the "hydrophilic" surfaces in the aqueous solution. This type of measurements

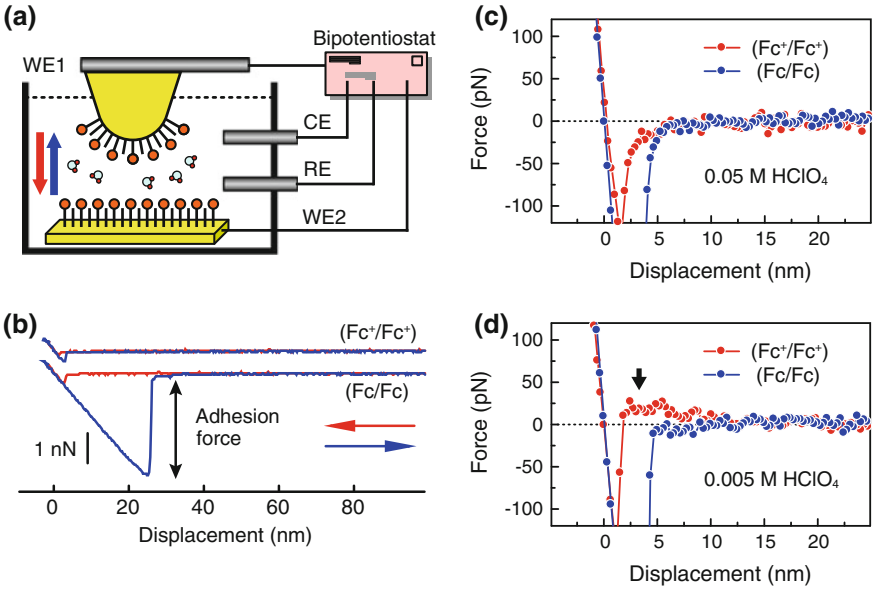

Fig. 21.5 **a** Schematic of force curve measurements for a tip and an electrode modified with electroactive molecules. *WE*, *RE*, *CE* indicate working, reference, and counter electrodes, respectively. **b** Typical force curves recorded at different tip and sample potentials in 0.05 M $HClO_4$. **c** Averaged approach curves in (**b**). **d** Averaged approach curves taken in 0.005 M $HClO_4$

enables us to conduct interfacial energy mapping of the sample by changing the tip position. Figure 21.5c, d is the results of approach curves by changing the oxidation state of the Fc-terminated SAMs and the electrolyte concentration. While the electrolyte concentration does not alter the force-displacement curves in the case of neutral Fc/Fc, the decrease of the concentration enhances the repulsive force between positively charged Fc^+-terminated SAMs (Fc^+/Fc^+) (see arrow in Fig. 21.5d). These results are consistent with the longer Debye length of 0.005 M $HClO_4$ aqueous solution (4.3 nm) compared to that of 0.05 M solution (1.4 nm).

As demonstrated in Fig. 21.5, the force curve measurement using contact-mode EC-AFM has been a useful technique to obtain the physicochemical properties at the electrified interfaces. However, so-called jump-in-contact problem is inevitable for contact-mode AFM (see force curves less than 5 nm in Fig. 21.5c, d). Since true atomic resolution images were taken by Fukuma et al. in 2005 [16], FM-AFM has become the most promising tool for microscopic investigations of liquid/solid interfaces. Thus, one can expect that FM-AFM measurements in the electrochemical environment (EC-FM-AFM) provide the key data for revealing unknown electrochemical issues, which cannot be obtained by EC-STM and contact-mode EC-AFM.

21.2 EC-FM-AFM

21.2.1 Instruments of EC-FM-AFM

Figure 21.6a shows the schematic of our first EC-FM-AFM apparatus [17]. The modification of commercial tapping mode AFM (5500 SPM, Agilent Technology) was performed to reduce the deflection sensor noise according to the literature by Fukuma et al. [18]. To oscillate the cantilever always at its resonant frequency while keeping constant amplitude and to accurately detect the frequency shift due to interactions, a digital oscillation controller using a phase locked loop (PLL) (OC4, Nanonis) was used (Digital PLL controller in Fig. 21.6a). The tip potential can be independently controlled by using bipotentiostat.

Figure 21.6b is the photograph of the electrochemical cell (Agilent Technology), filled with about 0.3 ml electrolyte solution. Large volume of the electrolyte solution is necessary for EC-FM-AFM measurements to realize the reproducible insertion of the reference and counter electrodes. So-called meniscus method, where liquid bridges the tip and the sample with its surface tension, may not be appropriate. In the case of aqueous solutions, the oxidized Au wire and flame-annealed Pt wire are used as a quasi-reference Au/AuO_x electrode and a counter electrode, respectively. Because the electrochemical setup is independent of the AFM apparatus, the electrochemical measurement, such as CV, can be performed during EC-FM-AFM operation. If one cannot prepare the large sample with respect to the size of a cantilever holder, a special modification of the electrochemical cell is required to perform precise electrochemical measurements. We note that the temperature and gas environment can be controlled by several units not depicted in Fig. 21.6a.

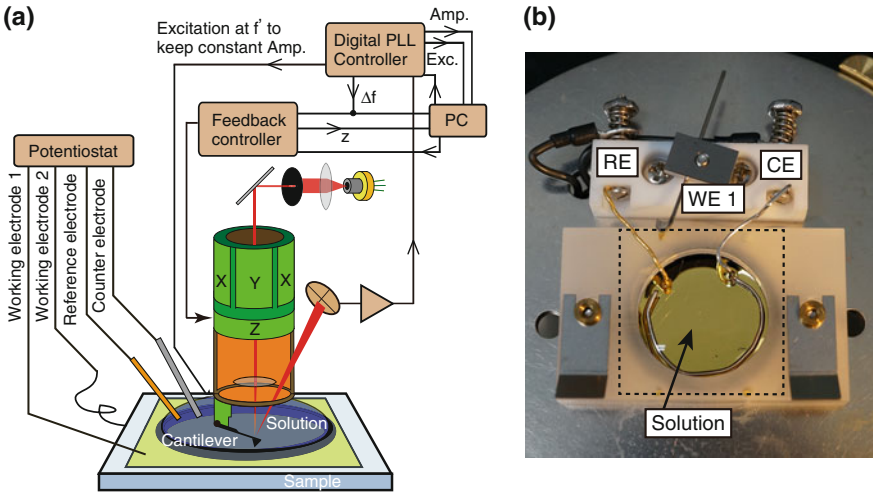

Fig. 21.6 **a** Schematic of EC-FM-AFM. **b** Photograph of an electrochemical cell. *Dotted rectangle* represents the typical sample size

21.2.2 Soft Imaging of Adsorbates

At first, we compare EC-STM and EC-FM-AFM images of the same sample. Figure 21.7a–c shows series of EC-FM-AFM images of Fc islands embedded in *n*-alkanethiol SAM on an Au(111) electrode [17], the same system as in Fig. 21.4. Protrusions observed in Fig. 21.7a represent neutral Fc islands and their height was determined to be 0.51 ± 0.17 nm, consistent with the expected height difference between the Fc derivative and surrounding *n*-alkanethiol matrix. The value of height difference indicates that the EC-FM-AFM tip traces the surface topology. When the sample potential was shifted to higher potential to oxidize the Fc moieties, the height difference increased by 0.44 ± 0.20 nm (Fig. 21.7b). This height change was found to be reversible against potential control, as shown in Fig. 21.7c, d. We note that the tip potential was always set to the sample potential ($E_{\mathrm{bias}} = E_{\mathrm{sample}} - E_{\mathrm{tip}} = 0$).

Since the pioneering work by Chidsey, a tremendous number of studies have been reported in the literature concerning electrochemical properties of Fc-terminated SAMs [19, 20]. Ellipsometry and surface plasmon resonance (SPR) studies have shown that the film thickness of the Fc-terminated SAMs increases with the oxidation of Fc moieties [21–23]. Uosaki et al. performed cyclic voltammetry of the Fc-terminated SAMs in various concentrations of $HClO_4$ solutions and proposed that the electron-transfer process accompanies the 1:1 ion-pair formation between Fc^+ moieties and ClO_4^- anions (Fig. 21.7e) [24]. According to in situ SPR study [23], the increase of the film thickness upon Fc oxidation was about 0.1 nm, indicating that the thickness change alone is not enough to explain the increase of height difference in our EC-FM-AFM study. Because the van der Waals radii of ClO_4^- anion is

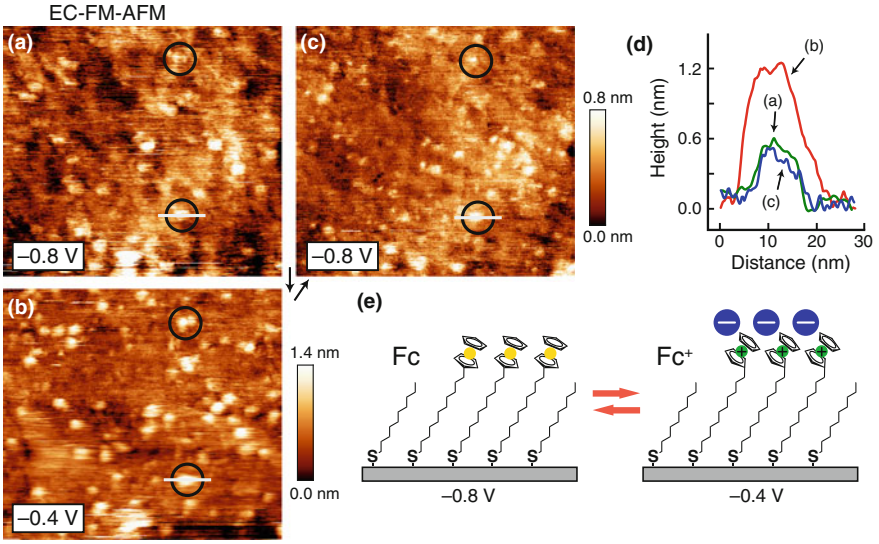

Fig. 21.7 Series of EC-FM-AFM images ($\Delta f = +528$ Hz, $A_{p-p} = 1.00$ nm) of $FcC_{11}H_{22}SH$ islands embedded in $C_{10}H_{21}SH$ SAM (176×159 nm^2) in 0.1 M $HClO_4$ at different E_s and E_t potentials. **a**, **c** $E_s = E_t = -0.8$ V, and **b** $E_s = E_t = -0.4$ V versus Au/AuO_x. Image **c** was recorded after acquisition of (**b**), showing the reproducibility of the image contrast at the $FcC_{11}H_{22}SH$ islands. **d** A comparison of line profiles at a selected $FcC_{11}H_{22}SH$ island indicated by a horizontal line on each image. **e** Schematic representation of the local structure change. Upon oxidation of Fc moieties, ClO_4^- anions coordinate to the Fc^+ moieties

about 0.5 nm and consistent with the observed height difference, we consider that the EC-FM-AFM tip traces the ion-paired ClO_4^- anions on the Fc^+-terminated islands. Although several experiments such as anion species and concentration dependencies are required for the conclusive assignment, we demonstrated that EC-FM-AFM reveals the physical height difference of soft materials in contrast to the case of EC-STM.

As a next example, EC-FM-AFM studies of a molecular adsorbate on highly oriented pyrolytic graphite (HOPG) electrode, which cannot be visualized by EC-STM, are shown in Fig. 21.8 [25]. The adsorbate molecule used is a phenalenyl derivative, 4,8,12,16-tetra-*tert*-butyl-s-indaceno[1,2,3-cd:5,6,7-c′d′]diphenalene (TTB-IDPL) , whose molecular structure is superimposed in Fig. 21.8a. The phenalenyl derivatives are expected to be applied in electronic devices due to their reversible electron transfer ability and graphene-like electronic structure [26]. It is known that Faraday current based on the electron transfer of TTB-IDPL film on HOPG increases with potential cycling to higher potential [27]. One of the possible reasons for current increase is the structural change of TTB-IDPL film upon the potential cycling. Many attempts to visualize TTB-IDPL molecules by EC-STM were unsuccessful presumably due to the peering off the adsorbate molecules by the tip.

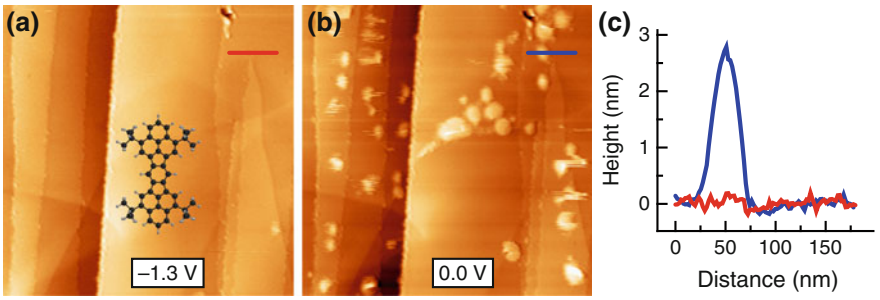

Fig. 21.8 **a**, **b** Series of EC-FM-AFM images ($1\times1\,\mu m^2$, $E_t = 0.48\,V$, $\Delta f = +290\,Hz$, $A_{p-p} = 0.62\,nm$) of a TTB-IDPL film on an HOPG electrode in 0.1 M $HClO_4$ at different E_s, indicating that a reversible change of the assembly of the TTB-IDPL molecules by E_s. *Inset* shows the molecular structure of TTB-IDPL (*black* carbon atom, *grey* hydrogen atom). **a** $E_s = -1.3\,V$, **b** $E_s = 0.0\,V$ versus Au/AuO_x, respectively. **c** Line profiles of images (**a**) and (**b**)

In contrast to the case of EC-STM, EC-FM-AFM images of TTB-IDPL adsorbates are successfully obtained as 1∼2 nm high agglomerates on HOPG at −1.3 V, indicating the advantage of EC-FM-AFM for imaging fragile materials. The height of the molecular agglomerates increases with the increase of sample potential up to 0 V with concomitant decrease of the lateral size. When the sample potential is shifted to higher potential (0.5 V, close to the oxygen evolution potential) and then the original lower potential is applied (−1.3 V), the TTB-IDPL adsorbates are no longer observed, as shown in Fig. 21.8a. Surprisingly, TTB-IDPL film is again observed after changing the sample potential to 0 V, and these disappearance and appearance of the film at −1.3 and 0 V, respectively, are found to be reversible against potential cycling. This observation indicates that when the adsorbate-substrate and adsorbate-adsorbate interactions are small enough, the adsorbate film structure is drastically changed with the change of the interfacial energy between the electrolyte/electrode interface, which alters by electrochemical potential. Adsorption/desorption of anions on HOPG [28] is a possible factor to change the solution–electrode interfacial energy. This example demonstrated that EC-FM-AFM imaging with small applying force enables us to study the potential-dependent structural change of fragile adsorbate aggregates, which was not recognized by other electrochemical and in situ measurements.

21.2.3 Solvation Structures by Force Curves

Because the structural change of fragile adsorbate aggregates was found to be triggered by the interfacial energy between the electrolyte/electrode interface, we performed force curve measurements of the bare HOPG electrode in electrolyte solutions using EC-FM-AFM [29]. Figure 21.9a shows a typical approach force curve taken

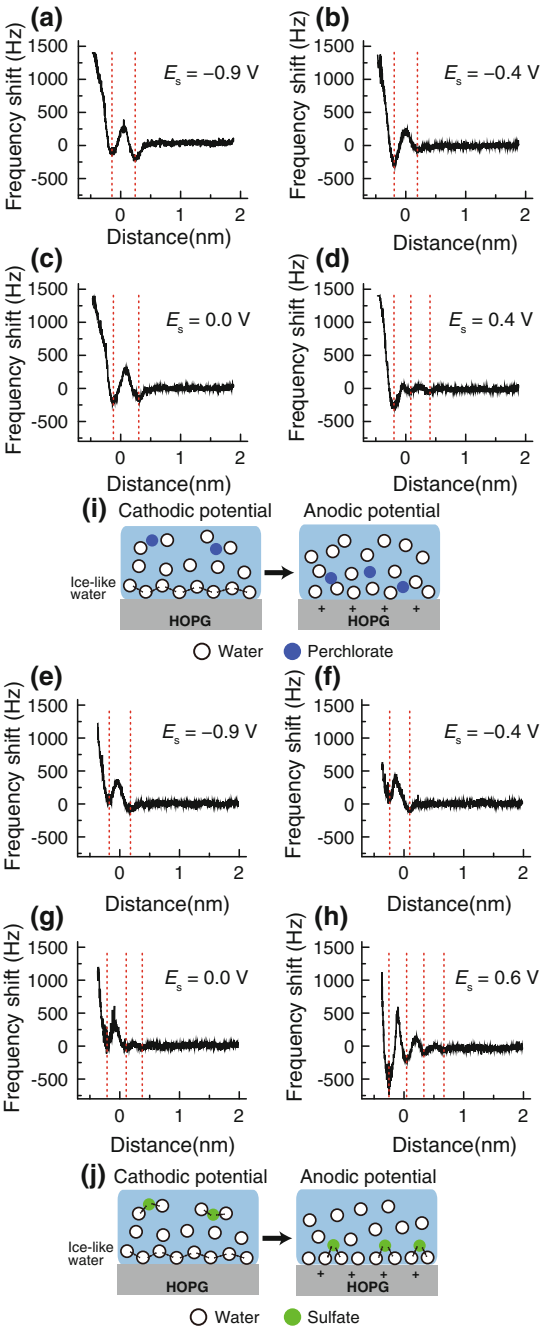

Fig. 21.9 **a–d** Frequency shift versus distance curves ($E_t = -0.90$ V, $A_{p-p} = 0.25$ nm) between a cantilever tip and an HOPG electrode taken at different E_s in 0.1 M $HClO_4$. **e–h** Frequency shift versus distance curves ($E_t = -0.90$ V, $A_{p-p} = 0.24$ nm) taken in 0.1 M H_2SO_4. *Red broken lines* indicate the valleys of force profiles. **i**, **j** Possible schematic presentations of potential-dependent structures of the interfaces in each aqueous solution

in 0.1 M $HClO_4$ aqueous solution at −0.9 V versus Au/AuO_x, which was positive against $E_{pzc} \sim -1.2$ V [30]. One can notice a decaying oscillatory profile indicative of structural hydration forces with two clearly visible valleys. While the obtained curve is qualitatively similar to that obtained close to an HOPG substrate in ultrapure water by Suzuki et al., the period of the oscillation was about 0.4 nm, slightly larger than the previous report (0.32 nm) [31]. Note that approach and retract force curves obtained by FM-AFM are similar with each other, in contrast to those taken by the contact-mode.

Application of positive potential up to 0 V only slightly changed the frequency shift versus distance curve, as shown in Fig. 21.9b, c. The drastic change was observed at 0.4 V, where the number of apparent valleys increased to three, and the period of oscillations reduced to about 0.3 nm.

We also performed corresponding measurements in 0.1 M H_2SO_4 aqueous solution to confirm the anion dependence on the force curve. At moderate potentials (−0.9 V ∼ −0.4 V), obtained force curves are qualitatively similar to those obtained in 0.1M $HClO_4$ aqueous solution at the same range of potential (Fig. 21.9e, f). The number of apparent valleys increased to three, and the period of oscillations reduced to about 0.3 nm at 0 V, as shown in Fig. 21.9g. Further potential increase to 0.6 V drastically altered the shape of the frequency shift versus distance curve, where the number of apparent valleys increased to four, and the amplitude of oscillatory frequency shift apparently enhanced (Fig. 21.9h). All the potential dependent changes of the force curves were reversible against potential cycling.

In order to quantify the frequency shift versus distance curves obtained above, the conversion of the measured frequency shift to force was performed by the well-established method of Sader and Jarvis [32]. The shape of resulting force versus distance curves was almost similar to the original data [29]. The recent theoretical consideration based on statistical mechanics indicated that the force versus distance curve $f(z)$ taken in water is represented by the simple function of the density profile of water molecules $\rho(z)$ by the following equation if the AFM tip is assumed to be a water molecule,

$$f(z) = k_B T \frac{d}{dz} \ln \rho(z) \tag{21.6}$$

where k_B is Boltzmann constant, T is temperature [33, 34]. Thus, the decaying oscillatory profile obtained by EC-FM-AFM is related to the modulation of local density of water at the electrified interfaces. Increase of the number of valleys and decrease of the period of oscillations at positive potential (far from pzc) indicate the compact hydration layers induced by the positive charge at the electrode surface.

The results that the water molecules respond to the surface charge as a function of applying potential are consistent with pictures of the electric double layer model. The classical model, however, is not able to explain the following two observations. First, we found that the shape of the force curves did not change distinctly at the moderate potential, but drastically changed at the higher potential. According to in situ IR measurements of an Au(111) electrode in aqueous solutions by Osawa and co-workers, peak intensity assigned to the interfacial water is known to increase

nonlinearly at far from pzc, which is correlated with adsorption of ions on Au(111) [6–8]. This observation is consistent with our EC-FM-AFM results on the HOPG electrode.

Second, the drastic change of the force curves at the highest potential differed depending on the anion species in electrolyte solutions; while ClO_4^- decreased the intensity of oscillatory profile, SO_4^{2-} (or HSO_4^-) increased the intensity. These observations indicate that when the anions are attracted to the positively charged electrode surface, interface water changes their density profile due to the presence of the anions. According to the previous studies of bulk aqueous solutions [35], the ClO_4^- anion is hydrophobic and is classified as a "structure breaker", which means that water molecules next to the anion are believed to be highly disordered and thus the hydrogen bonding network is highly broken down. On the other hand, the SO_4^{2-} (or HSO_4^-) anion is hydrophilic and is classified as a "structure maker", which means that water molecules next to the anion are believed to be ordered and thus the hydrogen bonding network is formed. These properties are consistent with our force curve results, if one assumes that the strength of the hydrogen bond network determines the density profile of interfacial water. Possible schematic potential-dependent interface structures in each electrolyte are shown in Fig. 21.9i, j.

The experimental analysis of the potential profile at the interface, which determines the reactivity of an electrochemical species, seems to be difficult, because the electric potential is determined by the distribution of both electrolyte ions and water molecules. Especially, the direct detection of electrolyte ions by AFM tip is unrealistic due to the very low concentration of the ions at usual electrolyte concentration; i.e. the number densities of water and electrolyte ion in 0.1 M solution are 33 and 0.06 nm^{-3}, respectively, and protons in bulk solutions diffuse more than 100 nm during one cantilever oscillation ($\sim 10^{-5}$ s). The anion dependence of force curves obtained above indicates that the molecular scale behavior of electrolyte ions can be indirectly investigated by EC-FM-AFM. We note that Kilpatrick et al. recently reported the ion species and concentration dependences of force curves at the electrolyte/mica interfaces [36].

21.3 Outlook

As described in previous sections, EC-FM-AFM measurements enable us to realize molecular scale pictures of electrolyte/electrode interface under electrochemical environment, which was not achieved by EC-STM nor contact-mode EC-AFM. However, there still remain many issues to be solved for understanding and designing the complicated electrochemical interfaces. Some of the challenging issues will be described below.

First, most of the classical electric double layer models assumed that physical quantities such as the density profile of solvent and electrolyte ions are homogeneous parallel to the electrode surface [1]. Recent force mapping studies using FM-AFM

in liquids, however, revealed that the obtained force curve clearly depends on the lateral position of the solid surface [37–39], indicating the importance of inhomogeneous treatment of electrified interface. Ichii et al. have shown the force mapping data of an Au(111) electrode in an ionic liquid taken by tuning fork-based EC-FM-AFM [40]. Figure 21.10a shows the two-dimensional force mapping data at −0.4 V versus Pt electrode, at which any electrochemical reactions were not detected by CV measurements. Clear multiple stripes along the x direction were observed with a period of 0.83 nm, corresponding to the ion-pair diameter of ionic liquid (0.89 nm). This observation indicates the presence of multiple solvation layers on the Au(111) electrode. When the electrode potential decreased to −1.2 V (onset of the reduction of trace water), the number of solvation layers decreased to only one layer (Fig. 21.10b). Furthermore, the solvation layers completely disappeared at −1.6 V (Fig. 21.10c), indicating that the reduction of water destructed the solvation layers of the ionic liquid. Interestingly, all the force mapping data are inhomogeneous along x-direction. The relationship between the inhomogeneity and the electrode structure (or others) seems to be quite important for understanding the local environment at the interface. For the details of force mapping studies, authors refer the reader to Chaps. 19, 20 in this book.

We note that ionic liquids are useful alternative electrolyte solutions for the molecular scale investigation of electrified interface because they are composed of only cation and anion. Ionic liquid/solid interfaces with and without potential control have been studied by various groups for two decades, but there remain many open-questions [41]. After the pioneering work of Atkin et al. [42, 43], AFM studies of ionic liquid/solid interfaces have been reported so far, including various dynamic mode studies; FM-AFM [40, 44–47], phase modulation AFM [48], and amplitude modulation AFM [49, 50]. These studies might extend our knowledge of electrified interfaces.

Second, force curve and force mapping measurements reveal only the information concerning local density profile of electrolyte solutions. In other words, individual atomic positions cannot be realized by usual AFM-based techniques. Because electric potential profile determined by the atomic positions is the most important information for understanding electrochemical reactions at the electrified interfaces, experimental data need to be compared to the theoretically obtained density profile to reconstruct the electric potential profile. In addition, one should be careful for the presence of AFM tip during experiment, because the tip may interact with electrolyte solutions as strong as sample electrode and alter the density profile on it. Several groups have already reported the comparison between the force curve data taken in aqueous solution and the density profile obtained by classical molecular dynamics (MD) or three dimensional reference interaction site model (3D-RISM) simulation [38, 39, 51]. Some of the simulation studies explicitly include the effect of an AFM tip [52–55]. Such complementary study should be useful for the electrochemical interfaces as well.

Finally, we note the importance of simultaneous measurements of EC-STM and EC-FM-AFM. Almost all the applications of electrochemistry except for capacitor-related ones, involve the electrochemical reactions at the electrified interfaces. This

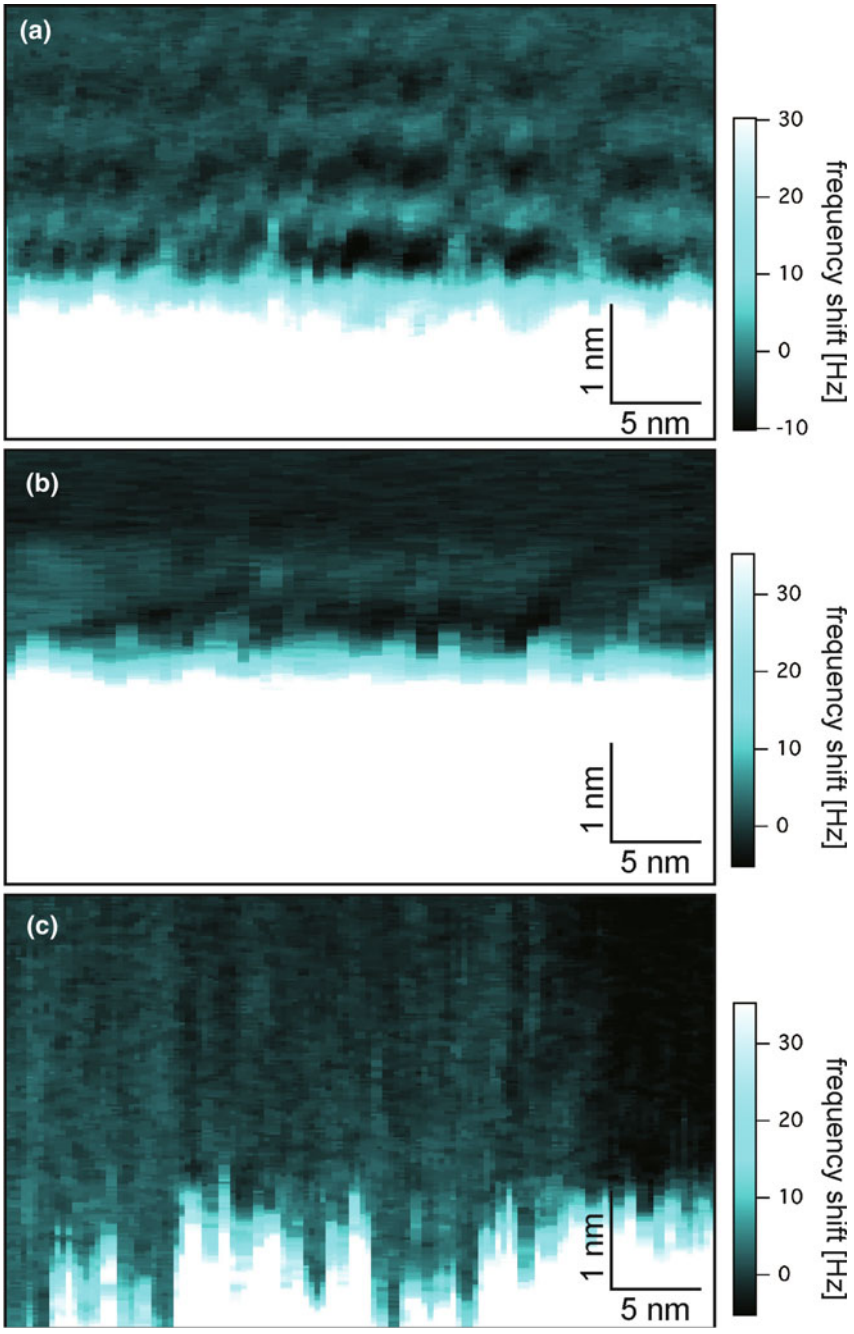

Fig. 21.10 Two-dimensional Δf maps ($A_{\mathrm{p-p}} = 0.125\,\mathrm{nm}$) obtained on an ionic liquid/Au(111) interface at different E_s. **a** $E_s = -0.4\,\mathrm{V}$, **b** $E_s = -1.2\,\mathrm{V}$, and **c** $E_s = -1.6\,\mathrm{V}$ versus Pt electrode. The lateral and vertical directions correspond to the x and z directions, respectively. (Reused with permission from Negami et al. [40] Copyright 2012, The Electrochemical Society)

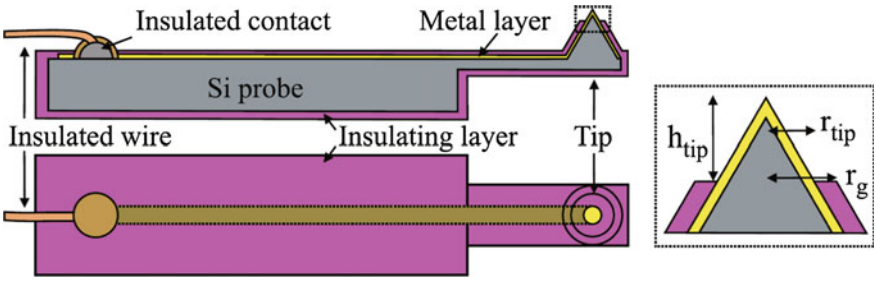

Fig. 21.11 Schematics of a wired and insulated conductive probe used for EC-AFM and EC-STM combined experiment. The *zoomed frame* illustrates the geometric parameters of the tip used to model its electrochemical properties. (Reused with permission from Wandlowski et al. [58] Copyright 2013, IOP Publishing)

means that the knowledge of the electric double layer itself is not enough to providing useful information to electrochemist. One of the most important concerns of electrochemistry is the kinetics of the electron transfer at the interfaces. Thus the molecular scale understanding of kinetic parameters such as reorganization energy, by which the activation energy for the electron transfer reactions can be estimated, is prerequisite for the sophisticated electrochemical devices. In the research field of surface electrochemistry using EC-STM, the estimation method of the reorganization energy of the individual electroactive molecule has already been established [56, 57]. Hence, simultaneous measurements of EC-STM and EC-FM-AFM can provide the kinetic parameters with the microscopic structural information of electric double layer. Several groups have reported the fabrication of special conducting AFM tip covered by insulating materials except at the very end for current measurements, as shown in Fig. 21.11 [58]. Thus, simultaneous measurements of EC-STM and EC-FM-AFM are ready to be performed for electrochemical issues.

Acknowledgments The authors are most grateful to Ken-ichi Umeda and Toru Utsunomiya for their contributions to develop the basis for this research field. We also acknowledge Yasukazu Hirao, Takashi Kubo, and Toshiaki Enoki for fruitful discussion. This work was partially supported by Grant-in-Aid for Scientific Research No. 24-2584 and No. 20001006 from the Ministry of Education, Culture, Sports, Science, and Technology, Japan, and by Funding Program for Next Generation World-Leading Researchers (GR071) from Japan Society for the Promotion of Science (JSPS).

References

1. A.J. Bard, L.R. Faulkner, *Electrochemical Methods: Fundamentals and Applications*, 2nd edn. (Wiley, New York, 2001)
2. R.A. Marcus, N. Sutin, Biochim. Biophys. Acta **811**, 265 (1985)
3. J. Wang, A.J. Davenport, H.S. Isaacs, B.M. Ocko, Science **255**, 1416 (1992)

4. M.F. Toney, J.N. Howard, J. Richer, G.L. Borges, J.G. Gordon, O.R. Melroy, D.G. Wiesler, D. Yee, L.B. Sorensen, Nature **368**, 444 (1994)
5. T. Kondo, J. Morita, K. Hanaoka, S. Takakusagi, K. Tamura, M. Takahashi, J. Mizuki, K. Uosaki, J. Phys. Chem. C **111**, 13197 (2007)
6. K. Ataka, T. Yotsuyanagi, M. Osawa, J. Phys. Chem. **100**, 10664 (1996)
7. K. Ataka, M. Osawa, Langmuir **14**, 951 (1998)
8. M. Osawa, M. Tsushima, H. Mogami, G. Samjeské, A. Yamakata, J. Phys. Chem. C **112**, 4248 (2008)
9. R. Sonnenfeld, P.K. Hansma, Science **232**, 211 (1986)
10. K. Itaya, Prog. Surf. Sci. **58**, 121 (1998)
11. U. Zhumaev, A.V. Rudnev, J.F. Li, A. Kuzume, T.H. Vu, T. Wandlowski, Electrochim. Acta **112**, 853 (2013)
12. Y. Yokota, K. Fukui, T. Enoki, M. Hara, J. Phys. Chem. C **111**, 7561 (2007)
13. A.A. Gewirth, B.K. Niece, Chem. Rev. **97**, 1129 (1997)
14. J.M. Serafin, A.A. Gewirth, J. Phys. Chem. B **101**, 10833 (1997)
15. Y. Yokota, T. Yamada, M. Kawai, J. Phys. Chem. C **115**, 6775 (2011)
16. T. Fukuma, K. Kobayashi, K. Matsushige, H. Yamada, Appl. Phys. Lett. **87**, 034101 (2005)
17. K. Umeda, K. Fukui, Langmuir **26**, 9104 (2010)
18. T. Fukuma, M. Kimura, K. Kobayashi, K. Matsushige, H. Yamada, Rev. Sci. Instrum. **76**, 053704 (2005)
19. H.O. Finklea, in *Electroanalytical Chemistry*, vol. 19, ed. by A.J. Bard, I. Rubinstein (Marcel Dekker, New York, 1996), pp. 109–335
20. K. Uosaki, Electrochemistry **67**, 1105 (1999)
21. T. Ohtsuka, Y. Sato, K. Uosaki, Langmuir **10**, 3658 (1994)
22. G. Valincius, G. Niaura, B. Kazakevičienė, Z. Talaikytė, M. Kažemėkaitė, E. Butkus, V. Razumas. Langmuir **20**, 6631 (2004)
23. X. Yao, J. Wang, F. Zhou, J. Wang, N.J. Tao, J. Phys. Chem. B **108**, 7206 (2004)
24. K. Uosaki, Y. Sato, H. Kita, Langmuir **7**, 1510 (1991)
25. T. Utsunomiya, Y. Yokota, T. Enoki, Y. Hirao, T. Kubo, K. Fukui, Carbon **77**, 184 (2014)
26. K. Nakasuji, T. Kubo, Bull. Chem. Soc. Jpn. **77**, 1791 (2004)
27. T. Utsunomiya, Y. Yokota, T. Enoki, Y. Hirao, T. Kubo, K. Fukui, Carbon **63**, 196 (2013)
28. B. Schnyder, D. Alliata, R. Kötz, H. Siegenthaler, Appl. Surf. Sci. **173**, 221 (2001)
29. T. Utsunomiya, Y. Yokota, T. Enoki, K. Fukui, Chem. Commun. **50**, 15537 (2014). doi:10.1039/C4CC07093C
30. K.K. Cline, M.T. McDermott, R.L. McCreery, J. Phys. Chem. **98**, 5314 (1994)
31. K. Suzuki, N. Oyabu, K. Kobayashi, K. Matsushige, H. Yamada, Appl. Phys. Express **4**, 125102 (2011)
32. J.E. Sader, S.P. Jarvis, Appl. Phys. Lett. **84**, 1801 (2004)
33. M. Watkins, B. Reischl, J. Chem. Phys. **138**, 154703 (2013)
34. K. Amano, K. Suzuki, T. Fukuma, O. Takahashi, H. Onishi, J. Chem. Phys. **139**, 224710 (2013)
35. Y. Marcus, *Ion Solvation* (Wiley, New York, 1985)
36. J.I. Kilpatrick, S.H. Loh, S.P. Jarvis, J. Am. Chem. Soc. **135**, 2628 (2013)
37. T. Fukuma, Y. Ueda, S. Yoshioka, H. Asakawa, Phys. Rev. Lett. **104**, 016101 (2010)
38. K. Kimura, S. Ido, N. Oyabu, K. Kobayashi, Y. Hirata, T. Imai, H. Yamada, J. Chem. Phys. **132**, 194705 (2010)
39. K. Kobayashi, N. Oyabu, K. Kimura, S. Ido, K. Suzuki, T. Imai, K. Tagami, M. Tsukada, H. Yamada, J. Chem. Phys. **138**, 184704 (2013)
40. M. Negami, T. Ichii, K. Murase, H. Sugimura, ECS Trans. **50**, 349 (2012)
41. A.A. Kornyshev, J. Phys. Chem. B **111**, 5545 (2007)
42. R. Atkin, G.G. Warr, J. Phys. Chem. C **111**, 5162 (2007)
43. J.J. Segura, A. Elbourne, E.J. Wanless, G.G. Warr, K. Voïtchovsky, R. Atkin, Phys. Chem. Chem. Phys. **15**, 3320 (2013)
44. T. Ichii, M. Fujimura, M. Negami, K. Murase, H. Sugimura, Jpn. J. Appl. Phys. **51**, 08KB08 (2012)

45. Y. Yokota, T. Harada, K. Fukui, Chem. Commun. **46**, 8627 (2010)
46. Y. Yokota, H. Hara, T. Harada, A. Imanishi, T. Uemura, J. Takeya, K. Fukui, Chem. Commun. **49**, 10596 (2013)
47. Y. Yokota, H. Hara, Y. Morino, K. Bando, A. Imanishi, T. Uemura, J. Takeya, K. Fukui, Appl. Phys. Lett. **104**, 263102 (2014)
48. T. Ichii, M. Negami, M. Fujimura, K. Murase, H. Sugimura, Electrochemistry **82**, 380 (2014)
49. A. Labuda, P. Grütter, Langmuir **28**, 5319 (2012)
50. A. Labuda, K. Kobayashi, Y. Miyahara, P. Grütter, Rev. Sci. Instrum. **83**, 053703 (2012)
51. P. Spijker, T. Hiasa, T. Musso, R. Nishioka, H. Onishi, A.S. Foster, J. Phys. Chem. C **118**, 2058 (2014)
52. M. Tsukada, N. Watanabe, M. Harada, K. Tagami, J. Vac. Sci. Technol. B **28**, C4C1 (2010)
53. M. Watkins, A.L. Shluger, Phys. Rev. Lett. **105**, 196101 (2010)
54. M. Watkins, M.L. Berkowitz, A.L. Shluger, Phys. Chem. Chem. Phys. **13**, 12584 (2011)
55. B. Reischl, M. Watkins, A.S. Foster, J. Chem. Theory Comput. **9**, 600 (2013)
56. J. Zhang, A.M. Kuznetsov, I.G. Medvedev, Q. Chi, T. Albrecht, P.S. Jensen, J. Ulstrup, Chem. Rev. **108**, 2737 (2008)
57. A.V. Rudnev, I.V. Pobelov, T. Wandlowski, J. Electroanal. Chem. **660**, 302 (2011)
58. I.V. Pobelov, M. Mohos, K. Yoshida, V. Kolivoska, A. Avdic, A. Lugstein, E. Bertagnolli, K. Leonhardt, G. Denuault, B. Gollas, T. Wandlowski, Nanotechnology **24**, 115501 (2013)

Chapter 22
High-Speed Atomic Force Microscopy

Takayuki Uchihashi, Noriyuki Kodera and Toshio Ando

Abstract High-speed atomic force microscopy (HS-AFM) has now been established that can capture protein molecules in action at submolecular spatial and sub-100 ms temporal resolution, without disturbing their biological function. In fact, various application studies on proteins have demonstrated this capability and brought important discoveries that cannot be achieved by other approaches. Moreover, recent progress of HS-AFM techniques has been extending its use to the observation of dynamic events occurring in larger samples including live cells and isolated intracellular organelles. This review mostly focuses on various techniques that have led to the achievement of these capabilities of HS-AFM, together with brief descriptions of typical application studies of proteins.

22.1 Introduction

AFM is a leading-edge driving force for the creation of new techniques, new research areas and new nanotech industries. Since the birth of AFM, its technology has been continuously advanced and extended in various directions. For example, efforts have been carried out to pursue the ultimate high spatial resolution and force sensitivity

T. Uchihashi · T. Ando (✉)
Department of Physics, Institute of Science and Engineering, Kanazawa University, Kakuma-machi, Kanazawa 920-1192, Japan
e-mail: tando@staff.kanazawa-u.ac.jp

T. Uchihashi · N. Kodera · T. Ando
Bio-AFM Frontier Research Center, Institute of Science and Engineering, Kanazawa University, Kakuma-machi, Kanazawa 920-1192, Japan
e-mail: uchihast@staff.kanazawa-u.ac.jp

T. Uchihashi · T. Ando
CREST, Japan Science and Technology Agency, 4-1-8 Honcho, Kawaguchi 332-0012, Japan

N. Kodera
PRESTO, Japan Science and Technology Agency, 4-1-8 Honcho, Kawaguchi 332-0012, Japan
e-mail: nkodera@staff.kanazawa-u.ac.jp

© Springer International Publishing Switzerland 2015

S. Morita et al. (eds.), *Noncontact Atomic Force Microscopy*,
NanoScience and Technology, DOI 10.1007/978-3-319-15588-3_22

of AFM. Consequently, it has now become possible to visualize even sub-atomic structures [1], distinguish the species of atoms on a solid surface [2] and resolve single electron spins [3]. These ultimate capabilities are based on the high quality mechanical resonance of cantilevers or quartz tuning forks [4] in vacuum. In non-vacuum usage of AFM, efforts have been directed to the acquisition of local material property maps of objects, in addition to their surface topography. The local material properties that have been acquired are elastic and adhesive properties [5, 6], magnetic and electric properties [7, 8], heat conductivity [9] and others. Similarly, various AFM systems have been developed that are combined with fluorescence microscopy, Raman spectroscopy, infrared spectroscopy, acoustic techniques [10, 11] and microwave techniques [12]. Some of the developed instruments are now of practical use for the inspection of industrial products. Moreover, AFM has been adapted to develop techniques for surface nano-processing, such as nano-printing [13] and nano-lithography [14]. Thus, beyond the initial aim and perspective, the AFM technology has been quickly extended into various directions and used in diverse areas.

In stark contrast to the remarkable rapid advances mentioned above, the slow scan and hence the low imaging rate of AFM has remained unimproved until very recently. Even now in 2014 when we are writing this chapter, more than 99 % of all AFM instruments that are in use worldwide remain slow. Maybe, this delay of progress would arise from the fact that the use of AFM has mainly been focused on the acquisition of high-resolution images of objects and force spectroscopy data. As a matter of course, high imaging rates cannot be anticipated in-vacuum NC-AFM because the high quality mechanical resonance of the probes is incompatible with fast response to an exerted force, and because there may not be many interesting dynamic phenomena to visualize in vacuum, at the nanometer scale. However, in gas and liquid environments, there are many interesting dynamic phenomena to study at the nanometer scale. In particular, most of biomolecular phenomena occur dynamically in aqueous solutions. Therefore, it may be understandable that one of the biophysicists writing this chapter (TA) embarked on the development of high-speed AFM (HS-AFM) in 1993. His group continued to work towards its materialization [15, 16] and finally demonstrated the innovative power of HS-AFM by capturing dynamics images of protein molecules in action: for example, bacteriorhodopsin in response to light [17], myosin V walking on actin filaments [18], rotor-less F_1-ATPase undergoing rotary propagation of conformational changes [19] and celluloses moving on cellulose fibers while hydrolyzing the fibers [20]. However, note that the initial attempt to increase the imaging rate of AFM was made by Quate and colleagues in 1991 to acquire wide-area images of semiconductor wafers [21] and produce nano-patterns on wide-area surfaces in a relatively short time [22] (a historical view of HS-AFM development is described elsewhere [23]). In addition to biomolecular phenomena for which the merit of HS-AFM has plainly been put forth, there are an array of dynamic phenomena occurring in liquids which are worth to be visualized at high rates: for example, corrosion reactions of metallic materials, electrochemical reactions represented by those in batteries, catalytic reactions, cleaning by detergents and dissolution of photoresists. Except for the dissolution of photoresist [24], these

dynamic phenomena have never been visualized at the nanometer scale and enough time resolution. As aimed by the Quate group, the high-speed performance is also important even in the acquisition of still images of topography and material property maps of surfaces because it permits in-depth and wide-area analysis of the surfaces within realistic time periods. These significant merits to be brought by high-speed imaging have recently been recognized in the AFM community. As a result, a number of researchers in various areas, including mechanical engineering and control engineering, have now been participating in developing techniques that may serve to improve the imaging rate of AFM. However, most of these studies focus on only one of various techniques involved in AFM. Therefore, it is often difficult to judge the actual usefulness of developed techniques.

Thus far, HS-AFM has been established only in in-liquid AFM and used most exclusively for biological studies. However, there must be a definite demand for increasing the speed performance of any type of AFM instruments and more generally any type of scanning probe microscopy (SPM) instruments. This chapter is dedicated mostly to describing HS-AFM techniques not only of the authors' group but also of others, which, we hope, will be good references for future developers of HS-SPM instruments. Before technical details, theoretical considerations are given to provide a quantitative relationship that determines the maximum possible imaging rate as a function of various parameters. After technical descriptions, representative HS-AFM imaging studies are presented. Finally, this chapter is closed with future prospects of HS-AFM.

22.2 Theoretical Considerations

The highest possible imaging rate of AFM, $R_{\max}$ frames/s (fps), is a function of various parameters and depends on the imaging mode. Here we quantitatively describe $R_{\max}$ in tapping mode AFM that employs a raster scan of the sample stage in the horizontal plane. For simplicity, the sample surface is assumed to have a sinusoidal shape with a periodicity λ and the maximum height h_0 in the XZ plane; height h varies as $h(x) = (h_0/2) \times [\sin(2\pi x/\lambda) + 1]$. When the sample stage is moved in the X-direction at velocity V_s and no feedback scan of the Z-scanner is performed, the sample height under the cantilever tip changes with time as $h(t) = (h_0/2) \times [\sin(2\pi ft) + 1]$, as shown with the solid line in Fig. 22.1a (here, the frequency f is given by $f = V_s/\lambda$). By feedback operation, the Z-scanner is moved at feedback frequency f in the direction opposite to the sample height. Because of the time delay τ_0 in the closed-loop feedback control, the Z-scanner is moved so that the sample-stage height $Z(t)$ changes as $Z(t) = -(h_0/2) \times [\sin(2\pi ft - \theta_0) + 1]$, where $\theta_0 = 2\pi f\tau_0$ is a phase delay in the sample surface tracing by feedback scan (the broken line in Fig. 22.1a). Therefore, the sample surface height $H(t)$, when viewed from the cantilever, cannot look perfectly flat but changes as

$$H(t) = h(t) + Z(t) = h_0 \sin(\theta_0/2) \times \cos(2\pi ft - \theta_0/2), \tag{22.1}$$

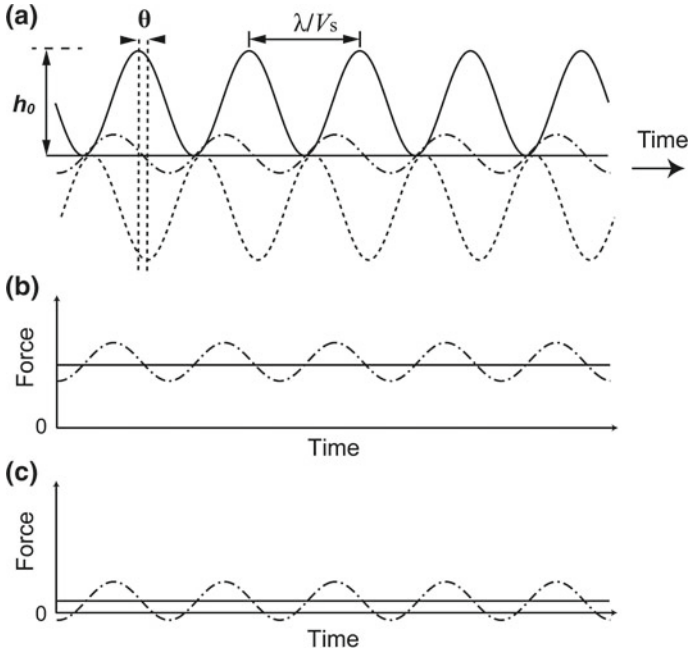

Fig. 22.1 Effect of feedback delay on the tip force exerted onto the sample. **a** Movement of Z-scanner (*broken line*) tracing the sinusoidally shaped sample surface (*solid line*; spatial periodicity, λ; temporal periodicity, λ/V_s; amplitude, $h_0/2$) that is being scanned in the X-direction at velocity V_s. Because of the delay of the Z-scanner movement, tracing error (*dashed line*) is produced. **b** Tip force (*dashed line*) exerted onto the sample when the set point force (*solid line*) corresponding to the set point amplitude is relatively large. **c** Tip force (*dashed*) exerted onto the sample when the set point force (*solid*) is set at a small value. The negative force cannot be exerted but becomes zero due to complete loss of tip-sample interaction when attractive tip-sample interaction is negligible

as shown with the dashed line in Fig. 22.1a. $H(t)$ represents the feedback error. Because of this error, the tapping force exerting from the oscillating cantilever tip to the sample cannot be maintained constant at the set point force (solid line in Fig. 22.1b) but varies; larger forces are exerted in the uphill regions of the sample, whereas weaker forces are exerted in the downhill regions, as shown with the dashed line in Fig. 22.1b. When the excessive force exerting on the sample is too excessive, we have to decrease the set point force (solid lines in Fig. 22.1c). This can be done by setting the cantilever set point amplitude A_s closer to the free oscillation amplitude A_0 (in other words, the dimensionless set point r defined as $r \equiv A_s/A_0$ is set closer to 1). However, this new setting results in a situation where the tip force to act on the sample in steep downhill regions becomes negative or zero (dashed line in Fig. 22.1c). Even under this situation, the tip can be kept in contact with the sample, if a sufficient attractive interaction (i.e., negative force) occurs between the tip and the sample. However, in the case of biological samples in physiological buffer solutions, the attractive tip-sample interaction is negligibly small and therefore the tip easily

loses contact. Once the contact is lost, it takes time for the tip to land on the sample surface again (like parachuting), because the error signal is saturated at a small value, $A_0(1-r)$, irrespective of how far the tip is apart from the sample surface at its bottom swing. Thus, it is now clear that the sample fragility significantly limits the largest allowable phase delay $\theta_{\max}$ and hence the maximum possible scan speed $V_s^{\max}$. In other words, low-invasive imaging is hard to be made compatible with high-speed imaging.

In general, the bandwidth f_B of closed feedback systems is defined by the feedback frequency at which $\pi/4$ radian (or 45°) phase delay occurs in the feedback control, i.e., $f_B = 1/(8\tau_0)$. Therefore, the $V_s^{\max}$ can be given by $V_s^{\max} = \lambda f_B \times \theta_{\max}/(\pi/4)$. Under the imaging conditions of the scan range in the X-direction W and the number of scan lines N, an image acquisition time T is given by $T = 2WN/V_s$. Thus, the maximum possible imaging rate $R_{\max}$ is given by

$$R_{\max} = 2\lambda f_B \theta_{\max}/(\pi WN). \tag{22.2}$$

Next, we quantitatively estimate how significantly $\theta_{\max}$ is limited by the tip-parachuting effect, assuming that attractive tip-sample interactions are negligibly small. The condition under which no complete loss of tip-sample contact occurs is given by $H(t) + A_0(1-r) > 0$ at any time, which results in

$$A_0(1-r) - h_0 \sin(\theta_0/2) > 0. \tag{22.3}$$

Under the conditions of $A_0 = h_0/5$ and $r = 0.9$ that are often employed for low-invasive imaging of protein molecules in solutions [25], equation (22.3) gives $\theta_0 < 0.013 \times \pi$ radian (i.e., $\theta_{\max} = 0.013 \times \pi$). This small value of $\theta_{\max}$ limits the highest possible feedback frequency to $\sim f_B/20$. As such, $R_{\max}$ is significantly restrained by the tip-parachuting problem. Thus, it is evident that HS-AFM applicable to fragile biological samples would not be materialized without finding a new feedback control technique that can eliminate the parachuting problem. As will be described later, such a technique has already been devised [26].

To increase the feedback bandwidth f_B, the time delay τ_0 of the closed-loop feedback control system has to be significantly reduced. To do so, the time delay of every device contained in the feedback loop has to be dramatically reduced. In the following sections, details of technical developments for this accomplishment are described.

22.3 Cantilever and Tip

The cantilever is a component most critical in accomplishing a high-speed imaging capability of AFM. Its mechanical properties significantly affect the bandwidth of feedback control. First of all, in the tapping mode, the probe tip should tap the sample surface at least once for each pixel of the image. Therefore, the cantilever's

first resonant frequency f_c should be high. The transient response of cantilever's oscillation amplitude to tip-sample contact should also be fast. The response rate is given by $\pi f_c/Q_c$, where Q_c is a quality factor. It may not be difficult to increase f_c by making the cantilever stiffer. However, a stiff cantilever exerts a large tapping force onto the sample and hence easily damages fragile samples. The first resonant frequency f_c and the spring constant k_c of a rectangular cantilever with thickness d, width w and length L are expressed as follows:

$$f_c = 0.56\frac{d}{L^2}\sqrt{\frac{E}{12\rho}} \tag{22.4}$$

and

$$k_c = \frac{wd^3}{4L^3}E, \tag{22.5}$$

where E and ρ are the Young's modulus and density of the material used, respectively. As is clear from these equations, the two demands, high f_c and small k_c, inherently conflicts and can only be achieved by miniaturization of the cantilever.

Small cantilevers have advantages in achieving not only high-speed imaging but also high sensitivity of force detection. The force detection sensitivity of AFM is generally limited by the extent of cantilever's thermal motion that is governed by the spring constant and the temperature; its average amplitude is given by $\sqrt{k_B T/k_c}$, where k_B is Boltzmann's constant and T is the temperature in Kelvin of measurement. The cantilever's thermal fluctuations in deflection are distributed over a frequency range from zero to slightly higher than f_c. Therefore, the thermal noise spectrum density becomes smaller for a cantilever with a higher f_c. In tapping-mode AFM, the frequency region used for imaging is approximately the imaging (or feedback) bandwidth centered at f_c. Thus, under a given k_c, the measurement of cantilever oscillation amplitude is less affected by thermal noise when cantilevers with higher f_c are used. Moreover, shorter cantilevers provide higher sensitivity in the optical beam deflection (OBD) detection of cantilever deflection, because the OBD method detects an angle change of a cantilever which follows $\Delta\varphi = 3\Delta z/(2L)$, where Δz and $\Delta\varphi$ are the displacement and angle change of the free end of the cantilever, respectively [27].

In the fabrication of small cantilevers with small k_c, silicon nitride (Si_3N_4) is usually used as a material. Its Young's modulus and density are $E = 2.9 \times 10^{11}$ N/m^2 and $\rho = 3200$ kg/m^3, respectively. For instance, when $f_c = 3$ MHz and $k_c = 0.2$ N/m are demanded for cantilevers, their feasible dimensions are $L \sim 7\,\mu$m, $d \sim 0.1\,\mu$m and $w \sim 1\,\mu$m, approximately one-tenth of those of conventional cantilevers. Several groups have attempted to fabricate small cantilevers [28–33]. Cantilevers satisfying both high f_c and small k_c have been successfully developed by Olympus, using low-pressure chemical vapor deposition (LP-CVD) that can precisely control the thickness of a Si_3N_4 film [31]. The custom-made small cantilevers that we are currently using have dimensions of $L = 6$–$7\,\mu$m, $w = 2\,\mu$m and $d = 90$ nm,

which provide $f_c = \sim 3.5$ MHz in air, $f_c = \sim 1.2$ MHz in water, $k_c = \sim 0.2$ N/m and $Q_c = \sim 2.5$ in water (Fig. 22.2). Their back side is coated with a gold film with a thickness of ~20 nm to gain enough reflectivity of light for the OBD detection of cantilever deflection. Unfortunately, the state-of-the-art cantilevers are not yet placed on the market. Somewhat larger cantilevers, BL-AC10DS-A2 (Olympus: f_c in air 1.5 MHz, f_c in water 600 kHz, and $k_c \sim 0.1$ N/m) or USC-F1.2-k0.15 (NanoWorld: f_c in air 1.2 MHz, f_c in water ~500 kHz, and $k_c \sim 0.15$ N/m), are available in the market. It may be possible to fabricate smaller cantilevers with higher f_c, without increasing k_c larger than 0.1 N/m. However, a smaller cantilever with $w < 1\mu$m could not be of practical use because of difficulty of focusing a laser beam onto such a small cantilever.

As mentioned above, the small cantilevers developed by Olympus are fabricated by thin film deposition of Si_3N_4, not by anisotropic etching of a single silicon crystal. Because of this fabrication method, the cantilevers do not have a sharp tip but a beak-like structure with an apex size of $>20 \times 20\,\text{nm}^2$ as shown in Fig. 22.3 (the size varies chip to tip), which is not sharp enough to obtain high-spatial resolution images. To

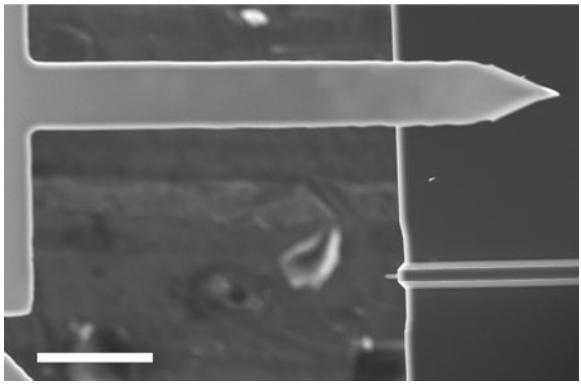

Fig. 22.2 SEM micrograph of a conventional AFM cantilever (*upper*) and a small cantilever (*lower*). Scale bar, 50 μm

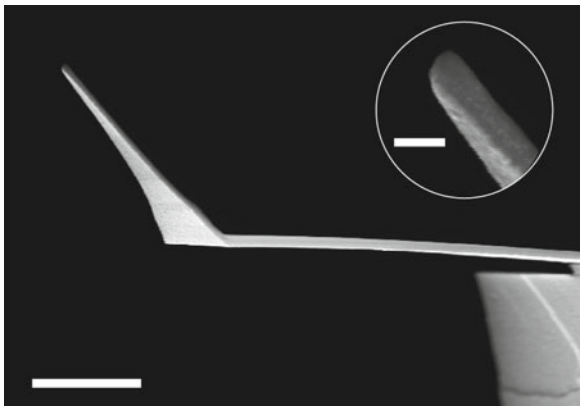

Fig. 22.3 SEM micrograph of a beak-like structure at the free end of an Olympus small cantilever (Scale bar, 1 μm). An *inset* is a magnified view of the end of the beak-like tip (Scale bar, 100 nm)

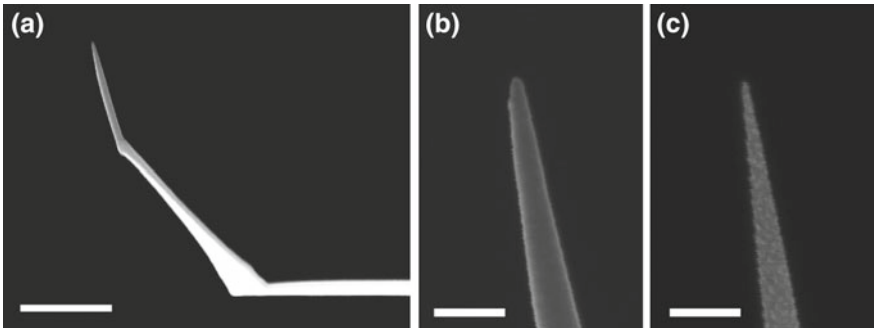

Fig. 22.4 SEM micrographs of EBD tips. **a** Entire view of the EBD tip on the original beak-like tip (Scale bar, 1 μm). The EBD tip ends **b** before and **c** after plasma etching. Scale bars, 100 nm

improve the sharpness, Olympus has grown a sharp carbon nanofiber tip on the beak-like tip. This type of small cantilevers, BL-AC10FS-A2, with mechanical properties similar to those of BL-AC10DS-A2, are also available in the market but expensive. Instead, we grow a sharp tip on the original beak-like tip by irradiating a focused electron beam in the organic gas atmosphere, which is termed the electron-beam deposition (EBD) [34–37]. Sublimable phenol powder is used as an organic gas source in the following way. The powder is placed in a small container with small holes (∼0.1 mm in diameter) in the lid. The cantilevers are attached onto the container lid using a conductive adhesive tape. Then, the container is placed in a scanning electron microscope (SEM) chamber. In the spot mode operation of the SEM, the electron beam of 20 kV is irradiated through an aperture of 20 μm onto the pointed end of the beak-like tip. Under these conditions, a needle composed of amorphous carbon grows at a rate of ∼20 nm/s. The electron beam is usually irradiated for 1 min, resulting in ∼1 μm long EBD tip deposition as shown in Fig. 22.4a. A typical radius of the EBD-tip end is ∼25 nm (Fig. 22.4b). To sharpen it, the cantilever is subjected to plasma etching in argon gas for 3–5 min. This process results in tip-end radius of ∼4 nm (Fig. 22.4c). The mechanical durability of this sharp tip is high enough to capture many images. The EBD tip can be completely removed by plasma etching in oxygen over several hours. Therefore, we can reuse the small cantilever as long as it has no damage and keeps enough light reflexibility.

22.4 OBD System for Small Cantilevers

The OBD method to detect cantilever deflection is simple and easy to use but several cares are required for adapting it to small cantilevers, achieving high sensitive and high bandwidth detection, and minimizing the effect of laser light on biological samples.

Schäffer et al. first reported an OBD system for small cantilevers [38]. A single high numerical aperture (NA) lens was used to have a small focused spot size (7 μm in diameter). The same lens was used to collect and collimate the laser beam reflected back from the cantilever. The collimated reflected laser beam was guided to the photodiode position sensor. However, the short working distance of the single high NA lens restricts the design of the AFM head. Instead of using a single lens, we have been using an objective lens with NA = 0.45 and a long working distance of 8 mm (CFI Plan Fluor ELWD 20×C, Nikon) [15] (Fig. 22.5). The resulting spot size of focused 670 nm laser beam is ~3 μm in diameter. Because of this strong focusing, the laser power is attenuated to ~0.5 mW in order to avoid heating the sample. The absence of sample heating was proven by the HS-AFM observation of myosin V molecules moving on actin filaments, where the moving velocity was shown to be identical to those observed by fluorescence microscopy under the same buffer solution and temperature (room temperature) conditions [18]. The same objective lens is also used for the inverted optical microscope integrated with the HS-AFM system to

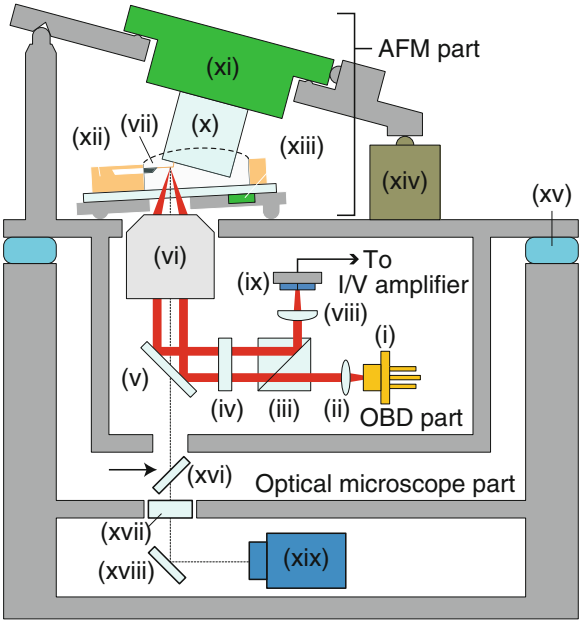

Fig. 22.5 Schematic illustration showing the HS-AFM head integrated with an inverted type of optical microscope. The OBD system comprises *(i)* laser diode, *(ii)* collimator lens, *(iii)* polarization beam splitter, *(iv)* λ/4 plate, *(v)* dichroic mirror, *(vi)* infinity-corrected objective lens, *(viii)* beam shaping lens, and *(ix)* split photodiode. The other devices are *(vii)* cantilever, *(x)* sample stage, *(xi)* high-speed scanner, *(xii)* cantilever holder with liquid cell (*thick dashed line* represents a liquid meniscus), *(xiii)* piezoactuator for cantilever excitation, *(xiv)* stepping motor, *(xv)* soft elastic gels, *(xvi)* dichroic mirror for additional illuminations, *(xvii)* infinity-corrected tube lens, *(xviii)* mirror, *(xix)* digital camera. *Thin dotted line* represents the optical path for the observation of the cantilever and the focused laser spot (See Fig. 22.6)

view the cantilever and the sample stage (more details are given below). To avoid the return of the scattered or reflected laser light into the laser diode, these OBD systems separate the incident and reflected laser beams using a quarter-wavelength plate and a polarization beam splitter (Fig. 22.5).

However, the polarization beam separation method is not perfect. Some of the reflected or scattered laser beam is sometimes incident to the laser diode. When it is incident to the optical resonator of the laser diode, the laser emission becomes unstable and hence noisy due to an "optical feedback" effect [39]. Moreover, some of the scattered light or the laser beam reflected from other objects than the cantilever is sometimes incident to the photodiode position sensor, which optically interferes with the laser beam reflected back from the cantilever and hence produces interference noise. To minimize the return of the reflected laser beam from other objects to the laser diode, one can introduce the incident beam to the objective lens at a slightly off-centered position so that the incident and reflected laser beams pass through different optical paths. Moreover, one can modulate the laser power with an RF signal of 300–500 MHz [39]. By this modulation, the laser oscillation mode is changed from single-mode to multimode. Compared to the single mode, the multimode is much less sensitive to the optical feedback and less coherent and hence less susceptible to optical interference effect. This RF modulation system is implemented in the OBD system of our HS-AFM setup [16].

The reflected light from the cantilever that is collected and collimated by the objective lens is slightly converged and fed into the photodiode position sensor that is a four-segmented Si-PIN photodiode (S6695-01, Hamamatsu Photonics) with a small junction capacitance of 3 pF and a high cutoff frequency of 40 MHz. The photocurrent signal from each segment is converted to voltage and amplified with a fast I/V amplifier and then all the voltage signals are fed into a custom-made signal conditioner with 20 MHz bandwidth to produce an differential output signal proportional to cantilever deflection, as well as a sum signal proportional to the total intensity of laser light incident to the photodiode position sensor. In our typical setup, the OBD detection sensitivity is 50–100 mV/nm, and the deflection noise density is $<$100 fm/$\sqrt{\text{Hz}}$ in water when a laser power of 0.5 mW is used [40].

As mentioned above, our HS-AFM head is combined with a laboratory-made inverted optical microscope that shares the objective lens with the OBD system. This combined system allows easy positioning of the sample stage and the cantilever (Fig. 22.6). The OBD system, to which the objective lens is fixed, is hung from the top base plate of the AFM head (Fig. 22.5). Moreover, the base plate is mechanically uncoupled from the optical microscope using soft elastic gels (e.g., P-N30L, Proseven) (Fig. 22.5). This design effectively shuts out mechanical vibrations that are traveling from the optical microscope with low resonant frequencies.

The optical microscope has an additional optical port (not shown in Fig. 22.5) through which another illumination light can be introduced to the objective lens to irradiate the sample. This light irradiation has been used to image photo-induced structural changes of bacteriorhodopsin [17, 41, 42] and photo-degradations of π-conjugated polymer chains [43]. It has also been used to quickly release functional ligands such as Ca^{2+} and ATP from caged compounds and then observe conforma-

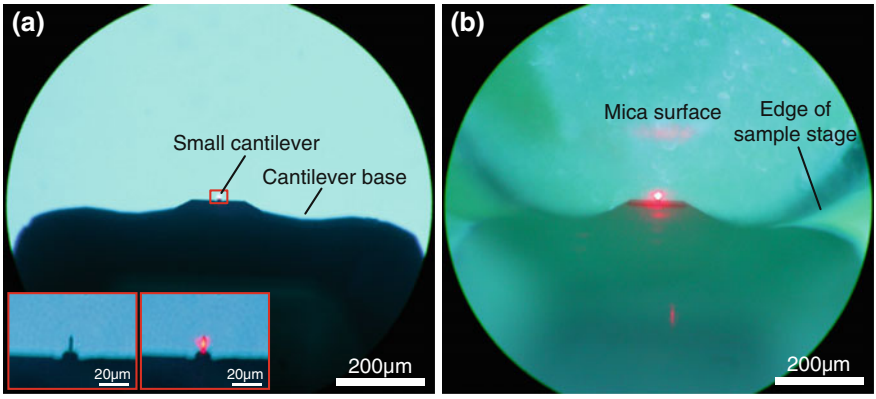

Fig. 22.6 Optical microscopic views of a small cantilever and a sample stage. **a** Low-magnification view of the cantilever without the sample stage. *Insets* show high-magnification views of the *red rectangle region* around the cantilever: *left*, without incident laser; *right*, with incident laser. **b** Low-magnification view of the cantilever when the sample surface is close to the cantilever

tional changes of proteins caused by the interaction with the released ligands [44, 45]. In these applications, the wavelength of the laser diode used in the OBD system sometimes has to be changed from usual 670 nm so that photo-sensitive samples are not affected by the laser beam, as has been done in the above mentioned studies of bacteriorhodopsin, where an infrared laser diode was used in the OBD system.

In addition to the OBD systems described above, other OBD systems or different methods to detect the deflection of small cantilevers have been proposed and used. A method that uses a Fabry-Perot interferometer for in-liquid frequency modulation (FM)-AFM achieved 3 μm focused spot size and a deflection noise density of <3 fm/$\sqrt{\text{Hz}}$ [46, 47]. Fukuma et al. also achieved a similar noise density in-liquid FM-AFM using an OBD system with a highly stabilized laser and a laser driver implemented with an RF signal superposition circuit. This low noise density enabled atomic resolution imaging in liquid [48, 49]. However, note that such a low noise density also requires the use of stiffer cantilevers with small thermal vibration amplitude. The laser diode in an OBD system can be replaced with a superluminescent diode that is low coherent and hence less susceptible to the effects of optical feedback and interference [50].

22.5 Fast Amplitude Detector

Since the Q value of small cantilevers is 2–3 in aqueous solution, the cantilever oscillation amplitude quickly changes when the tip makes contact with the sample surface. Therefore, amplitude detection should be performed at every oscillation cycle. However, RMS-DC converters or lock-in amplifiers used in conventional tapping-mode

AFM setups require at least several oscillation cycles to output an accurate amplitude signal. This is because a low-pass filter is used to remove high harmonic components from the oscillation signal. In the early high-speed AFM setup, a peak-hold method was used, in which the peak and bottom voltages of the oscillation signal were sampled by a sample-and-hold (S/H) circuit and then their difference was output as an amplitude signal [15]. This amplitude detector is fastest that can output the amplitude signal at every half cycle of oscillation. A drawback of this method is that the output is strongly affected by the cantilever's thermal motion because only two data points in the deflection signal are sampled.

In the current high-speed AFM setup, the other type of method, called the Fourier method, is used [16, 51], where the Fourier sine and cosine coefficients (A and B, respectively) of the fundamental frequency component of the deflection signal are calculated and then their root-mean-square, $\sqrt{A^2 + B^2}$, is output as the amplitude. Therefore, the amplitude signal can be detected every oscillation cycle. Since the deflection signal is integrated over a cycle, it provides a less noisy amplitude signal than the peak-hold method. A custom-designed Fourier amplitude detector (Fig. 22.7) composed of analog/digital hybrid circuits has been developed (T3510-01, Tsujicon, Japan), in which a high-performance digital signal processor (DSP) and a field-programmable gate array (FPGA) (StratixIII, Altera Corp., USA) are combined with high-bandwidth analog-to-digital (14 bit, 150 MSPS) and digital-to-analog (14 bit, 12 MSPS) converters. This system can also simultaneously calculate the phase of cantilever oscillation relative to the cantilever's excitation signal, allowing fast phase imaging in tapping mode. Figure 22.8 shows the deflection signal of an oscillating cantilever (red lines) and the amplitude signal (blue lines) detected with the Fourier method. In this measurement, the sinusoidally oscillating cantilever tip was made in

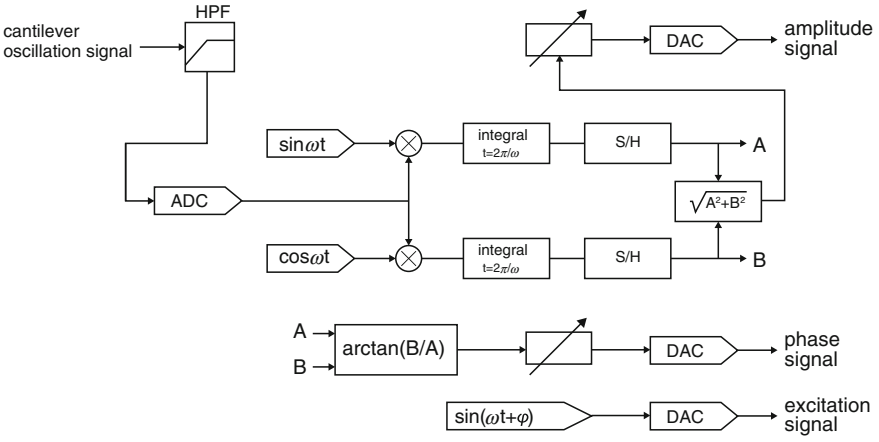

Fig. 22.7 Circuit diagram of Fourier method type of fast amplitude and phase detector

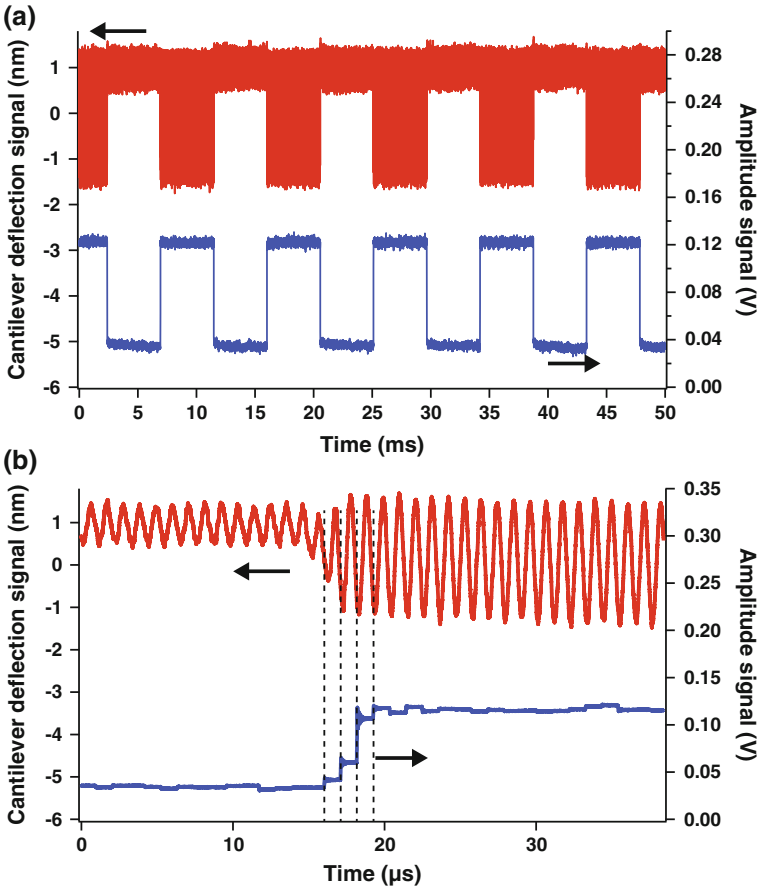

Fig. 22.8 Response of the amplitude detector output to square-wave changes of the cantilever oscillation amplitude. A cantilever is oscillated at 930 kHz in liquid. The Z-scanner was moved up and down by a square wave signal so that the tip was made in contact with the sample periodically. The cantilever's deflection signal and the amplitude signal detected by the Fourier method are plotted by *red* and *blue lines*, respectively. The *broken lines* in (**b**) indicate timings when the output from the amplitude detector is updated

contact periodically with the sample surface that was moved up-and down in a square wave. One can see that the amplitude signal quickly responses to the square-wave changes in the sample Z-position (Fig. 22.8a) and that the output signal is renewed at every oscillation cycle (Fig. 22.8b).

22.6 Scanner

The scanner to be used in high-speed AFM has to meet requirements of both high bandwidth and accuracy in mechanical positioning. The first requirement is most difficult to be achieved because the scanner is composed of macroscopic components such as piezoelectric actuators and supporting mechanical bases. Unwanted mechanical vibrations that limit the operation bandwidth are easily generated by the excitation of flexural vibrations of the mechanical structure. To minimize the generation of unwanted vibrations, piezoactuators with high resonant frequencies and a rigid mechanical structure are needed as well as a novel control strategy to damp unavoidable vibrations. The control for vibration damping is important particularly in the Z-scanner to be driven at high frequencies as well as in wide-area XY-scanners with low resonant frequencies. Moreover, wide-area scanners are susceptible to the effects of inherent nonlinear displacement of piezoactuators and crosstalk between displacements in the X- and Y-axes. Therefore, additional techniques to suppress or compensate for these effects are required. The following sections describe underlying techniques to fulfil these requirements.

22.6.1 Piezoelectric Actuator

Selection of piezoactuators is essential in achieving a high-speed scanner because their resonant frequencies are a major factor that restricts the scan frequency. Among several types of piezo-based actuators, a hollow tube-shaped piezoactuator is one of the simplest designs to achieve three-axis motion and hence has been most commonly used in conventional AFM systems. However, it has a low resonant frequency because of the large length-to-diameter ratio. The first resonant frequency of a tube scanner is typically less than 1 kHz. A shear mode piezoactuator can have a high resonant frequency because of its compact geometry and stiff mechanical property [52]. However, its displacement coefficient (i.e., displacement per voltage) is relatively small, which limits the application range of AFM. Alternatively, a tuning-fork based scanner has been used for video-rate AFM, where the X-scanner is oscillated sinusoidally at the tuning-fork's resonant frequency [53]. However, it has a drawback of non-linear displacement. Although the sinusoidal scan in the X-direction would not excite the scanner's mechanical resonances but makes an AFM image distorted in the X-direction. Generally, stack piezoactuators, which are widely used in commercial flexure-guided nanopositioners, can have both large displacement coefficients and high resonant frequencies. Therefore, stack piezoactuators are probably most suitable for high-speed scanners.

Among the X-, Y-, and Z-scanners, the Z-scanner should have the fastest response without overshoot or oscillation. Its response rate is one of the major factors that determine the bandwidth of feedback control to maintain the tip-sample interaction force constant. We have used different types of stack piezoactuators, depending on

the required displacement ranges. One end of the Z-piezoactuator is usually fixed onto a supporting base that is scanned in the X- and Y-directions. By this holding of the Z-piezoactuator, its resonant frequency becomes half the original one in free oscillation. Furthermore, the mass of the sample stage attached to the other end of the Z-piezoactuator further lowers the resonant frequency. To minimize the mass addition, we use a light glass rod of 1.5–2 mm in diameter and 2 mm long (10–15 mg) as a sample stage. This rod is glued onto the top of the Z-piezoactuator using nail polish.

As to the X-scanner that is scanned in a triangle wave, its resonant frequency should ideally be about 20 times higher than the fundamental frequency of the triangle wave. However, lower resonant frequencies are acceptable because the driving signal is predetermined and therefore feedforward control for vibration damping can be used, as described in Sect. 22.7.2.

22.6.2 Scanner Design

The scanner should be designed to be mechanically rigid so that excitation of unwanted vibrations can be prevented. A flexure-guided mechanism is most suitable for fast scanners because they can be monolithically machined from a single piece of metal block and hence no assembling parts are needed except for piezoactuators. Figure 22.9a illustrates a high-speed scanner that has been used for narrow-area high-speed imaging of biomolecular samples. The whole structure is machined monolithically from a stainless steel (SUS304) block. The thickness of each flexure is 0.4 mm. Two sets of flexure guides are combined in a serial-kinematic configuration; that is, the Y-scanner displaces the XZ-block that is connected to the base frame with two pairs of flexures, while within the XZ-block the X-scanner displaces the Z-scanner that is connected to the frame of the XZ-block with a pair of flexures

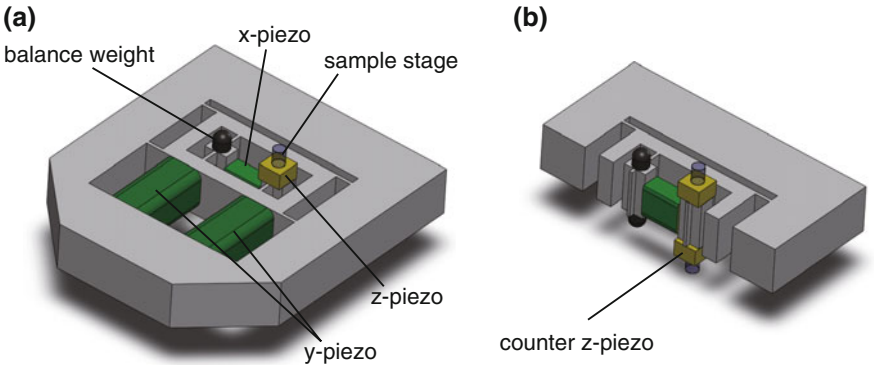

Fig. 22.9 HS-AFM scanner for relatively narrow area scan. The maximum san ranges are 1.3 μm in *X*, 3 μm in *Y* and 1.6 μm in *Z*. **a** Whole and **b** cross-sectional views of the scanner

(see Fig. 22.9a). This serial-kinematic configuration results in an asymmetric structure with respect to the X- and Y-scanners but is adequate because the X-scanner is scanned much faster than the Y-scanner. This configuration has another advantage; it does not suffer from parasitic, off-axis motion and can minimize crosstalk between the three-axis displacements [54]. When a symmetric structure with respect to the X- and Y-scanners is needed, a parallel-kinematic configuration can be employed, as described [55, 56], although this configuration is usually apt to suffer from crosstalk between X- and Y-displacements [54].

Quick displacement of a piezoactuator exerts impulsive force to its supporting base, which causes vibrations of the base and surrounding structures, and in turn, of the piezoactuator itself. To circumvent this problem, the mass center of the X-piezoactuator is managed to be kept stationary by its holding with two identical pairs of flexures at the ends and by the attachment of a balance weight to the counter side (Fig. 22.9a). The mass of the balance weight is adjusted to be similar to the sum of the mass of the Z-piezoactuator and the glass rod sample stage. A similar counterbalancing method is also applied to the Z-scanner. Two identical piezoactuators are attached to the opposite faces of the supporting base as shown in Fig. 22.9b. Both Z-piezoactuators are displaced simultaneously to the same extent in the opposite direction. Thus, the impulsive forces exerted to the supporting base are cancelled with each other [15, 16]. In addition to these devices to suppress unwanted vibrations, the vacant gaps in the scanner are filled with an elastomer to passively damp vibrations. This passive damping is effective in suppressing low-frequency vibrations. In this scanner (Fig. 22.9), stack piezoactuators with dimensions $3 \times 3 \times 2\,\mathrm{mm}^3$ (PL033.30, Physik Instrumente GmbH, Germany; nominal unloaded displacement, 2.2 μm at 100 V; nominal resonant frequency in free oscillation, 600 kHz) are used for the Z-scanner. The resonant frequency and maximum displacement of the Z-scanner with a sample stage are ∼180 kHz and ∼1.6 μm at 100 V, respectively. For the X- and Y-scanners, stack piezoactuators with dimensions $2 \times 3 \times 5\,\mathrm{mm}^3$ (AE0203D04F, Tokin-NEC, Japan; nominal unloaded displacement, 3 μm at 100 V; nominal resonant frequency in free oscillation, 260 kHz) and $5 \times 5 \times 10\,\mathrm{mm}^3$ (AE0505D08F, Tokin-NEC, Japan; nominal unloaded displacement 6 μm at 100 V; nominal resonant frequency in free oscillation, 138 kHz) are used, respectively. The resonant frequencies of these piezoactuators assembled in the scanner are ∼50 kHz and ∼12 kHz, respectively. The maximum displacements of the X- and Y-scanners are ∼1.3 μm and ∼3 μm, respectively.

For wide-area scanning over $\sim 20 \times 20\ \mu\mathrm{m}^2$, there are two ways to achieve such large displacements: one uses long piezoactuators without displacement magnification mechanisms, as has been designed in [55], whereas another uses relatively long piezoactuators together with displacement magnification mechanisms [56]. For wider-area scanning over $> 20 \times 20\ \mu\mathrm{m}^2$, magnification mechanisms are needed because the displacement range of stack piezoactuators with dimensions adequate for HS-AFM systems is limited. Figure 22.10a shows our wide-area scanner with the maximum scan range of $\sim 46 \times 46\ \mu\mathrm{m}^2$ at 100 V [56], where the third-class leverage mechanism is employed to magnify the displacements of the X- and Y-piezoactuators (Fig. 22.10b). This scanner is monolithically machined from an

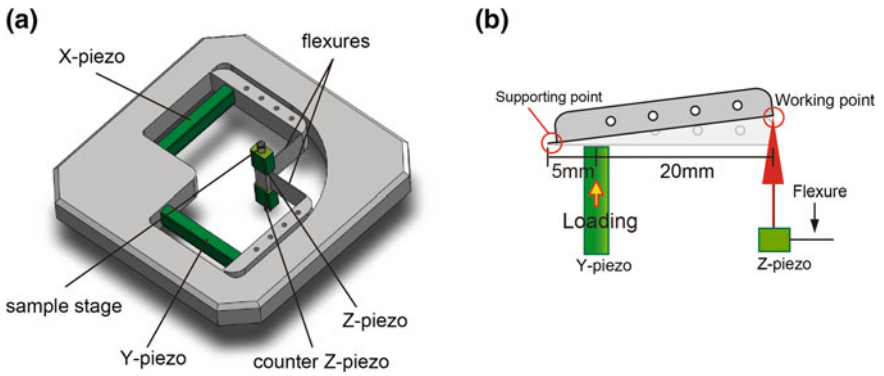

Fig. 22.10 HS-AFM scanner for wide-area scan. The maximum scan ranges are 46 μm in *X* and *Y* and 2.4 μm in *Z*. **a** Whole view of the wide-areas scanner. **b** Leverage-based displacement magnification mechanism

aluminum (A5052) block. The X- and Y-scanners are arranged in a parallel-kinematic configuration. That is, the identical X- and Y-scanners are arranged symmetrically with respect to the supporting base to which the Z-piezoactuator is attached. In this configuration, the fast axis can be chosen arbitrarily for the raster scanning. In the leverage mechanism, the entire lever length is 25 mm and the point of effort to which a piezoactuator is glued is 5 mm distant from the fulcrum; i.e., the designed lever ratio is five. Piezoactuator (AE0203D16F, Tokin-NEC, Japan) used for the X- and Y-scanners have dimensions of $2 \times 3 \times 20\,\text{mm}^3$, a nominal unloaded displacement of 11.6 μm at 100 V and a resonant frequency of 69 kHz. This parallel-kinematic configuration is susceptible to mechanical vibrations and crosstalk between the X- and Y-displacements. Furthermore, nonlinear displacements of the X- and Y-scanners are manifested in a wide-area imaging. These drawbacks have been overcome by feedforward control techniques described in the next sections. A stack piezoactuator (AE0203D04F, Tokin-NEC, Japan) is glued onto the top of the supporting base that is to be moved in the X- and Y-directions. The same type of piezoactuator is also glued to the bottom side of the supporting base as a counterbalance, similar to the small-area scanner.

22.7 Control Techniques

In HS-AFM systems, control techniques are required in various aspects: maintenance of the tip-sample interaction force at its set point, damping of mechanical vibrations of the scanner, compensation for non-linear and coupled displacements in the scanner, and others. In conventional AFM systems, digital controllers are widely used that are based on DSP or FPGA. One of the major advantages of digital controllers is their flexibility. That is, the controllers can be renewed by the update of software or

algorithm without alteration of hardware. Moreover, digital controllers allow us to use sophisticated control schemes that have been proposed to improve the feedback control performance and positioning accuracy in AFM systems [57–64]. However, the time delays involved in digital controllers, such as those required for analog-to-digital (AD) and digital-to-analog (DA) conversions and digital calculations, are not negligible, even when the most advanced digital electronics with highest speed performance are used. We should note that the time delays of mechanical devices of HS-AFM systems (i.e., cantilevers and scanners) have already been shortened significantly. In this current state, the time delay in digital controllers would become a major rate-limiting factor. Considering this advancement, we have been employing an analog proportional-integral-derivative (PID) controller for feedback control of the tip-sample interaction. Moreover, we have developed several control techniques to make high-speed imaging compatible with low-invasive imaging as well as to compensate for non-linear and coupled displacements in the scanner and drift of cantilever excitation efficiency. The following sections describe the details of these control techniques.

22.7.1 Active Damping of Z-scanner Vibrations

The response speed of resonant systems increases with increasing resonant frequency and decreasing quality factor Q. As described in Sect. 22.6, a fast Z-scanner can be built using small stack piezoactuators with high resonance frequencies and the counterbalancing method. However, the Q value of small stack piezoactuators is generally ∼20 or higher (Fig. 22.11a), meaning that there is still room for improving the response speed of the Z-scanner. For cantilevers, an active Q-control technique has been developed to increase their sensitivity to tip-sample interaction by increasing the Q value [65–67]. Conversely, this technique has been used to increase the response speed of cantilevers by decreasing the Q value [68, 69]. In principle, this technique can be applied to any resonant systems.

The Z-scanner motion can be approximately treated as a damped harmonic oscillator driven by external force $F(t)$:

$$m\ddot{z} + \gamma\dot{z} + kz = F(t), \tag{22.6}$$

where m is the mass of the Z-scanner, γ is the damping constant, and k is the spring constant of the Z-scanner, respectively. To decrease the Q value ($= \sqrt{mk}/\gamma$) while keeping the resonant frequency, the damping constant should be increased. To do so, a force proportional to $-\dot{z}$, i.e., $-G\dot{z}$ ($G > 0$), is added to the external force so that the effective Q value (Q_{eff}) decreases to $\sqrt{mk}/(\gamma + G)$. To accomplish this control, the velocity of the Z-scanner should be measured in real time but it is difficult to do so. Instead of measuring the displacement or velocity of the Z-scanner, one can monitor the output signal from a "mock Z-scanner" that is an LRC circuit characterized with a transfer function similar to that of the real Z-scanner [70]. As the transfer function

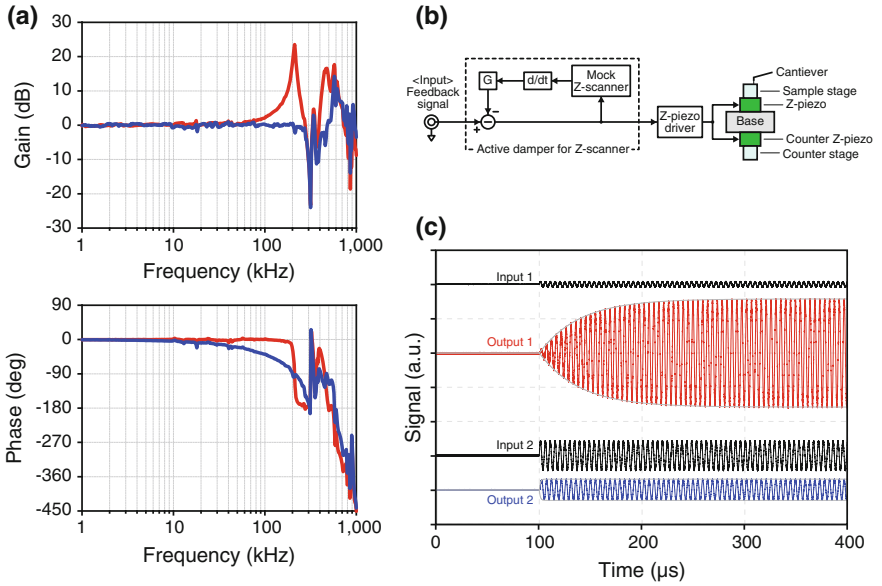

Fig. 22.11 Mock Z-scanner-based method to damp Z-scanner vibrations. **a** Frequency response of the Z-scanner. *Top*, amplitude response; *bottom*, phase response. Without active damping (*red lines*), the first resonant peak appears at 211 kHz, with Q = 28. As the phase of the Z-scanner shows an up-and-down feature around the first and second resonant peaks, the Z-scanner's resonators are connected in parallel. With active damping (*blue lines*), Q_{eff} was set at 0.7. **b** Schematic of the active damping method. The feedback signal (output from the PID controller) is fed to the active damping circuit. The "mock Z-scanner" constructed with an LCR circuit has a very similar frequency response to that of the real Z-scanner. **c** Effect of active damping on the transient response of the Z-scanner. "Input 1" and "Input 2" are the driving signals for the Z-scanner without and with active damping, respectively. The Z-scanner started to be driven at 100 μs by the sinusoidal wave signals of 211 kHz. "Output 1" (*red line*) and "Output 2" (*blue line*) are the responses of the Z-scanner without and with active damping, respectively. *Thin gray lines* represent the envelope curves of the Z-scanner displacements, which indicate the transient changes in the amplitude of the Z-scanner oscillation. The settling times (τ) were 39.0 and 1.0 μs in the cases of without and with active damping, respectively. These values were well consistent with the expectation from the relationship of $\tau = Q/\pi f$, where f was 211 kHz

of the real Z-scanner can be well approximated by that of a second-ordered low-pass filter, the LRC circuit can be easily constructed. This Q-control system is depicted in Fig. 22.11b. This simple method is quite effective in damping Z-scanner vibrations (Fig. 22.11a) and hence in increasing the Z-scanner's response speed (Fig. 22.11c). Although the phase delay is pronounced when Q_{eff} is reduced to 0.5, it can be improved by applying an inverse transfer function compensation, as demonstrated [70]. For practical use, Q_{eff} is set to the critical damping condition (i.e., $Q_{eff} \sim 0.7$). When the resonant frequency of the Z-scanner is high enough so that it would not be excited during imaging, Q_{eff} can be set at 1–3 to avoid pronouncing the phase delay.

22.7.2 Control Techniques to Damp XY-scanner Vibrations

The driving signal for X-directional scan is generally an isosceles triangle wave as a function of time. High harmonic frequency components contained in the vertices of the triangular wave would excite the X-scanner. When the first resonant frequency of the X-scanner is not high enough, this excitation generates fatal vibrations at the X-scanner's resonant frequencies, as exemplified in Fig. 22.12b. To eliminate the generation of unwanted vibrations by raster scanning, non-raster scan patters, such as spiral- [71, 72], cycloid- [73] and Lissajous- [74, 75] patterns, have been proposed. Although these non-raster scan patterns contain no higher harmonic frequencies, the procedures for producing the scan signals, reconstructing the image, and compensating for the nonlinear effects of the piezoactuators are complicated. Moreover, the cantilever tends to be twisted by a lateral dragging force component perpendicular to the lever arm, which would hampers the accurate sample height measurement. Even for wide-area scanners with low resonant frequencies, we still use raster scan but combine two simple methods to suppress the generation of unwanted vibrations in the X-scanner: inversion-based feedforward damping [16, 76, 77] and a modified triangular wave with reduced higher harmonics [16, 78].

The inversion-based feedforward damping is carried out as follows. Supposing that the waveform of X-scan is isosceles triangles characterized by amplitude X_0 and fundamental angular frequency ω_0, its Fourier transform is given by

$$F(\omega) = 2\pi X_0 \left[\frac{1}{2}\delta(\omega) - \frac{2}{\pi^2} \sum_{k=-\infty}^{+\infty} \frac{1}{k^2}\delta(\omega - k\omega_0) \right] \quad (k : odd) \tag{22.7}$$

To move the X-scanner characterized by a transfer function $G(s)$ in the isosceles triangle waveform, the driving signal X(t) sent to the X-piezoactuator is given by the inverse Fourier transform of constant-gained $F(\omega)/G(i\omega)$, which is expressed as

$$X(t) = g \times \left[\frac{X_0}{2} - \frac{4X_0}{\pi^2} \sum_{k=1}^{+\infty} \frac{1}{k^2} \frac{1}{G(ik\omega_0)} \cos(k\omega_0 t) \right] \quad (k : odd), \tag{22.8}$$

where g is the constant gain. We calculate (22.8) in advance to obtain numerical values of X(t) and output them in succession from a computer through a D/A converter. The black line in Fig. 22.12c shows the modified triangular wave obtained after filtration of a triangular wave through an inverse transfer function $1/G(i\omega)$ that is constructed using the frequency response of the X-scanner shown in Fig. 22.12a. Here, the filtered triangular wave is constructed with the first 20 terms in the Fourier cosine series of an isosceles triangle function. The vibrations observed in the absence of the feedforward damping are significantly suppressed by this damping method. In principle, this damping method can extend the bandwidth of the X-scanner, but in practice the limited gain and driving current of a piezodriver at high frequencies limit the bandwidth extension. Moreover, the frequency response of the X-scanner varies

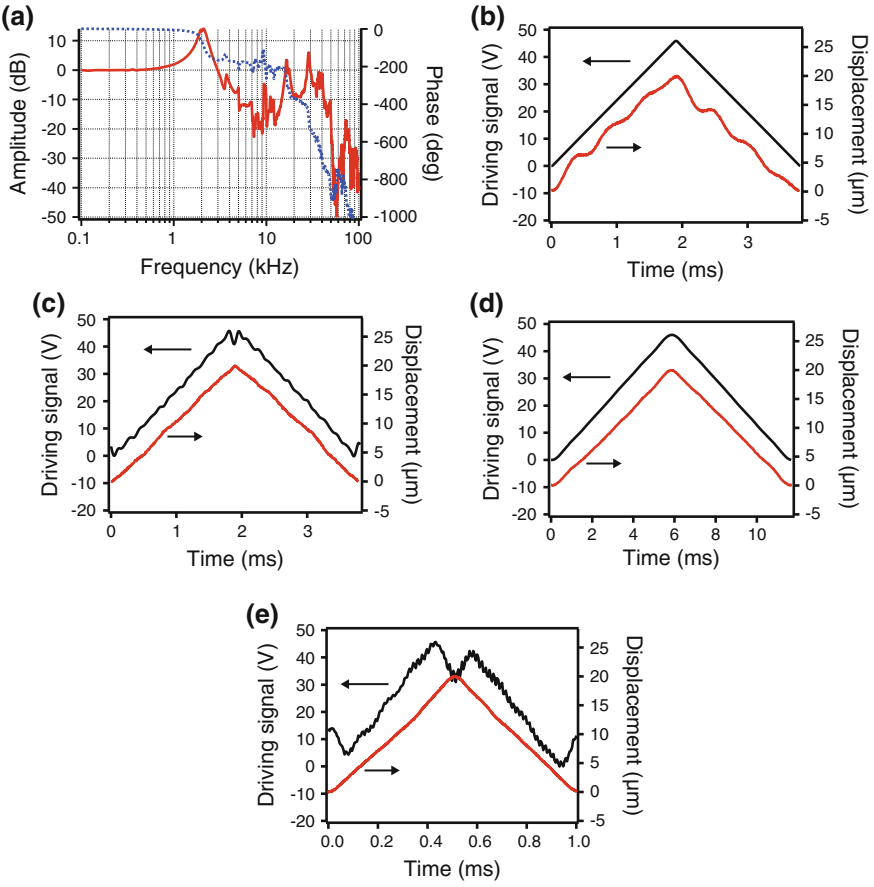

Fig. 22.12 Effects of vibration damping on X-scanner displacement of wide-area scanner. **a** Frequency spectra of mechanical response of the X-scanner (*red line*, amplitude; *blue line*, phase). **b** Driving signal of 256 Hz with a non-modified triangular wave (*black line*) and corresponding displacement (*red line*). **c** Driving signal of 256 Hz with a triangular wave form modified by inverse compensation (*black line*) and corresponding displacement (*red line*). **d** Driving signal of 85 Hz with a rounded triangular wave form containing harmonics up to the ninth order (*black line*) and corresponding displacement (*red line*). **e** Driving signal of 1 kHz obtained after modification by inverse compensation of a rounded triangular wave form containing harmonics up to the ninth-order (*black line*) and corresponding displacement (*red line*)

to some extent depending on the sample attached. Therefore, vibration damping to a practical extent cannot be achieved by this method alone. Therefore, an additional method (simple rounding of the vertices of the triangular wave) is combined.

The simple rounding method is carried out as follows. An isosceles triangular wave is composed of a cosine wave with the fundamental frequency and an infinite series of its odd higher harmonics. By omitting higher harmonic components in this series, we can easily generate a triangular wave with round vertices. As shown in

Fig. 22.12a, the amplitude gain of the X-scanner starts to increase around 500 Hz. Assuming that the gain tolerance is less than 1 dB, the highest frequency of harmonics to be included in the driving signal should be lower than ∼780 Hz, judging from the frequency response shown in Fig. 22.12a. To scan at 85 Hz, the highest harmonics should be less than the ninth order (i.e., 745 Hz). Figure 22.12d shows a rounded triangular wave constructed from harmonics up to the ninth order (black line) and the corresponding displacement of the X-scanner (red line). The displacement does not show noticeable vibrations. The nonlinear scan range is about 10 % of the full scan range, which is much smaller than that when a sinusoidal scan wave is used. Figure 22.12e shows the driving signal and the measured displacement of the X-scanner when the two damping methods are combined. Here, the rounded triangular wave containing higher harmonics up to the ninth order was filtered through an inversed transfer function constructed using the measured frequency response. Thus, the scanning frequency was able to be extended up to ∼1 kHz even for the wide-area scanner with the first resonant frequency of 2 kHz.

In raster scan, a sawtooth wave is usually used for the Y-directional scan. The quick return to the scan origin along the Y-direction, which is performed after the completion of line scans in the X-direction, generates large vibrations. This vibration generation can easily be suppressed by slowing the scan speed. The time delay added by this slow scan is negligible because it is much shorter than the frame imaging time.

22.7.3 Compensation for Nonlinearity and Crosstalk

Piezoelectric materials have hysteresis between driving voltage and displacement. In the X- and Y-directional scan, the positioning error by hysteresis is generally 10–15 % of the full scan range [79], which causes considerable image distortion such as local elongation and compression, especially for wide-area imaging, as demonstrated with a 10 μm-pitch square grid image (Fig. 22.13a). To eliminate image distortion, closed-loop compensation is often used in commercial AFM systems. In the closed-loop compensation, the displacement sensor is incorporated into the scanner to monitor the displacements of the X- and Y-piezoactuators. The monitored displacements are used to regulate the driving signal by feedback control so that the piezoactuators are linearly displaced. This approach enables precise positioning and is tolerant to aging variation of the nonlinearity of the piezoactuators. However, the closed-loop compensation makes the scanner assembly complicated because of the implementation of the displacement sensors. Moreover, the bandwidth of high-precision displacement sensors is too low compared to the bandwidth required for high-speed scanners. On the other hand, open-loop compensation based on pre-measured nonlinear behaviors [80] does not require modification of the scanner and guarantees high-speed performance, although the accuracy would not be as superb as closed-loop compensation.

We applied open-loop compensation to the above wide-area scanner in the following way. The hysteresis curves of the X- and Y-scanners are first measured with a

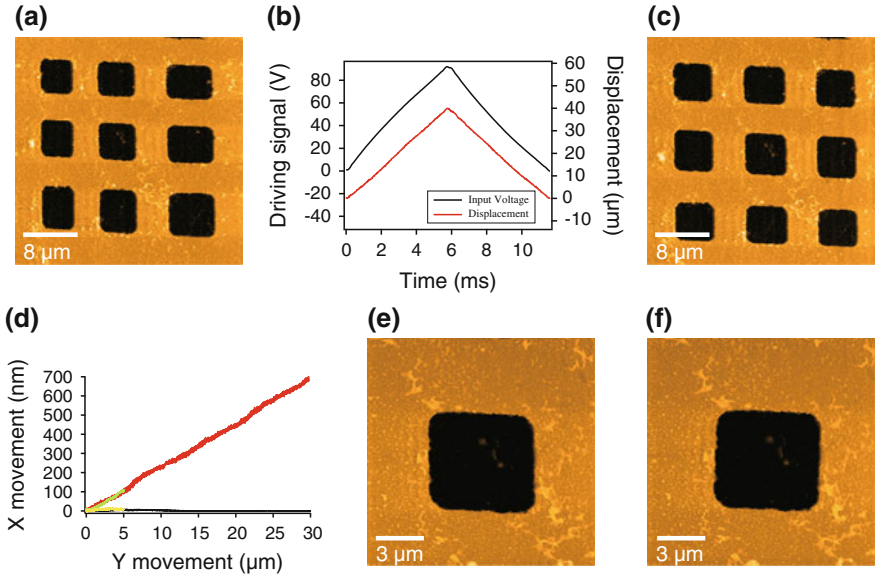

Fig. 22.13 Compensation for nonlinear behavior of piezoactuators and crosstalk between X- and Y-scanning. **a** AFM image of a test grating sample with a pitch of 10 μm obtained without compensation for nonlinear hysteresis (imaging rate, 7 s/frame; pixels, 256 × 256). **b** Driving signal of 85 Hz with a triangular wave form modified by open-loop compensation for hysteresis (*black line*) and corresponding displacement (*red line*). **c** AFM image of the same grating sample obtained with compensation for hysteresis (imaging rate, 7 s/frame; pixels, 256 × 256). **d** Sample stage displacement in the X-direction as a function of Y-scanner displacement. Displacement ranges of Y-scanner are 5 μm (*green line*) and 30 μm (*red line*). *Yellow* and *black lines* represent displacements in the X direction when compensation for crosstalk is applied to Y-scanner displacements of 5 and 30 μm, respectively. **e** AFM image of the grating sample obtained without compensation for crosstalk (scan range, 15 × 15 μm^2, imaging rate, 7 s/frame, pixels, 256 × 256). **f** AFM image of the grating sample obtained with compensation for crosstalk (scan range, 15 × 15 μm^2; imaging rate, 7 s/frame; pixels, 256 × 256)

displacement sensor and then fitted by fourth-order polynomial functions. Although higher-order polynomial functions give better fitting, the fourth-order fitting is good enough in practice to compensate for the nonlinearity. The driving voltage signal not processed for inverse vibration damping is constructed using the inverse functions of the fitted hysteresis curves. Then, this driving signal is further processed by the vibration damping methods mentioned above. Figure 22.13b shows the effect of hysteresis compensation on the displacement of the X-scanner. The black line indicates a driving signal of 85 Hz constructed by open loop compensation, while the red line indicates the corresponding displacement of the X-scanner. The outwardly (ascending regime) and inwardly (descending regime) distorted curves of the driving signal reflect the compensation for the nonlinear hysteresis. The X-scanner is displaced linearly in both expansion and contraction regimes. As a result, the distortion of the grating image is much improved as shown in Fig. 22.13c.

In addition to the nonlinear behavior of the piezoactuators, crosstalk between the X- and Y-scanners is an issue to be resolved for accurate high-speed imaging. Interference between the X- and Y-scanners is inevitable in wide-area scanners that employ the parallel-kinematic configuration. The crosstalk ratio is 0.017 in our wide-area scanner; when the sample stage is moved by 1 μm along one axis, it is also moved by 17 nm along the other axis (Fig. 22.13d). To eliminate the crosstalk effect, an appropriate fraction of the voltage applied to the X (or Y)-piezoactuator is subtracted from the driving signal for the Y (or X)-piezoactuator. This simple method minimizes the coupled movement of the sample stage, irrespective of the displacement range. As a result, the images of square grid holes with rhombic distortion shown in Fig. 22.13e is converted to images with much less distortion, as shown in Fig. 22.13f.

22.7.4 Dynamic PID Controller

Biological phenomena occurring in biomolecules proceed through delicate intramolecular and intermolecular interactions. To observe biomolecular processes using HS-AFM, the tip-sample interaction force should be kept as small as possible. Under the condition of cantilever's free oscillation amplitude A_0 and amplitude set point $A_s = rA_0$, the average tapping force $\langle F_{ts} \rangle$ exerted on the sample from an oscillating cantilever tip is given by

$$\langle F_{ts} \rangle = \frac{k_c A_0}{Q_c} \sqrt{1 - r^2} \tag{22.9}$$

To achieve small $\langle F_{ts} \rangle$ with a given cantilever, the cantilever free oscillation amplitude A_0 has to be set at a small value, and moreover the dimensionless amplitude set point r has to be set close to 1 [81].conditions result in tip parachuting, as described in Sect. 22.2. This problem cannot be solved by the increase of the feedback gain because it induces overshoot in the uphill regions of the sample, resulting in the instability of the feedback operation. However, if the feedback gain can be increased only in the downhill regions of the sample, this difficult problem can be solved.

To accomplish such gain control, we first need to know in real time whether the sample is being scanned in its downhill regions or uphill regions. As described in Sect. 22.2, in the uphill regions the cantilever oscillation amplitude A becomes smaller than the set point amplitude A_s, whereas in the downhill regions A becomes larger than A_s. Using this general rule, we developed a new PID controller called "dynamic PID controller", in which the feedback gain is automatically tuned depending on the relative magnitude of A compared to a threshold level A_H [26]. As shown in Fig. 22.14a, A_H is set at A_s or between A_s and A_0. When A exceeds A_H, an artificial error signal proportional to $(A - A_H)$ is added to the true error signal (Fig. 22.14a, b). The resulting large error signal produces a large feedback signal, which remarkably shortens the parachuting time or prevents the cantilever tip from getting into the parachuting state (Fig. 22.14c). This favorable effect can occur even when r is set up to ~0.9. In fact, the feedback bandwidth becomes independent of r so long as r

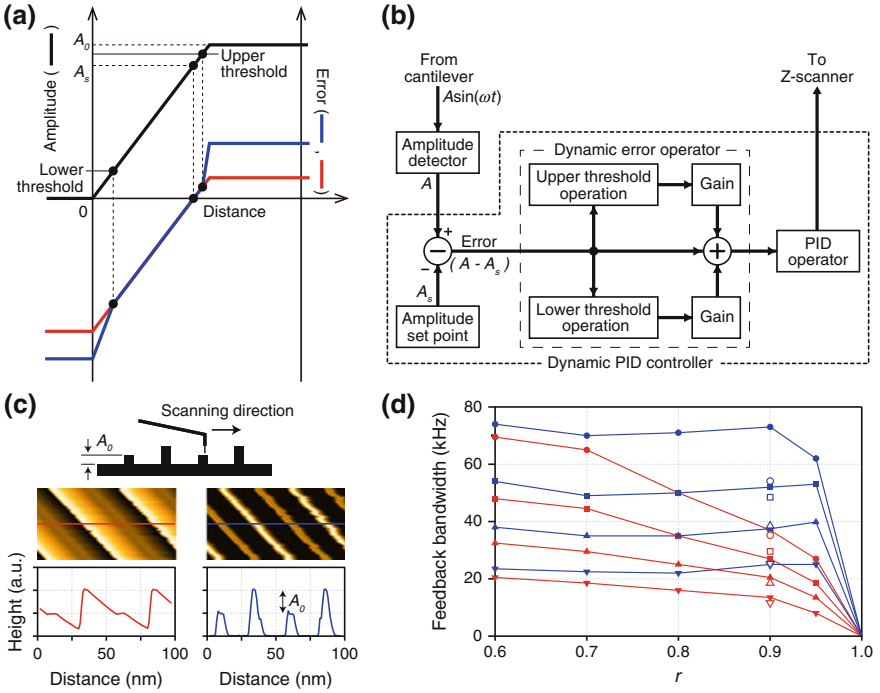

Fig. 22.14 Dynamic PID controller and its effect on feedback bandwidth. **a** Principle of dynamic PID controller. *Black solid line* shows cantilever oscillation amplitude versus distance curve. *Red* and *blue lines* show error versus distance curves for conventional PID control and dynamic PID control, respectively. **b** Circuit diagram of the dynamic PID controller. A dynamic error operator is inserted between the error signal output terminal and the input terminal of the conventional PID operator. Dynamic error signal manipulation is carried out using a precision diode circuit. **c** AFM images of a pseudo-sample surface with rectangle patterns with two different heights. *Top row* shows the schematic of the pseudo-sample surface. *Middle row* shows AFM images taken using the conventional (*left*) and dynamic PID controllers (*right*), respectively. These images were obtained using a mock AFM system [26]. *Bottom row* shows the height profiles along the *red* and *blue lines* drawn in the Pseudo-AFM images. Simulation condition used in the mock AFM system: Cantilever, resonant frequency 1.2 MHz and quality factor 3; Z-scanner, resonant frequency 150 kHz and quality factor 0.5; Sample, height of the lower rectangle A_0 and height of the higher rectangle $2A_0$; the feedback amplitude set point $r = 0.9$; the line scan speed 1 mm/s (1 kHz); Scanning direction from *left* to *right*. **d** Effect of the dynamic PID controller on the feedback bandwidth as a function of the amplitude set point. *Red* and *blue* colored data sets were obtained using the conventional and dynamic PID controllers, respectively. *Filled* and *opened* marks represent the data points obtained by the mock AFM system and the real AFM system (at only $r = 0.9$), respectively. The sample heights for data points of circles, squares, triangles and inverted triangles were $0.2 \times A_0$, $0.5 \times A_0$, $1.0 \times A_0$ and $2.0 \times A_0$, respectively. The other simulation conditions of the mock AFM system were same as that used in (**c**)

is set at less than ∼0.9 (Fig. 22.14d). Thus, this control method makes high-speed imaging compatible with low-invasive imaging to a significant extent. In addition, this gain tuning method can be applied to a situation where the cantilever tip suddenly

encounters an object with significantly large height. In this case, another threshold level A_L is set at a very small value between A_s and zero (Fig. 22.14a, b). When A becomes smaller than A_L, an artificial error signal proportional to $(A - A_L)$ is added to the true error signal. This error signal manipulation can alleviate the event where the cantilever tip gets into a strong contact with the sample.

22.7.5 Drift Compensator

High-speed and low-invasive AFM imaging of biological molecules is typically performed under the condition of $1 < A_0 < 3\,\text{nm}$ and $r = 0.8$–0.9. In order to make the dynamic PID control effective under this condition, both low-noise cantilever oscillation amplitude signal and stable cantilever excitation are required. The former requirement can be satisfied by the Fourier method-based amplitude detector as mentioned in Sect. 22.5. However, the latter requirement is not easy to be met. The cantilever excitation instability is caused by two effects. One is temperature increase in the piezoactuator that is continuously oscillated to excite the cantilever. This temperature increase results in decrease of oscillation efficiency of the piezoactuator. The other is a shape change of the buffer solution in the liquid cell. When A_0 decreases, A also decreases. The feedback control system misinterprets this decrease of A as a consequence of strong tip-sample contact and therefore withdraws the sample stage from the cantilever, which eventually resulting in complete detachment of the tip from the sample surface.

Because there is no direct way to measure A_0 during imaging, it is difficult to maintain A_0 at its initial value. When A_0 is gradually decreasing, A is maintained at its set point by feedback control. However, the tip-sample interaction force is not maintained constant but gradually decreasing. Therefore, it is possible to detect the decrease of A_0 if a signal sensitive to the tip-sample interaction force is available. When a cantilever tip sinusoidally oscillating at f_c taps the sample surface, its sinusoidal oscillation is distorted, resulting in production of higher harmonic components $(2f_c, 3f_c, \ldots)$. The time-averaged amplitude of the second harmonic oscillation can be used as an indicator of drift in A_0 [82]. The second harmonic amplitude can be maintained constant using a slow integral-controller whose time constant is longer than the image acquisition time (Fig. 22.15a). In this way, the amplitude of driving signal for the cantilever-excitation piezoactuator can be controlled to maintain A_0 at its initial value [26]. This drift compensation method works effectively (Fig. 22.15b). Using this method together with the dynamic PID controller, we can perform stable low-invasive and high-speed imaging even under the condition of $A_0 = 1\,\text{nm}$ and $r \sim 0.95$.

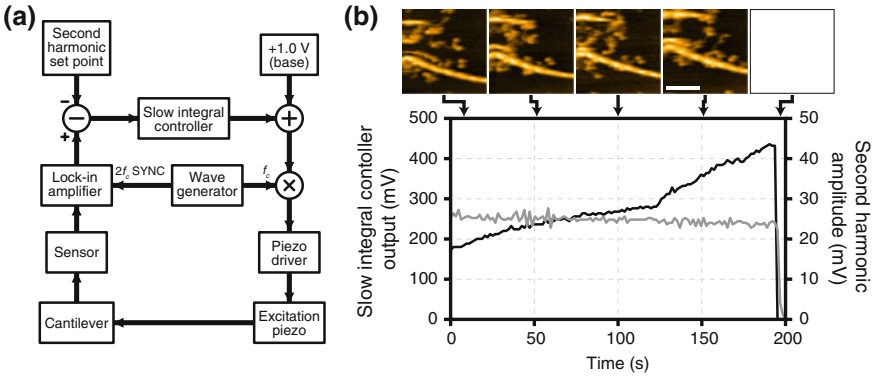

Fig. 22.15 Compensation for drift of cantilever excitation power. **a** Circuit diagram of the drift compensator. The lock-in frequency of the lock-in amplifier is the synchronized second harmonic frequency ($2f_c$) of the cantilever oscillation. **b** Successive AFM images of myosin V molecules bound to actin filaments captured using the drift compensator. The *lower graph* shows the time courses of the output signal from the slow integral controller (*black line*) and the second harmonic amplitude (*gray line*), respectively. The *top row* AFM images were captured at the times indicated by the *arrows*. Imaging conditions: $A_0 = 2.5$ nm; $r = 0.92$; scanning area, 250×250 nm^2; frame rate, 10 fps. At 3 min, the drift compensator was switched off. After that, no image was obtained because of complete detachment of the cantilever tip form the sample surface. Scale bar, 100 nm; Z-scale, 0–11 nm

22.8 HS-AFM Imaging of Protein Molecules in Action

After the completion of development of various devices and techniques described above, HS-AFM was established around 2008. Since then, its innovative power has been continuously demonstrated by the visualization of several types of dynamic events occurring in protein systems (see Reviews [83–85]). These dynamic events include mechanical actions, dynamic interactions with partners, self-assembly processes, diffusion and interactions in membranes, structural transitions, and others. Most of the visualized dynamic events were able to be interpreted straightforwardly without intricate analyses and hypotheses. More importantly, most of the studies brought important discoveries impossible to be made with other approaches, and therefore, provided significant insights into the functional mechanism of the observed protein systems. In this section, HS-AFM imaging studies on myosin V and an intrinsically disordered protein FACT protein are described. For other proteins systems, see [84].

22.8.1 Myosin V

Myosin V (M5) is a member of the myosin superfamily and functions as a cargo transporter in cells. M5 consists of two identical heavy chains, each of which has a

N-terminal motor domain, a neck (also called "lever-arm") domain bound to six light chains (calmodulins or calmolulin-like proteins), a tail region with a proximal α-helix domain to form a dimerized coiled-coil region and a distal C-terminal cargo binding domain [86]. Single molecules of M5 move processively along actin filaments over long distances [87, 88] with a large step size (~36 nm) [87, 89]. This processivity has allowed us to trace the motor action continuously using single-molecule fluorescent microscopy and optical-trap nanometry, enabling the investigation of motor properties of M5. Single molecule studies have demonstrated that M5 moves along actin filaments in a "hand-over-hand" manner [90, 91], consuming one ATP molecule per forward step [92]. However, the protein molecules themselves are invisible in these single molecule observations. Although the structural information has been obtained in detail by electron microscopy [93–96] and X-ray crystallography [97, 98], it has been limited to static snapshots. As such, a comprehensive understanding of the motor mechanism, especially the chemo-mechanical coupling mechanism, has not been achieved until our direct observation of M5 molecules in dynamic action by HS-AFM [18].

To visualize M5 molecules moving along actin filaments with HS-AFM, actin filaments should be immobilized on a surface, while M5 should be free from the surface and interact only with the immobilized actin filaments. To meet these conditions, a mica supported lipid bilayer containing a biotin-lipid was used [99]. On this surface, partially biotinylated actin filaments were immobilized though streptavidin molecules with a low surface density. Successive AFM images captured in the presence of ATP clearly showed individual M5-HMM (tail-truncated myosin V) molecules moving processively with discrete ~36 nm steps (Fig. 22.16a). In the two-headed bound M5-HMM, the neck-motor domain junction appears smooth in the leading head (L-head) but is V-shaped in the trailing head (T-head) without exception. The short coiled-coil tail slightly tilts towards the direction opposite to the moving direction of M5-HMM. These features are fully consistent with those observed by electron microscopy [93]. Furthermore, the detailed stepping process including "hand-over-hand" movement was successfully visualized when the surface density of streptavidin molecules was increased (Fig. 22.16b). The extra amounts of streptavidin molecules worked as moderate obstacles to the stepping. Notably, after the T-head detached from actin, the nearly straight L-head swung from the back leaning orientation to the forward leaning orientation. This observation provided the first direct evidence for the swinging lever-arm motion initially proposed by Huxley for muscle myosin [100]. Thus, the long-lasted debate on this swinging-lever arm hypothesis is now settled and therefore this brilliant idea is no longer a hypothesis [101, 102].

Even under the nucleotide-free condition, both heads of M5-HMM were bound to the same actin filament. However, unlike in the presence of nucleotides, where the T-head almost always (>95 %) took a nearly straight conformation (slightly curved outward), the L-head often exhibited a sharply kinked conformation and alternated back and forth between this conformation and the nearly straight conformation. The sharp kink is likely to occur to release the large strain accumulated in the neck, suggesting that the neck-motor domain junction is stiffer in the absence of nucleotides than that of the nucleotide-bound head. The sharply kinked conformation adopted

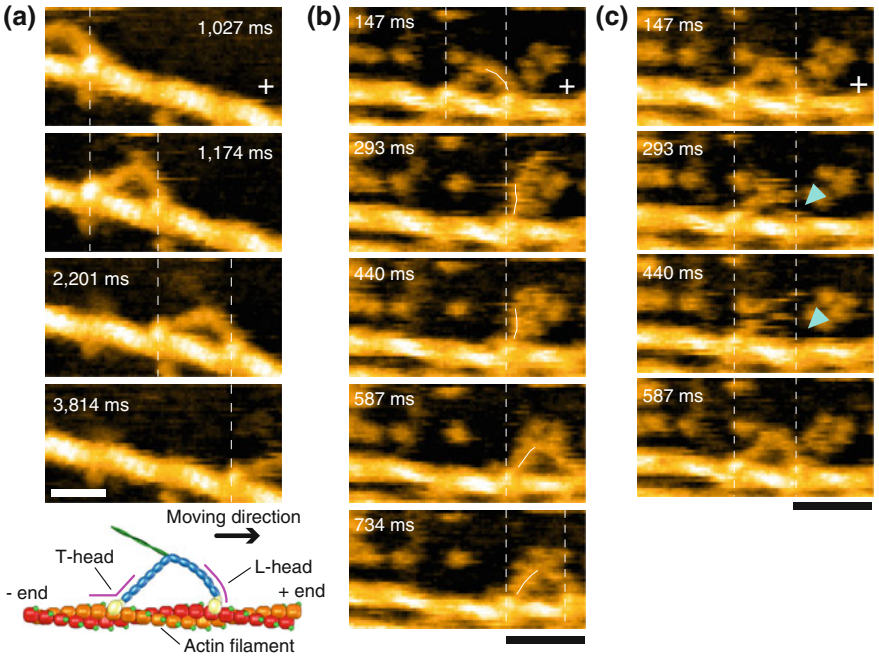

Fig. 22.16 HS-AFM images showing M5-HMM behaviors. **a** Successive AFM images showing unidirectional processive movement of M5-HMM (*upper panels*; scale bar, 30 nm) and schematic showing two-headed bound M5-HMM (*bottom*). **b** Successive AFM images that captured the stepping behavior of M5-HMM (scale bar, 50 nm). The swinging lever-arm is highlighted with the *thin white lines*. **c** Successive AFM images showing a foot stomp event that occurs at the L-head. *Light-blue arrowheads* indicate the detached L-head. The *vertical dashed lines* drawn in the AFM images show the centers of mass of the motor domains, and the *plus signs* indicate the plus ends of actin filaments. These AFM images were taken at 7 fps in a buffer solution containing 1 μM ATP

by the L-head under the nucleotide-free condition can provide a useful indicator of whether or not the L-head contains a nucleotide. Even in the presence of 0.1 μM ATP, the L-head neck was mostly straight (>98 %), suggesting that the L-head almost always retains ADP until the T-head binds to ATP and then detaches from actin. In the presence of low concentrations of ADP, the L-head exhibited alternate switching between the straight and sharply kinked conformations. From the proportion and lifetime of the straight L-head as a function of ADP concentration, the ADP dissociation rate constant k was estimated to be $k = 0.1\,s^{-1}$. The ADP dissociation rate constant of 0.1 s^{-1} means that, on average, one ADP is released from the L-head every 10 s. However, M5-HMM walks many steps during 10 s. As such, the sequential events of ADP release, the subsequent ATP binding, and the resulting head dissociation take place solely at the T-head, which is the basis underlying the processive hand-over-hand walking. This mechanism had been inferred from various indirect experiments [103, 104] but was clearly and directly demonstrated by the HS-AFM observation.

The HS-AFM observations mentioned above provided corroborative visual evidence for previously found or speculated molecular actions of M5. However, HS-AFM observations also brought new discoveries of the chemo-mechanical coupling in M5. During the two-headed bound state, both motor domains frequently exhibited brief dissociation and reassociation on the same actin filament (Fig. 22.16c), whereas M5-HMM remained at approximately the same position on the filament. This behavior was termed "foot stomp". The foot stomp at the L-head raises an important question about the chemo-mechanical coupling in this motor. The briefly detached L-head does not carry bound Pi because Pi is immediately released from the head following the initial attachment of the ADP-Pi-bound head to actin [105]. Nevertheless, the detached ADP-bound L-head rebound to actin still in the back leaning orientation, and then swung its lever-arm forward upon T-head detachment from actin, very similar to the normal step process. This indicated that tension generation for forward movement can occur without transitioning through the ADP-Pi bound state, but directly in the ADP-bound state. Thus, the tension generation for forward movement does not seem to require chemical energy be supplied by ATP hydrolysis. This surprising view was further confirmed by the HS-AFM observation of the two-headed bound M5-HMM in the presence of ADP; the short coiled-coil tail sometimes unwound, after which the monomerized L-head immediately rotated to the forward leaning orientation, very similar to the swinging lever-arm motion occurring in walking M5. This new view on the chemo-mechanical coupling in tension generation and lever-arm swing must be the case not only in M5 but also in all members of the myosin superfamily. This issue of chemo-mechanical coupling and chemical energy usage is described in detail elsewhere [84, 106, 107]. Because this new idea has not been able to be acquired from conventional biophysical and biochemical approaches, this HS-AFM study clearly demonstrates that direct observations of proteins in dynamic action is a powerful new approach to understanding how the proteins function.

22.8.2 Intrinsically Disordered Proteins

Until recently, it has long been believed that all functional proteins adopt a defined three-dimensional ordered structure. In other words, disordered proteins have been believed to be denatured and hence not functional. However, it has recently been recognized that a large fraction of functional proteins do not adopt an ordered structure either entirely or partly. This new class of proteins is referred to as intrinsically disordered proteins (IDPs) [108–111]. Based on a computational genomic analysis, ~30 % of eukaryotic proteins are mostly disordered, and more than 50 % of eukaryotic proteins have intrinsically disordered regions (IDRs) consisting of more than 40 consecutive amino acid residues [112]. In eukaryote, IDPs more frequently exist in nucleus rather than in cytoplasm and often play roles as regulators in transcription, translation and cellular signal transduction [113–115].

Various studies have been performed to understand how IDPs can function and interact with partner molecules [116–118]. In this context, various structural analyses of IDPs have been attempted but it has been difficult to reveal the structure because IDRs are very thin and flexible and transit among many conformers. For example, X-ray crystallography cannot be used because IDRs hamper crystallization. Electron microscopy also cannot be used because IDRs are too thin to be visualized. Therefore, rather indirect methods have often been used and combined to localize and characterize IDRs, such as circular dichroism, proteolysis, small angle X-ray scattering and others. Of course, NMR spectroscopy has been best instrumental in specifying IDRs within an IDP [119–121]. However, NMR spectroscopy can only determine the local structure of IDPs with molecular weights of less than 50 kDa (usually less than 20 kDa). In addition, NMR suffers from the inherent ensemble averaging, and hence, the individual structures populated in the conformational ensemble cannot be determined from NMR data.

As a model IDP, *Drosophila melanogaster* facilitates chromatin transcription (FACT) protein (dFACT) expressed in *E. coli* was used to examine whether HS-AFM would be able to visualize the thin and flexible structure of IDRs [122]. dFACT is a heterodimer consisting of SSRP1 and SPT16 subunits, each of which is predicted to have a long IDR [123–125]. HS-AFM successfully visualized two tail-like structures with different lengths, protruding from the main body of dFACT. Using dFACT mutants, in which either predicted IDRs were deleted, the tail-like structures were verified to be IDRs. It was also confirmed that the longer and shorter IDRs belong to SSRP1 and SPT16, respectively. Note that in the visualization of IDRs the sample cannot be dried because IDRs become too thin to be visualized, meaning that conventional AFM cannot be used for the identification of IDRs because IDRs move fast in solution.

Both two IDRs of dFACT exhibited undulation motion. To characterize the IDRs, the end-to-end distances R of the IDRs were measured, from the averages of which their microscopic persistence lengths L_p were estimated. Interestingly, both IDRs gave a similar value of $L_p \sim 1.1$ nm, in spite of the different amino acid sequences. This value is significantly longer than those of typical ordered proteins, 0.36–0.5 nm [126, 127] and even that of the putative random coil region of titin (i.e., the PEVK region), 0.4–2.5 nm (0.93 nm on average) [128]. Thus, the long L_p is a fingerprint of IDRs [122]. A recent HS-AFM study on other IDPs gave a similar value of L_p [129]. This quantitatively similar property of IDRs can be used to estimate the number of amino acids N_{aa} contained in an IDR, because the following relationship exists:

$$\langle R^2 \rangle = 4L_p \times N_{aa} \times \langle d_{aa} \rangle, \tag{22.10}$$

where $\langle d_{aa} \rangle$ represents the average distance between two adjacent amino acids.

IDRs are frequently subjected to post-translational modifications, including phosphorylation, acetylation, methylation, sumoylation and ubiquitination [130–132]. The IDR of the SSRP1 subunit of dFACT can be phosphorylated. By the phosphorylation, the binding of nucleosomal DNA to dFACT is inhibited [133]. To elucidate this

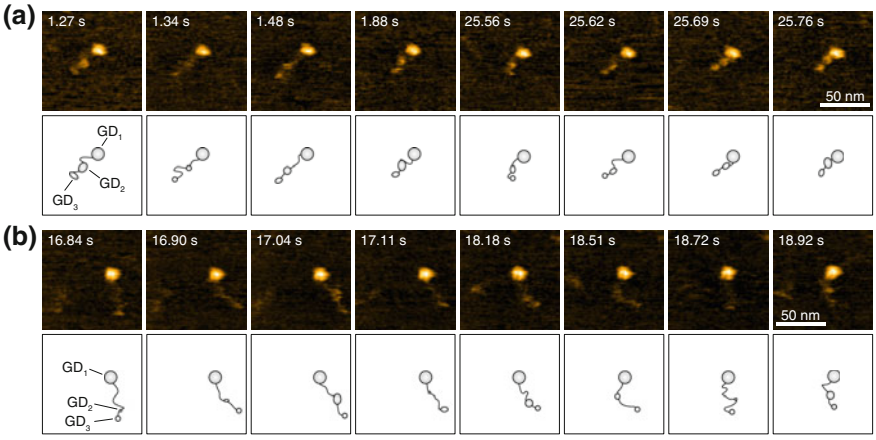

Fig. 22.17 Clips of successive HS-AFM images showing an IDP, dFACT. **a** Phosphorylated form (dFACT-WT) and **b** nonphosphorylated form (dFACT-10SA). The images were taken at 67.08 ms/frame. The time stamp of each image is shown in the *upper left*. Scan area, 100 × 100 mm^2 with 80 × 80 pixels; Z-scale, 4.0 nm. The observed molecular features of dFACT are schematized under the AFM images, which were drawn freehand by tracing the AFM images by visual estimation. *Gray-colored ellipses* and *black thick solid lines* represent the globular domains and IDRs, respectively

inhibitory mechanism, the HS-AFM images of fully phosphorylated form (dFACT-WT) were compared to those of nonphosphorylated form (dFACT-10SA) expressed in Sf9 insect cells [134]. The IDR of SPT16 subunit was deleted from both constructs. As shown in Fig. 22.17, the both constructs exhibited a large globular domain (GD_1), from which a flexible tail-like IDR was protruded, as previously observed [122]. In addition, small globular domains were observed on the middle of the IDR and at the distal end of the IDR. These were termed GD_2 and GD_3, respectively. GD_3 exhibited similar characteristics between the two constructs, whereas GD_2 was temporally appearing and disappearing, with different lifetimes between the two constructs. The GD_2 of dFACT-WT exhibited a longer lifetime in the globular state and larger height than those of dFACT-10SA. Moreover, the mean length of the IDR between GD_1 and GD_2 was shorter by ∼2 nm in dFACT-WT than in dFACT-10SA. Because the position of GD_2 is consistent with the position of the HMG domain that is known to interact with nucleosomal DNA, these observations suggest that the phosphorylated IDR between GD_1 and GD_2 tends to interact with the HMG domain and that this interaction prohibits the HMG domain from interacting with nucleosomal DNA [134]. As has been demonstrated in these studies as well as in other studies on different IDPs (the Archaeal Hef protein consisting of the helicase and nuclease domains [135] and the bacterial flagellar hook-length control protein FliK [136]), HS-AFM is a powerful tool to identify and characterize IDPs [137].

22.9 Future Prospects

Thus far, the innovative power of HS-AFM has been demonstrated in a limited number of proteins. There is, however, no doubt that HS-AFM will be more extensively used in the near future to understand not only the functional mechanism of a diverse array of proteins but also various non-biological dynamic phenomena occurring in liquids at the nanometer scale. To finalize this chapter, we briefly describe the future prospects for further progress of HS-AFM techniques.

The feedback bandwidth of HS-AFM is currently ~100 kHz, which corresponds to the highest possible imaging rate of ~15 fps when protein molecules are targets. This rate limit arises mainly from the limited miniaturization of cantilevers and partly from other devices including the OBD detector. Here we examine whether or not we can increase the feedback bandwidth up to 1 MHz and hence the imaging rate to ~150 fps. To achieve this rate in the tapping mode, the cantilevers made of Si_3N_4 have to have a resonant frequency of ~10 MHz in water whilst the spring constant is kept similar to that of current small cantilevers (~0.2 N/m). Supposing that the damping effect of aqueous solutions on the resonant frequency is similar between the current and expected cantilevers, this resonant frequency in water corresponds to ~35 MHz in air. Under the conditions of $k_c = 0.2$ N/m and width $w = 300$ nm (approximately corresponding to a minimized spot size of focused laser beam), the thickness-to-length ratio d/L is estimated to be ~0.021 from (22.5). From this ratio and (22.4), the resonant frequency in air, f_c, is given by $f_c = 32.3/L$. Therefore, to achieve $f_c = 35$ MHz, L and d should be 0.92 μm and 19 nm, respectively. To focus a laser beam onto such a small cantilever, we have to use an objective lens with a high numerical aperture >0.7 but the incident laser beam with a large incident angle >44° would be interrupted by the supporting base of the cantilever. Considering this interruption effect, the minimum length should be $L \sim 2$ μm, which corresponds to $d \sim 42$ nm and the highest possible $f_c \sim 16$ MHz in air. This frequency is ~4.6 times higher than that of our currently smallest cantilevers. This high resonant frequency may allow us to achieve $R_{max} \sim 70$ fps. To achieve this imaging rate, the X-scanner has to be scanned at ~7 kHz, while the Z-scanner has to be scanned at ~460 kHz. These numbers appear to be still within a feasible range, considering the scan ranges required for imaging protein molecules (~100 nm for the XY-directions and ~50 nm for the Z-direction) and available piezoactuators. To go beyond $R_{max} = 70$ fps, we have to discard the tapping mode and instead use the torsional mode [138] because the resonant frequency of torsional cantilever vibrations is much higher than that of flexural vibrations. Then, the factors that limit R_{max} would be piezoactuators and the mass of the sample stage.

In the HS-AFM system described above, the sample stage is scanned in three directions, while the cantilever chip is stationary. This type of system simplifies the AFM head structure because the focused spot position of the laser beam for OBD detection can be stationary. However, this configuration does not allow us to use a large sample stage. Moreover, it does not allow us to combine HS-AFM with fluorescence microscopy or various optical techniques, thus limiting the expandability

of HS-AFM. Recently, we developed the tip-scan type of HS-AFM system, in which the focused laser beam of the OBD detector precisely tracks the XY-motion of the cantilever [139]. This tracking is carried out by tilting, around orthogonal two axes, a dichroic mirror that reflects the laser beam. By placing this tip-scan HS-AFM system on an inverted type of fluorescence microscope, HS-AFM and total internal reflection fluorescence microscopy (TIRFM) images can be simultaneously captured, as demonstrated [139]. This combined tip-scan mode HS-AFM allows us to introduce various optical techniques. For example, optical tweezers can be installed in the combined system. This system will allow us to visualize a single biological molecule under external force. This visualization will provide a new opportunity to study the effect of applied force on the action of the molecule as well as detailed unfolding and refolding processes of the molecule. It is also possible to introduce tip-enhanced fluorescence microscopy that is based on the highly enhanced electric field formed in the close vicinity of a laser-illuminated metal or silicon tip [140, 141]. Tip-enhanced fluorescence microscopy has resolution <10 nm [142]. Therefore, this installation will materialize super-resolution/high-speed fluorescence microscopy combined with HS-AFM. As such, further progress will be expected to extend both speed performance and functionality of HS-AFM.

References

1. F.J. Giessibl, S. Hembacher, H. Bielefeldt, J. Mannhart, Science **289**, 422 (2000)
2. Y. Sugimoto, P. Pou, M. Abe, P. Jelinek, R. Perez, S. Morita, O. Custance, Nature **446**, 64 (2007)
3. D. Rugar, R. Budakian, H.J. Mamin, B.W. Chui, Nature **430**, 329 (2004)
4. F.J. Giessibl, Appl. Phys. Lett. **73**, 3956 (1998)
5. B. Cappela, G. Dietler, Surf. Sci. Rep. **34**, 1 (1999)
6. J.P. Cleveland, B. Anczykowski, A.E. Schmid, V.B. Elings, Appl. Phys. Lett. **72**, 2613 (1998)
7. R.A. Oliver, Rep. Prog. Phys. **71**, 076501 (2008)
8. U. Hartmann, Annu. Rev. Mater. Sci. **29**, 53 (1999)
9. B. Gotsmann, M.A. Lantz, Nat. Mater. **12**, 59 (2012)
10. U. Rabe, W. Arnold, Appl. Phys. Lett. **64**, 1493 (1994)
11. O. Kolosov, K. Yamanaka, Jpn. J. Appl. Phys. **32**, L1095 (1993)
12. L. Zhang, Y. Ju, A. Hosoi, A. Fujimoto, Rev. Sci. Instrum. **81**, 123708 (2010)
13. M. Jaschke, H.-J. Butt, Langmuir **11**, 1061 (1995)
14. R.D. Piner, J. Zhu, F. Xu, S. Hong, C.A. Mirkin, Science **283**, 661 (1999)
15. T. Ando, N. Kodera, E. Takai, D. Maruyama, K. Saito, A. Toda, Proc. Natl. Acad. Sci. U.S.A. **98**, 12468 (2001)
16. T. Ando, T. Uchihashi, T. Fukuma, Prog. Surf. Sci. **83**, 337 (2008)
17. M. Shibata, H. Yamashita, T. Uchihashi, H. Kandori, T. Ando, Nat. Nanotechnol. **5**, 208 (2010)
18. N. Kodera, D. Yamamoto, R. Ishikawa, T. Ando, Nature **468**, 72 (2010)
19. T. Uchihashi, R. Iino, T. Ando, H. Noji, Science **333**, 755 (2011)
20. K. Igarashi, T. Uchihashi, A. Koivula, M. Wada, S. Kimura, T. Okamoto, M. Penttila, T. Ando, M. Samejima, Science **333**, 1279 (2011)
21. R.C. Barrett, C.F. Quate, J. Vac. Sci. Technol. B **9**, 302 (1991)
22. S.C. Minne, J.D. Adames, G. Yaralioglu, S.R. Manalis, A. Atalar, C.F. Quate, Appl. Phys. Lett. **73**, 1742 (1998)

23. T. Ando, T. Uchihashi, N. Kodera, D. Yamamoto, A. Miyagi, M. Taniguchi, H. Yamashita, Pflügers Archiv-Eur. J. Physiol. **456**, 211 (2008)
24. T. Itani, J.J. Santillan, Appl. Phys. Express **3**, 061601 (2010)
25. T. Uchihashi, N. Kodera, T. Ando, Nat. Protoc. **7**, 1193 (2012)
26. N. Kodera, M. Sakashita, T. Ando, Rev. Sci. Instrum. **77**, 083704 (2006)
27. D. Sarid, *Scanning Force Microscopy: With Applications to Electric, Magnetic, and Atomic Forces* (Oxford University Press, New York, 1994)
28. G.E. Fantner, G. Schitter, J.H. Kindt, T. Ivanov, K. Ivanova, R. Patel, N. Holten-Andersen, J. Adams, P.J. Thurner, I.W. Rangelow, P.K. Hansma, Ultramicroscopy **106**, 881 (2006)
29. J.A. Harley, T.W. Kenny, Appl. Phys. Lett. **75**, 289 (1999)
30. S. Hosaka, K. Etoh, A. Kikukawa, H. Koyanagi, J. Vac. Sci. Technol. B **18**, 94 (2000)
31. M. Kitazawa, K. Shiotani, A. Toda, Jpn. J. Appl. Phys. **42**, 4844 (2003)
32. M.B. Viani, T.E. Schaffer, A. Chand, M. Rief, H.E. Gaub, P.K. Hansma, J. Appl. Phys. **86**, 2258 (1999)
33. D.A. Walters, J.P. Cleveland, N.H. Thomson, P.K. Hansma, M.A. Wendman, G. Gurley, V. Elings, Rev. Sci. Instrum. **67**, 3583 (1996)
34. T. Fujii, M. Suzuki, M. Miyashita, M. Yamaguchi, T. Onuki, H. Nakamura, T. Matsubara, H. Yamada, K. Nakayama, J. Vac. Sci. Technol. B **9**, 666 (1991)
35. B. Hubner, H.W.P. Koops, H. Pagnia, N. Sotnik, J. Urban, M. Weber, Ultramicroscopy **42**, 1519 (1992)
36. H.Y. Ximen, P.E. Russell, Ultramicroscopy **42**, 1526 (1992)
37. J.H. Kindt, G.E. Fantner, J.B. Thompson, P.K. Hansma, Nanotechnology **15**, 1131 (2004)
38. T.E. Schäffer, J.P. Cleveland, F. Ohnesorge, D.A. Walters, P.K. Hansma, J. Appl. Phys. **80**, 3622 (1996)
39. T. Fukuma, M. Kimura, K. Kobayashi, K. Matsushige, H. Yamada, Rev. Sci. Instrum. **76**, 126110 (2005)
40. T. Uchihashi, N. Kodera, T. Ando, in *Atomic Force Microscopy in Nanobiology*, ed. by K. Takeyasu. Development of High-Speed AFM and Its Biological Applications (Pan Stanford Publishing, Singapore, 2014), p. 143
41. M. Shibata, T. Uchihashi, H. Yamashita, H. Kandori, T. Ando, Angew. Chem. Int. Ed. Engl. **50**, 4410 (2011)
42. H. Yamashita, K. Inoue, M. Shibata, T. Uchihashi, J. Sasaki, H. Kandori, T. Ando, J. Struct. Biol. **184**, 2 (2013)
43. K. Shinohara, N. Kodera, T. Oohashi, J. Polym. Sci., Part A: Polym. Chem. **48**, 4103 (2010)
44. T. Ando, N. Kodera, Y. Naito, T. Kinoshita, K. Furuta, Y.Y. Toyoshima, Chem. Phys. Chem. **4**, 1196 (2003)
45. T. Ando, N. Kodera, T. Uchihashi, A. Miyagi, R. Nakakita, H. Yamashita, K. Matada, J. Surf. Sci. Nanotechnol. **3**, 384 (2005)
46. B.W. Hoogenboom, P.L.T.M. Frederix, J.L. Yang, S. Martin, Y. Pellmont, M. Steinacher, S. Zach, E. Langenbach, H.J. Heimbeck, Appl. Phys. Lett. **86**, 074101 (2005)
47. B.W. Hoogenboom, H.J. Hug, Y. Pellmont, S. Martin, P.L.T.M. Frederix, D. Fotiadis, A. Engel, Appl. Phys. Lett. **88**, 193109 (2006)
48. T. Fukuma, K. Onishi, N. Kobayashi, A. Matsuki, H. Asakawa, Nanotechnology **23**, 135706 (2012)
49. H. Asakawa, Y. Katagiri, T. Fukuma, Jpn. J. Appl. Phys. **52**, 110109 (2013)
50. A. Colom, I. Casuso, F. Rico, S. Scheuring, Nat. Commun. **4**, 2155 (2013)
51. J. Kokavecz, Z. Toth, Z.L. Horvath, P. Heszler, A. Mechler, Nanotechnology **17**, S173 (2006)
52. M.J. Rost, L. Crama, P. Schakel, E. van Tol, G.B.E.M. van Velzen-Williams, C.F. Overgauw, H. ter Horst, H. Dekker, B. Okhuijsen, M. Seynen, A. Vijftigschild, P. Han, A.J. Katan, K. Schoots, R. Schumm, W. van Loo, T.H. Oosterkamp, J.W.M. Frenken, Rev. Sci. Instrum. **76**, 053710 (2005)
53. L.M. Picco, L. Bozec, A. Ulcinas, D.J. Engledew, M. Antognozzi, M.A. Horton, M.J. Miles, Nanotechnology **18**, 044030 (2007)
54. Y.K. Yong, S.O.R. Moheimani, B.J. Kenton, K.K. Leang, Rev. Sci. Instrum. **83**, 121101 (2012)

55. C. Braunsmann, T.E. Schäffer, Nanotechnology **21**, 225705 (2010)
56. H. Watanabe, T. Uchihashi, T. Kobashi, M. Shibata, J. Nishiyama, R. Yasuda, T. Ando, Rev. Sci. Instrum. **84**, 053702 (2013)
57. G. Schitter, F. Allgower, A. Stemmer, Nanotechnology **15**, 108 (2004)
58. G. Schitter, P. Menold, H.F. Knapp, F. Allgower, A. Stemmer, Rev. Sci. Instrum. **72**, 3320 (2001)
59. Q. Zou, K.K. Leang, E. Sadoun, M.J. Reed, S. Devasia, Asian J. Control **6**, 164 (2004)
60. A. Stemmer, G. Schitter, J.M. Rieber, F. Allgower, Eur. J. Control **11**, 384 (2005)
61. Y. Wu, Q.Z. Zou, IEEE Trans. Control Syst. Technol. **15**, 936 (2007)
62. S. Necipoglu, S.A. Cebeci, Y.E. Has, L. Guvenc, C. Basdogan, IEEE Trans. Nanotechnol. **10**, 1074 (2011)
63. J. Otero, H. Guerrero, L. Gonzalez, M. Puig-Vidal, Sensors **12**, 686 (2012)
64. M.W. Fairbairn, S.O.R. Moheimani, IEEE Control Syst. **33**, 46 (2013)
65. B. Anczykowski, J.P. Cleveland, D. Kruger, V. Elings, H. Fuchs, Appl. Phys. A: Mater. Sci. Process. **66**, S885 (1998)
66. J. Tamayo, A.D.L. Humphris, A.M. Malloy, M.J. Miles, Ultramicroscopy **86**, 167 (2001)
67. J. Tamayo, A.D.L. Humphris, R.J. Owen, M.J. Miles, Biophys. J. **81**, 526 (2001)
68. T. Sulchek, R. Hsieh, J.D. Adams, G.G. Yaralioglu, S.C. Minne, C.F. Quate, J.P. Cleveland, A. Atalar, D.M. Adderton, Appl. Phys. Lett. **76**, 1473 (2000)
69. M. Antognozzi, M.D. Szczelkun, A.D.L. Humphris, M.J. Miles, Appl. Phys. Lett. **82**, 2761 (2003)
70. N. Kodera, H. Yamashita, T. Ando, Rev. Sci. Instrum. **76**, 053708 (2005)
71. I.A. Mahmood, S.O.R. Moheimani, B. Bhikkaji, IEEE Trans. Nanotechnol. **10**, 203 (2011)
72. T.R. Meyer, D. Ziegler, C. Brune, A. Chen, R. Farnham, N. Huynh, J.M. Chang, A.L. Bertozzi, P.D. Ashby, Ultramicroscopy **137**, 48 (2014)
73. Y.K. Yong, S.O.R. Moheimani, I.R. Petersen, Nanotechnology **21**, 365503 (2010)
74. A. Bazaei, Y.K. Yong, S.O.R. Moheimani, Rev. Sci. Instrum. **83**, 063701 (2012)
75. T. Tuma, J. Lygeros, V. Kartik, A. Sebastian, A. Pantazi, Nanotechnology **23**, 185501 (2012)
76. Y. Li, J. Bechhoefer, Rev. Sci. Instrum. **78**, 013702 (2007)
77. G. Schitter, A. Stemmer, IEEE Trans. Control Syst. Technol. **12**, 449–454 (2004)
78. K.K. Leang, A.J. Fleming, Asian J. Control **11**, 144 (2009)
79. P. Ge, M. Jouaneh, IEEE Trans. Control Syst. Technol. **4**, 209 (1996)
80. B. Mokaberi, A.A.G. Requicha, IEEE Trans. Autom. Sci. Eng. **5**, 197 (2008)
81. T.R. Rodriguez, R. Garcia, Appl. Phys. Lett. **82**, 4821 (2003)
82. J. Schiener, S. Witt, M. Stark, R. Guckenberger, Rev. Sci. Instrum. **75**, 2564 (2004)
83. T. Ando, Nanotechnology **23**, 062001 (2012)
84. T. Ando, T. Uchihashi, S. Scheuring, Chem. Rev. **114**, 3120 (2014)
85. T. Ando, T. Uchihashi, N. Kodera, Annu. Rev. Biophys. **42**, 393 (2013)
86. R.E. Cheney, M.K. O'Shea, J.E. Heuser, M.V. Coelho, J.S. Wolenski, E.M. Espreafico, P. Forscher, R.E. Larson, M.S. Mooseker, Cell **75**, 13 (1993)
87. A.D. Mehta, R.S. Rock, M. Rief, J.A. Spudich, M.S. Mooseker, R.E. Cheney, Nature **400**, 590 (1999)
88. T. Sakamoto, I. Amitani, E. Yokota, T. Ando, Biochem. Biophys. Res. Commun. **272**, 586 (2000)
89. M. Rief, R.S. Rock, A.D. Mehta, M.S. Mooseker, R.E. Cheney, J.A. Spudich, Proc. Natl. Acad. Sci. U.S.A. **97**, 9482 (2000)
90. J.N. Forkey, M.E. Quinlan, M.A. Shaw, J.E. Corrie, Y.E. Goldman, Nature **422**, 399 (2003)
91. A. Yildiz, J.N. Forkey, S.A. McKinney, T. Ha, Y.E. Goldman, P.R. Selvin, Science **300**, 2061 (2003)
92. T. Sakamoto, M.R. Webb, E. Forgacs, H.D. White, J.R. Sellers, Nature **455**, 128 (2008)
93. M.L. Walker, S.A. Burgess, J.R. Sellers, F. Wang, J.A. Hammer 3rd, J. Trinick, P.J. Knight, Nature **405**, 804 (2000)
94. S. Burgess, M. Walker, F. Wang, J.R. Sellers, H.D. White, P.J. Knight, J. Trinick, J. Cell. Biol. **159**, 983 (2002)

95. N. Volkmann, H. Liu, L. Hazelwood, E.B. Krementsova, S. Lowey, K.M. Trybus, D. Hanein, Mol. Cell **19**, 595 (2005)
96. O.A. Oke, S.A. Burgess, E. Forgacs, P.J. Knight, T. Sakamoto, J.R. Sellers, H. White, J. Trinick, Proc. Natl. Acad. Sci. U.S.A. **107**, 2509 (2010)
97. P.D. Coureux, A.L. Wells, J. Menetrey, C.M. Yengo, C.A. Morris, H.L. Sweeney, A. Houdusse, Nature **425**, 419 (2003)
98. P.D. Coureux, H.L. Sweeney, A. Houdusse, EMBO J. **23**, 4527 (2004)
99. D. Yamamoto, T. Uchihashi, N. Kodera, H. Yamashita, S. Nishikori, T. Ogura, M. Shibata, T. Ando, Methods Enzymol. **475**, 541 (2010)
100. H.E. Huxley, Science **164**, 1356 (1969)
101. J.A. Spudich, Nat. Rev. Mol. Cell Biol. **2**, 387 (2001)
102. M.A. Geeves, Nature **415**, 129 (2002)
103. C. Veigel, S. Schmitz, F. Wang, J.R. Sellers, Nat. Cell Biol. **7**, 861 (2005)
104. T.J. Purcell, H.L. Sweeney, J.A. Spudich, Proc. Natl. Acad. Sci. U.S.A. **102**, 13873 (2005)
105. E.M. De La Cruz, A.L. Wells, S.S. Rosenfeld, E.M. Ostap, H.L. Sweeney, Proc. Natl. Acad. Sci. U.S.A. **96**, 13726 (1999)
106. T. Ando, FEBS Lett. **587**, 997 (2013)
107. N. Kodera, T. Ando, Biophys. Rev. **6**, 237 (2014)
108. H.J. Dyson, P.E. Wright, Annu. Rev. Phys. Chem. **47**, 369 (1996)
109. A.K. Dunker, C.J. Brown, J.D. Lawson, L.M. Iakoucheva, Z. Obradovic, Biochemistry **41**, 6573 (2002)
110. V.N. Uversky, Protein Sci. **11**, 739 (2002)
111. P. Tompa, *Structure and Function of Intrinsically Disordered Proteins* (Chapman and Hall/CRC, New York, 2009)
112. C.J. Oldfield, Y. Cheng, M.S. Cortese, C.J. Brown, V.N. Uversky, A.K. Dunker, Biochemistry **44**, 1989 (2005)
113. M. Fuxreiter, A. Toth-Petroczy, D.A. Kraut, A.T. Matouschek, R.Y. Lim, B. Xue, L. Kurgan, V.N. Uversky, Chem. Rev. **114**, 6806 (2014)
114. U. Jakob, R. Kriwacki, V.N. Uversky, Chem. Rev. **114**, 6779 (2014)
115. V.N. Uversky, V. Dave, L.M. Iakoucheva, P. Malaney, S.J. Metallo, R.R. Pathak, A.C. Joerger, Chem. Rev. **114**, 6844 (2014)
116. V.N. Uversky, S. Longhi, in *Instrumental Analysis of Intrinsically Disordered Proteins: Assessing Structure and Conformation*, ed. by V.N. Uversky. Protein and Peptide Science (Wiley, New Jersey, 2010)
117. V.N. Uversky, A. Dunker, in *Intrinsically Disordered Protein Analysis*, vol. 1, ed. by V.N. Uversky, A. Dunker. Methods in Molecular Biology, vol. 895 (Humana Press, New York, 2012)
118. V.N. Uversky, A. Dunker, in *Intrinsically Disordered Protein Analysis*, vol. 2, ed. by V.N. Uversky, A. Dunker. Methods in Molecular Biology, vol. 896 (Humana Press, New York, 2012)
119. H.J. Dyson, P.E. Wright, Chem. Rev. **104**, 3607 (2004)
120. M.R. Jensen, R.W. Ruigrok, M. Blackledge, Curr. Opin. Struct. Biol. **23**, 426 (2013)
121. M.R. Jensen, M. Zweckstetter, J.R. Huang, M. Blackledge, Chem. Rev. **114**, 6632 (2014)
122. A. Miyagi, Y. Tsunaka, T. Uchihashi, K. Mayanagi, S. Hirose, K. Morikawa, T. Ando, Chem. Phys. Chem. **9**, 1859 (2008)
123. R. Belotserkovskaya, S. Oh, V.A. Bondarenko, G. Orphanides, V.M. Studitsky, D. Reinberg, Science **301**, 1090 (2003)
124. T. Shimojima, M. Okada, T. Nakayama, H. Ueda, K. Okawa, A. Iwamatsu, H. Handa, S. Hirose, Genes. Dev. **17**, 1605 (2003)
125. T. Formosa, Biochim. Biophys. Acta. **1819**, 247 (2013)
126. D.J. Müller, W. Baumeister, A. Engel, Proc. Natl. Acad. Sci. U.S.A. **96**, 13170 (1999)
127. H. Dietz, M. Rief, Proc. Natl. Acad. Sci. U.S.A. **101**, 16192 (2004)
128. H. Li, A.F. Oberhauser, S.D. Redick, M. Carrion-Vazquez, H.P. Erickson, J.M. Fernandez, Proc. Natl. Acad. Sci. U.S.A. **98**, 10682 (2001)

129. S. Dora, N. Kodera, J. Habchi, D. Blocquel, A. Gruet, T. Mori, M. Lotti, M. Mizuguchi, S. Longhi, T. Ando (Submitted)
130. L.M. Iakoucheva, P. Radivojac, C.J. Brown, T.R. O'Connor, J.G. Sikes, Z. Obradovic, A.K. Dunker, Nucl. Acid. Res. **32**, 1037 (2004)
131. M. Fuxreiter, Mol. Biosyst. **8**, 168 (2012)
132. D. Vuzman, Y. Levy, Mol. Biosyst. **8**, 47 (2012)
133. Y. Tsunaka, J. Toga, H. Yamaguchi, S. Tate, S. Hirose, K. Morikawa, J. Biol. Chem. **284**, 24610 (2009)
134. M. Hashimoto, N. Kodera, Y. Tsunaka, M. Oda, M. Tanimoto, T. Ando, K. Morikawa, S. Tate, Biophys. J. **104**, 2222 (2013)
135. S. Ishino, T. Yamagami, M. Kitamura, N. Kodera, T. Mori, S. Sugiyama, T. Ando, N. Goda, T. Tenno, H. Hiroaki, Y. Ishino, J. Biol. Chem. **289**, 21627 (2014)
136. N. Kodera, K. Uchida, T. Ando, S. Aizawa, J. Mol. Biol. **427**, 406 (2015)
137. T. Ando, N. Kodera, Methods Mol. Biol. **896**, 57 (2012)
138. O. Sahin, S. Magonov, C. Su, C.F. Quate, O. Solgaad, Nat. Nanotechnol. **2**, 507 (2007)
139. S. Fukuda, T. Uchihashi, R. Iino, Y. Okazaki, M. Yoshida, K. Igarashi, T. Ando, Rev. Sci. Instrum. **84**, 073706 (2013)
140. O.F.J. Martin, C. Girard, Appl. Phys. Lett. **70**, 705 (1997)
141. L. Novotny, R.X. Bian, X.S. Xie, Phys. Rev. Lett. **79**, 645 (1997)
142. Z. Ma, J.M. Gerton, L.A. Wade, S.R. Quake, Phys. Rev. Lett. **97**, 260801 (2006)

Index

© Springer International Publishing Switzerland 2015

S. Morita et al. (eds.), *Noncontact Atomic Force Microscopy*,
NanoScience and Technology, DOI 10.1007/978-3-319-15588-3

S